SUMMER PROGRAM IN

GEOPHYSICAL FLUID DYNAMICS

WALSH COTTAGE
WOODS HOLE OCEANOGRAPHIC INSTITUTION
JUNE 20-AUGUST 26, 2011

Norman Lebovitz and Phil Morrison, codirectors

Preface

The theme for the Program in Geophysical Fluid Dynamics for the summer of 2011 was *Shear Turbulence: onset and structure.* Ten days of principal lectures by Fabian Waleffe and Rich Kerswell began the summer, and a large number of seminars on this and a variety of other topics then continued through the eighth week. These lectures are presented in these Proceedings and form (we believe) the most complete, connected account of this subject)

Eleven fellows from around the globe helped to record the principal lectures, and each carried out a project of his/her own, presented in seminar during the tenth and final week. All these lectures and projects are also presented in this Proceedings volume.

The further seminars presented throughout the summer by visitors and (in some cases) by GFD faculty are also listed here. The popular Sears Lecture was given by L. Mahadevan. The title was *On growth and form: geometry, physics and biology.* It was indeed popular, drawing a large and enthusiastic audience.

There exists a phenomenon called "fun" (sp?). This was embodied in various social gatherings. To name just two (there were others): the 4th of July barbecue, organized by the fellows; and the traditional gathering, at the end of the final week, at the home of George and Kim Veronis on Crooked Pond.

In addition there was softball. The GFD team had a winning season, the first in quite a while!

The coorganizers want to thank Jeanne Fleming and Janet Fields, our most visible links to WHOI, for their administrative expertise and unstinting help with the needs of the program, the visitors, the fellows and (not least) the coorganizers.

The GFD Program acknowledges continuing support from the US National Science Foundation through grant OCE-0824636 and the Office of Naval Research through grant N00014-09-1-0844. The program also receives support from the Woods Hole Oceanographic Institution. Fabian Waleffe's work was partially supported by the US National Science Foundation under Grant No. 0807349. Any opinions, findings, and conclusions or recommendations expressed in this material are those of the author(s) and do not necessarily reflect the views of the National Science Foundation.

2011 Lecturers

Fabian Waleffe

Richard Kerswell

2011 GFD Participants

First row, seated (left to right):

David Goluskin, Chao Ma, Zhan Wang, Giulio Mariotti, Fabian Waleffe, Martin Hoecker-Martinez, Matthew Alford

Second row (left to right):

Jack Whitehead (seated), Charles Doering, Evelyn Lunasin, Diego Del-Castillo-Negrete, James Anderson, Edward Johnson, Joseph Keller, George Veronis, Philip Morrison, Willem Malkus, Unknown, Lindsey Corson, Adele Morrison, Richard Kerswell, George Hagstrom, Keiji Kimura, Norman Lebovitz (standing)

Third row (left to right):

Ed Spiegel (standing), Karl Helfrich, Unknown, Stefan Llewellyn-Smith, Philip Hall, Greg Chini, Jan Feys, Andrew Crosby, John Gibson, John Platt, Friedrich Busse, Tobias Schneider, Sergei Chernyshenko, Samuel Potter, Matthew Chantry, Robert Deegan

Not pictured: Michael Allshouse, Alexander Balk, Dwight Barkley, John Bowman, John Burke, Colm-cille Caulfield, Predrag Cvitanovic, Paul Dellar, Bruno Eckhardt, Francesco Fedele, Boris Galperin, Michael Graham, Philip Hall, Daniel Henningson, Tomoaki Itano, Keith Julien, Genta Kawahara, Patrice LeGal, L. Mahadevan, Thomas Mullin, Joseph Parker, Leslie Smith, Andrew Stewart, Jean-Luc Thiffeault, Yue-Kin Tsang, Laurette Tuckerman, Lennaert van Veen, Divakar Viswanath

Contents

I The following six lectures are by Fabian Waleffe University of Wisconsin **13**

1 Shear Turbulence: Onset and Structure
notes by Martín Hoecker-Martínez and Chao Ma
revised and *massively* expanded by FW
WHOI GFD Lecture 1, June 20, 2011 **15**

1.1 Introduction . . . 15
1.1.1 Navier-Stokes equations . . . 16
1.1.2 Laminar pipe flow . . . 17
1.1.3 Shear flows . . . 19
1.1.4 Transition threshold . . . 20
1.2 Linear Theory: exponential and algebraic growth . . . 23
1.2.1 Exponential growth . . . 23
1.2.2 Algebraic growth, redistribution of base flow . . . 23
1.2.3 Transient growth, non-normal and Jordan matrices . . . 26
1.3 Transition threshold: mechanisms and scalings . . . 28
1.3.1 Transient growth + nonlinear feedback and $\epsilon \sim R^{-3}$ . . . 28
1.3.2 Benney-Gustavsson mechanism and $\epsilon \sim R^{-2}$ . . . 28
1.3.3 Waleffe-Kim-Hamilton mechanism and $\epsilon \sim R^{-3}$ . . . 30
1.3.4 Chapman's viscous correction of the WKH mechanism . . . 31
1.3.5 Nonlinear saturation of linear transient growth and '$\epsilon = \infty$' . . . 33
1.3.6 SSP and $\epsilon \sim R^{-3/2}$, R^{-2} . . . 34
1.3.7 Derived SSP and $\epsilon \sim R^{-1}$ . . . 36
1.3.8 Summary of transition models and threshold scalings . . . 38
1.4 Transition threshold: experiments . . . 39
1.4.1 Theodorsen's horseshoes . . . 42
1.4.2 An argument for $R^{-1.4}$? . . . 45

2 Overview of turbulent shear flows
notes by Giulio Mariotti and John Platt
revised by FW
WHOI GFD Lecture 2, June 21, 2011 **51**

2.1 Reynolds decomposition . . . 51
2.2 Laminar and Inertial Scalings of the Drag τ_w . . . 53

2.3 Energy Dissipation Rate $\mathcal{E} = \tau_w U/h$ 54
2.4 Kolmogorov spectrum and Energy cascade 56
2.5 *Turbulent* Kinetic Energy 59
2.6 Upper bound on drag and dissipation 61
2.7 Mean flow phenomenology 62

3 Stability of Shear Flow
notes by Zhan Wang and Sam Potter
Revised by FW
WHOI GFD Lecture 3, 6/22/2011 **71**
3.1 Nonlinear stability 71
3.2 Linear stability 73
3.3 Energy equation 75

4 Stability of Shear Flow: part 2
notes by Matthew Chantry and Lindsey Ritchie
Revised by FW
WHOI GFD Lecture 4, 6/23/2011 **79**
4.1 Necessary conditions for linear instability 79
4.1.1 Linear stability of Couette, Poiseuille and Kolmogorov 82
4.1.2 Inviscid results 83
4.2 Rayleigh's piecewise linear models 84
4.3 Instability from viscosity and no-slip 87
4.4 Failures of linear theories 88
4.5 3D, nonlinear 'instability' 89

5 Feedback on vertical velocity. Rotation, convection, self-sustaining process.
Notes by Andrew Crosby, Keiji Kimura, Adele Morrison
Revised by FW
WHOI GFD Lecture 5, 24 June 2011 **93**
5.1 Redistribution of streamwise velocity 93
5.2 Rotation induced shear instability 95
5.3 Thermal convection and the Lorenz model 97
5.4 SSP Model 100

6 Exact Coherent States
Notes by Chao Ma and Samuel Potter
Revised by FW
WHOI GFD Lecture 6, June 27, 2011 **109**
6.1 Shear enhanced dissipation 109
6.2 $R^{-1/3}$ in lower branch exact coherent states 112
6.3 SSP model with critical layers 112
6.4 SSP and Exact Coherent States 115
6.4.1 Bifurcation from streaky flow 115
6.4.2 Homotopy of exact coherent states 120
6.4.3 'Optimum' channel Traveling Wave 121
6.5 Turbulence: onset and structure in state space 122

6.5.1 Conclusion 126

II The following four lectures are by Richard Kerswell University of Bristol 129

7 Transition Scenarios: Normality vs Non-Normality 131
7.1 Transition scenarios 131
7.1.1 Supercritical scenario 131
7.1.2 Subcritical scenarios 132
7.1.3 Normality vs Non-normality 134
7.1.4 Transient growth 136
7.2 Bifurcation Analysis 136
7.2.1 Energy stability 137
7.2.2 Linear stability 138

8 Edge Tracking – Walking the Tightrope 143
8.1 Approach 143
8.2 First Calculations 146
8.3 Developments 147
8.3.1 Varying Re 147
8.3.2 Geometry and use of Invariant Subspaces 150
8.3.3 Larger Geometries 151

9 Triggering Transition: Towards Minimal Seeds 157
9.1 Introduction 157
9.2 Linear transient energy growth (non-modal analysis) 158
9.2.1 Matrix-based method 158
9.2.2 Matrix-free method – Variational method 159
9.3 Non-linear optimization 162
9.4 Results 163
9.4.1 Pipe flow 164
9.4.2 PCF 166

10 Turbulence: Transient or Sustained? 171

III The Fellows' Projects 185

1 Constraints on low order models: The cost of simplicity
Martin Hoecker-Martinez: Advisor, Phil Morrison
Oregon State University 187
1.1 Introduction 187
1.1.1 Equations of Motion 187

1.1.2 Flow parameters . . . 189
1.1.3 Truncation . . . 189
1.2 Examination of Low Order Models . . . 191
1.2.1 Detailed Liouville . . . 191
1.2.2 Hamiltonian . . . 196
1.3 Conclusion . . . 198

2 On One-Fluid MHD Models with Electron Inertia
Keiji Kimura
Kyoto University **201**
2.1 Introduction . . . 201
2.2 Limitation and Energy Conservation of Inertial MHD Model . . . 202
2.3 Classification of Inertial MHD Model in terms of Energy Conservation . . . 204
2.4 Equilibrium States with No Flow – Grad-Shafranov Equation . . . 207
2.4.1 Modified Grad-Shafranov Equation in a "Straight Torus" with Constant Density . . . 207
2.4.2 Modified Grad-Shafranov Equation in a "Straight Torus" . . . 209
2.4.3 Modified Grad-Shafranov Equation in a Torus with Constant Density 211
2.4.4 Summary of Modified Grad-Shafranov equation in IMHD model . . . 213
2.5 Incompressible Equilibrium States with Flow . . . 214
2.5.1 The Situation $\mathbf{S}V \propto \mathbf{S}j$ . . . 214
2.5.2 Beltrami – "Jeltrami" Flow . . . 215
2.6 Conclusions and Discussions . . . 215

3 Traversing the edge: a study of turbulent decay
Matthew Chantry
University of Bristol **219**
3.1 Introduction . . . 219
3.2 Methods . . . 221
3.3 Statistical analysis . . . 222
3.4 Edge geometry . . . 225
3.5 Conclusion . . . 236
3.6 Acknowledgments . . . 240

4 A low dimensional model for shear turbulence in Plane Poiseuille Flow: an example to understand the edge
Giulio Mariotti
Boston University **243**
4.1 Introduction . . . 243
4.2 Model description . . . 244
4.3 Analysis of the system . . . 247
4.4 Bifurcation analysis . . . 247
4.4.1 Bifurcation at R_t . . . 248
4.4.2 Description of the periodic orbit . . . 248

4.5 Structure of the edge . . . 249
4.5.1 $R > R_t$ . . . 249
4.5.2 $R < R_t$ . . . 251
4.6 Discussion . . . 252
4.7 Conclusion . . . 253
4.8 Acknowledgment . . . 254

5 Upstream basin circulation of rotating, hydraulically controlled flows
Adele Morrison
Australian National University **267**
5.1 Introduction . . . 267
5.1.1 Motivation . . . 267
5.1.2 Overview . . . 268
5.1.3 Potential vorticity balance of the upstream basin circulation . . . 269
5.1.4 Review of previous studies of upstream basin flows . . . 271
5.2 Laboratory experiments . . . 273
5.2.1 Apparatus and procedure . . . 273
5.2.2 Qualitative description of the flows . . . 274
5.3 Numerical simulations . . . 276
5.3.1 Methods . . . 276
5.3.2 Simulations of the experiments . . . 277
5.3.3 Potential vorticity balance . . . 279
5.4 Conclusions and further work . . . 282
5.5 Acknowledgements . . . 283

6 Islands in locally-forced basin circulations
Sam Potter
Princeton University **287**
6.1 Abstract . . . 287
6.2 Introduction . . . 287
6.2.1 Simple gyre circulations . . . 287
6.2.2 Gyre circulation with islands . . . 289
6.3 This report . . . 290
6.3.1 β-plume circulation . . . 291
6.4 The laboratory . . . 291
6.5 Numerics . . . 293
6.5.1 Vertically-walled island . . . 293
6.5.2 Island with topography . . . 294
6.5.3 Increasing non-linearity . . . 295
6.6 Conclusions . . . 295
6.6.1 Future Work . . . 296

7 Stability analysis of two-layer immiscible viscous fluids in an inclined closed tube

Zhan Wang
University of Wisconsin **307**
7.1 Introduction . . . 307
7.2 Formulation . . . 309
7.2.1 Governing equation . . . 309
7.2.2 Linearization . . . 311
7.3 Linear stability analysis . . . 313
7.3.1 Stokes flow . . . 313
7.3.2 General case . . . 314
7.4 Weakly nonlinear model for long wave perturbation . . . 315
7.5 Conclusion . . . 318
7.6 Acknowledgements . . . 318
7.7 Appendix A. derivation of base shear flow . . . 319
7.8 Appendix B. boundary conditions on the interface . . . 320
7.9 Appendix C. numerical method . . . 321

8 Elliptic vortex patches: coasts and chaos
Andrew Crosby
Cambridge University **327**
8.1 Introduction . . . 327
8.2 Problem description . . . 328
8.2.1 Elliptic moment model . . . 329
8.2.2 Representing an ellipse . . . 330
8.2.3 Hamiltonian representation . . . 330
8.3 Motion along a coast . . . 332
8.3.1 Comparison with contour dynamics code . . . 334
8.3.2 Background tide . . . 336
8.4 Motion around a corner . . . 339
8.4.1 Corner trapping by an external flow . . . 345
8.5 Application to more complicated geometries . . . 346
8.5.1 Flow around an island . . . 349
8.6 Motion around a pair of islands . . . 350
8.7 Conclusion . . . 353
8.8 Future directions . . . 353
8.9 Acknowledgements . . . 354

9 On Brownian Motion in a Fluid with a Plane Boundary
Chao Ma
University of Colorado **357**
9.1 Introduction . . . 357
9.2 Behavior of Brownian particles in different time regimes . . . 359
9.3 Brownian Motion in whole space $\mathbb{R}^3$ . . . 360
9.4 Brownian Motion in the Half Space $\mathbb{R}^+ \times \mathbb{R}^2$ . . . 362

10 Localized solutions for Plane Couette Flow: a continuation study **371**
John Platt
Harvard University
10.1 Introduction . . . 371
10.2 Review of the first localized solution . . . 373
10.3 Continuation of second solution . . . 375
10.3.1 Isolas . . . 376
10.3.2 Searching for snaking . . . 379
10.3.3 Bifurcation behavior summary . . . 380
10.4 Symmetry breaking during localization . . . 381
10.5 Discussion . . . 384

11 Maximizing the heat flux in steady unicellular porous media convection **389**
Lindsey T. Corson
St. Andrews University
11.1 Introduction . . . 389
11.2 Problem formulation . . . 390
11.3 Numerical simulations . . . 392
11.3.1 Solution structure . . . 396
11.4 Asymptotic reduction . . . 399
11.4.1 Core . . . 402
11.4.2 Momentum boundary layer . . . 404
11.4.3 Thermal boundary layer . . . 405
11.5 Time-dependent numerical simulations . . . 405
11.6 Conclusion . . . 409

IV Lectures and Visitors **413**

1 Lecture Schedule **415**

2 Visitors **425**

Part I

The following six lectures are by Fabian Waleffe University of Wisconsin

Lecture 1

Shear Turbulence: Onset and Structure

notes by Martín Hoecker-Martínez and Chao Ma
revised and *massively* expanded by FW
WHOI GFD Lecture 1, June 20, 2011

1.1 Introduction

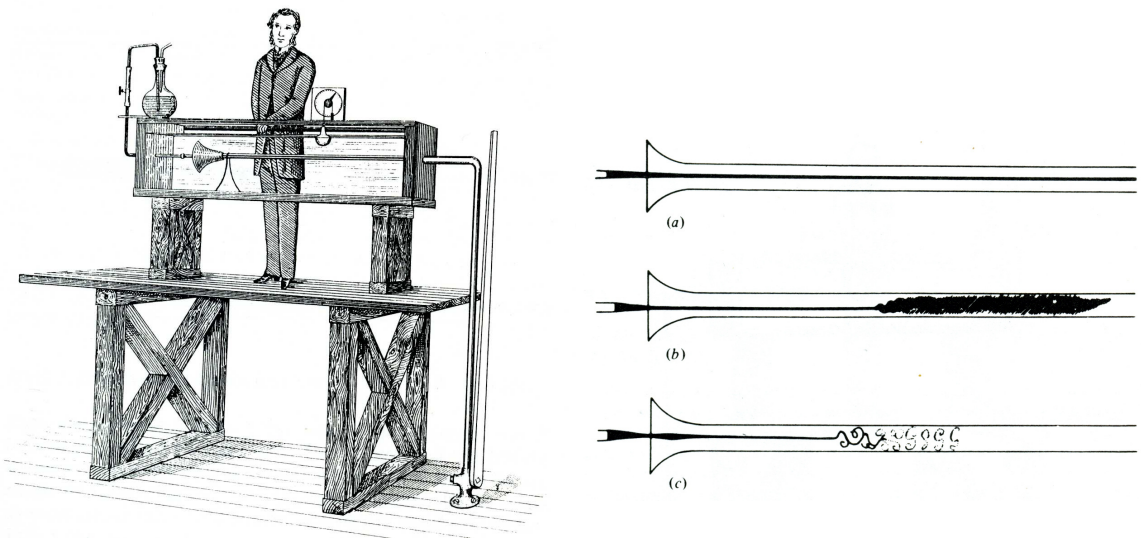

Figure 1.1: Reynolds' 1883 experiment, still operating at the University of Manchester, UK. Water flows down a long pipe and ink is introduced at the pipe centerline. On the right are the original drawings showing the dye filament in laminar flow (a), and the rapid mixing of the dye and water when the Reynolds number is larger than about 2000 in (b). (c) shows details of vortical structures in turbulent flow, visualized with a spark.

A classic series of educational fluid mechanics films is available online at

`http://web.mit.edu/hml/ncfmf.html`

The film on *Turbulence* provides an excellent visual introduction to turbulence in shear flows and reproduces the seminal experiments of Osborne Reynolds [24] on the transition from laminar to turbulent flow in a pipe, illustrated in Fig. 1.1. The 2011 *Annual Review of Fluid Mechanics* article by Tom Mullin [21] provides many fascinating historical details and is also highly recommended reading.

Transition to turbulence results from the non-linearity of the governing Navier-Stokes equations and the relevant non-dimensional quantity is the Reynolds number

$$R \equiv \frac{UL}{\nu} \tag{1.1}$$

where U and L are characteristic velocity and length scales, respectively — such as the average (or 'bulk') flow speed and the diameter of the pipe — and ν is the kinematic viscosity of the fluid (*e.g.* $\nu \approx 10^{-5}$ m^2/s for air, and $\nu \approx 10^{-6}$ m^2/s for water). Pipe flow will typically be in a turbulent state when the Reynolds number is larger than about 2000 and laminar below that. For flow of water ($\nu \approx 10^{-6}$ m^2/s), in a pipe of diameter D=10cm = 0.1m, turbulent flow is observed for bulk velocities U greater than about a mere 2 cm/s = 0.02 m/s.

1.1.1 Navier-Stokes equations

Although most fluids are compressible, the fundamental study of turbulence can be simplified if we consider an idealized incompressible flow. This is equivalent to assuming that the speed of sound in our medium, $c = \sqrt{(\partial P/\partial \rho)_S}$ (≈ 340 m/s in air and 1500 m/s in water), is much greater than any velocity in the fluid. The Navier-Stokes equations for constant density fluid flow (for a derivation see for example Acheson [2, Chap. 6] or Batchelor [4, Sect. 3.2]) are

$$\nabla \cdot \mathbf{v} = 0 \tag{1.2}$$

$$\partial_t \mathbf{v} + \mathbf{v} \cdot \nabla \mathbf{v} + \nabla p = \nu \nabla^2 \mathbf{v} \tag{1.3}$$

where $\mathbf{v} = \mathbf{v}(\mathbf{r}, t)$ is the fluid velocity at position $\mathbf{r} \in \mathbb{R}^3$ at time t, ∇ is the del operator, $p = p(\mathbf{r}, t)$ is the *kinematic* pressure (*i.e.* the pressure divided by the constant mass density ρ) and $\nu > 0$ is the *kinematic* viscosity and $\nabla^2 = \nabla \cdot \nabla$ is the Laplacian. The standard boundary condition for a viscous fluid is no-slip at the wall, that is $\mathbf{v}_{fluid} = \mathbf{v}_{wall}$.

For incompressible flow, the pressure p is purely *mechanical*, not thermodynamic. The pressure is determined by the flow and the incompressibility constraint $\nabla \cdot \mathbf{v} = 0$, and there is no need for an equation of state. In fact, taking the divergence of (1.3) and using $\nabla \cdot \mathbf{v} = 0$, yields a Poisson equation for the pressure

$$\nabla^2 p = -\nabla \cdot (\mathbf{v} \cdot \nabla \mathbf{v}) \tag{1.4}$$

where $\nabla \cdot (\mathbf{v} \cdot \nabla \mathbf{v}) = \nabla \mathbf{v} : \nabla \mathbf{v} = (\partial_i v_j)(\partial_j v_i) = S_{ij} S_{ij} - \Omega_{ij} \Omega_{ij}$ in cartesian index notation, where $\partial_i = \partial/\partial x_i$ and $S_{ij} = (\partial_i v_j + \partial_j v_i)/2$, $\Omega_{ij} = (\partial_i v_j - \partial_j v_i)/2$ are the deformation and rotation rate tensors, respectively. Thus, the pressure gradient in (1.3) is in fact a *non-local, nonlinear term* for the Navier-Stokes equations. The nonlinearity of the Navier-Stokes equations is $\mathbf{v} \cdot \nabla \mathbf{v} + \nabla p$, with the pressure solving the elliptic Poisson equation (1.4).

However, there are difficulties, misunderstandings and controversies regarding the boundary conditions needed to solve the Poisson equation (1.4), as discussed in Rempfer [23]. The dream is that the pressure boundary conditions can be decoupled from the velocity – a Neumann boundary condition $\partial p/\partial n = 0$ where n is normal to the wall, for instance – so that one could update the velocity in time using (1.3) then update the pressure from (1.4) using the updated velocity. Such methods are usually referred to as *Pressure Poisson equation* (PPE) formulations. Such decoupling is not correct in general, and PPE formulations, as well as the related *fractional step methods*, may have particular difficulties with *steady*, *traveling wave* and *time-periodic* solutions of the Navier-Stokes equations. Such solutions are precisely the focus of these lectures. A general approach is to enforce the incompressibility constraint $\nabla \cdot \mathbf{v} = 0$ *ab initio* through a streamfunction-type (*i.e.* divergence-free) formulation for $\mathbf{v}$ and eliminate the pressure by taking the curl ($\nabla \times (\cdot)$) of the Navier-Stokes equations (1.3) or projecting those equations onto the space of divergence-free functions. The v, η and 'poloidal-toroidal' representations fall under this general category of methods.

1.1.2 Laminar pipe flow

For flow in a nominally infinitely long pipe of radius a, driven by an imposed constant pressure gradient $dp_0/dx < 0$ in the axial streamwise direction x, GFD fellows easily verify that the Navier-Stokes equations (1.2), (1.3), have the parabolic solution

$$\mathbf{v} = \left(1 - \frac{r^2}{a^2}\right) U_c \, \hat{\mathbf{x}} \tag{1.5}$$

where $r = \sqrt{y^2 + z^2}$ is the distance to the pipe centerline, U_c is the centerline velocity, $\hat{\mathbf{x}}$ is the unit vector in the pipe direction and

$$\frac{dp_0}{dx} = -\nu \frac{4U_c}{a^2}. \tag{1.6}$$

This is the *laminar* pipe flow solution, first found by Poiseuille [21] from his experimental data. Averaging (1.5) over the pipe cross section A, yields the laminar bulk velocity

$$U = \frac{1}{\pi a^2} \int_A \hat{\mathbf{x}} \cdot \mathbf{v} \, dA = \frac{2}{a^2} U_c \int_0^a r \left(1 - \frac{r^2}{a^2}\right) dr = \frac{U_c}{2} \tag{1.7}$$

which is simply half the centerline velocity for *laminar* pipe flow. This simple relationship is not true for *turbulent* pipe flow.

Defining the Reynolds number $R = UD/\nu$ in terms of the bulk velocity U and the pipe diameter $D = 2a$, we can write a non-dimensional form of the relationship (1.6) between the pressure gradient and the laminar flow velocity, with $U_c = 2U$ from (1.7). This yields the the *friction factor*

$$f \equiv \left|\frac{dp_0}{dx}\right| \frac{D}{\frac{1}{2}U^2} = 64 \frac{\nu}{UD} = \frac{64}{R}. \tag{1.8}$$

Thus in laminar pipe flow, the friction factor f is inversely proportional to the Reynolds number, $f = 64/R$. In experiments, this laminar flow regime is typically observed only for $Re \lesssim 2000$. For higher Reynolds number, the friction factor transitions to a much weaker

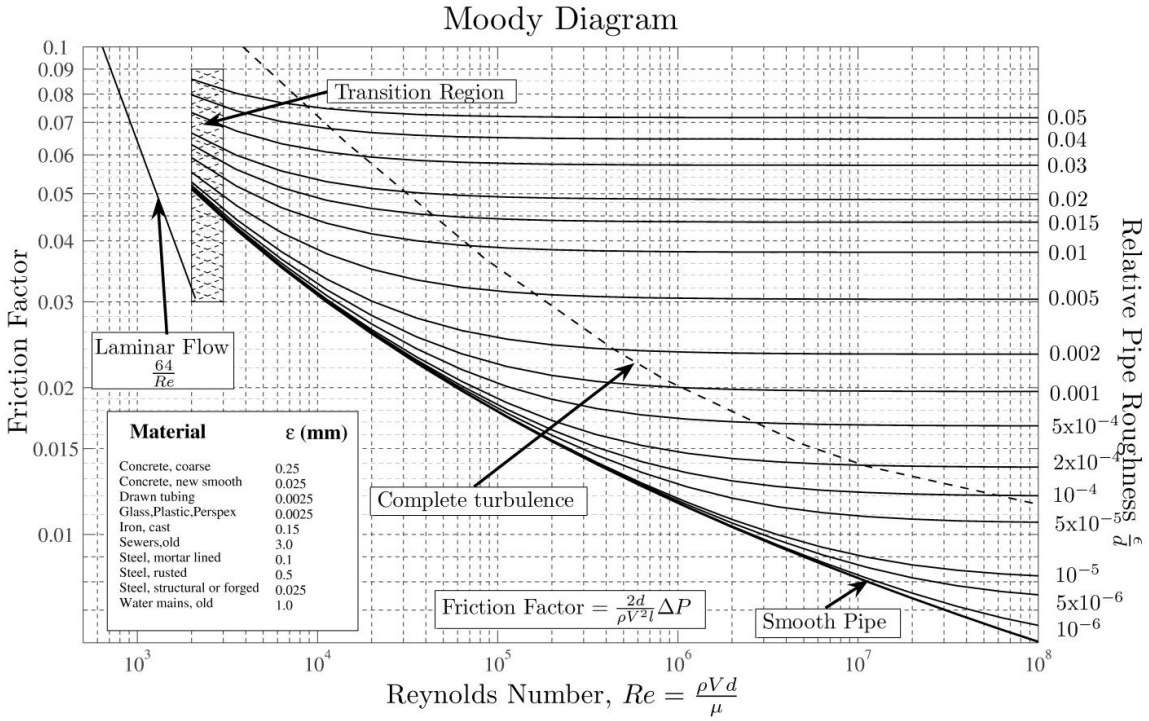

Figure 1.2: Moody diagram (from `http://en.wikipedia.org/wiki/Moody_chart`) showing the friction factor f as a function of Reynolds number $R = UD/\nu$ (eqn. (1.8)). Each curve is associated with a surface roughness of the pipe. On this plot $V \equiv U$ is the bulk velocity, $d \equiv D$ is the pipe diameter, $\mu = \rho\nu$ is the dynamic viscosity, and $\Delta P/(\rho l) = |dP_0/dx|$. The laminar flow friction law $f = 64/R$ is experimentally observed only for $R \lesssim 2,000$, even for smooth pipes. For $R \gtrsim 2000$, the drag associated with turbulent flow is much larger than it would be for laminar flow at the same Reynolds number. 'Complete turbulence' is loosely defined as the region where the friction factor is independent of Reynolds number. At $R = 10^5$, $f \approx 0.018$ is about 30 times larger than the laminar value $64/R$.

dependence on Reynolds number, perhaps asymptoting to a non-zero constant as illustrated in the Moody diagram well-known to engineers (Fig. 1.2).

However, transition is more complex than suggested by the Moody diagram. Reynolds achieved laminar pipe flow up to $R \approx 13\,000$ and Pfenniger's world record is about 100 000 [21]. Meseguer and Trefethen's [20] numerical calculations of the Navier-Stokes equations linearized about the laminar flow (1.5) show stability up to $R = 10^7$. Based on this experimental and numerical evidence, laminar pipe flow is believed to be *linearly stable for all Reynolds numbers.* However, no complete mathematical proof of linear stability is known to date.

1.1.3 Shear flows

Pipe flow is only one example of a *shear flow*, that is, a flow whose velocity varies in the direction perpendicular to the flow direction. Shear flows are a fundamental and ubiquitous class of fluid flow owing to the viscosity of real fluids and the no-slip boundary condition. Whenever a fluid flows by a wall, the no-slip boundary condition will lead to the generation of shear near the wall. This is the classic *Prandtl boundary layer* (Fig. 1.3) that can diffuse away from the wall temporally or spatially and even separate, shedding vortices (Fig. 1.4) (see *e.g.* [2], [4] for further information about this important and complex problem)

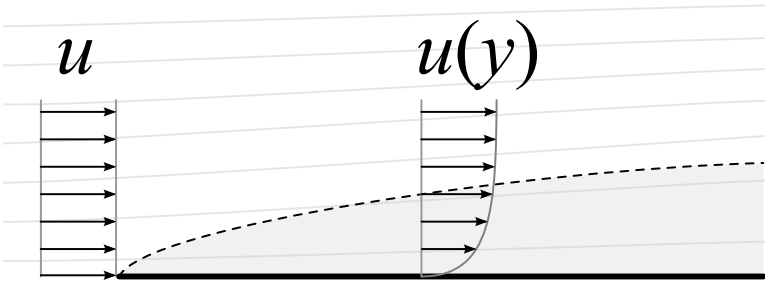

Figure 1.3: Shear flow developing spatially from viscosity and no-slip boundary condition as a fluid flows over a semi-infinite flat plate. The velocity is strongly dependent on the wall-normal y direction in a narrow *boundary layer* near the wall but only weakly dependent on the streamwise direction x. In laminar flow, the boundary layer thickness δ scales as $\sqrt{\nu x/U_\infty}$. (From `http://en.wikipedia.org/wiki/Boundary_layer`)

This process of boundary layer development and possible vortex shedding occurs at the entrance to the pipe in Reynolds' experiment. The vortex shedding at the entrance has a strong effect on the onset of turbulence and it is to eliminate those perturbations that Reynolds used a funnel, as shown in Fig. 1.1. With careful control of the entrance flow and geometry, one obtains the fully developed, steady laminar pipe flow (1.5) that can be routinely observed up to $Re \approx 20\,000$.

Other canonical 'fully developed' shear flows are plane Poiseuille (a.k.a. channel) flow and plane Couette flow, sketched in Fig. 1.5. Plane Poiseuille flow is the flow driven by a pressure gradient in-between two infinitely long, parallel fixed planes and the laminar solution is $\mathbf{v} = (1 - y^2/h^2)\, U_c\, \hat{\mathbf{x}}$ where y is the wall-normal direction and the walls are

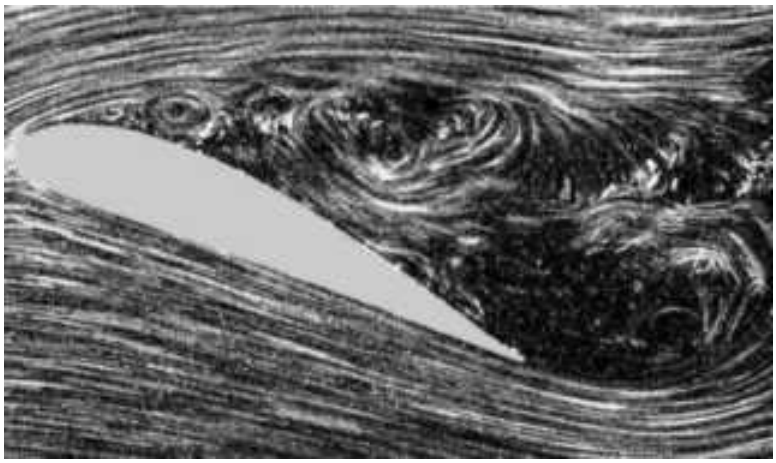

Figure 1.4: Boundary layer separation around an airfoil. This airfoil is *stalled*, the lift has collapsed, drag as increased, the flow is unsteady and turbulent behind the airfoil and vortices are continuously shed from the top front of the airfoil.
(from `http://en.wikipedia.org/wiki/Boundary_layer_separation`).

located at $y = \pm h$. Plane Couette flow is the flow between two infinite parallel walls and driven by the motion of those walls in opposite directions. The laminar plane Couette flow is $\mathbf{v} = U_w y/h\,\hat{\mathbf{x}}$ where the walls are at $y = \pm h$ and move at velocities $\pm U_w \hat{\mathbf{x}}$, respectively.

Plane Couette flow is linearly stable for *all* Reynolds numbers $R > 0$, as proved by Romanov [25], but experiments and simulations show transition to turbulence for $R = U_w h/\nu \gtrsim 350$. Contrary to its stable cylindrical cousin, plane Poiseuille flow has a linear instability for $R_c = U_c h/\nu > 5772$, where U_c is the centerline velocity and h the half-channel height. For plane Poiseuille flow, the bulk velocity $U = 2U_c/3$, so linear instability occurs for $R = UH/\nu > (4/3)\,5772 = 7696$, based on the bulk U and the full channel height $H = 2h$. This linear instability is an intriguing instability that originates from viscosity *and* the no-slip boundary condition, as anticipated by Prandtl. This instability is governed by the Orr-Sommerfeld equation and was first revealed by the pioneering analyses of Heisenberg for channel flow in 1924 and Tollmien for the Blasius boundary layer flow in 1929 [9]. This instability is very weak and delicate, small changes in the flow or geometry can suppress it. In any case, transition to turbulence is observed for $R_c = U_c h/\nu \gtrsim 1500$ in channel flow, well below the linear instability threshold [19].

1.1.4 Transition threshold

If plane Couette and pipe flows are stable to infinitesimal perturbations but experiments show transition to turbulence, this transition must result from *finite amplitude effects*. This is also the case in plane Poiseuille and boundary layer flows, where transition is observed at significantly lower Reynolds number than predicted by linear analysis, and on much faster time scales than the slow viscous time scale of linear eigenmodes. In those cases, Morkovin coined the term *'bypass transition'* – transition that bypasses the linear instability process.

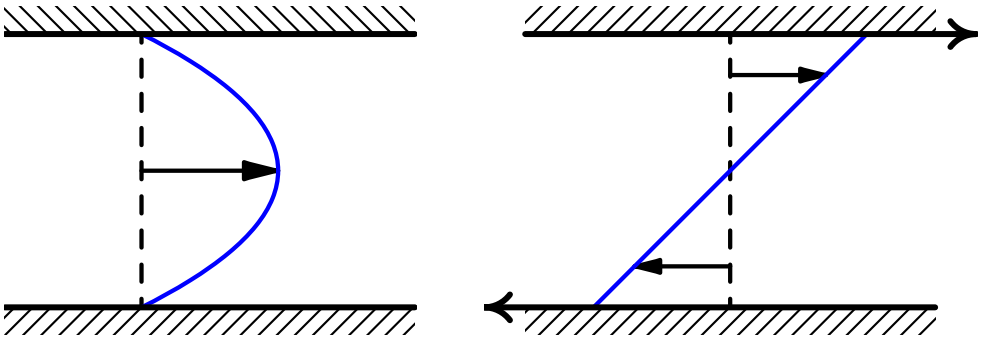

Figure 1.5: Canonical shear flows: pressure driven pipe and channel flows with a parabolic velocity profile $\mathbf{v} = (1 - y^2)\,\hat{\mathbf{x}}$ (*left*) and wall driven plane Couette flow with laminar velocity profile $\mathbf{v} = y\,\hat{\mathbf{x}}$ (*right*), where $\hat{\mathbf{x}}$ is the flow direction, y is the (signed) distance to the (midplane) centerline. The walls are at $y = \pm 1$, the centerline velocity is 1 for pipes and channels, and the wall velocities are ± 1 for Couette.

Onset of turbulence is thus a Reynolds number *and* amplitude dependent phenomenon.

A natural question therefore is to ask whether there is a scaling relating the *threshold* transition amplitude, ϵ say, to the Reynolds number R, perhaps a power law scaling

$$\epsilon \sim R^a \tag{1.9}$$

where we expect $a < 0$. Surprisingly, this question does not seem to have been articulated before Trefethen *et al.* in 1993 [29, TTRD hereafter]. Closely related questions, and more specific nonlinear mechanisms, were being investigated before TTRD, but the focus was on inviscid processes, therefore those investigations focused on the relations between *time scale* and *amplitude*, rather than *Reynolds number* and *amplitude*. That the two questions are closely related can be understood as follows.

Non-dimensionalizing the velocity by a characteristic velocity U, length scales by a characteristic length L, time by L/U and kinematic pressure by U^2, the Navier-Stokes equations (1.3) have the same form but with ν replaced by $1/R$

$$\partial_t \mathbf{v} - \frac{1}{R}\nabla^2 \mathbf{v} = -\mathbf{v} \cdot \nabla \mathbf{v} - \nabla p \tag{1.10}$$

where the right hand side is a quadratic nonlinearity since ∇p projects $\mathbf{v} \cdot \nabla \mathbf{v}$ onto the space of divergence-free fields (1.4). If ϵ is a measure of the amplitude of $\mathbf{v}$, we could estimate

$$\partial_t \mathbf{v} \sim \frac{\epsilon}{T}, \qquad \frac{1}{R}\nabla^2 \mathbf{v} \sim \frac{\epsilon}{R}, \qquad \mathbf{v} \cdot \nabla \mathbf{v} + \nabla p \sim \epsilon^2 \tag{1.11}$$

where T is a time scale to be determined. In the limit of large Reynolds number, $R \to \infty$, an inertial, inviscid scaling for (1.10) is then

$$\frac{\epsilon}{T} \sim \epsilon^2 \quad \Rightarrow \quad T \sim \frac{1}{\epsilon} \tag{1.12}$$

suggesting that the essential time scale for a non-trivial nonlinear process would be $T \sim 1/\epsilon$. This is much faster than the standard nonlinear time scale for nonlinear waves (*e.g.* Duffing oscillator, weakly nonlinear pendulum, nonlinear Schrödinger, ...) where the nonlinear time scale is $T \sim 1/\epsilon^2 \gg 1/\epsilon$, for small ϵ. The latter results from the fact that the quadratic interaction of a 'wave' or Fourier mode ϵe^{ikx} of amplitude ϵ and wavenumber k, generates a harmonic $\epsilon^2 e^{i2kx}$ of amplitude ϵ^2 and wavenumber $2k$. That harmonic then interacts with the complex conjugate of the fundamental wave ϵe^{-ikx} to provide nonlinear feedback $\epsilon^3 e^{ikx}$ onto the fundamental wave, but only at order ϵ^3, not ϵ^2. The nonlinear wave balance in that case is not (1.12) but $\epsilon/T \sim \epsilon^3$ yielding the slow nonlinear time scale $T \sim 1/\epsilon^2$ (recall that ϵ is small and measures relative departure from an equilibrium).

Now if instead of $R \to \infty$ with large but finite T, we focus instead on *steady* as in steady state and traveling waves, or *statistically steady* as in periodic or turbulent solutions, that is $T \to \infty$ with Re large but finite, the nonlinear balance and time scale argument (1.12) for (1.10) now yields

$$\frac{\epsilon}{R} \sim \epsilon^2 \quad \Rightarrow \quad \epsilon \sim \frac{1}{R} \tag{1.13}$$

and we interpret this as a measure of the minimum perturbation amplitude that could balance viscous damping – a *threshold amplitude*. Again this is a much smaller amplitude than the classical weakly nonlinear balance where feedback on the fundamental occurs at order ϵ^3 and the balance is $\epsilon/R \sim \epsilon^3$ not ϵ^2, yielding $\epsilon \sim 1/\sqrt{R} \gg 1/R$.

The simple balance (1.13) thus suggest that $a = -1$ in (1.9), stronger than the classic weakly nonlinear scaling that would have $a = -1/2$. However, while the scalings (1.12), (1.13) certainly apply to the *'subcritical logistic' equation*[1]

$$\frac{du}{dt} = -\frac{u}{R} + u^2, \tag{1.14}$$

that does have the threshold amplitude $u = 1/R$, it remains to be shown whether they do apply to the Navier-Stokes equations (1.10). Indeed, the brief discussion of classic weakly nonlinear feedback occurring at the weaker ϵ^3 instead of ϵ^2, suggests that the scalings (1.12) and (1.13) may not be allowed by the Navier-Stokes nonlinearity and it is necessary to investigate explicit nonlinear mechanisms for shear flows. The linear terms also require more investigation since they are trickier than the mere viscous damping in (1.14).

Decompose the full velocity $\mathbf{v}$ into a laminar flow $\mathbf{U}$ plus a perturbation $\mathbf{u}$. Substituting $\mathbf{v} = \mathbf{U}+\mathbf{u}$ into the Navier-Stokes equations (1.10), we obtain the equations for the solenoidal perturbation $\mathbf{u}$ in the schematic form

$$\frac{\partial \mathbf{u}}{\partial t} - \frac{1}{R}\nabla^2 \mathbf{u} = L(\mathbf{u}) + N(\mathbf{u}, \mathbf{u}) \tag{1.15}$$

where $N(\mathbf{u}, \mathbf{u})$ is a quadratic nonlinearity and $L(\mathbf{u}) = N(\mathbf{U}, \mathbf{u}) + N(\mathbf{u}, \mathbf{U})$ is linear in $\mathbf{u}$. Pressure is once again hidden in each of those operators to project them onto the space of solenoidal fields, so $N(\mathbf{u}, \mathbf{u}) = -\mathbf{u} \cdot \nabla \mathbf{u} - \nabla p$. The perturbation $\mathbf{u}$ is solenoidal $\nabla \cdot \mathbf{u} = 0$ and satisfies homogeneous boundary conditions, $\mathbf{u} = 0$ at no-slip walls since $\mathbf{U}$ satisfies $\mathbf{U}_{wall} = \mathbf{v}_{wall}$. Before looking into specific mechanisms and possible threshold exponent

[1] This 'subcritical logistic' equation is sometimes used to suggest that the Navier-Stokes equations could develop a singularity for sufficiently large initial amplitudes.

a in (1.9), we first discuss some characteristics of the linear operator $L(\mathbf{u})$ for shear flows which was ignored in the 'fully nonlinear' scalings (1.11) and (1.13).

1.2 Linear Theory: exponential and algebraic growth

1.2.1 Exponential growth

A linear stability analysis of the laminar flow $\mathbf{U}$ consists of studying the linearized equations

$$\frac{\partial \mathbf{u}'}{\partial t} - \frac{1}{R}\nabla^2 \mathbf{u}' = L(\mathbf{u}') \tag{1.16}$$

which is (1.15) for $\mathbf{u} = \epsilon \mathbf{u}'$ in the limit $\epsilon \to 0$, the 'infinitesimal amplitude' limit. If this linearized equation admits solutions that are *growing for all times*, then the laminar flow $\mathbf{U}$ is unstable. Growing perturbations typically have the form of *exponentially* growing eigenmodes of (1.16), solutions of the form $\mathbf{u}'(\mathbf{r}, t) = e^{\lambda t}\mathbf{u}(\mathbf{r})$ where λ is the temporal eigenvalue, with $\Re(\lambda) > 0$ for instability, and $\mathbf{u}(\mathbf{r})$ is the *eigenmode*. For example, the simple 2-by-2 model

$$\frac{d}{dt}\begin{pmatrix} u \\ v \end{pmatrix} = \begin{pmatrix} -k_u^2/R & 1 \\ \sigma^2 & -k_v^2/R \end{pmatrix}\begin{pmatrix} u \\ v \end{pmatrix}, \tag{1.17}$$

where k_u, k_v and σ are real and positive, has two exponential eigenmodes, one of which is growing if $R > k_u k_v/\sigma$.

The linear analysis of exponentially growing modes for shear flows is exceedingly delicate and was a central problem in Applied Mathematics for many decades beginning with the reduction of the problem to the *Orr-Sommerfeld equation*, derived independently by Orr in 1907 and Sommerfeld in 1908, and followed by the intricate asymptotic analyses of that equation by Heisenberg (1924), Tollmien (1929, 1935, 1947), Schlichting (1933), C.C. Lin (1945, 1955, 1957, 1961) and the more rigorous and general analyses of Morawetz (1951) and Wasow (1953), among many others. Orszag (1971) provided accurate numerical solution of the Orr-Sommerfeld equation using Chebyshev polynomials, for moderate Reynolds number, and that work demonstrated the usefulness of *spectral methods* for fluid dynamics computations.

As mentioned in sect. 1.1.3, the result of those many decades of studies is that there is essentially *no* exponentially growing mode for viscous shear flows. It is proved that there are none in plane Couette flow [25]; there is strong evidence that there are none in pipe flow [20, 21]; there is a weak *viscous* growing mode in plane Poiseuille flow first identified by Heisenberg and a similar, slightly more significant, mode for Blasius boundary layer flow, first studied by Tollmien and Schlichting. Those weakly growing modes are called *Tollmien-Schlichting waves* [9], but Heisenberg already understood in 1924 that these weakly growing viscous linear modes did not explain the onset of turbulence in shear flows, ... and that may be partly why he quickly switched to developing the matrix formulation of quantum mechanics!

1.2.2 Algebraic growth, redistribution of base flow

Thus, as an analogy to shear flows, the model problem (1.17) should have $\sigma = 0$ and be stable for all $0 < R < \infty$. Degenerate *algebraic* instability can occur in (1.17) when $\sigma = 0$

and $R = \infty$,

$$\frac{d}{dt}\begin{pmatrix} u \\ v \end{pmatrix} = \begin{pmatrix} 0 & 1 \\ 0 & 0 \end{pmatrix}\begin{pmatrix} u \\ v \end{pmatrix}, \tag{1.18}$$

the coupling matrix $\left(\begin{smallmatrix} 0 & 1 \\ 0 & 0 \end{smallmatrix}\right)$ is a *Jordan block*, it has the repeated eigenvalue $\lambda = 0$ but more importantly it has *only one* eigenvector, namely $(u, v) = (1, 0)$. Initial conditions $(u, v) = (0, 1)$ yield the algebraic pseudo-mode $(u, v) = (t, 1)$ since (1.18) is simply $dv/dt = 0$, $du/dt = v$. The general solution of (1.18) for initial conditions $(u, v) = (u_0, v_0)$ at $t = 0$ is

$$\begin{pmatrix} u \\ v \end{pmatrix} = u_0\begin{pmatrix} 1 \\ 0 \end{pmatrix} + v_0\begin{pmatrix} t \\ 1 \end{pmatrix}, \tag{1.19}$$

$v = v_0$ is constant but induces an algebraic growth $u = u_0 + v_0 t$.

Such algebraic growth is *generic* for the *inviscid linear* dynamics about shear flows. To show this, consider a general plane parallel shear flow $\mathbf{U} = U(y)\hat{\mathbf{x}}$, where x is streamwise and y shearwise. Substituting $\mathbf{v} = U(y)\hat{\mathbf{x}} + \mathbf{u}$ in (1.3) yields

$$\begin{aligned} \frac{\partial u}{\partial t} + U\frac{\partial u}{\partial x} + v\frac{dU}{dy} \quad &+\mathbf{u}\cdot\nabla u = -\frac{\partial p}{\partial x} + \frac{1}{R}\nabla^2 u, \\ \frac{\partial v}{\partial t} + U\frac{\partial v}{\partial x} \qquad\quad &+\mathbf{u}\cdot\nabla v = -\frac{\partial p}{\partial y} + \frac{1}{R}\nabla^2 v, \\ \frac{\partial w}{\partial t} + U\frac{\partial w}{\partial x} \qquad\quad &+\mathbf{u}\cdot\nabla w = -\frac{\partial p}{\partial z} + \frac{1}{R}\nabla^2 w, \end{aligned} \tag{1.20}$$

where $U = U(y)$ is the laminar shear flow profile and $\mathbf{u} = (u, v, w)$ in cartesian coordinates (x, y, z) with $\nabla\cdot\mathbf{u} = \partial u/\partial x + \partial v/\partial y + \partial w/\partial z = 0$. For streamwise independent perturbations, $\partial/\partial x = 0$, and linearizing in $\mathbf{u}$, (1.20) reduces to

$$\begin{aligned} \frac{\partial u}{\partial t} + v\frac{dU}{dy} \quad &= \qquad\quad \frac{1}{R}\nabla^2 u, \\ \frac{\partial v}{\partial t} \qquad\quad &= -\frac{\partial p}{\partial y} \quad +\frac{1}{R}\nabla^2 v, \\ \frac{\partial w}{\partial t} \qquad\quad &= -\frac{\partial p}{\partial z} \quad +\frac{1}{R}\nabla^2 w, \end{aligned} \tag{1.21}$$

and $\nabla\cdot\mathbf{u} = 0$ reduces to $\partial v/\partial y + \partial w/\partial z = 0$. Eliminating p and w, we obtain

$$\begin{aligned} \frac{\partial u}{\partial t} + v\frac{dU}{dy} \quad &= \frac{1}{R}\nabla^2 u, \\ \frac{\partial}{\partial t}\nabla^2 v \qquad &= \frac{1}{R}\nabla^2\nabla^2 v, \end{aligned} \tag{1.22}$$

where $\nabla^2 = \partial^2/\partial y^2 + \partial^2/\partial z^2$ for streamwise independent perturbations. For planar geometries, the no-slip boundary conditions $\mathbf{u} = 0$ yields $u = v = \partial v/\partial y = 0$ at the walls, the latter following from $\partial v/\partial y + \partial w/\partial z = 0$ since $w = \partial w/\partial z = 0$ along the walls.

For inviscid flow, $R = \infty$, (1.22) is conceptually identical to the simple model (1.18) and a non-zero vertical velocity will remain constant, $v = v_0$, but induce an algebraic growth of the streamwise velocity perturbation u

$$\frac{\partial u}{\partial t} = -v_0\frac{dU}{dy} \quad \Rightarrow \quad u = u_0 - v_0\frac{dU}{dy}\,t. \tag{1.23}$$

This is the linearization of a simple *redistribution of streamwise velocity $U(y)$ by the shearwise velocity perturbation v*. If, for instance, $U' = dU/dy > 0$ and $v > 0$, then lower velocity U is lifted upward by the perturbation v leading to a negative streamwise velocity perturbation $u = -v_0 U' t < 0$. This simple algebraic growth was perhaps first investigated by Benney and Lin in 1960 [7], rediscovered by Ellingsen and Palm in 1975 [10] and Gustavsson and Hultgren in 1980 and 1990, *e.g.* [12, 15, 11]. This redistribution was dubbed the *'lift-up mechanism'* by Marten Landahl, although it is actually *'pull-down'* when $v < 0$, and 'lift-up' usually comes with 'pull-down' because of conservation of volume. This is a trivial 'mechanism' yet an essential part of any instability or self-sustaining process that redistributes background momentum to release energy from the background shear.

But *linear* fluid dynamics is not *physical* fluid dynamics. Algebraic growth *for all times* cannot occur for bounded flows, even in the inviscid limit. Consider plane Couette flow $U(y) = y$ for $-1 \le y \le 1$. The largest perturbation that can be achieved is to 'lift-up' velocity $U = -1$ from the bottom wall all the way to the top wall and obtain $u = -2$ at $y = 1$, or likewise to 'pull-down' velocity $U = 1$ from the top wall all the way to the bottom wall, obtaining $u = 2$ at $y = -1$. Thus $|u| < 2$ in plane Couette and this is a strict upper bound since $v = 0$ at the walls, so it is actually not possible to lift-up or pull-down all the way from one wall to the other. In linear theory, *lift-up* can go on forever appearing mathematically as algebraic growth from the linearized advection term $v\,dU/dy$, but in real flows, lift-up does not go on forever. The term *redistribution* of streamwise velocity better captures the inherent limitation of the underlying simple advection of the background shear by the perturbation. If slow fluid is lifted up and fast fluid pulled down, then the mean shear has been reduced. Hence, there are obvious physical limits to the algebraic growth (1.19), (1.23), that would appear as nonlinear saturation effects in a more complete analysis. These and other issues are discussed in [31, 32] and in section 1.3.5, briefly, system (1.18) $\dot{u} = v$, $\dot{v} = 0$ with its algebraic growth $u = v_0 t$ is merely the linearization of

$$\frac{d}{dt}\begin{pmatrix} M \\ u \\ v \end{pmatrix} = \begin{pmatrix} -uv \\ Mv \\ 0 \end{pmatrix}, \tag{1.24}$$

about $M = 1$, $u = 0$, $v = 0$. System (1.24) does not have algebraic growth, it simply has continual *redistribution* of the mean shear M into *'streaks'* u then back to M, with a periodic general solution $M = M_0 \cos(v_0 t) - u_0 \sin(v_0 t)$, $u = u_0 \cos(v_0 t) + M_0 \sin(v_0 t)$, $v = v_0$.

Viscous details: Stokes eigenmodes

For finite R, it is clear that (1.22) has exponentially *decaying* eigenmodes with $u \neq 0$ but $v = 0$, and exponentially decaying v eigenmodes that force a *transient growth* of u with ultimate exponential decay. The former are simple eigenmodes of the heat equation for u, with even modes

$$u = \cos\left((2n-1)\frac{\pi}{2}y\right)\, e^{i\gamma z} \tag{1.25}$$

and odd modes

$$u = \sin(n\pi y)\, e^{i\gamma z} \tag{1.26}$$

for no-slip $u = 0$ at $y = \pm 1$, with $n = 1, 2, \ldots$ The latter are *Stokes eigenmodes* for v, *i.e.* the solutions of $\nabla^2\nabla^2 v = \lambda\nabla^2 v$. For channel geometries with no-slip walls at $y = \pm 1$, GFD fellows easily derive or at least verify that the Stokes eigenmodes consist of even modes

$$v = \left(\frac{\cosh\gamma y}{\cosh\gamma} - \frac{\cos\beta y}{\cos\beta}\right) e^{i\gamma z} \qquad \text{with} \qquad \gamma\tanh\gamma + \beta\tan\beta = 0 \tag{1.27}$$

and odd modes

$$v = \left(\frac{\sinh\gamma y}{\sin\gamma} - \frac{\sin\beta y}{\sin\beta}\right) e^{i\gamma z} \qquad \text{with} \qquad \frac{\gamma}{\tanh\gamma} - \frac{\beta}{\tan\beta} = 0 \tag{1.28}$$

where γ is a spanwise z wavenumber. The hyperbolic terms satisfy $\nabla^2 v = 0$ and show up to enforce the clamped boundary conditions $v = \partial v/\partial y = 0$ at $y = \pm 1$. The trigonometric terms satisfy $\nabla^2 v = -(\beta^2 + \gamma^2)\ v$, so these Stokes eigenmodes decay like $e^{-(\beta^2+\gamma^2)t/Re}$ although β is different for each mode, and there is a discrete infinity of β's for each γ. A simple graphical analysis quickly shows that, for each $\gamma \neq 0$, the even modes (1.27) have $\beta = \beta_n$ with $(2n-1)\pi/2 < \beta_n < n\pi$ with $n = 1, 2, \ldots$ and $\beta_n \sim n\pi$ for n large, or γ small. Likewise, the odd modes have $n\pi < \beta_n < (2n+1)\pi/2$ and $\beta_n \sim (2n+1)\pi/2$ for large n or small γ, with $n = 1, 2, \ldots$.

1.2.3 Transient growth, non-normal and Jordan matrices

Hence, the simple model (1.17) with $\sigma = 0$

$$\frac{d}{dt}\begin{pmatrix} u \\ v \end{pmatrix} = \begin{pmatrix} -k_u^2/R & 1 \\ 0 & -k_v^2/R \end{pmatrix}\begin{pmatrix} u \\ v \end{pmatrix}, \tag{1.29}$$

is almost an exact model of (1.22). For smallest viscous damping, $k_u^2 = \pi^2/4 + \gamma^2$ and $k_v^2 = \beta_1^2 + \gamma^2$ with $\pi/2 < \beta_1 < \pi$ the smallest solution of $\gamma\tanh\gamma + \beta\tanh\beta = 0$. These smallest k_u^2 and k_v^2 correspond to the first even modes for both (1.25) and (1.27) and $k_v^2 > k_u^2$.

System (1.29) does not have exponential growth and it does not have the algebraic growth for all times of the degenerate system (1.18), it has exponential decay and possible *transient algebraic growth* of u with ultimate exponential decay. The general solution of (1.29) is

$$\begin{pmatrix} u \\ v \end{pmatrix} = u_0\, e^{-\nu k_u^2 t}\begin{pmatrix} 1 \\ 0 \end{pmatrix} + v_0\, e^{-\nu k_v^2 t}\begin{pmatrix} \frac{e^{\delta t}-1}{\delta} \\ 1 \end{pmatrix}, \tag{1.30}$$

where $\nu = 1/R \geq 0$ and $\delta = \nu(k_v^2 - k_u^2) \geq 0$, and the limit $R \to \infty$ is indeed (1.19). All components of (1.30) decay exponentially, except for the *forced response* u_f of u to v which is such that

$$\frac{u_f}{v_0} = e^{-\nu k_v^2 t}\ \frac{e^{\delta t} - 1}{\delta} = \frac{e^{-\nu k_u^2 t} - e^{-\nu k_v^2 t}}{\delta} = e^{-\nu k_u^2 t}\ \frac{1 - e^{-\delta t}}{\delta}, \tag{1.31}$$

and this forced response is bounded from below and from above by

$$t\ e^{-\nu k_v^2 t} \leq \frac{u_f}{v_0} \leq t\ e^{-\nu k_u^2 t}. \tag{1.32}$$

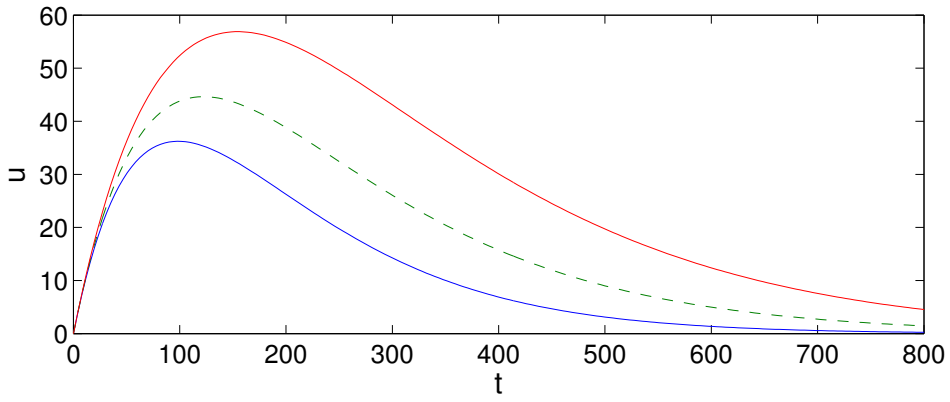

Figure 1.6: The forced response u_f/v_0 in (1.31), dashed, bracketed by the Jordan block bounds (1.32) for $R = 1000$ and $k_u^2 = \pi^2/4 + \gamma^2 \approx 6.4674$, $k_v^2 = \beta_1^2 + \gamma^2 \approx 10.1551$ for $\gamma = 2$ and $\beta_1 \approx 2.4809$ (1.27).

These bounds follow easily from $1 + x \leq e^x$ and $1 - x \leq e^{-x}$ for all real x (here $x \equiv \delta t$) and the equality occurs only at $t = 0$ if $\delta \neq 0$ or for all t if $\delta = 0$. These bounds are interesting since they show that *the forced response is bounded by the forced responses of the degenerate forms of system (1.29),* that is (1.29) with $k_u \to k_v$ or $k_v \to k_u$ (Fig. 1.6). When both diagonal elements are $-\nu k_u^2$ or $-\nu k_v^2$, system (1.29) is again a Jordan block with only one eigenvector. The solution of those degenerate systems are (1.30) in the limit $\delta \to 0$ where $(e^{\delta t} - 1)/\delta \to t$ with k_u or k_v in both exponentials, depending on the case.

System (1.29) is not degenerate when $\delta = (k_v^2 - k_u^2)/R \neq 0$, there are two eigenvectors but those eigenvectors are almost parallel when $\delta \ll 1$ and become parallel as $\delta \to 0$. That system with $\delta \neq 0$ is *non-normal*[2] – its eigenvectors are not orthogonal except in the very viscous limit $R \to 0$. Non-normal systems have been emphasized and studied by Trefethen and co-workers and discussed at length by Schmid and Henningson in the context of shear flows [26], although that focus on general non-normal operators may be unnecessarily abstract for shear flows where there is a natural decoupling into exponentially decaying modes for v with a *forced response* of the streamwise velocity perturbation u, as illustrated in (1.22) and the model (1.29). The bounds (1.32) also suggests that the *transient growth* associated with highly non-normal matrices – matrices with almost parallel eigenvectors – are tightly bounded by nearby degenerate systems (*i.e.* containing Jordan blocks) and that the initial conditions that lead to large transient growth are simply *orthogonal to the existing incomplete set of eigenvectors.* For the degenerate forms of (1.29), the only eigenvector is $(1, 0)$ and the initial condition giving most transient growth is $(0, 1)$.

It is now a simple Calculus exercise to show that the forced response (1.31) starts at $u_f = 0$ when $t = 0$, grows like $v_0 t$ for $(k_u^2 + k_v^2)t \ll R$ and ultimately decays like $(v_0/\delta)\, e^{-\nu k_u^2 t}$

[2] *Normal* is in the sense of *orthogonal* here. An *orthogonal* matrix has columns orthogonal to each other. A *normal* matrix has *eigenvectors* orthogonal to each other.

for $t \gg 1/\delta$, while reaching a maximum of

$$\max(u_f) = v_0 \, \frac{R}{k_v^2} \, \exp\left(-k_u^2 \, \frac{\ln k_v^2 - \ln k_u^2}{k_v^2 - k_u^2}\right) \tag{1.33}$$

at time

$$t_* = R \, \frac{\ln k_v^2 - \ln k_u^2}{k_v^2 - k_u^2} = R \, \frac{\ln(k_v^2/k_u^2)}{k_v^2 - k_u^2}. \tag{1.34}$$

Hence, there is a maximum growth of $O(v_0\, R)$ for u_f occurring at a time of $O(R)$.

1.3 Transition threshold: mechanisms and scalings

1.3.1 Transient growth + nonlinear feedback and $\epsilon \sim R^{-3}$

Our discussions in the previous sections makes clear that the 'subcritical logistic' model $du/dt = -u/R + u^2$, eqn. (1.14), is too simple for shear flows, but a more plausible model might be

$$\frac{d}{dt}\begin{pmatrix} u \\ v \end{pmatrix} = \begin{pmatrix} -\nu k_u^2 & 1 \\ 0 & -\nu k_v^2 \end{pmatrix}\begin{pmatrix} u \\ v \end{pmatrix} + \begin{pmatrix} 0 \\ u^2 \end{pmatrix}. \tag{1.35}$$

This is model (1.29) with $\nu = 1/R$ but with a quadratic nonlinear feedback from u onto v. If ϵ is a measure of the initial v_0, that is simply $\epsilon = v_0$ for this simple model, the transient growth of u will lead to a maximum $u \sim v_0 R = \epsilon R$, yielding a quadratic interaction $u^2 \sim \epsilon^2 (R)^2$ that must balance the viscous damping v/R to reach the *transition threshold*. The transition scenario is

$$v_0 = \epsilon \;\longrightarrow\; u \sim \epsilon R \implies v \sim u^2 R \sim \epsilon^2 R^3 \sim \epsilon \tag{1.36}$$

and the threshold scaling would be $\epsilon \sim R^{-3}$ with $a = -3$ in (1.9). TTRD [29] and Baggett and Trefethen [3] discuss similar simple models to illustrate *'nonlinear recycling of [transiently amplified] outputs into inputs'*.

However there are at least two basic reasons why such simple models are not valid models for Navier-Stokes. First, direct nonlinear feedback as in (1.35) is not allowed in the Navier-Stokes equations, and many other classic nonlinear and weakly nonlinear systems, as we already briefly discussed in section 1.1.4. Second, there is in fact virtually *no* 'nonlinear recycling of outputs into inputs' and the primary nonlinear effect of transient growth is actually to wipe out the background shear and saturate the growth, not regenerate 'optimal' disturbances. This is exactly true for the strongly amplified x-independent disturbances, as we prove in section 1.3.5, although not exactly true for more weakly amplified *oblique* disturbances, and this has led to sustained confusion among people who have been seduced by linear non-normal operators but have shied away from detailed analysis of nonlinear interactions. These issues are illustrated using simple models in the following.

1.3.2 Benney-Gustavsson mechanism and $\epsilon \sim R^{-2}$

Benney and Gustavsson (1981) [6] knew that streamwise independent perturbations induce a strong redistribution of streamwise velocity but do not trigger transition inducing nonlinear

effects. They searched then for a mechanism based on a *pair of oblique perturbations* and involving transient growth in the case of *direct resonance* – when $k_u^2 = k_v^2$ in (1.29) – and the limit of high R. Later studies of linear transient growth emphasized that direct resonances is not necessary for large growth, as discussed here in section 1.2.3 and figure 1.6. However, oblique disturbances in shear flows travel in the streamwise x direction, that is, the diagonal terms in (1.29) are complex in general and their imaginary parts do not scale like $1/R$, then large and distinct imaginary parts shut down the growth by phase shifting of the forcing v and the forced u. Thus, although exact 'direct resonance' is not necessary for large transient growth, it still remains that the imaginary parts of the eigenvalues for the v and η modes of oblique disturbances must be sufficiently close to each other for growth to occur.

Let v denote the amplitude of the vertical (*i.e.* shearwise) y velocity for a pair of oblique perturbations, and η represent the amplitude of the corresponding perturbation vertical vorticity ($\eta = \partial_z u - \partial_x w$). The latter η substitutes for the transient amplified streamwise velocity u in the x-independent dynamics. Benney and Gustavsson suggested the transition scenario

$$v = \epsilon \longrightarrow \eta \sim \epsilon t \Longrightarrow V, N \sim (\epsilon^2 t^2) \Longrightarrow v \sim (\epsilon^2 t^2)(\epsilon t)t = \epsilon^3 t^4, \tag{1.37}$$

in the limit of high R, where v and η are the amplitudes of $e^{i(\alpha x \pm \gamma z)}$ perturbations with linear eigenstructures in y, V and N are the amplitudes of v and η for the harmonics $e^{i2(\alpha x \pm \gamma z)}$ or $e^{i2\gamma z}$ and '$\longrightarrow$' is the linear transient growth, the first '$\Longrightarrow$' is the nonlinear interactions $\eta\eta$ and $\eta\eta^*$ and the second '$\Longrightarrow$' is the nonlinear interactions $V\eta$ and $N\eta$. This led them to suggest a nonlinear mechanism occurring on a time scale $t \sim 1/\sqrt{\epsilon}$, the time scale when the nonlinear feedback on v is of the order of the original amplitude $\epsilon^3 t^4 \sim \epsilon$, as laid out in (1.37).

In essence, what Benney and Gustavsson said is what we already discussed in sect. 1.1.4, for Navier-Stokes, and many other physical nonlinear systems, if a mode v linearly creates a mode u it does not make sense to have the quadratic interaction of the latter, u^2, directly feedback onto v. For instance, if v and u correspond to $e^{i(\alpha x \pm \gamma z)}$ then u^2 would be associated with the harmonic $e^{i2(\alpha x \pm \gamma z)}$ and the latter is orthogonal to the original modes, so we cannot have u^2 forcing of v as in (1.35). However, it is possible to have feedback at the next order of nonlinear interaction. In the context of our simple models, Benney and Gustavsson in effect said that (1.35) cannot be a suitable model for shear flows, but a possible model could be

$$\frac{d}{dt}\begin{pmatrix} u \\ v \end{pmatrix} = \begin{pmatrix} -\nu k_u^2 & 1 \\ 0 & -\nu k_v^2 \end{pmatrix}\begin{pmatrix} u \\ v \end{pmatrix} + \begin{pmatrix} 0 \\ u^3 \end{pmatrix}, \tag{1.38}$$

with a *cubic* nonlinear feedback u^3 onto v, not quadratic feedback u^2. In the inviscid limit, $\nu = 1/R \to 0$, this model has the scalings $dv/dt = u^3 \sim \epsilon^3 t^3$, so $v \sim \epsilon^3 t^4$ as in (1.37), while the *threshold scaling* is $\nu k_v^2 v = u^3 = (v/(\nu k_u^2))^3$ with $v = \epsilon$, yielding

$$\frac{\epsilon}{R} \sim (\epsilon\, R)^3 \quad \Leftrightarrow \quad \epsilon \sim R^{-2} \tag{1.39}$$

with $a = -2$ in (1.9). This is weaker than $\epsilon \sim Re^{-3}$ in (1.36) but still a very strong mechanism, especially compared to the classic weakly nonlinear scaling of a system such as $du/dt = -u/R + u^3$ for which $\epsilon \sim R^{-1/2}$. However, there is doubt as to the relevnace of this model as discussed in the next section.

1.3.3 Waleffe-Kim-Hamilton mechanism and $\epsilon \sim R^{-3}$

Waleffe *et al.* (1991) [37] suggested that the Benney-Gustavsson mechanism might in fact be much stronger because of several additional transient amplifications that could occur. They considered the scenario

$$v = \epsilon \longrightarrow \eta \sim \epsilon t \Longrightarrow V \sim (\epsilon^2 t^2)t \longrightarrow N \sim \epsilon^2 t^4 \Longrightarrow v \sim (\epsilon^2 t^4)(\epsilon t)t = \epsilon^3 t^6, \tag{1.40}$$

with feedback thus occurring when $\epsilon \sim \epsilon^3 t^6$ on the time scale $t \sim \epsilon^{-1/3}$ much faster than the Benney-Gustavsson $t \sim \epsilon^{-1/2}$. In essence, Waleffe *et al.* suggested that the dynamics of V and N could not be neglected and that a more powerful mechanism for shear flows might be modeled by

$$\frac{d}{dt}\begin{pmatrix} U \\ V \\ u \\ v \end{pmatrix} = \begin{pmatrix} -\nu k_U^2 & 1 & 0 & 0 \\ 0 & -\nu k_V^2 & 0 & 0 \\ 0 & 0 & -\nu k_u^2 & 1 \\ 0 & 0 & 0 & -\nu k_v^2 \end{pmatrix} \begin{pmatrix} U \\ V \\ u \\ v \end{pmatrix} + \begin{pmatrix} 0 \\ uu \\ 0 \\ uU \end{pmatrix}. \tag{1.41}$$

In this model, u and v represent the amplitudes of horizontal and vertical velocities, respectively, for *oblique* perturbations, $e^{i(\gamma z \pm \alpha x)}$ modes say, while U and V represent horizontal and vertical velocities for spanwise perturbations (x-independent), $e^{i2\gamma z}$ modes. Thus u and U in (1.41) represent the horizontal velocities associated with vertical *vorticity* modes η and N in (1.40) and that scenario corresponds to (1.41) for $\nu = 0$ and initial conditions $v = \epsilon$ with $u = U = V = 0$.

Both v and V lead to linear transient growth of u and U respectively, both from the 'lift-up' of the background laminar shear flow, showing up mathematically with the 1's on the off diagonal in (1.41). The quadratic interaction u^2 does not feedback on v but it forces V corresponding to an $e^{i2\gamma z}$ spanwise mode, which creates a large U and finally the nonlinear interaction uU feeds back on the original v. This yields the transition scenario

$$v = \epsilon \longrightarrow u \sim \epsilon R \Longrightarrow V \sim \epsilon^2 R^3 \longrightarrow U \sim \epsilon^2 R^4 \Longrightarrow v \sim \epsilon^3 R^6 \sim \epsilon, \tag{1.42}$$

and thus a threshold scaling $\epsilon \sim R^{-3}$.

So, is $\epsilon \sim Re^{-3}$, the same scaling as in the naive model (1.35), possible in shear flows?! Waleffe *et al.* [37] investigated these mechanisms using careful analysis of full Navier-Stokes simulations and showed that the nonlinear generation of V came from vv terms not uu, the latter being essentially zero! [37, Fig. 4], thus nonlinear interactions *completely bypassed the linear transient growth* of u that was occurring simultaneously. The forcing of v from uU was not analyzed but is also believed to be insignificant at transitional Reynolds numbers. Thus, the nonlinear forcing of v and V could be, for instance,

$$\frac{d}{dt}\begin{pmatrix} U \\ V \\ u \\ v \end{pmatrix} = \begin{pmatrix} -\nu k_U^2 & 1 & 0 & 0 \\ 0 & -\nu k_V^2 & 0 & 0 \\ 0 & 0 & -\nu k_u^2 & 1 \\ 0 & 0 & 0 & -\nu k_v^2 \end{pmatrix} \begin{pmatrix} U \\ V \\ u \\ v \end{pmatrix} + \begin{pmatrix} 0 \\ vv \\ 0 \\ vV \end{pmatrix}. \tag{1.43}$$

with nonlinearities arising from v and V, not from the transiently amplified u and U. Transient growth of u and U occurs in (1.43) but is *not* involved in transition. System (1.43) has a threshold $\epsilon \sim R^{-1}$ from the scenario

$$v = \epsilon \Longrightarrow V \sim \epsilon^2 R \Longrightarrow v \sim \epsilon^3 Re^2 \sim \epsilon. \tag{1.44}$$

Keeping uU instead of vV for the v forcing would yield a threshold $\epsilon \sim R^{-2}$, while a Uv term would yield $\epsilon \sim R^{-3/2}$.

These observations also negate the Benney-Gustavsson scaling (1.39) since there would be no u^3 but instead perhaps only a v^3 in (1.38), leading back to the weakly nonlinear $\epsilon \sim R^{-1/2}$. Thus, careful analysis of numerical simulations must be made since many linear and nonlinear processes are occurring concurrently in full numerical simulations but they may not have cause and effect connections. *The nonlinear interactions leading to transition could completely bypass the linear transient growth.*

1.3.4 Chapman's viscous correction of the WKH mechanism

Chapman (2002) [8] — apparently unaware of earlier work[3] by Waleffe, Kim and Hamilton [37] on the Benney-Gustavsson mechanism and the self-sustaining process [13, 31, 32, 33, 34, 35]— considered transition scenarios essentially identical to that discussed in section 1.3.3. His toy model (2.6)–(2.9) which reads

$$\frac{d}{dt}\begin{pmatrix}\phi_1\\ \psi_1\\ \phi_2\\ \psi_2\end{pmatrix} = \begin{pmatrix}-\epsilon_c & 1 & 0 & 0\\ 0 & -2\epsilon_c & 0 & 0\\ 0 & 0 & -\delta & 1\\ 0 & 0 & 0 & -2\delta\end{pmatrix}\begin{pmatrix}\phi_1\\ \psi_1\\ \phi_2\\ \psi_2\end{pmatrix} + \begin{pmatrix}0\\ \phi_2^2\\ 0\\ \phi_1\phi_2\end{pmatrix}. \tag{1.45}$$

is essentially identical to model (1.41). The exact correspondence between Chapman's (2.6–9) and (1.41) is

$$(\phi_1, \psi_1, \phi_2, \psi_2) \equiv (U, V, u, v). \tag{1.46}$$

The order of Chapman's variables (ϕ, ψ) has been reversed from his (2.6)–(2.9) to match (1.41) and the double Jordan block-like structure.

Unfortunately, Chapman uses 'ϵ' for the viscous decay rate of the streaks $\phi_1 \equiv U$, which we call νk_U^2, while we have used ϵ for perturbation amplitude, so we use ϵ_c for his ϵ to distinguish from ours. He uses δ for our νk_u^2. He assumes that $k_V^2 = 2k_U^2$ and $k_v^2 = 2k_u^2$, but this is inconsequential for our questions of threshold scalings and mechanisms.

Chapman correctly includes the possibility that the viscous decay rates of streamwise-independent (his ϵ_c) and oblique modes (his δ, with $0 < \epsilon_c \ll \delta \ll 1$) scale differently with R, while we assumed[4] in section 1.3.3 that both scale like R^{-1}. The stronger decay rate represented by Chapman's $\delta \gg \epsilon_c$ arises from the critical layer structure of oblique eigenmodes of the linearized operators. That critical layer structure has a scale of $O(R^{-1/3})$

[3] An obvious failure of the JFM review process

[4] In the original Benney-Gustavsson and Waleffe *et al.* work, the focus was on nonlinear time scales in the $R \to \infty$ limit as discussed in sections 1.1.4, 1.3.2, 1.3.3.

thus the effective wavenumbers k_u and k_v for oblique linear eigenmodes in (1.41) are both $O(R^{1/3})$ and $\delta = \nu k_u^2 \sim R^{-1}R^{2/3} = R^{-1/3}$.

The two time scales ϵ_c^{-1} and δ^{-1} in Chapman's model lead to two different scenarios with different scalings. His scenario (i) has $\psi_1 \equiv V$ transiently amplifying $\phi_1 \equiv U$ to an amplitude $1/\epsilon_c \equiv R/k_U^2$. That in itself will not trigger transition since it is obvious in (1.41), (1.45) that the nonlinear term vanishes identically if $\phi_2 \equiv u = 0$. The idea is that $\phi_1 \equiv U$ leads to an instability of the oblique modes $\phi_2 \equiv u, \psi_2 \equiv v$. To illustrate this and obtain the scaling we can rewrite Chapman's (2.8), (2.9), the ϕ_2 and ψ_2 equations in (1.45), in the matrix form

$$\frac{d}{dt}\begin{pmatrix}\phi_2\\ \psi_2\end{pmatrix} = \begin{pmatrix}-\delta & 1\\ \phi_1 & -2\delta\end{pmatrix}\begin{pmatrix}\phi_2\\ \psi_2\end{pmatrix} \tag{1.47}$$

where $\delta > 0$ and this readily suggests that if $\phi_1 \gtrsim 2\delta^2$ there might be growth of ϕ_2 and ψ_2 that might be interpreted as an instability of the 'streaks' $\phi_1 \equiv U$. A *streak instability* is a key part of the *self-sustaining process* discussed in sections 1.3.6, 1.3.7 below, and during a decade before Chapman's work [37, 13, 31, 32, 33, 34, 35], but what we have here is not quite a 'streak instability', it is an instability of the laminar shear (the 1 in the top right corner of the matrix in (1.47)) coupled with the streak amplitude $\phi_1 \equiv U$. A streak instability would have $\phi_1 \equiv U$ in *both* off-diagonal elements as in [33, eqns. (13)-(15)] and an inviscid ($\delta = 0$) growth rate of U, instead of $\sqrt{U} \equiv \sqrt{\phi_1}$ as in (1.47).

Since ψ_1 amplifies ϕ_1 to $\phi_1 \sim \psi_1/\epsilon_c$, we can therefore conclude with Chapman that something similar to a 'streak instability' might occur if $\phi_1 \sim \psi_1/\epsilon_c \gtrsim \delta^2$. This growth would be on the $1/\delta$ time scale, much faster than the slower $1/\epsilon_c$ time scale. Scenario (i) therefore is

$$\psi_1 \longrightarrow \phi_1 \sim \frac{1}{\epsilon_c}\psi_1 \rightsquigarrow \psi_2, \phi_2 \Longrightarrow \psi_1 \quad \text{if} \quad \psi_1 \gtrsim \epsilon_c\delta^2. \tag{1.48}$$

where '$\longrightarrow$', '$\rightsquigarrow$' and '$\Longrightarrow$' denote linear amplification, instability and nonlinear feedback, respectively. If $\epsilon_c \sim R^{-1}$ and $\delta \sim R^{-1}$ this would yield a $\psi_1 \sim R^{-3}$ threshold as in (1.42), but if $\delta \sim R^{-1/3}$ as for oblique linear modes in shear flows, then the threshold would be $\psi_1 \sim R^{-5/3}$.

Chapman's scenario (ii) begins with the oblique rolls, $\psi_2 \equiv v$ that linearly amplify $\phi_2 \equiv u$ which quadratically forces $\psi_1 \equiv V$ that linearly amplifies $\phi_1 \equiv U$ and the quadratic interaction $\phi_1\phi_2 \equiv Uu$, at last, feeds back onto the original $\psi_2 \equiv v$. But there is a catch! now the initial transient growth of ϕ_2 occurs (and peaks) on the faster time scale $1/\delta$ and ψ_1 only reaches $\sim \phi_2/\delta$ on that time scale. Diagrammatically,

$$\psi_2 \longrightarrow \phi_2 \sim \frac{1}{\delta}\psi_2 \Longrightarrow \psi_1 \sim \frac{1}{\delta}\phi_2^2 \longrightarrow \phi_1 \sim \frac{1}{\epsilon_c}\psi_1 \Longrightarrow \psi_2 \sim \frac{1}{\delta}\phi_1\phi_2 \tag{1.49}$$

putting it all together yields $\psi_2 \sim \psi_2^3/(\epsilon_c\delta^5)$ and the threshold scaling $\psi_2 \sim \epsilon_c^{1/2}\delta^{5/2}$ [8, Fig. 3]. For $\epsilon_c \sim R^{-1}$ and $\delta \sim R^{-1}$, the threshold would be $\psi_2 \sim R^{-3}$ as in (1.42), but for $\delta \sim R^{-1/3}$ the threshold would be $\psi_2 \sim R^{-4/3}$.

This is all very well, however a key problem is that it is built on the *assumption* that the quadratic interactions uu and Uu of the transiently amplified disturbances, $U \equiv \phi_1$ and $u \equiv \phi_2$ are the dominant nonlinear interactions, as in the naive model (1.35), the Benney-Gustavsson model (1.38) and the Waleffe, Kim & Hamilton model (1.41). Those nonlinear terms appear to be almost non-existent according to the numerical analysis of

[37] as discussed in the previous section, so these transition scenarios and thresholds are likely to not be the effective scenarios for Navier-Stokes.

1.3.5 Nonlinear saturation of linear transient growth and '$\epsilon = \infty$'

Transient amplification by a factor of R only occurs for streamwise x independent perturbations, $\partial/\partial x = 0$, but nonlinear feedback does *not* occur for such disturbances. In fact, x-independent perturbations form an *invariant manifold for shear flows for which the laminar flow is the global attractor*, that is, x-independent perturbations stay x-independent and the cross-stream velocities v, w decouple from the transiently amplified streamwise velocity u, thus v, w decay viscously and u eventually returns to zero. This was proved by Joseph and Tao in 1963 [17], see also [16]. The proof is straightforward. Consider (1.20) with $\partial/\partial x = 0$, then $\mathbf{u} \cdot \nabla = v\partial_y + w\partial_z$ and v and w decouple from u, then multiply the v equation by v, the w equation by w, add the resulting equations and integrate over the cross-section. Integration by parts and the boundary conditions eliminate the advection and pressure terms and we are left with

$$\frac{d}{dt}\int_A \frac{v^2+w^2}{2}\, dA = -\frac{1}{R}\int_A \left(|\nabla v|^2 + |\nabla w|^2\right) dA \;\leq 0 \tag{1.50}$$

where A is the flow cross-section and dA is its area element. Thus v and $w \to 0$ and in that limit the u equation becomes a simple heat equation and $u \to 0$ also. This is a fully nonlinear result but only for x-independent perturbations. There is transient growth of u but no nonlinear feedback on v.

The primary nonlinear effect, in fact, is to *reduce the transient growth of u by reducing the background shear*. A model for streamwise independent perturbations in a shear flow, more physical than (1.29), is then [31]

$$\frac{d}{dt}\begin{pmatrix} S \\ U \\ V \end{pmatrix} = \begin{pmatrix} -\nu k_S^2 & 0 & 0 \\ 0 & -\nu k_U^2 & 1 \\ 0 & 0 & -\nu k_V^2 \end{pmatrix}\begin{pmatrix} S \\ U \\ V \end{pmatrix} + \begin{pmatrix} -UV \\ SV \\ 0 \end{pmatrix} \tag{1.51}$$

for which $S = U = V = 0$ is the global attractor since $V \to 0$, then U and S also $\to 0$.

In model (1.51), V induces transient growth of U that leads to $-UV < 0$ that creates $S < 0$ which reduces the forcing of U from V to $(1+S)V < V$, but there is no transition since there is no feedback on V. S models the perturbation of the mean shear so that the total mean shear is $M = 1 + S$. The nonlinearity creates a 'Reynolds stress', $-UV$, that reduces the shear from 1 to $M = 1 + S < 1$ and the 'lift-up' term creating U is then $(1+S)V = MV$ instead of V.

Note that the nonlinearity is energy conserving and

$$\frac{1}{2}\frac{d}{dt}\left(S^2 + U^2 + V^2\right) = UV - \nu\left(k_S^2 S^2 + k_U^2 U^2 + k_V^2 V^2\right) \tag{1.52}$$

which is entirely analogous to the perturbation energy equation in shear flows[5]

$$\frac{1}{2}\frac{d}{dt}\int_V |\mathbf{u}|^2 dV = \int_V -uv\frac{dU}{dy}dV - \nu\int_V |\nabla\mathbf{u}|^2 dV. \tag{1.53}$$

The latter is obtained by dotting the full perturbation equations (1.20) with $\mathbf{u}$ and integrating by parts over a volume V with periodic or vanishing perturbations on its boundary.[9, §53]

The S equation in (1.51) is inspired by the mean flow equation, that is, let $\mathbf{v} = U(y)\hat{\mathbf{x}} + \mathbf{u} = U(y)\hat{\mathbf{x}} + \bar{u}(y,t)\hat{\mathbf{x}} + \tilde{\mathbf{u}}$ where $U(y)\hat{\mathbf{x}}$ is the laminar flow and $\bar{u}(y,t)\hat{\mathbf{x}}$ is the average of $\mathbf{u}$ over x and z with $\tilde{\mathbf{u}}$ the remaining fluctuating part. Averaging the x component of the Navier-Stokes equations (1.3) yields the mean flow perturbation equation

$$\partial_t \bar{u} = -\partial_y \overline{\tilde{u}\tilde{v}} + \nu\partial_y^2 \bar{u}, \tag{1.54}$$

which leads to the S equation in (1.51) if we assume a reasonable shape for $\overline{\tilde{u}\tilde{v}}$, say $\cos^2(\pi y/2)$ with s being the amplitude of a $\pi^{-1}\sin\pi y$ shape for $\bar{u}(y,t)$, for instance.

This is only a justification for the model, not a derivation, but (1.51) does capture the 'fully nonlinear' physics of streamwise independent shear flows. The model is in fact linear since V is decoupled from S and U. Model (1.51) captures the full physics of *redistribution of streamwise velocity*, $(1+S)V$ in the U equation together with $-UV$ in the S equation, not simply the linearized *lift-up* which is merely the V term in the U equation. Substituting $S = M - 1$ in (1.51) yields

$$\frac{dM}{dt} = \nu k_S^2(1-M) - UV, \qquad \frac{dU}{dt} = -\nu k_U^2 U + MV, \qquad \frac{dV}{dt} = -\nu k_V^2 V \tag{1.55}$$

which is the viscous version of system (1.24).

1.3.6 SSP and $\epsilon \sim R^{-3/2}$, R^{-2}

Waleffe [30] proposed a different mechanism — the Self-Sustaining Process (SSP)— that was later developed in a series of papers [37, 13, 31, 33], culminating in the construction of 'exact coherent states' for the full 3D Navier-Stokes equations [34, 35, 36]. The self-sustaining process was inspired by work of Benney (1984) [5] and experiments of Acarlar and Smith (1987) [1]. This process can be illustrated by a low order model that begins with the good model of x-independent dynamics (1.51), with x-independent modes S, U, V. We know from sect. 1.3.5 that such x-independent mean flows cannot be self-sustained, so we need an x-dependent fluctuation to obtain a self-sustaining process. Call that fluctuation w for 'wave' and assume that it has a simple $e^{i\alpha x}$ form in x, with w^* the amplitude of $e^{-i\alpha x}$ since the total flow must be real. The model is [31, 32]

$$\frac{d}{dt}\begin{pmatrix} S \\ U \\ V \\ w \end{pmatrix} = \begin{pmatrix} -\nu k_S^2 & 0 & 0 & 0 \\ 0 & -\nu k_U^2 & 1 & 0 \\ 0 & 0 & -\nu k_V^2 & 0 \\ 0 & 0 & 0 & -\nu k_w^2 \end{pmatrix}\begin{pmatrix} S \\ U \\ V \\ w \end{pmatrix} + \begin{pmatrix} -UV \\ SV - ww^* \\ ww^* \\ Uw - Vw \end{pmatrix}. \tag{1.56}$$

[5]Note that there is a sign difference between the hydrodynamics (1.22) and our models since $uv < 0$ from 'lift-up' for $dU/dy > 0$ but our models have $UV > 0$ (these U's are the forced response from V). This is only a difference in definition that can be removed by defining the flow so that $dU/dy < 0$ or considering that the V in our models in fact corresponds to $-V$ and 'pull-down' in the hydrodynamics.

This is model (1.51) with an extra w equation and a series of nonlinear interactions associated with w. The model reduces to (1.51) when $w = 0$, *i.e.* when the flow is x-independent.

This model contains not just the 'lift-up' of background laminar shear — the '1' in the row U, column V of the matrix — but the complete *redistribution* of the mean shear $M = 1+S$ by V that necessarily comes with the reduction of the mean shear $M = 1+S < 1$ by the Reynolds stress $-UV$. This redistribution leads to the formation of large x-independent streamwise velocity fluctuations U whose nonlinear self-interactions U^2 are non-existent (unlike models (1.35, 1.38, 1.41)) but that may be unstable to an x-dependent $e^{i\alpha x}$ 'wave' of amplitude w. The nonlinear interaction ww^* of that mode with its complex conjugate $e^{-i\alpha x}$ yields a *negative feedback* on U, since the latter provides the energy source for w, but also a *positive feedback* on V. The latter comes with a negative feedback on w and the nonlinear term is energy conserving so the energy equation for (5.32) is

$$\frac{1}{2}\frac{d}{dt}\left(S^2 + U^2 + W^2 + w^2\right) = UV - \nu\left(k_S^2 S^2 + k_U^2 U^2 + k_V^2 V^2 + k_w^2 w^2\right) \tag{1.57}$$

again entirely analogous to the hydrodynamic equivalent (1.53).

This mechanism is more complex and involves more physical steps. Models (1.35, 1.38, 1.41) are all essentially 2-steps: linear transient amplification of ϵ into ϵR followed by quadratic interactions of the transiently amplified perturbation yielding *presumed* feedback onto ϵ. Model (5.32) involves redistribution of mean shear and therefore 'nonlinear' reduction of mean shear, with exponential instability of transiently amplified fluctuations and various quadratic interactions of the latter growing mode leading to self-sustenance. We call it a *process* — the *self-sustaining process* — since it involves more steps.

Transition will not happen if $w \equiv 0$ in (5.32) since w will stay zero and the model then reduces to (1.51) which will always decay to $S = U = V = 0$. The transition scenario based on this process is not as straightforward because the w equation is linear in w and does not directly determine its amplitude. The V, U and S equations yield, respectively,

$$V \sim w^2 R, \qquad U \sim (1+S)w^2R^2 - w^2 R, \qquad S \sim -Uw^2R^2. \tag{1.58}$$

This mean shear reduction $S < 0$ must not shut down production of U, so we need $(1+S)V \gtrsim w^2 + U/R$ and substituting for S and V from (1.58) this requires $w^2R^2 \gtrsim (1 + w^4R^4)U$ to sustain U. We also need $U - V - \nu k_w^2 \gtrsim 0$ to sustain w and since $V \sim w^2R$ and $\nu = 1/R$ that requires $U \gtrsim (1 + w^2R^2)/R$. Sustenance of U and w thus requires

$$\frac{1 + w^2R^2}{R} \lesssim U \lesssim \frac{w^2R^2}{1 + w^4R^4} \tag{1.59}$$

which, in the limits $w\,R \ll 1$ and $w\,R \gg 1$, yields

$$R^{-3/2} \lesssim w \lesssim R^{-3/4}. \tag{1.60}$$

This would suggest a threshold exponent $a = -3/2$ in (1.9) with the transition scenario

$$w \sim R^{-3/2} \Longrightarrow V \sim R^{-2} \longrightarrow U \sim R^{-1},\, S \sim R^{-2} \rightsquigarrow w, \tag{1.61}$$

although we can also imagine the scenario

$$V \sim R^{-2} \longrightarrow U \sim R^{-1},\, S \sim R^{-2} \rightsquigarrow w \sim R^{-3/2} \Longrightarrow V \sim R^{-2} \tag{1.62}$$

where w arises from an instability of U and quickly grows to $w \sim R^{-3/2}$ to sustain the original V perturbation. This closely related scenario would have a threshold exponent $a = -2$ in (1.9) as discussed in [3].

These (1.61), (1.62) are the scalings of *lower branch* steady states for (5.32) as given in [33, eqn. (24)]. The *upper branch* steady state for (5.32) pushes against the upper bound of (1.60) and has the scaling $w \sim R^{-3/4}$, $V \sim R^{-1/2}$, $U \sim R^{-1/2}$, $(1+S) \sim R^{-1}$ as given in [32, 33].

1.3.7 Derived SSP and $\epsilon \sim R^{-1}$

Model (5.32) was first presented at a Center for Turbulence Research seminar in 1990 but did not trigger much interest among engineers heavily involved into cutting-edge high resolution 3D numerical simulations of turbulent flows. The model did not appear in print until 1995 [31], prompted by the publication of models similar to (1.35) in TTRD [29]. Many simple models were proposed and analyzed in the mid 1990's [3], but few had any direct connection with the Navier-Stokes equations. A derivation of (5.32) from the Navier-Stokes equations was therefore attempted by Galerkin truncation as in the derivation of the well-known Lorenz-Saltzmann model of convection and chaos.

That derivation showed that a key interaction is missing in (5.32), there should be a $-(1+S)w \equiv -Mw$ term in the w equation arising from the differential advection of that x-dependent mode by the mean shear $M = 1+S$ (modes A, B, C, D, E in [33, eqn. (10)] are coupled through M). For small S this is a large extra damping for w that has a direct impact on the transition threshold question. Thus the model should be

$$\frac{d}{dt}\begin{pmatrix} S \\ U \\ V \\ w \end{pmatrix} = \begin{pmatrix} -\nu k_S^2 & 0 & 0 & 0 \\ 0 & -\nu k_U^2 & 1 & 0 \\ 0 & 0 & -\nu k_V^2 & 0 \\ 0 & 0 & 0 & -\nu k_w^2 \end{pmatrix} \begin{pmatrix} S \\ U \\ V \\ w \end{pmatrix} + \begin{pmatrix} -UV + ww^* \\ SV - ww^* \\ ww^* \\ Uw - Vw - (1+S)w \end{pmatrix} \tag{1.63}$$

which is (5.32) with an extra $+ww^*$ in the S equation and an extra $-(1+S)w$ in the w-equation. The energy equation is still (1.57) since we have merely added *redistribution* terms that exchange energy between S and w but do not change the total energy. That last term in the w equation now includes a linear term, $-w$, and it is better therefore to rewrite the model in terms of the total mean shear $M = (1+S)$, instead of the perturbation from laminar shear S, in which case (1.63) becomes

$$\frac{d}{dt}\begin{pmatrix} M \\ U \\ V \\ w \end{pmatrix} = \begin{pmatrix} -\nu k_S^2\, M \\ -\nu k_U^2\, U \\ -\nu k_V^2\, V \\ -\nu k_w^2\, w \end{pmatrix} + \begin{pmatrix} -UV + ww^* \\ MV - ww^* \\ ww^* \\ (U - V - M)w \end{pmatrix} + \begin{pmatrix} \nu k_S^2 \\ 0 \\ 0 \\ 0 \end{pmatrix}. \tag{1.64}$$

The '1' in row U, column V of the linear coupling matrix in (1.63) has disappeared, it has been absorbed in the nonlinear term MV in the U equation in (6.11). The remaining matrix is now 'normal,' in fact it is diagonal and has been multiplied with the state vector. The full nonlinear term is energy conserving as in the Navier-Stokes equations, and a forcing

has appeared to maintain the mean shear. Again, (6.11) is simply (1.63) with the change of variable $S = M - 1$. The laminar solution is $M = 1$, $U = V = w = 0$. The total energy equation reads

$$\frac{1}{2}\frac{d}{dt}\left(M^2 + U^2 + V^2 + w^2\right) = \nu k_S^2(1 - M) - \nu\left(k_U^2 U^2 + k_V^2 V^2 + k_w^2 w^2\right) \tag{1.65}$$

in lieu of (1.57). This energy equation shows that the total energy decays if $M > 1$, in other words $M < 1$ for transition.

As in model (5.32), transition will not happen if $w = 0$ and determining the amplitude of w requires more delicate analysis. There are several cancellations and to keep track of them clearly it is better to label each interaction with distinct coefficients as in [33, eqn, (20)], but here we label only the (M, w) interaction for simplicity. Let $\sigma_m > 0$ be the coefficient of interaction between M and w, so $ww^* \to \sigma_m ww^*$ in the M equation and $-Mw \to -\sigma_m Mw$ in the w-equation. The V, U and M equations yield the scalings

$$V \sim w^2 R, \qquad U \sim Mw^2R^2 - w^2R, \qquad M \sim 1 + \sigma_m w^2 R - Uw^2R^2 \tag{1.66}$$

instead of (1.58). Production of U requires $MV \gtrsim k_u^2 U/R + ww^*$ and production of w requires $U \gtrsim \sigma_m M + V + k_w^2/R$. Substituting for M and V from (1.66) into these inequalities gives, respectively,

$$(1 + \sigma_m w^2 R)w^2R^2 - w^2R \gtrsim (1 + w^4R^4)\, U, \tag{1.67}$$

and

$$(1 + \sigma_m w^2R^2)\, U \gtrsim \sigma_m + \sigma_m^2 w^2 R + w^2 R + \frac{1}{R}. \tag{1.68}$$

Eliminating U between those two inequalities gives

$$(1 + \sigma_m w^2R^2)\left((1 + \sigma_m w^2R)w^2R^2 - w^2R\right) \gtrsim (1 + w^4R^4)\left(\sigma_m + \sigma_m^2 w^2 R + w^2 R + \frac{1}{R}\right), \tag{1.69}$$

yielding

$$R\,X \;\gtrsim\; \sigma_m R + 1 + (\sigma_m^2 + 1)X + X^2 + X^3 \tag{1.70}$$

where $X \equiv w^2R^2$. This is related to the fixed point equation in [33, eqn. (21)] but all constants have been set to 1, except for σ_m to help keep track of cancellations that occurred in deriving this inequality. The 1 has been kept on the right hand side of (1.70) so that the inequality reduces to (1.59) when $\sigma_m = 0$. The bounds on w follow from investigating the two extremes $X \ll 1$ and $X \gg 1$. For $X \ll 1$ and $R \gg 1$, inequality (1.70) reduces to $\sigma_m \lesssim X$ so the smallest $X \sim 1$, not $X \ll 1$. For $X \gg 1$ the inequality reduces to $X^3 \lesssim R\,X$ and since $X \equiv w^2R^2$ these two limits provide the bounds on w

$$R^{-1} \lesssim w \lesssim R^{-3/4}, \tag{1.71}$$

suggesting that $a = -1$ in (1.9). The transition scenario would be

$$w \sim R^{-1} \Longrightarrow V \sim R^{-1} \longrightarrow U \sim M < 1 \;\rightsquigarrow w \tag{1.72}$$

or

$$V \sim R^{-1} \longrightarrow U \sim M < 1 \;\rightsquigarrow w \sim R^{-1} \Longrightarrow V \sim R^{-1} \tag{1.73}$$

with w quickly growing to $w \sim R^{-1}$ from the instability of U in the latter case. In either case, this gives $\epsilon \sim R^{-1}$ for the transition threshold.

Again these (1.72), (1.73) are the scalings of the lower branch steady solution [33, eqn. (23)] for model (6.11), while the upper limit of (1.71) yields the scaling of the upper branch steady solution [32, 33], that is $w \sim R^{-3/4}$, $V \sim R^{-1/2}$, $U \sim R^{-1/2}$, $M \sim R^{-1}$.

1.3.8 Summary of transition models and threshold scalings

The transient growth models (1.35), (1.38), (1.41), (1.43), (1.45) show transition thresholds ranging from $\epsilon \sim R^{-3}$ to $\epsilon \sim R^{-1}$, depending on which *nonlinear* interactions do or do not actually occur. The smallest thresholds and most negative exponents correspond to models that *assume* the 'nonlinear recycling' of transiently amplified disturbances into 'optimal' disturbances, but this has not been explicitly demonstrated in the Navier-Stokes equations. On the contrary, long ago, Waleffe, Kim & Hamilton [37] presented evidence suggesting that such nonlinear interactions are nil to negligible. Yet Chapman's later work [8] still assumes but does not demonstrate the predominance of those same nonlinear interactions of transiently amplified disturbances. His threshold scaling predictions are thus wanting.

Those transient growth models (1.35), (1.38), (1.41), (1.45) are all *weakly nonlinear* in the sense that the mean shear stays at its laminar value of 1 and the perturbations essentially consist of interacting eigenmodes of the linearized Navier-Stokes equations, *i.e.* eigenmodes of the Orr-Sommerfeld and Squire equations. Indeed, much of Chapman's analysis [8, §5] centers on estimating the *eigenvalues* of these linear operators in spite of the emphasis on non-normal algebraic growth. The models (1.41), (1.45) are superficially similar to the SSP model (6.11), they are 4th order with quadratic nonlinearity, and they *assume* an interaction $Uu \equiv \phi_1\phi_2$ in the v equation that superficially appears to be a 'streak instability' when coupled with the v term in the u equation (sect. 1.3.4). However, the models (1.41), (1.45) are not actually models of transition since the mean shear remains at its laminar value 1 and the Uu term would be the weak nonlinear interaction of Squire modes (eigenmodes of the vertical vorticity η equation linearized about the laminar flow) instead of a real streak instability with its own eigenmodes.

So far, the only model that stands up to closer analysis of the Navier-Stokes nonlinearities is the SSP (sect. 1.3.7) with its $\epsilon \sim R^{-1}$ scaling. In the SSP model (6.11), the mean shear M provides the energy source for U through V but tends to destroy w that regenerates V. For transition in that model, the mean shear M must be reduced from its laminar value of 1 and the streaks U must be $O(1)$, in that sense, it is a fully nonlinear model as indicated by the $\epsilon \sim R^{-1}$ threshold scaling. In the SSP, w corresponds to an eigenmode of a spanwise varying streaky flow $(U(y,z),0,0)$, not of the laminar flow [31, 33, 34, 36]. This strong nonlinearity is reflected in our model building that started from a linear system with a Jordan block-like structure in (1.18) but ended with a system (6.11) with multiple energy-conserving nonlinear redistribution terms where the Jordan-block structure is not anymore a relevant point of view, it is now all about nonlinear interactions, and determination of the threshold scaling is more involved because of the stronger nonlinearity. We have gone from a *non-normal linear* system to a *normal nonlinear* system [32].

Finally, a point often overlooked in the discussion of transition processes is that the very existence of a *threshold* is closely connected with the existence of *unstable nonlinear states*. This is already clear in the subcritical logistic equation (1.14) $\dot{u} = -u/R + u^2$ where the threshold $u = 1/R$ *is* an unstable steady state. In the SSP model (6.11) the threshold is not identical to the 'lower branch' steady state but the transition scenario (1.72) is closely connected to it. The existence of fully resolved 3D nonlinear lower branch steady states with the proper scaling in plane Couette flow (fig. 1.7) indicates that the threshold $\epsilon \sim R^{-1}$ is indeed relevant for transition in the full Navier-Stokes equations. Indeed, all aspects of the SSP, (1) the creation of streaks together with mean shear reduction, (2) the streak instability and (3) the direct nonlinear feedback from that instability onto the x-independent rolls (often called 'streamwise rolls'), have been explicitly verified for the fully resolved Navier-Stokes equations [33, 34, 36]. The SSP model (6.11), albeit simplistic, faithfully captures the essence of a process that appears to be fundamental for transition *and* turbulence in shear flows and that has been fully vetted through the construction of fully resolved unstable nonlinear states in the Navier-Stokes equations, not just in low order models (figs. 1.7,1.8).

1.4 Transition threshold: experiments

Figure 1.9 is from Hof, Juel & Mullin (2003) [14] and shows a threshold amplitude scaling like R^{-1} for transition to turbulence in a pipe. The disturbance consists of one pulse of fluid injected tangentially through 6 equispaced holes of 0.5mm in a long pipe (15.7m) with a 20mm diameter. The transition amplitude is independent of the duration Δt of the injection provided it is long enough, that is provided the length $\ell = U\Delta t$ is greater than about 3 diameters, where U is the bulk velocity. The amplitude $\epsilon = \Phi_{inj}/\Phi_{pipe}$ is measured as the ratio of the disturbance mass flux to the pipe mass flux where Φ = velocity $\times$ area, and the Reynolds number is based on the bulk velocity and pipe diameter. The data is very well fitted by a power law $\epsilon \sim R^{-1}$. Other disturbances have since been used such as normal jets as well as fewer jets [21].

From the SSP point of view (Sect. 1.3.7), we may interpret these experiments as introducing streamwise[6] rolls V, sufficiently large in scale and amplitude and sufficiently long to develop streaks U that can be unstable. The streak instability is inflectional in nature and requires sufficiently small streamwise wavenumbers α. In practice we expect spanwise scales of the order of the pipe radius and streamwise scales about 2 to 3 times larger than that as discussed in SSP papers [31, 33, 36]. However the jets obviously introduce a range of scales from the 0.5mm holes to the pipe diameter 20mm so there is complex transient fluid behavior.

Figure 1.10 shows more recent data in pipe flow. The Re^{-1} line on that plot is a fit to various data sets (not shown) corresponding to perturbations in the form of jets (one or more) through the pipe wall as in fig. (1.9). A second set of data is also shown for 'push-pull' disturbances, where fluid is injected and sucked from two neighboring holes with no net injected mass flux. That second set of data shows a $R^{-1.4}$ scaling. That scaling is associated

[6] 'Streamwise rolls' have their axis in the streamwise direction, hence they are streamwise independent. Their wavenumber is actually spanwise.

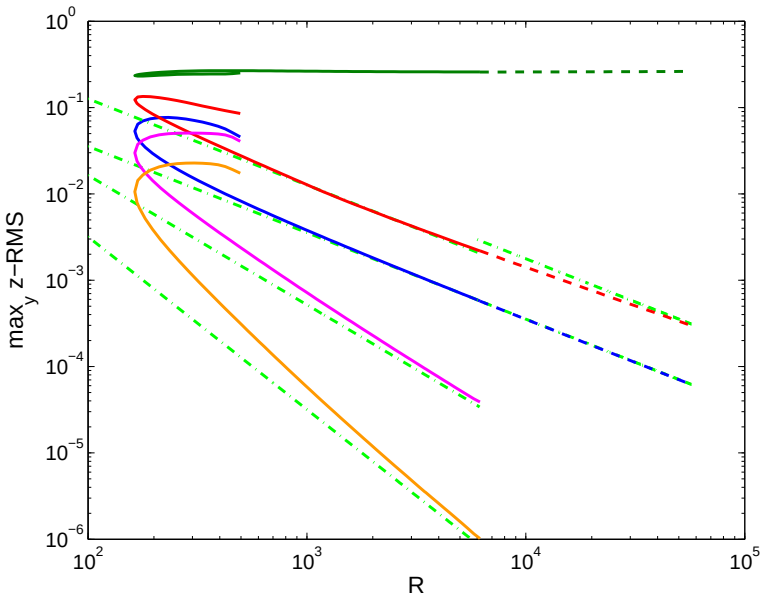

Figure 1.7: Scaling of 3D unstable lower branch steady solutions of the Navier-Stokes equations in plane Couette flow (see Wang, Gibson & Waleffe [38]). The streaks U (top green curve) are $O(1)$, independent of R. The rolls V scale like R^{-1} (blue curve, 3rd from top), the fundamental wave $e^{i\alpha x}$ corresponding to w in the SSP model (6.11) scales like $R^{-11/12}$ in this norm, slightly weaker than R^{-1} because of a critical layer structure (red curve, 2nd from top). The bottom two curves (purple and orange) correspond to the 2nd and 3rd x harmonics, $e^{i2\alpha x}$ and $e^{i3\alpha x}$, respectively. All harmonics are negligible for $R \gtrsim 6\,000$ and the solution is continued up to $R \approx 60\,000$ without them. The Reynolds number is based on the half channel height and the half wall velocity difference and this definition yields a Reynolds number that is about 4 times smaller than the typical pipe flow Reynolds number. In other words, this plane Couette $R = 60\,000$ corresponds to $Re \approx 240\,000$ in pipe flow.

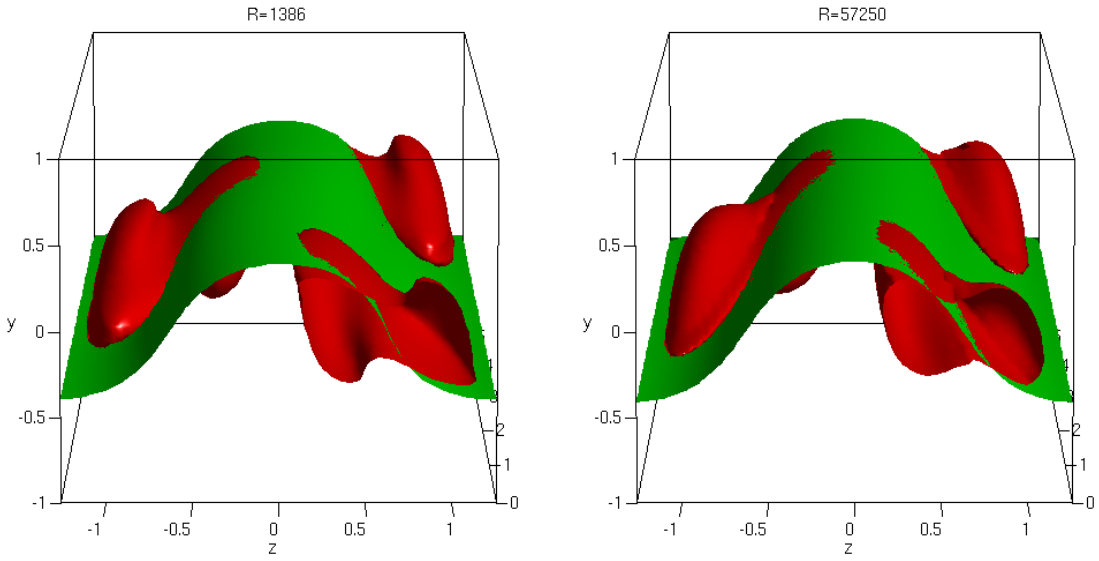

Figure 1.8: Visualization of the plane Couette flow lower branch steady state at $R = 1386$ (left) and $R = 57250$ (right) [38] whose scaling is shown in figure 1.7. The flow is in the x direction (in and out of the page) and the total streamwise velocity $u = \hat{\mathbf{x}} \cdot \mathbf{v} = 1$ at $y = 1$ and $u = -1$ at $y = -1$. The green isosurface is $u = 0$ and would be a flat sheet at $y = 0$ for the laminar flow but here it is warped with an $O(1)$ deformation as a result of the $O(1)$ streaks U in (6.11) and the $O(1)$ reduction of the mean shear M in (6.11). The red isosurfaces are the level set $Q = 0.6 \max(Q)$ where $2Q = \nabla^2 p = \Omega_{ij}\Omega_{ij} - S_{ij}S_{ij}$ (see eqn. (1.4)), a standard but crude attempt to visualize vortices. These red isosurfaces correspond to a combination of the streamwise rolls and the fundamental wave, the 2nd and 3rd curves from the top in fig. 1.7 and have small magnitude. Note that the two figures are almost identical in spite of the huge difference in Reynolds number.

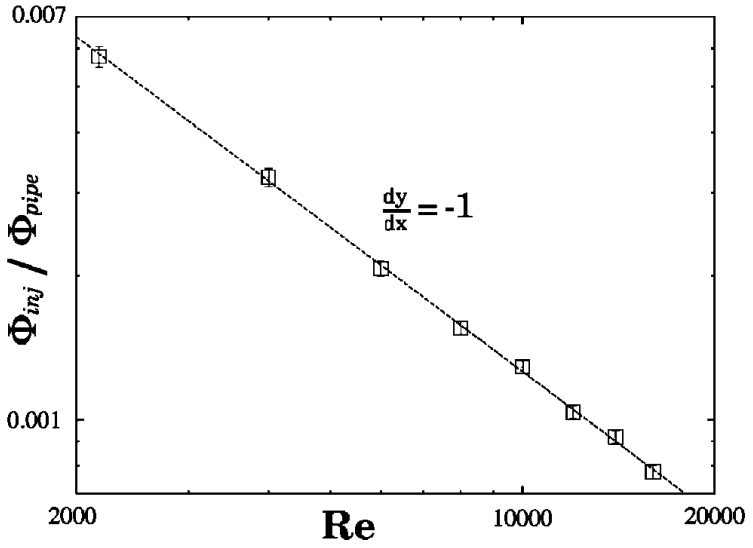

Figure 1.9: Transition threshold in pipe flow scaling as R^{-1}, from [14].

with the development of trains of hairpin/horseshoe vortices before transition to turbulence, in contrast to the R^{-1} disturbances that led to an abrupt transition. An example of the development of hairpin vortices is shown in figure 1.11. 'Hairpin' and 'horsehoe' are used to describe similar vortex structures. The term 'hairpin' is often used for small structures, especially those observed in turbulent shear flows, and 'horseshoe' for larger structures, although this is qualitative and subjective, there is no precise definition of the structures associated with those terms.

The development of these hairpin structures is a transient effect but one should be careful not to quickly associate it with the linear transient growth of non-normal operators. The latter is associated in this context with the linearization of the Navier-Stokes equations about a laminar shear flow $\mathbf{v} = U(y)\hat{\mathbf{x}}$. The linearized equations are separable in the cross-flow coordinates x and z and time t. The result is a set of *dispersive* Fourier modes, $\hat{\mathbf{u}}(y)e^{i(\alpha x+\gamma z-\omega t)}$, that are not orthogonal, but do form a complete set. Each of these modes evolves and travels independently of the other modes and it is quite unlikely that linear evolution of such modes captures the highly coherent development of hairpin vortices shown in fig. 1.11. The development of hairpin vortices is undoubtedly a *nonlinear process* leading to such highly coherent structures formed from the roll-up and stretching of vortex sheets.

1.4.1 Theodorsen's horseshoes

Horseshoe vortices in turbulent shear flows were predicted in the 1950's by Theodorsen who suggested that they were the 'molecules' of [shear] turbulence [27, 28] and drew the sketch shown in figure 1.12. He based his prediction of horseshoe vortices on an analysis of the vorticity equation, the curl of the Navier-Stokes equations (1.3)

$$\partial_t \boldsymbol{\omega} + \mathbf{v} \cdot \nabla \boldsymbol{\omega} = \boldsymbol{\omega} \cdot \nabla \mathbf{v} + \nu \nabla^2 \boldsymbol{\omega} \tag{1.74}$$

where $\boldsymbol{\omega} = \nabla \times \mathbf{v}$ is the curl of the velocity $\mathbf{v}$, thus $\nabla \cdot \boldsymbol{\omega} = 0$.

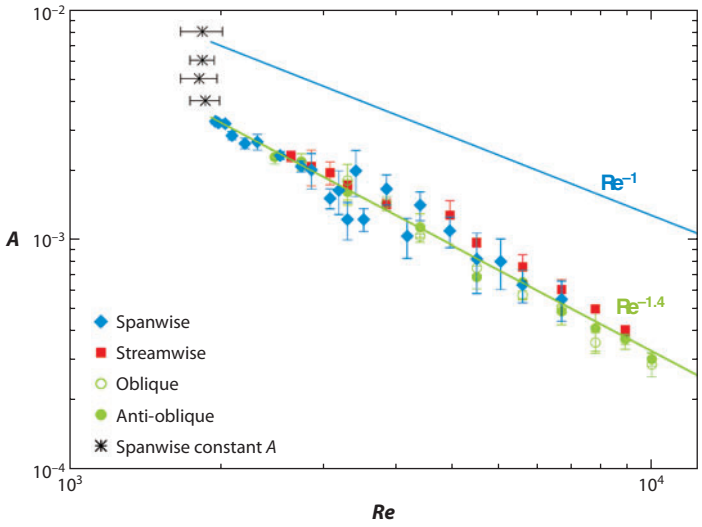

Figure 1.10: Transition threshold in pipe flow from [21, 22]. Here Re is the Reynolds number based on bulk velocity and pipe diameter and A is the threshold amplitude defined as the mass flux of the disturbance normalized by the mass flux in the pipe. The Re^{-1} line is a fit to various data sets (not shown on this figure) corresponding to perturbations in the form of jets (one or more) through the pipe wall [22, Fig. 3]. The lower data sets correspond to smaller scale 'push-pull' disturbances, with the push-pull axis oriented in various ways (spanwise, streamwise, etc.), and that data is fitted by a $Re^{-1.4}$ line.

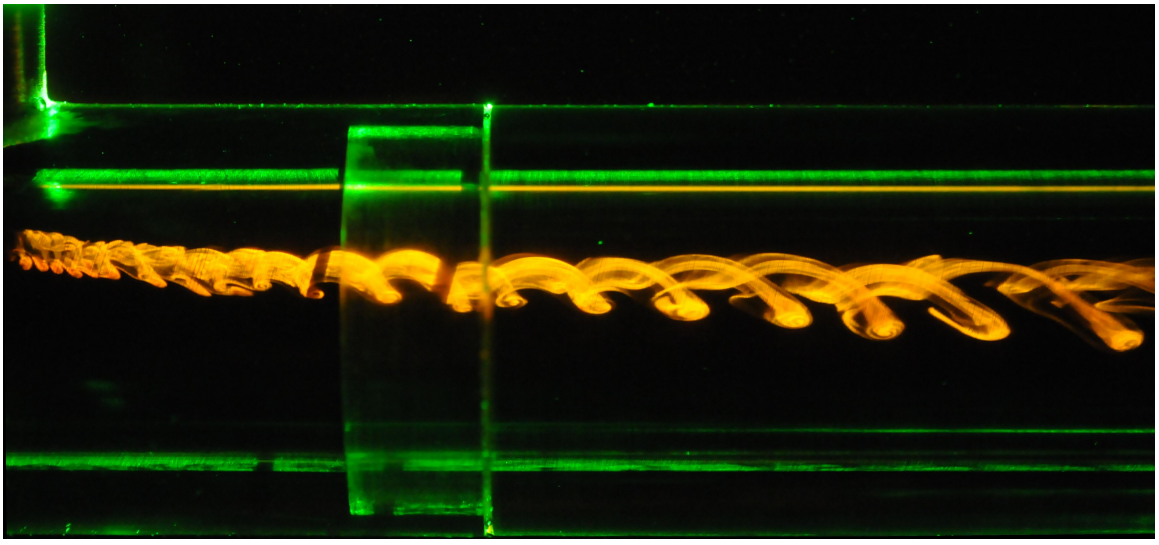

Figure 1.11: Hairpin vortices developing from a small jet in pipe flow (photograph by Finn Box in the Mullin Lab). This is the typical transient behavior of the disturbance leading to the $R^{-1.4}$ scaling in fig. 1.10.

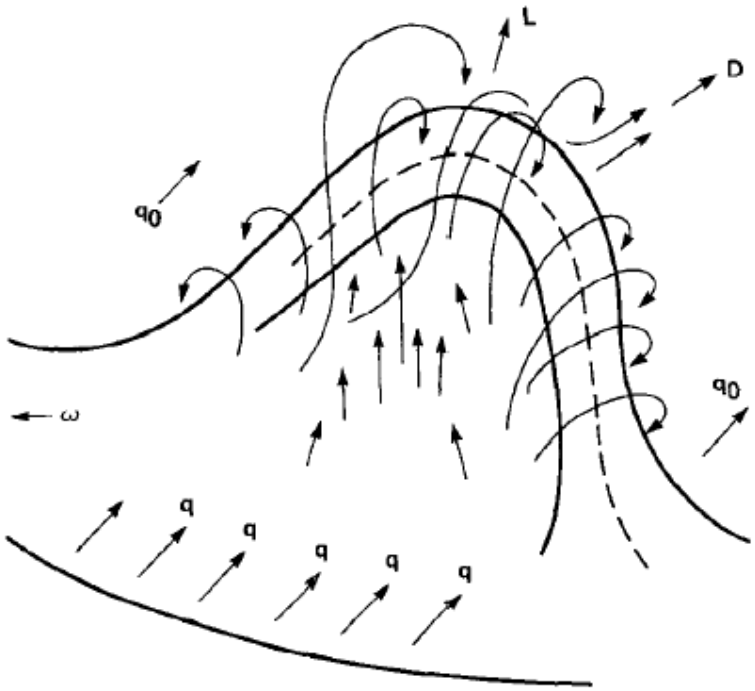

Figure 1.12: Hairpin/Horseshoe vortex postulated to be the 'molecule of shear turbulence' by Theodorsen in 1952. Here $\mathbf{q}$ is the fluid velocity and L and D are the lift and drag on the horseshoe structure [27].

His picture, reproduced in fig. 1.12, is compelling and horseshoe structures have since been observed as ubiquitous features in turbulent shear flows, but his mathematical justification for those structures is mostly hand-waving and laced with not quite correct statements. Theodorsen considers the enstrophy equation, obtained by dotting (1.74) with $\boldsymbol{\omega}$,

$$\frac{D}{Dt}\frac{\omega^2}{2} = \boldsymbol{\omega}\cdot(\boldsymbol{\omega}\cdot\nabla\mathbf{v}) + \nu\,\boldsymbol{\omega}\cdot\nabla^2\boldsymbol{\omega} \tag{1.75}$$

where $D/Dt = \partial_t + \mathbf{v}\cdot\nabla$ is the material derivative and $\omega^2 = \boldsymbol{\omega}\cdot\boldsymbol{\omega}$. He states that $\boldsymbol{\omega}\cdot(\boldsymbol{\omega}\cdot\nabla\mathbf{v}) = \omega^2 dv_s/ds$ where s is arclength along the local vortex line and $v_s = \mathbf{v}\cdot\boldsymbol{\omega}/\omega$ is the velocity component in the direction of the vortex line. This is not correct in general. If $\mathbf{s}$, $\mathbf{n}$, $\mathbf{b}$ represent an orthonormal Frenet-Serret frame along the vortex line, with $\mathbf{s} = \boldsymbol{\omega}/\omega$ and $\mathbf{v} = v_s\mathbf{s} + v_n\mathbf{n} + v_b\mathbf{b}$ then

$$\boldsymbol{\omega}\cdot(\boldsymbol{\omega}\cdot\nabla\mathbf{v}) = \omega^2\,\mathbf{s}\cdot\frac{d}{ds}(v_s\mathbf{s} + v_n\mathbf{n} + v_b\mathbf{b}) = \omega^2\left(\frac{dv_s}{ds} - \kappa v_n\right) \tag{1.76}$$

where κ is the curvature of the vortex line. He argues that the viscous terms $\boldsymbol{\omega}\cdot\nabla^2\boldsymbol{\omega}$ is negative and thus that $\boldsymbol{\omega}\cdot(\boldsymbol{\omega}\cdot\nabla\mathbf{v})$ is positive 'on average' for stationary turbulent flows. The viscous term

$$\boldsymbol{\omega}\cdot\nabla^2\boldsymbol{\omega} = \nabla^2\frac{\omega^2}{2} - \nabla\boldsymbol{\omega} : \nabla\boldsymbol{\omega}^T \tag{1.77}$$

and the 2nd term is negative since $\nabla\boldsymbol{\omega} : \nabla\boldsymbol{\omega}^T = (\partial_j\omega_i)(\partial_j\omega_i) \geq 0$, but the first term can be positive. These considerations do not explain the horseshoe structure however.

It appears that the basic reason for Theodorsen's horseshoe proposal is to maximize enstrophy production *by the mean shear*, that is to maximize $\boldsymbol{\omega}\cdot(\boldsymbol{\omega}\cdot\nabla\mathbf{v})$ for $\mathbf{v} = U(y)\hat{\mathbf{x}}$ in which case $\boldsymbol{\omega}\cdot(\boldsymbol{\omega}\cdot\nabla\mathbf{v}) = \omega_x\omega_y\,dU/dy$ and the rate of enstrophy production, that is $\boldsymbol{\omega}\cdot(\boldsymbol{\omega}\cdot\nabla\mathbf{v})/\omega^2 = (\omega_x\omega_y\,dU/dy)/(\omega_x^2 + \omega_y^2 + \omega_z^2)$ is maximized for $\omega_x = \omega_y$ with $\omega_z = 0$. There are two constraints on this optimum. First, since $\nabla\cdot\boldsymbol{\omega} = 0$, vortex lines cannot terminate at a point in the fluid. Second, very close to the wall, the vorticity must be $\boldsymbol{\omega} \approx \omega_z\hat{\mathbf{z}}$. Putting all these things together: (1) vortex lines starting in the spanwise $\hat{\mathbf{z}}$ direction near the wall, (2) turning in the 45° direction $\omega_x \approx \omega_y > 0$, $\omega_z \approx 0$ to maximize stretching by the mean shear, (3) turning back when $dU/dy \approx 0$ so that $\omega_x \approx \omega_y < 0$ again maximizes stretching and (4) smoothly connects back to the $\hat{\mathbf{z}}$ direction near the wall, leads to the very plausible horseshoe structure sketched in fig. 1.12. It seems clear from Theordorsen's depiction of *lift* and *drag* on the horseshoe — forces that are quadratic in the relative velocity — that this is implicitly a *coherent nonlinear structure*, not the linear dispersion of laminar flow eigenmodes.

1.4.2 An argument for $R^{-1.4}$?

Theodorsen's reasons for the horseshoe/hairpin vortex thus appear to be *quasi-linear*. The hairpin vortex must be nonlinear to hold itself together in a coherent packet, but the basic reason for the shape of the vortex appears to be merely stretching by the mean. If ℓ is the scale and v the velocity amplitude of the initial perturbation (*i.e.* the small jet or push-pull disturbance in the pipe experiments), we require that the perturbation's Reynolds number

be of $O(1)$ for that perturbation to 'roll-up' and create a small coherent vortical structure, that is

$$\frac{v\ell}{\nu} \gtrsim O(1). \tag{1.78}$$

Now for 'optimal' vortex stretching by the mean shear, we require that $\omega dU/dy \gtrsim \nu\nabla^2\omega$, that is

$$\frac{U}{h} \gtrsim \frac{\nu}{\ell^2} \iff \frac{\ell^2}{h^2} \gtrsim \frac{\nu}{Uh} = \frac{1}{R}. \tag{1.79}$$

where ℓ is an estimate for the vortex core and h is the pipe radius or the channel half-height. The meaning of this equation is that 'optimal' (*i.e.* 45° orientation) stretching of the vortex by the mean shear must at least balance the diffusion on the scale of the vortex core.

In the pipe experiments, the threshold amplitude is taken as the ratio of the perturbation mass flux $\approx v\ell^2$, to the pipe flux $\approx Uh^2$. Combining (1.78) and (1.79) yields

$$\frac{v\ell^2}{Uh^2} \gtrsim \frac{\nu}{Uh}\frac{\ell}{h} \gtrsim R^{-3/2}, \tag{1.80}$$

which is not $R^{-1.4}$ but close to it. Note that this is not an argument for transition but a quasi-linear argument for creation and amplification of hairpin vortices.

One issue with this argument is that ℓ is taken as both the size of the vortex core and of the initial perturbation. In the pipe experiments with $R^{-1.4}$ scaling [22], the scale of the push-pull disturbance is fixed at 1mm (two 1mm holes, 1mm apart) and the pipe radius is 20mm so $\ell/h \approx 0.05$ which seems large enough to satisfy (1.79), but these are mere scaling arguments and there may be significant hidden constant factors. For single jet disturbances with R^{-1} scaling, Peixinho and Mullin [22, Fig. 2(b)] show a scaling $vd/\nu \gtrsim (D/d)^{1/2}$ for the *jet* Reynolds number at fixed $R = 2500$, where d and D are the hole and pipe diameters, respectively. This shows that small holes require stronger jets, perhaps to lead to vortical structures with a size ℓ large enough to satisfy (1.78), (1.79). This suggests that the steeper scaling $R^{-1.4}$ instead of R^{-1} might be a small hole/low Reynolds number effect, although the Peixinho & Mullin $R^{-1.4}$ data is provided for a significant Reynolds number range.

Recent experimental studies of transition in plane Poiseuille flow by Lemoult, Aider and Wesfreid (2012) [19] show transition induced by a continuous small jet with $v/U \sim R^{-1}$ and a steeper scaling closer to $R^{-3/2}$ for low Reynolds number. The latter experiments document the development and persistence of hairpin vortices, especially in transitional states not laminar but not fully transitioned either. Thus the role of hairpin vortices and the threshold scaling remain to be clarified. In particular, small jets in cross-flows introduce multi-scale perturbations (the diameter of the jet and the thickness of the shear layer around that jet) that lead to the development of multiple vortex structures, such as a large scale counter-rotating vortex pair as well as smaller horseshoe (or necklace) vortices, possibly coupled to 'upright vortices' ([18] but the flow regimes are quite different from fig. 1.11). It may be that the visualizations draw our attention to the smaller scale trains of quasi-linear hairpin vortices but that it is really the larger scale counterrotating vortex pair that redistributes the mean to create streaks on the scale of the pipe radius and trigger the turbulent transition.

Bibliography

[1] M. Acarlar and C. Smith, *A study of hairpin vortices in a laminar boundary layer*, J. Fluid Mech., 175 (1987), pp. 1–41 and 45–83.

[2] D. Acheson, *Elementary Fluid Dynamics*, Oxford University Press, 1990.

[3] J. S. Baggett and L. N. Trefethen, *Low-dimensional models of subcritical transition to turbulence*, Physics of Fluids, 9 (1997), pp. 1043–1053.

[4] G. Batchelor, *An Introduction to Fluid Dynamics*, Cambridge Mathematical Library, Cambridge University Press, 2000.

[5] D. Benney, *The evolution of disturbances in shear flows at high Reynolds numbers*, Stud. Applied Math., 70 (1984), pp. 1–19.

[6] D. J. Benney and L. H. Gustavsson, *A new mechanism for linear and nonlinear hydrodynamic instability*, Stud. Applied Math., 64 (1981), pp. 185–209.

[7] D. J. Benney and C. C. Lin, *On the secondary motion induced by oscillations in a shear flow*, Physics of Fluids, 3 (1960), pp. 656–657.

[8] S. J. Chapman, *Subcritical transition in channel flows*, Journal of Fluid Mechanics, 451 (2002), pp. 35–97.

[9] P. Drazin and W. Reid, *Hydrodynamic Stability*, Cambridge University Press, Cambridge, UK, 1981.

[10] T. Ellingsen and E. Palm, *Stability of linear flow*, Physics of Fluids, 18 (1975), pp. 487–488.

[11] L. H. Gustavsson, *Energy growth of three-dimensional disturbances in plane Poiseuille flow*, Journal of Fluid Mechanics, 224 (1991), pp. 241–260.

[12] L. H. Gustavsson and L. S. Hultgren, *A resonance mechanism in plane Couette flow*, Journal of Fluid Mechanics, 98 (1980), pp. 149–159.

[13] J. Hamilton, J. Kim, and F. Waleffe, *Regeneration mechanisms of near-wall turbulence structures*, J. Fluid Mech., 287 (1995), pp. 317–348.

[14] B. Hof, A. Juel, and T. Mullin, *Scaling of the turbulence transition threshold in a pipe*, Phys. Rev. Lett., 91 (2003), p. 244502.

[15] L. S. Hultgren and L. H. Gustavsson, *Algebraic growth of disturbances in a laminar boundary layer*, Physics of Fluids, 24 (1981), pp. 1000–1004.

[16] D. D. Joseph and W. Hung, *Contributions to the nonlinear theory of stability of viscous flow in pipes and between rotating cylinders*, Archive for Rational Mechanics and Analysis, 44 (1971), pp. 1–22. 10.1007/BF00250825.

[17] D. D. Joseph and L. N. Tao, *Transverse Velocity Components in Fully Developed Unsteady Flows*, Journal of Applied Mechanics, 30 (1963), pp. 147–148.

[18] R. M. Kelso, T. T. Lim, and A. E. Perry, *An experimental study of round jets in cross-flow*, Journal of Fluid Mechanics, 306 (1996), pp. 111–144.

[19] G. Lemoult, J.-L. Aider, and J. E. Wesfreid, *Experimental scaling law for the subcritical transition to turbulence in plane Poiseuille flow*, Phys. Rev. E, 85 (2012), p. 025303.

[20] A. Meseguer and L. N. Trefethen, *Linearized pipe flow to Reynolds number* 10^7, J. Comput. Phys., 186 (2003), pp. 178–197.

[21] T. Mullin, *Experimental studies of transition to turbulence in a pipe*, Annual Review of Fluid Mechanics, 43 (2011), pp. 1–24.

[22] J. Peixinho and T. Mullin, *Finite-amplitude thresholds for transition in pipe flow*, Journal of Fluid Mechanics, 582 (2007), pp. 169–178.

[23] D. Rempfer, *On boundary conditions for incompressible Navier-Stokes problems*, Applied Mechanics Reviews, 59 (2006), pp. 107–125.

[24] O. Reynolds, *An experimental investigation of the circumstances which determine whether the motion of water shall be direct or sinuous, and of the law of resistance in parallel channels.*, Proceedings of the Royal Society of London, 35 (1883), pp. 84–99.

[25] V. Romanov, *Stability of plane-parallel Couette flow*, Functional Anal. & its Applic., 7 (1973), pp. 137–146.

[26] P. Schmid and D. Henningson, *Stability and Transition in Shear Flows*, no. v. 142 in Applied Mathematical Sciences, Springer, 2001.

[27] T. Theodorsen, *Mechanism of turbulence*, in Proceedings of 2nd Midwestern Conference on Fluid Mechanics, Ohio State University, 1952, pp. 1–18.

[28] ——, *The structure of turbulence*, in Technical Note, vol. 31, University of Maryland, The Institute for Fluid Dynamics and Applied Mathematics, 1954, pp. 21–27.

[29] N. Trefethen, A. Trefethen, S. Reddy, and T. Driscoll, *Hydrodynamic stability without eigenvalues*, Science, 261 (1993), pp. 578–584.

[30] F. Waleffe, *Proposal for a self-sustaining process in shear flows*, Unpublished Center for Turbulence Research manuscript, available at `www.math.wisc.edu/~waleffe/ECS/sspctr90.pdf`, (1990).

[31] ——, *Hydrodynamic stability and turbulence: Beyond transients to a self-sustaining process*, Stud. Applied Math., 95 (1995), pp. 319–343.

[32] ——, *Transition in shear flows: Nonlinear normality versus non-normal linearity*, Phys. Fluids, 7 (1995), pp. 3060–3066.

[33] ——, *On a self-sustaining process in shear flows*, Phys. Fluids, 9 (1997), pp. 883–900.

[34] ——, *Three-dimensional coherent states in plane shear flows*, Phys. Rev. Lett., 81 (1998), pp. 4140–4148.

[35] ——, *Exact coherent structures in channel flow*, J. Fluid Mech., 435 (2001), pp. 93–102.

[36] ——, *Homotopy of exact coherent structures in plane shear flows*, Phys. Fluids, 15 (2003), pp. 1517–1543.

[37] F. Waleffe, J. Kim, and J. Hamilton, *On the origin of streaks in turbulent shear flows*, in Turbulent Shear Flows 8: selected papers from the Eighth International Symposium on Turbulent Shear Flows, Munich, Germany, Sept. 9-11, 1991, F. Durst, R. Friedrich, B. Launder, F. Schmidt, U. Schumann, and J. Whitelaw, eds., Springer-Verlag, Berlin, 1993, pp. 37–49.

[38] J. Wang, J. Gibson, and F. Waleffe, *Lower branch coherent states in shear flows: transition and control*, Phys. Rev. Lett., 98 (2007), p. 204501.

Lecture 2

Overview of turbulent shear flows

notes by Giulio Mariotti and John Platt
revised by FW
WHOI GFD Lecture 2, June 21, 2011

A brief review of basic concepts and folklore in shear turbulence.

2.1 Reynolds decomposition

Experimental measurements show that turbulent flows can be decomposed into well-defined averages plus fluctuations, $\mathbf{v} = \bar{\mathbf{v}} + \mathbf{v}'$. This is nicely illustrated in the *Turbulence* film available online at `http://web.mit.edu/hml/ncfmf.html` that was already mentioned in Lecture 1.

In experiments, the average $\bar{\mathbf{v}}$ is often taken to be a time average since it is easier to measure the velocity at the same point for long times, while in theory it is usually an *ensemble average* — an average over many realizations of the same flow. For numerical simulations and mathematical analysis in simple geometries such as channels and pipes, the average is most easily defined as an average over the homogeneous or periodic directions.

Given a velocity field $\mathbf{v}(x, y, z, t)$ we define a mean velocity for a shear flow with laminar flow $U(y)\hat{\mathbf{x}}$ by averaging over the directions (x, z) perpendicular to the shear direction y,

$$\bar{\mathbf{v}} = \lim_{L_x, L_z \to \infty} \frac{1}{L_x L_z} \int_{-L_z/2}^{L_z/2} \int_{-L_x/2}^{L_x/2} \mathbf{v}(x, y, z, t) \mathrm{d}x \mathrm{d}z = \overline{U}(y, t)\hat{\mathbf{x}}. \tag{2.1}$$

The mean velocity is in the x direction because of incompressibility and the boundary conditions. In a pipe, the average would be over the streamwise and azimuthal (spanwise) direction and the mean would depend only on the radial distance to the pipe axis, and (possibly) time. Now we apply this averaging to the incompressible Navier-Stokes equations,

$$\frac{\partial \mathbf{v}}{\partial t} + \mathbf{v} \cdot \nabla \mathbf{v} = -\nabla p + \nu \nabla^2 \mathbf{v} \quad , \quad \nabla \cdot \mathbf{v} = 0. \tag{2.2}$$

Using the incompressibility condition $\nabla \cdot \mathbf{v} = 0$ we can rewrite the momentum equation in conservative form,

$$\frac{\partial \mathbf{v}}{\partial t} + \nabla \cdot (\mathbf{v}\mathbf{v}) = -\nabla p + \nu \nabla^2 \mathbf{v}. \tag{2.3}$$

We split the flow into a mean part and a fluctuation,

$$\mathbf{v} = \overline{U}(y,t)\hat{\mathbf{x}} + \mathbf{v}' \tag{2.4}$$

Averaging the Navier-Stokes equations (2.3) over x and z yields the *mean flow equation*

$$\frac{\partial \overline{U}}{\partial t} + \frac{\partial \overline{uv}}{\partial y} = -\frac{dP_0}{dx} + \nu \frac{\partial^2 \overline{U}}{\partial y^2}, \tag{2.5}$$

where $\mathbf{v}' = (u, v, w)$ in cartesian coordinates and the overline $\overline{()}$ denotes the average over x and z. To arrive at this mean flow equation, we used the divergence theorem and the fact that $\overline{\mathbf{v}'} = 0$. The mean pressure gradient $\overline{\partial P/\partial x} = dP_0/dx$ is not zero in pressure-driven channel and pipe flows where the pressure has the form $P = P_0(x) + p(\mathbf{r}, t)$ with dP_0/dx a fixed constant and $p(\mathbf{r}, t)$ is the flow induced pressure required to maintain incompressibility. For fixed flux, as in the Mullin pipe flow experiments [11], the mean pressure gradient can fluctuate in time to maintain the total mass flux.

For sufficiently large domains and sufficiently large Reynolds number, the flow in a pipe or channel is *statistically steady*, so the mean values are independent of t.[1] For statistically steady flow, the mean flow equation (2.5) reduces to

$$\frac{d\overline{uv}}{dy} = -\frac{dP_0}{dx} + \nu \frac{d^2 \overline{U}}{dy^2}. \tag{2.6}$$

Integrating (2.6) from the bottom wall at $y = -h$ to the top wall at $y = h$ gives $0 = -2h\frac{dP_0}{dx} + \nu \left.\frac{d\overline{U}}{dy}\right|_h - \nu \left.\frac{d\overline{U}}{dy}\right|_{-h}$ since $u = v = 0$ at the walls, leading to

$$-\frac{dP_0}{dx} = \frac{\tau_w}{h} \tag{2.7}$$

where $\tau_w = \nu \left. d\overline{U}/dy\right|_{-h} = -\nu \left. d\overline{U}/dy\right|_h$ is the shear stress on the bottom wall and top wall, by symmetry.

Plane Couette flow is driven by moving walls situated at $y = \pm h$ with velocities $\mathbf{v} = \pm U\hat{\mathbf{x}}$ and there is no imposed pressure gradient. Integrating equation (2.6) with $dP_0/dx = 0$ from the bottom wall where $u = v = 0$ to y gives

$$\nu \frac{d\overline{U}}{dy} - \overline{uv} = \tau_w, \tag{2.8}$$

where $\tau_w = \nu \, d\overline{U}/dy|_h$ is the stress on the bottom wall. Equation (2.8) states that the mean *stress* on the fluid layer below y is constant across the channel in Couette flow. The first term on the left hand-side of (2.8), $\nu \, d\overline{U}/dy$, is the mean viscous stress from the fluid above level y onto the fluid layer below y. The second term, $-\overline{uv}$, is the *Reynolds stress* that arises from the net vertical transport of streamwise momentum by the fluctuations, again from the fluid above y into the fluid layer below y. The two stresses add up to a constant total stress for Couette flow, τ_w. Note that these are all *kinematic* stresses, stress divided by fluid density ρ, so the actual total stress is $\rho\tau_w$.

[1] This is a reasonable assumption, verified experimentally and numerically. However, our recent discoveries of time-periodic solutions in plane Couette flow [4], [7], [15] show that is is possible to have time-dependent averages, in general.

2.2 Laminar and Inertial Scalings of the Drag τ_w

First we look at Couette flow, as described by equation (2.8). We try to find appropriate scalings for the two terms on the left hand side using the obvious scalings for velocity and length, U and h, the half-wall velocity difference and the half-channel height, respectively. We can scale the viscous and Reynolds stress terms in (2.8) as

$$\nu \frac{d\overline{U}}{dy} \sim \frac{\nu U}{h}, \qquad -\overline{uv} \sim U^2, \tag{2.9}$$

away from the walls, yielding the total stress as

$$\tau_w \sim \frac{\nu U}{h} + U^2 = \frac{\nu U}{h}\left(1 + \frac{Uh}{\nu}\right) = \frac{\nu U}{h}\left(1 + R\right) \tag{2.10}$$

where $R = Uh/\nu$ is the Reynolds number for Couette flow. This correctly suggests that for $R \ll 1$, the viscous stress $\nu d\overline{U}/dy$ dominates and we have *laminar scaling*

$$\tau_w \sim \frac{\nu U}{h} \quad \Rightarrow \quad \frac{\tau_w}{U^2} \sim \frac{1}{R}, \tag{2.11}$$

where τ_w/U^2 is a *friction factor*, as in the Moody diagram of Lecture 1. For $R \gg 1$, the Reynolds stress $-\overline{uv}$ dominates and we have *inertial scaling*

$$\tau_w \sim U^2 \quad \Rightarrow \quad \frac{\tau_w}{U^2} \sim 1. \tag{2.12}$$

This corresponds to the $R \gg 1$ portion of the Moody diagram labeled *'complete turbulence,'* where the friction factor τ_w/U^2 is roughly independent of Reynolds number R and would correspond to drag being dominated by the Reynolds stress $-\overline{uv}$ scaling as U^2.

Next we look at the scalings for channel flow. Now our equation is (2.6) with (2.7),

$$\nu \frac{d^2\overline{U}}{dy^2} - \frac{d\overline{uv}}{dy} = -\frac{\tau_w}{h}. \tag{2.13}$$

This equation states that the mean *force* on a fluid layer between y and $y + dy$ is a negative constant in channel flow to balance the positive pressure force $-dP_0/dx = \tau_w/h$. Scaling (2.13) as in (2.9)

$$\nu \frac{d^2\overline{U}}{dy^2} \sim -\frac{\nu U}{h^2}, \qquad \frac{d\overline{uv}}{dy} \sim \frac{U^2}{h}, \tag{2.14}$$

away from the walls, yields

$$\frac{\tau_w}{h} \sim \nu \frac{U}{h^2} + \frac{U^2}{h} \sim \nu \frac{U}{h^2}\left(1 + R\right). \tag{2.15}$$

This leads to the same results as in Couette flow, namely that the drag at the wall τ_w has the laminar scaling $\tau_w \sim \nu U/h$, corresponding to a friction factor $\tau_w/U^2 \sim 1/R$ for low R (2.11) and the inertial scaling $\tau_w \sim U^2$ for large R (2.12). The drag at the wall is the pressure gradient times the half-height, $\tau_w = -h\, dP_0/dx$, as derived in (2.7).

2.3 Energy Dissipation Rate $\mathcal{E} = \tau_w U/h$

We now look at the the Kinetic Energy (KE) budget for the total flow (mean plus fluctuation). The KE equation is obtained by the scalar product between the velocity $\mathbf{v}$ and the NS equation (4.10), yielding

$$\frac{\partial}{\partial t}\left(\frac{1}{2}|\mathbf{v}|^2\right) + \mathbf{v}\cdot\nabla\left(\frac{1}{2}|\mathbf{v}|^2\right) + \mathbf{v}\cdot\nabla p = -\frac{dP_0}{dx}\hat{\mathbf{x}}\cdot\mathbf{v} + \nu\,\mathbf{v}\cdot\nabla^2\mathbf{v}. \tag{2.16}$$

Equation (2.16) is then averaged over the whole domain V, that is $V^{-1}\int_V(\cdots)dV$ as a limit process in the homogeneous directions x and z, as in (2.1), or with periodic boundary conditions as in numerical simulations. The advection and flow-induced pressure terms vanish upon integration since $\nabla\cdot\mathbf{v} = 0$ implies that $\mathbf{v}\cdot\nabla(*) = \nabla\cdot(\mathbf{v}(*))$, then the integral of these divergences become surface integrals, by the divergence theorem, and the boundary integrals vanish because of no flow through the walls and/or periodic boundary conditions. The viscous term $\mathbf{v}\cdot\nabla^2\mathbf{v} = \nabla^2|\mathbf{v}|^2/2 - \nabla\mathbf{v}:\nabla\mathbf{v}^T$ where $\mathbf{A}:\mathbf{B} \equiv A_{ij}B_{ji} = \mathrm{trace}(\mathbf{A}\cdot\mathbf{B})$, so $\nabla\mathbf{v}:\nabla\mathbf{v}^T = (\partial_i v_j)(\partial_i v_j) \equiv |\nabla\mathbf{v}|^2 \geq 0$ is positive definite.

For channel flow in statistically steady state, we obtain

$$\underbrace{-\frac{dP_0}{dx}\,\frac{1}{V}\int_V \hat{\mathbf{x}}\cdot\mathbf{v}dV}_{\textit{energy input rate}} = \underbrace{\frac{\nu}{V}\int_V |\nabla\mathbf{v}|^2 dV}_{\textit{energy dissipation rate}} = \mathcal{E} \geq 0, \tag{2.17}$$

since $\mathbf{v} = 0$ at the walls. This relation can be written

$$\frac{\tau_w}{h}\,U = \mathcal{E} \tag{2.18}$$

where $\tau_w/h = -dP_0/dx$, from (2.7), is the force per unit mass with τ_w the stress at the wall, $U = V^{-1}\int_V \hat{\mathbf{x}}\cdot\mathbf{v}\,dV$ is the bulk velocity and $\mathcal{E}$ is the energy dissipation rate per unit mass.

For plane Couette flow driven by the motion of the walls, with $dP_0/dx = 0$, the viscous term $\mathbf{v}\cdot\nabla^2\mathbf{v} = \nabla^2|\mathbf{v}|^2/2 - \nabla\mathbf{v}:\nabla\mathbf{v}^T$ provides both the energy input and output. The KE equation reads

$$\frac{\nu}{V}\int_V \nabla\cdot\nabla\left(\frac{1}{2}|\mathbf{v}|^2\right)\,dV = \frac{\nu}{V}\int_V |\nabla\mathbf{v}|^2 dV \geq 0. \tag{2.19}$$

The divergence theorem applied to the left hand side yields

$$\begin{aligned}\frac{\nu}{V}\int_V \nabla\cdot\nabla\left(\frac{|\mathbf{v}|^2}{2}\right)\,dV &= \frac{\nu}{V}\int_{y=h}\hat{\mathbf{y}}\cdot\nabla\left(\frac{|\mathbf{v}|^2}{2}\right)dA - \frac{\nu}{V}\int_{y=-h}\hat{\mathbf{y}}\cdot\nabla\left(\frac{|\mathbf{v}|^2}{2}\right)dA \\ &= \frac{\nu}{V}\int_{y=h} u\frac{\partial u}{\partial y}dA - \frac{\nu}{V}\int_{y=-h} u\frac{\partial u}{\partial y}\,dA = \frac{\tau_w}{h}\,U\end{aligned} \tag{2.20}$$

since $u = U$ on the top wall at $y = h$ and $u = -U$ at $y = -h$ with $v = w = 0$ on both walls, and $\tau_w = \nu A^{-1}\int_{y=-h}\frac{\partial u}{\partial y}\,dA = \nu A^{-1}\int_{y=h}\frac{\partial u}{\partial y}\,dA$ is the mean stress on the bottom wall with surface area A, equal to the mean stress from the top wall onto the fluid and $V = 2Ah$. These surface integrals may have to be interpreted as limits as $A\to\infty$, as in (2.1). Using

(2.20), the KE equation for Couette flow (2.19) can also be written in the compact form (2.18),

$$\frac{\tau_w}{h}\, U = \mathcal{E} \tag{2.21}$$

but this U is the half wall velocity difference in plane Couette flow, instead of the bulk velocity in (2.18), and h is the half channel height in both cases.

The energy input/dissipation balance (2.18), (2.21), for pipe, channel and plane Couette flow, shows that there is a direct relationship between the scaling of the wall stress τ_w (the *drag*) and the scaling of the energy dissipation rate $\mathcal{E}$. For laminar scaling (2.11), (2.15) for 'small' Reynolds number $R = Uh/\nu$ (meaning smaller than a few 100's for the typical definitions of R in shear flows)

$$\tau_w \sim \frac{\nu U}{h} \quad \Leftrightarrow \quad \mathcal{E} \sim \nu \frac{U^2}{h^2}, \tag{2.22}$$

while the inertial scaling (2.12), (2.15) for large $R = Uh/\nu$,

$$\tau_w \sim U^2 \quad \Leftrightarrow \quad \mathcal{E} \sim \frac{U^3}{h}. \tag{2.23}$$

The remarkable fact about the inertial scaling (2.23) is that the wall stress

$$\tau_w = \nu \left.\frac{d\overline{U}}{dy}\right|_{wall} \tag{2.24}$$

which is necessarily transmitted from the fluid to the wall by viscosity, and the energy dissipation rate (2.17), (2.29)

$$\mathcal{E} = \nu \left\langle |\nabla \mathbf{v}|^2 \right\rangle = 2\,\nu \left\langle \mathbf{S} : \mathbf{S} \right\rangle, \tag{2.25}$$

where the brackets $\langle\ \rangle$ denote volume average, which also arises from viscosity, would both be *independent* of ν for sufficiently large R according to (2.23). This requires boundary layers of thickness $\sim \nu/U$ on average, much smaller than a stagnation point boundary layer thickness $\sim \sqrt{\nu/S}$, where S is a strain rate. The $\sqrt{\nu/S}$ boundary layer is to satisfy no-slip at $y = 0$ for the outer stagnation point flow $\mathbf{v} = (Sx, -Sy, 0)$ in incompressible flow (*e.g.* [1, §2.5]). It is not clear if and how one can obtain a ν/U boundary layer on a smooth wall in incompressible flow.

Note on the energy dissipation rate

The expression for the energy dissipation rate $\mathcal{E}$ in (2.17) is not correct in general. The viscous term $\nu\nabla^2\mathbf{v}$ in the Navier-Stokes equation (4.10) arises from the divergence of the stress tensor $\mathbf{T} = \nu(\nabla\mathbf{v} + \nabla\mathbf{v}^T) = 2\nu\mathbf{S}$, where $\mathbf{S}$ is the strain rate tensor, then $\nabla\cdot\mathbf{T} = \nu\nabla^2\mathbf{v}$ because $\nabla\cdot(\nabla\mathbf{v})^T = \nabla(\nabla\cdot\mathbf{v}) = 0$, since $\nabla\cdot\mathbf{v} = 0$. In the kinetic energy equation, then,

$$\nu\,\mathbf{v}\cdot\nabla^2\mathbf{v} = \nu\,\nabla\cdot((\nabla\mathbf{v})\cdot\mathbf{v}) - \nu\,\nabla\mathbf{v} : \nabla\mathbf{v}^T \tag{2.26}$$

is equal to

$$\mathbf{v}\cdot(\nabla\cdot\mathbf{T}) = \nabla\cdot(\mathbf{T}\cdot\mathbf{v}) - \mathbf{T} : \mathbf{S}, \tag{2.27}$$

where symmetry of the stress tensor $\mathbf{T} = \mathbf{T}^T$ has been used in (2.27) to obtain $\mathbf{T} : \nabla\mathbf{v}^T = T_{ij}\partial_i v_j = T_{ij}(\partial_i v_j + \partial_j v_i)/2 = T_{ij}S_{ji} = \mathbf{T} : \mathbf{S}$. Integration over the domain shows that the second form (2.27) yields the proper energy input rate on the boundaries, since, by the divergence theorem

$$\int_V \nabla \cdot (\mathbf{T} \cdot \mathbf{v}) \; dV = \int_{\partial V} \mathbf{f} \cdot \mathbf{v} \; dS \tag{2.28}$$

where $\mathbf{f} = \mathbf{n} \cdot \mathbf{T}$ is the stress on the surface boundary ∂V of the volume V, with unit outward normal $\mathbf{n}$, by definition of the stress tensor $\mathbf{T}$. Hence the energy dissipation rate per unit mass arises from the 2nd term on the right hand side of (2.27)

$$\mathcal{E} = \frac{1}{V}\int_V \mathbf{T} : \mathbf{S} \; dV = \frac{1}{V}\int_V 2\nu \, \mathbf{S} : \mathbf{S} \; dV \geq 0, \tag{2.29}$$

not from the 2nd term of (2.26), $\nu \, \nabla\mathbf{v} : \nabla\mathbf{v}^T$.

Subtracting (2.26) from (2.27) and canceling out factors of ν shows that the expressions $\nabla\mathbf{v} : \nabla\mathbf{v}^T$ and $2\,\mathbf{S} : \mathbf{S}$ differ by a divergence,

$$2\,\mathbf{S} : \mathbf{S} = \nabla\mathbf{v} : \nabla\mathbf{v}^T + \nabla \cdot (\mathbf{v} \cdot \nabla\mathbf{v}). \tag{2.30}$$

The divergence term on the right hand side integrates to

$$\int_V \nabla \cdot (\mathbf{v} \cdot \nabla\mathbf{v}) dV = \int_{\partial V} \mathbf{v} \cdot (\nabla\mathbf{v}) \cdot \mathbf{n} \, dS \tag{2.31}$$

and that boundary term vanishes for periodic boundary conditions, or for $\mathbf{v} = 0$ on ∂V, or for *flat* boundaries for which $\mathbf{n}$ is constant so $(\nabla\mathbf{v}) \cdot \mathbf{n} = \nabla(\mathbf{v} \cdot \mathbf{n})$ and there is no flow through the walls, $\mathbf{v} \cdot \mathbf{n} = 0$, so $\mathbf{v} \cdot (\nabla\mathbf{v}) \cdot \mathbf{n} = \mathbf{v} \cdot \nabla(\mathbf{v} \cdot \mathbf{n}) = 0$ on ∂V.

Thus, the expressions (2.17) and (2.29) for $\mathcal{E}$ are equal for pipe and plane channel and Couette flows, but they differ for cylindrical Couette flow, for instance. The difference is most striking for rigid body rotation for which $\mathbf{v} = (-\Omega y, \Omega x, 0)$ and $\nabla\mathbf{v} : \nabla\mathbf{v}^T = 2\Omega^2$ but $2\,\mathbf{S} : \mathbf{S} = 0$.

2.4 Kolmogorov spectrum and Energy cascade

The study of turbulence spawned a new branch in the 1930's when researchers went beyond the study of mean flows $\overline{U}(y)$ and started focusing on the turbulent fluctuations. Experiments measured *two-point correlations* $\langle \mathbf{v}(\mathbf{r}')\mathbf{v}(\mathbf{r}) \rangle$, where the average denoted by the brackets $\langle \; \rangle$ is typically a time average in practice or an ensemble average in theory. G.I. Taylor introduced the concept of *homogeneous turbulence* where those time or ensemble averages are assumed to depend only on the two-point separation $\mathbf{s} = \mathbf{r}' - \mathbf{r}$ but not on location, *e.g.*

$$\langle \mathbf{v}(\mathbf{r}')\mathbf{v}(\mathbf{r}) \rangle = \mathbf{R}(\mathbf{s}), \tag{2.32}$$

that is $\langle v_i(\mathbf{r}')v_j(\mathbf{r}) \rangle = R_{ij}(\mathbf{s})$ in cartesian index notation. The possible time dependence of these correlations will be kept implicit in this section. For fully developed turbulent flow in a pipe or channel at sufficiently high Reynolds number, the turbulence is observed to

be homogeneous in the azimuthal (or spanwise) and streamwise directions, sufficiently far from the entrance and exit to the pipe, and from the sides in channels. The statistics are strongly dependent on the distance to the wall, near the walls, but become approximately homogeneous sufficiently far from the wall. Sufficiently far is best measured in *wall units* (typically denoted with a '+' and sometimes called 'plus-units')

$$\delta^+ = \frac{\nu}{\sqrt{\tau_w}} \tag{2.33}$$

where $\tau_w = \nu \, d\overline{U}/dy|_w$ is the (kinematic) stress at the wall (2.24) which has units of velocity squared. For laminar scaling (2.11),

$$\tau_w \sim \nu \frac{U}{h} \quad \Rightarrow \quad \delta^+ \sim \sqrt{\frac{\nu h}{U}}, \tag{2.34}$$

but for inertial scaling (2.12), the wall unit would be much smaller

$$\tau_w \sim U^2 \quad \Rightarrow \quad \delta^+ \sim \frac{\nu}{U}. \tag{2.35}$$

In practice, 'sufficiently far' means distances from the wall greater than about $50\,\delta^+$.

The theory of *homogeneous turbulence*, where the statistics are invariant under translations, quickly specialized to the study of *isotropic turbulence* where the statistics are also independent of rotations and reflections. For the two-point correlation (2.32), that involves vector quantities $\mathbf{v}$ and introduces the special direction $\mathbf{s} = \mathbf{r}' - \mathbf{r}$, this implies

$$\langle \mathbf{v}(\mathbf{r}')\mathbf{v}(\mathbf{r}) \rangle = u_{rms}^2 \Big(F(s)\, \hat{\mathbf{s}}\hat{\mathbf{s}} + G(s)\, (\mathbf{I} - \hat{\mathbf{s}}\hat{\mathbf{s}}) \Big) \tag{2.36}$$

in dyadic notation, where s is the magnitude and $\hat{\mathbf{s}}$ the direction of $\mathbf{s} = s\,\hat{\mathbf{s}}$ and $\mathbf{I}$ is the identity tensor, or

$$\langle v_i(\mathbf{r}')v_j(\mathbf{r}) \rangle = u_{rms}^2 \left(F(s)\frac{s_i s_j}{s^2} + G(s) \left(\delta_{ij} - \frac{s_i s_j}{s^2} \right) \right) \tag{2.37}$$

in cartesian index notation, where δ_{ij} is the Kronecker delta and s_i are the cartesian components of $\mathbf{s} = \mathbf{r}' - \mathbf{r}$. The root mean square velocity is $u_{rms}^2 = \langle \mathbf{v} \cdot \mathbf{v} \rangle / 3$. Equation (2.36) $\equiv$ (2.37), says that the correlation depends only on the distance s between the two points and whether the velocity components are parallel or perpendicular to $\mathbf{s}$. Incompressibility, $\nabla \cdot \mathbf{v} = 0$ applied to (2.36), (2.37), yields

$$s\frac{dF}{ds} + 2(F - G) = 0 \tag{2.38}$$

relating $G(s)$ to $F(s)$, so the two-point velocity correlation tensor (2.32) is fully determined by the *longitudinal auto-correlation function*,

$$F(s) \equiv \frac{\langle u_1(\mathbf{r} + s\mathbf{e}_1)\, u_1(\mathbf{r}) \rangle}{u_{rms}^2} \tag{2.39}$$

in homogeneous isotropic turbulence. The reader should consult the books by Pope [13] or Sagaut and Cambon [14] for further information about homogeneous turbulence.

In homogeneous isotropic turbulence, the flow is assumed to take place in an infinite 3D euclidean space, maintained by a statistically steady and isotropic force but there are no mean flows, no walls and no drag. Thus the relationship (2.18), between the wall drag τ_w and the energy dissipation rate $\mathcal{E}$ is lost, although there is of course a similar relationship involving energy input by the statistically homogeneous, isotropic force.

In the Kolmogorov theory of isotropic turbulence, the energy dissipation rate $\mathcal{E}$ is the dominant quantity, it is the *energy cascade rate,* with energy input at the forcing scale ℓ_I cascading to ever smaller scales by nonlinear distortion down to sufficiently small scales where the energy is finally dissipated by viscosity. Kolmogorov estimated those small dissipation length scales by dimensional analysis based on $\mathcal{E}$ that has units L^2T^{-3} and viscosity ν with units L^2T^{-1}, so the *Kolmogorov dissipation length scale*, is

$$\ell_K \sim \left(\frac{\nu^3}{\mathcal{E}}\right)^{1/4}. \tag{2.40}$$

Dissipation on those scales would be achieved by turbulent velocity fluctuations of magnitude

$$u_K \sim (\nu\mathcal{E})^{1/4}, \tag{2.41}$$

with

$$\mathcal{E} \sim \nu \frac{u_K^2}{\ell_K^2} \sim \frac{u_{rms}^3}{\ell_I} \tag{2.42}$$

independent of ν, where $3u_{rms}^2 = \langle \mathbf{v}\cdot\mathbf{v}\rangle$ and ℓ_I is the energy input scale.

Kolmogorov's theory also predicts a scaling for the *Energy spectrum*

$$E(k) \sim \mathcal{E}^{2/3}\, k^{-5/3} \tag{2.43}$$

where $\int_0^\infty E(k)dk = \langle \mathbf{v}\cdot\mathbf{v}\rangle/2 = 3u_{rms}^2/2$ and $E(k)dk$ is the energy per unit mass in the wavenumber band $[k, k+dk]$. In isotropic turbulence, the energy spectrum $E(k)$ fully determines the Fourier transform $\Phi_{ij}(\mathbf{k})$ of the two point correlation tensor $R_{ij}(\mathbf{s})$ defined in (2.32)

$$\Phi_{ij}(\mathbf{k}) = \frac{E(k)}{4\pi k^2}\left(\delta_{ij} - \frac{k_i k_j}{k^2}\right) \tag{2.44}$$

where

$$\Phi_{ij}(\mathbf{k}) \equiv \frac{1}{(2\pi)^3}\int_{\mathbb{R}^3} R_{ij}(\mathbf{s})\, e^{-i\mathbf{k}\cdot\mathbf{s}} dV_{\mathbf{s}} \tag{2.45}$$

$$R_{ij}(\mathbf{s}) = \int_{\mathbb{R}^3} \Phi_{ij}(\mathbf{k})\, e^{i\mathbf{k}\cdot\mathbf{s}} dV_{\mathbf{k}} \tag{2.46}$$

with $dV_{\mathbf{s}}$ the volume element for $\mathbf{s}\in\mathbb{R}^3$ and $dV_{\mathbf{k}}$ the volume element for $\mathbf{k}\in\mathbb{R}^3$, so $dV_{\mathbf{s}} = ds_1 ds_2 ds_3$ and $dV_{\mathbf{k}} = dk_1 dk_2 dk_3$ in cartesian coordinates and $k = |\mathbf{k}|$. The energy spectrum $E(k)$ can be related to $F(s)$, the longitudinal auto-correlation (2.39), although the relationship is non-trivial

$$u_{rms}^2 F(s) = 2\int_0^\infty E(k)\left(\frac{\sin(ks)}{(ks)^3} - \frac{\cos(ks)}{(ks)^2}\right) dk. \tag{2.47}$$

A simpler relationship can be derived from (2.37), (2.44) and (2.46)

$$R_{ii}(\mathbf{s}) = u_{rms}^2\,(F(s) + 2G(s)) = 2\int_{\mathbb{R}^3} \frac{E(k)}{4\pi k^2}\, e^{i\mathbf{k}\cdot\mathbf{s}} dV_{\mathbf{k}} = 2\int_0^\infty E(k)\frac{\sin(ks)}{ks} dk. \qquad (2.48)$$

The Kolmogorov spectrum (2.43) occurs in the *inertial range* $\ell_I \gg k^{-1} \gg \ell_K$ where the wavelengths k^{-1} are much smaller than the energy input scale ℓ_I but much larger than the Kolmogorov dissipation scale ℓ_K. Defining the Reynolds number for homogeneous isotropic turbulence as

$$R = \frac{u_{rms}\,\ell_I}{\nu} = \frac{\mathcal{E}^{1/3}\ell_I^{4/3}}{\nu}. \qquad (2.49)$$

Using (2.40) then gives

$$\frac{\ell_I}{\ell_K} = \frac{\mathcal{E}^{1/4}\ell_I}{\nu^{3/4}} \equiv R^{3/4}. \qquad (2.50)$$

providing a rule of thumb, first proposed by S.A. Orszag, that the numerical resolution scales like $N \sim R^{9/4}$ for direct numerical simulation of 3D isotropic turbulence, where N is the total number of Fourier modes (or grid points) required to resolve the turbulent flow. A sketch of the energy spectrum with the inertial range (2.43) and the dissipation range for $k \gtrsim (\ell_K)^{-1}$ is shown in figure 2.1.

Since $\mathcal{E}$ is assumed to be independent of ν for sufficiently large Reynolds numbers, with $\mathcal{E} \sim u_{rms}^3/\ell_I$, eqn. (2.42) as in the inertial scaling (2.23), the Kolmogorov dissipation length (2.40) scales like $\nu^{3/4}$, smaller than the classic $\sqrt{\nu}$ boundary layer scaling, but *larger* than the inertial boundary layer scaling ν/U in turbulent channels and pipes (2.35). Thus, although the inertial scaling $\mathcal{E} \sim U^3/h$ in channels and pipes (2.23) and the Kolmogorov scaling $\mathcal{E} \sim u_{rms}^3/\ell_I$ are similar, there is a noteworthy difference between the two: the Kolmogorov scaling is achieved by small dissipation scales $\sim \nu^{3/4}$ throughout the volume of fluid, while the inertial scaling in shear flows over smooth walls requires small boundary layers $\sim \nu/U$ to transfer the momentum between the fluid and the walls, so $\tau_w = \nu\, d\overline{U}/dy|_w \sim U^2$, and would achieve ν-independent $\mathcal{E}$ through dissipation in those small boundary layers.

The Kolmogorov picture of turbulence is a *cascade of energy to smaller and smaller scales,* from the energy input scale ℓ_I down to the Kolmogorov dissipation scale $\sim \nu^{3/4}$, together with a *decoherence of the motions at different scales so that small scales are nearly isotropic.* In contrast, the inertial scaling (2.23) in shear flows appears to call for a *coherent transport of momentum over the height of the channel,* from one wall to the other wall in plane Couette flow for instance, transporting U over distance h to sustain boundary layers of thickness $\sim \nu/U$, on average. It is also known that in turbulent shear flows, the turbulence energy input occurs at small scales near the wall, not on the large scale of the channel.

2.5 *Turbulent* Kinetic Energy

In section 2.3, we derived a basic relation between the *drag* τ_w and the total *energy dissipation rate* $\mathcal{E}$. Here, we derive an equation for the fluctuations from the mean flow in turbulent channel flows. We return to the Reynolds decomposition $\mathbf{v} = \bar{\mathbf{v}} + \mathbf{v}'$ with $\mathbf{v} = \overline{U}(y,t)\hat{\mathbf{x}}$ in channels (2.4) and $\mathbf{v}' = (u, v, w)$ in cartesian coordinates. Substituting $\mathbf{v} = \overline{U}(y,t)\hat{\mathbf{x}} + \mathbf{v}'$ in

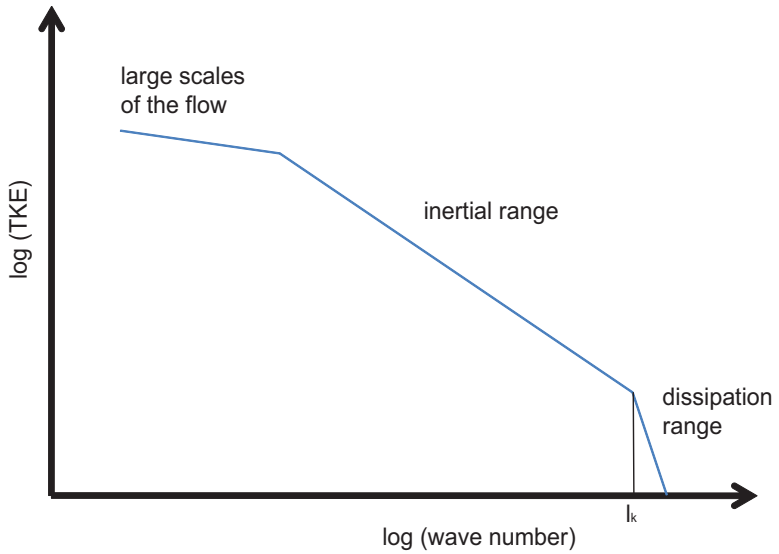

Figure 2.1: Sketch of the Turbulent Kinetic Energy spectrum $E(k)$ where k is wavenumber and $E(k)dk$ is the kinetic energy in the wavenumber band $[k, k+dk]$, according to the Kolmogorov scaling theory. Energy enters the flow at low wavenumbers (large scales) and cascades through the inertial range (2.43) to the dissipation scales (2.40) where it is dissipated.

the Navier-Stokes equations (2.3) and subtracting the mean flow equation (2.5) yields the equation for the turbulent fluctuations

$$\frac{\partial \mathbf{v}'}{\partial t} + \overline{U}\frac{\partial \mathbf{v}'}{\partial x} + v\frac{\partial \overline{U}}{\partial y}\hat{\mathbf{x}} + \nabla\cdot(\mathbf{v}'\mathbf{v}') - \frac{\partial \overline{uv}}{\partial y}\hat{\mathbf{x}} = -\nabla p' + \nu\nabla^2\mathbf{v}', \tag{2.51}$$

where $\overline{U}$ and $\overline{uv}$ are functions of y and t in general. Dotting this equation (2.51) with $\mathbf{v}'$ and averaging over the whole volume using the divergence theorem, incompressibility $\nabla\cdot\mathbf{v}' = 0$ and the boundary conditions, yields the kinetic energy of the fluctuations

$$\frac{d}{dt}\left\langle \frac{|\mathbf{v}'|^2}{2} \right\rangle = \underbrace{\left\langle (-uv)\frac{\partial \overline{U}}{\partial y} \right\rangle}_{Production} - \underbrace{\nu\left\langle |\nabla\mathbf{v}'|^2 \right\rangle}_{Dissipation \geq 0} \tag{2.52}$$

where the brackets $\langle\cdots\rangle \equiv V^{-1}\int_V \cdots dV$ denote a volume average, $|\nabla\mathbf{v}'|^2 = \partial_i u_j \partial_i u_j$ in cartesian index notation (but recall (2.30) in general), and the $\mathbf{v}'\cdot\hat{\mathbf{x}}\,\partial_y\overline{uv} = u\,\partial_y\overline{uv}$ term vanishes upon averaging over horizontal planes since $\bar{u} = 0$. This fluctuating kinetic energy equation should be contrasted with the mean kinetic energy equation obtained by multiplying the mean flow equation (2.5) by $\overline{U}$ and averaging over the volume to obtain

$$\frac{d}{dt}\left\langle \frac{\overline{U}^2}{2} \right\rangle = \frac{\tau_w}{h}U - \left\langle (-uv)\frac{\partial \overline{U}}{\partial y} \right\rangle - \nu\left\langle \left(\frac{\partial \overline{U}}{\partial y}\right)^2 \right\rangle \tag{2.53}$$

where $\tau_w U/h$ arises as in section 2.3 and U is the bulk velocity in channel flow, but the half wall velocity difference in plane Couette flow, in either case $\tau_w U/h$ is the energy input per

unit mass from the pressure gradient or the wall drag. Evidently, the 'production' term in (2.52) appears with the opposite sign in the mean flow kinetic energy (2.53) and is a transfer term extracting energy from the mean flow $\overline{U}$ to feed the fluctuations $\mathbf{v}'$. Adding up (2.52) and (2.53) leads back to the total kinetic energy equation of section 2.3, that reduces to (2.18), (2.21) for statistically steady flow. For statistically steady state, the fluctuation kinetic energy equation (2.52) becomes

$$\frac{1}{2h}\int_{-h}^{h}(-\overline{uv})\frac{d\overline{U}}{dy}\,dy = \nu\,\left\langle|\nabla\mathbf{v}'|^2\right\rangle \geq 0. \tag{2.54}$$

where the brackets $\langle\cdots\rangle$ denote a volume average and the overline $\overline{(\cdots)}$ denotes a horizontal average. This equation states that $(-\overline{uv})$ and $d\overline{U}/dy$ must have the same sign, on average, in order to sustain the turbulent fluctuations.

2.6 Upper bound on drag and dissipation

Malkus [10] proposed a theory of turbulent convection and of shear turbulence where he invoked concepts of *marginal stability*, *existence of a smallest scale* and *maximization of heat flux or momentum transport*. This led Howard [5, 6] and Busse [2] to derive bounds on heat flux in convection and momentum transport in shear flow.

For plane Couette flow, the idea is to look for the field $\mathbf{v}' = (u, v, w)$ that maximizes the drag τ_w (2.8) for a given U subject to various constraints including the boundary conditions $\overline{U} = \pm U$ and $\mathbf{v}' = 0$ at $y = \pm h$, incompressibility $\nabla\cdot\mathbf{v}' = 0$ and the fluctuation energy equation (2.54). The expression (2.8) for the total stress,

$$\tau_w = \nu\frac{d\overline{U}}{dy} - \overline{uv} \tag{2.55}$$

can be averaged over the fluid layer $-h \leq y \leq h$ to obtain

$$\tau_w = \frac{\nu U}{h} - \langle uv\rangle \tag{2.56}$$

since $\overline{U}(y = \pm h) = \pm U$ and τ_w is constant, and where the brackets $\langle\cdots\rangle$ denote a volume average. While $\nu d\overline{U}/dy$ and $-\overline{uv}$ in (2.8) are functions of y that add up to the drag τ_w, equation (2.56) expresses the drag as a the laminar value $\nu U/h$ plus a nonlinear, turbulent contribution $-\langle uv\rangle$. Normalizing (2.56) by U^2 yields

$$\frac{\tau_w}{U^2} = \frac{1}{R} - \frac{\langle uv\rangle}{U^2} \tag{2.57}$$

showing the $1/R$ scaling of the *friction factor* τ_w/U^2 (recall the Moody diagram of Lecture 1) in laminar flow where $\langle uv\rangle = 0$.

Eliminating τ_w between (2.55) and (2.56) gives $\nu d\overline{U}/dy = \nu U/h + \overline{uv} - \langle uv\rangle$ which we can then use to eliminate the mean shear $d\overline{U}/dy$ in the fluctuation energy equation (2.54) to obtain the constraint

$$-\langle uv\rangle\frac{U}{h} + \frac{1}{\nu}\Big(\langle\overline{uv}\rangle^2 - \langle\overline{uv}^2\rangle\Big) = \nu\,\left\langle|\nabla\mathbf{v}'|^2\right\rangle \tag{2.58}$$

since $\langle\overline{uv}\rangle = \langle uv\rangle$. The $1/\nu$ term on the left hand side is negative definite and can be written $\langle\overline{uv}\rangle^2 - \langle\overline{uv}^2\rangle = -\langle(\overline{uv} - \langle uv\rangle)^2\rangle$, thus (2.58) shows that we need $\langle uv\rangle < 0$ to sustain turbulent fluctuations. In the standard non-dimensionalization of velocities by U and lengths by h, the energy constraint (2.58) reads

$$-\langle uv\rangle = R\left\langle(\overline{uv} - \langle uv\rangle)^2\right\rangle + \frac{1}{R}\left\langle|\nabla\mathbf{v}'|^2\right\rangle \geq 0 \tag{2.59}$$

with the Reynolds number $R = Uh/\nu$. The upper bound problem is then to find the field $\mathbf{v}' = (u, v, w)$, with $\nabla\cdot\mathbf{v}' = 0$ and $\mathbf{v}' = 0$ on the boundaries, that maximizes $-\langle uv\rangle$ subject to the energy constraint (2.59) for fixed Reynolds number R. Busse [2] uses a different convention and normalization and actually solves for the minimum Reynolds number for a given momentum transport $\mu \equiv -\langle uv\rangle \geq 0$. Busse argues that the optimum solution is streamwise x independent and solves the problem approximately using so-called 'multi-α solutions' that provide the interesting multi-scale optimum field shown in figure 2.2.

Doering and Constantin [3] have developed a different 'background flow' approach to bounds on flow quantities and Kerswell [8] has shown the relationship between the Howard-Busse and the Doering-Constantin approaches. Plasting and Kerswell [12] obtain the bound

$$\frac{\tau_w}{h}U = \mathcal{E} < 0.034\frac{U^3}{h} \tag{2.60}$$

for plane Couette flow in the limit $R = Uh/\nu \to \infty$, where U is the half wall velocity difference and h is the half distance between the walls.

2.7 Mean flow phenomenology

We now consider some features of a fully turbulent (*i.e.* R well above transition) shear flow near a solid boundary. The following arguments are discussed in Kundu and Cohen [9, p. 570] and Pope [13, Chap. 7]. We consider the case where the boundary roughness is small, so it does not affect the flow. In this section we think of y as the distance to the (bottom) wall, not to the centerline as earlier in these notes.

Prandtl (1925) proposed that at sufficiently large Reynolds number $R = Uh/\nu \gg 1$, in a region sufficiently close to the wall $y \ll h$, the mean velocity profile $\overline{U}(y)$ should have a universal form, independent of h. This is in the spirit of the inertial scaling discussed earlier. Indeed, the drag at the wall $\tau_w = \nu d\overline{U}/dy|_{wall}$ is a function of the bulk or wall velocity U, the half channel height h and the kinematic viscosity ν, in general, but in non-dimensional form this reads

$$\tau_w = U^2 f(R) \tag{2.61}$$

for some function $f(R)$ where $R = Uh/\nu$ is the Reynolds number. This should be obvious enough but follows more generally from the 'Buckingham Pi theorem'. Recall that the plot of τ_w/U^2 as a function of R is the *Moody diagram* shown for pipe flow in lecture 1. The assumption of *inertial scaling* is that $f(R) \to$ *constant* as $R \to \infty$, an asymptotic regime labeled *'complete turbulence'* on the Moody diagram. This is equivalent to saying that for sufficiently large R, the drag at the wall τ_w is independent of the size of the channel h, which then implies that it is also independent of ν and can only be proportional to U^2, by

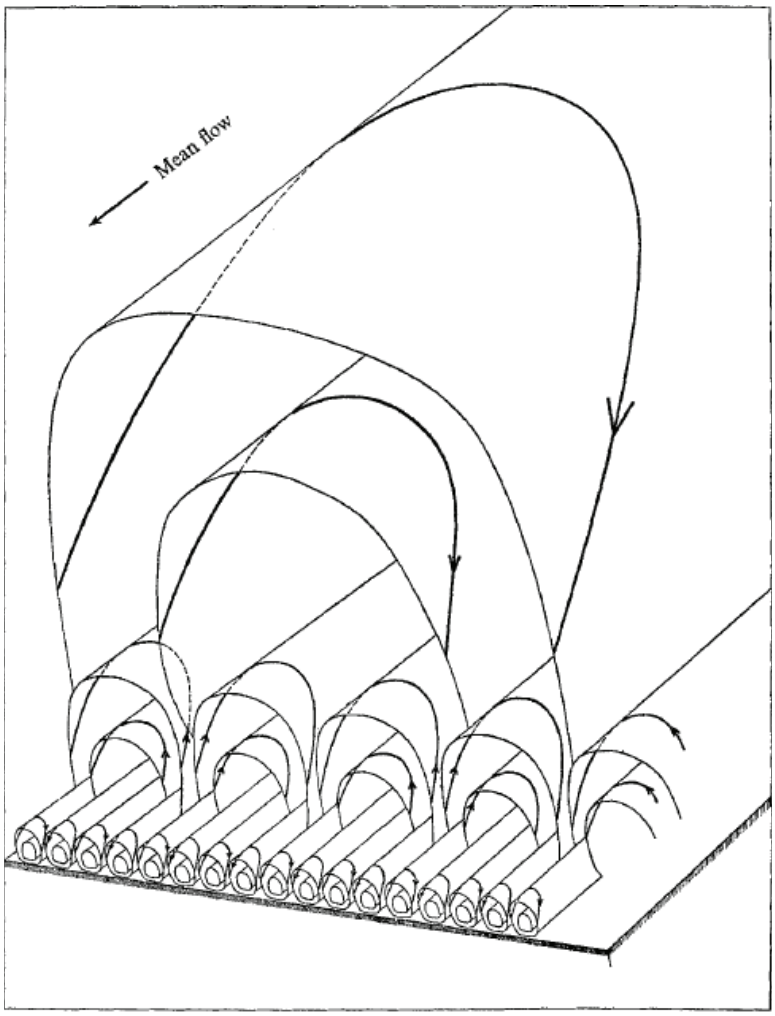

Figure 2.2: Qualitative sketch of the boundary-layer region of the vector field yielding maximum transport of momentum, from Busse [2]. The streamlines depict the fiuctuation field $\mathbf{v}' = (u, v, w)$ and show that $\langle uv \rangle < 0$ with $u > 0$ when $v < 0$ and $u < 0$ when $v > 0$.

dimensional analysis. It is also equivalent to making the assumption that τ_w is independent of ν as $R \to \infty$, in which case it is also independent of h by dimensional analysis.

The equation for the mean flow in plane Couette (2.8) can be written

$$\frac{d\overline{U}}{dy} = \frac{u_\tau^2}{\nu} + \frac{\overline{uv}}{\nu} \tag{2.62}$$

where it will be convenient to write the drag as $\tau_w = u_\tau^2$. In channel flow, integrating (2.6) over y with (2.7) gives

$$\frac{d\overline{U}}{dy} = \frac{u_\tau^2}{\nu}\left(1 - \frac{y}{h}\right) + \frac{\overline{uv}}{\nu}. \tag{2.63}$$

Recall that we have shifted the y coordinate so that the bottom wall is at $y = 0$ and the channel centerline is at $y = h$ for the purpose of this section, with $\overline{U}(0) = 0$ and $\overline{U}(2h) = 2U$ in plane Couette flow. From the boundary condition and incompressibility, $\nabla \cdot \mathbf{v}' = 0$, we have u, v, $\partial v/\partial y \to 0$ as $y \to 0$ and $d\overline{U}/dy \to u_\tau^2/\nu$ as $y \to 0$ so $\overline{U} \sim u_\tau^2 y/\nu$ in both Couette and channel flow. This suggests introducing the *friction velocity* u_τ (often written u_*) and the *'wall unit'* δ^+,

$$u_\tau \equiv \sqrt{\tau_w}, \qquad \delta^+ \equiv \frac{\nu}{u_\tau}, \tag{2.64}$$

so that in wall units the asymptotic relation $\overline{U} \sim u_\tau^2 y/\nu$ as $y \to 0$ simply reads

$$\overline{U}^+ \sim y^+ \tag{2.65}$$

where $\overline{U}^+ = \overline{U}/u_\tau$ and $y^+ = y/\delta^+ = y u_\tau/\nu$. Experiments and simulations show that (2.65) holds in $0 \le y^+ \lesssim 5$, a region that is called the *viscous sublayer*. The *friction Reynolds number* is then defined as

$$R_\tau = \frac{u_\tau h}{\nu} = \frac{h}{\delta^+}, \tag{2.66}$$

and the channel centerline in wall units is at $y^+ = R_\tau$. In laminar flow, $\tau_w \sim \nu U/h$ so $R_\tau \sim \sqrt{R}$ for 'low' R but the inertial scaling $\tau_w \sim U^2$ gives $R_\tau \sim R$ for large R. Pope [13, p. 279] gives the approximation $R_\tau \approx 0.09 R^{0.88}$ for turbulent channel flow, but see also (2.78) and (2.80) below, for a linear relationship up to a log correction.

These considerations suggest that it may be more appropriate to use u_τ as the characteristic velocity for the mean profile $\overline{U}(y)$ instead of the bulk or wall velocity U and $\delta^+ = \nu/u_\tau$ as the length scale instead of h. So the mean profile $\overline{U}(y)$ depends on u_τ, h, ν and y but by dimensional analysis (and the Pi theorem if necessary) we can write in full generality

$$\frac{d\overline{U}}{dy} = \frac{u_\tau^2}{\nu}\, f(y^+, R_\tau) \tag{2.67}$$

for some function $f(\cdot,\cdot)$ such that $\lim_{y^+ \to 0} f(y^+, R_\tau) = 1$, for any R_τ, as follows from (2.62) and (2.63). Note that $y/h = y^+/R_\tau$. Prandtl's *law of the wall* postulates that

$$\lim_{\substack{R_\tau \to \infty \\ y^+ \, fixed}} f\left(y^+, R_\tau\right) = \Phi(y^+), \tag{2.68}$$

and therefore

$$\frac{d\overline{U}}{dy} \approx \frac{u_\tau^2}{\nu}\,\Phi(y^+), \tag{2.69}$$

for arbitrary but fixed y^+ as $R_\tau \to \infty$, *i.e.* for $y \ll h$ with $R_\tau \gg 1$. Equation (2.69) can be written $d\overline{U}^+/dy^+ \approx \Phi(y^+)$ and there is indeed good experimental and numerical evidence that the mean profile *scales in wall units*, that is, mean profiles corresponding to different R_τ will 'collapse' onto one another when plotted in wall units, $\overline{U}^+(y^+)$.

The law of the wall (2.69) implies that $\overline{U}(y)$ is independent of h for $y/h \to 0$. The von Karman *log law* can then be derived by assuming further that $d\overline{U}/dy$ is also independent of ν for sufficiently large y^+, this would require both $\delta^+ \ll y \ll h$, and require $R_\tau = h/\delta^+ \gg 1$. Recall that in the inertial scaling $\tau_w \sim U^2$ is independent of both h and ν. For $d\overline{U}/dy$ in (2.69) to be independent of ν requires $\Phi(y^+) \sim 1/y^+$ giving $d\overline{U}/dy \sim u_\tau/y$. This is equivalent to $d\overline{U}^+/dy^+ \sim 1/y^+$ and yields

$$\overline{U}^+ \approx \frac{1}{\kappa}\ln(y^+) + C, \tag{2.70}$$

where κ is known as the von Karman constant. Experiments and simulations show that $\kappa \approx 0.41$ and $C \approx 5.2$ and the log law (2.70) holds approximatively in $30\,\delta^+ \lesssim y \lesssim 0.3\,h$. The region $5 \lesssim y^+ \lesssim 30$ where the mean velocity profile transitions from the viscous behavior $\overline{U}^+ \sim y^+$ (2.65) to the log law (2.70) is called the *buffer region*.

Von Karman (1930) derived the log law using unsatisfying mixing length arguments and 2D flow considerations, instead of the reasoning presented above. Millikan (1938) provided a more satisfying asymptotic 'overlap' argument (see *e.g.* [9]) that matches Prandtl's law of the wall for $y \ll h$ to the *velocity defect law* that applies for $y \gg \delta^+$. Prandtl's law of the wall (2.69) can be written

$$\overline{U}(y) \sim u_\tau\, F(y^+), \tag{2.71}$$

or $\overline{U}^+ \sim F(y^+)$ where $\overline{U}^+ = \overline{U}/u_\tau$, with $F(y^+) \sim y^+$ as $y^+ \to 0$ (2.65) and $dF/dy^+ = \Phi(y^+)$. This law applies for $y \ll h$ and $R_\tau \gg 1$. There is a similar *velocity defect law* that would apply for $y \gg \delta^+ = \nu/u_\tau$. By dimensional analysis, we can write

$$\overline{U}(y) - \overline{U}_C = u_\tau\, g(\eta, R_\tau) \tag{2.72}$$

for some function $g(\cdot,\cdot)$, where $\overline{U}_c$ is the centerline velocity and $\eta \equiv y/h$ with $y = 0$ at the wall to the channel center at $y = h$. The *velocity defect law* states that the velocity defect, $\overline{U}(y) - \overline{U}_C$, depends only on u_τ and $\eta = y/h$ but not ν

$$\overline{U}(y) - \overline{U}_C \sim u_\tau\, G(\eta) \tag{2.73}$$

for $R_\tau \to \infty$ with $\eta = y/h = y^+/R_\tau$ fixed but arbitrary. In the overlap region, $\delta^+ \ll y \ll h$, both equations (2.71) and (2.73) should hold and

$$\frac{dU}{dy} \sim \frac{u_\tau^2}{\nu}\frac{dF}{dy^+}, \tag{2.74}$$

$$\frac{dU}{dy} \sim \frac{u_\tau}{h}\frac{dG}{d\eta}. \tag{2.75}$$

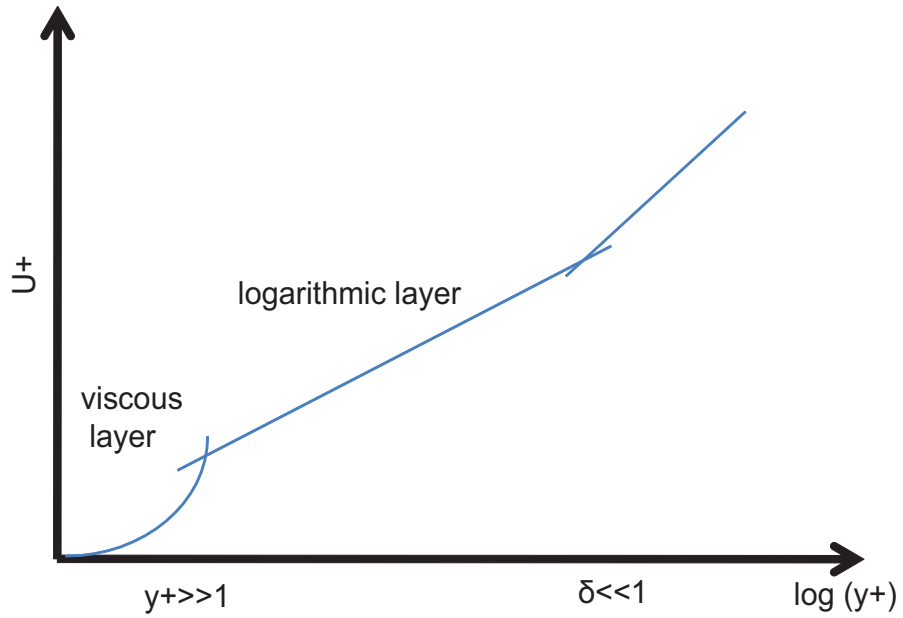

Figure 2.3: Sketch of the 'Law of the Wall' with its viscous sublayer $\overline{U}^+ \sim y^+$ for $y^+ \lesssim 5$ and the log region $\overline{U}^+ \sim \kappa^{-1} \ln y^+ + C$ for $30 \lesssim y^+ \lesssim 0.3R_\tau$.

Multiplying both equations by y/u_τ yields

$$y^+ \frac{dF}{dy^+} \sim \eta \frac{dG}{d\eta} \tag{2.76}$$

since $y^+ = yu_\tau/\nu$ and $\eta = y/h$. Considering $R_\tau \to \infty$ with y^+ fixed but arbitrary gives

$$y^+ \frac{dF}{dy^+} \sim \lim_{\eta \to 0} \left(\eta \frac{dG}{d\eta} \right) \equiv \frac{1}{\kappa} \tag{2.77}$$

where κ is the von Karman constant and this yields the log law (2.70).

The von Karman log law (2.70) is a good approximation to the mean velocity in most of the channel except for a small viscous region with $y^+ \lesssim 30$, *i.e.* $y \lesssim 30\nu/u_\tau$ and a small deviation near the center of the channel. It can therefore be used to derive an approximation to the friction factor $\tau_w/U^2 = f(R)$ for large R. Integrating the log law (2.70) from $y^+ \approx 30$ to the centerline at $y^+ = R_\tau \gg 1$ and dividing by the half size of the channel in wall units, R_τ, gives the bulk velocity U as

$$\frac{U}{u_\tau} = \frac{R}{R_\tau} \approx \frac{1}{R_\tau} \int_{30}^{R_\tau} \left(\frac{\ln y^+}{\kappa} + C \right) dy^+ \approx \frac{\ln R_\tau}{\kappa}, \tag{2.78}$$

for $R_\tau \gg 1$. Defining $u_\tau/U = \sqrt{\lambda}$ where $\lambda = \tau_w/U^2$ is a friction factor, equation (2.78) gives

$$\frac{1}{\sqrt{\lambda}} = \frac{R}{R_\tau} \approx 2.44 \ln R_\tau = 2.44 \ln \left(R\sqrt{\lambda} \right) \tag{2.79}$$

for $1/\kappa \approx 2.44$, for channel flow. The friction factor is often defined as $2\tau_w/U^2$ in the literature, so watch out for factors of 2. In any case, the friction factor would not be quite R independent as $R \to \infty$ and there would be a relatively small log correction to that inertial scaling.

For plane Couette flow, we could simply evaluate (2.70) at the centerline $y = h$ so $y^+ = R_\tau$ where $\overline{U} = U$ (since $\overline{U}(0) = 0$ and $\overline{U}(2h) = 2U$ in the convention of this section) to obtain

$$\frac{U}{\sqrt{\tau_w}} \equiv \frac{U}{u_\tau} \equiv \frac{R}{R_\tau} \approx \frac{1}{\kappa} \ln R_\tau + C \tag{2.80}$$

and therefore

$$\frac{\tau_w U}{h} = \mathcal{E} \approx \frac{1}{(5.2 + 2.44 \ln R_\tau)^2} \frac{U^3}{h}, \tag{2.81}$$

using $C \approx 5.2$ and $\kappa \approx 0.41$. Again, there would be a log correction to the inertial scaling. A good engineer would adjust all the constants to fit the data as well as possible, but our purpose here was only to give a brief introduction to turbulence folklore.

Bibliography

[1] D. Acheson, *Elementary Fluid Dynamics*, Oxford University Press, 1990.

[2] F. H. Busse, *Bounds for turbulent shear flow*, Journal of Fluid Mechanics, 41 (1970), pp. 219–240.

[3] C. R. Doering and P. Constantin, *Energy dissipation in shear driven turbulence*, Phys. Rev. Lett., 69 (1992), pp. 1648–1651.

[4] J. Hamilton, J. Kim, and F. Waleffe, *Regeneration mechanisms of near-wall turbulence structures*, J. Fluid Mech., 287 (1995), pp. 317–348.

[5] L. N. Howard, *Heat transport by turbulent convection*, Journal of Fluid Mechanics, 17 (1963), pp. 405–432.

[6] L. N. Howard, *Bounds on flow quantities*, Annual Review of Fluid Mechanics, 4 (1972), pp. 473–494.

[7] G. Kawahara and S. Kida, *Periodic motion embedded in Plane Couette turbulence: regeneration cycle and burst*, J. Fluid Mech., 449 (2001), pp. 291–300.

[8] R. Kerswell, *Unification of variational principles for turbulent shear flows: the background method of doering-constantin and the mean-fluctuation formulation of howard-busse*, Physica D: Nonlinear Phenomena, 121 (1998), pp. 175 – 192.

[9] P. Kundu and I. Cohen, *Fluid Mechanics*, Academic Press, Elsevier, 2010.

[10] W. V. R. Malkus, *Outline of a theory of turbulent shear flow*, Journal of Fluid Mechanics, 1 (1956), pp. 521–539.

[11] T. Mullin, *Experimental studies of transition to turbulence in a pipe*, Annual Review of Fluid Mechanics, 43 (2011), pp. 1–24.

[12] S. C. Plasting and R. R. Kerswell, *Improved upper bound on the energy dissipation rate in plane Couette flow: the full solution to Busse's problem and the Constantin–Doering–Hopf problem with one-dimensional background field*, Journal of Fluid Mechanics, 477 (2003), pp. 363–379.

[13] S. Pope, *Turbulent Flows*, Cambridge University Press, 2000.

[14] P. Sagaut and C. Cambon, *Homogeneous Turbulence Dynamics*, Cambridge University Press, 2008.

[15] D. Viswanath, *Recurrent motions within plane Couette turbulence*, J. Fluid Mech., 580 (2007), pp. 339–358.

Lecture 3

Stability of Shear Flow

notes by Zhan Wang and Sam Potter
Revised by FW
WHOI GFD Lecture 3, 6/22/2011

A look at energy stability, valid for all amplitudes, and linear stability for shear flows.

3.1 Nonlinear stability

Associated Navier-Stokes equation:

$$\partial_t \mathbf{v} + \mathbf{v}\cdot\nabla\mathbf{v} + \nabla P = \mathbf{F} + \nu\nabla^2\mathbf{v} \quad \text{with} \quad \nabla\cdot\mathbf{v} = 0 \tag{3.1}$$

In this equation $\nu = R^{-1}$ is the nondimensional viscosity coefficient, where R is the Reynolds number. Let us assume a base flow $\mathbf{U}(\mathbf{x},t)$ that is a known solution to equation (7.1) driven by the body force $\mathbf{F}$ (*e.g.* an imposed pressure gradient $\mathbf{F} = -\hat{\mathbf{x}}\, dP_0/dx$ in channel flow, or gravity for flow down an inclined channel) and/or the boundary conditions. Next we perturb the flow as $\mathbf{v} = \mathbf{U} + \mathbf{u}$ where $\mathbf{u} = (u, v, w)$ represents the perturbation. We plug this $\mathbf{v}$ into equation (7.1) which yields:

$$\partial_t\big(\mathbf{U}+\mathbf{u}\big) + \mathbf{U}\cdot\nabla\mathbf{U} + \mathbf{u}\cdot\nabla\mathbf{U} + \mathbf{U}\cdot\nabla\mathbf{u} + \mathbf{u}\cdot\nabla\mathbf{u} + \nabla\big(P+p\big) = \mathbf{F} + \nu\nabla^2\big(\mathbf{U}+\mathbf{u}\big) \tag{3.2}$$

Since $\mathbf{U}$ is a solution of equation (7.1) the associated terms cancel and we get the perturbation equation:

$$\partial_t\mathbf{u} + \mathbf{U}\cdot\nabla\mathbf{u} + \mathbf{u}\cdot\nabla\mathbf{U} + \mathbf{u}\cdot\nabla\mathbf{u} + \nabla p = \nu\nabla^2\mathbf{u} \tag{3.3}$$

with the incompressible constraint $\nabla\cdot\mathbf{u} = 0$. For the domain V with fixed boundary ∂V, the boundary condition for $\mathbf{u}$ is homogeneous, namely, $\mathbf{u}\big|_{\partial V} = 0$ or periodic. Note that the decomposition $\mathbf{v} = \mathbf{U} + \mathbf{u}$ into a *base flow* plus a *perturbation* is different from the Reynolds decomposition $\mathbf{v} = \bar{\mathbf{v}} + \mathbf{v}'$ into a *mean* plus a *fluctuation*. The base flow $\mathbf{U}$ is a solution of the Navier-Stokes equations and is independent of the perturbation $\mathbf{u}$, but the mean flow is $\bar{\mathbf{v}}$ is not a solution of Navier-Stokes and is coupled to the fluctuations $\mathbf{v}'$ through the Reynolds stresses.

In order to calculate the total kinetic energy of the perturbation, we multiply equation (3.3) by $\mathbf{u}$ and integrate over the domain V

$$\int_V \mathbf{u}\cdot\Big(\partial_t\mathbf{u}+\mathbf{U}\cdot\nabla\mathbf{u}+\mathbf{u}\cdot\nabla\mathbf{U}+\mathbf{u}\cdot\nabla\mathbf{u}+\nabla p-\nu\nabla^2\mathbf{u}\Big)dV=0 \tag{3.4}$$

Direct computation using integration by parts and the incompressibility condition ($\nabla\cdot\mathbf{U}=\mathbf{0}\rightarrow\nabla\cdot\mathbf{u}=\mathbf{0}$) yields

$$\begin{aligned}\frac{d}{dt}\int_V\frac{|\mathbf{u}|^2}{2}dV &= \int_V -\mathbf{u}\cdot\nabla\mathbf{U}\cdot\mathbf{u}\,dV-\nu\int_V\nabla\mathbf{u}:\nabla\mathbf{u}^T\,dV\\ &\triangleq \underbrace{\int_V-\mathbf{u}\cdot\mathbf{S}\cdot\mathbf{u}\,dV}_{\text{Production}}-\underbrace{\nu\int_V|\nabla\mathbf{u}|^2\,dV}_{\text{Dissipation}}\end{aligned} \tag{3.5}$$

where $\mathbf{S}$ is the symmetric tensor strain rate tensor defined as $S_{ij}=\frac{1}{2}\big(\partial_iU_j+\partial_jU_i\big)$ and $u_iS_{ij}u_j=u_i(\partial_iU_j)u_j$ using Einstein summation and $\nabla\mathbf{u}:\nabla\mathbf{u}^T\triangleq(\partial_iu_j)(\partial_iu_j)=|\nabla u|^2+|\nabla v|^2+|\nabla w|^2\triangleq|\nabla\mathbf{u}|^2$. Since the dissipation term is always positive, if the production term is negative or zero the the flow is *absolutely stable*, that is, stable to any perturbation $\mathbf{u}$.

Example: Rigid body rotation is absolutely stable, since the production term is 0. In this case

$$\begin{aligned}\mathbf{U}&=\begin{pmatrix}0&-\Omega&0\\ \Omega&0&0\\ 0&0&0\end{pmatrix}\begin{pmatrix}x\\ y\\ z\end{pmatrix}\Rightarrow\nabla\mathbf{U}=\begin{pmatrix}0&\Omega&0\\ -\Omega&0&0\\ 0&0&0\end{pmatrix}\\ S_{ij}&=\frac{1}{2}\big(\partial_iU_j+\partial_jU_i\big)\Rightarrow\mathbf{S}=\begin{pmatrix}0&0&0\\ 0&0&0\\ 0&0&0\end{pmatrix}.\end{aligned} \tag{3.6}$$

Definition (growth rate): We can think of the right hand side of (3.5) normalized by $2E\triangleq\int_V|\mathbf{u}|^2dV$ as a *growth rate* since if the perturbation had the form $\mathbf{u}\triangleq e^{\lambda t}\widehat{\mathbf{u}}(\mathbf{x})$, as would be the case for time independent $\mathbf{U}$ in the linear limit, we would have $|\mathbf{u}|^2=\exp(2\sigma t)|\widehat{\mathbf{u}}|^2$ and $(2E)^{-1}dE/dt=\sigma=\Re(\lambda)$, so σ, the real part of λ, is called the *growth rate*. We have $-\mathbf{u}\cdot\mathbf{S}\cdot\mathbf{u}\leqslant\lambda_{\max}\mathbf{u}\cdot\mathbf{u}$ where $\lambda_{\max}$ is the largest eigenvalue of the real and symmetric $(-\mathbf{S})$. Manipulating the right hand side of equation (3.5) gives

$$\begin{aligned}\sigma &\triangleq \frac{\int_V-\mathbf{u}\cdot\mathbf{S}\cdot\mathbf{u}dV}{\int_V|\mathbf{u}|^2dV}-\frac{\nu\int_V|\nabla\mathbf{u}|^2dV}{\int_V|\mathbf{u}|^2dV}\\ &\leqslant \frac{\lambda_{\max}\int_V|\mathbf{u}|^2dV}{\int_V|\mathbf{u}|^2dV}-\frac{\nu\int_V|\nabla\mathbf{u}|^2dV}{\int_V|\mathbf{u}|^2dV}\leqslant\lambda_{\max}\end{aligned} \tag{3.7}$$

and this provides a simple upper bound on the growth rate of any instability.

Theorem (Serrin 1959): For any steady solution $\mathbf{U}$ there exists a critical Reynolds number $Re_1>0$ such that for any flow with $Re\leqslant Re_1$, the system is absolutely stable. See [2, §53.1] or [1, §9.6].

Next let's turn to shear base flows, *i.e.* $\mathbf{U} = U(y)\hat{\mathbf{x}}$ and

$$\mathbf{S} = \begin{pmatrix} 0 & \frac{U'}{2} & 0 \\ \frac{U'}{2} & 0 & 0 \\ 0 & 0 & 0 \end{pmatrix}, \quad \text{where} \quad U' \triangleq \frac{dU}{dy} \tag{3.8}$$

The corresponding kinetic energy takes the form

$$\frac{d}{dt}\int_V \frac{|\mathbf{u}|^2}{2} dV = \int_V -uv\frac{dU}{dy} dV - \nu \int_V |\nabla \mathbf{u}|^2 dV \tag{3.9}$$

that is very similar to the fluctuation energy equation derived in lecture 2, but again the production term there involved the mean shear rate $d\overline{U}/dy$ that depends on the Reynolds stress $\overline{uv}$, while here we have the base shear rate dU/dy that is independent of uv. For shear flows, the growth rate $\sigma < \max(U'/2)$ (assuming $U' \geq 0$) and this maximum would require very large Reynolds numbers $\nu = 1/R \to 0$ and $u = -v$ with $w = 0$, localized near the max of U'. In the case of nondimensional Couette flow $U(y) = y$, the energy equation reads

$$\frac{d}{dt}\int_V \frac{|\mathbf{u}|^2}{2} dV = \int_V -uv\, dV - \nu \int_V |\nabla \mathbf{u}|^2 dV \tag{3.10}$$

From this equation it can be seen that $-uv > 0$ occurring somewhere in the domain V is a necessary condition for instability. Turning to the energy stability of shear flows, if we define the critical value ν_E

$$\nu_E \triangleq \max \frac{\displaystyle\int_V -uv\frac{dU}{dy} dV}{\displaystyle \nu \int_V |\nabla \mathbf{u}|^2 dV} \tag{3.11}$$

it directly follows that

$$\frac{d}{dt}\int_V \frac{|\mathbf{u}|^2}{2} dV \leqslant (\nu_E - \nu) \int_V |\nabla \mathbf{u}|^2 dV. \tag{3.12}$$

The inequality (3.12) shows that the perturbation is stable if $\nu_E < \nu \Leftrightarrow R < 1/\nu_E \triangleq R_E$. This is a sufficient condition for stability and is known as the *absolute stability threshold*. Therefore an argument for absolute stability turns into an optimization problem (3.11) with the constraints $\nabla \cdot \mathbf{u} = \mathbf{0}$ and $\mathbf{u}\big|_{\partial V} = 0$

Remark: For Couette flow, the critical Reynolds number for absolute stability is about 20.7, see [2, §53.1].

3.2 Linear stability

The flow is decomposed into a base flow $\mathbf{U}$ and a perturbation about the base flow $\mathbf{u}$

$$\mathbf{v} = \mathbf{U} + \mathbf{u}. \tag{3.13}$$

Plugging into the Navier-Stokes equations and neglecting the quadratic nonlinearity $\mathbf{u}\cdot\nabla\mathbf{u}$ gives

$$\partial_t\mathbf{u} + \mathbf{U}\cdot\nabla\mathbf{u} + \mathbf{u}\cdot\nabla\mathbf{U} + \nabla p = \nu\nabla^2\mathbf{u}. \tag{3.14}$$

The base flow is now taken to be a shear flow, $\mathbf{U} = U(y)\hat{\mathbf{x}}$. Taking the curl of (3.14) and dotting with the vertical unit vector $\hat{\mathbf{y}}$ gives

$$(\partial_t + U\partial_x - \frac{1}{R}\nabla^2)\eta = -\partial_z v\,\frac{dU}{dy} \tag{3.15}$$

where $\eta = \hat{\mathbf{y}}\cdot\nabla\times\mathbf{u}$ is the vertical component of the vorticity and $v = \hat{\mathbf{y}}\cdot\mathbf{u}$ is the vertical component of the perturbation velocity. Taking the curl of (3.14) twice and dotting with the vertical unit vector gives

$$(\partial_t + U\partial_x - \frac{1}{R}\nabla^2)\nabla^2 v - \partial_x v\frac{d^2U}{dy^2} = 0. \tag{3.16}$$

Equations (3.15) and (3.16) are known as the Squire and Orr-Sommerfeld equations, respectively. Note that the v equation (3.16) is decoupled from the η equation (3.15). There are two basic kinds of boundary conditions at the walls of the channel. One is no-slip boundary condition $u = v = w = 0$ which implies there is no perturbation at the walls. In the Orr-Sommerfeld equation this boundary condition takes the form $v = 0$, $v_y = -u_x - w_z = 0$ and $\eta = u_z - w_x = 0$. The other is 'free slip' boundary conditions (*i.e.* stress or Neumann boundary conditions on the full flow) $v = u_y = w_y = 0$ which implies $v = 0$, $\eta_y = u_{yz} - w_{xz} = 0$ and $v_{yy} = -u_{xy} - w_{zy} = 0$ at the walls of the channel. Next we turn to the Fourier analysis of the Orr-Sommerfeld system, since $U = U(y)$ only, equations (3.15) and (3.16) admit solutions of the form

$$\eta(x,y,z,t) = \hat{\eta}(y)e^{\lambda t}e^{i(\alpha x+\gamma z)}$$
$$v(x,y,z,t) = \hat{v}(y)e^{\lambda t}e^{i(\alpha x+\gamma z)}$$

where λ is a complex-valued growth rate, α and γ are the real streamwise and spanwise wavenumbers, respectively, and $\hat{\eta}(y)$ and $\hat{v}(y)$ are complex functions. Plugging the above forms of v and η into equations (3.15) and (3.16) gives

$$\left[\lambda + i\alpha U - \frac{1}{R}(D^2 - k^2)\right]\hat{\eta} = -i\gamma\hat{v}U' \tag{3.17}$$

$$\left[\lambda + i\alpha U - \frac{1}{R}(D^2 - k^2)\right](D^2 - k^2)\hat{v} - U''i\alpha\hat{v} = 0 \tag{3.18}$$

where a prime indicates a y-derivative, $D = d/dy$, and $k^2 = \alpha^2 + \gamma^2$. Equation (3.18) can be simplified by multiplying through by k/α

$$\left[\widetilde{\lambda} + ikU - \frac{1}{\widetilde{R}}(D^2 - k^2)\right](D^2 - k^2)\hat{v} - U''ik\hat{v} = 0 \tag{3.19}$$

where $\widetilde{\lambda} = \lambda k/\alpha$ and $\widetilde{R} = R\alpha/k$.

Squire's theorem. Equation (3.19) is (3.18) with $\alpha \equiv k$ and rescaled growth rate and

Reynolds number. Therefore a three dimensional perturbation with wavenumbers (α, γ) at Reynolds number R with growth rate λ is mathematically equivalent to a two dimensional perturbation with wavenumbers $(k, 0)$ but with Reynolds number $\widetilde{R} = R\,\alpha/k \leq R$ and growth rate $\Re(\widetilde{\lambda}) = \Re(\lambda)k/\alpha \geq \Re(\lambda)$. In other words, for any 3D unstable mode (α, γ) there is a 2D unstable mode $(\sqrt{\alpha^2+\gamma^2}, 0)$ with *larger* growth rate at a *lower* Reynolds number. This is Squire's Theorem [3], [2]. Another way to derive this result, is to let $\alpha U(y) = k\widetilde{U}(y)$ in (3.19) and conclude that a 3D perturbation is equivalent to a 2D perturbation with a weaker shear flow $\widetilde{U}(y) = \alpha U(y)/k$.

Furthermore, it is easy to show that the homogeneous η equation, that is (3.17) with $v = 0$ has only damped modes (multiply the homogeneous equation by η^* the conjugate of η, integrate from wall to wall and add the complex conjugate of the result to show that $\lambda + \lambda^* = 2\sigma \leq 0$). This is physically obvious since (3.17) is an advection diffusion equation when $v = 0$, in fact the decay of $\int_V \eta^2 dV$ for $v = 0$ can be shown for the full linear PDE (3.15). Thus the eigenvalue problem for (3.15), (3.16), reduces to the consideration of the Orr-Sommerfeld equation (3.19) for 2D perturbations only. Note that equation (3.17) with $v \neq 0$ exhibits *transient growth* for 3D perturbations with $\partial_z v \neq 0$, as discussed in lecture 1. The physical mechanism behind this is the redistribution of streamwise velocity $U(y)$ by the perturbation v to create u perturbations and $\eta = \partial_z u - \partial_x w$.

3.3 Energy equation

From Squire's theorem it suffices to consider (3.18) with $k = \alpha$

$$\left[\lambda + i\alpha U - \frac{1}{R}(D^2 - \alpha^2)\right](D^2 - \alpha^2)\hat{v} - U'' i\alpha\hat{v} = 0. \tag{3.20}$$

The equation for the complex conjugate $\hat{v}^*$ reads

$$\left[\lambda^* - i\alpha U - \frac{1}{R}(D^2 - \alpha^2)\right](D^2 - \alpha^2)\hat{v}^* + U'' i\alpha\hat{v}^* = 0. \tag{3.21}$$

since $U(y)$, α and R are real and where λ^* is the complex conjugate of λ. Doing the following surgery: $\hat{v}^* \cdot (3.20) + \hat{v} \cdot (3.21)$ and integrating from the bottom of the domain $(y = y_1)$ to the top of the domain $(y = y_2)$ yields

$$(\lambda + \lambda^*) \underbrace{\int_{y_1}^{y_2} \left(|Dv|^2 + \alpha^2|v|^2\right) dy}_{\text{kinetic energy}} = \underbrace{\int_{y_1}^{y_2} U'T dy}_{\text{production}} - \underbrace{\frac{2}{R}\int_{y_1}^{y_2} |\phi|^2 dy}_{\text{dissipation}}. \tag{3.22}$$

Here $T \triangleq i\alpha(\hat{v}D\hat{v}^* - \hat{v}^*D\hat{v}) \equiv -\alpha^2\overline{uv}$, and $\phi \triangleq (D^2 - \alpha^2)\hat{v}$ with

$$\int_{y_1}^{y_2} |\phi|^2 dy = \int_{y_1}^{y_2} |D^2 v - \alpha^2 v|^2 dy = \int_{y_1}^{y_2} \left(|D^2\hat{v}|^2 + 2\alpha^2|D\hat{v}|^2 + \alpha^4|\hat{v}|^2\right) dy \geq 0. \tag{3.23}$$

It is noted that when doing the integration by parts, the boundary condition $\hat{v}\big|_{\partial V} = 0$ is used, and either $D\hat{v}\big|_{\partial V} = 0$ or $D^2\hat{v}\big|_{\partial V} = 0$ can be applied to lead the same equality (3.22). In other words, (3.22) holds for both *no-slip* and *free-slip* boundary conditions.

Equation (3.22) is simply the version of (3.9) for 2D eigensolutions $v = \hat{v}(y)e^{\lambda t}e^{i\alpha x}$ with $u = \hat{u}(y)e^{\lambda t}e^{i\alpha x} = (i/\alpha)D\hat{v}\ e^{\lambda t}e^{i\alpha x}$ to satisfy $\partial_x u + \partial_y v = 0$ and the 'Reynolds stress' for such a perturbation is

$$-\overline{uv} = -\left(\hat{u}^*\hat{v} + \hat{u}\hat{v}^*\right)e^{2\sigma t} = \frac{i}{\alpha}\left(\hat{v}D\hat{v}^* - \hat{v}^*D\hat{v}\right)e^{2\sigma t} \equiv \frac{T}{\alpha^2}e^{2\sigma t} \tag{3.24}$$

where $2\sigma = \lambda + \lambda^*$ and $\overline{uv}$ is the horizontal average of uv. Likewise, $\phi = (D^2 - \alpha^2)\hat{v}$ is effectively the z component of vorticity $\omega_z = \partial_x v - \partial_y u = (i\alpha\hat{v} - (i/\alpha)D^2\hat{v})\,e^{\lambda t}e^{i\alpha x} = (-i/\alpha)\phi(y)\,e^{\lambda t}e^{i\alpha x}$.

For *free-slip* boundary conditions, $\hat{v} = D^2\hat{v} = 0$ at the walls, we can derive a useful form of the *enstrophy equation*, *i.e.* an equation for the integral of vorticity squared. Consider $\int_{y_1}^{y_2}\left[(D^2-\alpha^2)\hat{v}^* \cdot (3.20) + (D^2-\alpha^2)\hat{v}\cdot(3.21)\right]dy = 0$ to obtain

$$(\lambda+\lambda^*)\int_{y_1}^{y_2}|\phi|^2dy = \underbrace{-\int_{y_1}^{y_2}U'''T\,dy}_{\text{production}} - \underbrace{\frac{2}{R}\int_{y_1}^{y_2}\left[|D\phi|^2 + \alpha^2|\phi|^2\right]dy}_{\text{dissipation}\geq 0} \tag{3.25}$$

It follows directly that $U''' = 0$ implies linear stability for free-slip, that is $2\sigma = \lambda + \lambda^* \leq 0$. In other words plane Couette flow $U(y) = y$ and plane Poiseuille flow $U(y) = 1 - y^2$, in $-1 \leq y \leq 1$, are linearly stable for free-slip (*i.e.* imposed stress) boundary conditions as well as any combination of Couette and Poiseuille $U(y) = a + by + cy^2$, among other flows. We'll discuss this further in the next lecture.

The enstrophy equation (3.25) only holds under free-slip boundary condition, since $\hat{v}\big|_{\partial V} = D^2\hat{v}\big|_{\partial V} = 0$ leads to the cancelation of the boundary terms in integration by parts but a boundary term of indefinite sign subsists for no-slip $\hat{v} = D\hat{v} = 0$ at the walls. The physical meaning of these boundary terms is that vorticity can be generated (or destroyed) at the walls for no-slip but not for free-slip.

Bibliography

[1] D. Acheson, *Elementary Fluid Dynamics*, Oxford University Press, 1990.

[2] P. Drazin and W. Reid, *Hydrodynamic Stability*, Cambridge University Press, Cambridge, UK, 1981.

[3] H. Squire, *On the stability of three-dimensional disturbances of viscous flow between parallel walls*, Proc. Roy. Soc. Lond. A, 142 (1933), pp. 621–628.

Lecture 4

Stability of Shear Flow: part 2

notes by Matthew Chantry and Lindsey Ritchie
Revised by FW
WHOI GFD Lecture 4, 6/23/2011

We derive necessary conditions for linear instability of shear flows and prove linear stability of plane Couette, Poiseuille and Kolmogorov flows for *viscous* flow with *stress* boundary conditions (*i.e.* free-slip perturbations) thereby generalizing well-known *inviscid* stability results. We give a straightforward derivation of classic inviscid results by combining the perturbation energy and enstrophy equations. We then summarize the stability of various canonical shear flows and conclude the implications of energy stability and linear theory. Furthermore, we examine inflectional instabilities and introduce their role in the self-sustaining process.

4.1 Necessary conditions for linear instability

In the previous lecture the full flow $\mathbf{v}$ has been decomposed into a base shear flow $U(y)\hat{\mathbf{x}}$ and a perturbation $\mathbf{u}$. The Navier-Stokes equations have been linearized about the base flow $U(y)\hat{\mathbf{x}}$ and this led us to the Squire and Orr-Sommerfeld equation after elimination of the pressure. Since the equations for $\mathbf{u}$ have been linearized and its coefficients depend only on $U(y)$, we can reduce the solution to the consideration of perturbations of the form $\mathbf{u} = \hat{\mathbf{u}}(y)e^{\lambda t}e^{i\alpha x}e^{i\gamma z}$ with α, γ real (*i.e.* Fourier-Laplace expansion of $\mathbf{u}$). Then *Squire's theorem* shows that it suffices to consider 2D perturbations ($\gamma = 0$) to investigate exponentially growing modes, that is solutions with $2\Re(\lambda) = \lambda + \lambda^* = 2\sigma > 0$. We define $\lambda = \sigma - i\omega$ where $i^2 = -1$ and σ and ω are real.

We derived an energy and enstrophy equation for those linear 2D perturbations and both equations include a production term that involves the perturbation 'Reynolds stress' $-\overline{uv} \equiv \alpha^{-2}T(y)e^{2\sigma t}$, where

$$T(y) = -\alpha^2\left(\hat{u}^*\hat{v} + \hat{u}\hat{v}^*\right) = i\alpha\left(\hat{v}D\hat{v}^* - \hat{v}^*D\hat{v}\right), \tag{4.1}$$

such that $T = 0$ at the walls at $y = y_1$ and $y = y_2$ since $v = 0$ there. We write $D \equiv d/dy$ for compactness. We drop the hat over $\hat{v}$ below.

The perturbation energy equation derived in the previous lecture implies that for an instability, $\sigma > 0$, we must have

$$2\sigma \int \left(|Dv|^2 + \alpha^2|v|^2\right) + \frac{2}{R}\int |\phi|^2 = \int U'T = -\int (U - U_0)\, T' > 0, \tag{4.2}$$

where $\int(\cdots)$ is short for $\int_{y_1}^{y_2}(\cdots)dy$, the integral from the bottom wall at $y = y_1$ to the top wall at y_2, the prime $(\cdot)' \equiv D(\cdot) \equiv d(\cdot)/dy$, that is $U' = dU/dy$, $U'' = d^2U/dy^2$,... The function $\phi = (D^2 - \alpha^2)v$ is effectively the perturbation vorticity (see lecture 3).[1]

Equation (4.2) follows from multiplying the Orr-Sommerfeld equation (4.17) by v^*, integrating over the full channel from $y = y_1$ to y_2 using integration by parts and taking the real part of the result. The last expression in (4.2) was obtained by integration by parts of $\int U'T$ and U_0 is an arbitrary constant since $\int U_0 T' = U_0 \int T' = 0$ because $T = 0$ at the walls.

For *free-slip* boundary conditions, that is $v = D^2v = 0$ at the walls (corresponding to stress boundary conditions on the full flow, that is $\mathbf{v}\cdot\hat{\mathbf{y}} = 0$ with $\partial_y \mathbf{v}_\parallel$ fixed), the perturbation enstrophy equation derived in lecture 3 reads

$$2\sigma \int |\phi|^2 + \frac{2}{R}\int \left(|D\phi|^2 + \alpha^2|\phi|^2\right) = \int U''T' = \int (-U''')T \; > 0, \tag{4.3}$$

and the enstrophy production $\int U''T' = \int(-U''')T$ should be positive for an instability $\sigma > 0$. This equation was obtained by multiplying the Orr-Sommerfeld equation (4.17) by $\phi^* = (D^2 - \alpha^2)v^*$, integrating over the channel using multiple integrations by parts then taking the real part of the integral equation (*i.e.* adding its complex conjugate). This yields the enstrophy equation (4.3) together with the boundary term

$$\frac{1}{R}\Big[\phi^* D\phi + \phi D\phi^*\Big]_{y_1}^{y_2} \tag{4.4}$$

on the right hand side of (4.3). This boundary term vanishes for $v = D^2v = 0$ on the boundary since $\phi = D^2v - \alpha^2 v$. For no-slip, $v = Dv = 0$, the boundary term (4.4) is sign indefinite and corresponds to the generation or destruction of enstrophy at the walls.

Now, since $\phi = (D^2 - \alpha^2)v$, integration by parts with $v = 0$ at the walls gives

$$\int |\phi|^2 = \int \left(|D^2v|^2 + 2\alpha^2|Dv|^2 + \alpha^4|v|^2\right) \tag{4.5}$$

so we can combine the energy and enstrophy equation taking (4.3) - α^2 (4.2) to obtain

$$2\sigma \int \left\{|D^2v|^2 + \alpha^2|Dv|^2\right\} + \frac{2}{R}\int |D\phi|^2 = \\ -\int (U''' + \alpha^2 U')T = \int \left(U'' + \alpha^2(U - U_0)\right)T' \; > 0. \tag{4.6}$$

[1] In the classical literature, *e.g.* [1, Chap. 4], it is common to use a streamfunction $\phi(y)$ for the Rayleigh and Orr-Sommerfeld equations, we prefer to use the vertical velocity v in those equations and our $\phi = (D^2 - \alpha^2)v$ is effectively the vorticity, $\omega = \partial_x v - \partial_y u = (i\alpha)^{-1}\phi(y)e^{\lambda t}e^{i\alpha x}$.

We can go even further and take (4.6) - β^2 (4.2) to obtain

$$2\sigma \int \left\{ \left(|D^2 v|^2 - \beta^2 |Dv|^2 \right) + \alpha^2 \left(|Dv|^2 - \beta^2 |v|^2 \right) \right\} + \frac{2}{R} \int \left(|D\phi|^2 - \beta^2 |\phi|^2 \right) =$$
$$- \int \left(U''' + (\alpha^2 + \beta^2) U' \right) T = \int \left(U'' + (\alpha^2 + \beta^2)(U - U_0) \right) T' \quad (4.7)$$

The left hand side of (4.7) is not necessarily positive even for $\sigma > 0$ unless β is small enough. Indeed, the left hand side consists of integrals of the form $\int (|Df|^2 - \beta^2 |f|^2)$ and each of these integrals will be positive provided $\beta \leq \pi/2$ for free slip boundary conditions $v = D^2 v = \phi = 0$ at the walls at $y = \pm 1$ since for such functions one can show by variational calculus that

$$\int_{-1}^{1} |Dv|^2 dy \geq \frac{\pi^2}{4} \int_{-1}^{1} |v|^2 dy, \quad (4.8)$$

$$\int_{-1}^{1} |D\phi|^2 dy \geq \frac{\pi^2}{4} \int_{-1}^{1} |\phi|^2 dy, \quad (4.9)$$

$$\int_{-1}^{1} |D^2 v|^2 dy \geq \frac{\pi^2}{4} \int_{-1}^{1} |Dv|^2 dy, \quad (4.10)$$

so the left hand side of (4.7) will always be positive if $\sigma > 0$ (instability) and $\beta^2 \leq \pi^2/4$. This yields another necessary condition for instability

$$- \int \left(U''' + \left(\alpha^2 + \frac{\pi^2}{4} \right) U' \right) T = \int \left(U'' + \left(\alpha^2 + \frac{\pi^2}{4} \right) (U - U_0) \right) T' \geq 0. \quad (4.11)$$

Condition (4.11) is expressed for a domain normalized to $-1 \leq y \leq 1$, for $y_1 \leq y \leq y_2$ the factor $\pi^2/4$ should be replaced by π^2/H^2, with $H = y_2 - y_1$.

Thus for a linear shear flow instability, $\sigma > 0$, we must have positive energy production $\int U'T = -\int (U - U_0)T' > 0$ from (4.2), always, as well as condition (4.11) for *viscous flow with free-slip* perturbations. Note that (4.11) together with (4.2) includes and therefore supersedes (4.3) and (4.6) and we obtain the necessary conditions for linear instability for *viscous flow with free-slip*, or for *inviscid flow*,

$$\boxed{\int (-U''')\, T \;\geq \left(\alpha^2 + \frac{\pi^2}{H^2} \right) \int U'\, T \;> 0} \quad (4.12)$$

which, after integration by parts with $T = 0$ at the walls, can also be written as

$$\boxed{\int U'' T' \;\geq \left(\alpha^2 + \frac{\pi^2}{H^2} \right) \int (U_0 - U)\, T' \;> 0} \quad (4.13)$$

where $H = y_2 - y_1$ is the total channel height, U_0 is an arbitrary constant, $\int \equiv \int_{y_1}^{y_2} dy$ and $T = T(y)$ is the perturbation Reynolds stress (4.1).

4.1.1 Linear stability of Couette, Poiseuille and Kolmogorov

The enstrophy equation (4.3) allows us to conclude that plane Couette flow $U = y$, plane Poiseuille flow $U = 1 - y^2$ and any combination of Couette and Poiseuille $U = a + by + cy^2$ for any constant a, b, c (*i.e.* shear flow driven by both a pressure gradient and imposed stress at the walls) are *linearly stable* for *inviscid or viscous flow with free-slip*, since all these flows have $U''' = 0$ and no enstrophy production, therefore $\sigma < 0$ for any $0 \le R < \infty$ from (4.3).[2]

Condition (4.12), or (4.13), allows us to show linear stability for *free-slip* of the *Kolmogorov flow*

$$U(y) = \frac{\sin(\beta y)}{\sin \beta} \tag{4.14}$$

whenever $\beta \le \pi/2$. The Kolmorogov flow (5.28) is normalized so $U(\pm 1) = \pm 1$ as for Couette flow which it asymptotes to for $\beta \to 0$, and we can take $\beta \ge 0$ without loss of generality. The Kolmogorov flow is an *inflectional profile* with a vorticity maximum at $y = 0$. For (5.28), we have $-U''' = \beta^2 U' = \beta^3 \cos(\beta y)/\sin\beta$ so instability of the *wall-bounded* Kolmogorov flow requires, from (4.12), that

$$\int_{-1}^{1} \cos(\beta y)\, T\, dy > 0 \qquad \text{and} \qquad \beta^2 \ge \alpha^2 + \frac{\pi^2}{4}, \tag{4.15}$$

where $T(y)$ is defined in (4.1), so Kolmogorov flow (5.28) with $0 \le \beta \le \pi/2$ is linearly stable. This includes Couette flow for $\beta \to 0$ and the flow $U(y) = \sin(\pi y/2)$ used in the derivation of the SSP model [9], as well as all sinusoidal profiles between those two flows.

Lou Howard (1997, private communication) provided a proof for the linear stability of the $U = \sin(\pi y/2)$ viscous flow with free-slip perturbations used in [9]. His proof made use of the energy (4.2) and enstrophy (4.3) equations and $U'' = (-\pi^2/4)U$ for $U = \sin \pi y/2$ to eliminate the production terms through the combination (4.3) - $\pi^2/4$ (4.2).

Linear instability for *inviscid* or *viscous* flow with *no-slip or free-slip* requires positive perturbation energy production $\int U'T > 0$ from (4.2). If we could show that $U'T \ge 0$ *pointwise*, for instance, then we could generalize the classic Rayleigh and Fjortoft theorems of inviscid flow (see below) to *viscous* flow with *free-slip* perturbations. Indeed if we *assume* that $U'T$ is positive pointwise, not just on average as required by (4.12), then

$$\int (-U''')T' = \int \left(\frac{-U'''}{U'}\right) U'T \;\le \max_y \left(\frac{-U'''}{U'}\right) \int U'T$$

and (4.12) would yield the necessary condition[3]

$$\max_{y_1 \le y \le y_2} \left(\frac{-U'''}{U'}\right) \ge \alpha^2 + \pi^2/H^2. \tag{4.16}$$

[2] We stress again that these results only apply to viscous flows with *stress* boundary conditions, that is, $\mathbf{v}\cdot\mathbf{n}$ and $\partial_n \mathbf{v}_\parallel$ fixed (*i.e.* fixed stress $\nu\partial_n \mathbf{v}_\parallel$), where $\mathbf{n}$ is the unit normal to the wall and $\mathbf{v}_\parallel = \mathbf{v} - (\mathbf{v}\cdot\mathbf{n})\mathbf{n}$ is parallel to the wall. From incompressibility, this yields $v = D^2 v = 0$ at the walls. For no-slip, (4.3) has an extra boundary term of indefinite sign.

[3] as claimed in the lecture but flagged by Matt Chantry as only valid for $U'T \ge 0$ pointwise, which we have not shown. Good eye, Matt!

This would be a stronger version of Fjortoft's theorem, implying for instance that a flow such as $U = y^3$ with $U' = 3y^2 \geq 0$ and $U''' = 6 > 0$ could not be unstable but other inflectional flows such as $U = \tanh(\beta y)$ could be unstable provided β is large enough. This would be a nice result since the linear stability of shear flows (see *e.g.* [1, Chap. 4]) is in an unsatisfactory state of affairs, with classic inflectional instability results derived only for *inviscid* flows. If we could extend those results to *viscous* flow with *free-slip*, this would certify that the difference is not between inviscid or viscous flow, but between free-slip or no-slip, as numerical calculations indicate. The physical difference arising because no-slip allows the generation of enstrophy at the walls but free-slip or viscosity-free do not.

4.1.2 Inviscid results

The energy (4.2) and enstrophy (4.3) integrals, and the instability conditions (4.12), (4.13), still apply for *inviscid flow* with $1/R \equiv 0$ in which case the *Orr-Sommerfeld equation* for $v(y)$

$$\left[\lambda + i\alpha U - \frac{1}{R}(D^2 - \alpha^2)\right](D^2 - \alpha^2)v - U'' i\alpha v = 0. \tag{4.17}$$

reduces to the *Rayleigh equation*

$$(U - c)(D^2 - \alpha^2)v - U''v = 0 \tag{4.18}$$

with $\lambda \triangleq -i\alpha c$, that is $c = i\lambda/\alpha = \omega/\alpha + i\sigma/\alpha$ for $\lambda = \sigma - i\omega$ with $i^2 = -1$ and σ, ω real. So an instability for Rayleigh's equation occurs when $\Im(c) = \sigma/\alpha > 0$, taking $\alpha > 0$ without loss of generality. The only boundary condition for Rayleigh's equation is no-flow through the walls, that is $v = 0$ at $y = y_1$ and y_2.

Rayleigh's equation (4.18) allows us to derive an expression for T', the Reynolds force. Substituting for $D^2 v$ from (4.18) into $T' \equiv DT = dT/dy$ calculated from (4.1) gives

$$T' = i\alpha(vD^2v^* - v^*D^2v) = 2\sigma \frac{U''}{|U - c|^2} |v|^2 \tag{4.19}$$

hence T' has the sign of U'' when $\sigma = \Re(\lambda) > 0$ (instability).

Rayleigh's theorem (1880). Since $T = 0$ at the walls (4.1), T' and therefore U'' *must change sign in the domain for instability.* Thus U'' must vanish somewhere in the domain but not everywhere (Couette flow) since $\sigma = 0$ from (4.2) and (4.19) when $1/R \equiv 0$ and $U'' = 0$ everywhere.

Fjortoft's theorem (1950). Substituting for T' from (4.19) into (4.2) shows that instability requires $(U_0 - U)U'' \geq 0$ somewhere in the domain, for any U_0, which again gives Rayleigh's theorem that U'' must change sign in the domain. Picking $U_0 = U(y_s) = U_s$ where $U''(y_s) = 0$, so both $U_s - U$ and U'' change sign when y crosses y_s, gives the perturbation energy equation (4.2) as

$$\int_{y_1}^{y_2} \left(|Dv|^2 + \alpha^2|v|^2\right) dy = \int_{y_1}^{y_2} \frac{(U_s - U)U''}{|U - c|^2} |v|^2 \, dy \; \geq 0, \tag{4.20}$$

for $\sigma \neq 0$ and *Fjortoft's theorem* that $(U_s - U)U'' \geq 0$ somewhere in the domain is necessary for instability. This implies linear stability of flows such as $U = y^3$ for which $(U_s - U)U'' =$

$-6y^4 \leq 0$, but possible instability of flows such as $U = \sin(\beta y)/\sin\beta$ that have $U'' = \beta^2(U_s - U)$, see *e.g.* [1, Fig. 4.2].

We can go further by substituting for T' from (4.19) into (4.11) or (4.13), with $U_0 = U_s$, to find that $(U'')^2 \geq (\alpha^2 + \pi^2/H^2)(U_s - U)U''$ somewhere in the domain. If we now *assume* that $(U_s - U)U'' \geq 0$ everywhere, we obtain that

$$\max_{y_1 \leq y \leq y_2} \left(\frac{U''}{U_s - U} \right) \geq \alpha^2 + \frac{\pi^2}{H^2} \tag{4.21}$$

is necessary for instabilitym where H is the full height of the channel. This implies stability of the Kolmorogov flows $U = \sin(\beta y)/\sin\beta$ when $|\beta| \leq \pi/H$ as we already established for viscous flow with free-slip, but now also includes other similar flows such as $U = \tanh\beta y$ which are only unstable for β large enough (left to the reader). Condition (4.21) effectively contains the results of Friedrichs (1942) and Drazin and Howard (1966) [1, p. 133, 134]. Our derivation is more straightforward but the result is not quite identical since Friedrichs provides an expression for a neutral wavenumber. Condition (4.21) shows that inflectional instabilities are larger scale instabilities, that is, they require $0 \leq \alpha^2 \leq \beta_s^2 - \pi^2/H^2$, where $\beta_s^2 \equiv \max(U''/(U_s - U))$.

Since the production integral on the right hand side of (4.20) can written for any constant U_0 in place of U_s and in particular for $U_0 = c_r = \Re(c)$, and since $|U - c|^2 = (c_r - U)^2 + c_i^2$ with $c_i = \Im(c) = \sigma/\alpha$, we can infer that while $U'' = 0$ somewhere is necessary for instability, the maximum instability ($\max c_i$) occurs for values of c_r that tend to maximize $U''/(c_r - U)$ and functions $v(y)$ that are largest near those maxima. For profiles that are anti-symmetric about the inflection point, such as $U = \sin\beta y$ or $\tanh\beta y$, this will likely be for $c_r = U_s$.

4.2 Rayleigh's piecewise linear models

Rayleigh's eigenvalue problem (4.18) is difficult to solve when $U(y)$ is a smoothly varying function (figure 4.1(a)). However, if $U(y)$ is defined as a piecewise linear function (as shown in figure 4.1(b)), then the solutions of Rayleigh's equation are simple exponential or hyperbolic functions which must satisfy certain matching conditions at a discontinuity of $U(y)$ or $U'(y)$ [1].

The matching conditions can be derived by going back to the primitive equations [1, §23] and [8, §6.2.1] and the reader should study those derivations. Here, we start from Rayleigh's equation (4.18) and imagine a continuous deformation from a smooth profile to a piecewise linear profile, for instance a continuous deformation of $U = \tanh(y/h)$ into the piecewise linear profile in fig. 4.1(b)). Then Rayleigh's equation applies but $U'' \to \infty$ at corners and 0 everywhere else, *i.e.* U'' tends to a sum of Dirac delta functions and Rayleigh's equation implies that $D^2v \to \infty$ at those points also, to balance the U'' divergences. That is, the jumps in U' must be balanced by jumps in v' as governed by Rayleigh's equation. Indeed, Rayleigh's equation (4.18) can be rewritten in the form

$$\big((U - c)v' - U'v\big)' - \alpha^2(U - c)v = 0, \tag{4.22}$$

and integrating (4.22) across a vanishing rapid transition region for U', say from $y = y_0 - \epsilon$

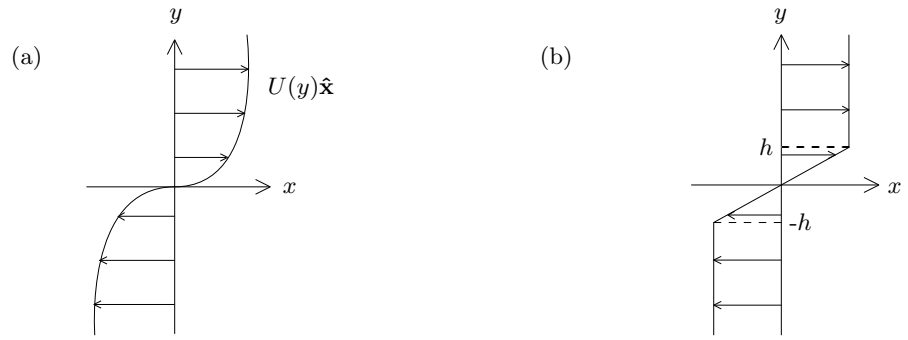

Figure 4.1: (a) Unbounded smooth shear flow. (b) Piecewise-linear unbounded shear flow.

to $y = y_0 + \epsilon$ with $\epsilon \to 0^+$ gives the jump condition

$$\Big[(U-c)v' - U'v\Big]_{y_0^-}^{y_0^+} = 0. \tag{4.23}$$

This jump condition corresponds to continuity of pressure [1, §23] and [8, §6.2.1].

If we also allow for jumps in U, these must be matched by jumps in v and that balance is revealed by rewriting (4.22) as

$$\left((U-c)^2\left(\frac{v}{U-c}\right)'\right)' - \alpha^2(U-c)v = 0. \tag{4.24}$$

which shows that $v/(U-c)$ cannot jump since such a jump could not be balanced in Rayleigh's equation. Thus, the jump conditions for v at a jump of U is

$$\left[\frac{v}{U-c}\right]_{y_0^-}^{y_0^+} = 0. \tag{4.25}$$

A discontinuous U profile corresponds to the Kelvin-Helmholtz model with a sharp interface between two differentially moving fluid layers. The jump condition (4.25) corresponds to the linearized material interface condition [1, §23] and [8, §6.2.1].

Away from jumps, when the velocity profile is piecewise linear, $U'' = 0$, and so Rayleigh's stability equation (4.18) has the general solution

$$v(y) = Ae^{\alpha y} + Be^{-\alpha y} \tag{4.26}$$

for arbitrary constants A,B. Therefore, we can use conditions (4.23) and (4.25) to match solutions of the form (4.26) to solve any problem with a piecewise linear velocity profile.

For the piecewise linear unbounded shear flow, we take

$$U(y) = \begin{cases} U_0 & \text{if } y \geq h, \\ U_0 y/h & \text{if } -h \leq y \leq h, \\ -U_0 & \text{if } y \leq -h, \end{cases} \tag{4.27}$$

as in figure 4.1b. Note that $U'' = (-U_0/h)\delta(y-h) + (U_0/h)\delta(y+h)$ where $\delta(\cdot)$ is the Dirac delta function and that U'' *changes sign*. We could consider this problem as the limit for $\epsilon \to 0^+$ of the smooth profile with $U'' = (-U_0/h)G(y-h,\epsilon) + (U_0/h)G(y+h,\epsilon)$ where $G(y,\epsilon) = (\pi\epsilon)^{-1/2}\exp(-y^2/\epsilon)$ is the standard Gaussian.

Solving (4.18) for (4.27) with $v \to 0$ as $y \to \pm\infty$ gives

$$v(y) = \begin{cases} Ae^{-\alpha(y-h)} & \text{if } y > h, \\ Be^{\alpha y} + Ce^{-\alpha y} & \text{if } -h < y < h, \\ De^{\alpha(y+h)} & \text{if } y > -h, \end{cases} \tag{4.28}$$

with $\alpha > 0$ (and D here is a constant not the d/dy shorthand as before). Since U is continuous, the jump condition (4.25) reduces to continuity of v at $y = \pm h$, hence

$$\begin{aligned} A &= Be^{\alpha h} + Ce^{-\alpha h}, \\ D &= Be^{-\alpha h} + Ce^{\alpha h}. \end{aligned} \tag{4.29}$$

It is now convenient to let

$$\hat{c} = \frac{c}{U_0}, \quad \hat{\alpha} = \alpha h, \tag{4.30}$$

(or equivalently taking h and U_0 has length and velocity scales leading to $h \equiv 1$ and $U_0 \equiv 1$) then applying the jump condition (4.23) at $y = \pm h$, substituting for A and D from (4.29) gives

$$\begin{aligned} \big(2\hat{\alpha}(1-\hat{c}) - 1\big)Ce^{\hat{\alpha}} &= Be^{-\hat{\alpha}}, \\ \big(2\hat{\alpha}(1+\hat{c}) - 1\big)Be^{\hat{\alpha}} &= Ce^{-\hat{\alpha}}, \end{aligned} \tag{4.31}$$

which after elimination of B and C yields $\big((2\hat{\alpha}-1)^2 - 4\hat{\alpha}^2\hat{c}^2\big) = e^{-4\hat{\alpha}}$ and

$$\hat{c}^2 = \frac{(1-2\hat{\alpha})^2 - e^{-4\hat{\alpha}}}{4\hat{\alpha}^2}, \tag{4.32}$$

such that $\hat{c}^2 \to -1$ as $\hat{\alpha} \to 0$, $\hat{c}^2 = 0$ at $\hat{\alpha} \approx 0.63$ and $\hat{c}^2 < 0$ in $0 < \hat{\alpha} \lesssim 0.63$. A negative $\hat{c}^2$ means $c = c_r + ic_i$ with $c_r = 0$ and $c_i = \pm|c|$, hence instability. The growth rate (4.18) $\lambda = -i\alpha c = \alpha c_i$ is real when c^2 is negative. Define $\hat{\lambda} = \hat{\alpha}\hat{c}_i = \alpha c_i(h/U_0)$, so $\hat{\lambda} = \lambda(h/U_0)$ and this non-dimensional growth rate is plotted in fig. 4.2 as a function of the non-dimensional wavenumber $\hat{\alpha} = \alpha h$.

Kelvin-Helmholtz. The limit $h \to 0$ yields the Kelvin-Helmholtz model with $\hat{\alpha} = \alpha h \to 0$ in (4.32) yielding $\hat{c}^2 \to -1$ so $c = \pm iU_0$ and $\lambda = -i\alpha c = \pm\alpha U_0$. The Kelvin-Helmholtz model is *ill-posed* since $\lambda = \alpha U_0$ can be as large as one desires by taking α large enough, but Rayleigh's piecewise linear model with a length scale h, eqns. (4.27), (4.32) and fig. 4.2, is well-posed and gives a qualitatively and quantitatively valid picture of the instability that only occurs for $\alpha \lesssim 0.63/h$. Although, 'Kelvin-Helmholtz instability' is often used to describe general inflectional instability and vortex roll-up, the Kelvin-Helmholtz model is a bit too singular to provide insights into the instability for smooth profiles $U(y)$. The Rayleigh model (4.27) is more physical and shows that the instability results from the interaction between two regions where $U''/(c_r - U)$ is large and positive with U'' of opposite signs. Valis [8, §6.2.4] provides a useful interpretation of the instability as an interaction between edge waves for the Rayleigh model.

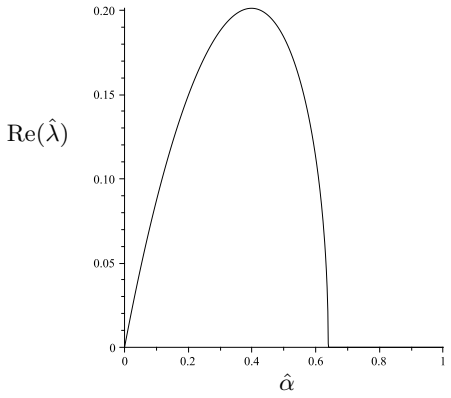

Figure 4.2: Growth rate $\hat{\lambda} = \hat{\alpha}\hat{c}_i = \alpha c_i(h/U_0)$ with c given by equation (4.32). The flow is unstable for $\hat{\alpha} = \alpha h < 0.63$.

Reynolds stress. The perturbation Reynolds stress is given by (4.1)

$$-\overline{uv} = \frac{i}{\alpha}\left(v\frac{dv^*}{dy} - v^*\frac{dv}{dy}\right). \tag{4.33}$$

In the case of piecewise linear unbounded shear flow (4.28) this gives

$$-\overline{uv} = \begin{cases} 0 & \text{if } y > h, \\ 2i(BC^* - B^*C) & \text{if } -h < y < h, \\ 0 & \text{if } y > -h. \end{cases} \tag{4.34}$$

then eliminating C using (4.31) with $c = ic_i$ and $\hat{\sigma} = \hat{\alpha}\hat{c}_i > 0$ gives

$$-\overline{uv} = 4\hat{\sigma}|B|^2 e^{2\hat{\alpha}} > 0 \tag{4.35}$$

in $-h < y < h$, where $\hat{\alpha} = \alpha h$ and $\hat{\sigma} = \sigma(h/U_0)$ with $\sigma = \alpha c_i > 0$ for an unstable mode. Therefore, constant positive perturbation Reynolds stress $-\overline{uv}$ occurs throughout the shear layer and $U'T \geq 0$ pointwise (4.2) (but this is for the inviscid problem). The Reynolds stress $-\overline{uv}$ transports momentum from $y = h$ to $y = -h$ and vice-versa. The Reynolds *force* onto the mean flow $-d\overline{uv}/dy$ consists of two delta functions, one negative at $y = h$ and a positive at $y = -h$, slowing down the mean at $y = h$ and speeding it up at $y = -h$.

4.3 Instability from viscosity and no-slip

Remarkably, viscosity and *no-slip* at the walls can lead to linear instability even for flows with $U''' = 0$, such as plane Poiseuille flow $U = 1 - y^2$, that are stable for free-slip as shown in sect. 4.1. In plane Poiseuille flow, Heisenberg [2] found a weak linear 2D instability, that occurs at $R \simeq 5772$ [4] and disappears as $R \to \infty$. In boundary layer flows Tollmien [7] and

Schlichting [6] demonstrated a weak 2D instability which has a critical Reynolds number of approximately $R \simeq 500$ and again disappears as $R \to \infty$. However, unlike the previous two flows, Romanov [5] proved that plane Couette flow is linearly stable for all values of R (although this was already believed since the work of Hopf (1914), [1, §31.1]). While pipe flow (or Hagen-Poiseuille flow) has not been proven linearly stable for all R, it is believed to be so, and this has been shown up to $Re \simeq 10^5$ experimentally and $R \simeq 10^7$ computationally (see lecture 1). When the no-slip boundary conditions are replaced by free-slip boundary conditions for the perturbations then we showed earlier in sect. 4.1 that plane Poiseuille and Couette flows are linearly stable for all R. The instability for viscous flow with no-slip in channel flow arises because of the generation of vorticity at the boundary (4.4). This is a delicate process because viscosity leads to dissipation of enstrophy in the bulk as well as generation of enstrophy at the boundary (4.3), these two viscous effects are of the same order and oppose each other.

(Note: A lecture on the Orr-Sommerfeld equation for $R < \infty$, with a look at Heisenberg and Tollmien's work and critical layers was skipped in the GFD program.)

4.4 Failures of linear theories

We now summarise the results derived from linear theory in the last two lectures. From the previous lecture we have the governing linear equations

$$\left(\frac{\partial}{\partial t} + U\frac{\partial}{\partial x} - \frac{1}{Re}\nabla^2\right)\eta = -U'\frac{\partial v}{\partial z}, \tag{4.36}$$

$$\left(\frac{\partial}{\partial t} + U\frac{\partial}{\partial x} - \frac{1}{Re}\nabla^2\right)\nabla^2 v - U''\frac{\partial v}{\partial x} = 0, \tag{4.37}$$

where $v = \hat{\mathbf{y}} \cdot \mathbf{v}$ and $\eta = \hat{\mathbf{y}} \cdot \nabla \times \mathbf{v} = \partial_z u - \partial_x w$. For $v = 0$, we can show that $\eta \to 0$ for $\eta = 0$ or $\partial_n \eta = 0$ at the walls, since the homogeneous η equation is an advection diffusion equation. Exponential instabilities therefore can only originate from the v equation and Squire's theorem (lecture 3) shows that 2D (x, y), that is independent of the spanwise direction z, are more unstable than 3D disturbances. However, the canonical shear flows (Couette, Poiseuille, pipe) do not have a linear instability, except for a weak linear instability for *viscous* plane Poiseuille flow with *no slip* at the walls.

Energy stability on the other hand (lecture 3 and [1, §53.1]) shows that 2D perturbations depending on (y, z) only, independent of the streamwise direction x, lead to the lowest Reynolds number below which the flow is absolutely stable. Hence linear stability theory and energy stability theory give, literally, *orthogonal* results!

The x-independent perturbations of energy stability theory lead to the largest initial perturbation energy growth since they maximize production over dissipation (lecture 3), but such x independent perturbations ultimately decay. We discussed this in lecture 1 and

can show it by considering the *full* non-linear Navier-Stokes equations with no x-dependence,

$$\begin{aligned}
&\frac{\partial u}{\partial t} + \cancelto{0}{u\frac{\partial u}{\partial x}} + v\frac{\partial u}{\partial y} + w\frac{\partial u}{\partial z} = \cancelto{0}{-\frac{\partial p}{\partial x}} + F + \frac{1}{R}\nabla^2 u,\\
&\frac{\partial v}{\partial t} + \cancelto{0}{u\frac{\partial v}{\partial x}} + v\frac{\partial v}{\partial y} + w\frac{\partial v}{\partial z} = -\frac{\partial p}{\partial y} + \frac{1}{R}\nabla^2 v,\\
&\frac{\partial w}{\partial t} + \cancelto{0}{u\frac{\partial w}{\partial x}} + v\frac{\partial w}{\partial y} + w\frac{\partial w}{\partial z} = -\frac{\partial p}{\partial z} + \frac{1}{R}\nabla^2 w,
\end{aligned} \tag{4.38}$$

where $\mathbf{v} = (u, v, w)$ and where F in the u equation is a driving body force. The continuity equation reduces to $\nabla \cdot \mathbf{v} = \partial_y v + \partial_z w = 0$. Hence, the equations for v and w decouple from the equation for u and the latter is a *passive scalar* forced by F and redistributed by v, w. This decoupling implies that v and w do not have any forcing and therefore they decay because of viscosity, no matter their initial amplitude [3]. This was discussed and proved in lecture 1. The proof is simple and consists in deriving the equation for the cross-stream kinetic energy $\int_A (v^2 + w^2)$ where A is the cross-section and showing that $\frac{d}{dt}\int_A (v^2 + w^2) = -(1/R)\int_A \left(|\nabla v|^2 + |\nabla w|^2\right) \leq 0$.

These x-independent perturbations also lead to the largest linear growth of the perturbation energy. For such perturbations, $\eta = \partial_z u - \partial_x w$ reduces to

$$\eta = \frac{\partial u}{\partial z},$$

and we can therefore integrate equation (4.36) with respect to z to recover the streamwise $u = U(y) + \tilde{u}$ velocity equation (4.38) linearized about the base shear flow $U(y)$

$$\frac{\partial \tilde{u}}{\partial t} - \frac{1}{R}\nabla^2 \tilde{u} = -vU'. \tag{4.39}$$

Hence, x-independent but z-dependent $v(y, z)$ perturbations can generate large perturbations of streamwise velocity u and large $\eta = \partial_z u$. However, they eventually decay in the linear theory *as well as* in the full x-independent nonlinear theory, as there is no feedback upon v. The reader is referred to the discussions and models in lecture 1.

4.5 3D, nonlinear 'instability'

Thus linear theory of shear flows fails. Energy stability and upper bound theories (lecture 2) suggest x-independent perturbations as most effective at initial perturbation energy growth and maximum momentum transport and energy dissipation, but truly x-independent perturbations always decay, for all amplitudes. So we need a *nonlinear, 3D* theory. Ouch!

Yet, we're not far. The x-independent perturbations indeed are very good at redistributing the streamwise velocity u and transporting momentum, that is maximizing $-\overline{uv}$ and perturbation energy production $-\overline{uv}\,U'$. This is clear from equation (4.39) which for large R gives $\tilde{u} \sim -vU't$ so $-\overline{uv} \sim \overline{v^2}\,U't$.

These perturbations are necessarily spanwise z dependent, otherwise continuity and the boundary conditions would require $v = 0$. These perturbations typically introduce z-inflections in the streamwise velocity profile and those lead to instabilities of inflectional type, but as a result of z inflections, not y inflections as in the classical linear theory. These inflectional instabilities extract energy and momentum from the u-fluctuations of course and will therefore *accelerate* the return to the laminar flow, *unless* they manage to regenerate v. This seems like a lot of ifs, however that is essentially the fundamental *self-sustaining process* that leads to the possibility of 3D, nonlinear states disconnected from the laminar flow, and ultimately the sustenance of turbulent shear flows. The self-sustaining process will be written up in more detail in the next lectures. (There was lots of hand-waving and jumping around by the lecturer that is difficult to write-up).

Bibliography

[1] P. Drazin and W. Reid, *Hydrodynamic Stability*, Cambridge University Press, Cambridge, UK, 1981.

[2] W. Heisenberg, *On stability and turbulence of fluid flows. (Über stabilität und turbulenz von flüssigkeitsströmen.)*, Trans. from Annalen der Phys., 74,15 (1924), pp. 577–627.

[3] D. D. Joseph and L. N. Tao, *Transverse Velocity Components in Fully Developed Unsteady Flows*, Journal of Applied Mechanics, 30 (1963), pp. 147–148.

[4] S. Orszag, *Accurate solution of the Orr-Sommerfeld stability equation.*, J . Fluid Mech., 50 (1971), pp. 659–703.

[5] V. Romanov, *Stability of plane-parallel Couette flow*, Functional Anal. & its Applic., 7 (1973), pp. 137–146.

[6] H. Schlichting, *Zur entstehung der turbulenz bei der plattenstromung.*, Nachr. Ges. Wiss. Göttingen, Math. Phys. Klasse, (1933), pp. 182–208.

[7] W. Tollmien, *Über die Entstehung der Turbulenz.*, Nachr. Ges. Wiss. Göttingen, Math. Phys. Klasse, (1929), pp. 21–44.

[8] G. K. Vallis, *Atmospheric and Oceanic Fluid Dynamics*, Cambride University Press, 2006.

[9] F. Waleffe, *On a self-sustaining process in shear flows*, Phys. Fluids, 9 (1997), pp. 883–900.

Lecture 5

Feedback on vertical velocity. Rotation, convection, self-sustaining process.

Notes by Andrew Crosby, Keiji Kimura, Adele Morrison
Revised by FW
WHOI GFD Lecture 5, 24 June 2011

We have shown in the previous lectures that the $-vU'$ term in the u equation, that is $\partial_t u = -vU' + \cdots$, is the key term leading to momentum transport $-\overline{uv} \sim \overline{vv}U't$ and perturbation energy production $-\overline{uv}\,U' \sim \overline{vv}(U')^2 t > 0$. This term is the redistribution of streamwise velocity that releases energy from the background shear to enable bifurcation to turbulent flow. However, in shear flows we have not yet identified a mechanism that can feedback from the u fluctuation to v, thus v creates just the right u through the $-vU'$ advection term, but how is v sustained? In this lecture, we first review two *linear* mechanisms of feedback on v involving extra physics, (1) through the Coriolis term in rotating shear flow, (2) through buoyancy in Rayleigh-Bénard convection. We derive the famous Lorenz model for convection, then consider a similar model for shear flows that illustrates the mechanisms involved in the *nonlinear* feedback from u to v, yielding a self-sustaining process for shear flows $v \to u \to \cdots \to v$. This is the model that was already discussed in lecture 1.

5.1 Redistribution of streamwise velocity

In this lecture we will consider the mechanisms that lead to a 3D nonlinear self-sustaining process in shear flows. Let us first consider what this may look like in plane Couette flow. If we introduce a perturbation in the y-direction (in this case $v > 0$), such as a cross-stream jet, the perturbation will create so-called *streamwise rolls,* as shown in Figure 5.1, that is a flow $\mathbf{v} = (0, v(y,z), w(y,z))$ as a result of incompressibility and the boundary conditions.[1] The streamwise rolls redistribute the streamwise velocity, by advecting negative momentum

[1]Streamwise rolls have their axis in the streamwise direction and they are streamwise-independent. Their horizontal wavevector $\mathbf{k}_H = (k_x, k_z) = (0, k_z)$ is actually pointing in the spanwise direction z.

($u < 0$) up and towards $z = 0$ (where $z = 0$ is defined as the position of the jet) and positive momentum ($u > 0$) down and away from $z = 0$.

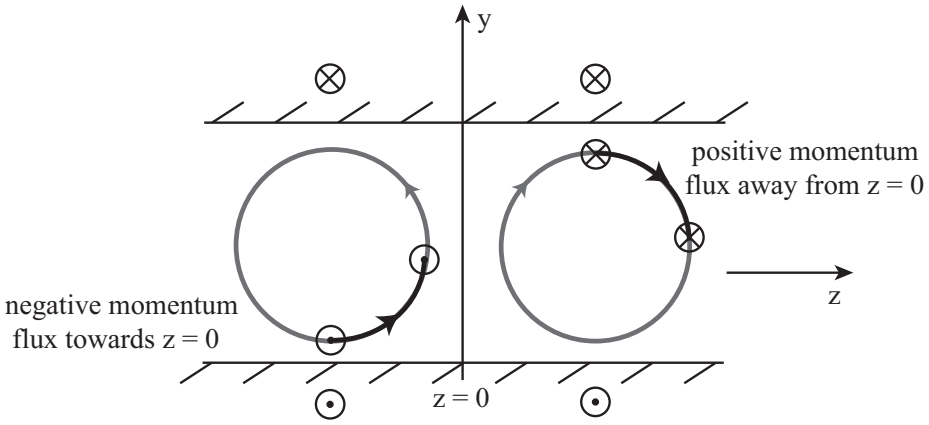

Figure 5.1: Streamwise rolls redistribute the momentum of the mean shear from the bottom wall up and toward $z = 0$ and from the top wall down and away from $z = 0$. The mean shear flow is into and out of the screen.

The redistribution of the streamwise momentum results in a pattern of so-called *streaks* in u, with low streamwise velocity at the position of the jet. 'Streaks' refers to the patterns made by hydrogen bubbles released in the near wall region of turbulent shear flows. In theory, they refer to spanwise fluctuations of the streamwise velocity u, that is the departure of the x averaged u, $\overline{u}^x(y,z)$ from the x and z averaged u, $\overline{u}(y)$, so the streaks are defined as $\overline{u}^x(y,z) - \overline{u}(y)$ (with t implicit). Figure 5.2 shows that the perturbation induces streaks of faster and slower streamwise flow. The profile of u now has inflection points, but in the spanwise z direction, and so we may expect it to be unstable.

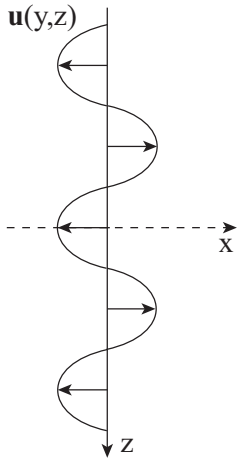

Figure 5.2: Top view: Streamwise rolls redistribute the mean shear creating streaks.

However, in order for the flow to bifurcate from the laminar flow, it is not enough to have rolls $(0, v(y,z), w(y,z))$ creating unstable streaky flow $(u(y,z), 0, 0)$, we need feedback

from the streak instability into the rolls sufficient to lead to a self-sustaining process. To investigate whether a mechanism exists to feedback on the v perturbation, let us consider the energy stability discussed in earlier lectures. If the perturbations are independent of the streamwise x direction, we can separate out the streamwise from the cross-stream components as follows:

$$\frac{d}{dt}\int \frac{u^2}{2} dV = \int \left(-uvU'\right) dV - \frac{1}{R}\int |\nabla u|^2 dV \tag{5.1}$$

$$\frac{d}{dt}\int \frac{v^2+w^2}{2} dV = -\frac{1}{R}\int \left(|\nabla v|^2 + |\nabla w|^2\right) dV \tag{5.2}$$

It is evident from eqn. (5.2) that there is dissipation, but no production, of the cross-stream components. Therefore a further mechanism is needed if the rolls and streaks created by the initial perturbation are to be sustained.

We can further investigate the feedbacks between the streamwise rolls and streaks by considering the streamwise and cross-stream linearized momentum equations eliminating any x dependence (see lectures 1 and 4)

$$\partial_t u - \frac{1}{R}\nabla^2 u = -vU' \tag{5.3}$$

$$\partial_t v - \frac{1}{R}\nabla^2 v + \partial_y p = 0 \tag{5.4}$$

$$\partial_t w - \frac{1}{R}\nabla^2 w + \partial_z p = 0 \tag{5.5}$$

with the pressure $p(y,z,t)$ enforcing $\partial_y v + \partial_z w = 0$ and where $U' = dU/dy$ is the shear rate of the laminar base flow. Equation 5.3 further emphasises the creation of streaks from the streamwise rolls; an updraft $v > 0$ creates $u < 0$, while a downdraft $v < 0$ creates $u > 0$, assuming $U' > 0$. However the cross-stream velocities v, w are decoupled from the streamwise velocity u and therefore the rolls will decay.

5.2 Rotation induced shear instability

One method of creating feedback from u onto v is to add rotation to our system of plane Couette flow. Let us consider rotation of the form $\Omega\hat{\mathbf{z}}$, with $\Omega > 0$. The linearized momentum equations in the rotating frame involve the *Coriolis force* $-2\Omega\hat{\mathbf{z}} \times \mathbf{v} = (2\Omega v, -2\Omega u, 0)$ (the centrifugal force is absorbed into the pressure gradient) and read

$$\partial_t u - \frac{1}{R}\nabla^2 u = -vU' + 2\Omega v \tag{5.6}$$

$$\partial_t v - \frac{1}{R}\nabla^2 v + \partial_y p = -2\Omega u \tag{5.7}$$

with the same w equation (5.5). The Coriolis force adds a feedback from u to v. The Coriolis force is energy conserving since it is always orthogonal to $\mathbf{v}$. However, in the presence of background shear U', the advection of U by v creates u that is rotated into v by the Coriolis term and this can lead to a linear instability. As shown previously in

Figure 5.1, a positive perturbation in v will lead to a negative perturbation in u, assuming $U' > 2\Omega$ via the advection of mean shear (5.6). Coriolis $-2\Omega u$ in the v equation (5.7) turns this negative u into a positive feedback on v, thereby sustaining the rolls and destabilizing the flow. Ignoring diffusion and the pressure gradient, equations (5.6) and (5.7) suggest instability when

$$2\Omega(U' - 2\Omega) > 0, \tag{5.8}$$

for a base flow $U(y)\hat{\mathbf{x}}$ and rotation $\Omega\hat{\mathbf{z}}$. Thus, too much rotation $|U'| < 2|\Omega|$ will lead to stability and any rotation in the direction of the shear vorticity (*i.e.* $U'\,\Omega < 0$) will also stabilize, but a bit of rotation in the direction *opposite* to the shear flow vorticity (*i.e.* $U' > 2\Omega > 0$ or $U' < 2\Omega < 0$) will lead to linear instability as a result of shear redistribution and the Coriolis force.

This simple outline of rotating plane Couette flow is a way of understanding the classic 'centrifugal' instability seen in Taylor-Couette flow, in which fluid contained within two concentric cylinders is unstable *when the inner cylinder rotates faster than the outer cylinder,* and indicate that that classic instability should perhaps be called 'Coriolis instability' instead of 'centrifugal'. The rolls and streaks in Taylor-Couette flow are shown in Figure 5.3. Placing a plane Couette flow on a rotating table leads to similar 'Taylor vortices' as done in experiments by Tillmark and Alfredsson.

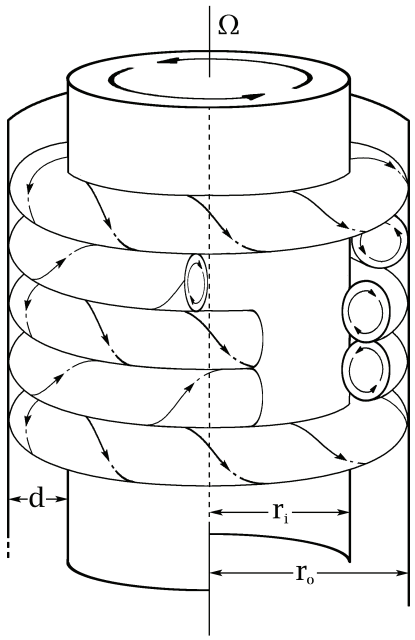

Figure 5.3: Toroidal vortices in Taylor-Couette flow (by M. Minbiole and R. M. Lueptow)

5.3 Thermal convection and the Lorenz model

A second method of creating feedback onto the cross-stream velocity perturbations v, w is to add a thermal gradient. We consider the Boussinesq thermal convection between planes, *i.e.* Rayleigh-Bénard convection (see Figure 5.4), especially in the weakly nonlinear regime, and derive qualitatively the reduced system of ODEs known as the Lorenz model.

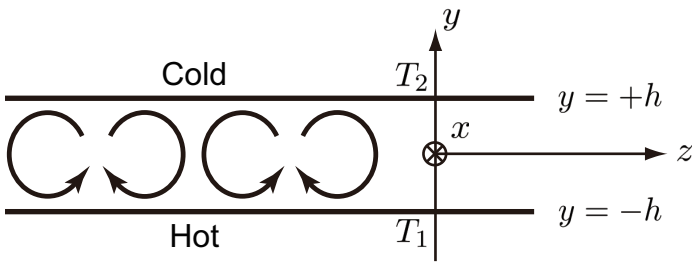

Figure 5.4: Schematic picture of Rayleigh-Bénard convection. Gravity acts downward in the $-\hat{\mathbf{y}}$ direction.

The governing equations of Boussinesq thermal convection between planes are

$$\frac{\partial \mathbf{u}}{\partial t} + (\mathbf{u}\cdot\nabla)\mathbf{u} + \nabla p = g\alpha T\hat{\mathbf{y}} + \nu\nabla^2\mathbf{u}, \tag{5.9}$$

$$\nabla\cdot\mathbf{u} = 0, \tag{5.10}$$

$$\frac{\partial T}{\partial t} + (\mathbf{u}\cdot\nabla)T = \kappa\nabla^2 T, \tag{5.11}$$

where $\mathbf{u}$ is the velocity, $-g\hat{\mathbf{y}}$ is the acceleration of gravity, T the temperature[2] departure from some mean temperature so that the density $\rho \approx \rho_0(1-\alpha T)$ with $\alpha \geq 0$ the thermal expansion coefficient, ν the kinematic viscosity and κ the thermal diffusivity. The distance between the two plates is $H = 2h$ and the temperature of the lower plate is T_1 at $y = -h$ and the upper plate is at T_2 at $y = h$, with $T_1 + T_2 = 0$. Thermal convection occurs when the temperature difference $\Delta T = T_1 - T_2$ is larger than a certain threshold. The base temperature profile is

$$T = T_c = -\frac{\Delta T}{H}y, \tag{5.12}$$

which the conductive state solution of (5.9), (5.10) and (5.11) with $\mathbf{u} = 0$, for all values of the parameters. Buoyancy $g\alpha T_c\,\hat{\mathbf{y}}$ in (5.9) is balanced by an hydrostatic pressure.

(1) Insert rolls. We choose the boundary conditions as free-slip at the walls, that is $v = \partial_y w = \partial_y^2 v = 0$, this is a physically reasonable boundary condition that is mathematically convenient since it allows the representation of the velocity by Fourier modes. We insert a 'streamwise roll' into the flow that can be taken as

$$v = V(t)\cos(\beta y)\cos(\gamma z), \tag{5.13}$$

[2]Here, T is *temperature*, not the perturbation Reynolds stress that appeared in earlier lectures!

where $v = \hat{\mathbf{y}}\cdot\mathbf{u}$ and $\beta = \pi/(2h)$ so $v = \partial_y^2 v = 0$ at $y = \pm h$ and γ is an arbitrary wavenumber. We choose the flow in the (y, z) plane to match the shear flow problem (fig. 5.1). From incompressibility $\partial_y v + \partial_z w = 0$, the z velocity $w = \hat{\mathbf{z}} \cdot \mathbf{u}$ must be

$$w = \frac{\beta}{\gamma} V(t) \sin(\beta y) \sin(\gamma z), \tag{5.14}$$

with $\partial_y w = 0$ at $y = \pm h$ since $\beta = \pi/(2h)$. So this $\mathbf{u} = (0, v, w)$ flow (5.13), (5.14) as the shape of the rolls sketched in Figure 5.4 and satisfies the boundary conditions $v = \partial_y w = \partial_y^2 v = 0$ at $y = \pm h$.

(2) Rolls redistribute temperature. Let $T = T_c(y) + \tilde{T}(y, z, t)$, that is, the conductive profile (5.12) plus a perturbation $\tilde{T}$. Then, (5.11) becomes

$$\frac{\partial \tilde{T}}{\partial t} + \mathbf{u} \cdot \nabla \tilde{T} = -v \frac{dT_c}{dy} + \kappa \nabla^2 T \tag{5.15}$$

which is entirely similar to the streamwise velocity perturbation equation in shear flows (5.3) (and earlier lectures). Inserting the v mode (5.13) into the temperature equation (5.15) with $T_c = -y\Delta T/H$ shows that the $-v dT_c/dy = v\,\Delta T/H$ term generates a thermal perturbation of the form

$$\tilde{T} = T_{11}(t) \cos(\beta y) \cos(\gamma z) + \cdots, \tag{5.16}$$

that is the rolls (5.13) redistribute the linear temperature profile (5.12) inducing a temperature fluctuation $\tilde{T}$ that has the same spatial form as v. The nonlinear term $\mathbf{u} \cdot \nabla \mathbf{u}$ for (5.13), (5.14) can be absorbed into the pressure gradient,[3] so it does not distort the velocity field. If it did (for different rolls, say for no-slip), we would assume at this stage that the rolls are weak so $\nabla \times (\mathbf{u} \cdot \nabla \mathbf{u})$ is small.

(3) Temperature fluctuation feedback onto rolls. The temperature fluctuation $\tilde{T}$ (5.16) yields a buoyancy fluctuation $g\alpha\tilde{T}\hat{\mathbf{y}}$ in the momentum equation (5.9) that perfectly feeds back on the v mode (5.13). These $V \to T_{11} \to V$ interactions through the base state $T_c(y)$ will lead to thermal instability provided this feedback can overcome the viscous and thermal damping of the V and T_{11} modes, as shown below (5.27).

(4) Mean temperature gradient reduction. The 'next' effect[4] is the interaction between the rolls (5.13) and the induced fluctuation $\tilde{T}$ (5.16), in the temperature equation (5.15). This interaction arises from the advection term $-\mathbf{u} \cdot \nabla \tilde{T}$ in (5.15) for v, w and $\tilde{T}$ as in (5.13), (5.14), (5.16), then after a simple calculation

$$-\mathbf{u} \cdot \nabla \tilde{T} = -v \frac{\partial \tilde{T}}{\partial y} - w \frac{\partial \tilde{T}}{\partial z} = \frac{\beta}{2}\, V\, T_{11}\, \sin(2\beta y) + \cdots \tag{5.17}$$

so this interaction generates a $\sin(2\beta y)$ temperature fluctuation, which is a modification of the mean temperature profile $\overline{T}(y, t)$, that is the z (and x) averaged temperature profile.

[3] $\nabla \times (\mathbf{u}\cdot\nabla\mathbf{u}) = \mathbf{u}\cdot\nabla\omega\hat{\mathbf{x}}$ where $\omega = \partial_y w - \partial_z v$ for this 2D flow. Using a streamfunction $v = \partial_z \psi$, $w = -\partial_y \psi$ gives $\mathbf{u} \cdot \nabla\omega = (\partial_y\psi\partial_z - \partial_z\psi\partial_y)(\partial_y^2 + \partial_z^2)\psi$. Now for (5.13), $\psi = (V/\gamma)\cos\beta y \sin\gamma z$ and $\nabla^2\psi = -(\beta^2 + \gamma^2)\psi$ so $\mathbf{u} \cdot \nabla\omega = 0$. Thus $\mathbf{u} \cdot \nabla\mathbf{u} = \nabla\chi$, indeed $\chi = \left(\cos 2\beta y - (\beta^2/\gamma^2)\cos 2\gamma z\right) V^2/4$.

[4] All these effects take place simultaneously but here we identify a cause and effect sequence, starting with a small stirring of the fluid, then analyzing the dynamical consequences of that stirring.

We label this mode the T_{20} mode since it is a temperature mode with y wavenumber 2β and z wavenumber 0, hence the *'two-zero'* (20) mode. This reduction of the mean temperature gradient will lead to a reduction of the T_{11} forcing and saturation of the instability.

Therefore, the temperature distribution has the form

$$T = -y\frac{\Delta T}{H} + T_{11}(t)\cos(\beta y)\cos(\gamma z) + T_{20}(t)\sin(2\beta y) + \cdots . \tag{5.18}$$

together with the velocity field $\mathbf{u} = (0, v, w)$ with v and w as in (5.13), (5.14). The cause-effect chain that we have in mind being $V \longrightarrow T_{11} \longrightarrow V \Longrightarrow T_{20} \Longrightarrow T_{11}$, where as in the scenarios of lecture 1, a $\longrightarrow$ indicates a linear interaction (that is between the base flow and a fluctuation) and a $\Longrightarrow$ a nonlinear interaction between fluctuations. Note that amplitude-wise $T_{11} \sim V$, $T_{20} \sim VT_{11} \sim V^2$ and the feedback from V and T_{20} onto T_{11} is of order $VT_{20} \sim V^3$.

We have identified a physically consistent set of modal interactions and can truncate the expansion at this level. In general, this truncation will be valid only for sufficiently small amplitude V since other modes are generated. We truncate the above formulation using what is known as the Galerkin truncation or projection, that is we substitute these expansions for v, w and $\tilde{T}$ into the equations and throw away higher order modes such as $\cos 2\gamma z$, $\cos 3\beta y$, etc. In the Galerkin truncated system, the dependent variables are the modal amplitudes $V(t)$, $T_{11}(t)$ and $T_{20}(t)$, thus we reduce the complete set of PDEs (5.9), (5.10), (5.11) to 3 ODEs.

The temperature equation (5.15) is easy enough, but the $\mathbf{u}$ equation is complicated by the pressure gradient needed to enforce incompressibility. For 2D flow, we can eliminate pressure and $\mathbf{u}$ using a streamfunction, or as in the derivation of the Orr-Sommerfeld equation by taking $\hat{\mathbf{y}} \cdot (\nabla \times \nabla(*)) = (\partial_y \nabla - \hat{\mathbf{y}}\nabla^2) \cdot (*) \equiv \boldsymbol{P}_v \cdot (*)$, so $\boldsymbol{P}_v \cdot \mathbf{u} = -\nabla^2 v$ and $\boldsymbol{P}_v \cdot \nabla\varphi = 0$. Applying this $\boldsymbol{P}_v$ operator to (5.9) yields

$$\partial_t \nabla^2 v = \nu\nabla^2\nabla^2 v + g\alpha\nabla_\perp^2 T + \boldsymbol{P}_v \cdot (\mathbf{u} \cdot \nabla\mathbf{u}) \tag{5.19}$$

where $\nabla^2 = \partial_x^2 + \partial_y^2 + \partial_z^2$ and $\nabla_\perp^2 = \partial_x^2 + \partial_z^2$ and $\mathbf{u}$ follows from v and incompressibility in 2D flow, and $\boldsymbol{P}_v \cdot (\mathbf{u} \cdot \nabla\mathbf{u}) = 0$ for (5.13). Additional $\eta = \hat{\mathbf{y}} \cdot \nabla \times \mathbf{u}$ and mean flow equations would be needed for general 3D flow but (5.19) together with (5.15) suffice for 2D flow. Then for v and T as in (5.13) and (5.18), equations (5.15) and (5.19) yield the governing equations for the modal amplitudes $V(t)$, $T_{11}(t)$ and $T_{20}(t)$,

$$\begin{aligned}
\frac{dV}{dt} + \nu_{11}V &= g_{11}\,T_{11}, \\
\frac{dT_{11}}{dt} + \kappa_{11}T_{11} &= V\tfrac{\Delta T}{H} \quad -\beta\,VT_{20}, \\
\frac{dT_{20}}{dt} + \kappa_{20}T_{20} &= \tfrac{\beta}{2}\,VT_{11},
\end{aligned} \tag{5.20}$$

where

$$\nu_{11} = \nu(\beta^2+\gamma^2), \quad \kappa_{11} = \kappa(\beta^2+\gamma^2), \quad \kappa_{20} = \kappa(4\beta^2), \quad g_{11} = g\alpha\frac{\gamma^2}{\beta^2+\gamma^2} \tag{5.21}$$

and $\beta = \pi/(2h) = \pi/H$. This is the famous Lorenz model of convection.[5] One solution of these equations is $V = T_{11} = T_{20} = 0$ which corresponds to the conductive state. Linearizing about that state yields

$$\begin{aligned} \frac{dV}{dt} + \nu_{11} V &= g_{11} T_{11}, \\ \frac{dT_{11}}{dt} + \kappa_{11} T_{11} &= V \tfrac{\Delta T}{H}, \end{aligned} \tag{5.25}$$

which has an unstable mode $V(t) = e^{\lambda t}\hat{V}$, $T_{11}(t) = e^{\lambda t}\hat{T}_{11}$ if $g_{11}\Delta T/H > \nu_{11}\kappa_{11}$, that is for

$$\frac{g\alpha\Delta T}{H}\frac{\gamma^2}{\beta^2+\gamma^2} > \nu\kappa(\beta^2+\gamma^2)^2 \tag{5.26}$$

or in non-dimensional form with $\hat{\beta} = \beta H = \pi$ and $\hat{\gamma} = \gamma H$

$$Ra \equiv \frac{g\alpha\Delta T H^3}{\nu\kappa} > \frac{(\pi^2+\hat{\gamma}^2)^3}{\hat{\gamma}^2} \geq \frac{27\pi^4}{4} \approx 657.5, \tag{5.27}$$

where Ra is the non-dimensional *Rayleigh number* and the minimum $Ra = 27\pi^4/4 = Ra_c$ value for onset of convection with free-slip occurs at $\hat{\gamma} = \gamma H = \pi/\sqrt{2}$.

This, of course, is just the beginning of the story since the simple nonlinear model (5.20) has some rather interesting chaotic nonlinear dynamics as first studied by E. Lorenz (1963), and for the the full PDEs (5.9), (5.10), (5.11), this is just the onset of convection leading to multiscale turbulence for larger Ra, much beyond the range of validity of the simple Lorenz model.

5.4 SSP Model

In the previous sections we have illustrated instabilities that result from the interactions $v \to u \to v$ thanks to base velocity redistribution $-vdU/dy$ and the Coriolis force, and from the interaction $v \to T_{11} \to v$ thanks to mean temperature redistribution $-vdT/dy$ and buoyancy in convection. In bare shear flows, there is no direct linear feedback from $u \to v$, but there are more involved 3D nonlinear mechanisms that provide that crucial feedback. The entire set of mechanisms is called the *self-sustaining process* and we illustrate it here with a low order model similar in spirit to the Lorenz model of convection.

From the earlier energy stability result (Equation 5.2) we know that unless we have variation of the velocity in the x direction any perturbations must eventually die out (possibly after some initial transient growth) thus any successful model must include such variation.

[5] The standard non-dimensional form of the Lorenz model is

$$\frac{dx}{d\tau} = \sigma(y-x), \tag{5.22}$$

$$\frac{dy}{d\tau} = -y + rx - xz, \tag{5.23}$$

$$\frac{dz}{d\tau} = -bz + xy, \tag{5.24}$$

where $\tau = \kappa_{11}t$, $\sigma = \nu/\kappa$, $r = g_{11}(\Delta T)/(\nu_{11}\kappa_{11}H)$, $b = \kappa_{20}/\kappa_{11}$ and $x = \beta V/(\sqrt{2}\kappa_{11})$, $y = \beta/(\sqrt{2}\kappa_{11})(g_{11}/\nu_{11})T_{11}$, $z = (\beta/\kappa_{11})(g_{11}/\nu_{11})T_{20}$.

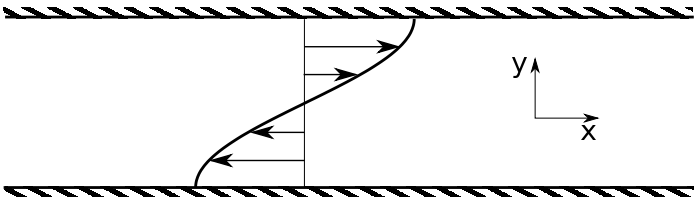

Figure 5.5: Wall-bounded Kolmogorov flow, $U = \sin \beta y$ with $\beta y = \pm\pi/2$ at the walls, is stable for all Reynolds numbers for free-slip perturbations, as proved in lecture 4.

The SSP model was already described in lecture 1 and was first described in [2, 3]. The model can be derived by Galerkin truncation from the full Navier-Stokes equations [4], and some mode linking.

Brief derivation

We consider a wall-bounded Kolmogorov flow with free-slip at the walls, figure 5.5. This will allow us to use Fourier modes to represent the flow and lead to a simpler and cleaner model than other shear flows with no-slip.

$$\mathbf{U}(y,t) = M(t)\sin(\beta y)\hat{\mathbf{x}} \tag{5.28}$$

with $\beta = \pi/2$ and the walls at $y = \pm 1$. We assume that this flow is maintained by a body force, so that the evolution of M in the absence of any perturbations is given by

$$\dot{M} + \frac{1}{R}M = \frac{1}{R}, \tag{5.29}$$

for which one solution is simply $M = 1$ and R is the Reynolds number. We proved in lecture 4 that this wall-bounded Kolmogorov flow is stable for all Reynolds numbers for free-slip perturbations.

As before we consider an initial perturbation consisting of rolls whose axes are in the x direction, see Figure 5.1, and flow in the y and z directions as follows:

$$\begin{aligned} v &= V(t)\ \cos(\beta y)\cos(\gamma z), \\ w &= \frac{\beta}{\gamma}V(t)\ \sin(\beta y)\sin(\gamma z) \end{aligned} \tag{5.30}$$

this $V(t)$ mode satisfies incompressibility $\partial_y v + \partial_z w = 0$ and the free-slip boundary conditions $v = \partial_y w = \partial_y^2 v = 0$ at $\beta y = \pm\pi/2$. This is the same rolls as in the Lorenz model (5.13). The vertical component, v, of these perturbations advects momentum associated with the background flow and leads to a perturbation of the velocity in the x direction, which to leading order has structure

$$u = U(t)\cos(\gamma z), \tag{5.31}$$

these are the *streaks* and the need for this mode arises from the redistribution of the base shear (5.28) by the rolls (5.30), so

$$v\partial_y \mathbf{U} + w\partial_z \mathbf{U} = \beta V M \cos\gamma z\ (\cos\beta y)^2 \hat{\mathbf{x}} = \frac{\beta}{2}\, V M \cos\gamma z\ (1 + \cos 2\beta y)\ \hat{\mathbf{x}}.$$

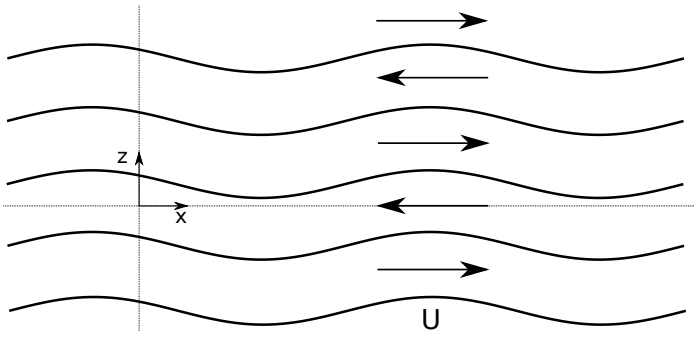

Figure 5.6: Inflectional instability viewed from below.

The $\cos 2\beta y$ was dropped in the derivation in [4] but it might be better to keep it and define the streaks as $U(t)\cos\gamma z\ (1+\cos 2\beta y)$. Moehlis *et al.* [1] have considered small modifications of the 8 mode model in [4] that includes a few such adjustments of the mode definitions. In any case, there is a VM forcing of U and likewise the advection by the rolls of the streaks $u\hat{\mathbf{x}}$ with u as in (5.31) gives

$$v\partial_y u + w\partial_z u = -\beta\, VU\ \sin\beta y\,(\sin\gamma z)^2 = -\frac{\beta}{2}VU\ \sin\beta y\,(1-\cos 2\gamma z)$$

and this gives a negative feedback on the base flow (5.28). Again we truncate the $\cos 2\gamma z$ contribution.

At this level, our Galerkin truncation for the redistribution of the base flow (5.28) by the streamwise rolls (5.30) has the form

$$\begin{aligned} \dot{M} + \tfrac{1}{R}M &= \tfrac{1}{R} - UV \\ \dot{U} + \tfrac{1}{R}U &= VM \\ \dot{V} + \tfrac{1}{R}V &= 0 \end{aligned} \tag{5.32}$$

where the dot $\dot{(\ )} \equiv d/dt$ and the coefficients have been set to 1 to highlight the structure of the interactions as clearly as possible. However, as our motion is still independent of the x direction, there is nothing to regenerate the vertical motion V and all perturbations will eventually die out. Viewed from above the flow now has strips of faster and slower flowing fluid, the streaks U (5.31) sketched in Figure 5.2, which have been generated by the advection of the mean shear M by the rolls V. This streaky flow has inflection points in the spanwise z direction and hence we might expect it to be unstable to an inflectional instability as discussed in lecture 4. This instability provides a mechanism for introducing the variation in the x direction that we know is vital to sustain the perturbations. This inflectional instability of $U\cos\gamma z\hat{\mathbf{x}}$ will consist of the growth of 'streak-sloshing' mode, illustrated in Figure 5.6, that is most simply represented by a spanwise velocity perturbation periodic in x, that is

$$w = W(t)\cos(\alpha x) \tag{5.33}$$

(we could just as well choose $\sin\alpha x$, this is a phase choice that is inconsequential to the dynamics at this point). This spanwise perturbation should be added to the streamwise roll

contribution (5.30) so the full spanwise velocity at this level of truncation is

$$w = W(t)\cos(\alpha x) + \frac{\beta}{\gamma}V(t)\ \sin(\beta y)\sin(\gamma z) \tag{5.34}$$

Mode $\mathbf{\Psi}_{100} = (0, 0, \cos\alpha x)$ in (5.33) can grow from the U streak mode $\mathbf{\Psi}_{001} = (\cos\gamma z, 0, 0)$ but only through interaction with the velocity mode $(-\gamma\cos\alpha x \sin\gamma z,\ 0,\ \alpha\sin\alpha x\cos\gamma z)$ labelled $\mathbf{\Psi}_{101}$ in [4]. The $\mathbf{\Psi}$ modes are solenoidal, $\nabla\cdot\mathbf{\Psi} = 0$, and satisfy the boundary conditions. The details are left to [4] but the conceptual result is that we now have an x dependent mode $W(t)$ and interactions between U and W such that W grows from an instability of U, so the 'forcing' of W is in the form of a UW. Conceptually, the dynamics reads

$$\begin{array}{lcccc} \dot{M} + \frac{1}{R}M & = & \frac{1}{R} & -UV & \\ \dot{U} + \frac{1}{R}U & = & & VM & -W^2 \\ \dot{V} + \frac{1}{R}V & = & 0 & & \\ \dot{W} + \frac{1}{R}W & = & & & UW \end{array} \tag{5.35}$$

Unfortunately there is still no feedback on V so our perturbations must still die out. This is an important point rarely understood, *streak instability does not guarantee bifurcation from the laminar flow*. The streak instability could simply, as in model (5.35), destroy the streaks U created by V from M, and therefore accelerate the return of the flow to the laminar state $(M, U, V, W) = (1, 0, 0, 0)$.

In fact it is remarkably difficult to generate feedback on the streamwise rolls from the streak eigenmode interactions. This feedback requires the interaction of modes with opposite y-symmetry, *i.e.* an even mode interacting with an odd mode, and those modes arise from each other through interaction with the mean shear. Thus as observed in [4], the mean shear M plays the dual role of supplier of energy and momentum but also shaper of the streak instability in order to allow feedback on V from the nonlinear interaction of the streak instability eigenmode. It turns out that no less than five x-dependent modes are required before we can get feedback on V, [4, §III. A], giving an 8th order model. However we can simplify the model by kinematic linking of those 5 modes into a single complex mode of amplitude W, the details are spelled out in [4, §III. C] and the result conceptually is

$$\begin{array}{lcccccc} \dot{M} + \frac{1}{R}M & = & \frac{1}{R} & -UV & & & \\ \dot{U} + \frac{1}{R}U & = & & VM & -W^2 & & \\ \dot{V} + \frac{1}{R}V & = & 0 & & & & W^2 \\ \dot{W} + \frac{1}{R}W & = & & & UW & -VW & \end{array} \tag{5.36}$$

with, at last, feedback on V.

However, the derivation in [4] shows that these interactions are necessarily accompanied by a feedback from W to M, which can be interpreted as the unavoidable shearing of x dependent modes by the mean shear $M\sin\beta y\ \hat{\mathbf{x}}$ that tends to destroy the W mode and by conservation of energy, transfer that energy and momentum back to M. This is therefore a mean shear stabilizing term and it is key to the $1/R$ threshold discussed in lecture 1. The

complete model [4, eqn. (20)] is then

$$\begin{array}{rcccccc}
\left(\frac{d}{dt}+\frac{\kappa_m^2}{R}\right)M &=& \frac{\kappa_m^2}{R} & -\sigma_u UV & & & +\sigma_m W^2 \\
\left(\frac{d}{dt}+\frac{\kappa_u^2}{R}\right)U &=& & \sigma_u MV & -\sigma_w W^2 & & \\
\left(\frac{d}{dt}+\frac{\kappa_v^2}{R}\right)V &=& & & & \sigma_v W^2 & \\
\left(\frac{d}{dt}+\frac{\kappa_w^2}{R}\right)W &=& & & \sigma_w UW & -\sigma_v VW & -\sigma_m MW
\end{array} \tag{5.37}$$

where all κ^2 and σ are positive constants and $R > 0$ is the Reynolds number. This model (6.11) has a laminar flow $(M, U, V, W) = (1, 0, 0, 0)$, that is linearly stable for all Reynolds number. The nonlinear interactions conserve energy and

$$\frac{d}{dt}\left(\frac{M^2+U^2+V^2+W^2}{2}\right) = \kappa_m^2\frac{M}{R} - \frac{1}{R}\left(\kappa_m^2 M^2 + \kappa_U^2 U^2 + \kappa_V^2 V^2 + \kappa_W^2 W^2\right) \tag{5.38}$$

from which we see that the kinetic energy of the flow decays due to viscous dissipation with the only energy input coming from the forcing of the mean shear, as should be. This energy equation also shows that there is no blow-up since we have linear energy input with quadratic dissipation and any non-laminar statistically steady state must have $0 < M < 1$.

Brief analysis of the model

An analysis of the SSP model (6.11) is given in [4] and also in the notes for lecture 1. Although the laminar flow is stable for *all* Reynolds numbers, as is the case for the full linearized Navier-Stokes PDEs, the SSP model (6.11) allows the onset of non-trivial steady states for sufficiently large R. For those non-trivial states,

1. V redistribute M to create U. This is the $\sigma_u MV$ term, and $-\sigma_u UV$ is the corresponding 'Reynolds stress'.

2. the streaks U are unstable leading to the growth of W. This is the $\sigma_w UW$ term, this is an instability, not a direct forcing. The corresponding 'Reynolds stress' on U is the $-\sigma_w W^2$ term,

3. Ah, Ha! *nonlinear feedback* from W onto V, the $\sigma_v W^2$,

4. but also a feedback onto M, $\sigma_m W^2$, pushing up the transition threshold.

This process supports onset of non-trivial steady states for R above a critical value and these states arise from 'saddle-node' bifurcations, although typically *both states are unstable from onset*. Because of the higher dimensionality, both the saddle and the 'node' are unstable at onset. In the low order model, the upper branch of solutions (the node), gains stability at higher R. The bifurcation and scaling of W are sketched in Figure 5.7. The lower branch saddle scales like $W \sim R^{-1}$ and the upper branch like $W \sim R^{-3/4}$.

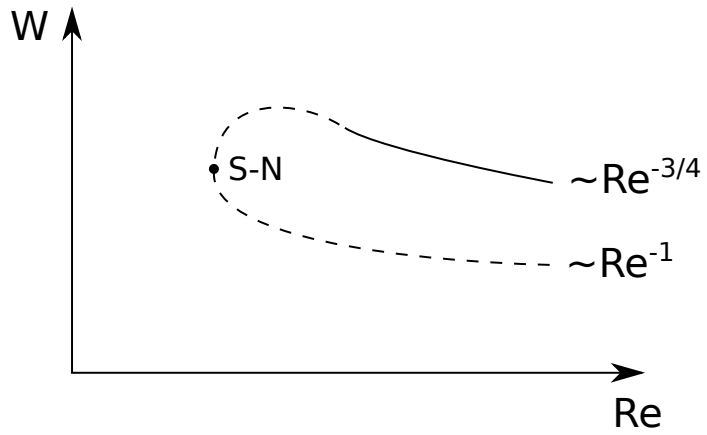

Figure 5.7: Non-trivial steady states of the SSP model (6.11), Re is the Reynolds number. The dashed line indicates instability of the solution. The laminar flow at $W = 0$ is stable for all Re.

Bibliography

[1] J. Moehlis, H. Faisst, and B. Eckhardt, *A low-dimensional model for turbulent shear flows*, New Journal of Physics, 6 (2004), pp. 56+17.

[2] F. Waleffe, *Hydrodynamic stability and turbulence: Beyond transients to a self-sustaining process*, Studies in Applied Mathematics, 95 (1995), pp. 319–343.

[3] F. Waleffe, *Transition in shear flows. nonlinear normality versus non-normal linearity*, Physics of Fluids, 7 (1995), pp. 3060–3066.

[4] F. Waleffe, *On a self-sustaining process in shear flows*, Physics of Fluids, 9 (1997), pp. 883–900.

Lecture 6

Exact Coherent States

Notes by Chao Ma and Samuel Potter
Revised by FW
WHOI GFD Lecture 6, June 27, 2011

Shear enhanced dissipation, $R^{1/3}$ scaling in shear flows. Critical layer in lower branch exact coherent states. SSP model modified to include critical layers. Construction of *exact coherent states* in full Navier-Stokes. Optimum traveling wave and near-wall coherent structures, 100+ streak spacing. Physical space structures of turbulence. State space structure of turbulence.

6.1 Shear enhanced dissipation

In the (quick) overview of the SSP model, we discussed how the shearing of x-dependent modes by the mean shear leads to a *positive* feedback on the mean flow. In the SSP model these are the W^2 term in the M equation and the $-MW$ term in the W equation. Although this interaction is not necessary for the self-sustaining process itself, it is the key effect that leads to the R^{-1} scaling of the transition threshold, and of the V and W components of the lower branch steady state (while U and $1-M$ are $O(1)$, see lectures 1 and 5).

Advection by a shear flow leads to enhanced dissipation and an $R^{-1/3}$ scaling characteristic of *linear* perturbations about shear flows, or evolution of a passive scalar. The $R^{-1/3}$ enhanced damping, instead of R^{-1}, was included by Chapman for the x-dependent modes in his modification of the WKH model (as discussed in lecture 1). However, that is because Chapman considers the weak nonlinear interaction of eigenmodes of the *laminar flow*, $U(y)$. In contrast, the basic description of the SSP consists of the weak nonlinear interaction of *streaky flow eigenmodes*, that is, neutral eigenmodes of the spanwise varying shear flow $U(y,z)$ consisting of the mean shear *plus* the streaks. An important aspect of the streaky flow $U(y,z)$ is that the mean shear has been reduced precisely to allow that instability, as illustrated by the SSP model where $\sigma_w U - \sigma_m M - \sigma_v V > 0$ is needed for streak instability and growth of W. So it is unclear *a priori* whether the $R^{-1/3}$ should apply to x-dependent modes in the SSP. In section 6.2 below we review the numerical evidence that the 3D nonlinear lower branch SSP states in plane Couette flow do have $R^{-1/3}$ critical layers as $R \to \infty$ [24]. But why $R^{1/3}$?

Back-of-the-envelope analysis. Consider plane channel flow with near-wall velocity profile $U(y) \simeq Sy$ (Figure 6.1), where S is the shear rate. Denote $\hat{\mathbf{x}}$ as the flow direction and $\hat{\mathbf{y}}$ as the shear direction. We introduce a small disturbance which we imagine as a little eddy

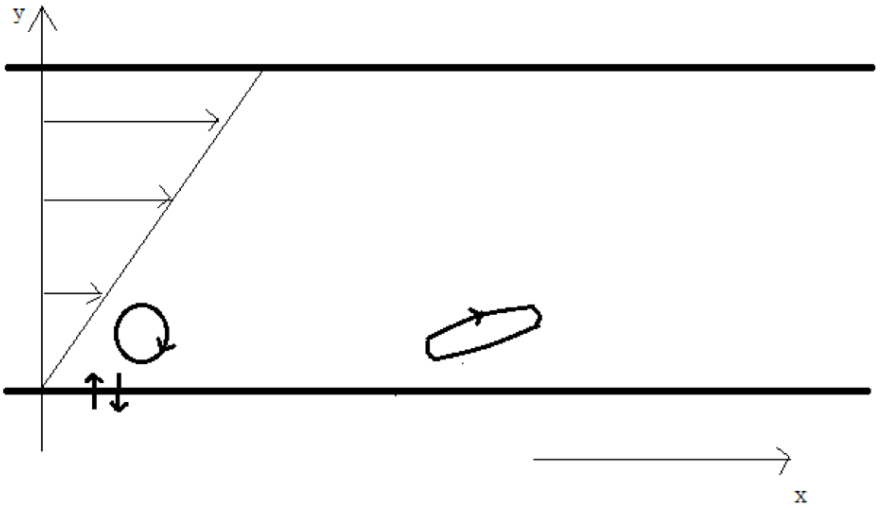

Figure 6.1: Shearing leads to enhanced dissipation and $R^{1/3}$ scaling.

with characteristic length ℓ_0, generated perhaps using a push-pull perturbation as in some of the experiments of Mullin *et al.* discussed in lecture 1 with the push-pull axis oriented streamwise (we consider only 2D flow here). We assume that the eddy Reynolds number is small so that the evolution of the eddy consists primarily of the distortion by the mean shear (so small eddy Reynolds number and 2D means none of the Theodorsen horseshoes discussed in lecture 1), that is the governing equation is the advection diffusion of spanwise vorticity $\omega = \partial_x v - \partial_y u$

$$(\partial_t + Sy\,\partial_x - \nu\nabla^2)\,\omega = 0. \tag{6.1}$$

The eddy will be stretched in the $\hat{\mathbf{x}}$ direction as a result of the differential advection,[1] and the major axis a of this now elliptical eddy will grow like $a \sim \ell_0\sqrt{1+(St)^2} \sim \ell_0 St$, while its minor axis b will decay like $b \sim \ell_0^2/a \sim \ell_0/(St)$, since area is conserved in this 2D incompressible flow. This is the back-of-the-envelope handling of the $Sy\partial_x$ term in (6.1) and we now estimate the dissipation $\nu\nabla^2 \sim -\nu/\ell^2$ where the relevant length scale ℓ here is the *smallest scale* which is $b \sim \ell_0/(St)$ for long times. So the diffusion term will give

$$\frac{d\omega}{dt} \sim -\nu\frac{(St)^2}{\ell_0^2}\,\omega \quad \Rightarrow \quad \omega \sim \omega_0\,\exp\left(-\nu\frac{S^2t^3}{3\ell_0^2}\right) \tag{6.2}$$

Note that we have used a d/dt instead of ∂_t since we have taken care of the advection and are effectively doing a Lagrangian analysis. In the absence of differential advection, we would have $\omega \sim \omega_0 \exp(-\nu St/\ell_0^2)$, so (6.2) is much smaller for $St > 3$, and differential advection leads to enhanced diffusion. In non-dimensional form, we can define a Reynolds

[1] Two material points at the same y do not separate, but two material points at the same x but ℓ_0 apart in y are differentially advected in x and the distance between them will be $\ell = \ell_0\sqrt{1+(St)^2}$.

number $R_0 = S\ell_0^2/\nu$ based on the length scale ℓ_0 and the velocity scale $S\ell_0$ and write (6.2) as

$$\frac{\omega}{\omega_0} \sim \exp\left(-\frac{(St)^3}{3R_0}\right) \tag{6.3}$$

where St is a nondimensional time based on the shear rate S and this shows that enhanced dissipation occurs on a time scale $St \sim R_0^{1/3}$. If we have a length scale, say h for the shear flow, then we can define a Reynolds number $R = Sh^2/\nu$ then $R_0 = R\,(\ell_0/h)^2$ and the enhanced dissipation occurs on the time scale $St \sim R^{1/3}(\ell_0/h)^{2/3}$, still scaling like $R^{1/3}$.

Didn't he say 'analysis'? Fellows uncomfortable with the back of an envelope should go with the flow $x = x_0 - Syt$ and consider $\omega = \omega(x_0, y, t)$ in terms of the Lagrangian coordinate $x_0 = x + Syt$ and y, t, then $(\partial/\partial x)_{y,t} = (\partial/\partial x_0)_{y,t}$ but

$$(\partial/\partial y)_{x,t} = (\partial/\partial y)_{x_0,t} - \ St\ (\partial/\partial x_0)_{y,t} \tag{6.4}$$

$$(\partial/\partial t)_{x,y} = (\partial/\partial t)_{x_0,y} - \ Sy\ (\partial/\partial x_0)_{y,t} \tag{6.5}$$

and (6.1) for $\omega(x_0, y, t)$ becomes

$$\frac{\partial\omega}{\partial t} = \nu\big(1 + (St)^2\big)\,\frac{\partial^2\omega}{\partial x_0^2} - 2\nu St\,\frac{\partial^2\omega}{\partial x_0 \partial y} + \nu\frac{\partial^2\omega}{\partial y^2} \tag{6.6}$$

that has solutions of the form $\omega = A(t)e^{i(\alpha x_0 + \beta_0 y)}$ with

$$A(t) = A_0 \exp\Big(-\nu\left((\alpha^2 + \beta_0^2)t - \alpha\beta_0 St^2 + \alpha^2 S^2 t^3/3\right)\Big), \tag{6.7}$$

which for $\alpha = 1/\ell_0$, $\beta_0 = 0$ gives

$$\omega = \omega_0\ \exp\left(-\nu\ \frac{t + S^2t^3/3}{\ell_0^2}\right), \tag{6.8}$$

that should reassure fellows of the validity of (6.2).

One can also use *Kelvin modes* and solve (6.1) (in an infinite domain in y) using solutions of the form $\omega = A(t)\exp(i\mathbf{k}(t)\cdot\mathbf{r})$, that is, Fourier modes with time-dependent wavevectors $\mathbf{k}(t)$. For (6.1), one finds $\mathbf{k}(t) = (\alpha, \beta_0 - \alpha St)$ and $dA/dt = -\nu k^2 A$ with $k^2 = \alpha^2 + (\beta_0 - \alpha St)^2$ and recover (6.7). Thus, shearing leads to wavenumbers that grow like St in the shear direction $\beta \sim -\alpha St$ or $k_y \sim -k_x St$ and this leads to enhanced damping.

In a *semi-infinite* domain, *e.g.* $0 \le y < \infty$, the advection diffusion equation (6.1)[2] has eigensolutions of the form $e^{\lambda t}e^{i\alpha x}f(y)$ where $f(y)$ can be expressed in terms of Airy functions with y length scales $\sim (\nu/(\alpha S))^{1/3}$ and $\Re(\lambda) \sim -(\nu\alpha^2 S^2)^{1/3}$. For a *bounded domain*, the eigenmodes have y scale $\sim (\alpha R)^{-1/3}$ and decay rates $\sim (\alpha R)^{-1/3}$, with α now the non-dimensionalized x wavenumber. The connection between the y scale and the decay rate follows from the form of the dissipation $\partial_t = \nu\nabla^2 \sim -\nu k^2$ where k is a wavenumber. In non-dimensional units, this is $\partial_t \sim -k^2/R$ with $k \sim R^{1/3}$ for scales $\sim R^{-1/3}$, thus

$$-\frac{k^2}{R} \sim -R^{-1/3}. \tag{6.9}$$

[2]for the y vorticity η with boundary condition $\eta = 0$ or $\partial_y\eta = 0$, or for $\partial_x\omega = (\partial_x^2 + \partial_y^2)v$ with no-slip $v = \partial_y v = 0$ or free-slip $v = \partial_y^2 v = 0$.

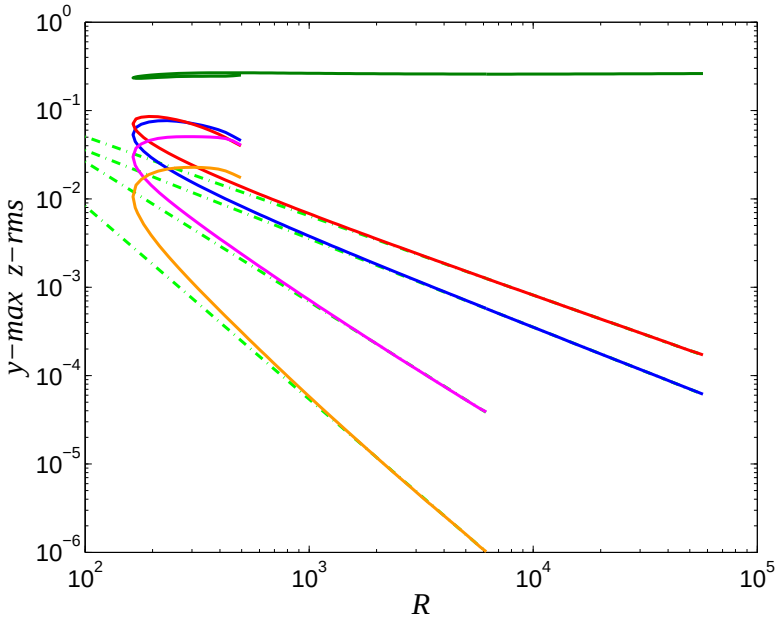

Figure 6.2: Scalings of the component of the lower branch steady state in plane Couette flow from [24]. The top curve (green) is the amplitude of the streaks $u_0(y,z) - \overline{U}(y) \sim O(1)$ as $R \to \infty$. The 2nd from the top (red) is $w_1 \sim R^{-1}$, the 3rd (blue) is $v_0, w_0 \sim R^{-1}$. The bottom two curves are the higher harmonics $\exp(i2\alpha x)$ (magenta) and $\exp(i3\alpha x)$ (orange) and they converge to zero faster than R^{-1}.

6.2 $R^{-1/3}$ in lower branch exact coherent states

Lower branch exact coherent states, that is the unstable 3D steady states calculated from the Navier-Stokes equations using Newton's method and the SSP phenomenology [18], show $R^{-1/3}$ critical layers as illustrated by the plane Couette flow steady states in [24]. Those calculations (up to about $R \approx 60\,000$) show that for large R the flow converges to a simple form

$$\mathbf{v} \to \mathbf{v}_0(y,z) + e^{i\alpha x}\mathbf{v}_1(y,z) + e^{-i\alpha x}\mathbf{v}_1^*(y,z) \tag{6.10}$$

such that $\mathbf{v}_0 = (u_0, v_0, w_0)$ has streaks $u_0(y,z) - \overline{u_0}(y) = O(1)$, but rolls v_0, $w_0 \sim O(R^{-1})$. The x-mode $\mathbf{v}_1(y,z)$ scales *almost* like R^{-1}, see Figure 6.2. The structure of this lower branch steady state is shown in Figure 6.3 and the gentle updraft and downdraft supporting $O(1)$ streaks is quite visible together with the critical layer structure of the wave mode $\mathbf{v}_1(y,z)$.

6.3 SSP model with critical layers

The SSP model [17] discussed in lectures 1 and 5 was intended as an as-simple-as-possible *low Reynolds number* model of the essential process in shear flow that leads to feedback from u onto the shearwise velocity v that creates u through the redistribution of the base

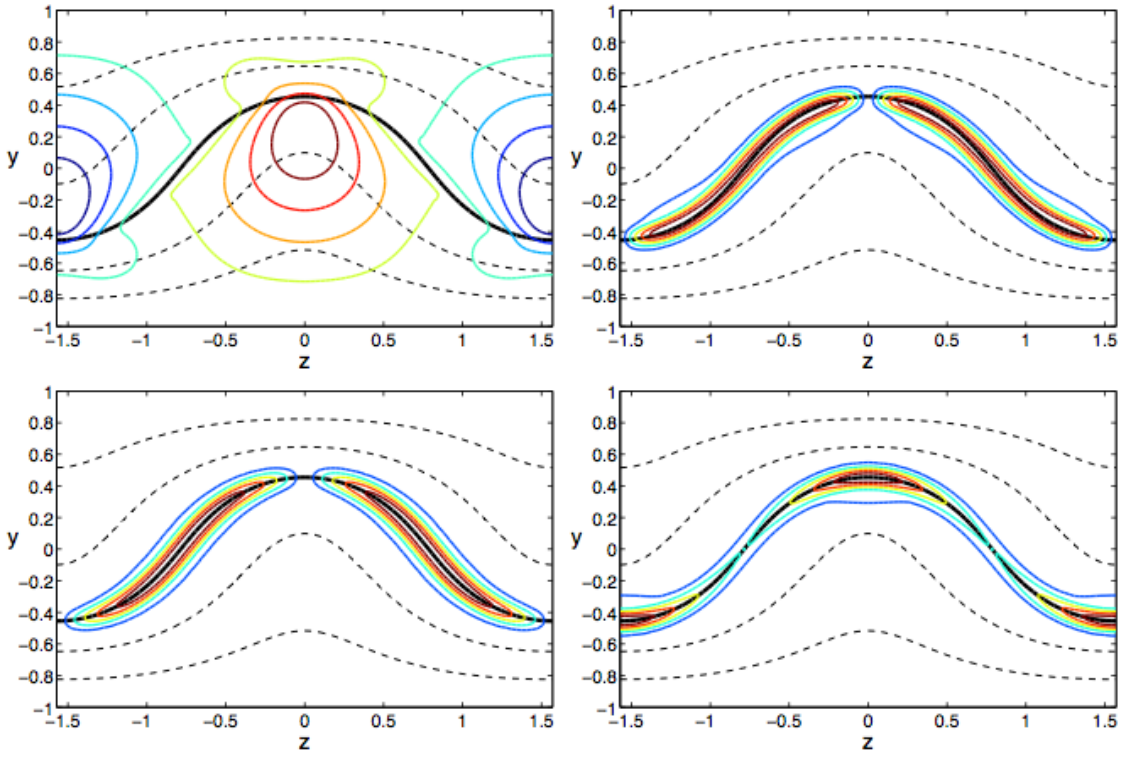

Figure 6.3: The lower branch plane Couette flow steady state for $\alpha = 1$, $\gamma = 2$, $R = 50\,171$. *Top left:* Contours of $u_0(y, z)$ (dashed, with $u_0 = 0$ thick solid) and $v_0(y, z)$ (color) showing updraft at $z = 0$ and downdraft at $z = \pm\pi/2$. *Top right:* $|u_1(y, z)|$. *Bottom left:* $|v_1(y, z)|$. *Bottom right:* $|w_1(y, z)|$. Note the concentration of u_1, v_1 and w_1 in a $R^{-1/3}$ layer about $u_0 = 0$. From [24].

shear ($\partial_t u \sim -v\,\partial_y \overline{U} + \cdots$), thereby leading to bifurcation from laminar flow. The model was derived from the Navier-Stokes equations through a Galerkin truncation procedure entirely similar to that needed to derive the Lorenz model of Rayleigh-Bénard convection. The latter is well-known to be physically valid *only* for Rayleigh numbers Ra close to the onset of convection at $Ra_c = 27\pi^4/4$, and the famous chaos of the Lorenz 3-mode model disappears for higher resolution, indeed the chaos is labelled as physically *spurious* [1].[3]

The 3-mode Lorenz model does capture the bifurcation from the conduction state to a *steady* convection state for $Ra \gtrsim Ra_c$ but for Ra not too far from Ra_c only ($Ra \lesssim 10Ra_c$). The 3-mode model is physically successful for relatively low Ra because the instability is linear and supercritical, *i.e.* it saturates at small amplitudes $\sim (Ra - Ra_c)^{1/2}$ [10]. Likewise the SSP 4-mode model [17] obtained by projection of the Navier-Stokes equations onto a few large scale Fourier modes is expected to be valid only for low R near onset of bifurcated states, but not as accurate as the Lorenz model since the SSP 4-mode model attempts to capture a nonlinear, finite amplitude bifurcation.

Nonetheless, the *lower branch steady states* do appear to result merely from the weakly nonlinear interaction of neutral streaky flow eigenmodes but those streaky flow eigenmodes contain $R^{-1/3}$ critical layers as we have seen. Thus the $R \to \infty$ scalings predicted by the low order model, namely $W \sim R^{-1}$ for the lower branch state (lecture 5 and [17]), may not be correct. Recall that the SSP 4-mode model reads

$$\begin{aligned}
\left(\frac{d}{dt} + \frac{\kappa_m^2}{R}\right) M &= \frac{\kappa_m^2}{R} - \sigma_u\, UV + \sigma_m\, W^2 \\
\left(\frac{d}{dt} + \frac{\kappa_u^2}{R}\right) U &= \sigma_u\, MV - \sigma_w\, W^2 \\
\left(\frac{d}{dt} + \frac{\kappa_v^2}{R}\right) V &= \sigma_v\, W^2 \\
\left(\frac{d}{dt} + \frac{\kappa_w^2}{R}\right) W &= \sigma_w\, UW - \sigma_v\, VW - \sigma_m\, MW
\end{aligned} \tag{6.11}$$

Since W is the amplitude of the only x-dependent mode in the SSP 4-mode model, it is the mode that we should correct for critical layers and its dissipation wavenumber κ_w should be $\kappa_w \sim R^{1/3}$ as $R \to \infty$, as discussed in the previous section. This gives a W decay rate scaling as $\kappa_w^2/R \sim R^{-1/3}$, instead of R^{-1}. The damping wavenumber κ_v for the rolls V also needs to be changed to $R^{1/3}$ in spite of it being x-independent. This is because the rolls are generated through the nonlinear interaction of the streak eigenmode of amplitude W that lives on the critical layer of thickness $\sim R^{-1/3}$ so the dissipation of the rolls occurs at that scale and $\kappa_v \sim R^{1/3}$ also. Likewise the nonlinear interaction coefficients σ_w, σ_v, σ_m scale like $R^{1/3}$ because those originate from the $\mathbf{u} \cdot \nabla \mathbf{u}$ nonlinearity, and when reduced to the V forcing for instance, [17, eqn. (6)], it involves only ∂_y and ∂_z derivatives, *i.e.* derivatives across the warped critical layer of thickness $R^{-1/3}$, so those derivatives scale like $R^{1/3}$. Thus because of the critical layer of the streak eigenmodes we expect

$$\kappa_v, \kappa_w \sim R^{1/3} \qquad \text{and} \quad \sigma_v, \sigma_w, \sigma_m \sim R^{1/3} \tag{6.12}$$

[3] There are constrained physical systems, *e.g.* the heated fluid loop [9] or the Malkus-Howard water-wheel nicely described in Strogatz's Nonlinear Dynamics and Chaos book, that are governed by the Lorenz equations and do show chaos.

but κ_m, κ_u and σ_u remain $O(1)$ because the mean shear M and streaks U are x-independent (so no shearing and critical layers for those modes) and they arise from the smooth redistribution of streamwise velocity by the large scale rolls V.

With these modifications, the lower branch steady state would have the $R \to \infty$ scaling U, $M \sim O(1)$ and $V \sim R^{-1}$ but

$$\frac{\kappa_v^2}{R} V = \sigma_v W^2 \;\Rightarrow\; R^{-4/3} \sim R^{1/3} W^2 \;\Rightarrow\; \boxed{W \sim R^{-5/6}} \tag{6.13}$$

This scaling matches the asymptotic analysis of Hall and Sherwin [4], and the plane Couette numerical results [24], but the asymptotic analysis of the full PDEs is a lot more involved.

6.4 SSP and Exact Coherent States

6.4.1 Bifurcation from streaky flow

OK, but how does one find the 3D Navier-Stokes solutions shown in section 6.2? There are several approaches nowadays, but the original robust approach that worked for plane Couette and plane Poiseuille with both no-slip and free-slip perturbations [18, 19, 20] as well as for pipe flow [2, 25, 11] is based on the self-sustaining process (SSP) shown schematically in Figure 6.4.

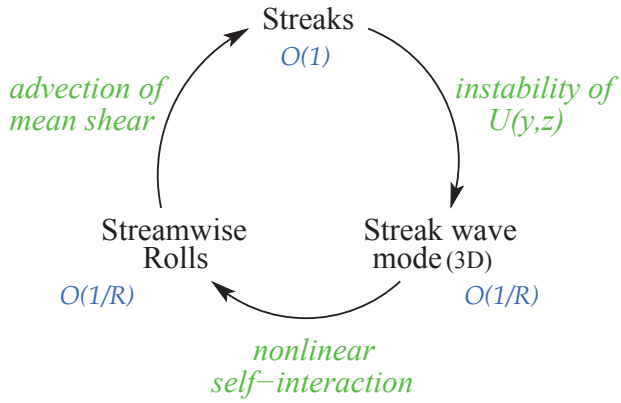

Figure 6.4: Schematic of the self sustaining process from [17]. Note that the scaling of the 'Streak wave mode' should now be corrected to $R^{-5/6}$.

The SSP was initially conceived as a periodic process where each element would occur in succession: (1) rolls redistribute streamwise velocity to create streaks, (2) streaky flow $U(y, z)$ develops an instability, (3) the nonlinear self-interaction of that instability (essentially an *oblique* vortex roll-up) regenerates the rolls. Indeed, the earliest test of the validity of this process [22, 5] using direct numerical simulations, showed a nearly periodic version of the process and truly time-periodic solutions were later isolated by Kawahara and Kida [6] and Viswanath [15].

But there are also equilibrated versions of the process where the rolls, streaks and streak eigenmode have just the right structure and amplitude to stay in mutually sustained steady or traveling wave equilibrium. The self-sustaining process theory can be used to find 3D steady state or traveling wave solutions of the full Navier-Stokes equations (NSE), *i.e.* the 3D NSE with sufficiently high resolution in all 3 directions. The solutions are represented in terms of Fourier-Chebyshev expansions, Fourier in the x and z directions and Chebyshev in the wall-normal y direction (see [20] for numerical details). The SSP-based procedure to do this [18] is

1. Add $\frac{F}{R^2}$ forcing of rolls $(0, v_0(y,z), w(y,z))$ to NSE $\Rightarrow O(\frac{1}{R})$ rolls, $O(1)$ streaks
2. Find F_c for *onset* of instability of $[u_0, v_0, w_0](y,z)$ for given α (or α_c for given F).
3. Use W (amp of $e^{i\alpha x}$ mode) as control parameter and continue to $F = 0$ (*Subcritical* bifurcation thanks to nonlinear feedback from wave mode onto rolls).

The parameter F is $O(1)$ and R is the Reynolds number [17, 18, 20]. This procedure is illustrated in Figures 6.5, 6.6 and 6.7 for free-slip plane Couette flow ('FFC' = 'Free-Free Couette') where it is particularly clean since the roll forcing has a simple form to yield the $v_0(y,z) = (F/R)\cos\beta y \ \cos\gamma z$ with $\beta = \pi/2$ from lecture 5. Here $F_c = 5$ for $\alpha \approx 0.49$ and $\gamma = 1.5$ at $R = 150$. $F = 0$, $W = 0$ is the laminar flow $u = y$ with $u = 0$ at $y = 0$ (the green surfaces in Figures 6.6, 6.7, the yellow surface is $u = -0.5$). For $F \neq 0$, we are forcing simple streamwise rolls seen as the red and blue tubes in Fig. 6.6 that redistribute the streamwise velocity u, warping the isosurfaces $u = constant$, to create a 2D streaky flow. Increasing F beyond a critical value F_c leads to an unstable streaky flow, although when F becomes too big, the rolls stir up the flow so much that the mean shear and streaks are wiped out and the streaky flow regains stability. This streaky flow for $\alpha = 0.49$, $\gamma = 1.5$, $R = 150$ is unstable for $5 < F < 18.3$ (*i.e.* fixed geometry, although we usually fix F and find the band of unstable α). Taking W, the normalized amplitude of the $e^{i\alpha x}$ mode, as the control parameter and increasing from $W = 0$ leads to the sequence of 3D steady states shown in figures 6.6 and 6.7 yielding to self-sustained states with no roll forcing ($F = 0$).

This procedure can be used in other flows: Rigid-Rigid Couette (*i.e.* no-slip at both walls), Rigid-Free Couette, Rigid-Free Poiseuille, Rigid-Rigid Poiseuille as well as in no-slip pipe flow [2, 25, 11] and duct flow (Kawahara *et al.*).

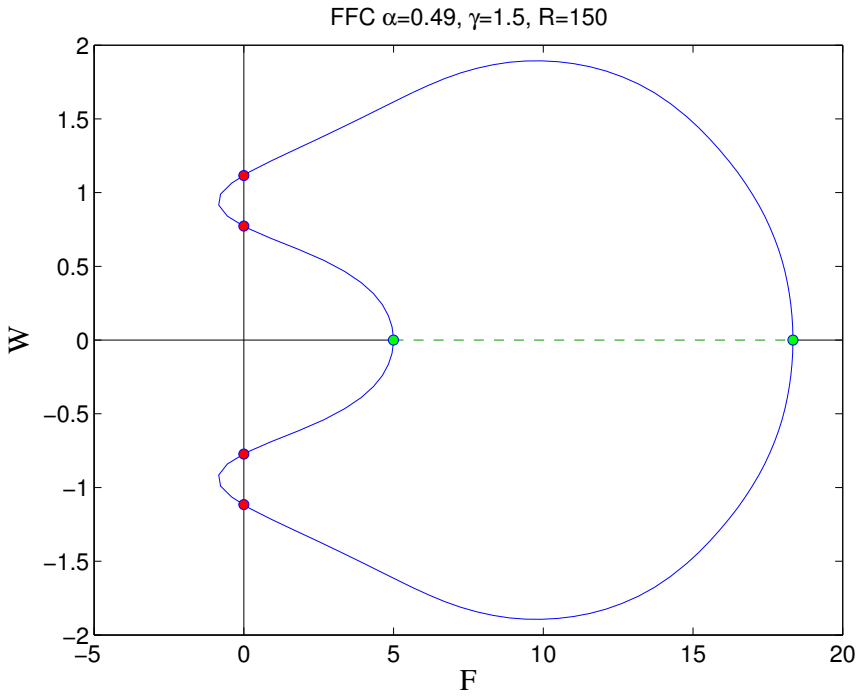

Figure 6.5: Bifurcation diagram for Free-Free Plane Couette Flow with $\alpha \approx 0.49$, $\gamma = 1.5$, $R = 150$, fixed. $F = W = 0$ is the laminar flow $U = y$. $W = 0$ corresponds to x-independent streaky flow with rolls and streaks when $F \neq 0$. The green markers at $W = 0$, $F = 5, 18.3$ are the streaky flow bifurcation points and the streaky flow is unstable between those markers (dashed line). The red markers at $F = 0$ indicate the self-sustained 3D steady states. Since W is the amplitude of the $e^{i\alpha x}$ mode, a change of sign of W corresponds to a half-period shift in x. This is for well-resolved spectral calculations of the full Navier-Stokes equations *not* the low-order model, although the low-order model has similar behavior.

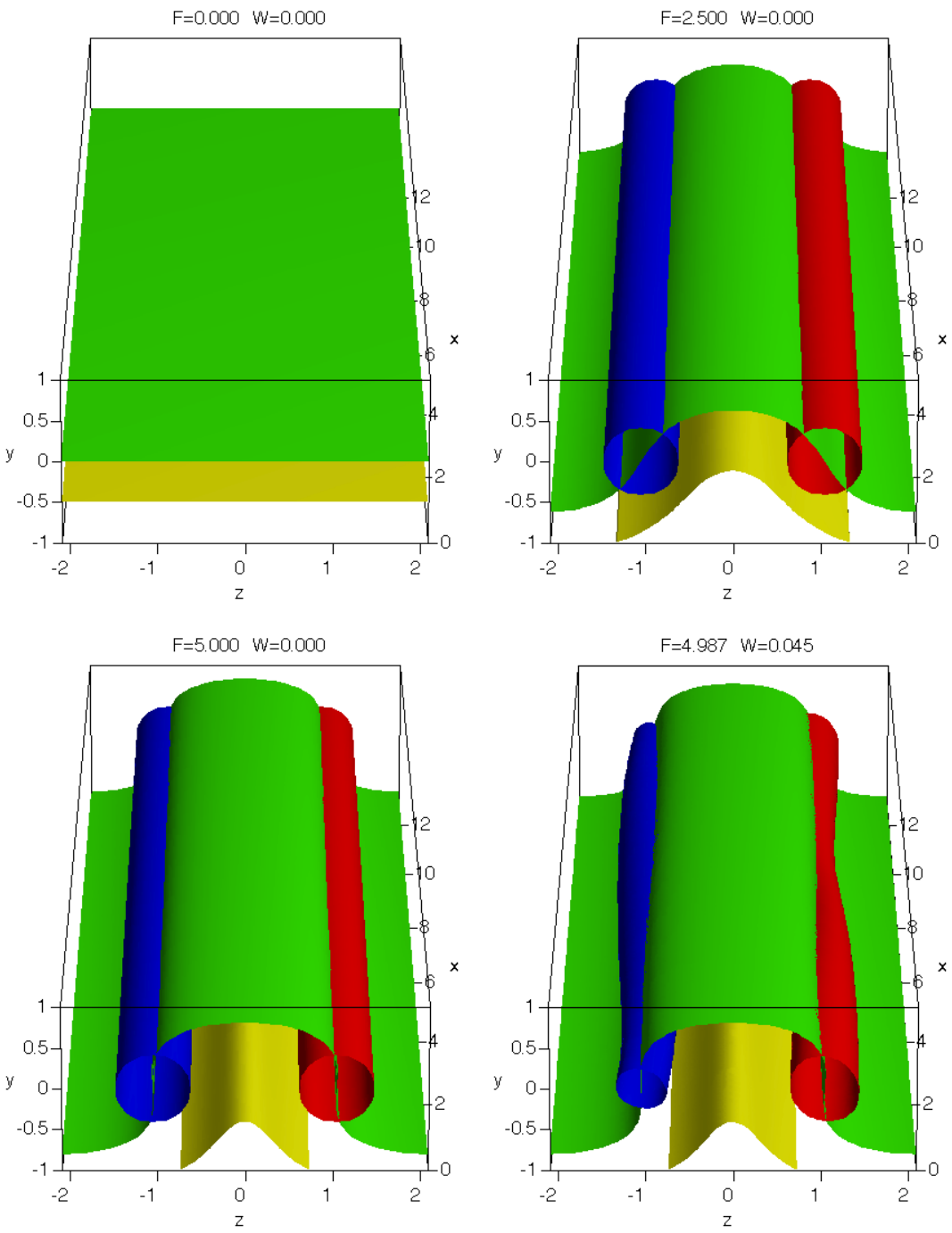

Figure 6.6: SSP construction of exact coherent states for Free-Free Plane Couette Flow. The green surfaces are $u = 0$, gold is $u = -0.5$. Red and blue correspond to positive and negative streamwise vorticity ω_x, respectively (80% of max). F is the normalized roll $v_0(y, z)$ amplitude and W is the normalized $e^{i\alpha x}$ streaky mode amplitude. First we increase F with $W = 0$ until the 2D streaky flow is unstable (bottom left), then we start increasing W with F free.

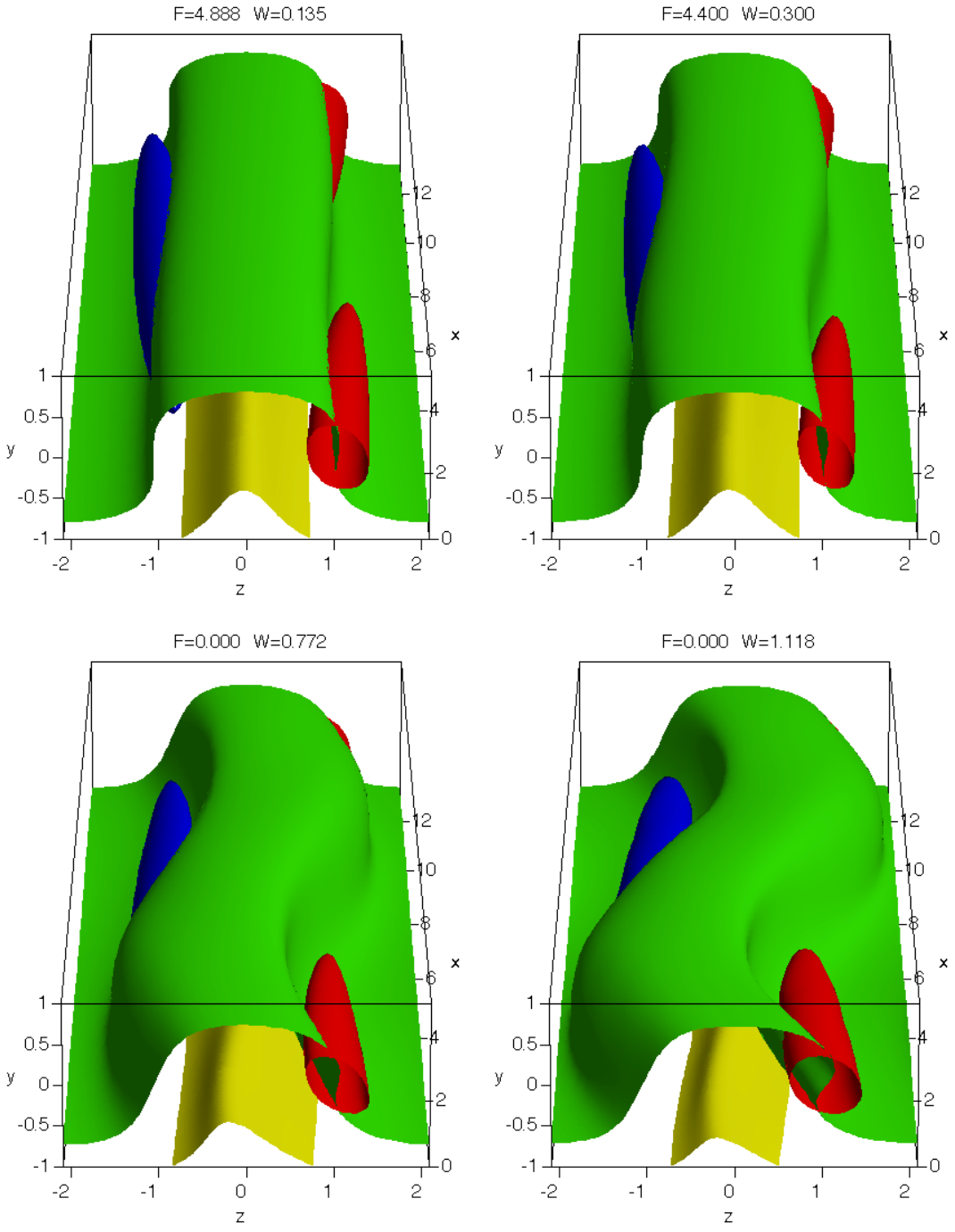

Figure 6.7: Continued from Fig. 6.6, we keep on increasing W and obtain a lower branch self-sustained steady state when $F = 0$ (bottom left) and an upper branch (bottom right). These are the upper two red markers in the bifurcation diagram Fig. 6.5.

6.4.2 Homotopy of exact coherent states

The solutions can also be easily 'deformed' into one another. For instance one can perform the homotopy from *Free-Free Couette* to *Rigid-Free Poiseuille*, this is a Newton continuation of the steady state Couette solutions to *traveling wave* Poiseuille solutions in a half-channel with no-slip at the bottom wall at $y = -1$ and free-slip at the centerline at $y = 1$. This is the homotopy

$$\begin{aligned} U_L(y) &= y + \mu\left(\frac{1}{6} - \frac{y^2}{2}\right) \\ (1-\mu)\frac{\partial u}{\partial y} + \mu\, u &= 0 \qquad \text{at} \qquad y = -1 \end{aligned} \tag{6.14}$$

and similarly for w at the wall, with $\mu = 0 \to 1$ to go from Couette with free slip at both walls to Poiseuille $U_L(y) = 1/6 + y - y^2/12$ with no-slip at the bottom wall, where $U_L(y)$ is the laminar flow and Poiseuille is normalized to be nearest to Couette. If this homotopy is performed at fixed W (amp of $e^{i\alpha x}$ mode) then R becomes the free parameter, since we are now only interested in self-sustained 3D states with no external roll forcing $F = 0$ (Figure 6.8).

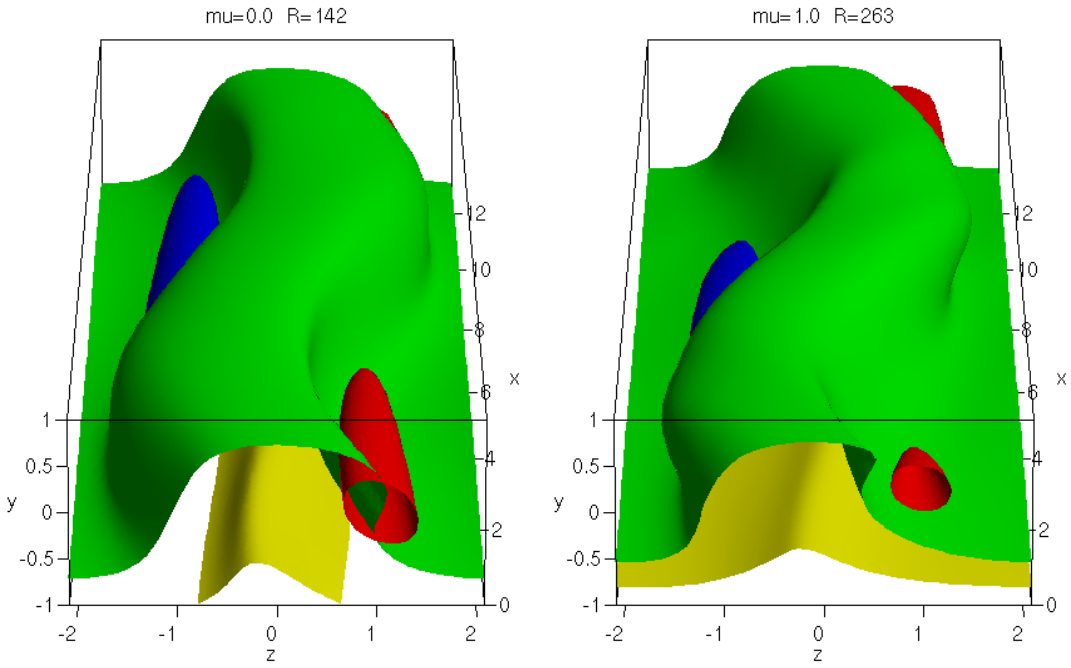

Figure 6.8: Homotopy (6.14) from free-free Couette $\mu = 0$ (left) to Rigid-free Poiseuille at $\mu = 1$ (right) [18, 19]. The gold $u = -0.5$ isosurface cannot be swept away with no-slip at $y = -1$ (right). The green isosurface on the right is $u - c = 0$ where c is the wave speed.

By 'homotopy' we mean to emphasize the very similar ('homo') shape ('topos') of the solutions in the various flows, *e.g.* free-slip Couette and no-slip Poiseuille, and the 'homotopy' procedure consists of a smooth deformation of one solution into the other. In contrast,

we used bifurcation from streaky flow to construct the solution from scratch and that is not smooth since it involves a bifurcation (sect. 6.4.1). In the literature, authors often refer to the latter as 'homotopy' as well, but we do not.

6.4.3 'Optimum' channel Traveling Wave

Once a self-sustained 3D steady state or traveling wave has been found, it is interesting to find its lowest onset Reynolds number. To do so we need to optimize the 3D solutions over the fundamental wavenumbers α and γ, *i.e.* over the wavelengths L_x and L_z in order to minimize the Reynolds number. This was done for a variety of flows, including Rigid-Rigid Couette where onset $R \approx 127.7$ and Rigid-Free Poiseuille where onset $R \approx 977$ (based on the laminar centerline velocity and the wall to centerline distance to compare to 5772 for onset of the weak 2D viscous no-slip instability). Note that there is a factor of 4 difference arising just from the different definitions of R in plane Couette and Poiseuille.

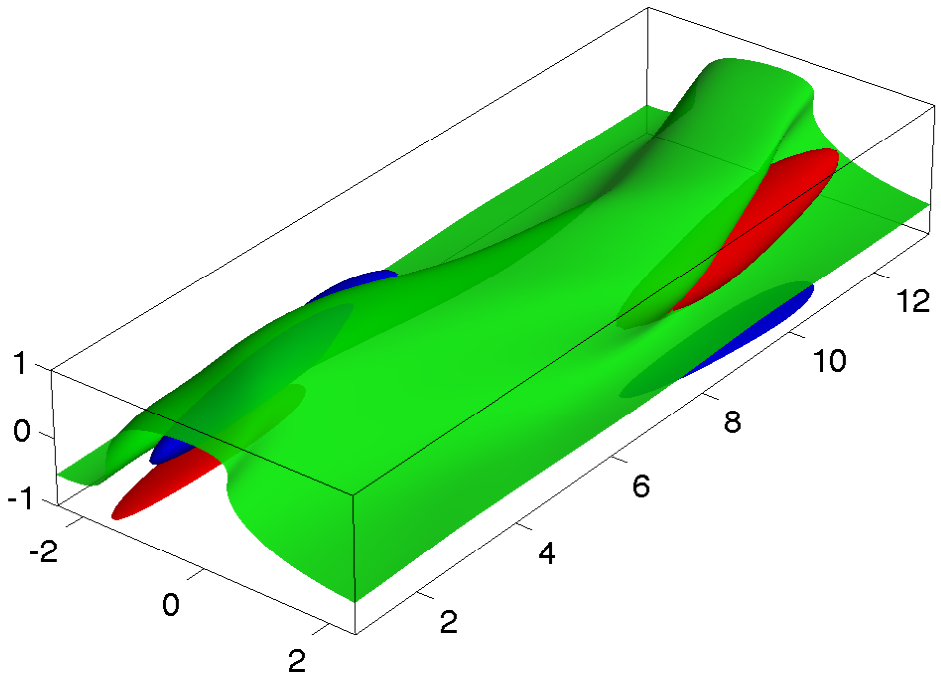

Figure 6.9: Channel flow traveling wave at onset Reynolds number $R_\tau \approx 44$ for $L_x^+ \approx 274$ and $L_z^+ \approx 105$ in wall units. This corresponds to a pressure gradient based Reynolds number (*i.e.* laminar centerline velocity and wall to centerline distance) of 977 [20]. R_τ is based on the friction velocity $u_\tau = \sqrt{\tau_w}$ and the wall to centerline distance. Wall or 'plus' units are based on ν/u_τ. Each vortex (red and blue isosurfaces) has a shear layer of opposite sign ω_x at the wall below it. The green isosurface is $u - c = 0$ where c is the traveling wave speed.

One remarkable result of this optimization is that the length scales for minimum onset Reynolds number turn out to be almost identical to the length scales that had long been observed for *coherent structures* in the near-wall region of turbulent channel flows, namely $L_x^+ \approx 300$, $L_y^+ \approx 50$ and $L_z^+ \approx 100$, the latter corresponding to the well-known 100+ streak spacing. This fits with the idea that those scales are the smallest scales for the self-sustaining process and the streak spacing is essentially an onset Reynolds number [16]. The structure of the traveling wave is also remarkably similar to the educed structure of near wall momentum transporting flows shown in Figure 6.10. Those observed structures consists of wavy low speed streaks flanked by staggered counterrotating quasi-streamwise vortices, exactly like the 3D traveling waves, hence the name of *exact coherent states* for the latter [19].

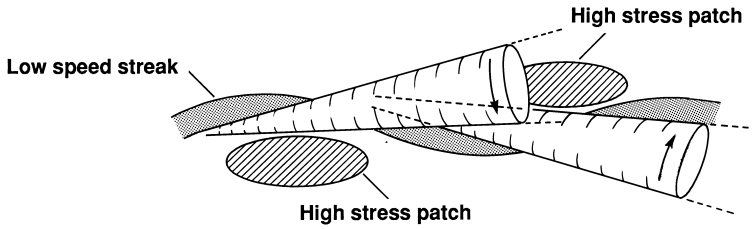

Figure 6.10: Near-wall coherent structure educed from turbulent channel data by Derek Stretch (1990) [14]. Note the wavy streak as the wavy green isosurface in Fig. 6.9 and the counterrotating quasi-streamwise vortices as the red and blue isosurfaces in Fig. 6.9, and the earlier Couette solutions in Fig. 6.7.

6.5 Turbulence: onset and structure in state space

We saw in sect. 6.4.1 how the exact coherent states — 3D steady states and traveling wave solutions of the Navier-Stokes equations — can be constructed by bifurcation from streaky flow in the (F, W) parameter space for fixed R, α, γ (Fig. 6.5). For fixed $F = 0$ these solutions arise from *saddle-node* bifurcations, also known as *out-of-the-blue-sky* bifurcations, in the (R, W) parameter plane, as shown in Figure 6.11. Although the drag of the upper branches grows quickly with Reynolds number, at least initially (we expect fixed (α, γ) solutions to eventually saturate), the lower branch solution quickly asymptotes to a constant *larger than the laminar drag*. These computations have been pushed to $R \approx 60\,000$ and the lower branch drag appears constant, consistent with Fig. 6.2 where the solution asymptotes to O(1) streaks. This suggest that these solutions never bifurcate from the laminar flow, not even at $R \to \infty$.

But all these upper and lower branches are *unstable from onset*, how then could they be relevant? We have already seen that their structure and length scales (*e.g.* the 100+ streak spacing) match very well with the observed near-wall coherent structures in turbulent shear flows, and the latter are clearly unstable, yet they are statistically ever present and control the momentum transport. Figure 6.12 provides other evidence of the relevance of unstable coherent states to turbulent flows that appear to oscillate around the upper

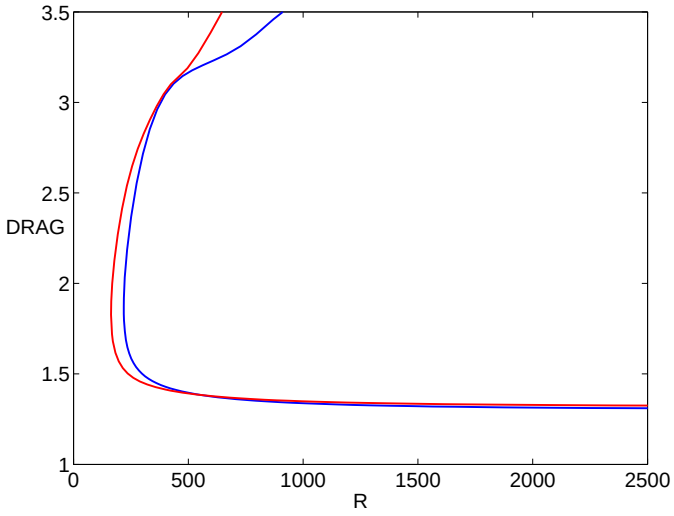

Figure 6.11: Rigid-rigid Couette bifurcation diagram for 3D steady states for $(\alpha, \gamma) = (1, 2)$ (red) and (1.14,2.5) (blue). Drag versus Reynolds number. Drag is non-dimensionalized by the laminar drag so this is a Nusselt number, $\tau_w/(\nu U/h)$ and Drag=1 is the laminar flow. The upper branch drag increases rapidly with R but the lower branch quickly asymptotes to a constant > 1. The solutions arise *out-of-the-blue-sky* but do not bifurcate from the laminar flow.

branches, suggesting that the upper branch is a good first approximation to the statistics of turbulent flows such as drag, energy dissipation, mean flows, ...

The lower branch on the other hand has the remarkable property of having only one unstable direction, at least in plane Couette flow except close to the nose of the bifurcation curve [24]. Starting in the unstable direction either leads quickly to turbulent flow, or in the opposite direction leads quickly back to laminar flow as shown in Figure 6.13. This suggests that the lower branch is the backbone of the laminar-turbulent boundary that would be the *stable manifold* of the lower branch. Further calculations by us and others have confirmed this role of the lower branch [12].

Figure 6.14 is an old cartoon (APS DFD 2001, [19], [21]) sketching how these exact coherent states and their stable and unstable manifold structure the state space. Gibson, Cvitanović and Halcrow [3] have produced a beautiful picture of the state space of plane Couette flow for given fundamental wavenumber (α, γ) and Reynolds number $R = 400$ that shows the role of the coherent states and their unstable manifolds in guiding the turbulent dynamics. Kawahara, Uhlmann and van Veen explore the relevance of invariant solutions for fully developed turbulent flows [7].

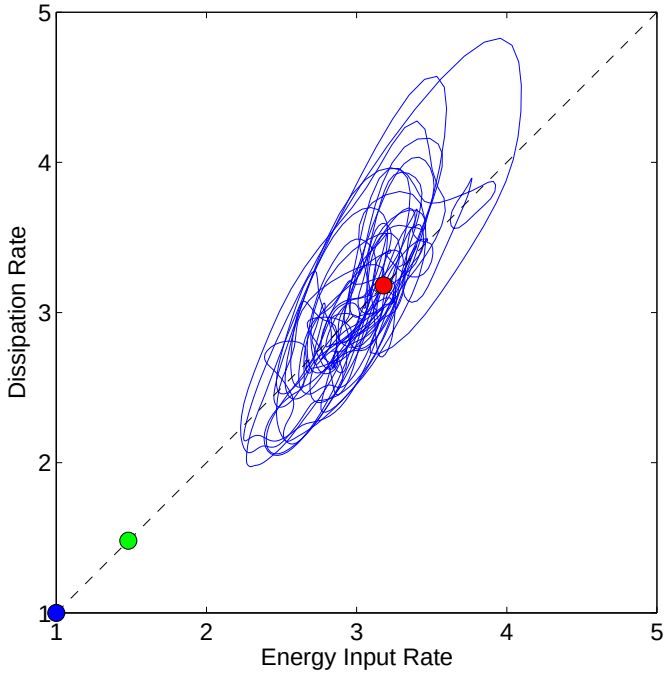

Figure 6.12: Rigid-rigid Couette 3D steady states for $(\alpha, \gamma) = (0.95, 1.67)$ in the total energy input rate $\tau_w U/h$ versus total energy dissipation rate $\mathcal{E}$ (lecture 2), normalized by laminar values so blue marker is laminar flow at (1,1). Green marker is lower branch, red marker is upper branch. The blue orbit is a DNS of turbulent flow for 2000 h/U time units for $(\alpha, \gamma) = (1.14, 1.67)$. Turbulent orbit was computed by Jue Wang using John Gibson's Channelflow code [24].

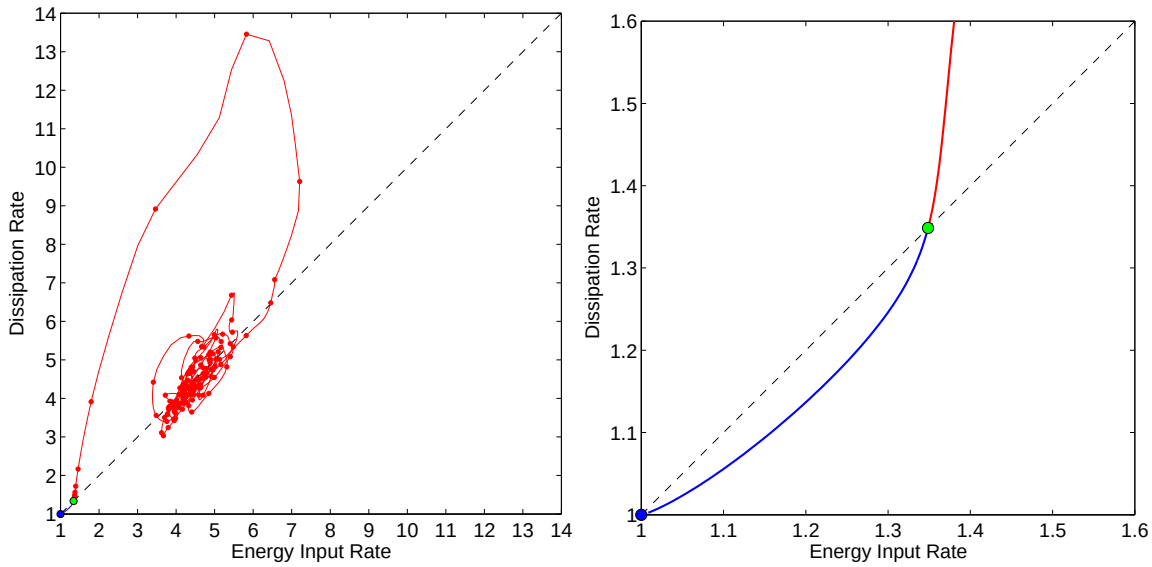

Figure 6.13: Rigid-rigid Couette for $(\alpha, \gamma) = (1, 2)$ at $R = 1000$. Starting on the positive (say) side of the lower branch unstable direction quickly leads to a turbulent flow that oscillates about upper branches (left). Starting on the opposite side quickly leads to a slow, reverse SSP, decay back to laminar. That is, the flow first loses its x dependence, then the rolls and streaks slowly decay back to laminar flow (right). Note the different scales. The dots on the red curve mark equal time intervals to show speed along the curve.

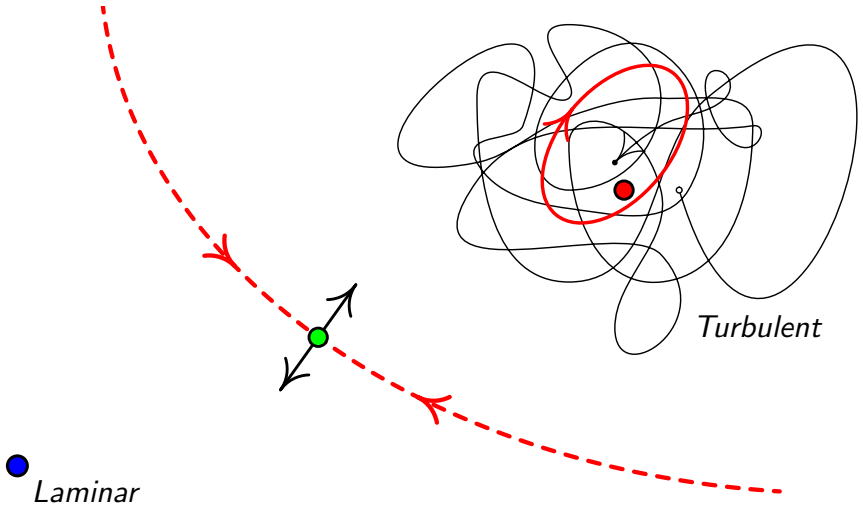

Figure 6.14: Schematic of the state space and role of the unstable exact coherent states. Laminar flow (blue) is stable for all R. Lower branch is the backbone of the laminar-turbulent boundary which is the stable manifold (red dashed) of the lower branch (green marker). The turbulent flow is an aperiodic oscillation about upper branches (red marker). There exists also unstable periodic orbits (red curve), that form the skeleton of the turbulent attractor.

6.5.1 Conclusion

These six lectures have been a quick and necessarily incomplete overview of the problem of turbulence onset and structure in basic flows such as flows in pipes and channels. The scientific study of this basic fluid dynamics problem started with the experiments of Reynolds and the analyses of Rayleigh in the 1880s and has been an active field of study ever since, splitting into several distinct directions such as stability theory, turbulence modeling and statistical theories of turbulence.

Linear stability theory of shear flows does not explain onset of turbulence but has many technical and physical peculiarities such as critical layers and (weak) instability arising from viscosity in channel but not in pipe, in pressure-driven but not wall-driven flows, yet turbulence in all these different flows is quite similar. Statistical theories have focused largely on homogeneous isotropic turbulence and disconnected drag from energy dissipation. The Kolmogorov picture of turbulence with its energy cascade concept and $k^{-5/3}$ energy spectrum is compelling, but has little if anything to say about momentum transport or heat flux in realizable wall-bounded flows. Numerical simulations and modern experimental visualization techniques such as PIV (particle image velocimetry) have revealed a myriad of coherent structures and a major challenge has been to decide how to identify and classify these observed structures and their interconnections, and figure out how to introduce them in models and theories.

Our work on exact coherent states reconnects turbulence onset to developed turbulence with its observed and educed coherent structures. The 100+ streak spacing of near-wall coherent structures in fully developed turbulent shear flows is closely related to, if not identical with, the critical Reynolds number for turbulence onset [16], [20]. In a little more than a decade, we have gone from the two well-known states of fluid flow, *laminar* and *turbulent*, to the discovery of a multitude of intermediate states, *unstable exact coherent states*. These states can be steady states or more generally traveling waves in plane Couette, Poiseuille, pipe and duct flows as well as time periodic solutions. The latter have been found mostly in plane Couette flow so far, by Kawahara and Kida [6], Viswanath [15] and many unpublished states found by John Gibson (but posted on his web page). Schneider, Gibson and Burke [13] have found spanwise localized states that bifurcate from the lower branch states close to the 'nose' of the saddle-node bifurcation. This bifurcation is directly connected to the Hopf bifurcation that was known to occur along the lower branch as we approached the saddle-node bifurcation [23], [24], and to the instability of the upper branch (the node) at onset.

Our cartoon (Fig. 6.14) is now too simplistic, there are many lower branches and upper branches, even snakes and ladders [13], and Eckhardt and co-workers have shown that there are more complex types of *'edge states'* on the laminar-turbulent boundary than mere traveling waves. Lebovitz [8] uses low order models to explore features of the laminar-turbulent boundary and shows that the 'edge' may not be a laminar-turbulent boundary but an invariant set separating the basin of attraction of the laminar state in two parts. We have discovered the unstable coherent scaffold of turbulent flows and, not surprisingly, it is rich and complex.

Bibliography

[1] J. H. Curry, J. R. Herring, J. Loncaric, and S. A. Orszag, *Order and disorder in two- and three-dimensional Bénard convection*, Journal of Fluid Mechanics, 147 (1984), pp. 1–38.

[2] H. Faisst and B. Eckhardt, *Traveling waves in pipe flow*, Phys. Rev. Lett., 91 (2003), p. 224502.

[3] J. F. Gibson, J. Halcrow, and P. Cvitanović, *Visualizing the geometry of state space in plane Couette flow*, Journal of Fluid Mechanics, 611 (2008), pp. 107–130.

[4] P. Hall and S. Sherwin, *Streamwise vortices in shear flows: harbingers of transition and the skeleton of coherent structures*, Journal of Fluid Mechanics, 661 (2010), pp. 178–205.

[5] J. Hamilton, J. Kim, and F. Waleffe, *Regeneration mechanisms of near-wall turbulence structures*, J. Fluid Mech., 287 (1995), pp. 317–348.

[6] G. Kawahara and S. Kida, *Periodic motion embedded in Plane Couette turbulence: regeneration cycle and burst*, J. Fluid Mech., 449 (2001), pp. 291–300.

[7] G. Kawahara, M. Uhlmann, and L. van Veen, *The significance of simple invariant solutions in turbulent flows*, Annu. Rev. Fluid Mech. 44 (2012), pp. 203–225.

[8] N. R. Lebovitz, *Boundary collapse in models of shear-flow transition*, Communications in Nonlinear Science and Numerical Simulation, 17 (2012), pp. 2095 – 2100.

[9] W. V. R. Malkus, *Non-periodic convection at high and low Prandtl number*, Mém. Soc. R. Sci. Liège, 4 (1972), pp. 125–128.

[10] W. V. R. Malkus and G. Veronis, *Finite amplitude cellular convection*, Journal of Fluid Mechanics, 4 (1958), pp. 225–260.

[11] C. C. T. Pringle and R. R. Kerswell, *Asymmetric, helical, and mirror-symmetric traveling waves in pipe flow*, Physical Review Letters, 99 (2007), p. 074502.

[12] T. Schneider, J. Gibson, M. Lagha, F. De Lillo, and B. Eckhardt, *Laminar-turbulent boundary in plane Couette flow*, Phys. Rev. E, 78 (2008), p. 037301.

[13] T. M. Schneider, J. F. Gibson, and J. Burke, *Snakes and ladders: Localized solutions of plane couette flow*, Phys. Rev. Lett., 104 (2010), p. 104501.

[14] D. Stretch, *Automated pattern eduction from turbulent flow diagnostics*, in Annual Research Briefs, Center for Turbulence Research, Stanford U., 1990, pp. 145–157.

[15] D. Viswanath, *Recurrent motions within plane Couette turbulence*, J. Fluid Mech., 580 (2007), pp. 339–358.

[16] F. Waleffe, *Proposal for a self-sustaining process in shear flows*, Working paper, available at `www.math.wisc.edu/~waleffe/ECS/sspctr90.pdf`, (1990).

[17] ——, *On a self-sustaining process in shear flows*, Phys. Fluids, 9 (1997), pp. 883–900.

[18] ——, *Three-dimensional coherent states in plane shear flows*, Phys. Rev. Lett., 81 (1998), pp. 4140–4148.

[19] ——, *Exact coherent structures in channel flow*, J. Fluid Mech., 435 (2001), pp. 93–102.

[20] ——, *Homotopy of exact coherent structures in plane shear flows*, Phys. Fluids, 15 (2003), pp. 1517–1543.

[21] ——, *Exact coherent structures in turbulent shear flows*, in Turbulence and Interactions: Keynote Lectures of the TI 2006 Conference, M. Deville, T.-H. Le, and P. Sagaut, eds., Springer, 2009, pp. 139–158.

[22] F. Waleffe, J. Kim, and J. Hamilton, *On the origin of streaks in turbulent shear flows*, in Turbulent Shear Flows 8: selected papers from the Eighth International Symposium on Turbulent Shear Flows, Munich, Germany, Sept. 9-11, 1991, F. Durst, R. Friedrich, B. Launder, F. Schmidt, U. Schumann, and J. Whitelaw, eds., Springer-Verlag, Berlin, 1993, pp. 37–49.

[23] J. Wang, *On lower branch Exact coherent structures in Turbulent shear flows*, Ph.D. Thesis, University of Wisconsin-Madison, 2007.

[24] J. Wang, J. Gibson, and F. Waleffe, *Lower branch coherent states in shear flows: transition and control*, Phys. Rev. Lett., 98 (2007), p. 204501.

[25] H. Wedin and R. Kerswell, *Exact coherent structures in pipe flow*, J. Fluid Mech., 508 (2004), pp. 333–371.

Part II

The following four lectures are by Richard Kerswell University of Bristol

Lecture 7

Transition Scenarios: Normality vs Non-Normality

7.1 Transition scenarios

Transition to turbulence in fluid systems can be broadly divided into two different classes: the 'supercritical' or the 'subcritical' scenario.

7.1.1 Supercritical scenario

In the supercritical scenario, there is a well-defined sequence of supercritical bifurcations in which the flow gradually becomes more complicated in space and time. For these flows, nothing happens (that is, all disturbances decay) below a well-defined value of a control parameter, e.g. the Reynolds number Re. The following commonly-referred-to values of the control parameter R (e.g. [19]) then effectively characterise the situation:

- R_E, the threshold below which any disturbances, both finite and infinitesimal, monotonically decay. This is known as the Energy stability threshold.
- R_L, the threshold for linear stability.
- R_G, the least R below which the basin of attraction of the laminar solution includes all states with the exception of a set of states of measure zero. R_G signals the emergence of another attractor beyond the laminar solution.

In the supercritical scenario where the first bifurcation from the base state is supercritical, $R_E \leq R_L = R_G$. The only interesting issue is then whether $R_E = R_L$ or $R_E < R_L$ so there is a gap.

Rayleigh-Bénard convection (RB) is an example of a flow in the supercritical scenario class (e.g. see [6], chapter 6). The motionless conductive state is provably absolutely stable (i.e. to *all* disturbances) until a certain value ($Ra_L = 1708$ for rigid-rigid boundary conditions, where Ra is the Rayleigh number) so $R_E = R_L = R_G = 1708$. Above this value, the flow undergoes a sequence of supercritical bifurcations.

Another member of the supercritical scenario class is Taylor-Couette flow (TC) with co-rotating cylinders. TC flow shows a succession of bifurcations and increasing complexity

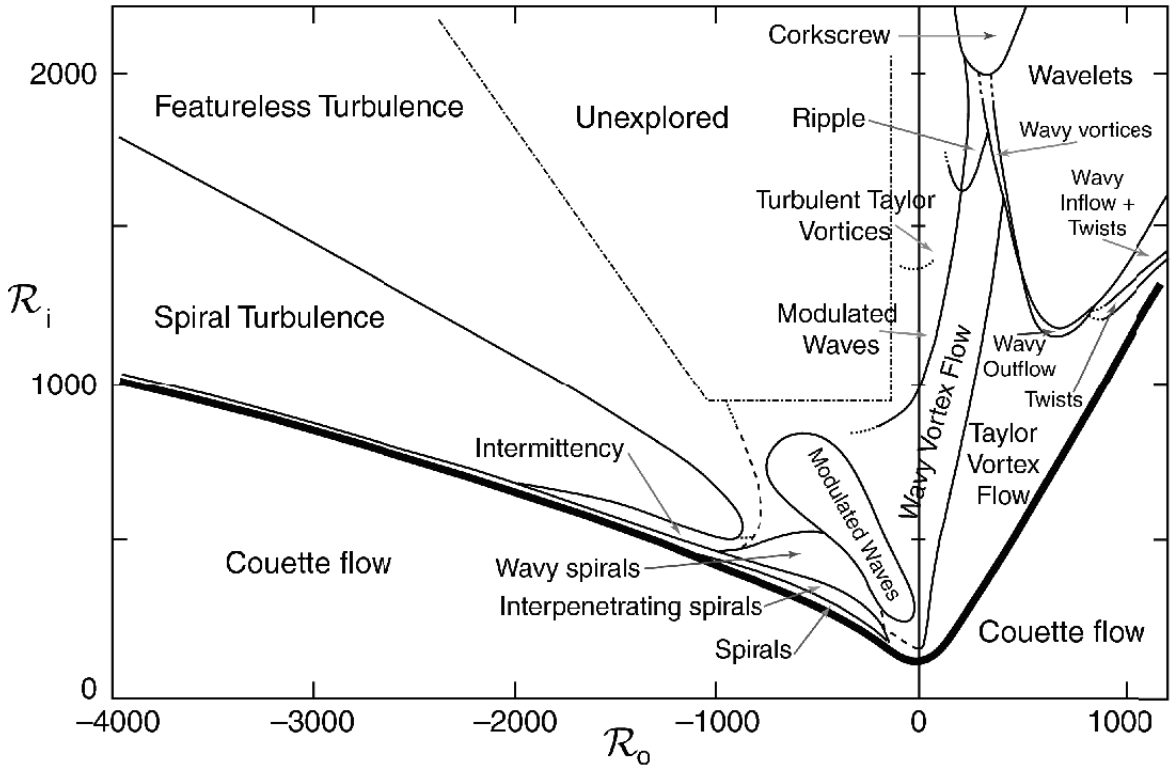

Figure 7.1: Phase diagram of patterns observed in Taylor-Couette flow as a function of the inner Reynolds number R_i and the outer Reynolds number R_o. The heavy line denotes the boundary between featureless flow below the line and patterned states above the line. (Redrawn from [1], see also [6], figure 7.8).

for $R := R_i > R_L > 0$ (increasing rotation rate of the inner cylinder and fixed outer cylinder rotation rate $R_o > 0$): see figure 7.1. Contrary to RB flow, $R_E < R_L = R_G$ which means that transient growth - an initial disturbance can initially grow in amplitude before eventually decaying away - is possible for $R_E < R < R_L$ with TC flow (see figure 7.2). The supercritical scenario is well-studied and understood.

7.1.2 Subcritical scenarios

In the subcritical scenario, as typified by wall-bounded shear flows, transition is sudden, noise-dependent and dramatic, i.e. the flow immediately becomes complicated. There is usually a region of bistability so that the laminar and turbulent states can coexist (in plane Couette and Hagen-Poiseuille flow, this region extends to infinite Re!). As a result this is the more interesting scenario where there has been considerable recent research activity and so will be the focus of my lectures. Flows in the subcritical scenario class cannot be sufficiently described by the three (established) parameters defined above. Therefore, as a first attempt in building up a more sophisticated picture, we introduce the following additional parameter values:

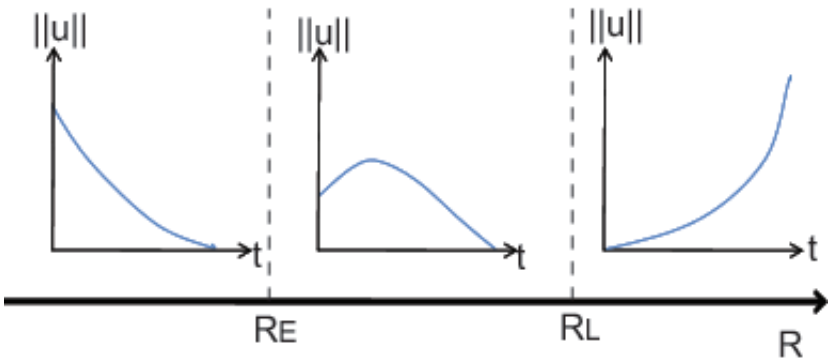

Figure 7.2: Sketch of different solution characteristics under different values of R for the supercritical scenario.

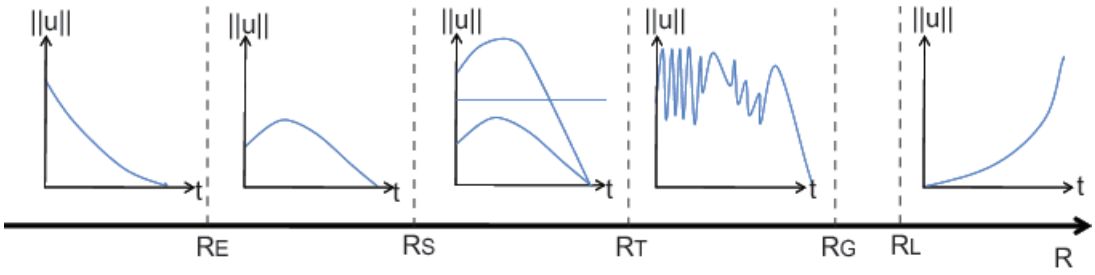

Figure 7.3: Sketch of different solution characteristics under different values of R for the subcritical scenario.

- R_S, the threshold above which there exists initial conditions with measure zero which do not convergence to the basic state. Or equivalently, there exists 'other' unstable exact solutions of the governing equations beyond the basic state.

- R_T, the threshold above which long-lived non-trivial flows exist. These flows look turbulent (characterised by positive Lyapunov exponents so nearby trajectories diverge) but may not be sustained if $R_T < R < R_G$.

For subcritical scenarios we have that $R_E < R_S, R_T \leq R_G$, where $R_S < R_T$ seems likely but is unproven and typically $R_G < R_L$ for wall-bounded shear flows like plane Poiseuille flow, plane Couette flow and Hagen-Poiseuille flow. The qualitative behaviour of a typical subcritical scenario is sketched in figure 7.3. For $R < R_E$ all solutions decay monotonically to the base state. For $R_E < R < R_S$ transient growth is possible of some disturbances. For $R_S < R < R_T$ at least one disturbance does not decay to the base state. For $R_T < R < R_G$ at least one solution experiences a 'long-lived' transient before eventually decaying. For $R_G < R < R_L$ the flow need not relaminarise when disturbed and finally, for $R > R_L$ the flow always evolves away from the base state. Table 7.1 emphasizes how the Rayleigh-Bénard problem differs from plane Poiseuille, plane Couette and Hagen-Poiseuille flows which are all in the subcritical scenario class.

	R_E	R_S	R_T	R_L
RB	$1708^{[8]}$	1708	1708	1708
PPF	$49.6^{[4]}$	$\leq 977^{+[20]}$	$2100^{[18]}$	$5772^{[13]}$
PCF	$20.7^{[8]}$	$\leq 127^{[12,\ 20]}$	$\sim 325^{[5]}$	$\infty^{[17]}$
HPF	$81.5^{[9]}$	$\leq 773^{*[15]}$	$\sim 1800^{[11]}$	$\infty^{\dagger}$

Table 7.1: The various thresholds for different flow types: Rayleigh-Bénard (RB), plane Poiseuille flow (PPF), plane Couette flow (PCF), and Hagen-Poiseuille flow (HPF). Source references are shown as superscripts and † indicates still unproven. $^{+}$ means R_S is based upon fixed pressure gradient whereas * means R_S based upon fixed mass flux. R_S for PPF based upon fixed mass flux is close to but strictly below 860 whereas HPF based upon pressure gradient is close to, but strictly below, 990.

7.1.3 Normality vs Non-normality

We now discuss the reasons for this very different behaviour which, because of the special form of the nonlinearity in the Navier-Stokes equation, can be largely traced back to the properties of the linear operator produced by linearising the Navier-Stokes equation around the basic state.

If $\mathbf{u}_{\text{tot}} = \mathbf{u}_{\text{lam}} + \hat{\mathbf{u}}$ so $\hat{\mathbf{u}}$ satisfies homogeneous boundary conditions (is real, at least C^2 and has finite kinetic energy), then the Navier-Stokes equation for the perturbation $\hat{\mathbf{u}}$ can be written as

$$\frac{\partial \hat{\mathbf{u}}}{\partial t} = L\hat{\mathbf{u}} + N(\hat{\mathbf{u}}, \hat{\mathbf{u}}), \tag{7.1}$$

$$\nabla \cdot \hat{\mathbf{u}} = 0, \tag{7.2}$$

where L and N are linear and nonlinear operators, respectively. If $\langle \mathbf{u}, \mathbf{v} \rangle := \int \mathbf{u}^*.\mathbf{v}\, dV$ where * indicates complex conjugation (redundant here for real $\hat{\mathbf{u}}$ but important when discussing the eigenfunctions and adjoint of L), then

$$\left\langle (L^+\mathbf{u}), \mathbf{v} \right\rangle := \langle \mathbf{u}, (L\mathbf{v}) \rangle \tag{7.3}$$

defines L^+, the adjoint of L and L is normal if and only if L^+ commutes with L i.e. $LL^+ = L^+L$. The eigenvalue spectrum of the linear operator L determines the linear stability of the base state $\mathbf{u}_{\text{lam}}$ with R_L defined by when $\max[\Re e(\text{eig}(L))] = 0$. Energy stability is derived by examining the instantaneous rate of change of the perturbation kinetic energy,

$$\frac{\partial}{\partial t}\langle \frac{1}{2}\hat{\mathbf{u}}^2 \rangle = \left\langle \hat{\mathbf{u}}, \frac{\partial \hat{\mathbf{u}}}{\partial t} \right\rangle = \langle \hat{\mathbf{u}}, (L\hat{\mathbf{u}}) \rangle = \tfrac{1}{2} \left\langle \hat{\mathbf{u}}, (L + L^+)\hat{\mathbf{u}} \right\rangle \tag{7.4}$$

since $\langle \hat{\mathbf{u}}, N(\hat{\mathbf{u}}, \hat{\mathbf{u}}) \rangle = 0$ (this is the special property of the Navier-Stokes equations referred to immediately above) and L can always be decomposed into 'symmetric' and 'antisymmetric' parts, $L = \frac{1}{2}(L+L^+)+\frac{1}{2}(L-L^+)$. Clearly there can only be energy growth if the right hand side of (7.4) is positive for at least one allowable $\hat{\mathbf{u}}$ (where 'allowable' is taken to mean a real incompressible velocity field which is twice-differentiable, satisfies the boundary conditions and has finite kinetic energy). Since $L + L^+$ is a self-adjoint (symmetric) operator, this can only happen if one of its eigenvalues is positive (recall all eigenvalues of a self-adjoint operator are real). If L is self-adjoint, then this is one and the same condition that the flow is linearly unstable so $R_E = R_L$. However, the weaker condition that L is normal is also sufficient. This is because if L has the (possibly complex) eigenvalue and eigenfunction pair $(\mu_i, \mathbf{v}_i)$ then L^+ has the equivalent pair $(\mu_i^*, \mathbf{v}_i)$ when L commutes with L^+. Then

$$\mathrm{eig}(\ \tfrac{1}{2}(L + L^+)\ ) = \Re e(\ \mathrm{eig}(L)\ ) \tag{7.5}$$

and so energy growth starts to occur precisely when an eigenvalue of L crosses into the right hand side of the complex plane. Hence

$$\text{Normality of } \ L \Rightarrow R_E = R_L \Rightarrow \text{supercriticality.} \tag{7.6}$$

The bifurcation at R_L has to be supercritical as the laminar state is the global attractor for $R < R_E$. The reverse direction is not valid, i.e. supercritically does *not* imply $R_E = R_L$ as we will see in the example of rotating plane Couette flow below.

A subcritical bifurcation at R_L implies $R_E < R_L$ and therefore the possibility of transient growth: for some (but not all) $\hat{\mathbf{u}}$, the perturbation energy will initially grow but ultimately decay for $R_E < R < R_L$. This means that an eigenvalue of $L + L^+$ must reach into the right hand side of the complex plane while no eigenvalue of L does so L has to be non-normal. In other words

$$\text{Non-Normality of } \ L \Leftarrow R_E < R_L \Leftarrow \text{subcriticality.} \tag{7.7}$$

The arrows cannot be reversed as non-normality does not imply $R_E < R_L$. It is theoretically possible (but presumably unusual) to have a non-normal operator where the largest eigenvalue of $(L + L^+)$ becomes positive precisely when the eigenvalue of largest real part for L crosses onto the right hand side of the complex plane. From a different perspective, non-normality of L implies that the eigenfunctions of L are non-orthogonal but this in itself is not sufficient to produce transient growth as the following example illustrates. Let $\mathbf{u} = \mathbf{v}e^{\lambda_1 t} + \mathbf{w}e^{\lambda_2 t}$ where λ_1 and λ_2 are negative and $\mathbf{v}.\mathbf{w} \neq 0$. If $\mathbf{v}^2 = c_1^2$, $\mathbf{w}^2 = c_2^2$, $\mathbf{v}.\mathbf{w} = \alpha c_1 c_2$ where $0 < \alpha^2 < 1$ and $\mathbf{c} = (c_1 \quad c_2)^T$, then

$$\frac{d\mathbf{u}^2}{dt}|_{t=0} = \mathbf{c}^T\mathbf{B}\mathbf{c} \quad \text{where} \quad \mathbf{B} := \begin{bmatrix} 2\lambda_1 & \alpha(\lambda_1+\lambda_2) \\ \alpha(\lambda_1+\lambda_2) & 2\lambda_2 \end{bmatrix}. \tag{7.8}$$

For no transient growth, $\mathbf{B}$ must be negative definite. Since $\mathbf{B}$ is symmetric this requires both of its eigenvalues to be negative which is the condition that $4\lambda_1\lambda_2 > \alpha^2(\lambda_1 + \lambda_2)^2$. This can always be achieved by choosing α small enough (thanks to Divakar Viswanath for this nice example).

So, in summary, if the linear operator is normal then $R_E = R_L$, otherwise the operator is non-normal which is a necessary but not sufficient condition for a subcritical bifurcation.

7.1.4 Transient growth

To illustrate the phenomenon of transient growth we consider a simple system of 2 ODEs given by

$$\frac{\mathrm{d}}{\mathrm{d}t}\begin{bmatrix} x(t) \\ \\ y(t) \end{bmatrix} = A\mathbf{x}(t) = \begin{bmatrix} -\dfrac{1}{Re} & 0 \\ 1 & -\dfrac{2}{Re} \end{bmatrix}\begin{bmatrix} x(t) \\ \\ y(t) \end{bmatrix} \tag{7.9}$$

where x represents rolls and y streaks (say). The operator A is non-normal since $AA^T \neq A^TA$ (transpose being the matrix equivalent of adjoint) and has eigenvalues $-1/Re$ and $-2/Re$. The initial rate of change of the 'energy' is

$$\frac{d}{dt}\mathbf{x}^2 = \mathbf{x}^T\left(A + A^T\right)\mathbf{x} \tag{7.10}$$

Since $A+A^T$ is symmetric, all that is needed to find initial growth is a positive eigenvalue and initial conditions with sufficient overlap with the corresponding eigendirection. The simple initial conditions $x(0) = y(0) = 1$ are adequate (providing $Re > 3$) since the solution,

$$\begin{bmatrix} x(t) \\ \\ y(t) \end{bmatrix} = \begin{bmatrix} 1 \\ \\ Re \end{bmatrix} e^{-t/Re} + \begin{bmatrix} 0 \\ \\ 1-Re \end{bmatrix} e^{-2t/Re} \sim \begin{bmatrix} 1 - \frac{t}{Re} + \mathcal{O}\left(\frac{t^2}{Re^2}\right) \\ 1 + \frac{Re-2}{Re}t + \mathcal{O}\left(\frac{t^2}{Re^2}\right) \end{bmatrix}, \tag{7.11}$$

has the initial energy behaviour

$$E(t) := \frac{1}{2}(x^2(t) + y^2(t)) = 1 + \frac{(Re-3)}{Re}t + \mathcal{O}\left(\frac{t^2}{Re^2}\right) \tag{7.12}$$

Although the rolls decay, there is enough initial growth in the streaks to give overall energy growth even though both eigenvalues of the system are negative.

7.2 Bifurcation Analysis

In wall-bounded shear flows, the linear operator is generically non-normal and therefore to understand the situation we need to find other nonlinear solutions which exist. There are a variety of methods that can be used, but the first (default) way is to use bifurcation analysis and nonlinear branch continuation techniques. Rotating plane Couette flow presents a beautifully accessible arena in which to illustrate this while also indicating how the first nonlinear solutions in plane Couette flow were found by Nagata [12]. The governing Navier-Stokes equations for an incompressible flow are

$$\frac{\partial \mathbf{u}_{\mathrm{tot}}}{\partial t} + 2\Omega\hat{\mathbf{z}} \times \mathbf{u}_{\mathrm{tot}} + \mathbf{u}_{\mathrm{tot}} \cdot \nabla \mathbf{u}_{\mathrm{tot}} + \nabla p = \frac{1}{Re}\nabla^2 \mathbf{u}_{\mathrm{tot}}, \tag{7.13}$$

$$\nabla \cdot \mathbf{u}_{\mathrm{tot}} = 0, \tag{7.14}$$

where $\mathbf{u}_{\mathrm{tot}}(x, \pm 1, z, t) = \pm\hat{\mathbf{x}}$ and $\mathbf{\Omega} = \Omega\hat{\mathbf{z}}$ is the spanwise rotation rate. As in §7.1.3, we define $\mathbf{u}_{\mathrm{tot}} = \mathbf{u}_{\mathrm{lam}} + \hat{\mathbf{u}}$, where $\hat{\mathbf{u}} := (\hat{u}, \hat{v}, \hat{w})$ is a (possibly large) perturbation to the laminar

base state $\mathbf{u}_{\rm lam} := y\hat{\mathbf{x}}$ so that the full perturbation equations are

$$\frac{\partial \hat{\mathbf{u}}}{\partial t} + 2\Omega\hat{\mathbf{z}} \times \hat{\mathbf{u}} + \mathbf{u}_{\rm lam} \cdot \nabla\hat{\mathbf{u}} + \hat{\mathbf{u}} \cdot \nabla\mathbf{u}_{\rm lam} + \hat{\mathbf{u}} \cdot \nabla\hat{\mathbf{u}} + \nabla\hat{p} = \frac{1}{Re}\nabla^2\hat{\mathbf{u}}, \tag{7.15}$$

$$\nabla \cdot \hat{\mathbf{u}} = 0, \tag{7.16}$$

where now $\hat{\mathbf{u}}(x, \pm 1, z, t) = \mathbf{0}$. Firstly, we compare the energy and linear stability thresholds for this problem.

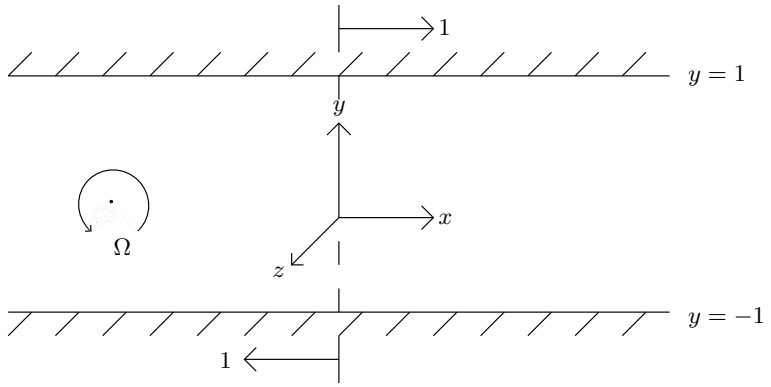

Figure 7.4: (Spanwise) Rotating Plane Couette flow

7.2.1 Energy stability

The energy equation is derived by taking the scalar product of $\hat{\mathbf{u}}$ with (7.15),

$$\begin{aligned}\langle \hat{\mathbf{u}} \cdot (7.15) \rangle = \frac{\partial}{\partial t}\langle \frac{1}{2}\hat{\mathbf{u}}^2 \rangle = &- \langle 2\Omega\hat{\mathbf{z}} \times \hat{\mathbf{u}} \cdot \hat{\mathbf{u}} \rangle - \langle \mathbf{u}_{\rm lam} \cdot \nabla \frac{1}{2}\hat{\mathbf{u}}^2 \rangle - \langle \hat{\mathbf{u}} \cdot \hat{\mathbf{u}} \cdot \nabla\hat{\mathbf{u}} \rangle \\ &- \langle \hat{\mathbf{u}} \cdot \nabla\mathbf{u}_{\rm lam} \cdot \hat{\mathbf{u}} \rangle - \langle \hat{\mathbf{u}} \cdot \nabla\hat{p} \rangle - \frac{1}{Re}\langle |\nabla\hat{\mathbf{u}}|^2 \rangle, \end{aligned} \tag{7.17}$$

(where

$$\langle (\ldots) \rangle := \int\int\int (\ldots) \mathrm{d}V = \lim_{L_x\to\infty} \lim_{L_z\to\infty} \frac{1}{4L_xL_z} \int_{-L_x}^{L_x} \int_{-L_z}^{L_z} \int_{-1}^{1} (\ldots) \mathrm{d}y\mathrm{d}z\mathrm{d}x \quad) \tag{7.18}$$

which simplifies to

$$\begin{aligned}\frac{\partial E}{\partial t} &= -\langle \hat{\mathbf{u}} \cdot \nabla\mathbf{u}_{\rm lam} \cdot \hat{\mathbf{u}} \rangle - \frac{1}{Re}\langle |\nabla\hat{\mathbf{u}}|^2 \rangle \\ &= \langle |\nabla\hat{\mathbf{u}}|^2 \rangle \left[-\frac{\langle \hat{\mathbf{u}} \cdot \nabla\mathbf{u}_{\rm lam} \cdot \hat{\mathbf{u}} \rangle}{\langle |\nabla\hat{\mathbf{u}}|^2 \rangle} - \frac{1}{Re} \right]. \end{aligned} \tag{7.19}$$

Hence, energy growth is possible only if $-\langle \hat{\mathbf{u}} \cdot \nabla\mathbf{u}_{\rm lam} \cdot \hat{\mathbf{u}} \rangle > \frac{1}{Re}\langle |\nabla\hat{\mathbf{u}}|^2 \rangle$ or, turning this around, there is a threshold Re_E defined as

$$\frac{1}{Re_E} \equiv \max_{\nabla.\hat{\mathbf{u}}=0, \hat{\mathbf{u}}(x,\pm1,z,t)=\mathbf{0}} \frac{-\langle \hat{\mathbf{u}} \cdot \nabla\mathbf{u}_{\rm lam} \cdot \hat{\mathbf{u}} \rangle}{\langle |\nabla\hat{\mathbf{u}}|^2 \rangle} \tag{7.20}$$

below which no energy growth is possible. After some manipulation, the eigenvalue problem for Re_E can be written as

$$\frac{1}{2}\left[\nabla \mathbf{u}_{\text{lam}} + (\nabla \mathbf{u}_{\text{lam}})^T\right] \cdot \hat{\mathbf{u}} + \nabla \hat{p} = \frac{1}{Re_E}\nabla^2 \hat{\mathbf{u}}, \tag{7.21}$$

which, since $\mathbf{u}_{\text{lam}} = y\hat{\mathbf{x}}$, simplifies to

$$\frac{1}{2}\begin{bmatrix}\hat{v}\\ \hat{u}\\ 0\end{bmatrix} + \nabla \hat{p} = \frac{1}{Re_E}\nabla^2 \hat{\mathbf{u}} \tag{7.22}$$

together with $\nabla.\hat{\mathbf{u}} = 0$ and $\hat{\mathbf{u}}(x, \pm 1, z) = \mathbf{0}$.

7.2.2 Linear stability

Linearising equation (7.15) gives

$$\frac{\partial \hat{\mathbf{u}}}{\partial t} + 2\Omega\hat{\mathbf{z}} \times \hat{\mathbf{u}} + \mathbf{u}_{\text{lam}} \cdot \nabla \hat{\mathbf{u}} + \hat{\mathbf{u}} \cdot \nabla \mathbf{u}_{\text{lam}} + \nabla \hat{p} = \frac{1}{Re}\nabla^2 \hat{\mathbf{u}}. \tag{7.23}$$

Assuming streamwise Taylor (2D) roll solutions of the form

$$\hat{\mathbf{u}}(\mathbf{x}, t) = \tilde{\mathbf{u}}(y)e^{ikz+\sigma t} \tag{7.24}$$

(known to be critical for the energy stability problem), (7.23) becomes

$$\sigma\tilde{\mathbf{u}} + \begin{bmatrix}(1-2\Omega)\tilde{v}\\ 2\Omega\tilde{u}\\ 0\end{bmatrix} + \nabla\tilde{p} = \frac{1}{Re}\nabla^2\tilde{\mathbf{u}}. \tag{7.25}$$

Comparing equation (7.25) to the energy stability equation (7.22) we see that when $\Omega = 1/4$, the operators from the energy and linear stability are identical providing $\sigma = 0$ also. This is a special case of a more general relationship between Re_E and Re_L which can be extracted by reducing (7.25) down to a problem in just $\tilde{v}$. Eliminating $\hat{w}$ using the incompressibility condition, $\hat{p}$ from $\hat{\mathbf{z}}.(7.25)$ and $\hat{u}$ from $\hat{\mathbf{x}}.(7.25)$ leaves

$$2Re^2\Omega(1-2\Omega)k^2\tilde{v} = -(D^2 - k^2 - \sigma Re)^2(D^2 - k^2)\tilde{v}, \tag{7.26}$$

to be solved subject to boundary conditions

$$\tilde{v} = D\tilde{v} = (D^2 - k^2 - \sigma Re)(D^2 - k^2)\tilde{v} = 0 \text{ at } y = \pm 1, \tag{7.27}$$

where $D := \mathrm{d}/\mathrm{d}y$. This system must be solved to find $Re_L = \min_k Re$ such that $\Re e(\sigma) = 0$. Conveniently, this can be done by comparing it to the Rayleigh-Bénard convection problem given by

$$k^2 Ra\,\tilde{w} = -(D^2 - k^2 - \sigma)^2(D^2 - k^2)\tilde{w} \tag{7.28}$$

with boundary conditions

$$\tilde{w} = D\tilde{w} = (D^2 - k^2 - \sigma)(D^2 - k^2)\tilde{w} = 0 \text{ at } y = \pm\frac{1}{2}, \tag{7.29}$$

where Ra is the Rayleigh number. This system has a well-known solution, with $\min_k Ra = 1708$ for $\sigma = 0$ and $k = 3.117$ (Drazin 2002, section 6.3 and the rigid-rigid case). Since the layer depth for Rayleigh-Bénard convection is standardly non-dimensionalised to be 1 whereas it is 2 here (e.g. compare positions of boundaries), the lengths in equations (7.26) and (7.27) need to be rescaled to make the connection exact. Letting $D^2 \to \frac{1}{4}D^2$, $k^2 \to \frac{1}{4}k^2$ and setting $\sigma = 0$ means the association

$$Re_L^2 = \frac{1708}{2^4[2\Omega(1-2\Omega)]} \tag{7.30}$$

can be made. The minimum of Re_L occurs when $\Omega = 1/4$ (as noticed above) where the linear operator is normal and so

$$\min_{k,\Omega} Re_L = 20.67 = Re_E. \tag{7.31}$$

More generally ($\Omega \neq 1/4$)

$$Re_L = \frac{Re_E}{\sqrt{8\Omega(1-2\Omega)}} \tag{7.32}$$

exceeds Re_E and the linear operator is non-normal. Notice also that $Re_L \to \infty$ for $\Omega \to 0$ and $1/2$. Beyond these values, there is no linear instability: the Rayleigh number in the analogous Rayleigh-Benard problem is then negative indicating that the stationary fluid is now hotter on its top surface than the bottom which is a very stable situation.

Figure 7.5 shows the bifurcation diagram for rotating plane Couette flow. The 2-dimensional steady solution surface emanating out of the bifurcation given by (7.32) is shown in blue. This is traced out by considering the velocity expansion

$$\begin{bmatrix} \mathbf{u}(y,z) \\ p(y,z) \end{bmatrix} = \sum_{l=-\infty}^{+\infty} \begin{bmatrix} \tilde{\mathbf{u}}_l(y) \\ \tilde{p}_l(y) \end{bmatrix} e^{ilkz} \tag{7.33}$$

truncated to some finite positive upper and negative lower values in l where k is the critical wavenumber (a weakly nonlinear solution would just have $l = 0, \pm 1, \pm 2$ only). The expansion functions $\tilde{\mathbf{u}}_l(y)$ and $\tilde{p}_l$ are typically themselves expanded in terms of basis functions in y so that the solution is represented by a doubly-indexed set of complex coefficients. Solutions are then found using root-finding algorithms invariably based upon the Newton-Raphson method. These 2D solutions become unstable to 3D steady disturbances (shown as a green curve). By tracing these solutions around in (Re, Ω) parameter space, Nagata [12] found that they pierced the $\Omega = 0$ plane for $Re \geq 125$ (later more accurately computed to be 127.7 [20]). These non-rotating steady 3D solutions (shown in red) were the first discovery of exact solutions to plane Couette flow beyond the simple constant shear state.

The rotating plane Couette system is also of interest in astrophysics for studying the fluid dynamics of accretion disks (e.g. [16]). A disk with an angular velocity profile of $\Omega^* \sim R^{-q}$ and a thin distant radial strip $R \in [R-1, R+1]$ (with $1 \ll R$) looks locally like rotating PCF with

$$\Omega = \frac{1}{q} \tag{7.34}$$

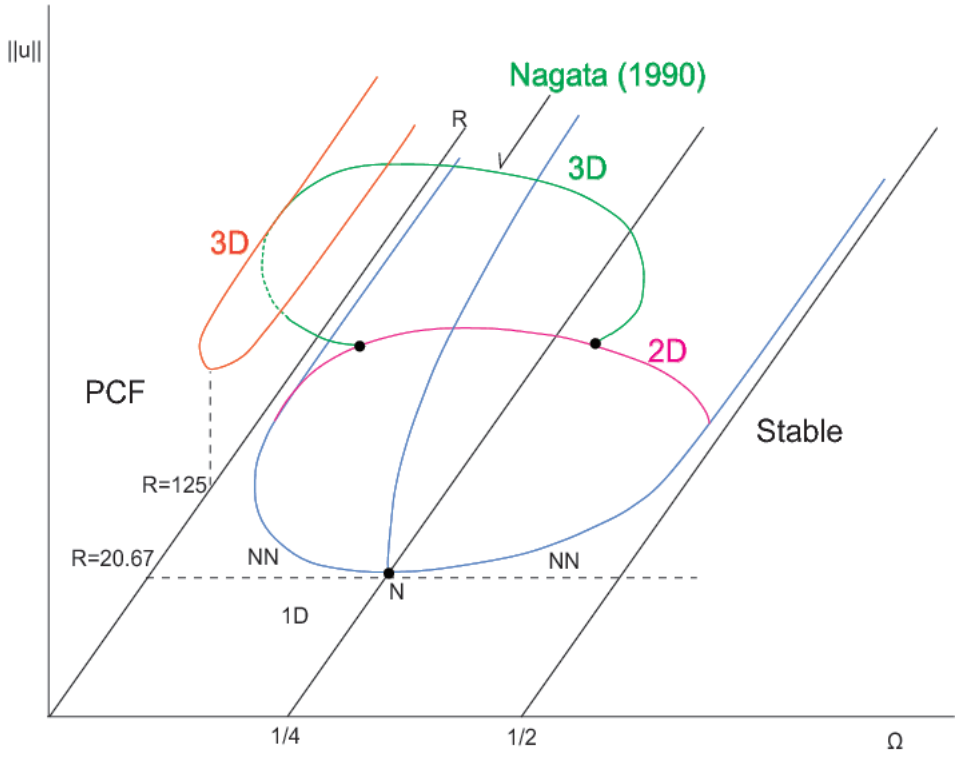

Figure 7.5: Bifurcation diagram for rotating plane Couette flow.

(relative to a non-dimensionalised shear of 1 across the domain as above). The astrophysical interest is in understanding what hydrodynamic processes can operate in a Keplerian disc which has $\Omega^* \sim R^{-3/2}$ or $\Omega = 2/3$ so as to enhance dissipative processes (see [2] for an introduction to the issues). However, the Rayleigh [10] (axisymmetric) stability criterion predicts that profiles with angular momentum increasing radially outwards i.e. $d(R^2\Omega^*)/dR > 0$ or $\Omega > 1/2$ are stable. This does not preclude non-axisymmetric (streamwise-dependent) instabilities or the existence of disconnected nonlinear solutions as in the plane Couette problem but these have yet to be found (e.g. [7, 16, 14] and [3] for a recent commentary).

Bibliography

[1] C. D. Anderek, S. S. Liu, and H. L. Swinney, *Flow regimes in a circular Couette system with independently rotating cylinders*, J. Fluid Mech., 164 (1986), pp. 155–183.

[2] S. A. Balbus, *Spinning discs in the lab*, Nature, 444 (2006), pp. 281–282.

[3] ——, *A turbulent matter*, Nature, 470 (2011), pp. 475–476.

[4] F. H. Busse, *Bounds on the transport of mass and momentum by turbulent flow between parallel plates*, Z. Angew. Math. Phys., 20 (1969), pp. 1–14.

[5] O. Dauchot and F. Daviaud, *Finite-amplitude perturbation and spots growth-mechanism in plane Couette flow*, Phys. Fluids, 7 (1995), pp. 335–343.

[6] P. G. Drazin, *Introduction to Hydrodynamic Stability*, Cambridge University Press, second ed., 2002.

[7] H. Ji, M. Burin, E. Schartman, and J. Goodman, *Hydrodynamic turbulence cannot transport angular momentum effectively in astrophysical disks*, Nature, 444 (2006), pp. 343–346.

[8] D. Joseph, *Nonlinear stability of the Boussinesq equations by the method of energy*, Arch. Rat. Mech. Anal., 22 (1966), pp. 163–184.

[9] D. D. Joseph and S. Carmi, *Stability of Poiseuille flow in pipes, annuli and channels*, Quart. Appl. Math., 26 (1969), pp. 575–599.

[10] Lord Rayleigh, *On the dynamics of revolving fluids*, Proc. R. Soc. Lond. A, 93 (1917), pp. 148–154.

[11] T. Mullin, *Experimental studies of transition to turbulence in a pipe*, Ann. Rev. Fluid Mech., 43 (2011), pp. 1–24.

[12] M. Nagata, *Three-dimensional finite-amplitude solutions in plane Couette flow: bifurcation from infinity*, J. Fluid Mech., 217 (1990), pp. 519–527.

[13] S. A. Orszag, *Accurate solution of the Orr-Sommerfeld stability equation*, J . Fluid Mech., 50 (1971), pp. 659–703.

[14] M. S. Paoletti and D. P. Lathrop, *Angular momentum transport in turbulent flow between independently rotating cylinders*, Phys. Rev. Lett., 106 (2011), p. 024501.

[15] C. C. T. Pringle and R. R. Kerswell, *Asymmetric, helical and mirror-symmetric travelling waves in pipe flow*, Phys. Rev. Lett., 99 (2007), p. 074502.

[16] F. Rincon, G. I. Ogilvie, and C. Cossu, *On the self-sustaining processes in Rayleigh-stable rotating plane Couette flows and subcritical transition to turbulence in accretion disks*, Astron. & Astrophys., 463 (2007), pp. 817–832.

[17] V. A. Romanov, *Stability of plane Couette flow*, Funkcional Anal. i Prolozen, 7 (1973).

[18] B. L. Rozhdestvensky and I. N. Simakin, *Secondary flows in a plane channel: their relationship and comparison with turbulent flows*, J. Fluid Mech., 147 (1984), pp. 261–289.

[19] P. J. Schmid and D. S. Henningson, *Stability and Transition in Shear Flows*, Springer, first ed., 2001.

[20] F. Waleffe, *Homotopy of exact coherent structures in plane shear flows*, Phys. Fluids, 15 (2003), pp. 1–18.

Lecture 8

Edge Tracking – Walking the Tightrope

In the subcritical transition scenario, there is typically a regime where the linearly stable basic state coexists with the turbulent state. The simplest model of this is a 1D system $\dot{y} = y(\frac{1}{2} - y)(y - 1)$ where the basic state is $y = 0$, the 'turbulent' state is $y = 1$ and there is an intermediate state $y = \frac{1}{2}$ which separates initial conditions which become turbulent (if $y(0) > \frac{1}{2}$ then $y(t) \to 1$ as $t \to \infty$) from those which laminarise (if $y(0) < \frac{1}{2}$ then $y \to 0$ as $t \to \infty$). The state $y = \frac{1}{2}$ is special in that it separates these two different types of behaviour and corresponds to neither (if $y(0) = 1/2$, $y(t) = 1/2 \; \forall t$). Identifying initial conditions which lead to this intermediate behaviour is crucial for understanding transition. An extra dimension is needed in our model to allow this intermediate behaviour to be non-trivial so consider the 2D system

$$\begin{aligned} \dot{x} &= -x + 10y, \\ \dot{y} &= y(10\mathrm{e}^{-0.01x^2} - y)\,(y - 1)\,, \end{aligned} \tag{8.1}$$

which, like the 1D model, has two stable equilibria and an unstable state. The line $y = 1$ separates initial conditions which will laminarise to $(0, 0)$ and those which become 'turbulent', that is, spiral into the fixed point at $\approx (14, 1.4)$: see figure 1. All points on $y = 1$ – here the basin boundary for the laminar and turbulent states or more generally called the 'edge' – are attracted to the relative attractor at $(10, 1)$ which is called the 'edge state' (this is a saddle point in 2D but an attractor for trajectories confined to the 1D edge). This lecture is about recent successes in identifying the edge state in realistic flows whereas the next will be concerned with identifying the closest point of approach of the edge to the laminar state[1].

8.1 Approach

The approach to finding the edge goes back to [17] (at least in fluid mechanics) and is based on simple bisection combined with direct numerical simulation (DNS). A turbulent velocity

[1] This will indicate the initial conditions of least energy which can trigger turbulence - if this distance is defined as $\sqrt{x^2 + y^2}$ and energy as $x^2 + y^2$, this would be the point $(0, 1)$ here.

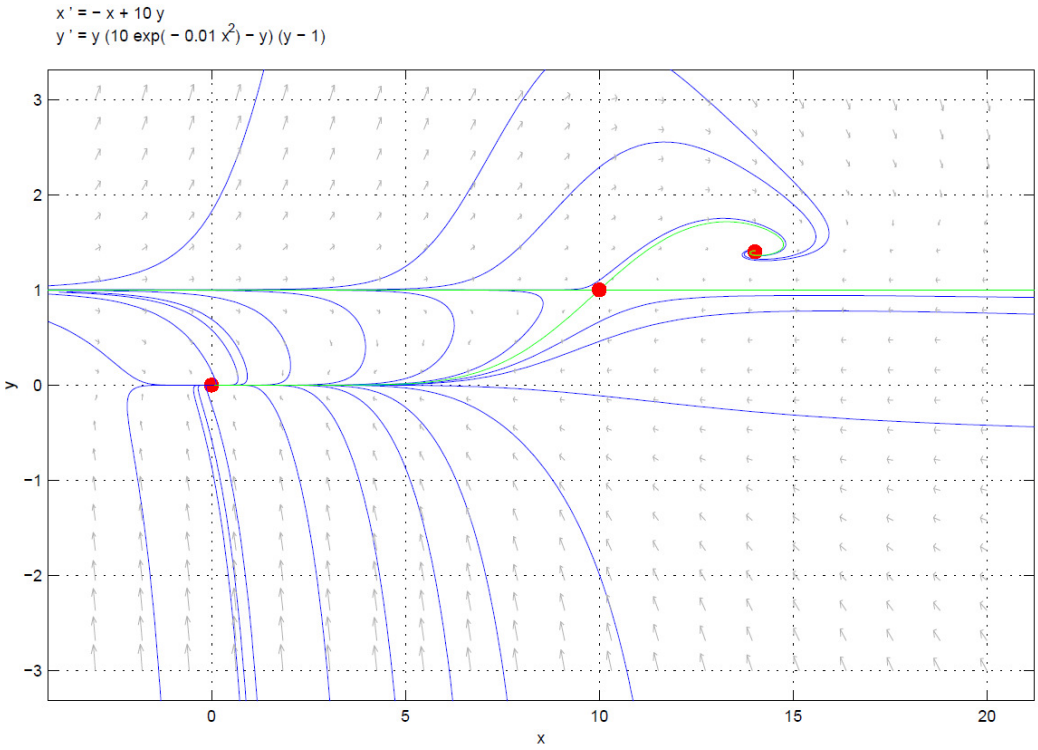

Figure 8.1: Phase plane of the 2D system (8.1) created using the free Matlab macro pplane6.m written by John Polking, Rice University, 1995. The laminar state is at $(0, 0)$, the edge state at $(10, 1)$ and the 'turbulent' state at $\approx (14, 1.4)$. The edge is the line $y = 1$.

field $\mathbf{u}_{turb}(\mathbf{x})$ generated by DNS is the starting point and is decomposed into a 2D part and a 3D part. Importantly, this 2D part is known in practice not to be able to initiate 3D turbulent state in plane Couette or pipe flow. In pipe flow, either azimuthally averaging or axial averaging can be used, i.e.

$$u_{2D} = \begin{cases} \frac{1}{2\pi} \int_0^{2\pi} u(r,\theta,z)\mathrm{d}\theta \\ \frac{1}{L} \int_0^{L} u(r,\theta,z)\mathrm{d}z \end{cases} \tag{8.2}$$

and then

$$\mathbf{u}_{3D}(\mathbf{x}) := \mathbf{u}_{turb}(\mathbf{x}) - \mathbf{u}_{2D}. \tag{8.3}$$

The key point is that these two velocity fields can be used to reconstruct an initial condition as follows

$$\mathbf{u}(\mathbf{x}, 0; \lambda) := \mathbf{u}_{2D} + \lambda \mathbf{u}_{3D}(\mathbf{x}) \tag{8.4}$$

where $\lambda \in [0, 1]$ is a free mixing ratio. $\mathbf{u}(\mathbf{x}, 0; 1) = \mathbf{u}_{turb}$ so that the DNS code will continue to follow the turbulent attractor whereas $\mathbf{u}(\mathbf{x}, 0; 0) = \mathbf{u}_{2D}$ and the flow must subsequently relaminarise. Given these contrasting behaviours, there must be (at least) one intermediate value λ^* where the flow neither becomes turbulent nor relaminarises. At this value $\mathbf{u}(\mathbf{x}, 0; \lambda^*)$ must be precisely on the edge and the flow has to subsequently walk the tightrope of the edge neither converging back to the laminar state nor swinging up to the turbulent state. The approach to finding λ^* is to successively bisect the n^{th} interval $[\lambda_l^n, \lambda_u^n]$ where λ_l causes relaminarisation and λ_u leads to turbulence. This requires initialising a DNS using $\mathbf{u}(\mathbf{x}, 0; \frac{1}{2}(\lambda_l + \lambda_u))$ and having some criterion for deciding if the flow is starting to relaminarise or become turbulent (obviously the quicker this decision is made, the faster the bisection technique). Typically, λ^* must be known to *considerable* accuracy to be able to track the edge for any length of time because of the edge's inherent instability. To illustrate this, let μ be the Lyapunov exponent which describes the rate at which trajectories diverge from the edge. Then if $|\lambda_u^n - \lambda_l^n| \leq 10^{-14}$ (e.g. double precision accuracy in Fortran), one could anticipate being able to shadow the edge for a time T where

$$e^{\mu T} \times 10^{-14} \lesssim 1. \tag{8.5}$$

Typically, for pipe flow at $Re = O(2500)$, $UT/D \approx 200 - 300$ (D pipe diameter and U bulk velocity along the pipe). Once λ^* has been found to this accuracy, the bisection approach can be restarted a little back from T, say $0.9T$, using the velocity fields $\mathbf{u}(\mathbf{x}, 0.9T; \lambda_l)$ and $\mathbf{u}(\mathbf{x}, 0.9T; \lambda_u)$ so that both velocity fields are still very similar albeit on different 'sides' of the edge. In this way a long-time edge-shadowing trajectory can be generated by piecing together different tracking sections. The edge-tracking technique relies on two ingredients for success.

1. The ability to quickly distinguish between two (and only two) different evolutions. A clear energy level separation between the turbulent state and the edge is usually sufficient.

2. The fact that the edge is a hypersurface and so can be reached by adjusting one parameter (or alternatively, there is only one unstable direction across the edge).

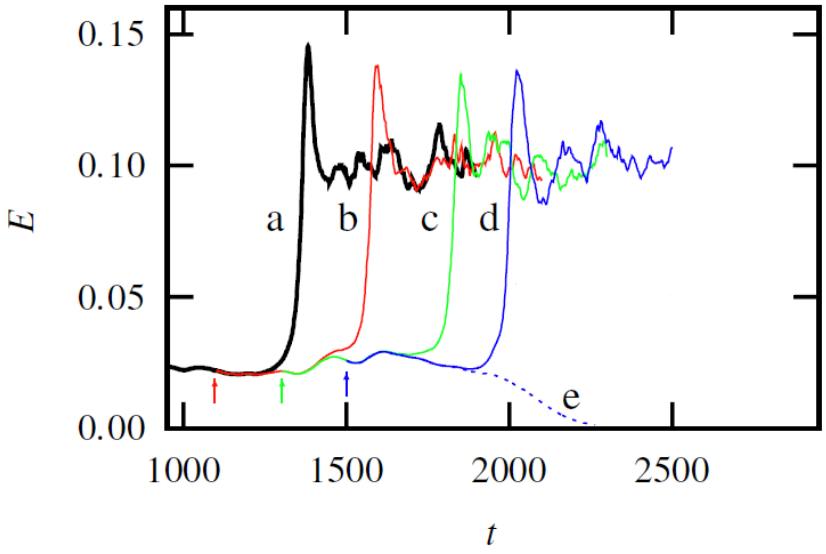

Figure 8.2: Perturbation energy traces of trajectories bounding the edge of chaos from [12]. Re=2875 and the pipe is $5\,D$ long.

It's worth remarking here that this bisection approach can identify more general hypersurfaces in phase space than basin boundaries since only different *initial* behaviours are needed. Whether the turbulent state is sustained or not is irrelevant for the mechanics of the procedure although this does, of course, influence the interpretation of the edge.

8.2 First Calculations

Following Toh & Itano's [17] first calculations, Skufca, Yorke & Eckhardt [16] treated a low-dimensional model of shear flow and then the first edge-tracking calculation in pipe flow was carried out in [12]. Figure 2 shows one of their edge trackings in a $5\,D$ pipe at $Re = 2875$. The first thing to notice is the characteristic way the trajectories leave the edge to swing up in energy to the turbulent state. The trajectory (d) and the relaminarising trajectory (e) both provide a good approximation to the edge dynamics until about $t \approx 1800$ when they start to separate. If the edge is followed for longer, chaotic dynamics are obtained as the 'edge state' (the limiting set). Interestingly, a time-average of the velocity field (see figure 3) over this attractor reveals a coherent large scale structure where streamwise rolls and streaks combine in a familiar way [4, 20]. A very similar-looking travelling wave (TW) was found soon afterwards [9] prompting the conclusion that this TW must be embedded in the edge state. The fact that some TWs could be part of the edge was an idea already gaining momentum [5, 19]. Figure 4 shows the effect of perturbing a typical lower branch TW along its most unstable direction (from [5], 'lower branch' meaning closer to the laminar state than the 'upper branch' in any sensible measure such as energy or dissipation). Depending on the sign of the perturbation, the evolution can either lead to the turbulent state (solid green line) or the laminar state (dashed green line). Hence this TW must be on the edge. Contrast

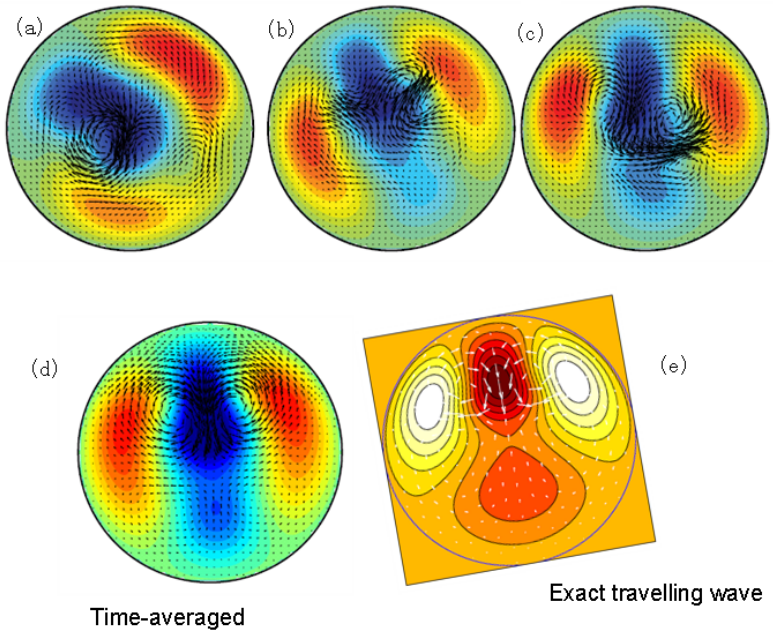

Figure 8.3: Edge trajectory snapshots, their time-average and an exact travelling wave calculated in [9].

this situation with perturbing an upper branch TW (figure 5) where the subsequent flow is turbulent whichever way the perturbation is applied. The consensus now is that the edge is made up of (at least) the union of all the stable manifolds of the lower branch TWs.

8.3 Developments

The significance of the edge state is that initial conditions which are just able to trigger transition should follow the edge, reach the edge state and then be ejected along its unstable manifold to the turbulent state. Hence, in some sense, it is an organising centre for transition (see [3] for a discussion). From another perspective, the edge-tracking technique can be viewed as a powerful new approach to finding nonlinear solutions of the Navier-Stokes equations. The edge state can change depending on the flow geometry (e.g. length of pipe), Re and the symmetries imposed on the flow (see examples below). Starting conditions for the tracking will also be important if the edge state is not the unique attractor on the edge. All of these aspects of the procedure have been explored and will now be briefly described.

8.3.1 Varying Re

Schneider & Eckhardt [11] examined how the typical edge state energy varies compared to the turbulent state for $Re \in [2000, 4000]$ in their $5\,D$ pipe. Figure 6 makes it clear that the separation of the edge and turbulence increases with Re. However, over this range of Re, the edge state remains chaotic (see [3] for even higher Re).

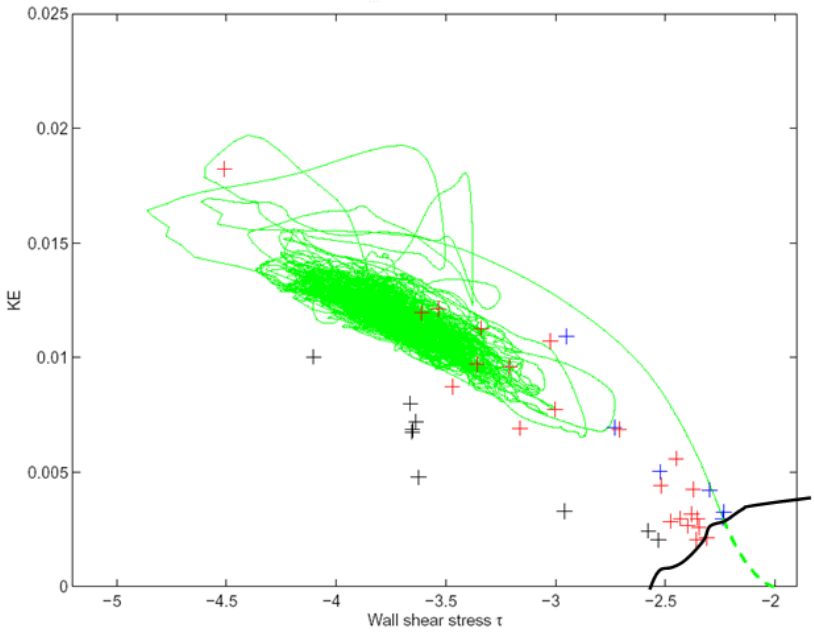

Figure 8.4: The disturbed kinetic energy per unit mass versus wall shear stress τ for a lower branch TW. The subsequent flow either becomes turbulent (solid green line) or tamely relaminarises (dashed green line). All the TWs known in 2007 to fit into a $5\,D$ pipe are plotted: 2-fold rotationally symmetric TWs(blue), 3-fold TWs(red) and 4-fold TWs(black). The non-smooth bold black separating line is supposed to indicate the edge. For details see [5].

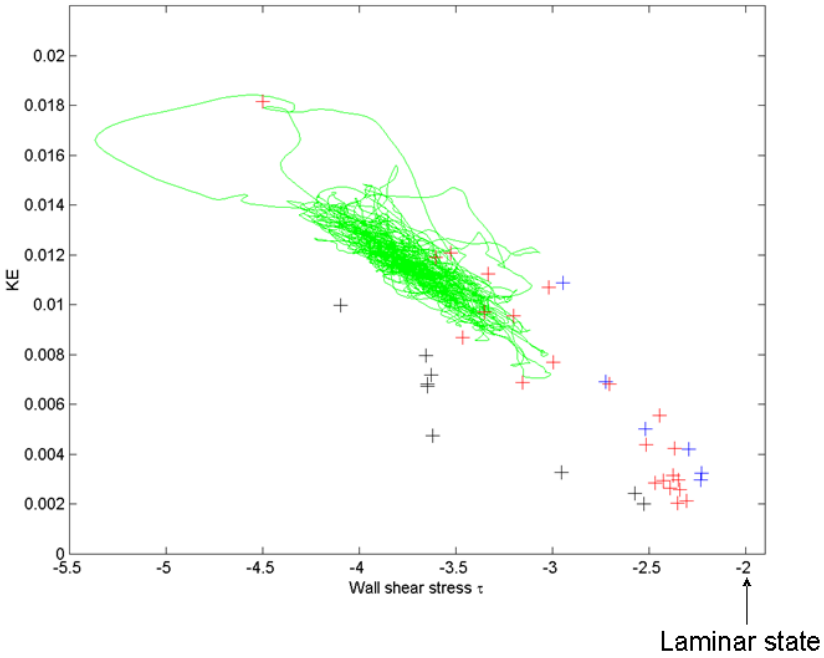

Figure 8.5: The disturbed kinetic energy per unit mass versus wall shear stress τ for a typical upper branch TW [5].

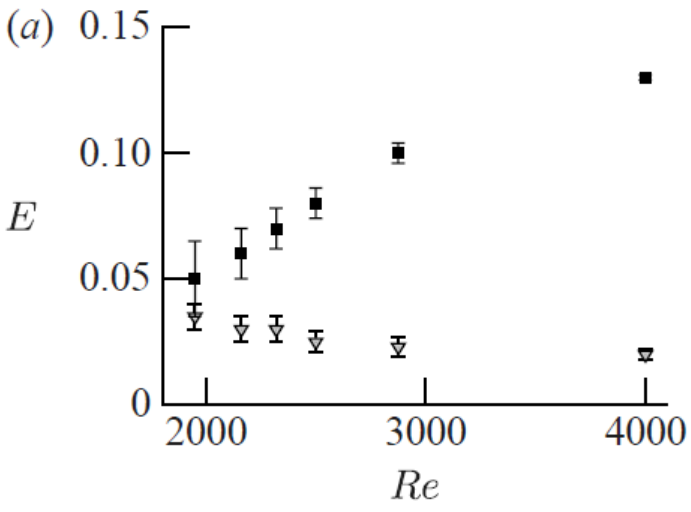

Figure 8.6: Typical energy of the edge trajectory (down triangles) and turbulence (black boxes) as a function of Re for a $5\,D$ pipe from [11].

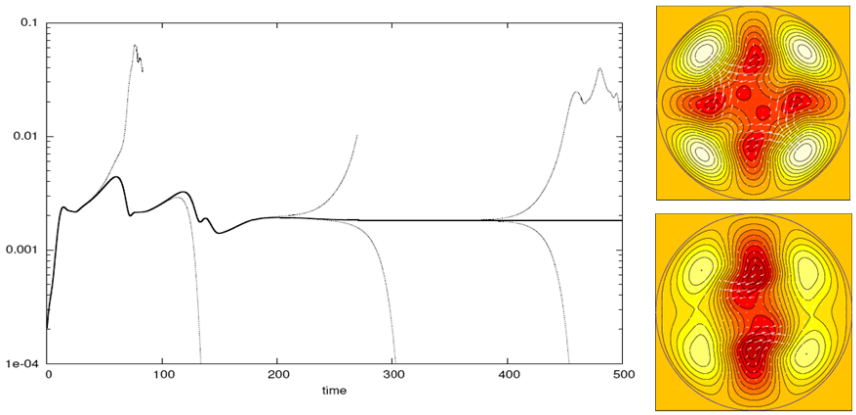

Figure 8.7: Energy contained in the axially dependent flow. The thick line indicates the edge trajectory and the thinner lines nearby trajectories which either relaminarize (energy decrease) or become turbulent (energy increases to a higher level). Pipe length is $2.5\,D$, $Re = 2400$ and the flow is calculated within the R_2-subspace [2]. The two cross-sections on the right indicate (at least) two travelling waves which are stable on the edge (the upper one corresponds to the trace on the left at large times).

8.3.2 Geometry and use of Invariant Subspaces

Duguet, Willis & Kerswell [2] looked at the edge state in a $2.5\,D$ pipe imposing R_2 symmetry (the flow is symmetric under a π rotation about its axis) at $Re = 2400$. The plot of E_{3d} (energy in the streamwise-dependent part of the flow) as a function of time is shown in figure 7. The edge energy is seen to quickly level off indicating an edge state with *constant* E_{3d} which corresponds to a TW solution (labelled $C3\_1.25$ in [2] and later renamed $N2$ in [10]). This finding was significant in two ways. It was the first identification of a TW using this technique (see also [13] who found a steady state in small geometry plane Couette flow at about the same time) but it was not the expected TW. Calculations in [5] had identified that a lower branch TW (in their nomenclature $2b\_1.25$, now known as $S2$) only had one unstable direction indicating that this would be a relative attractor in the edge. However, the TW found possessed an additional mirror symmetry never seen before. Thus it was the first demonstration of multiple edge states. Secondly, the realisation that such 'highly symmetric' TWs could exist led to whole new families of TWs being quickly discovered thereafter [10]. As Re increases, these waves turn out to appear *before* the original less-symmetric TWs found in [4, 20]. Plausibly, these latter waves arise from the former in symmetry-breaking bifurcations ([10] shows an example of this - S3 bifurcating off N3 - in their figure 8).

Duguet, Willis & Kerswell [2] also noticed that the edge trajectory in the $5\,D$ case at $Re = 2875$ occasionally dipped to low energy values and smoothened locally (see Figure 8 for an example). They realised that the flows at these local energy minima turn out to be very close to other (lower branch) TWs embedded in the edge but these are now saddles there rather than relative attractors. This clearly reinforces the picture of lower branch TWs embedded in the edge. The picture is then of the edge trajectory transiently visiting the neighbourhood of these (saddle) TWs before ultimately reaching an edge state (see

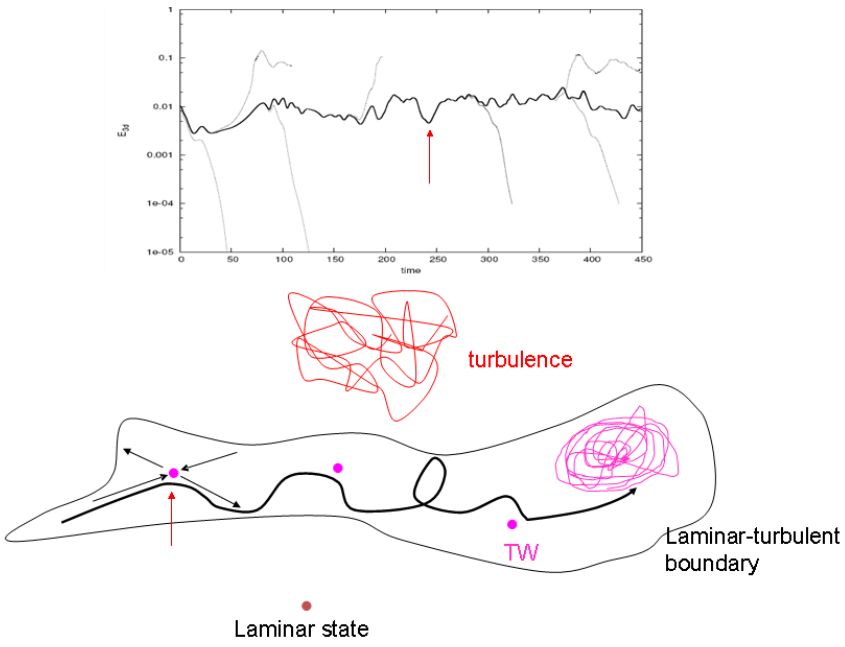

Figure 8.8: **Upper:** energy contained in the axially dependent modes on the edge for 5D pipe at $R_e = 2875$. The thick line indicates the edge trajectory. **Lower:** Schematic view of phase space. The surface separates initial conditions which relaminarize from those which become turbulent. An edge trajectory visiting three pink states is shown schematically [2].

Figure 8).

8.3.3 Larger Geometries

The bisection technique also works in larger geometries where the edge state turns out to be localised. This was first seen in the '$2 + \epsilon$' dimensional model of pipe flow [21] and then in fully 3 dimensional pipe flow [8]: see Figure 9. In both these cases, only spatiotemporally chaotic edge states are found. In plane Couette flow, however, spanwise-localised equilibrium and travelling wave solutions were found [15] in short (streamwise) and wide (spanwise) domains. These spanwise-localised solutions were later found to bifurcate off the spanwise-periodic solutions already known [14] suggesting that all strictly periodic solutions could have connected localised versions too (see the talk by Tobias Schneider in this volume). Opening up the flow even further by considerably lengthening the domain leads to an edge state also localised in the streamwise direction, albeit now chaotic [1, 15]. Intriguingly, this edge state resembles a turbulent spot (although the energies are lower) and highlights the large size of domains needed to see streamwise localisation. Figure 10 illustrates this latter point by comparing the small plane Couette flow domain originally used for edge-tracking [13] ($4\pi \times 2 \times 2\pi$ being the streamwise, cross-stream and spanwise dimensions respectively) with the short, wide domain ($4\pi \times 2 \times 8\pi$) and long, wide domain ($64\pi \times 2 \times 16\pi$) of [15]. It is currently an outstanding question as to whether fully localised equilibrium or TW solutions exist in wall-bounded shear flows.

There are still many issues surrounding the edge and efforts have started in very low

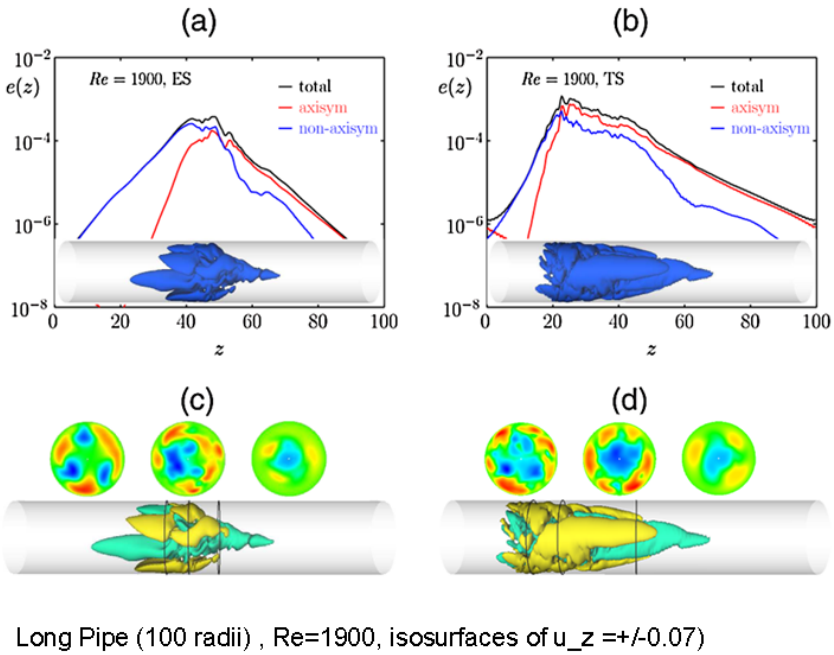

Figure 8.9: Localized edge state (ES) and turbulent state (TS) at $R_e = 1900$. Energy distribution of (a) the localized edge state and (b) a turbulent state. (c) and (d) show cross-sectional distributions of isosurfaces of the edge state and the turbulent state respectively, from [8].

dimensional models to unravel these [6, 7, 18].

Summary

- Edge tracking is possible if there are two different types of behaviour (which can easily be discerned). The subcritical scenario is ideal as the laminar and turbulent states co-exist. If these two states are locally stable, the edge represents the laminar-turbulent boundary. If they are not, then the edge is a hypersurface which divides initial conditions which experience different initial behaviour only.
- Edge tracking can find exact solutions if they are relative attractors on the edge or even if they are saddle points on the edge (with luck).
- Edge states act as organising centres for transitional flows.
- Edge states vary with Re, geometry of the flow and what symmetries are imposed.
- Edge tracking just needs a DNS code and patience.

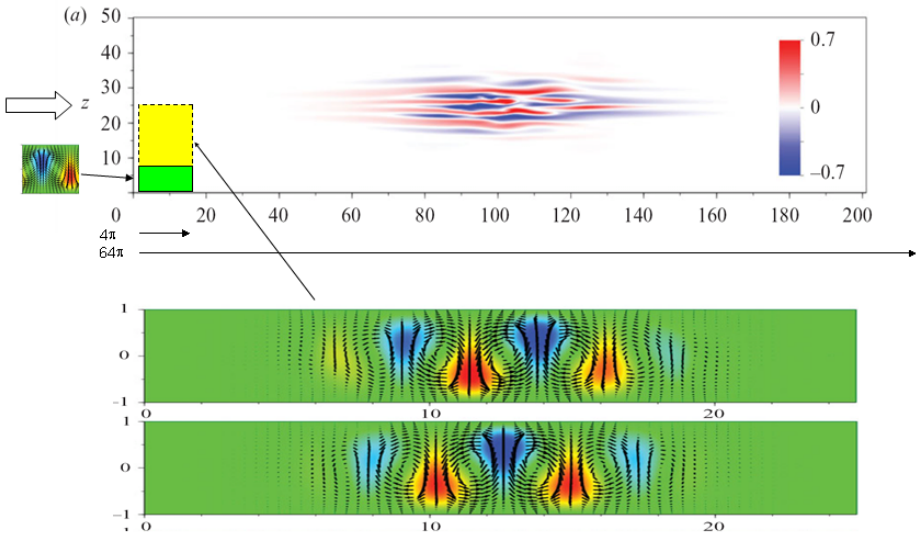

Figure 8.10: The small domain of [13] in which the edge state is a steady global state is shown as the lower left green rectangle (flow is left to right). The short wide box of [15] is shown as the lower left yellow rectangle (4 times wider than the green rectangle) with both dwarfed by the 16 times longer, wide box which captures a fully localised edge state. Underneath are shown the spanwise localised states found by edge tracking in the short wide box.

Bibliography

[1] Y. Duguet, P. Schlatter & D.S. Henningson, Localised edge states in plane Couette flow, Phys. Fluids, 21, 111701, 2009.

[2] Y. Duguet, A.P. Willis & R.R. Kerswell, Transition in pipe flow: the saddle structure on the boundary of turbulence, J. Fluid Mech., 613, 255-274, 2008.

[3] Y. Duguet, A.P. Willis & R.R. Kerswell, Slug genesis in cylindrical pipe flow, J. Fluid Mech., 663, 180–208, 2010.

[4] H. Faisst & B. Eckhardt, Traveling waves in pipe flow, Phys. Rev. Lett., 91, 224502, 2003.

[5] R.R. Kerswell & O.R. Tutty, Recurrence of travelling waves in transitional pipe flow, J. Fluid Mech., 584, 2007.

[6] N. Lebovitz, Shear-flow transition: the basin boundary, Nonlinearity 22, 2645-2655, 2009

[7] N. Lebovitz, Boundary collapse in models of shear-flow transition, Commun. Nonlin. Sci. Num. Sim *in press* 2011

[8] F. Mellibovsky, A. Meseguer, T.M. Schneider & B. Eckhardt, Transition in localized pipe flow turbulence, Phys. Rev. Lett., 103(5), 2009.

[9] C.C.T. Pringle & R.R. Kerswell, Asymmetric, helical, and mirror-symmetric traveling waves in pipe flow, Phys. Rev. Lett., 99(7), 2007.

[10] C.C.T. Pringle, Duguet, Y. & R.R. Kerswell, Highly symmetric travelling waves in pipe flow Phil. Trans. Roy. Soc. A, 367, 457-472, 2009.

[11] T.M. Schneider & B. Eckhardt, Edge states intermediate between laminar and turbulent dynamics in pipe flow, Phil. Trans. R. Soc. A, 367, 577-587, 2009.

[12] T.M. Schneider, B. Eckhardt & J.A. Yorke, Turbulence transition and the edge of chaos in pipe flow, Phys. Rev. Lett., 99(3), 2007.

[13] T.M. Schneider, J.F. Gibson, M. Lagha, F. De Lillo & B.Eckhardt, Laminar-turbulent boundary in plane Couette flow, Phys. Rev. E, 78(3), 2008.

[14] T.M. Schneider, J.F. Gibson & J. Burke, Snakes and ladders: localised solutions of plane Couette flow, Phys. Rev. Lett., 104, 104501, 2010.

[15] T.M. Schneider, D. Marinc & B. Eckhardt, Localized edge states nucleate turbulence in extended plane Couette cells, J. Fluid Mech., 646, 441-451, 2010.

[16] J.D. Skufca, J.A. Yorke & B. Eckhardt, Edge of chaos in a parallel shear flow, Phys. Rev. Lett., 96, 174101, 2006.

[17] S. Toh & T. Itano, Low-dimensional dynamics embedded in a plane Poiseuille flow turbulence: Traveling-wave solution is a saddle point?, ArXiv:physics/9905012, 1999.

[18] J. Vollmer, T.M. Schneider & B. Eckhardt, Basin boundary, edge of chaos and edge state in a two-dimensional model, New J. Phys. 11, 013040, 2009.

[19] J. Wang, J.F. Gibson & F. Waleffe Lower branch coherent states in shear flow: transition and control Phys. Rev. Lett., 98, 204501, 2007.

[20] H. Wedin & R.R. Kerswell, Exact coherent structures in pipe flow: travelling wave solutions, J. Fluid Mech., 508, 333–371, 2004.

[21] A.P. Willis & R.R. Kerswell, Turbulent dynamics of pipe flow captured in a reduced model: puff relaminarisation and localised 'edge' states, J. Fluid Mech., 619, 213-233, 2009.

Lecture 9

Triggering Transition: Towards Minimal Seeds

9.1 Introduction

In the previous lecture we discussed the edge and tracking it *forward* in time to a relative attractor - the edge state. This always seems to be on an energy plateau compared with other points and it is natural to ask what is the lowest energy attained by the edge. The initial condition corresponding to this point - the *minimal seed* - infinitesimally disturbed represents the easiest way (energetically) to trigger turbulence. In this lecture, we discuss a method of finding the minimal seed which, in some sense, manages to integrate *backwards* in time along the edge.

Some evidence that there is a disparity in energies on the edge was supplied recently by Viswanath and Cvitanović [13] who looked at shooting for the edge state in a short pipe of length πD (D is the pipe diameter). They took a combination of only three flow fields as an initial condition and searched for the lowest initial energy for which the ensuing flow would approach a particular travelling wave solution some time later. This travelling wave was chosen as the target since it is known to be embedded in the chaotic edge state in a $5D$ pipe [7]. They chose one of the initial flow fields as the travelling wave solution itself and the other two to be its two unstable eigenmodes, and found that the maximum growth ratio of the energy was $O(10^4)$ (see also [4]). Thus some regions of the edge have a much smaller energy level than the attracting plateau where the edge state resides. This suggests a strategy to identify the minimal seed which involves looking for the initial condition which experiences the largest energy growth. A brute force search over all possible initial conditions is not feasible but a variational approach is.

We define the growth of the energy at time T by the gain

$$G(T) := \max_{\mathbf{u}_0(\mathbf{x}),\ \nabla\cdot\mathbf{u}_0=0} \frac{\left\langle \frac{1}{2}|\mathbf{u}(\mathbf{x},T)|^2 \right\rangle}{\left\langle \frac{1}{2}|\mathbf{u}_0(\mathbf{x})|^2 \right\rangle}, \tag{9.1}$$

where $\mathbf{u}_0(\mathbf{x}) = \mathbf{u}(\mathbf{x}, t=0)$ and $\langle\cdot\rangle$ means the volume integration $\int \cdot\, dV$. It is this function

$G(T)$ that we want to maximise to find the minimal seed. We briefly discuss the matrix-based and a matrix-free variational methods to find the minimal seed of the linearised Navier-Stokes equations. Then we extend the matrix-free approach to investigate the fully nonlinear transient energy growth problem [8],[9].

9.2 Linear transient energy growth (non-modal analysis)

The non-dimensionalized linearized Navier-Stokes equation around the laminar flow $\mathbf{u}_{\text{lam}}$ is

$$\frac{\partial \mathbf{u}}{\partial t} + (\mathbf{u}_{\text{lam}} \cdot \nabla)\mathbf{u} + (\mathbf{u} \cdot \nabla)\mathbf{u}_{\text{lam}} + \nabla p = \frac{1}{Re}\nabla^2 \mathbf{u}, \tag{9.2}$$

where $\mathbf{u}$ is the perturbation of the laminar flow $\mathbf{u}_{lam}$ and Re is the Reynolds number. As normal we assume that the fluid is incompressible, $\nabla \cdot \mathbf{u} = 0$.

9.2.1 Matrix-based method

We can rewrite the linearized Navier-Stokes equation (9.2) in the form

$$\frac{\partial \mathbf{u}}{\partial t} = L\mathbf{u}, \tag{9.3}$$

where L is a linear operator, which has eigenvalues λ_j and eigenfunctions $\mathbf{q}_j$. Assuming that the set $\mathbf{q}_j$ is complete (but not necessarily orthogonal unless L is normal), then

$$\mathbf{u}_0(\mathbf{x}) = \sum_{j=1}^{\infty} a_j(0)\mathbf{q}_j(\mathbf{x}) \quad \Rightarrow \quad \mathbf{u}(\mathbf{x},t) = \sum_{j=1}^{\infty} a_j(t)\mathbf{q}_j(\mathbf{x}) \tag{9.4}$$

where $a_j(t) := a_j(0)\exp(\lambda_j t)$. Then

$$G(T;Re) = \max_{\mathbf{a(0)}} \frac{\langle\, \mathbf{u}^* \,.\, \mathbf{u} \,\rangle}{\langle\, \mathbf{u}_0^* \,.\, \mathbf{u}_0 \,\rangle} = \max_{\mathbf{a(0)}} \frac{\sum_i \sum_j a_i^*(T) a_j(T) \langle\, \mathbf{q}_i^* . \mathbf{q}_j \,\rangle}{\sum_i \sum_j a_i^*(0) a_j(0) \langle\, \mathbf{q}_i^* . \mathbf{q}_j \,\rangle}. \tag{9.5}$$

Truncating at some large but finite N (so things become finite-dimensional yet insensitive to the exact value of N) then $M_{ij} := \langle\, \mathbf{q}_i^* . \mathbf{q}_j \,\rangle$ is a Hermitian $n \times n$ matrix which can be reduced to another matrix F such that $F^*F = M$, then

$$G(T;Re) = \max_{\mathbf{a(0)}} \frac{[F\mathbf{a}(T)]^* . F\mathbf{a}(T)}{[F\mathbf{a}(0)]^* . F\mathbf{a}(0)} = \max_{\mathbf{a(0)}} \frac{[Fe^{\Lambda T}\mathbf{a}(0)]^* . Fe^{\Lambda T}\mathbf{a}(0)}{[F\mathbf{a}(0)]^* . F\mathbf{a}(0)} = ||Fe^{\Lambda T}F^{-1}||_2^2 \tag{9.6}$$

where $e^{\Lambda T} = \text{diag}(e^{\lambda_1 T}, e^{\lambda_2 T}, \ldots, e^{\lambda_N T})$ [11]. This can handled by standard Singular Value Decomposition (SVD) software to give the largest singular value. If L is normal, M and F are diagonal and

$$G(T;Re) = ||e^{\Lambda T}||_2^2 = \max_j \left| e^{\lambda_j T} \right|^2 = \max_j e^{2\Re e(\lambda_j)T} \tag{9.7}$$

so there can be no transient growth when L is linearly stable i.e. $\Re e(\lambda_j) \leq 0$ for all j.

This method is straightforward but only really computationally feasible for one-dimensional, or possibly two-dimensional problems because the size of the matrices becomes unwieldy and then unmanageable for three-dimensional problems. A better approach is the matrix-free method which, although incurring more start-up costs (e.g. building a time stepping algorithm), is extendable to include nonlinearity.

9.2.2 Matrix-free method – Variational method

In this section, we consider the use of a matrix-free variational method for finding the energy growth which involves time-stepping the linearised Navier-Stokes equations. Since the problem is linear, the initial energy can be rescaled to 1 and we consider the Lagrangian

$$\begin{aligned} G = G(\mathbf{u}, p, \lambda, \mathbf{S}\nu, \pi; T) &= \left\langle \frac{1}{2}|\mathbf{u}(\mathbf{x}, T)|^2 \right\rangle + \lambda \left\{ \left\langle \frac{1}{2}|\mathbf{u}(\mathbf{x}, 0)|^2 \right\rangle - 1 \right\} \\ &+ \int_0^T \left\langle \mathbf{S}\nu(\mathbf{x}, t) \cdot \left\{ \frac{\partial \mathbf{u}}{\partial t} + (\mathbf{u}_{\text{lam}} \cdot \nabla)\mathbf{u} + (\mathbf{u} \cdot \nabla)\mathbf{u}_{\text{lam}} + \nabla p - \frac{1}{Re}\nabla^2 \mathbf{u} \right\} \right\rangle dt \\ &+ \int_0^T \langle \pi(\mathbf{x}, t) \nabla \cdot \mathbf{u} \rangle \, dt \end{aligned} \tag{9.8}$$

where λ, $\mathbf{S}\nu$ and π are Lagrangian multipliers imposing the constraints that the initial energy is fixed, that the linearized Navier-Stokes equation (9.2) holds over $t \in [0, T]$ and the flow is incompressible (their corresponding Euler-Lagrange equations are respectively:

$$\left\langle \frac{1}{2}|\mathbf{u}(\mathbf{x}, 0)|^2 \right\rangle = 1, \tag{9.9}$$

$$\frac{\partial \mathbf{u}}{\partial t} + (\mathbf{u}_{\text{lam}} \cdot \nabla)\mathbf{u} + (\mathbf{u} \cdot \nabla)\mathbf{u}_{\text{lam}} + \nabla p - \frac{1}{Re}\nabla^2 \mathbf{u} = 0, \tag{9.10}$$

$$\nabla \cdot \mathbf{u} = 0.) \tag{9.11}$$

The Euler-Lagrange equation for the pressure p is

$$\begin{aligned} 0 &= \int_0^T \left\langle \frac{\delta G}{\delta p} \delta p \right\rangle dt = \int_0^T \langle (\mathbf{S}\nu \cdot \nabla)\delta p \rangle \, dt \\ &= \int_0^T \langle \nabla \cdot (\mathbf{S}\nu \delta p) \rangle \, dt - \int_0^T \langle \delta p (\nabla \cdot \mathbf{S}\nu) \rangle \, dt. \end{aligned} \tag{9.12}$$

which to vanish means

$$\mathbf{S}\nu = \mathbf{0} \ \text{ at boundary}, \tag{9.13}$$

$$\nabla \cdot \mathbf{S}\nu = 0. \tag{9.14}$$

Finally, considering variations in $\mathbf{u}$ (with the condition that $\delta\mathbf{u} = \mathbf{0}$ on the boundary):

$$\begin{aligned} \int_0^T \left\langle \frac{\delta G}{\delta \mathbf{u}} \cdot \delta \mathbf{u} \right\rangle &= \langle \mathbf{u}(\mathbf{x}, T) \cdot \delta \mathbf{u}(\mathbf{x}, T) \rangle + \lambda \langle \mathbf{u}(\mathbf{x}, 0) \cdot \delta \mathbf{u}(\mathbf{x}, 0) \rangle \\ &+ \int_0^T \left\langle \mathbf{S}\nu \cdot \left\{ \frac{\partial \delta \mathbf{u}}{\partial t} + (\mathbf{u}_{\text{lam}} \cdot \nabla)\delta \mathbf{u} + (\delta \mathbf{u} \cdot \nabla)\mathbf{u}_{\text{lam}} - \frac{1}{Re}\nabla^2 \delta \mathbf{u} \right\} \right\rangle dt \\ &+ \int_0^T \langle \pi \nabla \cdot \delta \mathbf{u} \rangle \, dt. \end{aligned} \tag{9.15}$$

The first term in the second line of the above equation can be reexpressed as

$$\begin{aligned}\int_0^T \left\langle \mathbf{S}\nu \cdot \frac{\partial \delta\mathbf{u}}{\partial t} \right\rangle dt &= \int_0^T \left\langle \frac{\partial}{\partial t}(\delta\mathbf{u} \cdot \mathbf{S}\nu) \right\rangle dt - \int_0^T \left\langle \delta\mathbf{u} \cdot \frac{\partial \mathbf{S}\nu}{\partial t} \right\rangle dt \\ &= \langle \delta\mathbf{u}(\mathbf{x},T) \cdot \mathbf{S}\nu(\mathbf{x},T) - \delta\mathbf{u}(\mathbf{x},0) \cdot \mathbf{S}\nu(\mathbf{x},0) \rangle - \int_0^T \left\langle \delta\mathbf{u} \cdot \frac{\partial \mathbf{S}\nu}{\partial t} \right\rangle dt,\end{aligned} \tag{9.16}$$

the second term as

$$\begin{aligned}\langle \mathbf{S}\nu \cdot \{(\mathbf{u}_{\text{lam}} \cdot \nabla)\delta\mathbf{u}\} \rangle &= \langle \nabla \cdot ((\mathbf{S}\nu \cdot \delta\mathbf{u})\mathbf{u}_{\text{lam}}) - \delta\mathbf{u} \cdot \{(\mathbf{u}_{\text{lam}} \cdot \nabla)\mathbf{S}\nu\} \rangle \\ &= - \langle \delta\mathbf{u} \cdot \{(\mathbf{u}_{\text{lam}} \cdot \nabla)\mathbf{S}\nu\} \rangle ,\end{aligned} \tag{9.17}$$

the third term as

$$\langle \mathbf{S}\nu \cdot \{(\delta\mathbf{u} \cdot \nabla)\mathbf{u}_{\text{lam}}\} \rangle = \left\langle \delta\mathbf{u} \cdot \left\{ \mathbf{S}\nu \cdot (\nabla \mathbf{u}_{\text{lam}})^{\mathrm{T}} \right\} \right\rangle (= \langle \delta u_i \ \nu_j \ \partial_i u_{\text{lam},j} \rangle). \tag{9.18}$$

and the fourth term as

$$\left\langle \mathbf{S}\nu \cdot \left(-\frac{1}{Re} \nabla^2 \delta\mathbf{u} \right) \right\rangle = - \left\langle \frac{1}{Re} \delta\mathbf{u} \cdot \nabla^2 \mathbf{S}\nu \right\rangle , \tag{9.19}$$

and finally the last term as

$$\begin{aligned}\langle \pi \nabla \cdot \delta\mathbf{u} \rangle &= \langle \nabla \cdot \pi \delta\mathbf{u} \rangle - \langle \delta\mathbf{u} \cdot \nabla\pi \rangle \\ &= - \langle \delta\mathbf{u} \cdot \nabla\pi \rangle .\end{aligned} \tag{9.20}$$

Combining all these gives

$$\begin{aligned}\int_0^T \left\langle \frac{\delta G}{\delta \mathbf{u}} \cdot \delta\mathbf{u} \right\rangle &= \langle \delta\mathbf{u}(\mathbf{x},T) \cdot \{\mathbf{u}(\mathbf{x},T) + \mathbf{S}\nu(\mathbf{x},T)\} \rangle \\ &\quad + \langle \delta\mathbf{u}(\mathbf{x},0) \cdot \{\lambda\mathbf{u}(\mathbf{x},0) - \mathbf{S}\nu(\mathbf{x},0)\} \rangle \\ &\quad + \int_0^T \left\langle \delta\mathbf{u} \cdot \left\{ -\frac{\partial \mathbf{S}\nu}{\partial t} - (\mathbf{u}_{\text{lam}} \cdot \nabla)\mathbf{S}\nu + \mathbf{S}\nu \cdot (\nabla \mathbf{u}_{\text{lam}})^{\mathrm{T}} - \nabla\pi - \frac{1}{Re} \nabla^2 \mathbf{S}\nu \right\} \right\rangle dt.\end{aligned} \tag{9.21}$$

For this to vanish for all allowed $\delta\mathbf{u}(\mathbf{x},T)$, $\delta\mathbf{u}(\mathbf{x},0)$ and $\delta\mathbf{u}$ means

$$\frac{\delta G}{\delta \mathbf{u}(\mathbf{x},T)} = 0 \quad \Rightarrow \quad \mathbf{u}(\mathbf{x},T) + \mathbf{S}\nu(\mathbf{x},T) = \mathbf{0} \tag{9.22}$$

$$\frac{\delta G}{\delta \mathbf{u}(\mathbf{x},0)} = 0 \quad \Rightarrow \quad \lambda\mathbf{u}(\mathbf{x},0) - \mathbf{S}\nu(\mathbf{x},0) = \mathbf{0} \tag{9.23}$$

$$\frac{\delta G}{\delta \mathbf{u}} = 0 \quad \Rightarrow \quad \frac{\partial \mathbf{S}\nu}{\partial t} + (\mathbf{u}_{\text{lam}} \cdot \nabla)\mathbf{S}\nu - \mathbf{S}\nu \cdot (\nabla \mathbf{u}_{\text{lam}})^{\mathrm{T}} + \nabla\pi + \frac{1}{Re} \nabla^2 \mathbf{S}\nu = \mathbf{0}. \tag{9.24}$$

The last equation is the 'dual (or adjoint) linearized Navier-Stokes equation'. This equation can only be integrated backwards in time because of the negative diffusion term. Figure 9.1 shows a diagram of a numerical method for iteratively solving these variational equations in order to construct the initial condition with maximum growth (e.g. [5]). The algorithm has the following steps.

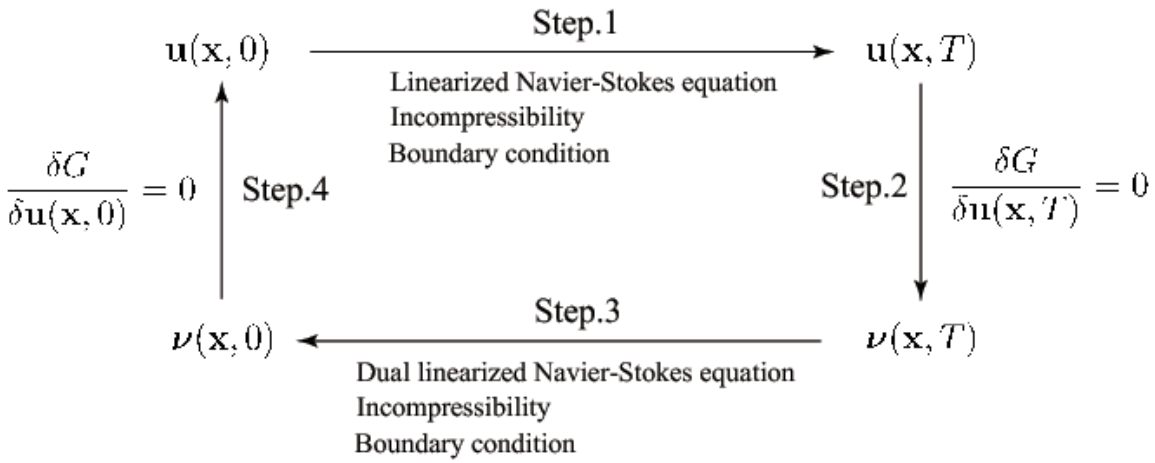

Figure 9.1: Diagram of iterative method.

Step.0 Choose an initial condition of the iterative method $\mathbf{u}^{(0)}(\mathbf{x},0)$ such that

$$\left\langle \frac{1}{2}\left\{\mathbf{u}^{(0)}(\mathbf{x},0)\right\}^2 \right\rangle = 1. \tag{9.25}$$

Then we construct $\mathbf{u}^{(n+1)}(\mathbf{x},0)$ from $\mathbf{u}^{(n)}(\mathbf{x},0)$ as follows:

Step.1 Time integrate the linearized Navier-Stokes equation (9.2) forward with incompressibility $\nabla \cdot \mathbf{u} = 0$ and boundary condition $\mathbf{u} = \mathbf{0}$ from $t = 0$ to $t = T$ with the initial condition $\mathbf{u}^{(n)}(\mathbf{x},0)$ to find $\mathbf{u}^{(n)}(\mathbf{x},T)$.

Step.2 Calculate $\mathbf{S}\boldsymbol{\nu}^{(n)}(\mathbf{x},T)$ using (9.22) which is then used as the *initial* condition for the dual linearized Navier-Stokes equation (9.24).

Step.3 Backwards time integrate the dual linearized Navier-Stokes equation (9.24) with incompressibility (9.14) and boundary condition (9.13) from $t = T$ to $t = 0$ with the 'initial' condition $\mathbf{S}\boldsymbol{\nu}^{(n)}(\mathbf{x},T)$ to find $\mathbf{S}\boldsymbol{\nu}^{(n)}(\mathbf{x},0)$.

Step.4 Using equation (9.23), a simple approach to calculating the correction of $\mathbf{u}^{(n)}$ is as follows:

$$\mathbf{u}^{(n+1)} = \mathbf{u}^{(n)} + \epsilon \left[\frac{\delta G}{\delta \mathbf{u}(\mathbf{x},0)}\right]^{(n)} \tag{9.26}$$

$$= \mathbf{u}^{(n)} + \epsilon \left(\lambda \mathbf{u}^{(n)}(\mathbf{x},0) - \mathbf{S}\boldsymbol{\nu}^{(n)}(\mathbf{x},0)\right), \tag{9.27}$$

with λ chosen such that

$$1 = \left\langle \frac{1}{2}\left\{\mathbf{u}^{(n+1)}(\mathbf{x},0)\right\}^2 \right\rangle \tag{9.28}$$

$$= \left\langle \frac{1}{2}\left[(1+\epsilon\lambda)\mathbf{u}^{(n)}(\mathbf{x},0) - \epsilon \mathbf{S}\boldsymbol{\nu}^{(n)}(\mathbf{x},0)\right]^2 \right\rangle. \tag{9.29}$$

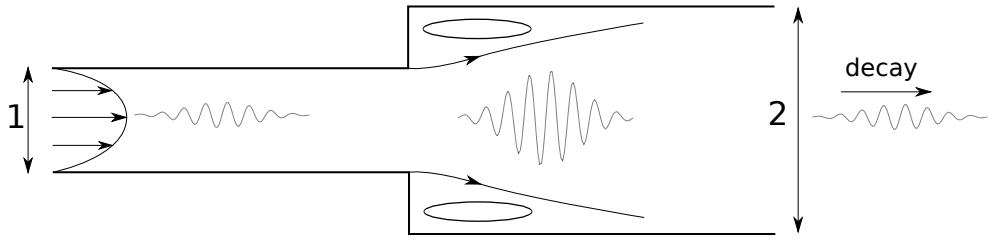

Figure 9.2: Initial noise is magnified as it passes through the pipe expansion before eventually decaying.

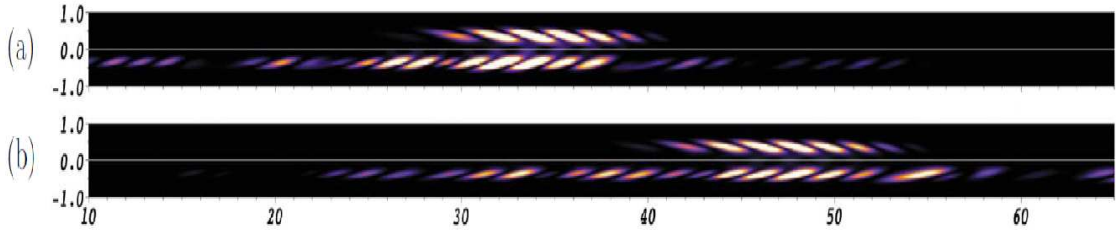

Figure 9.3: Comparison between noise-driven flows (bottom halves) and the linear optimal growth (top halves) for $Re = 900$ (upper) and $Re = 1200$ (lower) [1].

Here ϵ is a parameter of this iterative method and must be sufficiently small.

This last step moves $\mathbf{u}^{(n)}(\mathbf{x}, 0)$ in the direction of maximum ascent in order to increase $G(T)$. Iterating the last four steps typically converges to a local maximum of $G(T)$ [3], [5].

An example of the application of this method for finding linear optimum initial conditions is the case of expansion flow in a pipe [1], see Figure 9.2. Flow through an expansion in a pipe is a classical engineering problem which is not spatially homogeneous. The resulting linear-growth optimal can be compared with the numerical result of perturbing the flow with random noise, see Figure 9.3. The dominant spatial structure which grows out of the noise appears to agree well with the linear optimal.

9.3 Non-linear optimization

The matrix-free approach is, in principle, 'easily' extended to the non-linear problem. There are only two changes that need to be made to the Lagrangian G: the nonlinearity is added back to the linearised Navier-Stokes equation and the initial energy is explicitly set at E_0 which joins T as a free parameter of the problem. So

$$G(T, E_0; Re) = ... + \int_0^T \langle \mathbf{S}\nu \cdot (\mathbf{u} \cdot \nabla)\mathbf{u} \rangle \, dt + \lambda \left\{ \left\langle \frac{1}{2}\mathbf{u}^2(x, 0) \right\rangle - E_0 \right\} \tag{9.30}$$

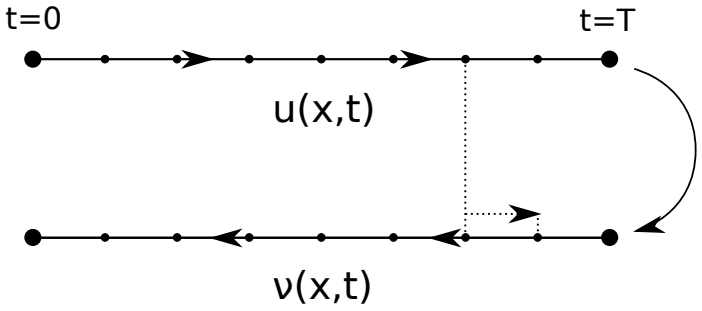

Figure 9.4: Checkpointing: during the calculation of $\mathbf{S}\nu(\mathbf{x},t)$ the velocity $\mathbf{u}(\mathbf{x},t)$ is recalculated in short sections from each checkpoint.

The change to a the non-linear term means that the part of the functional derivative of G with respect to $\mathbf{u}$ must be recalculated to get

$$\begin{aligned}\int_0^T \left\langle \frac{\delta G}{\delta \mathbf{u}} \cdot \delta \mathbf{u} \right\rangle dt &= \ldots + \int_0^T \langle \mathbf{S}\nu \cdot [\delta \mathbf{u} \cdot \nabla \mathbf{u} + \mathbf{u} \cdot \nabla \delta \mathbf{u}] \rangle \, dt \\ &= \ldots + \int_0^T \left\langle \delta \mathbf{u} \cdot [(\nabla \mathbf{u})^{\mathrm{T}} \cdot \mathbf{S}\nu - \mathbf{u} \cdot \nabla \mathbf{S}\nu] \right\rangle dt. \end{aligned} \tag{9.31}$$

Thus the dual Navier-Stokes equation becomes

$$-\frac{\partial \mathbf{S}\nu}{\partial t} + (\nabla[\mathbf{u} + \mathbf{u}_{lam}])^{\mathrm{T}} \cdot \mathbf{S}\nu - (\mathbf{u} + \mathbf{u}_{lam}) \cdot \nabla \mathbf{S}\nu - \nabla \pi - \frac{1}{Re} \nabla^2 \mathbf{S}\nu = 0. \tag{9.32}$$

The consequences of adding the non-linear term can be summarised as follows:

1. The full Navier-Stokes equations now need to be integrated forward in time.
2. The dual Navier-Stokes equation remains linear in $\mathbf{S}\nu$ but now depends on $\mathbf{u}(\mathbf{x},t)$.
3. The result now depends on *both* E_0 and T.

The added dependence of the dual equations on $\mathbf{u}(\mathbf{x},t)$ creates some problems numerically as this suggests that $\mathbf{u}(\mathbf{x},t)$ must be stored at every step of the forwards integration. For large systems the memory requirements associated with this are unfeasible so a method called 'checkpointing' is used instead. This involves storing $\mathbf{u}(\mathbf{x},t)$ at a reduced set of times or 'checkpoints' and then integrating forward in time again from each checkpoint as required when calculating $\mathbf{S}\nu$, see Figure 9.4. This method results in much reduced storage requirements but at the added cost of having to perform the forward integration twice per iteration.

9.4 Results

Before looking at some actual numerical results, we briefly consider what might happen. For a fixed value of T we could expect the algorithm to converge for energy values E_0 where it is not possible to trigger turbulence. However, once E_0 exceeds a threshold E_{thresh} where

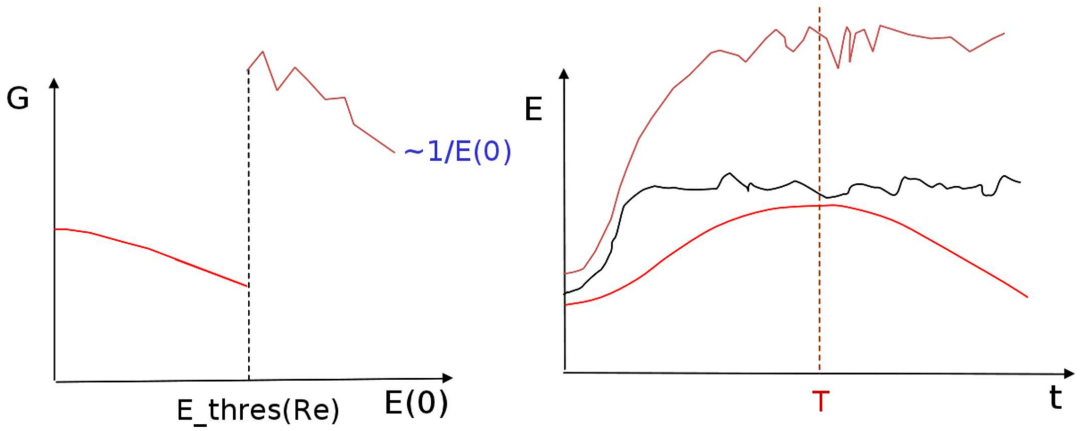

(a) Expected variation of G with E_0.

(b) Possible variations of E with t: turbulent (top), non-linear optimal (middle), linear optimal (bottom).

Figure 9.5: Expected results; the red curves correspond to the results of linear transient-growth analysis [12].

turbulence can be reached by some initial conditions, the algorithm should find these since they experience the larger energy growth. Then the algorithm should fail to converge due to the extreme sensitivity of the turbulence-triggering initial conditions to the exact turbulent energy level reached a fixed time later: see Figure 9.5.

9.4.1 Pipe flow

Pringle & Kerswell [8] numerically solved the nonlinear optimisation problem in the case of pipe flow using a short pipe with $L = \pi R$ (see also [2] for a boundary layer calculation). Figure 9.6 shows the growth G against E_0 at $Re = 1750$ which indicates how a new 3-dimensional optimal emerges at $E_0 \approx 10^{-5}$ to replace the 2-dimensional linear optimal. The optimisation time T was taken to be the time taken for the linear calculation to reach its maximum value of G to emphasize the effect of nonlinearity in the optimisation calculation. This, however, was too short a time for initial conditions to reach the turbulent state and convergence problems were encountered at $E_0 = 2 \times 10^{-5} < E_{thres}$ (similar issues were also found at $Re = 2250$).

The linear optimal is a well-known 2D structure as shown in Figure 9.7 (e.g. [12]). The optimum initial disturbance consists of a roll structure which then generates large velocity streaks before eventually decaying back to laminar flow. The structure of the new 3D optimal is much more complicated: see Figure 9.8. It initially consists of a radially-localised helical mode which unwinds to create rolls which then form streamwise streaks; the presence of these two distinct stages can be clearly seen from the two stages of growth in Figure 9.6b (see [9] for more details). When similar calculations are performed for longer pipes a localisation of the initial condition in the axial direction is also observed. This localised initial perturbation now also unrolls and expands in the streamwise direction to produce long streamwise rolls and ultimately streaks.

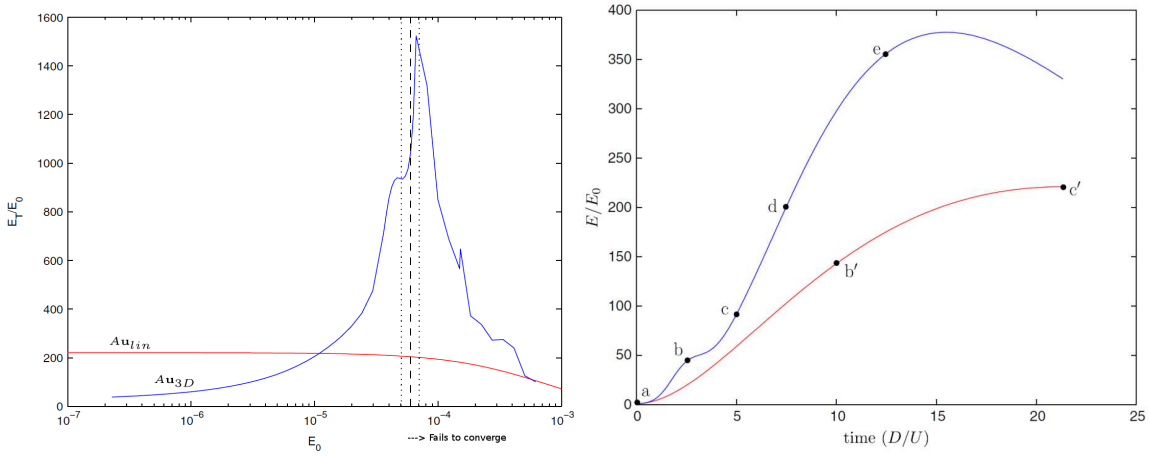

(a) Variation of G with E_0.

(b) Evolution of $G(t)$ with time for linear optimal (lower/red) and non-linear optimal (upper/blue).

Figure 9.6: Results of numerical calculation for short pipe [8].

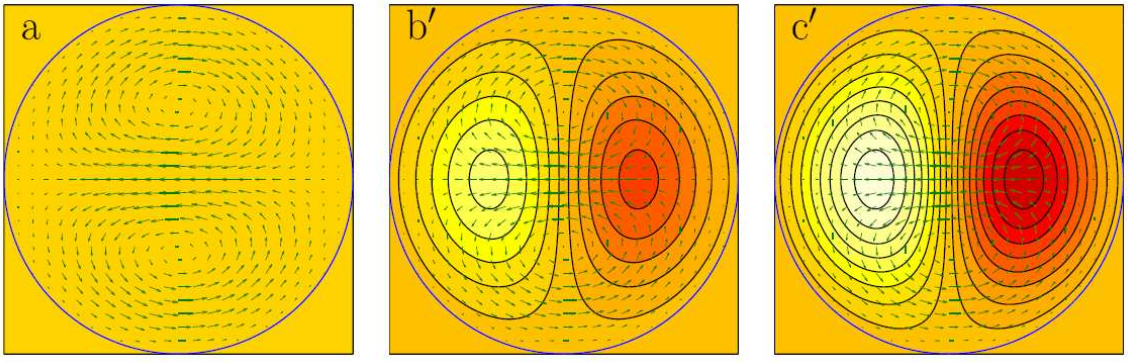

Figure 9.7: Linear optimal at three successive times. Colours represent streamwise velocity and the arrows represent velocity in the cross-section.

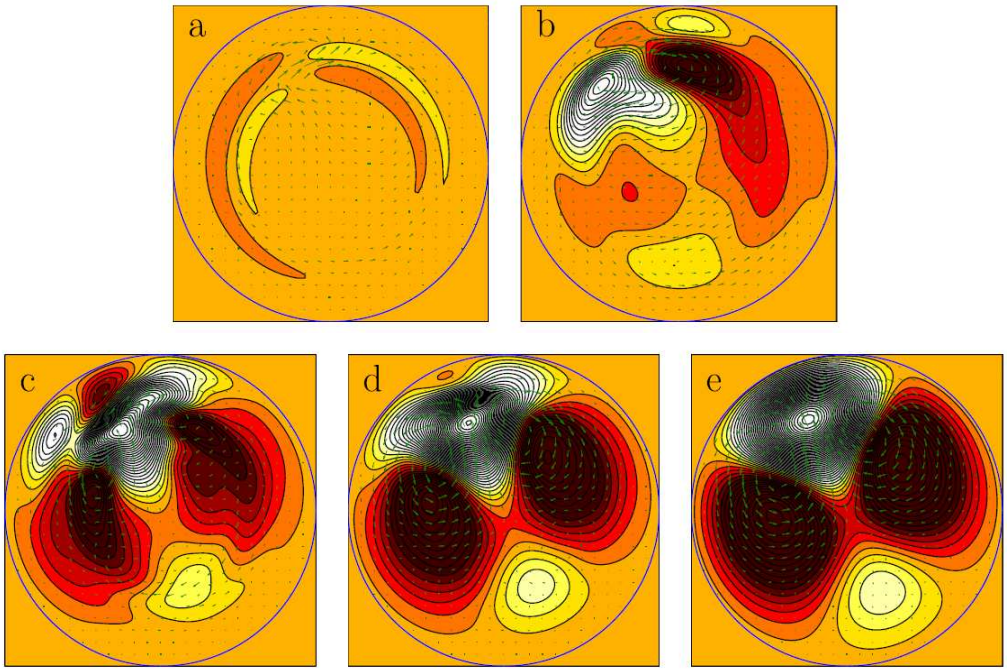

Figure 9.8: Non-linear optimal at five successive times. Colours represent streamwise velocity and the arrows represent velocity in the cross-section [8].

Two questions emerge from these preliminary results:

1. Can this approach be used to estimate E_{thresh}?
2. Does the non-linear optimal found correspond to the minimal seed for turbulence?

It is clearly possible that the extremum to which the numerical code converges may be a local maximum rather than the global maximum. This would result in too high a value of E_{thresh}. Even if the numerical code finds the correct value of E_{thresh}, it is possible that the non-linear optimum found does not become turbulent but rather the minimal seed is a different point on the same surface of E_0, see Figure 9.9. Further numerical results [9], however, suggest that the answer to the first question is 'yes' and the answer may also be 'yes' to the second as well.

9.4.2 PCF

Numerical optimisation calculations have also been performed for PCF [6]. However this work used a different choice of G choosing instead to look at the total dissipation

$$G' = \frac{1}{T}\int_0^T \left\langle \frac{1}{Re}|\nabla \mathbf{u}|^2 \right\rangle dt. \tag{9.33}$$

This functional was chosen based on the idea that turbulent flow is much more dissipative than laminar flow. The results of these calculations are shown in Figures 9.10 & 9.11.

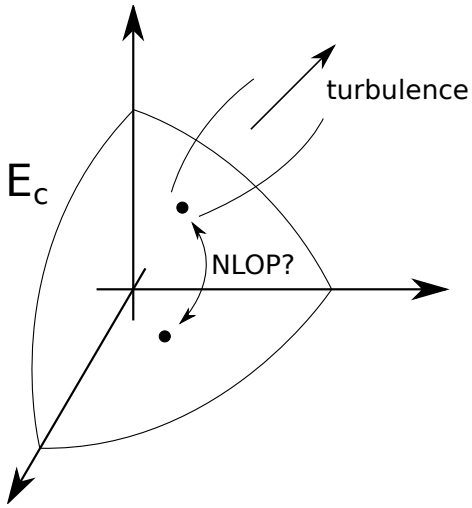

Figure 9.9: Does the non-linear optimal found numerical necessarily correspond to the minimal seed?

The increase in dissipation as the initial condition switches from remaining laminar to transitioning to turbulence is very clear. We also see a localisation of the initial perturbation as was previously observed for a long pipe. Optimising the energy growth for exactly the same flow configuration (geometry and Re) seems to produce the same estimate of E_{thres} [10]. This is consistent with the thinking developed in [9] where the exact functional used is not important but merely that the functional takes on enhanced values for turbulent flow states compared to their laminar counterparts. It should be clear that there is much to explore and understand in this promising new variational approach.

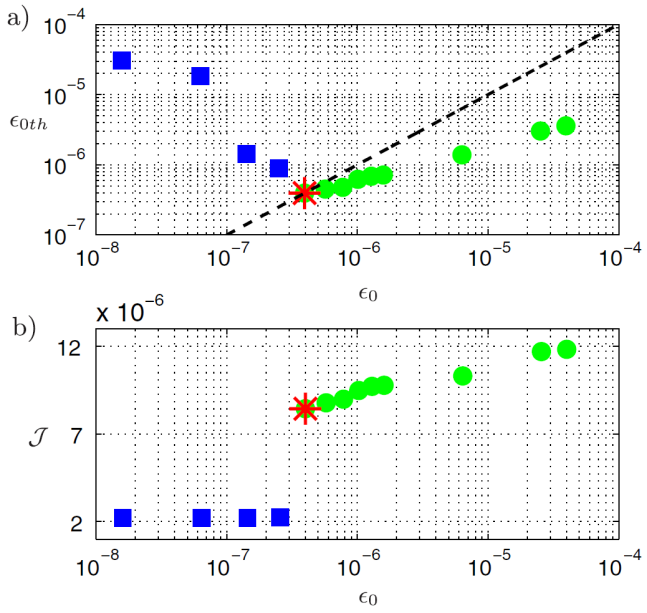

Figure 9.10: Variation of energy threshold for transition to turbulence with E_0 (top) and of dissipation with E_0 (bottom). Blue marks correspond to flows that remain laminar, green to those that transition to turbulence, and the red star to the non-linear optimal [6].

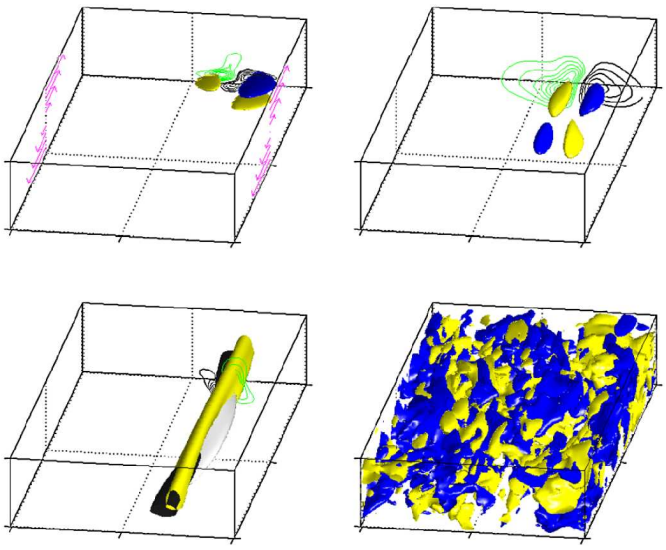

Figure 9.11: Evolution of the non-linear optimal with time [6].

Bibliography

[1] C. D. Cantwell, D. Barkley, and H. M. Blackburn, *Transient growth analysis of flow through a sudden expansion in a circular pipe*, Physics of Fluids, 22 (2010), p. 034101.

[2] S. Cherubini, P. De Palma, J.-C. Robinet, and A. Bottaro, *Rapid path to transition via nonlinear localized optimal perturbations in a boundary layer flow*, Phys. Rev. E, 82 (2010), p. 066302.

[3] P. Corbett and A. Bottaro, *Optimal perturbations for boundary layers subject to stream-wise pressure gradient*, Physics of Fluids, 12 (2000), pp. 120–130.

[4] Y. Duguet, L. Brandt, and B. R. J. Larsson, *Towards minimal perturbations in transitional plane Couette flow*, Phys. Rev. E, 82 (2010), p. 026316.

[5] A. Guégan, P. J. Schmid, and P. Huerre, *Optimal energy growth and optimal control in swept Hiemenz flow*, Journal of Fluid Mechanics, 566 (2006), pp. 11–45.

[6] A. Monokrousos, A. Bottaro, L. Brandt, A. Di Vita, and D. S. Henningson, *Nonequilibrium thermodynamics and the optimal path to turbulence in shear flows*, Phys. Rev. Lett., 106 (2011), p. 134502.

[7] C. C. T. Pringle and R. R. Kerswell, *Asymmetric, helical and mirror-symmetric travelling waves in pipe flow*, Phys. Rev. Lett., 99 (2007), p. 074502.

[8] ——, *Using nonlinear transient growth to construct the minimal seed for shear flow turbulence*, Phys. Rev. Lett., 105 (2010), p. 154502.

[9] C. C. T. Pringle, A. P. Willis, and R. R. Kerswell, *Minimal seeds for shear flow turbulence: using nonlinear transient growth to touch the edge of chaos*, Journal of Fluid Mechanics, 702 (2012), pp. 415–443.

[10] S. M. Rabin, C. P. Caulfield, and R. R. Kerswell, *Triggering turbulence efficiently in plane Couette flow*, Journal of Fluid Mechanics, subjudice (see arXiv:1111.6654).

[11] S. C. Reddy and D. S. Henningson, *Energy growth in viscous channel flows*, Journal of Fluid Mechanics, 252 (1993), pp. 209–238.

[12] P. J. Schmid and D. S. Henningson, *Optimal energy density growth in Hagen-Poiseuille flow*, Journal of Fluid Mechanics, 277 (1994), pp. 197–225.

[13] D. Viswanath and P. Cvitanović, *Stable manifolds and the transition to turbulence in pipe flow*, Journal of Fluid Mechanics, 627 (2009), pp. 215–233.

Lecture 10

Turbulence: Transient or Sustained?

Many realised in the 1980s that Chaos theory was not going to solve the problem of turbulence because it is an inherently spatiotemporal phenomenon (at least at low to intermediate Re). Pomeau [12][1] was the first to start thinking about turbulence from a statistical mechanical viewpoint by comparing spatiotemporal intermittency to directed percolation. Here, a spatial lattice of sites which individually can either be active ('turbulent') or passive ('laminar') is stochastically evolved in time using simple rules which incorporate information about neighbouring states. In the simplest models, there is one parameter p which defines the evolutionary strategy and then the challenge is to characterise the ensuing dynamics as a function of p. What typically emerges is that the order parameter $\rho(t)$ defined as the ensemble average of the lattice average of active sites (active=1, passive =0) asymptotes to 0 as $t \to \infty$ for $p \leq p_c$ where p_c is a critical value, whereas for $p > p_c$, $\lim_{t\to\infty} \rho(t) \sim (p-p_c)^\beta$ (there are universality classes defined by the exact value taken by the exponent β). What is important here is the idea that turbulence and the laminar state can coexist above a definite threshold (in Re) and the use of statistical techniques to characterise this via an order parameter (e.g. turbulent fraction in a domain).

These ideas were followed up most famously in 1998 by Bottin et al. [4] who conducted a series of plane Couette flow experiments in very large domains (non-dimensionalised as $380 \times 2 \times 70$ in the streamwise, cross-stream and spanwise directions respectively) so that the spatiotemporal behaviour near the transition threshold could be seen. The turbulent fraction of the flow, F_t as a function of time for various Re is shown in Figure 10.1. This plot emphasizes the temporal variability in F_t and the sensitivity of the flow to the initial conditions used (e.g. compare the two time signals for $Re = 322$). F_t is found to approach 0 eventually for all $Re < R_c \approx 323$, but long transients are found when $R_u \approx 312 < Re < R_c$ so that a long-time average which is non-zero can still be defined (all turbulence rapidly decays for $Re < R_u$). This is plotted verses Re in Figure 10.2.

Bottin et al. then applied a statistical approach to quantifying the transience of turbulence in the Re range $[R_u, R_c]$. They collected lifetime data from $50 - 120$ separate experiments and then estimated $P(T)$, the probability that the flow still remains turbulent

[1] Apparently, this work was mostly done at the Woods Hole summer program of 1985.

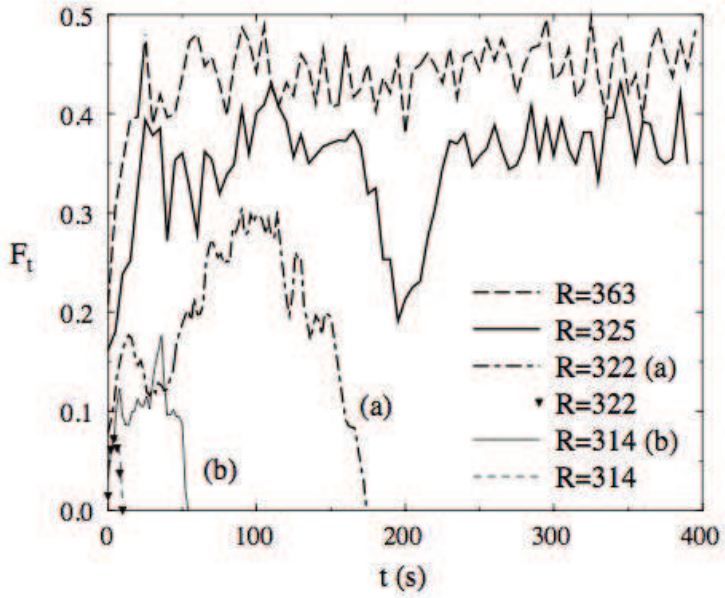

Figure 10.1: (From [4]) Turbulent fraction vs. time during typical runs at various values of Re.

after a time T: see Figure 10.3. The best fit lines drawn through the data at each Re indicate an exponential distribution of lifetimes

$$P(T) = e^{-T/\tau}, \tag{10.1}$$

(since $P(0) = 1$) where $\tau = \tau(Re)$ is the mean lifetime of the process. If $p(T)dT$ is the probability that the flow relaminarises in the time interval $[T, T + dT)$ (as $dT \to 0$), then

$$p(T) = \frac{1}{\tau} e^{-T/\tau} \tag{10.2}$$

and the half life (median) is $\tau \ln 2$. This distribution indicates that the relaminarisation process is *memoryless*, that is, the probability of relaminarising in the interval $[T, T + s)$ only depends on s and not T. Figure 10.3 also shows that flows at higher values of Re take longer to relaminarise. In fact plotting $1/\tau$ against Re indicated a linear relationship with an intercept ($\tau \to \infty$) at ≈ 323: see Figure 10.3. This is consistent with Re_c such that for $Re < Re_c$ the turbulence will always be transient with a finite half life, while for $Re > Re_c$ the half life is infinite and the turbulence sustained.

A similar statistical approach was also adopted numerically in *small* systems, that is, flow geometries where the flow is either globally laminar *or* turbulent: see Schmiegel & Eckhardt (1997) for plane Couette flow and Faisst & Eckhardt (2004) for pipe flow. The latter study was motivated by an experimental study by Daryshire & Mullin (1995) which showed no sharp border between initial conditions which lead to turbulence and those that did not. Faisst and Eckhardt found a similar situation when observing over a fixed period of time

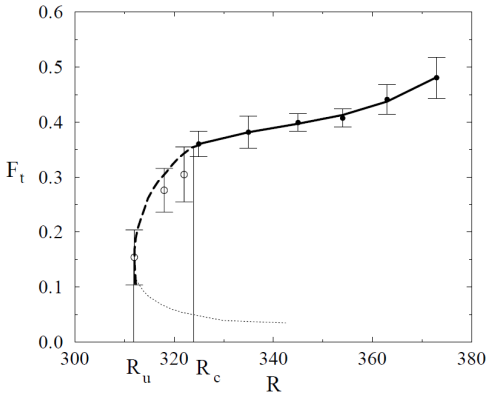

Figure 10.2: The time-averaged turbulent fraction against Re from [4]. $R_u = 312$ is the Re threshold below which turbulent patches rapidly decay (see Figure 10.1)). For $R_u < Re < R_c \approx 323$, there are long-lived turbulent transients. Above R_c, turbulence is sustained although since $F_t < 1$ it is not space-filling (the lower dotted line is a conjectured threshold).

in their short, $5D$ (5 diameters) long pipe across which they applied periodic boundary conditions and through which they enforced constant mass flux. They collected lifetime statistics based on repeatedly initializing a numerical simulation using a perturbation of fixed form but randomly varying its amplitude. 50-100 different runs were done for each Re and 8 values of Re chosen from the interval $[1600, 2200]$. As in [4], they found that $P(T) = e^{-T/\tau(Re)}$ - see Figure 10.4 - and estimated τ using the half life rather than the mean lifetime due to the cut off in the observation times imposed. Figure 10.5 shows that the mean lifetime τ increases rapidly with Re with the inset figure indicating that actually $\tau \to \infty$ as $Re \to 2250$. Faisst and Eckhardt speculated that for $Re < 2250$ where the turbulent lifetime is finite, there is a chaotic repeller while for $Re > 2250$ there is a chaotic attractor.

Further evidence for critical point behaviour in the transition to turbulence in a pipe was

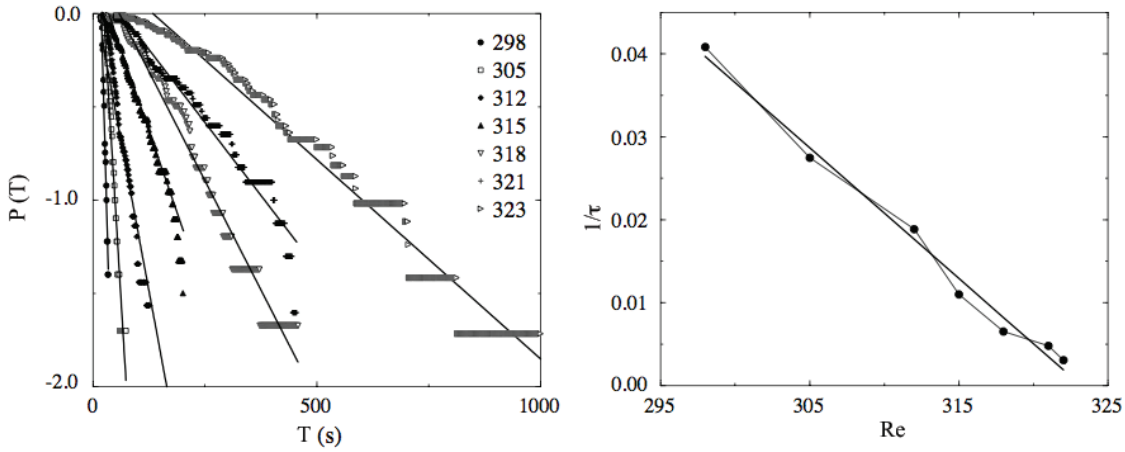

Figure 10.3: (From [4]) Left: cumulated lifetime distributions for turbulent transients at different values of $Re < Re_c$ indicating exponential decay (lin-log scales; solid lines are fits through the experimental data points). Right: variation of the inverse average decay time $1/\tau$ as a function of Re extrapolating to zero at $Re_c = 323$.

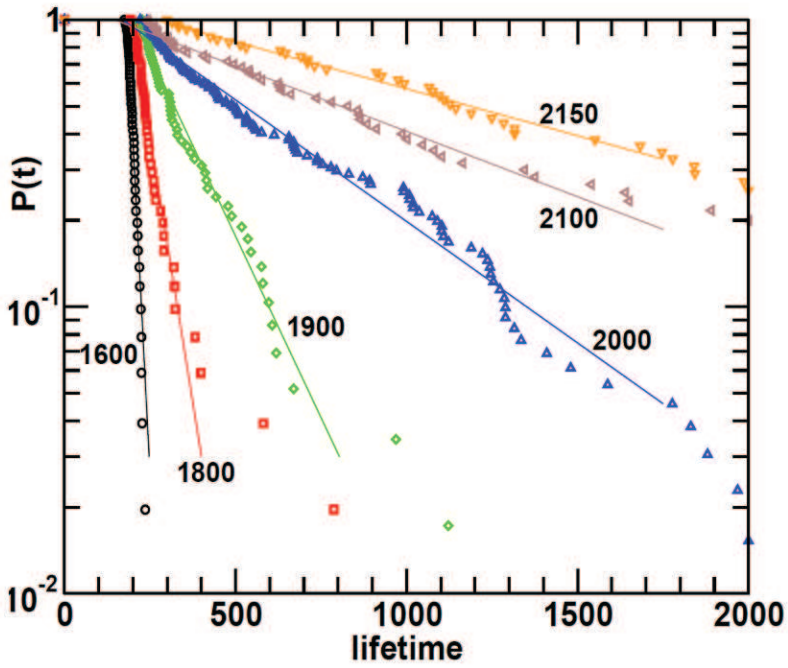

Figure 10.4: (From [6]) Probability for a single trajectory to still be turbulent after a time t for six Reynolds numbers as indicated.

presented by a novel experiment by Peixinho and Mullin in 2006 [11]. In their experimental setup (depicted in Figure 10.6a), a short duration perturbation was used to generate a

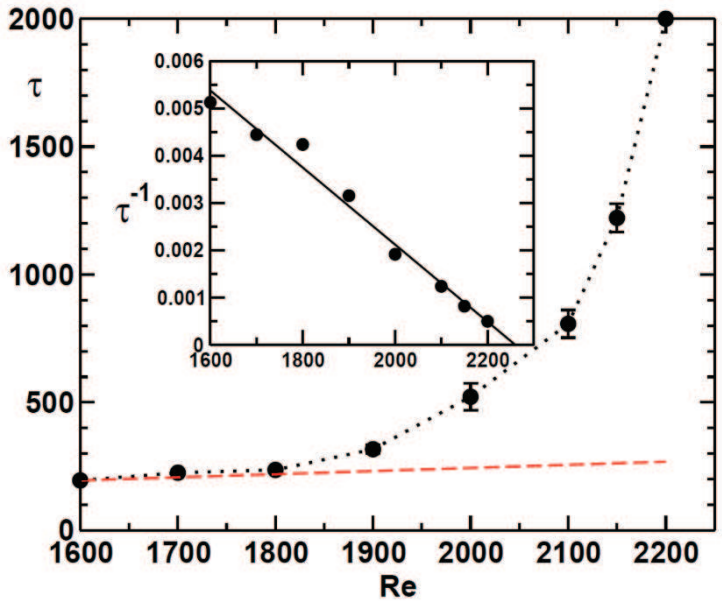

Figure 10.5: (From [6]) τ is found to increase rapidly with Re until the cut-off lifetime of 2000 at $Re = 2200$ is reached. The red dashed line shows the linear increas e in lifetime expected due to purely non-normal linear dynamics. The inset shows the inverse mean lifetime vs. Re and a linear fit, corresponding to a law $\tau(Re) \propto (Re_c - Re)^{-1}$, with $Re_c \approx 2250$.

localised puff at $Re = 1900$. The puff was allowed to advect $100D$ down the pipe so as to become independent of the initial conditions, at which point Re was lowered to the required value. The lifetime of the turbulence from this point onwards was then measured up to a maximum travel of $500D$ (their pipe was $785D$ long in total). The mean puff lifetime as a function of Reynolds number is shown in Figure 10.6b. In qualitative agreement with the conclusions of Faisst and Eckhardt's numerical simulations, the experiments showed that above a critical Reynolds number - estimated to be $Re_c \approx 1750 \pm 10$ - the lifetime of the puffs becomes infinite and turbulence is sustained.

An experimental and numerical study by Hof et al. in 2006 [8], however, failed to find any evidence for a critical Reynolds number. Instead, their results indicated that although the half life of turbulence increases rapidly with Re it never actually becomes infinite for finite Re so that pipe turbulence remains transient for *all* Re. Their experiments were performed using a longer (30m) and thinner (4mm diameter) *opaque* pipe which was non-dimensionally much longer at $7500D$ than Peixinho & Mullin's. Turbulent puffs were excited by injecting water through holes in the pipe (apparatus shown in Figure 10.7a). Since the pipe was opaque, the angle at which the jet exited the pipe was monitored to see if the puffs had survived or not (an exiting puff causes a small flicker in the jet). This meant survival distances were measured rather than survival times with the latter found assuming that the puff speed is uniform. Other differences with the experiments of Peixinho & Mullin (2006) included using fixed-pressure-gradient driving rather than constant mass flux and, since the pipe was opaque, the implicit assumption that puffs were always triggered by the

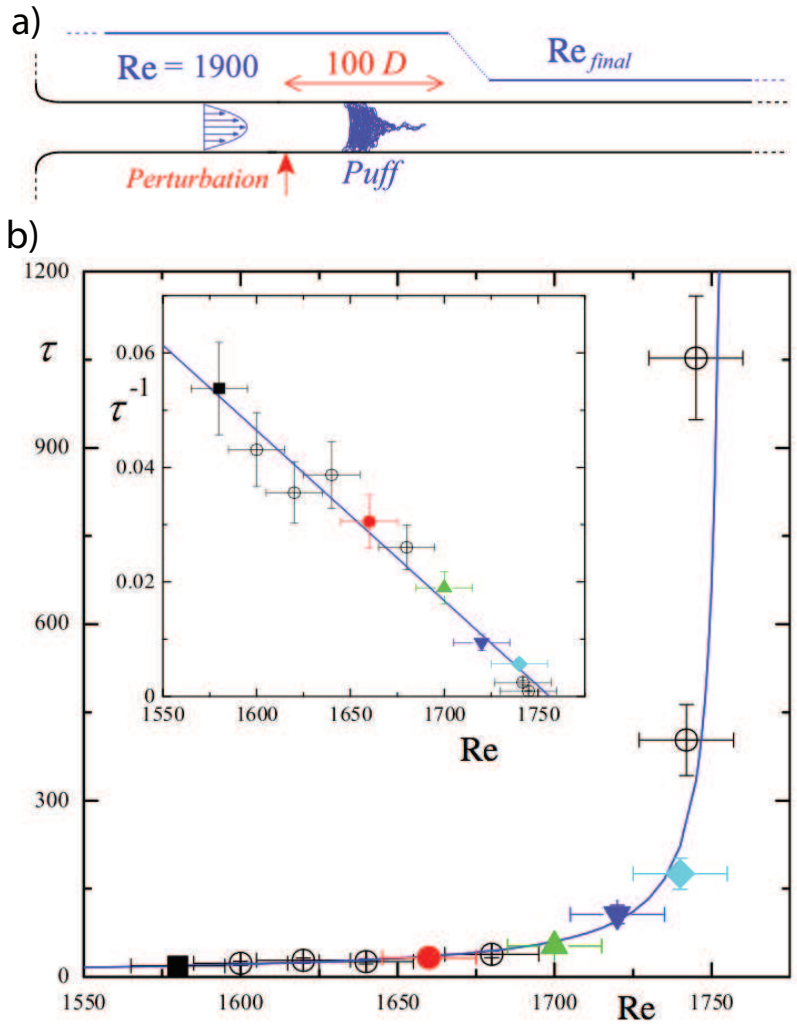

Figure 10.6: (From [11]) a) Schematic of flow control procedure. Laminar pipe flow was developed at $Re = 1900$ for $185D$ before a perturbation was injected (indicated by the arrow). The puff progressed downstream for $100D$ and Re was then reduced to a prescribed value. b) Variation of the mean lifetime as a function of Re and a fit, which indicates a sharp cutoff at $Re_c \approx 1750 \pm 10$. The inset is the inverse mean lifetime versus Re and a linear fit.

jets. These subtleties aside, their mean lifetime data (inset of Figure 10.7b) did not appear to fit the simple exponential implied by $\tau(Re) \propto (Re_c - Re)^{-1}$, as in [6] and [11]. Instead, they suggested an exponential relation between τ and Re, of the form

$$P(T;T_0) = e^{-(T-T_0)/\tau(Re)} \tag{10.3}$$

with lifetime given by

$$\frac{1}{\tau} = e^{(a+bRe)}$$

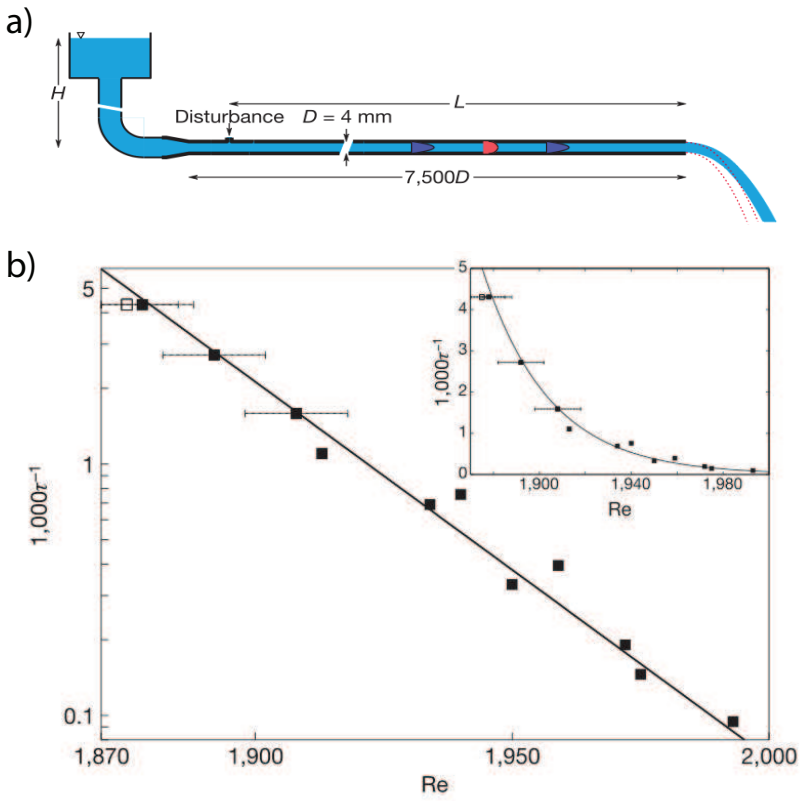

Figure 10.7: (From [8]) a) Sketch of the experimental apparatus. b) The reciprocal characteristic lifetimes as a function of Re for all experiments with $t_0 = 120D/U$, plotted on a log scale. Each data point required 400 to 500 measurements, with the total number of experiments underlying the figure exceeding 5,000. The straight line is an exponential fit to the data points. Inset, the same data replotted on a linear scale, underlining that they are not compatible with a diverging mean lifetime.

where a and b are constant fitting parameters. The significance of an exponential relationship is that there is no critical Reynolds number beyond which turbulent puffs are sustained for all times. The introduction of a shifted time origin T_0 was crucial in their data analysis: the best straight line fit needs to be shifted in time. The explanation for this was that the flow would take a finite time $\approx T_0$ to *reach* the turbulence state after the initial disturbance, so that $T - T_0$ would actually be the puff lifetime. Hof et al (2006) also redid the short pipe numerical computations of [6] to reach the same conclusion. Furthermore, they reprocessed Faisst & Eckhardt's original data incorporating a best-fitted time origin to confirm that this data also supported a lack of a critical Re.

Next to attack this problem were Willis & Kerswell in 2007 [15] who carried out numerical simulations in a pipe long enough (10 times longer than in [6]) to realistically capture the localised structure of a turbulent puff. The methodology for generating initial conditions mirrored that of [11], as puffs at a higher Re of 1900 were used as initial conditions for the numerical simulations at lower Re. Using 40-60 independent simulations per Re as

the computations were so costly, a critical Re_c was found with a value of ≈ 1870 and τ best fitted by

$$\tau = \alpha\,(1870 - Re)^{-1}\,,$$

where $\alpha = 2.4 \times 10^{-4}$, comparing favourably with the results of [11] who found

$$\tau = \alpha\,(1750 - Re)^{-1}\,,$$

with $\alpha = 2.8 \times 10^{-4}$.

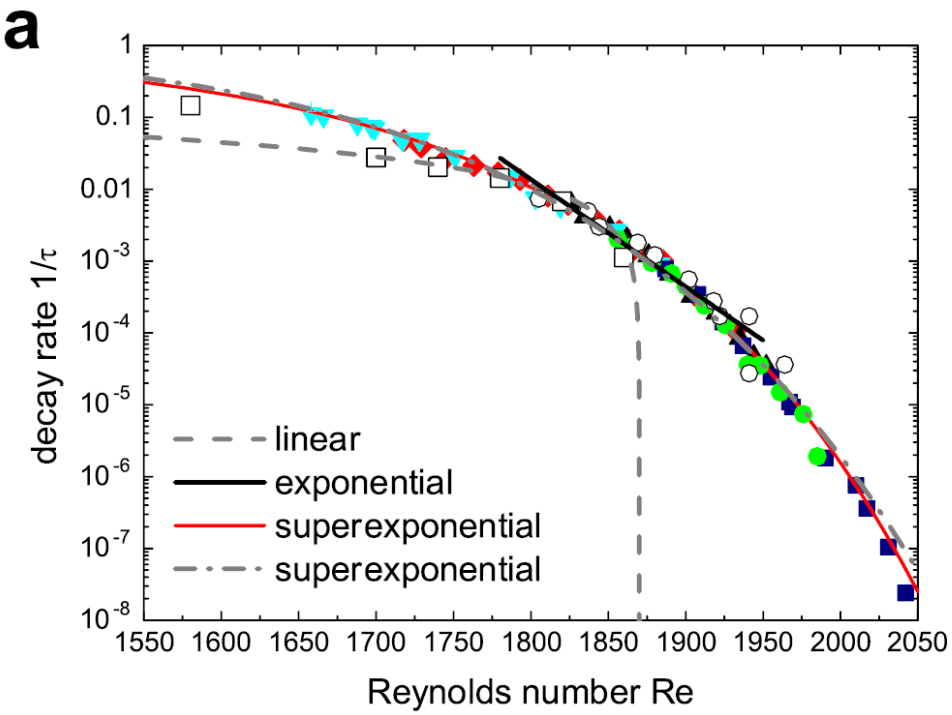

Figure 10.8: (From [7]) Decay rate $1/\tau$ plotted on a log linear scale against Re suggesting superexponential dependence of τ upon Re.

This result was countered by Hof et al. in 2008 [7] who presented results from four different physical experiments (pipe length $=600D$, $690D$, $2000D$ & $3600D$) in three different locations (Manchester, Delft and Göttingen) (see also the arXiv discussion articles arXiv:0707.2642 and arXiv.0707.2684). The authors also increased the number of observations taken compared to their previous paper [8]. From this greater data set, they revised their exponential dependence of τ upon Re to superexponential,

$$\tau \sim e^{\alpha Re} \Rightarrow \tau \sim e^{e^{\alpha Re}}\,.$$

This new relationship still implied that no finite value for Re_c existed (see Figure 10.8: note the last Re considered and the later work of [1] discussed below).

Further numerical work then started to be done in large domains. Initially, due to the extreme cost, these simulations were carried out working with reduced resolution in one

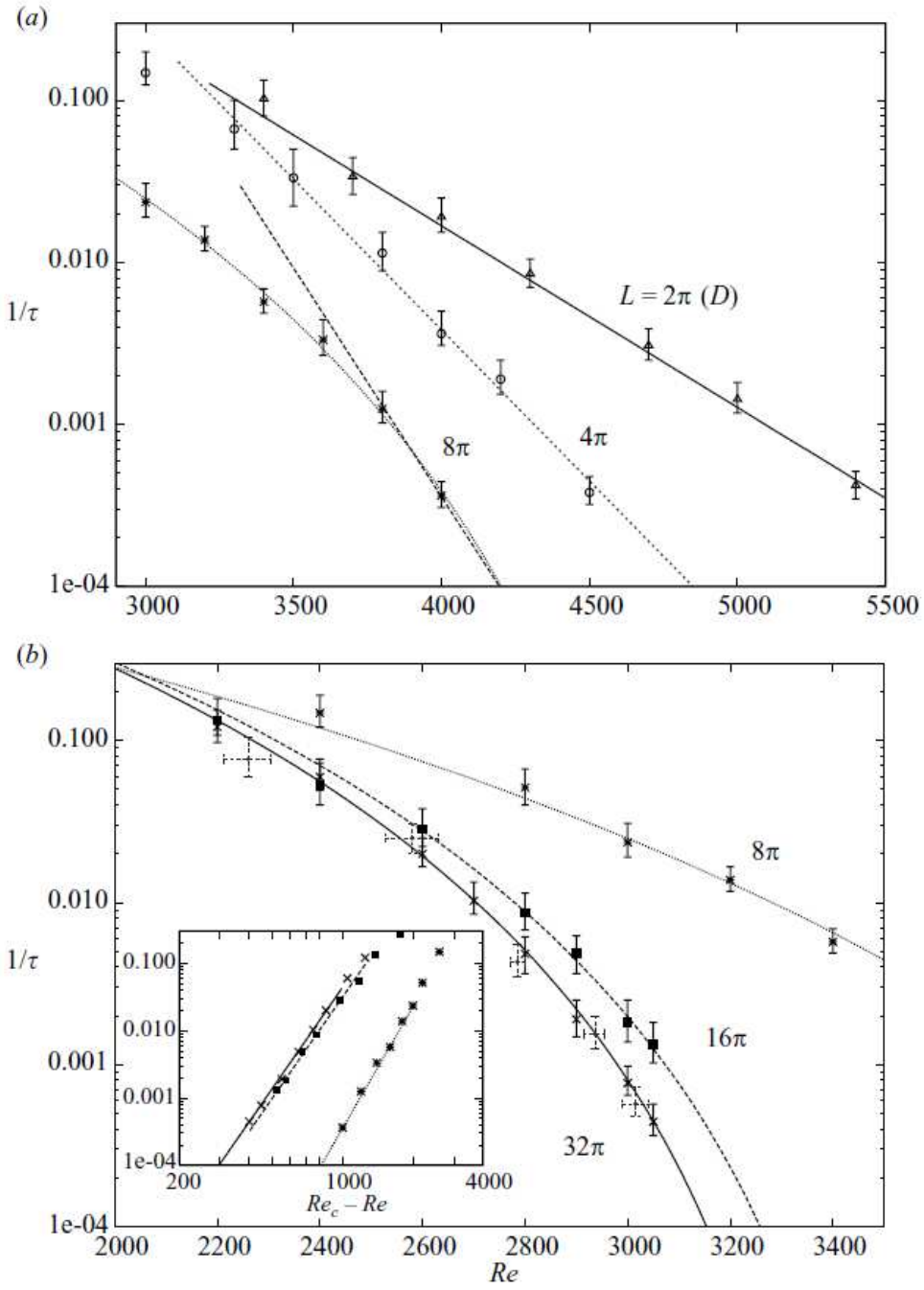

Figure 10.9: (From [16]) The sensitivity of lifetime (τ) to pipe length is shown with data generated using the $2+\epsilon$ dimensional model. The $1/\tau$ is plotted against Re for a range of pipe lengths from $2\pi\,D$ to $32\pi\,D \approx 100\,D$. The results suggest an infinite value of Re_c for pipes shorter than 8π and a finite value for longer pipes.

direction in order to ensure enough data was collected of long transients (e.g. Lagha & Manneville 2009, Willis & Kerswell 2009). The hope was that these reduced models would capture the real qualitative aspects of the problem, that is, whether there is a finite Re_c or not. In work by Lagha & Manneville [9] on plane Couette flow, the authors heavily reduced the resolution in the wall-normal direction, while maintaining the resolution in the two remaining directions. Using this approach they found evidence for a finite value for Re_c. Alongside this work, Willis & Kerswell [16] developed a similar reduction in pipe flow. Here the resolution reduction was made in the azimuthal direction, with just 3 Fourier modes retained in this direction ($m = 0, \pm 3$). Again the reduced model provided good qualitative comparisons with full DNS. Large numbers of simulations were carried out for both short and long pipes which suggested a transition in the relationship between τ and Re (Figure 10.9). For pipes too short to support localized turbulence, $Re_c = \infty$ with τ taking the form

$$\tau \sim e^{\alpha Re}.$$

When long pipes were studied, a different relationship emerged with a finite Re_c,

$$\tau \sim (Re_c - Re)^{\beta}.$$

The '2+ϵ' dimensional model of [16] was so much more efficient to run that the full 3 dimensional situation that $100D$ pipes could easily be handled and transients followed for $O(100)$ times longer. However, this was not fully exploited because as Re was increased the puffs started to delocalise or split to form 'slugs' (a turbulent state which aggressively expands). This highlighted the fact that extrapolating puff lifetime data to asymptotically large Re was actually irrelevant since the morphology of the turbulence changes. It took a later study (Avila et al. 2011, see below) to pursue this realisation to a logical conclusion.

In the meantime, further numerical work was attempted in the $50D$ pipe to collect even more data by fully harnessing a supercomputer. Using the same numerical code as in [15] with the same resolution, Avila et al [2] extended the results of [15] in Re, sample size and included pipes of length $100\,D$. Armed with much more data, the authors saw no statistical evidence for Re_c being finite within their range of $Re < 1900$ (Figure 10.10).

After this, Avila et al. 2011 [1] took measurements of a puff splitting in both numerical simulations and experimental work. They measured the lifetime of a puff before it underwent its first split to become two puffs, and calculated $S(T)$, the probability that a puff has not split by time T. Their results suggested this probability had an exponential (memoryless) form with a mean lifetime τ_s having a superexponential dependence on Re (Figure 10.11). By combining the plots of decay and splitting to see the crossover, a critical Reynolds number of 2040 was found beyond which, *on average*, a puff should survive. For Reynolds number smaller than this, puffs are more likely to decay than split, and therefore, on average to ultimately decay. In other words, below 2040 turbulence is transient, and above it, the expectation is that it will be sustained. Individual initial conditions at Reynolds numbers greater than 2040 can still lead to transient turbulence, but the expectation over an ensemble of runs is that more will yield turbulence at the end of a given time period (however long) than not.

The current conclusion is then the following. For small systems, all current evidence is that turbulence appears transient albeit with very large half life as Re increases. In large

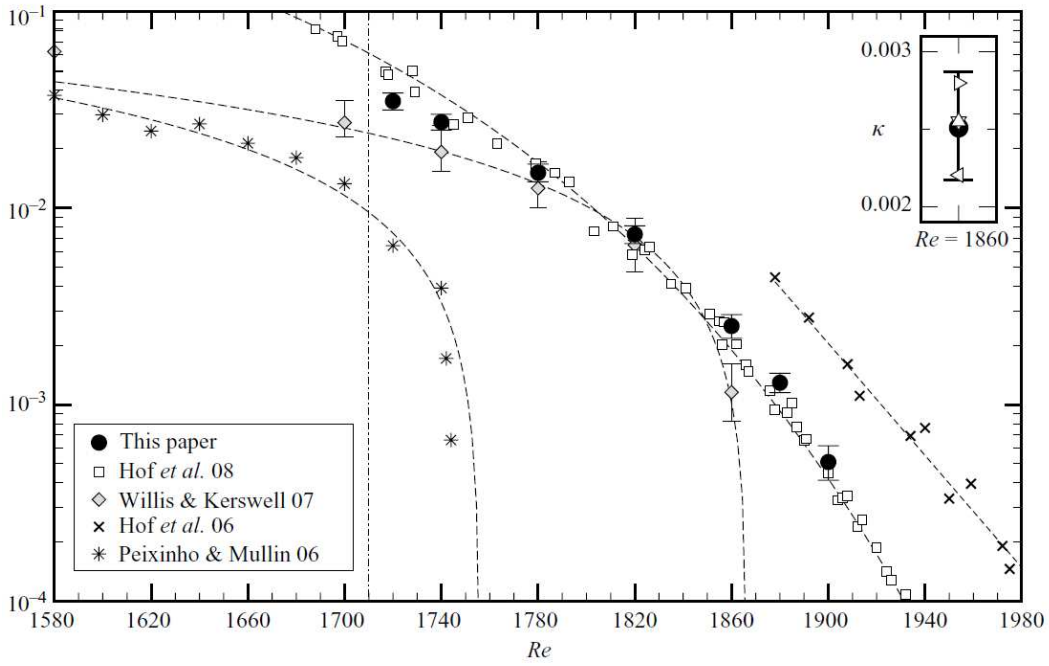

Figure 10.10: (From [2]) $1/\tau$ plotted against Re, summarising the recent work against their results which suggest a superexponential dependence of τ upon Re.

domains, however, the balance of evidence is that turbulence is ultimately sustained. The key difference between small and large systems is that in large systems, turbulent patches can independently exist in the flow. The spatial coupling between these turbulent patches appears crucial to achieve sustenance [10]. This realisation has led to a return of statistical approaches to modelling turbulence, most recently in the form of directed percolation [14] and other reduced models [3].

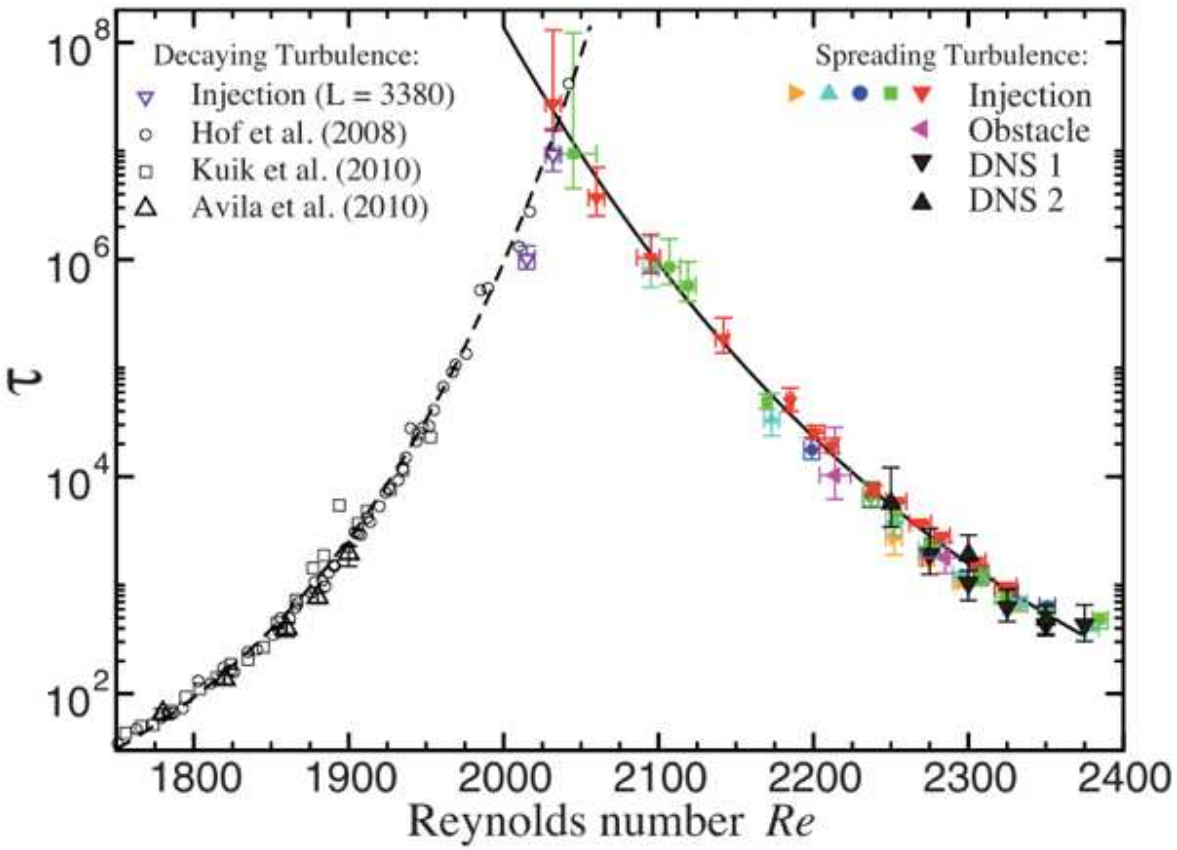

Figure 10.11: (From [1]) Mean lifetime before decay and the mean lifetime before splitting are plotted against Re (both experimental and numerical data shown).

Bibliography

[1] K. Avila, D. Moxey, A. de Lozar, M. Avila, D. Barkley, and B. Hof, *The onset of turbulence in pipe flow*, Science, **333** (2011), p. 192–196.

[2] M. Avila, A. P. Willis, and B. Hof, *On the transient nature of localized pipe flow turbulence*, J. Fluid Mech., **646** (2010), p. 127–136.

[3] D. Barkley, *Simplifying the complexity of pipe flow*, Phys. Rev. E, **84** (2011), 016309.

[4] S. Bottin, F. Daviaud, P. Manneville, and O. Dauchot, *Discontinuous transition to spatiotemporal intermittency in plane couette flow*, Europhys. Lett., **43** (1998), p. 171.

[5] A. G. Darbyshire and T. Mullin *Transition to turbulence in constant-mass-flux pipe-flow* J. Fluid Mech., **289** (1995), p. 83–114.

[6] H. Faisst and B. Eckhardt, *Sensitive dependence on initial conditions in transition to turbulence in pipe flow*, J. Fluid Mech., **504** (2004), p. 343–352.

[7] B. Hof, A. de Lozar, D. J. Kuik, and J. Westerweel, *Repeller or attractor? Selecting the dynamical model for the onset of turbulence in pipe flow*, Phys. Rev. Lett., **101** (2008) 214501.

[8] B. Hof, J. Westerweel, T. M. Schneider, and B. Eckhardt, *Finite lifetime of turbulence in shear flows*, Nature, **443** (2006), p. 59–62.

[9] M. Lagha and P. Manneville, *Modeling of plane Couette flow. I. Large scale flow around turbulent spots*, Phys. Fluids, **19** (2007) 094105.

[10] P. Manneville, *Spatiotemporal perspective on the decay of turbulence in wall-bounded flows*, Phys. Rev. E, **79** (2009) 025301.

[11] J. Peixinho and T. Mullin, *Decay of turbulence in pipe flow*, Phys. Rev. Lett., **96** (2006), p. 094501.

[12] Y. Pomeau, *Front motion, metastability and subcritical bifurcations in hydrodynamics*, Physica D, **23** (1986), p. 3–11.

[13] A. Schmiegel and B. Eckhardt, *Fractal stability border in plane Couette flow*, Phys. Rev. Lett., **79**, (1997), p. 5250-5253.

[14] M. Sipos and N. Goldenfeld, *Directed percolation describes lifetime and growth of turbulent puffs and slugs*, arXiv:1101.5835v2.

[15] A. P. Willis and R. R. Kerswell, *Critical behavior in the relaminarization of localized turbulence in pipe flow.*, Phys. Rev. Lett., **98** (2007) 014501.

[16] A. P. Willis and R. R. Kerswell, *Turbulent dynamics of pipe flow captured in a reduced model: puff relaminarization and localized 'edge' states*, J. Fluid Mech., **619** (2009), pp. 213–233.

Part III

The Fellows' Projects

Project 1

Constraints on low order models: The cost of simplicity

Martin Hoecker-Martinez: Advisor, Phil Morrison

Oregon State University

Low degree of freedom models have been proposed to understand the transition to turbulence and the coherent structures which form. The low order model on which the Self Sustaining Process [10] for turbulence in Couette flow is examined with respect to mean conservation laws of Fourier truncations Aspects of the non-dissipative limits of these models are studied. Transport equations and conservation laws are derived for Energy, vorticity and helicity. Connections are made between low order models and conservation laws and Lie algebras

1.1 Introduction

The transition from laminar to turbulent flow is of interest in bounded shear flow geometries. Laminar flows are advection free and mix only by molecular diffusion while turbulent flows are characterized by drastic increases in mixing rates. The change in mixing regimes is due to advective transport accessible to the turbulent state. Some flows can transition through a linear instability of the laminar flow. In contrast systems like plane Couette flow which are stable to infinitesimal perturbations exhibit transitions to turbulence for finite amplitude perturbations.

1.1.1 Equations of Motion

The governing equations of fluid flow can be constructed through two very different approaches. The most fundamental method of generating equations of fluid motion begins with a continuously labelled set of fluid particles from which a Hamiltonian is constructed[1]. From this Hamiltonian formulation conservation laws may in principle be derived using

[1]For a discussion of Hamiltonian dynamics of fluids see [4, 8]

Noether's theorem. For most fluids it is difficult to write an expression for the Hamiltonian in this manner as the natural co-ordinate system is advected with the particles.

An alternate approach constructs a set of partial differential equations which include specific conservation laws. This approach is also more amenable to inclusion of empirical equations of state and stress strain relations. The Navier-Stokes equations

$$\frac{\partial v}{\partial t} + v \cdot \nabla v = -\frac{1}{\rho}\nabla p + \frac{1}{\mathrm{R}}\nabla^2 v_i \tag{1.1}$$

$$\frac{\partial \rho}{\partial t} + \nabla \cdot \rho v = 0 \tag{1.2}$$

are derived in this manner, using assumptions about diffusion of fluid properties and conservation of mass and momentum. The parameter R is the Reynolds number which gives a measure of the relative influence of diffusion and advection. The ratio of advective and diffusive transports is given by the Reynolds number[7, 9, 6]

$$\mathrm{R} = \frac{UL}{\nu} \tag{1.3}$$

where U and L are characteristic velocity and length scales and ν is the molecular diffusivity.

These two modes of derivation can be bridged starting with governing equations from application of conservation laws then seeking to find a Hamiltonian system which is consistent with those dynamics. This requires an expression for the Hamiltonian H and a Poisson bracket operator $\{A, B\}$. The Poisson bracket is implicitly defined by the time evolution operator

$$\frac{\partial}{\partial t} A = \{A, H\} \tag{1.4}$$

For example in an ideal fluid is governed by the Euler equations

$$\frac{\partial v}{\partial t} + v \cdot \nabla v = -\frac{1}{\rho}\nabla p \tag{1.5}$$

$$\frac{\partial \rho}{\partial t} + \nabla \cdot \rho v = 0 \tag{1.6}$$

$$\frac{\partial s}{\partial t} + v \cdot \nabla s = 0 \tag{1.7}$$

and have a Hamiltonian takes of the form

$$H[v, \rho, s] = \iiint \frac{1}{2}\rho v \cdot v + \rho U(\rho, s)\ \mathrm{d}^3 r \tag{1.8}$$

where v is the velocity, ρ is density, s is entropy density and U is internal energy. The Poisson bracket for this system is found explicitly by [5, 4]

$$\begin{aligned} \{A, B\} = & -\iiint \frac{\delta A}{\delta \rho}\nabla \cdot \frac{\delta B}{\delta v} - \frac{\delta B}{\delta \rho}\nabla \cdot \frac{\delta A}{\delta v} \\ & + \frac{\nabla \times v}{\rho} \cdot \frac{\delta B}{\delta v} \times \frac{\delta A}{\delta v} \\ & + \frac{\nabla s}{\rho} \cdot \left(\frac{\delta A}{\delta s}\frac{\delta B}{\delta v} - \frac{\delta B}{\delta s}\frac{\delta A}{\delta v} \right) \mathrm{d}^3 r \end{aligned} \tag{1.9}$$

where $\frac{\delta A}{\delta v}$ is the functional derivative. It is from this middle road approach we take the inspiration for analysis of low order models of turbulence.

1.1.2 Flow parameters

Since the ideal fluid (1.5) is the limit as $\mathrm{R} \to \infty$ of the viscous fluid (1.1) it is instructive to describe some of the characteristics such flows. Before continuing the analysis we further restrict ourselves to incompressible flows. This replaces the density evolution equation with the requirement that velocity be divergence free $\nabla \cdot v = 0$. To highlight the differences between incompressible solutions to (1.5) and (1.1) we will focus on the evolution of three quantities. Kinetic energy $\frac{1}{2}v^2$, vorticity $\omega = \frac{1}{2}\nabla \times v$, and helicity $\omega \cdot v$ are governed by the transport equations

$$\frac{\partial}{\partial t}\frac{v^2}{2} = \nabla_i \left(-\frac{v_i P}{\rho} + \frac{1}{\mathrm{R}} \nabla_i \frac{v^2}{2} \right) - \frac{\left(\nabla_i u_j\right)^2}{\mathrm{R}} \tag{1.10}$$

$$\frac{\partial}{\partial t}\omega_i = \nabla_j \left(\omega_j v_i - v_j \omega_i + \frac{1}{\mathrm{R}} \nabla_j \omega_i \right) \tag{1.11}$$

$$\frac{\partial}{\partial t} v_i \omega_i = \nabla_i \left(\frac{\rho v^2 - 2P}{2\rho} \omega_i - v_i v_j \omega_j + \frac{\nabla_i \omega_j v_j}{\mathrm{R}} \right) - \frac{2\left(\nabla_j \omega_i\right)\left(\nabla_j v_i\right)}{\mathrm{R}}. \tag{1.12}$$

For the inviscid case the transport equations are a flux divergence and these quantities are conserved. When viscosity is introduced energy is damped and vorticity is made more homogeneous. The influence of diffusion on helicity is more complex, in addition to a homogenizing diffusive term there is an additional term whose sign is indeterminate.

At large but finite Reynolds number diffusion is weak and only has influence at very small length scales. This separation of scales is the basis of the Kolmogorov hypothesis where at intermediate scales the motion self-organizes so that there is a constant energy dissipation rate ϵ. The Kolmogorov length scale

$$\eta = \sqrt[4]{\nu^3/\epsilon} \propto \sqrt[4]{\frac{1}{\mathrm{R}}} \tag{1.13}$$

is the scale at which diffusion can dissipate all the energy input and sets a lower bound on the size of flow persistent features[9, 6].

1.1.3 Truncation

For very viscous flows the range of scales of motion available are limited, this has led to the exploration of low dimensional models of turbulent transitions [10, 3, 2]. Using a spectral decomposition of the flow these low order models retaining a subset of the modes which represent motion with the largest length scales and whose dynamics will be least damped. If density ρ is assumed to be constant (1.1) can be written in spectral form

$$\frac{\partial v(k)}{\partial t} + v(k) * ikv(k) = -\frac{1}{\rho} ikp(k) - \frac{1}{\mathrm{R}} k^2 v(k) \tag{1.14}$$

where $*$ is the convolution operator. Truncation changes the behaviour of the convolution operator by restricting the domain available in the spectral space to a set of amplitudes

Z_i. The result is a finite set of non-linear differential equations for the amplitude of the chosen modes. It is important to emphasize that the choice of which modes enter into the truncation can greatly effect the behaviour of the low dimensional system.

Projecting (1.1) into Fourier space $\hat{u}_i(k)$ imposes a strong constraint on the motion through phase space

$$\frac{\partial}{\partial \hat{u}_j(k)} \frac{\mathrm{d}\hat{u}_i(k)}{\mathrm{d}t} = 2\mathrm{i} \left(\delta_{ij} - \frac{k_i k_j}{k^2} \right) \hat{u}_m(0) k_m - \frac{1}{\mathrm{R}} k^2 \delta_{ij}. \tag{1.15}$$

Trajectories in the inviscid limit $\frac{1}{\mathrm{R}} \to 0$, with no mean flow $\hat{u}(0) = 0$ are divergence free. These divergence free trajectories additionally satisfy a Detailed Liouville where each term in the sum (1.15) is separately zero. This Detailed Liouville behaviour in Fourier space has been noted by [1] without the constraint on mean flow.

Some additional properties of the trajectories are low dimensional analogues of Flux-divergence conservation laws of the full partial differential equation. If Fourier modes are used for the decomposition there are some basic properties which all truncations will share. The volume average of these transport equations can be used to form additional constraints on the amplitudes of a Fourier decomposition. By Parceval's theorem mean kinetic energy is simply the sum of squares of Fourier amplitudes and must evolve according to

$$\sum_{i=1}^{N} Z_i \dot{Z}_i = -\frac{1}{\mathrm{R}} \sum_{i=1}^{N} \kappa_i^2 Z_i^2 \tag{1.16}$$

where κ_i is the wave vector for mode i. Similarly mean vorticity $\sum_{i=1}^{N} Z_i \omega(Z_i)$ and mean helicity $\sum_{i=1}^{N} Z_i \varpi(Z_i)$ must evolve according to

$$\sum_{i=1}^{N} \dot{Z}_i \omega(Z_i) = -\frac{1}{\mathrm{R}} \sum_{i=1}^{N} \kappa_i^2 Z_i \omega(Z_i) \tag{1.17}$$

$$\sum_{i=1}^{N} \dot{Z}_i \varpi(Z_i) = -\frac{2}{\mathrm{R}} \kappa_i \omega_j(Z) * \kappa_i u_j(Z) \tag{1.18}$$

where $u(Z_i)$, $\omega(Z_i)$, and $\varpi(Z_i)$ are the velocity, vorticity and helicity in mode Z_i when it has unit amplitude. Mean vorticity dynamics rarely contribute to low order truncations, it is common to have no modes with mean vorticity [2], one mode out of eight [10], or two modes out of nine [3]. Helicity dynamics are absent in low order models where all the included modes have zero helicity [10, 3, 2]. The absence of helicity is due to the choice of modes not the boundary conditions, in the domain used by [10, 3] a helical mode with similar wave-numbers to those included in the truncation is of the form

$$\vec{u} = \begin{pmatrix} \cos^2 \pi y \sin \pi y \\ 0 \\ \cos \pi y \sin^2 \pi y \end{pmatrix} \tag{1.19}$$

where the velocity spirals between the boundaries.

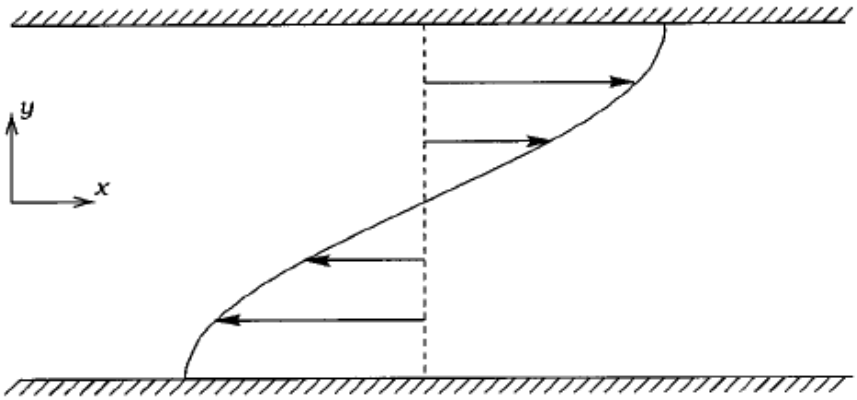

Figure 1.1: Mean flow mode M from [10]

1.2 Examination of Low Order Models

Analogously to how [5, 4] take the continuum equations for momentum balance in an ideal fluid we hope to connect the low order models of [10] to an underlying Hamiltonian system in the inviscid limit. With that goal in mind the necessary conditions of truncations are checked for the four and five dimensional systems proposed and both systems are found to behave in a manner inconsistent with a truncation. In the inviscid limit the fourth order system has atracting regions in phase space and can not be a Hamiltonian system.

1.2.1 Detailed Liouville

In the inviscid limit any Fourier truncation is expected to be divergence free in phase space. This Liouvillian character of trajectories implies there can not be any purely attracting regions in phase space once the effects of viscosity have been removed. Because the parent model is a truncation of Fourier modes and there is no mean flow there is the stronger condition that the trajectories have a Detailed Liouville behaviour (1.15). Using Z_i for the amplitude of the i^{th} Fourier mode in the truncation

$$\frac{\partial \dot{Z}_i}{\partial Z_i} = 0 \text{ no sum on } i. \tag{1.20}$$

The simplest low order model we consider is the fourthorder model from [10]. This model has a mean flow M figure 1.1 and three additional modes charachterized as streaks U, Stream-wise vorticies, and a Streak Instability W which are combined into a Self Sustaining Process figure 1.2. The governing equations

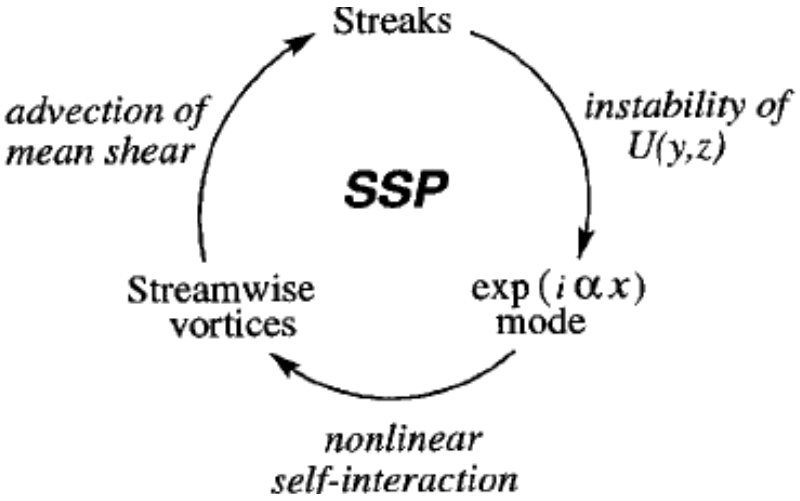

Figure 1.2: Self sustaining process from [10]

$$\text{Mean shear } \dot{M} = -UV + \Sigma_m W^2 - \frac{1}{R}(M-1) \tag{1.21}$$

$$\text{Streaks } \dot{U} = +MV + \Sigma_u W^2 - \frac{\kappa_u^2}{R}U \tag{1.22}$$

$$\text{Stream-wise Rolls } \dot{V} = +\Sigma_v W^2 - \frac{\kappa_v^2}{R}V \tag{1.23}$$

$$\text{Streak Instability } \dot{W} = -W(\Sigma_m M + \Sigma_u U + \Sigma_v V) - \frac{\kappa_w^2}{R}W \tag{1.24}$$

include a source term in the mean flow $\frac{1}{\mathrm{R}}(M-1)$ to model the input of energy from outside the system. The coupling constants $\Sigma_{m,u,v}$ arise from the convolution of the truncated modes. and are functions of the particular wave-numbers $\kappa_{u,v,w}$ chosen in the truncation. The equations have been made non-dimensional to minimize the number of constants. The fourth order model of [10] has an attracting orbit in the $\frac{1}{\mathrm{R}} \to 0$ limit is shown in figure 1.3

$$(M, U, V, W) = (M_0 \cos V_0 t, M_0 \sin V_0 t, V_0, 0). \tag{1.25}$$

This convergent behaviour in phase space indicated that the simplifying assumptions used to reduce the model from an eighth order truncation introduced non-physical dissipation.

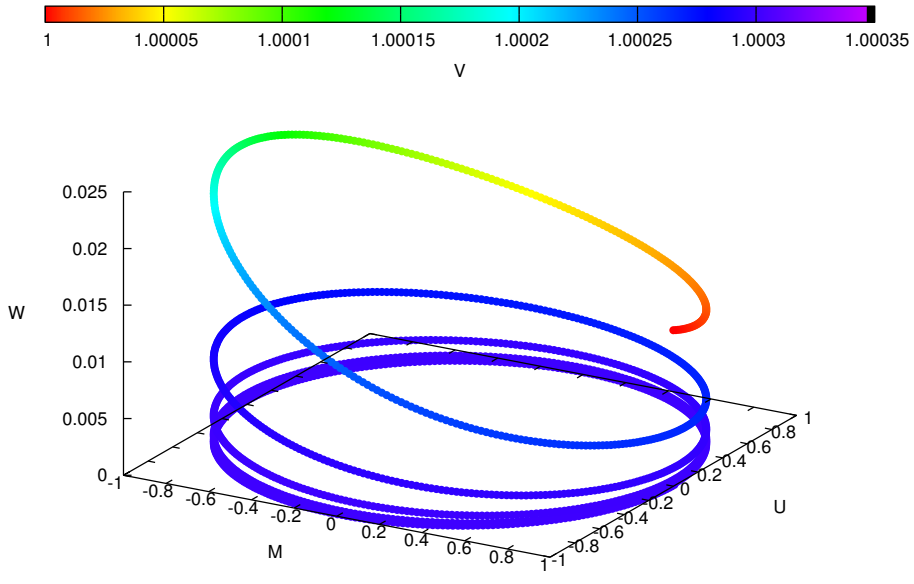

Figure 1.3: Attracting orbit of [10] 4 dimensional model in the limit $\frac{1}{\mathrm{R}} \to 0$. M, U, W are shown in projection and V is colored

The fifth order parent model

$$\text{Mean shear } \dot{M} = -UV + \Sigma_m AE - \frac{1}{R}(M-1) \tag{1.26}$$

$$\text{Streaks } \dot{U} = +MV + \Sigma_{ua} A^2 + \Sigma_{ue} E^2 - \frac{\kappa_u^2}{R} U \tag{1.27}$$

$$\text{Rolls } \dot{V} = +\Sigma_v AE - \frac{\kappa_v^2}{R} V \tag{1.28}$$

$$\dot{A} = -\frac{E}{2}(\Sigma_m M + \Sigma_v V) - \Sigma_{ua} UA - \frac{\kappa_a^2}{R} A \tag{1.29}$$

$$\dot{E} = -\frac{A}{2}(\Sigma_m M + \Sigma_v V) - \Sigma_{ue} UE - \frac{\kappa_e^2}{R} E \tag{1.30}$$

is non-divergent but fails the more stringent requrement of being Detailed Liouvillian (1.20). Using the fifth order model from [10] as a starting point a similar set of equations which

satisfies Detailed Liouville (1.20) is constructed

$$\begin{aligned}
\text{Mean shear } \dot{M} &= -UV + \Sigma_m AE - \frac{1}{R}(M-1) \\
\text{Streaks } \dot{U} &= +MV + \Sigma_u AE - \frac{\kappa_u^2}{R}U \qquad (1.31) \\
\text{Rolls } \dot{V} &= +\Sigma_v AE - \frac{\kappa_v^2}{R}V \\
\dot{A} &= -\frac{E}{2}(\Sigma_m M + \Sigma_u U + \Sigma_v V) - \frac{\kappa_a^2}{R}A \qquad (1.32) \\
\dot{E} &= -\frac{A}{2}(\Sigma_m M + \Sigma_u U + \Sigma_v V) - \frac{\kappa_e^2}{R}E \qquad (1.33)
\end{aligned}$$

where A^2 and E^2 have been replaced by a term proportional to AE in (1.27) and terms proportional to UA in (1.29) have been replaced by UE and vice-versa in (1.30). In the inviscid limit this new set of equations satisfies Detailed Liouville (1.20), as well as conservation of energy (1.16), and vorticity (1.17).

The stability of the laminar state equilibrium, where $M = 1$ and all others are zero, can be explored using energy stability. The laminar state L_i is globally stable with respect to the energy while

$$\frac{\mathrm{d}}{\mathrm{d}t}(Z_i - L_i)^2 \leq 0 \qquad (1.34)$$

for any system state Z_i. This criterion is dependent on the value of R, in fact the laminar state is stable only if both

$$\begin{aligned}
\mathrm{R} &\leq 2|\kappa_u \kappa_v| \qquad (1.35) \\
\mathrm{R} &\leq 2\left|\frac{\kappa_a \kappa_e}{\Sigma_m}\right| \qquad (1.36)
\end{aligned}$$

hold. The other equilibria of the system of equations can be found by solving the roots of a 5^{th} order polynomial, but the solution is not amenable to testing limiting behaviour. The equilibria criteria can be simplified into the relations

$$\begin{aligned}
U &= -\frac{\Sigma_m \Sigma_v M^2 + \frac{\Sigma_m \Sigma_u \kappa_v^2 - 2\kappa_a \kappa_e \Sigma_v}{R} M - \frac{2\kappa_a \kappa_e \Sigma_u \kappa_v^2}{R^2}}{\Sigma_u \Sigma_v M + \frac{\kappa_u^2 \Sigma_v^2 + \Sigma_u^2 \kappa_v^2}{R}} \qquad (1.37) \\
V &= \frac{\kappa_u^2 \Sigma_v U}{\Sigma_v R M + \Sigma_u \kappa_v^2} \qquad (1.38) \\
E^2 &= -\frac{\kappa_a \kappa_v^2 V}{\kappa_e \Sigma_v R} \qquad (1.39) \\
A^2 &= \frac{\kappa_e^2}{\kappa_a^2} E^2 \qquad (1.40)
\end{aligned}$$

in addition to the trivial solution $M = U = V = A = E = 0$. From these relations and

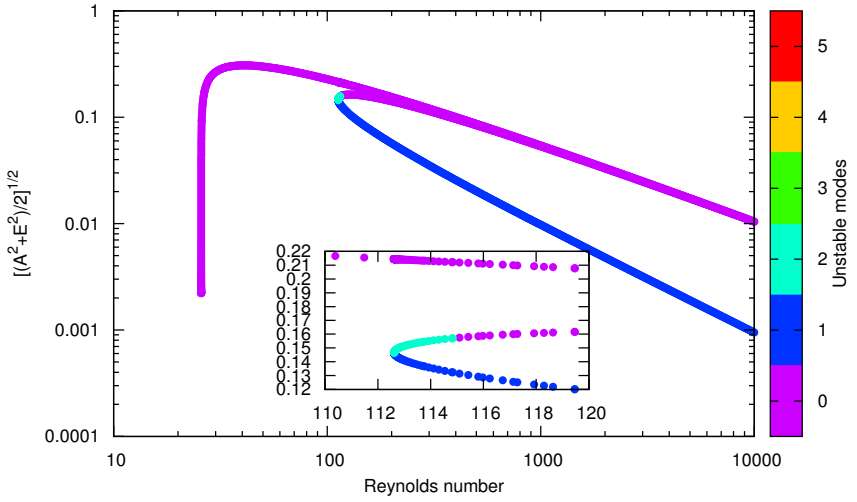

Figure 1.4: Equilibrium solutions as a function of Reynolds number, colored by number of unstable modes

(1.26) the limiting behaviour as $\mathrm{R} \to \infty$

$$M \rightarrow \frac{1}{1+\kappa_u^2 \frac{\Sigma_m^2}{\Sigma_u^2}} \tag{1.41}$$

$$U \rightarrow -\frac{\Sigma_m}{\Sigma_u} M \tag{1.42}$$

$$V \rightarrow -\frac{\Sigma_m \kappa_u^2}{\Sigma_u R} \tag{1.43}$$

$$E^2 \rightarrow \frac{\kappa_a \Sigma_m \kappa_v^2 \kappa_u^2}{\kappa_e \Sigma_u \Sigma_v R^2} \tag{1.44}$$

$$A^2 \rightarrow \frac{\kappa_e \Sigma_m \kappa_v^2 \kappa_u^2}{\kappa_a \Sigma_u \Sigma_v R^2} \tag{1.45}$$

which differs from both the zero and laminar solutions. At finite Reynolds number these solutions come in families where the sign of E, and A are arbitrary when (1.39) has real roots.

To continue to characterize the behavior of the system it is helpful to use numerical methods and integrate the equations of motion. Since the equilibria are insensitive to the sign of A or E and both the trivial and laminar states have $A = E = 0$ figure 1.4 plots $\sqrt{\frac{1}{2}(A^2 + E^2)}$ of the equilibria against Reynolds number. The laminar equilibrium becomes an unstable equilibrium at a Reynolds number between 20 and 30. The break in the graph

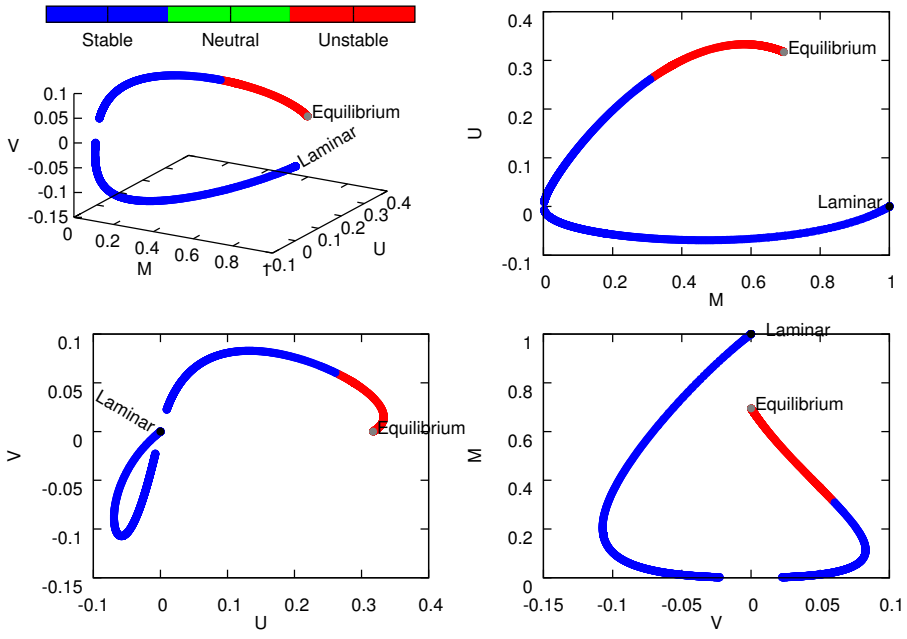

Figure 1.5: Equilibrium solutions colored by stability

in that region is due to the discrete step size taken in Reynolds number. Two additional unstable equilibria arise near R $\approx$ 113 unlike the equilibrium near R $\approx$ 20 which is stable. One equilibrium remains unstable for all Reynolds numbers while the other becomes stable for increasing Reynolds number.

The nature of this transition can be more easily seen in figures 1.5 and 1.6 where the equilibria are plotted in M, U, V space. The two curves show the two disjoint families of equilibrium of solutions. As Reynolds number is increased the laminar state smoothly transitions to a state of no motion. In contrast at moderate Reynolds number another set of solutions come into existence, an unstable equilibrium smoothly approaches the inviscid equilibrium state as Reynolds number increases. The other equilibrium is initially very unstable ubt quickly become stable and smoothly approaches the state of no motion. This show two co-existing stable equilibria which approach each other in the limit of large Reynolds number.

1.2.2 Hamiltonian

Having modified the five dimensional system to satisfy Detailed Liouville we now seek to find a Hamiltonian system from which it can be derived. The construction is simplified by the quadratic form of the energy

$$H = M^2 + U^2 + V^2 + A^2 + E^2 \tag{1.46}$$

where the H is chosen to emphasize that in the inviscid system the Hamiltonian is the energy. Now we need a co-ordinate transformation so that we can recover the equations of

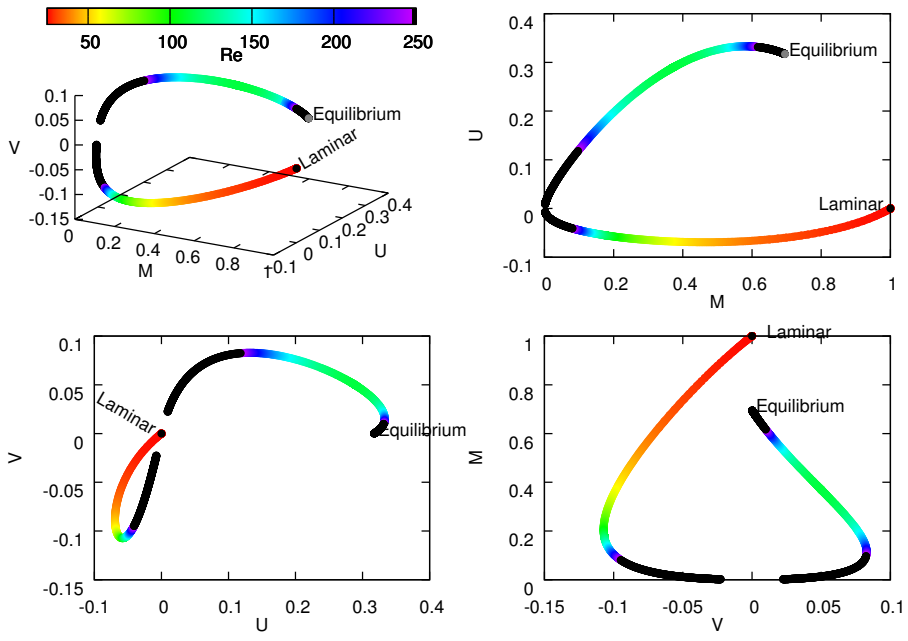

Figure 1.6: Equilibrium solutions colored by Reynolds number

motion using a Poisson bracket

$$\dot{Z}^i = \left\{ Z^i, H \right\}. \tag{1.47}$$

For finite dimension Hamiltonian systems the Poisson bracket used for time evolution can be written in a general from

$$\{f, g\} = \frac{\partial f}{\partial Z^i} J^{ij} \frac{\partial g}{\partial Z^j} \tag{1.48}$$

where J^{ij} is an anti-symmetric tensor which satisfies the Jacobi identity

$$S^{ijk} = J^{im} \frac{\partial J^{jk}}{\partial Z^m} + J^{jm} \frac{\partial J^{ki}}{\partial Z^m} + J^{km} \frac{\partial J^{ij}}{\partial Z^m} + = 0 \tag{1.49}$$

Because we are using a quadratic Hamiltonian and are enforcing Detailed Liouville the tensor J^{ij} is of the form

$$J^{ij} = C_k^{ij} Z^k \tag{1.50}$$

where C_k^{ij} form a Lie algebra. For four dimensional systems there are only two Lie algebras which give rise to full rank tensors J^{ij}, the two archetypal forms of the J tensor are

$$J^{ij} = \begin{pmatrix} 0 & -Z_1 & 0 & 0 \\ Z_1 & 0 & 0 & 0 \\ 0 & 0 & 0 & -Z_3 \\ 0 & 0 & Z_3 & 0 \end{pmatrix} \text{ or } \begin{pmatrix} 0 & -Z_3 & 0 & 0 \\ Z_3 & 0 & 0 & 0 \\ 0 & 0 & 0 & -Z_1 \\ 0 & 0 & Z_1 & 0 \end{pmatrix} \tag{1.51}$$

but neither admit linear co-ordinate transformations which reproduce the characteristics of the fourth order model of [10] such as non-normality. For the five dimensional case the

possible Lie algebras have not been exhausted but no J^{ij} which satisfies the Poisson bracket has been found which satisfies the Jacobi identity (1.49).

1.3 Conclusion

A non-dimensional version of the low order models in [10] have been shown to introduce an additional damping not present in the continuous system. Hamiltonian generalization of the fourth order model has been been excluded using properties of Lie algebras. The fifth order model [10] has been shown to violate the Detailed Liouville criterion, a simple substitution was introduced into the fifth order model to recover Detailed Liouville. The behaviour of this modified fifth order model is explored in detail and the stability and multiplicity of the equilibria is shown for a range of Reynolds numbers. No conclusive statement is made about the existence of a Hamiltonian parent model for the models of order higher than four. A trial form for the anti-symmetric tensors J^{ij} was found for both fifth order systems was found which satisfied time evolution as a Poisson bracket. The candidate tensors fail the Jacobi identiy, the time evolution only uniquely determines J^{ij} for systems of order three and less and no general statement can be made from the failure of of the Jacobi identity for these particular tensors.

Bibliography

[1] T. D. Lee, *On some statistical properties of hydrodynamical and magnetohydrodynamical fields*, Quarterly of Applied Mathematics, 10 (1952), pp. 69–74.

[2] G. Mariotti, *A low dimensional model for plane poiseuille flow.* Woods Hole Geophysical Fluid Dynamics Program, 2011.

[3] J. Moehlis, H. Faisst, and B. Eckhardt, *A low-dimensional model for turbulent shear flows*, New Journal of Physics, 6 (2004), p. 56.

[4] P. J. Morrison, *Hamiltonian description of the ideal fluid*, Reviews of Modern Physics, 70 (1998), pp. 467–521.

[5] P. J. Morrison and J. M. Greene, *Noncanonical hamiltonian density formulation of hydrodynamics and ideal magnetohydrodynamics*, Phys. Rev. Lett., 45 (1980), pp. 790–794.

[6] S. Pope, *Turbulent Flows*, Cambridge Univ. Press, 2000.

[7] O. Reynolds, *An experimental investigation of the circumstances which determine whether the motion of water shall be direct or sinuous, and of the law of resistance in parallel channels.*, Proceedings of the Royal Society of London, 35 (1883), pp. 84–99.

[8] R. Salmon, *Lectures on geophysical fluid dynamics*, Oxford University Press, USA, 1998.

[9] H. Tennekes and J. L. Lumley, *A First Course in Turbulence*, The MIT Press, 1972.

[10] F. Waleffe, *On a self-sustaining process in shear flows*, Physics of Fluids, 9 (1997), pp. 883–900.

Project 2

On One-Fluid MHD Models with Electron Inertia

Keiji Kimura

Kyoto University

We investigate the limitations of various MHD models that include electron inertia by considering expansion in terms of non-dimensional parameters, and by classifying those that have energy conservation. It is revealed that a correction term in the momentum equation, which is usually neglected, is needed to conserve the total energy. In order to investigate the effect of this correction term, a modified Grad-Shafranov equation is obtained in the "straight torus," i.e., where toroidal curvature is neglected, for the cases when the plasma has constant density or is barotropic. In the case with toroidal curvature, some conditions on the magnetic field in a torus are needed even if the plasma has constant density.

2.1 Introduction

The usual ideal magnetohydrodynamic (MHD) model is often used in various fields, for instance, in astrophysics, nuclear fusion and geophysics. Of course, as with all models, ideal MHD has some limitations, such as in a specific regions where magnetic reconnection takes place, which is considered to have an important role in energy transfer. Other effects can also be important and the MHD model may breakdown for other reasons. Consequently, many researchers have considered other MHD models (usually called extended MHD) and investigated their properties both analytically and numerically. However different researchers have used different extended MHD models [1, 3, 4, 10], and the relation and limitation between these models seems to be unknown. For all of these models the difference only exists in the generalized Ohm's law, with the momentum equation being the same as the usual MHD model.

Here we first classify models with electron inertial in terms of energy conservation; we find which models have an energy conservation law. Next, to investigate the effect of electron inertia, we try to generalize the Grad-Shafranov equation, which describes the equilibrium

state with no flow and axisymmetry in a torus [5, 6]. Finally, we introduce some equilibrium states with flow in an incompressible plasma.

This report is organized as follows. In Section 2.2 we discuss the limitations of some inertial MHD models and investigate their energy conservation. In Section 2.3, we classify some inertial MHD models in terms of energy conservation. In Section 2.4 we try to modify the Grad-Shafranov equation to include the effect of electron inertia term and in Section 2.5 we introduce some equilibrium states with constant density and with flow. Finally, Conclusions and discussions are given in Section 2.6.

2.2 Limitation and Energy Conservation of Inertial MHD Model

In this section we derive the asymptotically consistent inertial MHD (IMHD) model from a complete one-fluid model. We consider an electron-ion plasma that is completely ionized. The one-fluid model has been derived from kinetic theory (see e.g. [3, 2]) of charged particles, that is, a plasma. We begin with the model of Lüst [8] who derived the continuity equation, the momentum equation, and the generalized Ohm's law for the one-fluid model.

Using the fact that the electron mass is much lighter than the ion mass and assuming the plasma is quasi-neutral, we obtain the continuity equation, the momentum equation, and the generalized Ohm's law as follows:

$$
\begin{aligned}
0 &= \frac{\partial \rho}{\partial t} + \nabla \cdot (\rho \mathbf{S}V), \\
\rho \left(\frac{\partial \mathbf{S}V}{\partial t} + (\mathbf{S}V \cdot \nabla)\mathbf{S}V \right) &= -\nabla p + \mathbf{S}j \times \mathbf{S}B - \frac{m_e}{e}(\mathbf{S}j \cdot \nabla)\frac{\mathbf{S}j}{en}, \\
\mathbf{S}E + \mathbf{S}V \times \mathbf{S}B &= \frac{1}{\sigma}\mathbf{S}j + \frac{1}{en}(\mathbf{S}j \times \mathbf{S}B - \nabla p_e) \\
&\quad + \frac{m_e}{e^2 n}\left[\frac{\partial \mathbf{S}j}{\partial t} + \nabla \cdot (\mathbf{S}V\mathbf{S}j + \mathbf{S}j\mathbf{S}V) \right] \\
&\quad - \frac{m_e}{e^2 n}(\mathbf{S}j \cdot \nabla)\frac{\mathbf{S}j}{en},
\end{aligned}
$$

where ρ is the density of plasma, $\mathbf{S}V$ the bulk velocity, p the pressure, $\mathbf{S}j$ the current density, $\mathbf{S}B$ the magnetic field, m_e the electron mass, e the elementary charge, n the number density of each species of charged particles, $\mathbf{S}E$ the electric field, σ the conductivity, and p_e the electron pressure. Note that the momentum equation is equivalent to the summation of the momentum equations of the electron and ion species, and the generalized Ohm's law is the difference. Ohm's law can be viewed as representing the momentum equation of electron.

The last term on the right-hand-side of the momentum equation exists due to the electron inertia. We call the second term on the left-hand-side of the generalized Ohm's law the "nonlinear term," the first term on the right-hand-side the "collision term," the second term the "Hall term," and the third and fourth terms will be called the "electron inertia

terms." To compare the size of these terms, we use the following characteristic numbers:

$$\begin{aligned} Re_m &\equiv \frac{\text{Nonlinear term}}{\text{Collision term}} = \sigma\mu_0 UL, \\ C_H &\equiv \frac{\text{Hall term}}{\text{Collision term}} = \frac{\sigma B}{en}, \\ C_I &\equiv \frac{\text{Electron inertia term}}{\text{Collision term}} = \frac{\sigma m_e}{e^2 n\tau}, \end{aligned}$$

where U, L, B, and τ are the characteristic velocity scale, length scale, magnitude of magnetic field, and time scale of current change, respectively. The number Re_m is called the magnetic Reynolds number.

In this report we focus on the situation where the electron inertia term is much larger than the collision term and the Hall term; however, the nonlinear term is still considered to be large enough to be comparable with the electron inertia term, that is,

$$Re_m \gg 1,\ C_I \gg 1,\ \frac{C_I}{C_H} \gg 1.$$

Since the last relation is equivalent to

$$\frac{C_I}{C_H} = \frac{m_e}{eB}\frac{1}{\tau} = \frac{1}{\Omega_{Ge}\tau},$$

where Ω_{Ge} is the electron gyro-frequency, this relation can be interpreted as saying that the characteristic time scale of the current change is much shorter than the gyro-period of the electron.

Finally, we obtain the IMHD model given by the following equations:

$$0 = \frac{\partial \rho}{\partial t} + \nabla\cdot(\rho \mathbf{S}V), \tag{2.1}$$

$$\rho\left(\frac{\partial \mathbf{S}V}{\partial t} + (\mathbf{S}V\cdot\nabla)\mathbf{S}V\right) = -\nabla p + \mathbf{S}j\times\mathbf{S}B - \epsilon\,\frac{m_e}{e}(\mathbf{S}j\cdot\nabla)\frac{\mathbf{S}j}{en}, \tag{2.2}$$

$$\mathbf{S}E + \mathbf{S}V\times\mathbf{S}B = \epsilon\,\frac{m_e}{e^2 n}\left[\frac{\partial \mathbf{S}j}{\partial t} + \nabla\cdot(\mathbf{S}V\mathbf{S}j + \mathbf{S}j\mathbf{S}V)\right] - \delta\frac{m_e}{e^2 n}(\mathbf{S}j\cdot\nabla)\frac{\mathbf{S}j}{en}, \tag{2.3}$$

$$0 = \frac{\partial S}{\partial t} + (\mathbf{S}V\cdot\nabla)S, \tag{2.4}$$

where S is the entropy of the plasma and the last equation means the plasma is adiabatic. We have inserted book keeping parameters ϵ and δ to label terms, yet both of these have value unity. The above equations are to be solved with the pre-Maxwell's equations,

$$\begin{aligned} \nabla\cdot\mathbf{S}E &= 0, \\ \nabla\cdot\mathbf{S}B &= 0, \\ \nabla\times\mathbf{S}E &= -\frac{\partial \mathbf{S}B}{\partial t}, \\ \nabla\times\mathbf{S}B &= \mu_0\mathbf{S}j. \end{aligned}$$

Note that because of quasi-neutrality, the current density is solenoidal, that is,

$$\nabla \cdot \mathbf{S}j = 0.$$

Next, let us consider the energy of this IMHD model. Taking the dot product of $\mathbf{S}V$ and the momentum equation, the dot product of $\mathbf{S}j$ and the generalized Ohm's law, and from the pre-Maxwell equations, we obtain the following energy relation:

$$\begin{aligned} 0 = \frac{\partial}{\partial t}\left(\frac{1}{2}\rho|\mathbf{S}V|^2 + \rho U + \epsilon\frac{m_e}{e^2 n}\frac{|\mathbf{S}j|^2}{2} + \frac{|\mathbf{S}B|^2}{2\mu_0}\right) \\ + \nabla\cdot\left[\left(\frac{1}{2}\rho|\mathbf{S}V|^2 + p + \rho U + \epsilon\frac{m_e}{e^2 n}\frac{|\mathbf{S}j|^2}{2}\right)\mathbf{S}V \right. \\ \left. + \epsilon\frac{m_e}{e^2 n}(\mathbf{S}V\cdot\mathbf{S}j)\mathbf{S}j - \delta\frac{m_e}{2e^3n^2}|\mathbf{S}j|^2\mathbf{S}j + \frac{\mathbf{S}E\times\mathbf{S}B}{\mu_0}\right]. \end{aligned}$$

Because of the electron inertia the term $\dfrac{m_e}{e^2 n}\dfrac{|\mathbf{S}j|^2}{2}$ is included in the energy density term. Note that, from the generalized Ohm's law, $\mathbf{S}E$ includes the time derivative term $\epsilon\dfrac{m_e}{e^2 n}\dfrac{\partial \mathbf{S}j}{\partial t}$, so the above formulation is not in the usual conservation form.[1] However, upon integrating the above energy relation over the whole domain V with appropriate boundary conditions, it is revealed that the total energy H, which is defined as

$$H \equiv \int_V \left(\frac{1}{2}\rho|\mathbf{S}V|^2 + \rho U + \epsilon\frac{m_e}{e^2 n}\frac{|\mathbf{S}j|^2}{2} + \frac{|\mathbf{S}B|^2}{2\mu_0}\right) d\mathbf{S}r,$$

is conserved.

2.3 Classification of Inertial MHD Model in terms of Energy Conservation

In this section we consider the classification of some IMHD models in terms of the energy conservation. In order to classify these models, we label the different epsilon term the different epsilon as is shown in the following arguments.

[1] When we solve the governing equations (2.1)–(2.4) with the full Maxwell's equations, we obtain the following energy relation:

$$\begin{aligned} 0 = \frac{\partial}{\partial t}\left(\frac{1}{2}\rho|\mathbf{S}V|^2 + \rho U + \epsilon\frac{m_e}{e^2 n}\frac{|\mathbf{S}j|^2}{2} + \frac{|\mathbf{S}B|^2}{2\mu_0} + \frac{1}{2}\epsilon_0|\mathbf{S}E|^2\right) \\ + \nabla\cdot\left[\left(\frac{1}{2}\rho|\mathbf{S}V|^2 + p + \rho U + \epsilon\frac{m_e}{e^2 n}\frac{|\mathbf{S}j|^2}{2}\right)\mathbf{S}V \right. \\ \left. + \epsilon\frac{m_e}{e^2 n}(\mathbf{S}V\cdot\mathbf{S}j)\mathbf{S}j - \delta\frac{m_e}{2e^3n^2}|\mathbf{S}j|^2\mathbf{S}j + \frac{\mathbf{S}E\times\mathbf{S}B}{\mu_0}\right], \end{aligned}$$

and this relation is of the usual conservation form.

First, we consider the compressible IMHD model which is governed by pre-Maxwell's equations and by the following equations:

$$
\begin{aligned}
0 &= \frac{\partial \rho}{\partial t} + \nabla \cdot (\rho \mathbf{S}V), \\
\rho \left(\frac{\partial \mathbf{S}V}{\partial t} + (\mathbf{S}V \cdot \nabla)\mathbf{S}V \right) &= -\nabla p + \mathbf{S}j \times \mathbf{S}B - \epsilon_{\mathrm{EOM}} \frac{m_e}{e} (\mathbf{S}j \cdot \nabla) \frac{\mathbf{S}j}{en}, \\
\mathbf{S}E + \mathbf{S}V \times \mathbf{S}B &= \epsilon_{\mathrm{t}} \frac{m_e}{e^2 n} \frac{\partial \mathbf{S}j}{\partial t} + \epsilon_{\mathrm{ad}} \frac{m_e}{e^2 n} (\mathbf{S}V \cdot \nabla)\mathbf{S}j + \epsilon_{\mathrm{cp}} \frac{m_e}{e^2 n} \mathbf{S}j (\nabla \cdot \mathbf{S}V) \\
&\quad + \epsilon_{\mathrm{M}} \frac{m_e}{e^2 n} (\mathbf{S}j \cdot \nabla)\mathbf{S}V - \delta \frac{m_e}{e^2 n} (\mathbf{S}j \cdot \nabla) \frac{\mathbf{S}j}{en}, \\
0 &= \frac{\partial S}{\partial t} + (\mathbf{S}V \cdot \nabla) S,
\end{aligned}
$$

where S is the entropy and δ, ϵ_{t} (time derivative), ϵ_{ad} (advection), ϵ_{cp} (compressible), ϵ_{M} (related to EOM), ϵ_{EOM} (in EOM) are labels of these terms. In this system, the energy conservation is as follows:

$$
\begin{aligned}
&\frac{\partial}{\partial t} \left(\frac{1}{2} \rho |\mathbf{S}V|^2 + \rho U + \epsilon_{\mathrm{t}} \frac{m_e}{e^2 n} \frac{|\mathbf{S}j|^2}{2} + \frac{|\mathbf{S}B|^2}{2\mu_0} \right) \\
&\quad + \nabla \cdot \left[\left(\frac{1}{2} \rho |\mathbf{S}V|^2 + p + \rho U + \epsilon_{\mathrm{ad}} \frac{m_e}{e^2 n} \frac{|\mathbf{S}j|^2}{2} \right) \mathbf{S}V \right. \\
&\qquad \left. + \epsilon_{\mathrm{M}} \frac{m_e}{e^2 n} (\mathbf{S}V \cdot \mathbf{S}j)\mathbf{S}j - \delta \frac{m_e}{e^3 n^2} \frac{|\mathbf{S}j|^2}{2} \mathbf{S}j + \frac{\mathbf{S}E \times \mathbf{S}B}{\mu_0} \right] \\
&= (\epsilon_{\mathrm{t}} - \epsilon_{\mathrm{ad}}) \frac{m_e}{e^2 n} \frac{|\mathbf{S}j|^2}{2} \frac{\nabla \cdot (n \mathbf{S}V)}{n} + (\epsilon_{\mathrm{ad}} - \epsilon_{\mathrm{cp}}) \frac{m_e}{e^2 n} |\mathbf{S}j|^2 (\nabla \cdot \mathbf{S}V) \\
&\quad + (\epsilon_{\mathrm{M}} - \epsilon_{\mathrm{EOM}}) \frac{m_e}{e} \mathbf{S}V \cdot \left\{ (\mathbf{S}j \cdot \nabla) \frac{\mathbf{S}j}{en} \right\}.
\end{aligned}
$$

Then, since the ϵ_{t} term have to exist in this model because when deriving the IMHD model we evaluate the electron inertia term using the characteristic time scale of current change, we find that the total energy is conserved only when all the epsilon terms exist or ϵ_{t}, ϵ_{ad} and ϵ_{cp} exist. Therefore we conclude that the epsilon term in the momentum equation is very important to conserve the total energy in IMHD model.

Secondly, we consider the incompressible IMHD model which is governed by pre-Maxwell's equations and by the following equations:

$$
\begin{aligned}
\rho = \rho_0 = \text{const.} \quad &\Leftrightarrow \quad n = n_0 = \text{const.}, \\
\rho_0 \left(\frac{\partial \mathbf{S}V}{\partial t} + (\mathbf{S}V \cdot \nabla)\mathbf{S}V \right) &= -\nabla p + \mathbf{S}j \times \mathbf{S}B - \epsilon_{\mathrm{EOM}} \frac{m_e}{e^2 n_0} (\mathbf{S}j \cdot \nabla)\mathbf{S}j, \\
\mathbf{S}E + \mathbf{S}V \times \mathbf{S}B &= \epsilon_{\mathrm{t}} \frac{m_e}{e^2 n_0} \frac{\partial \mathbf{S}j}{\partial t} + \epsilon_{\mathrm{ad}} \frac{m_e}{e^2 n_0} (\mathbf{S}V \cdot \nabla)\mathbf{S}j \\
&\quad + \epsilon_{\mathrm{M}} \frac{m_e}{e^2 n_0} (\mathbf{S}j \cdot \nabla)\mathbf{S}V - \delta \frac{m_e}{e^3 n_0^2} (\mathbf{S}j \cdot \nabla)\mathbf{S}j.
\end{aligned}
$$

Note that ϵ_{cp} do not exist in the above equations because of the incompressibility. In this

system, the energy conservation is as follows;

$$\begin{aligned}
&\frac{\partial}{\partial t}\left(\frac{1}{2}\rho_0|\mathbf{S}V|^2+\epsilon_{\mathrm{t}}\frac{m_e}{e^2n_0}\frac{|\mathbf{S}j|^2}{2}+\frac{|\mathbf{S}B|^2}{2\mu_0}\right)\\
&\quad+\nabla\cdot\left[\left(\frac{1}{2}\rho_0|\mathbf{S}V|^2+p+\epsilon_{\mathrm{ad}}\frac{m_e}{e^2n_0}\frac{|\mathbf{S}j|^2}{2}\right)\mathbf{S}V\right.\\
&\qquad\left.+\epsilon_{\mathrm{M}}\frac{m_e}{e^2n_0}(\mathbf{S}V\cdot\mathbf{S}j)\mathbf{S}j-\delta\frac{m_e}{e^3n_0^2}\frac{|\mathbf{S}j|^2}{2}\mathbf{S}j+\frac{\mathbf{S}E\times\mathbf{S}B}{\mu_0}\right]\\
&=(\epsilon_{\mathrm{M}}-\epsilon_{\mathrm{EOM}})\frac{m_e}{e^2n_0}\mathbf{S}V\cdot\{(\mathbf{S}j\cdot\nabla)\mathbf{S}j\}\,.
\end{aligned}$$

Then it is revealed that total energy is conserved when $\epsilon_{\mathrm{M}}=\epsilon_{\mathrm{EOM}}=0$ or 1, and there are no other constraints against ϵ_{t} and ϵ_{ad}.

ϵ_{t}	ϵ_{ad}	ϵ_{cp}	ϵ_{M}	Ohm's law $\quad\mathbf{S}E+\mathbf{S}V\times\mathbf{S}B=$	ϵ_{EOM}	Conserved?
Compressible plasma						
1	1	1	1	$\frac{m_e}{e^2n}\left(\frac{\partial\mathbf{S}j}{\partial t}+\nabla\cdot(\mathbf{S}V\mathbf{S}j+\mathbf{S}j\mathbf{S}V)\right)$	1	OK!
1	1	1		$\frac{m_e}{e^2n}\left(\frac{\partial\mathbf{S}j}{\partial t}+\nabla\cdot(\mathbf{S}V\mathbf{S}j)\right)$		OK!
1				$\frac{m_e}{e^2n}\frac{\partial\mathbf{S}j}{\partial t}$		$\frac{m_e}{e^2n}\frac{\|\mathbf{S}j\|^2}{2}\frac{\nabla\cdot(n\mathbf{S}V)}{n}$
1	1			$\frac{m_e}{e^2n}\left(\frac{\partial\mathbf{S}j}{\partial t}+(\mathbf{S}V\cdot\nabla)\mathbf{S}j\right)$		$\frac{m_e}{e^2n}\|\mathbf{S}j\|^2(\nabla\cdot\mathbf{S}V)$
1	1	1	1	$\frac{m_e}{e^2n}\left(\frac{\partial\mathbf{S}j}{\partial t}+\nabla\cdot(\mathbf{S}V\mathbf{S}j+\mathbf{S}j\mathbf{S}V)\right)$		$\frac{m_e}{e}\mathbf{S}V\cdot\left\{(\mathbf{S}j\cdot\nabla)\frac{\mathbf{S}j}{en}\right\}$
Incompressible plasma						
1		−		$\frac{m_e}{e^2n_0}\frac{\partial\mathbf{S}j}{\partial t}$		OK!
1	1	−		$\frac{m_e}{e^2n_0}\left(\frac{\partial\mathbf{S}j}{\partial t}+(\mathbf{S}V\cdot\nabla)\mathbf{S}j\right)$		OK!
1	1	−	1	$\frac{m_e}{e^2n_0}\left(\frac{\partial\mathbf{S}j}{\partial t}+\nabla\cdot(\mathbf{S}V\mathbf{S}j+\mathbf{S}j\mathbf{S}V)\right)$	1	OK!
1	1	−	1	$\frac{m_e}{e^2n_0}\left(\frac{\partial\mathbf{S}j}{\partial t}+\nabla\cdot(\mathbf{S}V\mathbf{S}j+\mathbf{S}j\mathbf{S}V)\right)$		$\frac{m_e}{e^2n_0}\mathbf{S}V\cdot\{(\mathbf{S}j\cdot\nabla)\mathbf{S}j\}$

Table 2.1: Classification of some IMHD models in terms of energy conservation. The epsilons in the generalized Ohm's law are listed from the first to fourth columns, and the generalized Ohm's law is described in the fifth column. The epsilon in the momentum equation are listed in the sixth column. When the total energy is conserved "OK!" is written in the last column, otherwise the remaining terms are written in the last column. Note that in a incompressible plasma, there is no ϵ_{cp} term in the generalized Ohm's law, then we write − in the third column in a incompressible plasma.

We summarize the classification of some IMHD models in terms of the energy conservation in Table 2.1.

2.4 Equilibrium States with No Flow – Grad-Shafranov Equation

In the previous section we find that $\epsilon_{\rm EOM}$ term is very important to conserve the energy in the MHD model. Then in this section, to investigate the effect of this term, we try to modify the Grad-Shafranov (GS) equation ([5],[6]) which can be derived from the (ideal) MHD model and describe the equilibrium state with no flow in a torus and with toroidal axisymmetry, for example, the axisymmetric toroidal plasma in a tokamak.

2.4.1 Modified Grad-Shafranov Equation in a "Straight Torus" with Constant Density

Let us consider the Grad-Shafranov equation of plasma with constant density in a "straight torus," which means a torus with no curvature, that is, a cylinder. We assume that the plasma is steady and z-independent, where z means the axis of the cylinder. Then, using the cylindrical coordinate (r, θ, z), the magnetic field can be described as

$$\mathbf{S}B = B_z \mathbf{S}e_z + \mathbf{S}e_z \times \nabla\psi,$$

and the current density is

$$\mathbf{S}j = \frac{1}{\mu_0}\nabla \times \mathbf{S}B = \frac{1}{\mu_0}\left[\mathbf{S}e_z(\nabla_\perp^2\psi) - \mathbf{S}e_z \times (\nabla_\perp B_z)\right],$$

where B_z and ψ are both z-independent and

$$\nabla_\perp \equiv \mathbf{S}e_r\frac{\partial}{\partial r} + \mathbf{S}e_\theta\frac{1}{r}\frac{\partial}{\partial\theta},$$
$$\nabla_\perp^2 \equiv \frac{1}{r}\frac{\partial}{\partial r}\left(r\frac{\partial}{\partial r}\right) + \frac{1}{r^2}\frac{\partial^2}{\partial\theta^2},$$

and $\mathbf{S}e_r$, $\mathbf{S}e_\theta$ are the unit vector toward the radial and polar angle direction, respectively. Then the governing equations can be simplified to the following equations:

$$\mathbf{S}0 = -\nabla p + \mathbf{S}j \times \mathbf{S}B - \epsilon\frac{m_e}{e^2 n_0}(\mathbf{S}j \cdot \nabla)\mathbf{S}j, \tag{2.5}$$

$$\mathbf{S}0 = \nabla \times \mathbf{S}E = -\delta\frac{m_e}{e^3 n_0^2}\nabla \times [(\mathbf{S}j \cdot \nabla)\mathbf{S}j], \tag{2.6}$$

where p is also z-independent.

First we focus on the momentum equation (2.5). Considering the z component of the momentum equation, we obtain

$$0 = \left\{\psi - \tilde{\epsilon}\nabla_\perp^2\psi,\ B_z\right\},$$

where $\tilde{\epsilon} \equiv \epsilon m_e/(\mu_0 e^2 n_0)$ and

$$\{f, g\} \equiv \mathbf{S}e_z \cdot (\nabla_\perp f \times \nabla_\perp g),$$

where f and g are both z-independent [2] . Then we obtain the first constraint, that is,

$$\psi - \tilde{\epsilon}\nabla_\perp^2\psi \equiv L(B_z), \tag{2.7}$$

where L is an arbitrary function of B_z.

Taking the dot product of $\mathbf{S}j$ and the momentum equation, we obtain

$$\begin{aligned} 0 &= \left\{ \mu_0 p + \tilde{\epsilon}\ \frac{(\nabla_\perp^2\psi)^2}{2} + \tilde{\epsilon}\ \frac{|\nabla_\perp B_z|^2}{2}, B_z \right\}, \\ \Leftrightarrow \quad M(B_z) &\equiv \mu_0 p + \tilde{\epsilon}\ \frac{(\nabla_\perp^2\psi)^2}{2} + \tilde{\epsilon}\ \frac{|\nabla_\perp B_z|^2}{2}, \end{aligned} \tag{2.8}$$

where $M(B_z)$ is an arbitrary function of B_z, and this is the second constraint.

Taking the dot product of $\nabla_\perp\psi$ and the momentum equation and substituting the above two constraints (2.7) and (2.8), we obtain the third constraint described as

$$0 = \frac{dM}{dB_z} + \frac{dL}{dB_z}(\nabla_\perp^2\psi) + B_z - \tilde{\epsilon}(\nabla_\perp^2 B_z). \tag{2.9}$$

Considering $\epsilon \to 0$, the first constraint (2.7) means B_z is a function of ψ, that is, $B_z \equiv F(\psi)$, then the second constraint means p is also a function of ψ, and the third constraint becomes

$$\nabla_\perp^2\psi = -\mu_0\frac{dp}{d\psi} - F\frac{dF}{d\psi}, \tag{2.10}$$

which is the incompressible Grad-Shafranov equation in a "straight torus."

Next we consider the constraint from the δ term (2.6) with the above three constraints with finite ϵ. After some calculations, we obtain the following equation from (2.6):

$$\mathbf{S}0 = -\frac{dL}{dB_z}\nabla_\perp\psi \times \nabla_\perp B_z + \nabla \times (\nabla_\perp\psi \times \nabla_\perp B_z),$$

then we find that

$$\nabla_\perp\psi \times \nabla_\perp B_z \equiv \mathbf{S}0, \quad \Leftrightarrow \quad B_z \equiv F(\psi), \tag{2.11}$$

where F is an arbitrary function of ψ, and this is the fourth constraint.

¿From the first constraint (2.7) and the fourth one (2.11), $\nabla_\perp^2\psi$ is also a function of ψ. Then $|\nabla_\perp\psi|^2$ is also a function of ψ because of the relation that $\nabla_\perp^2 B_z = F''|\nabla_\perp\psi|^2 + F'\nabla_\perp^2\psi$ with the third constraint (2.9) and the fact that $\nabla_\perp^2\psi$ is a function of ψ. So we define

$$|\nabla_\perp\psi|^2 \equiv K(\psi).$$

Then, considering the second constraint (2.8) with the relation that $|\nabla_\perp B_z|^2 = F'^2|\nabla_\perp\psi|^2$, it is revealed that p is also a function of ψ.

[2] If $\{f, g\} = 0$, f is an arbitrary function of g, or g is an arbitrary function of f.

Finally, after some calculations, we obtain the following equation from the third constraint (2.9):

$$\nabla_\perp^2 \psi = -\frac{1}{1-\tilde{\epsilon}F'^2}(\mu_0 p' + FF') - \frac{\tilde{\epsilon}F'^2}{1-\tilde{\epsilon}F'^2}\frac{K'}{2}, \tag{2.12}$$

where prime means the derivative of ψ, and this is the modified incompressible Grad-Shafranov equation in a "straight torus." Note that when $\epsilon \to 0$, the above equation becomes the (usual) incompressible Grad-Shafranov equation in a "straight torus" already shown in (2.10).

2.4.2 Modified Grad-Shafranov Equation in a "Straight Torus"

Next, let us consider the Grad-Shafranov equation of compressible plasma in a "straight torus." Then the governing equations are

$$\mathbf{S}0 = -\frac{1}{m_e n}\nabla p + \frac{1}{m_e n}\mathbf{S}j \times \mathbf{S}B - \epsilon\left(\frac{\mathbf{S}j}{en}\cdot\nabla\right)\frac{\mathbf{S}j}{en}, \tag{2.13}$$

$$\mathbf{S}0 = \nabla \times \mathbf{S}E = -\delta\frac{m_e}{e}\nabla \times \left[\left(\frac{\mathbf{S}j}{en}\cdot\nabla\right)\frac{\mathbf{S}j}{en}\right]. \tag{2.14}$$

We assume p, n, B_z and ψ are all z-independent. Comparing the z component of momentum equation, we obtain the first constraint:

$$\left\{B_z, \psi - \epsilon\frac{m_e}{\mu_0 e^2}\frac{\nabla_\perp^2\psi}{n}\right\} = 0, \quad \Leftrightarrow \quad \psi - \epsilon\frac{m_e}{\mu_0 e^2}\frac{\nabla_\perp^2\psi}{n} \equiv L(B_z). \tag{2.15}$$

Taking the dot product of $\mathbf{S}j$ and the momentum equation (2.13), we obtain

$$0 = \frac{1}{n}[B_z,\ \mu_0 p] + \left[B_z,\ \epsilon\frac{m_e}{\mu_0 e^2}\frac{(\nabla_\perp^2\psi)^2}{2n^2} + \epsilon\frac{m_e}{\mu_0 e^2}\frac{|\nabla_\perp B_z|^2}{2n^2}\right], \tag{2.16}$$

and taking the dot product of $\nabla_\perp\psi$ and the momentum equation (2.13), we obtain

$$\begin{aligned} 0 = &-\nabla_\perp\psi\cdot\nabla_\perp(\mu_0 p) - (\nabla_\perp^2\psi)|\nabla_\perp\psi|^2 - \nabla_\perp\psi\cdot\nabla_\perp\left(\frac{B_z^2}{2}\right) \\ &- \epsilon\frac{m_e}{\mu_0 e^2}\frac{\nabla_\perp\psi}{n}\cdot\nabla_\perp\left(\frac{|\nabla_\perp B_z|^2}{2}\right) + \epsilon\frac{m_e}{\mu_0 e^2}\frac{(\nabla_\perp^2 B_z)}{n}\nabla_\perp\psi\cdot\nabla_\perp B_z \\ &+ \epsilon\frac{m_e}{\mu_0 e^2}\frac{1}{n^2}[B_z,\ n]\cdot[B_z,\ \psi], \end{aligned} \tag{2.17}$$

where we use the first constraint (2.15).

Next we focus on the constraint of δ term (2.14), and we can define the potential Φ as the following relation:

$$\begin{aligned} \left(\frac{\mathbf{S}j}{en}\cdot\nabla\right)\frac{\mathbf{S}j}{en} &= \frac{1}{\mu_0^2}\frac{1}{e^2n^2}\left[\nabla_\perp\left(\frac{|\nabla_\perp B_z|^2}{2}\right) - (\nabla_\perp^2 B_z)\nabla_\perp B_z \right. \\ &\qquad \left. -\frac{1}{n}\{B_z, n\}\,\mathbf{S}e_z \times (\nabla_\perp B_z)\right] + \frac{1}{\mu_0^2}\frac{1}{e^2 n}\left\{\frac{\nabla_\perp^2\psi}{n}, B_z\right\}\mathbf{S}e_z, \\ &\equiv \nabla\Phi = \nabla_\perp\Phi + \frac{\partial\Phi}{\partial z}\mathbf{S}e_z. \end{aligned}$$

Then, since n, B_z and ψ are all z-independent, it is revealed that

$$\frac{\partial}{\partial z}\left(\nabla_\perp \Phi\right) = \mathbf{S}0, \quad \text{and} \quad \frac{\partial}{\partial z}\left(\frac{\partial \Phi}{\partial z}\right) = 0,$$

therefore we obtain

$$C = \frac{\partial \Phi}{\partial z} = \frac{1}{\mu_0^2}\frac{1}{e^2 n}\left\{\frac{\nabla_\perp^2 \psi}{n}, B_z\right\},$$

where C is a constant. Using the constraint (2.15), the above equation becomes

$$C = \frac{1}{\epsilon\mu_0}\frac{1}{n}\left\{\psi, B_z\right\}.$$

Multiplying nB_z^2 by the above equation and integrating in the whole area S perpendicular to the z-axis,

$$\begin{aligned} C\int_S nB_z^2 dS &= \frac{1}{\epsilon\mu_0}\int_S B_z^2\left\{\psi, B_z\right\} dS \\ &= \frac{1}{\epsilon\mu_0}\int_S \psi\left\{B_z, B_z^2\right\} dS = 0, \end{aligned}$$

where we use $B_z = 0$ on the boundary ∂S. Since n is positive and $B_z^2 \neq 0$ in some region in the area S, the constant C must be 0. This fact means that the potential Φ is also z-independent, that is,

$$\frac{\partial \Phi}{\partial z} = 0, \quad \Leftrightarrow \quad \left\{\frac{\nabla_\perp^2 \psi}{n}, B_z\right\} = 0,$$

then it is revealed that $\nabla_\perp^2 \psi / n$ is an arbitrary function of B_z. Considering this fact with the first constraint (2.15), we find that ψ is a function of B_z, that is,

$$B_z \equiv F(\psi). \tag{2.18}$$

In this case, (2.16) becomes

$$0 = \frac{1}{n}[\psi,\ \mu_0 p] + [\psi,\ \epsilon\mu_0 m_e \Phi] = \frac{1}{n}[\psi,\ \mu_0 p] + \left[\psi,\ \epsilon\frac{m_e}{\mu_0 e^2}\frac{F'^2}{2n^2}|\nabla_\perp \psi|^2\right], \tag{2.19}$$

and (2.17) becomes

$$\begin{aligned} 0 &= -\nabla_\perp \psi \cdot \frac{\nabla_\perp(\mu_0 p)}{n} - FF'\frac{|\nabla_\perp \psi|^2}{n} \\ &\quad - \left(1 - \epsilon\frac{m_e}{\mu_0 e^2}\frac{F'^2}{2n}\right)\frac{\nabla_\perp^2 \psi}{n}|\nabla_\perp \psi|^2 - \epsilon\frac{m_e}{\mu_0 e^2}\frac{F'^2}{2n^2}\nabla_\perp \psi \cdot \nabla_\perp(|\nabla_\perp \psi|^2) \\ &= -\nabla_\perp \psi \cdot \frac{\nabla_\perp(\mu_0 p)}{n} - FF'\frac{|\nabla_\perp \psi|^2}{n} - \frac{\nabla_\perp^2 \psi}{n}|\nabla_\perp \psi|^2 - \epsilon\mu_0 m_e \nabla_\perp \psi \cdot \nabla_\perp \Phi. \end{aligned} \tag{2.20}$$

Let us consider the situation that the plasma is barotropic, that is, $p = p(n)$. We define the function P as

$$\nabla_\perp P \equiv \frac{1}{n(p)} \nabla_\perp p.$$

¿From (2.19), we obtain the following constraint:

$$P + \epsilon m_e \Phi \equiv \tilde{P}(\psi),$$

where $\tilde{P}$ is an arbitrary function of ψ. Since $\nabla_\perp^2 \psi / n$ is a function of B_z, and B_z is a function of ψ, that is, $\nabla_\perp^2 \psi / n \equiv G(\psi)$ where G is a function of ψ. And so (2.20) becomes

$$0 = -\mu_0 \tilde{P}' - \frac{FF'}{n} - G,$$

where prime means the derivative of ψ. Therefore we find that n is also a function of ψ. ¿From (2.19), it is revealed that $|\nabla_\perp \psi|^2$ is a function of ψ, that is, $|\nabla_\perp \psi|^2 \equiv K(\psi)$, where K is a function of ψ. Finally, after some calculations for (2.20), we obtain the following equation:

$$\nabla_\perp^2 \psi = -\frac{1}{1 - \epsilon \dfrac{m_e}{\mu_0 e^2 n} F'^2} \left(\mu_0 p' + FF' \right) - \frac{\epsilon \dfrac{m_e}{\mu_0 e^2 n} F'^2}{1 - \epsilon \dfrac{m_e}{\mu_0 e^2 n} F'^2} \frac{K'}{2}, \tag{2.21}$$

where prime means the derivative of ψ, and this is the modified Grad-Shafranov equation in a "straight torus." This includes the modified Grad-Shafranov equation with constant density in a "straight torus" which is described as (2.12).

2.4.3 Modified Grad-Shafranov Equation in a Torus with Constant Density

Thirdly, let us consider the Grad-Shafranov equation of plasma with constant density in a torus. We assume that the plasma is steady and ϕ-independent, where we use the cylindrical coordinate (R, ϕ, Z) and ϕ means the azimuth. In this case the magnetic field can be described as

$$\mathbf{S}B = B_\phi \mathbf{S}e_\phi + \frac{1}{R} \mathbf{S}e_\phi \times \nabla_\perp \psi,$$

where B_ϕ and ψ are both ϕ-independent. The current density can be described as

$$\mathbf{S}j = \frac{1}{\mu_0} \left[\frac{1}{R} (\Delta^* \psi) \mathbf{S}e_\phi + \frac{1}{R} \nabla_\perp (RB_\phi) \times \mathbf{S}e_\phi \right],$$

where $\nabla_\perp$ and Δ^* are defined as

$$\nabla_\perp \equiv \mathbf{S}e_R \frac{\partial}{\partial R} + \mathbf{S}e_Z \frac{\partial}{\partial Z},$$
$$\Delta^* \equiv R \frac{\partial}{\partial R} \left(\frac{1}{R} \frac{\partial}{\partial R} \right) + \frac{\partial^2}{\partial Z^2},$$

and $\mathbf{S}e_R$, $\mathbf{S}e_Z$ are the unit vector toward the radial and height direction, respectively. The governing equations are as follows:

$$\mathbf{S}0 = -\nabla p + \mathbf{S}j \times \mathbf{S}B - \epsilon \frac{m_e}{e^2 n_0}(\mathbf{S}j \cdot \nabla)\mathbf{S}j, \tag{2.22}$$

$$\mathbf{S}0 = \nabla \times \mathbf{S}E = -\delta \frac{m_e}{e^3 n_0^2}\nabla \times [(\mathbf{S}j \cdot \nabla)\mathbf{S}j]. \tag{2.23}$$

First we focus on the momentum equation (2.22). Comparing the ϕ component of this equation, we obtain the first constraint as follows:

$$\psi - \tilde{\epsilon}\Delta^*\psi \equiv L(RB_\phi), \tag{2.24}$$

where L is an arbitrary function of RB_ϕ and

$$\tilde{\epsilon} \equiv \epsilon \ \frac{m_e}{\mu_0 e^2 n_0}.$$

Taking the dot product of $\mathbf{S}j$ and the momentum equation, we also obtain the second constraint, that is,

$$M(RB_\phi) \equiv \mu_0 p + \tilde{\epsilon}\frac{(\Delta^*\psi)^2}{2R^2} + \tilde{\epsilon}\frac{|\nabla_\perp(RB_\phi)|^2}{2R^2}, \tag{2.25}$$

where M is an arbitrary function of RB_ϕ. Finally, taking the dot product of $\nabla_\perp\psi$ and the momentum equation and using the first and second constraints, we obtain the third constraint which is described as

$$0 = R^2\frac{dM}{d(RB_\phi)} + \frac{dL}{d(RB_\phi)}\Delta^*\psi - \tilde{\epsilon}\Delta^*(RB_\phi) + RB_\phi. \tag{2.26}$$

When $\epsilon \to 0$, using (2.24)– (2.26), we can obtain the (usual) Grad-Shafranov equation which is described as

$$\Delta^*\psi = -\mu_0 R^2 p' - FF',$$

where $p \equiv p(\psi)$ and $RB_\phi \equiv F(\psi)$, and prime means the derivative of ψ.

Next we consider the constraint of (2.23). This equation means

$$\begin{aligned}\nabla\Phi &\equiv (\mathbf{S}j \cdot \nabla)\mathbf{S}j \\ &= \nabla_\perp\left[\frac{|\nabla_\perp(RB_\phi)|^2}{2\mu_0^2R^2} + \frac{(\Delta^*\psi)^2}{2\mu_0^2R^2} - \frac{M}{\mu_0^2\tilde{\epsilon}}\right] \\ &\quad + \frac{1}{\mu_0^2\tilde{\epsilon}}\frac{1}{R^2}\left[-(\Delta^*\psi)\nabla_\perp\psi - RB_\phi\nabla_\perp(RB_\phi) + \nabla_\perp\psi \times \nabla_\perp(RB_\phi)\right].\end{aligned}$$

Therefore, we find

$$\frac{\partial}{\partial\phi}\nabla_\perp\Phi = \frac{\partial}{\phi}\frac{\partial\Phi}{\partial\phi} = 0, \quad \Leftrightarrow \quad \frac{\partial\Phi}{\partial\phi} = C,$$

where C is a constant.

If $C = 0$, that is, Φ is also ϕ-independent, then we find $RB_\phi \equiv F(\psi)$ where F is an arbitrary function of ψ. Then, from the first constraint (2.24) $\Delta^*\psi \equiv N(\psi)$ where N is an arbitrary function of ψ.

$$\mathbf{S}0 = \nabla \times \nabla\Phi = \frac{1}{\mu_0^2\tilde{\epsilon}}\frac{2}{R^3}\left(N + FF'\right)\mathbf{S}e_R \times \nabla_\perp\psi,$$

therefore we find that

$$N + FF' = 0, \quad \text{or} \quad \psi = \psi(R). \tag{2.27}$$

Especially the second situation that ψ is only a function of R and independent of Z may be unrealistic. Further analyses are needed.

If $C \neq 0$, the potential Φ becomes a multivalued function, so this means the domain must not be simply connected space. This situation is satisfied in a tokamak. Further analyses are also needed.

2.4.4 Summary of Modified Grad-Shafranov equation in IMHD model

	Straight torus	Torus
Plasma with constant density	3 constraints (2.7)– (2.9) are obtained.	3 constraints (2.24)– (2.26) are obtained.
	Modified GS (2.12) is obtained.	Only the condition (2.27) is obtained if $\partial\Phi/\partial\phi = 0$.
Compressible plasma	1 constraints (2.15) and 2 (weak) constraints (2.16), (2.17) are obtained.	??
	If barotropic, modified GS (2.21) is obtained.	???

Table 2.2: Summary of the constraints of the equilibrium states with no flow in a "straight torus" and a torus and the modified Grad-Shafranov (GS) equations. The upper row in each situation shows the result with considering only ϵ term in the momentum equation, while the lower row shows the result with considering both ϵ and δ terms. At compressible plasma in a "straight torus," "weak constraints" mean that these constraints are not the form that some values are purely the functions of another values but are simply the written formulation. We could not obtain any efficient conditions for compressible plasma in a torus and so '??' is written in the above table.

In Table 2.2, we summarize the constrains of the equilibrium states with no flow in a "straight torus" or a torus and the modified Grad-Shafranov equation obtained in the previous sections.

In "straight tori," the modified Grad-Shafranov equations are obtained with the assumption that the plasma is barotropic. In torus, however, because of its curvature, useful equations could not be obtained and only some conditions are obtained even if the plasma

has constant density. In compressible plasma in torus, there were no efficient results obtained. The physical interpretation of this effect of its curvature is a future work and further analyses are needed.

2.5 Incompressible Equilibrium States with Flow

In this section we introduce some equilibrium states in an incompressible plasma with flow, but further analyses are future works.

The governing equations are as follows:

$$\rho = \rho_0 = \text{const.} \quad \Leftrightarrow \quad n = n_0 = \text{const.}, \tag{2.28}$$

$$\mathbf{S}0 = -\nabla p + \mathbf{S}j \times \mathbf{S}B - \epsilon \frac{m_e}{e^2 n_0}(\mathbf{S}j \cdot \nabla)\mathbf{S}j - \rho_0(\mathbf{S}V \cdot \nabla)\mathbf{S}V, \tag{2.29}$$

$$\nabla\Phi = \mathbf{S}E = -\mathbf{S}V \times \mathbf{S}B + \epsilon \frac{m_e}{e^2 n_0}\left[(\mathbf{S}V \cdot \nabla)\mathbf{S}j + (\mathbf{S}j \cdot \nabla)\mathbf{S}V\right] - \delta \frac{m_e}{e^3 n_0^2}(\mathbf{S}j \cdot \nabla)\mathbf{S}j, \tag{2.30}$$

because the plasma is incompressible and

$$\mathbf{S}0 = \frac{\partial \mathbf{S}B}{\partial t} = -\nabla \times \mathbf{S}E \quad \Leftrightarrow \quad \mathbf{S}E \equiv \nabla\Phi.$$

2.5.1 The Situation $\mathbf{S}V \propto \mathbf{S}j$

We assume

$$\mathbf{S}V = C\frac{\mathbf{S}j}{en},$$

then the governing equations (2.28)– (2.30) become as follows;

$$0 = -\nabla p + \mathbf{S}j \times \mathbf{S}B - \left(C^2 \frac{\rho_0}{e^2 n_0^2} + \epsilon \frac{m_e}{e^2 n_0}\right)(\mathbf{S}j \cdot \nabla)\mathbf{S}j,$$

$$0 = \nabla\Phi + \frac{C}{en}\mathbf{S}j \times \mathbf{S}B - \left(2C\epsilon \frac{m_e}{e^3 n_0^2} - \delta \frac{m_e}{e^3 n_0^2}\right)(\mathbf{S}j \cdot \nabla)\mathbf{S}j.$$

If

$$2C\epsilon \frac{m_e}{e^3 n_0^2} - \delta \frac{m_e}{e^3 n_0^2} = \frac{C}{en}\left(C^2 \frac{\rho_0}{e^2 n_0^2} + \epsilon \frac{m_e}{e^2 n_0}\right)$$

and we define Φ as $\Phi \equiv -Cp/(en_0)$, the two equations are equivalent. Indeed, if $\delta = 0$,

$$C = \pm\sqrt{\epsilon \frac{m_e}{e^2 n_0 \rho_0}} = \pm\sqrt{\epsilon \frac{m_e}{m_i + m_e}},$$

and the governing equation becomes

$$0 = -\nabla p + \mathbf{S}j \times \mathbf{S}B - 2\epsilon \frac{m_e}{m_i + m_e}(\mathbf{S}j \cdot \nabla)\mathbf{S}j,$$

where $\nabla \times \mathbf{S}B = \mu_0 \mathbf{S}j$. Studying the physical meaning of the value of C is a future work.

2.5.2 Beltrami – "Jeltrami" Flow

In this section we consider the Beltrami – "Jeltrami" flow, which means the velocity and current density satisfy the following equations:

$$\nabla \times \mathbf{S}V = \lambda \mathbf{S}V,$$
$$\nabla \times \mathbf{S}j = \mu \mathbf{S}j,$$

where λ and μ are some functions in general. In this case the magnetic field satisfies the following equation:

$$\mathbf{S}B = \frac{\mu_0}{\mu}\mathbf{S}j + \nabla\chi,$$

where χ is an arbitrary harmonic function because $\mathbf{S}B$ is solenoidal. Then the governing equations (2.28)– (2.30) become as follows:

$$\nabla\tilde{p} = \mathbf{S}j \times \nabla\chi,$$
$$\nabla\tilde{\Phi} = -\mathbf{S}V \times \nabla\chi + \frac{\mu_0}{\mu}\left[1 + \left(\frac{m_e}{\mu_0 e^2 n_0}\right)\mu(\mu - \lambda)\right]\mathbf{S}j \times \mathbf{S}V,$$

where $\tilde{p}$ and $\tilde{\Phi}$ are defined as

$$\tilde{p} \equiv p + \rho_0\frac{|\mathbf{S}V|^2}{2} + \epsilon\frac{m_e}{e^2 n_0}\frac{|\mathbf{S}j|^2}{2},$$
$$\tilde{\Phi} \equiv \Phi + \epsilon\frac{m_e}{e^2 n_0}(\mathbf{S}V \cdot \mathbf{S}j) + \delta\frac{m_e}{e^3 n_0^2}\frac{|\mathbf{S}j|^2}{2}.$$

For simplicity, if μ, λ and χ satisfy the following relations,

$$\mu = \lambda, \quad \text{and} \quad \chi \equiv 0,$$

the governing equations becomes

$$\nabla\tilde{p} = 0,$$
$$\nabla\tilde{\Phi} = \frac{\mu_0}{\mu}\mathbf{S}j \times \mathbf{S}V.$$

2.6 Conclusions and Discussions

We have investigated limitations of IMHD model by introducing some non-dimensional parameters and classify IMHD models according to whether or not they conserve energy. It is revealed that the correction term $\frac{m_e}{e}(\mathbf{S}j \cdot \nabla)\frac{\mathbf{S}j}{en}$ in the momentum equation, which is usually neglected, is needed to conserve the total energy.

In order to investigate the effect of this correction term, we attempted to modify the Grad-Shafranov equation, which describes the equilibrium state in a torus with no flow, and obtain a modified Grad-Shafranov equation in a "straight torus" when the plasma is barotropic (the density being a function of the pressure). However, we were only ablte to

do this with some conditions on the magnetic field in a torus due to its curvature. The physical interpretation of this effect of curvature will be addressed in future work and further analyses are needed.

We also introduced some equilibrium states with constant density and with flow. One has $\mathbf{S}V$ proportional to $\mathbf{S}j$ and another was the Beltrami–"Jeltrami" flow. Concrete analyses of these will also be considered in future work.

The dispersion relation of the Alfven wave in usual MHD model is $\omega/k = V_A \cos\theta$, where ω is the frequency, k the wavenumber, $V_A \equiv \sqrt{B_0^2/(\mu_0\rho_0)}$ the speed of Alfven wave (B_0 is the magnitude of magnetic field and ρ_0 the density), and θ is the angle between the uniform magnetic field and the wavevector. On the other hand, the dispersion relation of the IMHD model is $\omega/k = V_A \cos\theta/\sqrt{1 + d_e^2 k^2}$, where $d_e^2 \equiv m_e/(\mu_0 e^2 n_0)$ (m_e is the electron mass, e the elementary charge and n_0 the number density) [9]. Therefore, higher wavenumber waves propagate more slowly in IMHD model than in usual MHD model. The same tendency can be found in the fast and slow magnetosonic waves. These facts suggest that the stability of some states can be changed by the effect of electron inertia, and this is this will also be considered in future work.

Acknowledgements

I would like to thank the Woods Hole Oceanographic Institution for the opportunity to participate in the 2011 Geophysical Fluid Dynamics Program. I am also grateful to Professor Philip J. Morrison for initiating this project and for his great and helpful advice, in spite of my poor English. Last but not least, I would like to thank to all the GFD Fellows for sharing this great experience with me at summer program, as well as to all the staff members for fruitful discussions. To participate in this GFD Program 2011, I was supported by a Grant in-Aid for the Global COE Program "Foundation of International Center for Planetary Science" from the Ministry of Education, Culture, Sports, Science and Technology (MEXT) of Japan.

Bibliography

[1] A. Bhattacharjee, Z. W. Ma, and X. Wang, "Impulsive reconnection dynamics in collisionless laboratory and space plasmas," *J. Geophys. Res.*, **104** (A7), 14, 543–14, 556 (1999).

[2] F. F. Chen, "Introduction to plasma physics and controlled fusion. Volume 1, Plasma physics," second edition, Springer, pp 346 (1984).

[3] R. Fitzpatrick, "The Physics of Plasmas," Lulu, pp261 (2008). (The PDF version can be obtained in http://farside.ph.utexas.edu/teaching/plasma/plasma.html)

[4] J.P. Freidberg, "Ideal magnetohydrodynamic theory of magnetic fusion system," *Rev. Modern Phys.*, **54**, 801–902 (1982).

[5] H. Grad and H. Rubin, "Hydromagnetic equilibria and force-free fields," Proceedings of the second UN Conf. on the Peaceful Uses of Atomic Energy, **31**, 190–197 (1958).

[6] V. D. Shafranov, "Plasma equilibrium in a magnetic field," Reviews of Plasma Phys. edited by M.A. Leontovitch (Consultants Bureau, New York), **2**, 103 (1966).

[7] M. A. Shay, J. F. Drake and B. N. Rogers, "Alfvénic collisionless magnetic reconnection and the Hall term," *J. Geophys. Res.*, **106**, 3759–3772 (2001).

[8] V. R. Lüst, "Über die Ausbreitung von Wellen in einem Plasma," *Fortschritte der Physik*, **7**, 503–558 (1959).

[9] P. J. Morrison with E. Tassi, "Notes on IMHD Waves" (2009, unpublished).

[10] V. M. Vasylinuas, "Theoretical models of magnetic field line merging, 1," *Rev. Geophys. Space Phys.*, **13**, 303–336 (1975).

Project 3

Traversing the edge: a study of turbulent decay

Matthew Chantry

University of Bristol

In this work the "edge of chaos" is studied to increase our understanding of turbulence in shear flows. The "edge" is a hypersurface in phase space which separates conditions which return to the laminar state from those which engage in turbulent dynamics. We tackle the subject of the geometry of the edge, and its involvement during the return to the laminar state. Here studying plane-Couette flow we observe the death of the self-sustaining process during decay and identify the processes which govern the decay rate. The report concludes with tests on the validity of edge geometry observed in low dimensional models.

3.1 Introduction

The study of Newtonian fluid flow through through a straight circular pipe was first carried out in the 19th century, where Hagen [1] and Poiseuille [2] separately studied the laminar flow which now carries both their names. This work was continued by Reynolds [3] who studied the transition from laminar flow to flow which is both temporally and spatially disordered, called turbulent flow. The Reynolds number $Re := UD/\nu$ governs this transition, where U is the mean speed, D the diameter and ν the kinematic viscosity. The laminar Hagen-Poiseuille flow is linearly stable for all values of Re, meaning that a finite amplitude disturbance is required to generate turbulent behaviour. The energy that the disturbance requires to trigger turbulence has been studied for many years, and depend sensitively upon the shape of the disturbance and the Reynolds number. The minimum value of the Reynolds number at which turbulence is seen varies between experiments but appears to lie in the range 1750-2300. It is thought that in this range of Re that there exists a chaotic saddle responsible for the dynamics, which may transition to a chaotic attractor for larger Re [4]. In this regime the lifetime of turbulence can vary strongly, so mean dynamics described by probability functions are used to demonstrate the behaviour. Faisst et al. [4] amongst

others showed that probability of turbulence surviving depends exponentially on the ratio of time, t, to a mean lifetime which depends upon Re. The relationship between Re and the mean lifetime is still a subject of research, both experimental and computational. In that work the discussion centres around the existence of a finite Re for which the probability of decay back to the laminar state is zero.

Pipe flow is one member of a class of shear flows which also include plane Couette flow, Taylor-Couette flow and boundary layer flow. Plane Couette flow (PCF) is the flow between two infinite plates, which are driven at constant speed in opposite directions. The flow shares all of the features discussed about (although with different critical Re), but for research has two advantages over pipe flow. The symmetry of the system allows the existence of fixed points solutions, whereas the simplest structure in pipe flow are travelling waves. The Cartesian geometry of PCF is computationally simpler than the cylindrical coordinate system of pipe flow.

The linear stability of the laminar states makes finding new solutions to the Navier-Stokes equations challenging, however recently new solutions have been found ([5], [6], [7], [8], [9], [10], [11], [12]). These solutions are fixed points (in PCF only), travelling waves which are steady under a translating reference frame and periodic orbits, many of which exhibit symmetries. These solutions are unstable but have both stable and unstable manifolds and are therefore saddle points in phase space. Kerswell [13] and others propose that these, and more solutions form a "skeleton" for the dynamics which can guide trajectories around the turbulent portion of phase space.

Within the last 10 years a new method has been implemented to find solutions in both pipe flow and PCF. The method, pioneered by Itano et al. [14], is to track the "Edge of Chaos", the hyper-surface surface which separates separates conditions which simply relaminarize from those which are subjected to turbulence. The edge therefore provides a minimum on the energy required to trigger turbulence, however there is no known method to use the edge to find this minimum energy point. By reducing the dynamics to only evolve along the edge, new structures have been found in both pipe flow and PCF ([15], [16], [17]). By evolving along the edge only, one unstable direction is removed, meaning solutions embedded in the edge with just one unstable direction in the full dynamics become local attractors within the dynamics of the edge. As discussed earlier, at low Reynolds number turbulence is transient and initial conditions experience sudden decay back to the laminar state. The edge can therefore not be considered a boundary for the basin of attraction of the laminar state, as conditions either side of the edge will decay. This therefore raises a question into the understanding of phase space in these systems. How do initial conditions on the "turbulent side" of the edge pass back to the laminar state and does there exist a unique point (or a small number of points) where this passing occurs? In particular geometries the edge contains simple attracting states, such as fixed points or travelling waves. In some of these situations, evidence points to a single global attracting state in the edge, to which all initial conditions on the edge converge, called the edge state. A secondary question of this work concerns the dynamical significance of this edge state during relaminarization. The point is significant within dynamics on the edge, and all initial conditions must, in some manner, pass by this edge, therefore the edge state may be important in this relaminarization process. We will attack this problem on two fronts. The first will examine the statistics of decay, and look for evidence of a unique "crossing" point. The second half will look to the

results of low-dimensional models and attempt to draw parallels between these and the full dynamics. In the next sections we will discuss the set-up used to investigate this problem, and present some statistical work on this problem. We will then look at previous work using low dimensional models to consider this problem, and compare these to the full dynamics. Finally we shall draw conclusions and discuss further work into this problem.

3.2 Methods

To examine the questions considered above we choose plane Couette flow as the shear flow for our investigation. This has been chosen for its simple geometry and the evidence for a single fixed point attracting edge state in a particular geometry (Schneider private communication 2011). As with pipe flow discussed above, no-slip boundary conditions at the wall are used, with periodic boundaries in the two remaining directions. The laminar flow is linearly stable and takes the form

$$\bar{\mathbf{u}} = Uy\ \hat{\mathbf{x}}, \tag{3.1}$$

where convention dictates that x takes the direction of the wall motion, y the wall normal direction and z the spanwise direction. The DNS is carried out in a Fourier by Chebyshev by Fourier domain, with an adaptive 3rd order Semi-implicit Backwards Differentiation timestep code written by Gibson ([23] [24]). The Reynolds number in this system is $Re := Uh/\nu$, where U is the wall speed, h is half the wall separation and ν the kinematic viscosity. For simplicity both U and h remain equal to one. We will study Reynolds numbers in the range $[340, 380]$ where turbulence exists but turbulent lifetimes are short (order 1000 time units). The domain is $[0, 4\pi] \times [-1, 1] \times [0, 2\pi]$, chosen for the existence of a single edge state, a member of the "Nagata" solution family [5], which is visualised in figure 3.1. We shall use the notation breaking the velocity field, $\bar{\mathbf{u}}$, into the laminar and perturbation parts, $\bar{\mathbf{u}} = y\ \hat{\mathbf{x}} + \mathbf{u}$. This study will begin with a statistical investigation into decaying turbulence, where trajectories will be aligned to decay at the same point in a new time t^* which is defined for each simulation as

$$t^* := t_{lam} - t, \tag{3.2}$$

where t_{lam} is the time such that

$$\int_V \mathbf{u} \cdot \mathbf{u}\ dV < 0.005. \tag{3.3}$$

This finds the time where the flow is sufficiently close to the laminar state to be considered as laminar. The results of this section are not qualitatively affected by the precise choice of this distance from the laminar state. For brevity we shall refer to this as the relaminarization time. We begin by simulating a large number of DNS runs from turbulent initial conditions until they reach the laminar state. Once aligned by their relaminarization times we can find the mean and standard deviation of the L2 norm of $\mathbf{u}$, and plot this against the relaminization time. In figure 3.2 we carry out this procedure for 100 evolutions at a Reynolds number of 380. Several observations can be made from this figure in answering the questions posed previously. The decay from the turbulent state begins approximately

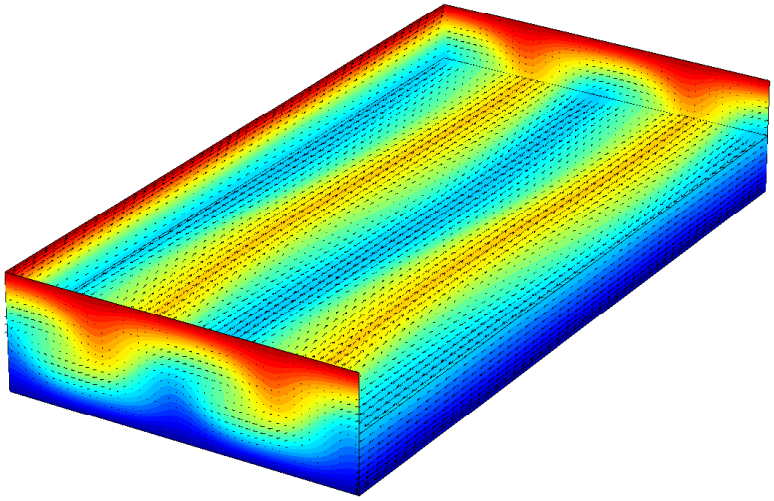

Figure 3.1: Visualization of the fixed point embedded in edge, which is an attractor when the dynamics are restricted to the edge. Colours indicate downstream velocity, with red flowing into the page and blue out of the page. Arrows plot cross stream velocity field.

500 time units before relaminarization time, and before this a statistically steady state is observed with approximately constant variance. During decay, while a decrease of variance is observed, trajectories do not converge until just prior to $t^* = 0$. This simple observation suggests an answer to one of the questions postulated above: does there exist a unique point for passing by the edge? If a unique point existed, one would expect to see the trajectories converge at an L2 norm value associated with the edge (~ 0.2). The result was robust to using a range of metrics to align the decaying trajectories, including E_{3D}, vorticity, and downstream vorticity. With all of these metrics no patterns in the decay emerged, therefore suggesting that this hypothesis is false.

3.3 Statistical analysis

We can use this approach to examine the physical properties of the flow during decay, and confirm the features expected from analytical and previous computational work. In figure 3.3 we plot the mean evolution of the L2 norm of 4 physical quantities during the last 1000 time units before decay, the velocity, the vorticity, the downstream vorticity and the "3D velocity". These first two are related to the energy and dissipation of the system respectively, and begin to decay simultaneously with similar relative gradients. The L2 norm of the downstream vorticity provides a measure for the downstream vorticies, or rolls, which redistribute the mean shear. This then creates downstream streaks, which can develop

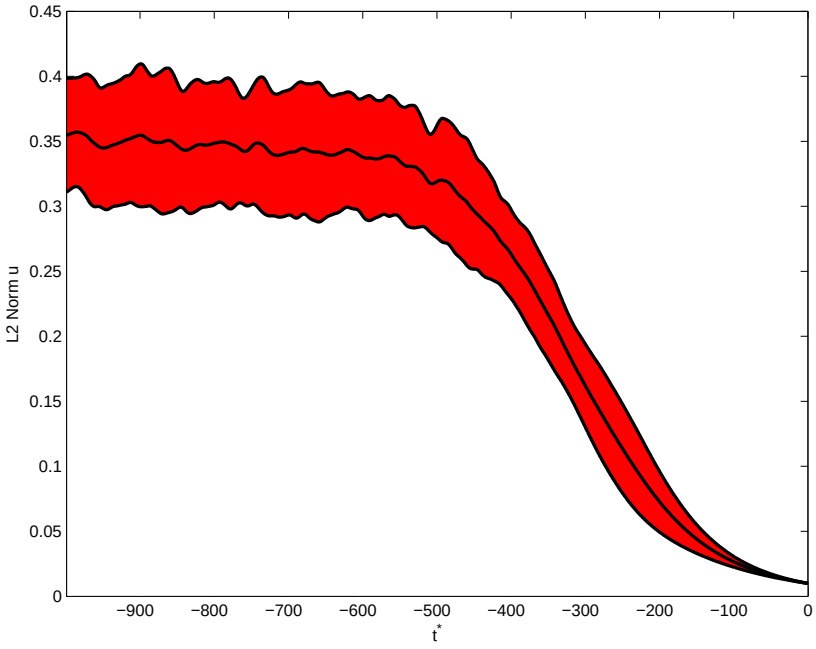

Figure 3.2: L2 Norm of perturbation velocity field $\mathbf{u}$ against t^*, the time before relaminarization. Plotted are the mean $\pm$ the standard deviation of 100 turbulent evolutions at $Re = 380$. Initial conditions generated from turbulence at slightly larger Re.

instabilities. These instabilities feedback into the rolls. This is called the self-sustaining process (SSP [18]), and plays a crucial role in the maintenance of turbulence. Therefore if the rolls are removed then the sustaining process is broken, and turbulent cannot be maintained. The results in frame (c) of figure 3.3 show that the L2 norm of the downstream vorticity begins to decay at the same time as the previous two metrics, however it decreases at greater relative rate. This results in no rolls existing for the final 200 time units of the decay. The final measure considered is the "3D velocity", $\mathbf{u}'$, the part of the velocity field which depends upon x.

$$\mathbf{u} = \frac{1}{L_x} \int \widetilde{\mathbf{u}} \, dx + \mathbf{u}' \tag{3.4}$$

The quantity is dynamically important to the maintenance of turbulence, the energy in this part of the velocity field we shall denote as E_{3D}. It can be shown in shear flows that a 2D perturbation cannot to lead to turbulence. From the view of the SSP this quantity measures the instabilities which complete the process and feedback upon the rolls. Frame (d) of figure 3.3 shows the evolution of this quantity before relaminarization. The beginnings of decay are observed in line with the other 3 quantities, with decay occurring at the same relative rate as downstream vorticity. Therefore we observe that the for the last 200 time units of decay the flow is two-dimensional with no downstream rolls, this leaves only downstream streaks (and a small amount of cross-stream flow). These findings therefore agree with the previous work, which suggested that downstream rolls and 3D flow are the first parts of the flow field to fully decay. After these two quantities have decayed the streak decay will govern the overall decay rate, which we shall now study.

Understanding the structure of the streaks during this decay will explain the variety of decays rates observed, as these are the only feature remaining during the final part of decay. In figure 3.4 frames (a) & (b) show the x-averaged[1] velocity for two different decay trajectories approximately 200 time units before relaminarization. Trajectories were chosen for displaying slow and fast decay respectively, i.e. shallow and steep decay rates during the final 200 time units of decay. Beyond this choice these trajectories are generic within their respective class (slow or fast decay). Obvious from the figure are the two different streak structures involved in the flow field, where streaks are indicated by waviness in the downstream velocity contours. Frame (a) has two streaks, one fast and one slow, whereas frame (b) has four streaks with two of each sign. The different length-scales involved with these flow fields explain the decay rates involved. In this regime the diffusion operator dominates the evolution, meaning that structures with small length-scales involved will decay at a faster rate compared to those with larger length-scales. The flow at this stage in decay is independent of x, and all flow-fields have similar dependence upon y leaving the z structure to set this rate. To further this work we consider the evolution of simple structures carrying the two and four streak pattern, members of the "Nagata" family of solutions. As previously discussed one member of this family, which has a four streak pattern (figure 3.1), is the edge state in the chosen geometry. However there exists a two streak member of the family, which also lies on the edge but has two unstable directions (and is therefore not an attracting structure on the edge). The x-averaged flow field for these solutions are plotted in frames (c) and (d) of figure 3.4. The comparisons between the decaying fields and

[1]Recall final decay is independent of x, therefore 2D visualization displays all flow features.

solution fields can be easily seen, but the solutions have sharper streak structure and retain downstream vorticity. We can study the length-scales involved in these fixed points and the decaying trajectories by by representing the z dependence of the flow-field through a Fourier decomposition. As these solutions belong to the same family, but are effectively solutions from two different box widths their dependence on the first few Fourier modes differs. The two streak solution contains a large amount of energy in the first mode, whereas the four streak solution contains none. The second Fourier mode will be the dominant term for the 4-streak solution, but be of lesser importance in the 2-streak solution. When these two solutions are perturbed in the correct unstable direction (to the "laminar side" of the edge) the solutions will smoothly decay to the laminar state. The decay of these states, with their different spanwise spectra will be a useful comparison for decaying turbulence. In figure 3.5 100 decaying trajectories are plotted, alongside the decay from the two states discussed all at the same Reynolds number. The striking feature of this figure is that the decay from two fixed points almost bounds the decay from turbulence. We can understand this by studying the spanwise Fourier modes during the last 200 time units of decay. Those decaying at a similar rate as the two streak solution, will have more energy in the first spanwise Fourier mode and little in the second. Whereas those decaying with the four streak solution will have little in the first spanwise Fourier mode and the majority in the second. Trajectories decaying at rates between these two "extremes" will have energy in both these modes in varying proportions which match the decay rate. An observation to made from this figure is that no decaying trajectory in our sample decayed at a significantly greater rate than the four streak fixed point. It appears within this domain all turbulence (in this range of Reynolds number) decays through a very simple streak structure. How this behaviour would change if a wider domain was used, or a larger Reynolds number set, remains a topic for further research. The author suggests that if the domain was sufficiently widened then turbulence would decay through a six streak structure, in addition to the two and four structures. It is not obvious that all decaying turbulence in this geometry should have streaks with such similar y-dependence, although the tight constraints of the domain might again be responsible. Studying the decay of other fixed points in this geometry would make for an interesting comparison with those discussed above. Are these two solutions special in the way they almost bound the decay, or is this a feature of fixed points?

3.4 Edge geometry

Through examining the statistics of the decay from turbulence we have gained insight into the processes involved, and evidence that a unique route past the edge does not exist. Beyond this fact we have learnt little about how the decaying trajectories pass the edge. In this section we will examine this issue with the aid of low dimensional models. Attempts to study low dimensional models for shear turbulence have been used in recent years with limited success. Waleffe [18] took the ideas behind his self-sustaining process to construct both eight and four mode ODE models, however these were limited by representing turbulence with a fixed point. These models did show that the physical processes behind turbulence could be captured in a small number of well chosen modes. Extensions to a nine mode model [19] and an eight mode PDE model [20] have made progress in capturing more detail but more modes makes the analysis more complex. In order to understand the edge

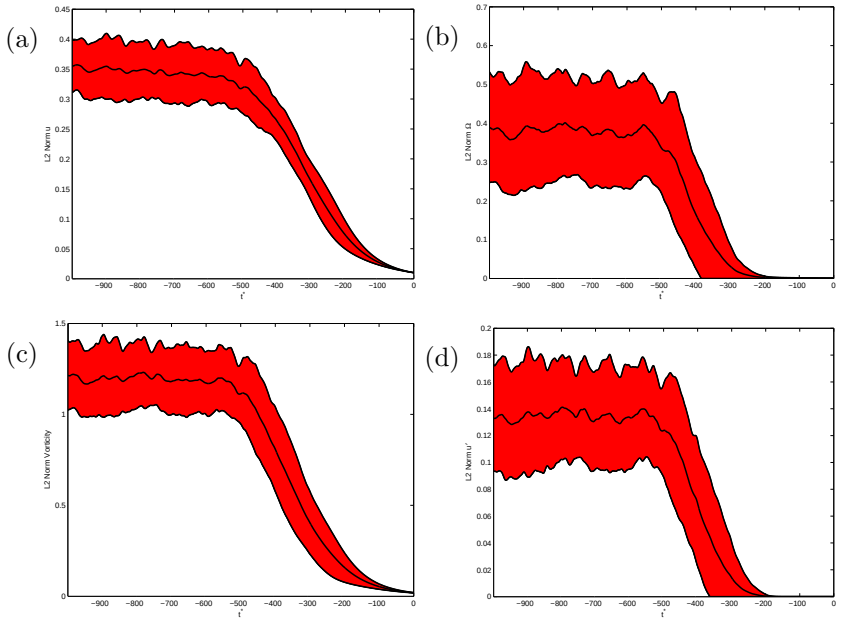

Figure 3.3: Evolution of the mean ± standard deviation for the L2 norm of 4 flow field quantities, (a) Velocity, (b) downstream vorticity, (c) vorticity & (d) "3D velocity". All experience decay approximately 500 time units before relaminarization, with faster relative decay rates for downstream vorticity and 3D velocity.

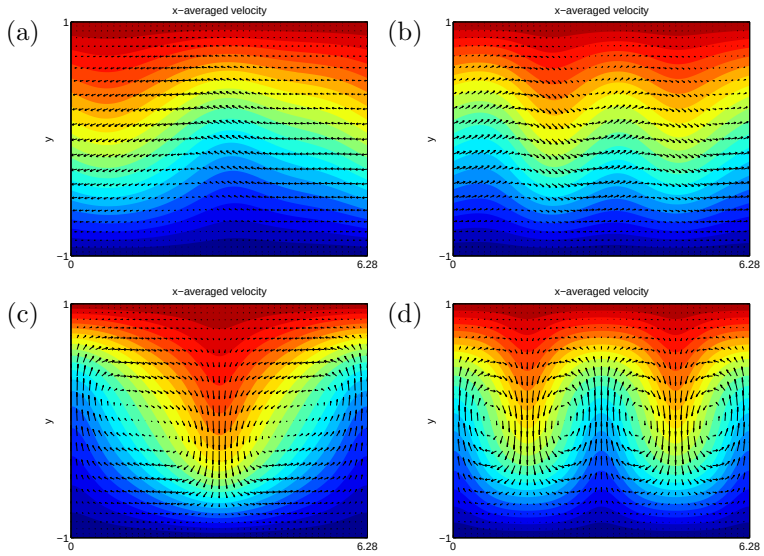

Figure 3.4: Frames (a), (b) show x-averaged flow fields 200 time units before decay. Solutions selected for demonstrating slow and fast relaminarization rates respectively. Frame (a) has two streaks, one fast at the centre of the domain, and one slow at the left edge. Frame (b) has four streaks, two fast and two slow. To be compared with frames (c) and (d) x-averaged flow field for members of the Nagata solution family. Frame (c) shows the longest spanwise wavelengths family member. Solution in frame (d) contains two copies of the Nagata solution in spanwise direction.

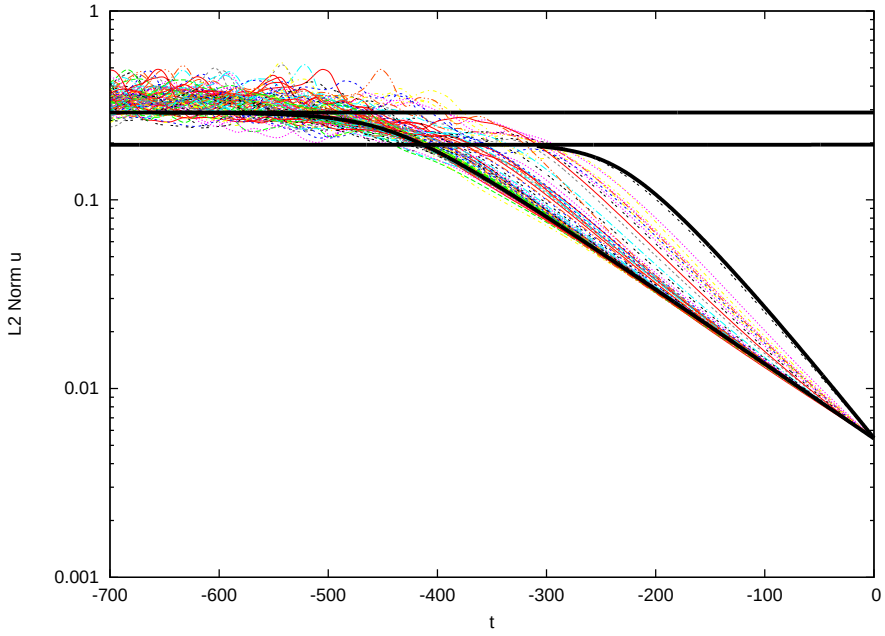

Figure 3.5: Coloured lines - L2 norm of the **u** against time for decaying trajectories. Black horizontal lines - indicate the value of L2 norm for the two solutions from figure 3.4 (higher line - two streak solution). Black lines - decay from fixed point solutions to the laminar state after perturbation. All decaying lines have been aligned by decay time.

Lebovitz examined the edge structure in Waleffe's four mode model [21]. He subsequently designed a two dimensional system which captured the same edge topology [22]. It is this two dimensional system which we will compare with the edge structure in the full system. The equations of the system are

$$\begin{aligned}\dot{x}_1 &= -\delta x_1 + x_2 + x_1 x_2 - 3x_2^2 \\ \dot{x}_2 &= -\delta x_2 - x_1^2 + 3x_1 x_2,\end{aligned} \tag{3.5}$$

where δ is the control parameter and surrogate for Reynolds number, which we will fix at 0.4. For this value of δ the system has 3 fixed point solutions. One is stable and located at $(0, 0)$ which will be the surrogate for the laminar state. One is an unstable saddle, called the lower branch (LB), which is the surrogate for the edge state. The final fixed point is unstable, called the upper branch (UB) and is the surrogate for the turbulent state. In figure 3.6 the three fixed points points are plotted alongside the manifolds of the edge state and a typical decay from near the upper branch point. The stable manifold of the edge state forms the edge in this system; near the edge state initial conditions below the edge decay to the laminar state, whereas points above the edge visit an area in phase space further from the laminar state before being attracted the laminar state. The feature captured by this model, and Waleffe's four order model, is that while the edge goes out to infinity in one direction, in the other it spirals infinitely many times around the upper branch point. An initial condition near the upper branch point will spiral outwards before passing around the edge on the way to the laminar state. It is this spiral feature that provides the route from the "turbulent" part of phase space to the "laminar state".

In this section we wish to answer the following. Does a higher dimensional equivalent of this behaviour occur in the full dynamics? It is obvious that we cannot simply plot the phase space of the full dynamics, so we need a test to compare the model with the full dynamics. We shall introduce the test in the reduced model before carrying out the same analysis in PCF. We begin with a trajectory spiraling out from the unstable equilibrium, and select several time points along the trajectory. At these points we shall calculate a new initial condition

$$\mathbf{x}_{in} = \lambda \mathbf{x} \tag{3.6}$$

in the model for a range of λ around $\lambda = 1$, the condition that recovers the original point on the relaminarizing trajectory. For each value of λ we will evolve the new initial condition and study the dynamics. A condition close to the surrogate for turbulence will be "above" the edge, therefore there exists a $\lambda \in [0, 1]$ for which a new condition lies below the edge and will quickly relaminarize. The subsequent behaviour is measured by a time average of the L2 norm of $\mathbf{x}$, (called the T measure), taken over a suitable time. The T measure should be considered a surrogate for the lifetime of the flow. Considering how this T measure changes with λ will locate the edge relative to the relaminarizing trajectory. A sudden and large change in the value of T denotes a transition across the edge. Figures 3.7 shows the evolution in phase space of the rescaled and original decaying trajectories, from an initial condition above and on the outside of the spiral structure. This measure of "turbulence" against λ is plotted in figure 3.8. The original trajectory decays quickly, as do those rescaled further from the laminar state. However for $\lambda < 0.97$ a large increase in the time average of the L2 norm is observed, this is caused by stepping across the edge meaning another spiral

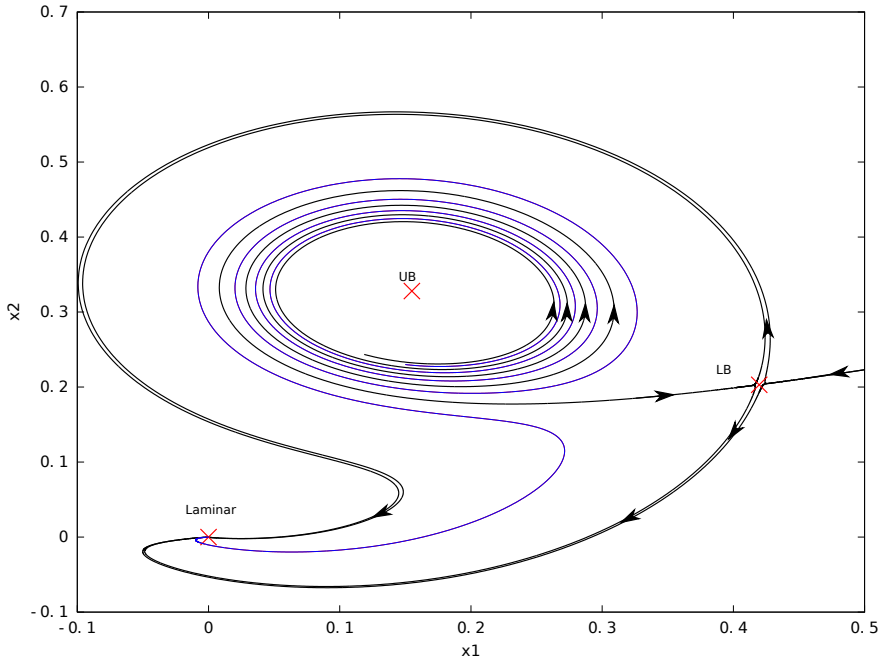

Figure 3.6: Phase space for 2D model. Red crosses indicate fixed points (increasing x_1) Laminar surrogate, Turbulence surrogate and Edge state surrogate. Black lines show the unstable and stable manifolds of the edge state. Stable manifold is the edge in this system. Blue line an example decaying trajectory beginning "near" turbulence.

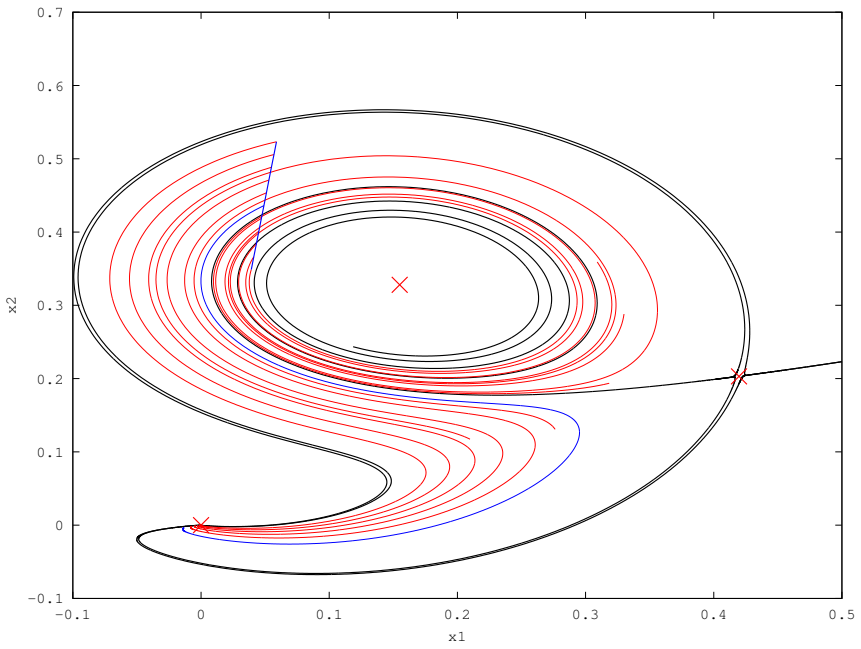

Figure 3.7: Phase space of the 2D model. Blue curving line denotes the trajectory decaying from "turbulence". Blue straight line shows range of rescaled initial conditions, the evolution of which are plotted in red. Original decaying point lies above the edge. Rescaled initial conditions span the edge.

must be completed before relaminarization. We will compare these results to the carrying out the same analysis at later point along the original trajectory, with results in figures 3.9 & 3.10. The original point lies below the edge, so the reverse λ scaling is observed. For $\lambda < 1.08$ trajectories relaminization quickly, but larger values lie the other side of the edge. The results from these two points highlight the transition that is made as a trajectory in this model passes around the edge on route to the laminar point. By using a relatively short time average of the L2 norm for our projection we restrict the edge crossings that we can observe. Crossing the outer-most loop of the spiral is captured as a transition, but the subsequent crossings of inner parts of the edge are not caught by this relatively short time average. By using this metric we observe a behaviour which is has a parallel in the full dynamics, which will be discussed later.

In the case of the low dimensional model the outcome of the test could be predicted from the phase portrait alone. Having studied this simple system the same analysis can be performed on the full dynamics and allow some interpretation of the complex behaviour of the edge. Before we can begin this work we should consider the methods previously used to study the edge. These methods have revolved around a bisection technique between an original turbulent state and another which smoothly relaminarizes. The criterion as to the turbulent or laminar evolution of the new flow field are usually energy or E_{3D} thresholds, with the turbulent threshold set just below the turbulent value of the metric.

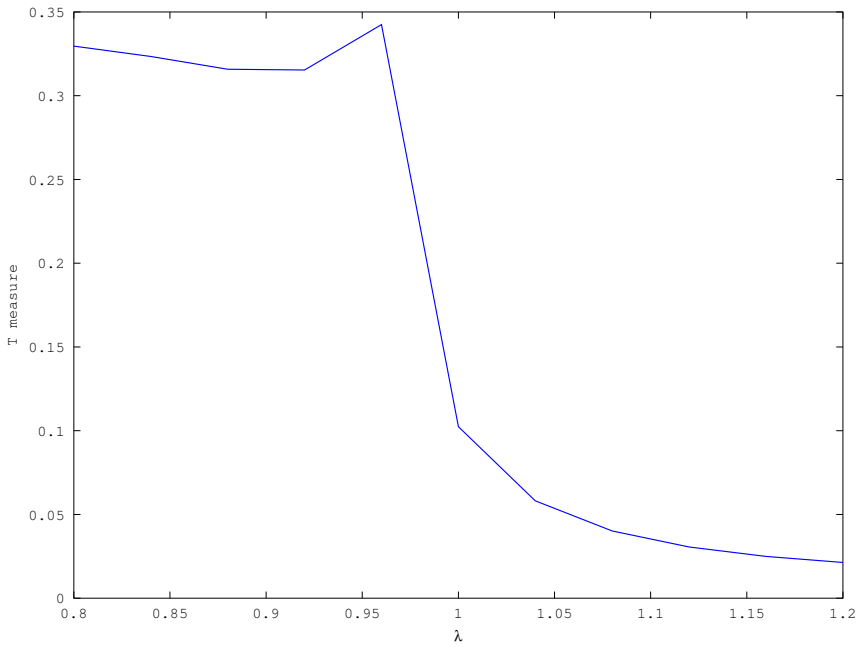

Figure 3.8: T measure against λ. Measures whether each initial condition maintains "turbulent" evolution during measure time. Values above 0.2 indicate "turbulent" evolution. Values below indicate decay to the laminar state.

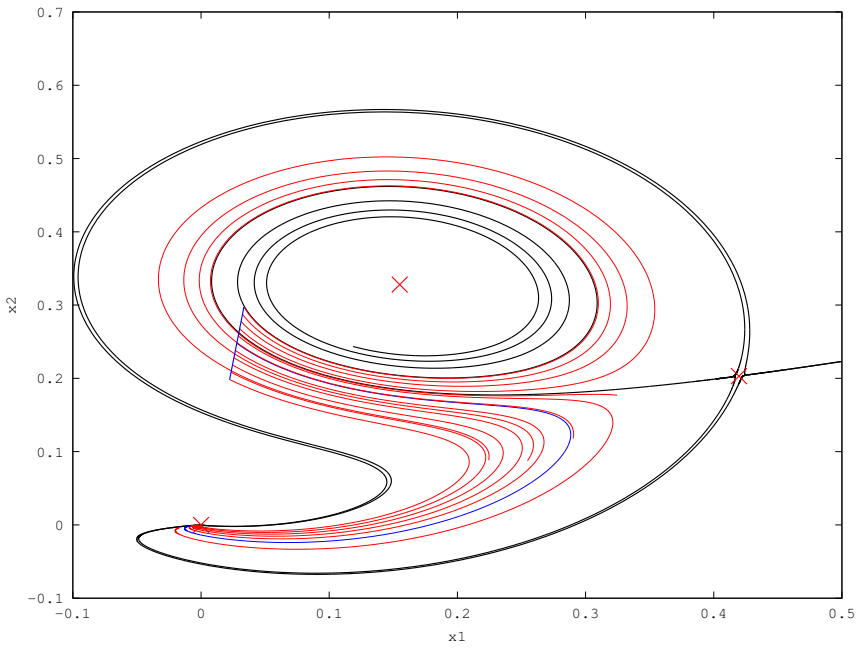

Figure 3.9: Phase space of the 2D model. Test this time carried out at later time on the original decaying trajectory. Initial condition now lies below the edge. Rescaled initial conditions still span the edge.

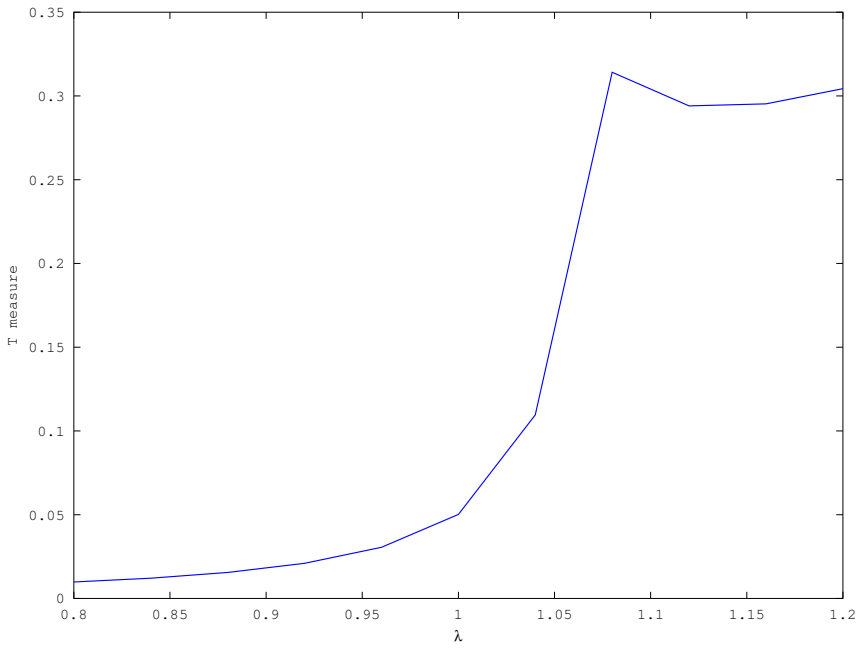

Figure 3.10: T measure against λ for second point on the trajectory. Graph confirms no edge beneath trajectory (smaller λ) but edge exists above (larger λ).

These techniques work well for finding the attracting objects embedded within the edge, but using this definition the edge will not be found near the turbulent part of phase space. This can be compared to using the T measure (with a short time average) to define the edge in the low dimensional model. If this was used, only the outer spiral of the edge would be detected. In the two dimensional model the edge is defined to be the stable manifold of the edge state, which removes the issue. In the full system, in geometries which have a single attracting edge state, we can use the same definition. While the edge state may be located using the bisection technique, we suggest that the edge is defined as the stable manifold of the edge state. It should be noted that this definition does not automatically solve the problem of tracking the edge near turbulent, which will be discussed later in this work. With this new definition of the edge, we can move forward to comparing the full dynamics with the low dimensional model.

The test begins with a single relaminarizing trajectory, along which two test points are selected. The flow fields at these points are rescaled using the same methodology as before,

$$\mathbf{u}_{in} = \lambda \mathbf{u} \tag{3.7}$$

where $\lambda = 1$ recovers the original dynamics. For each value of λ the initial condition is generated, evolved for a set time, and the time average of the L2 norm of $\mathbf{u}$ recorded (again called the T measure). Figure 3.11 shows the evolution of the L2 norm of $\mathbf{u}$ for the original trajectory and rescaled conditions for $\lambda \in [0.8, 1.3]$, and in figure 3.12 is plotted the T measure against λ. By choice the original trajectory decays quickly, as do its neighbours

in λ. However for both larger and smaller values of λ the T measure increases, indicating a crossing of the edge to turbulent dynamics on both sides of the point. A second region where trajectories decay exists at $\lambda \simeq 0.9$. The main point to receive is that there exists an edge (in this case several pieces of the edge) below the relaminarizing trajectory. The next step is to carry the process out at a later time, the results of which are presented in figures 3.13 & 3.14. A transition has occurred since the previous analysis, as there now exists no edge beneath the relaminarizing trajectory. Turbulent dynamics are only to be found by choosing $\lambda > 1.2$. While the results of conducting this test on the full dynamics are far more complicated than those of the low dimensional model, certain characteristics are maintained in both situations. Early in the decay, part of the edge exists beneath the trajectory in phase space. Yet later, this edge beneath is no longer present. This result is unsurprising given that by the definition of the edge this transition from one "side" to another has to occur. However the time and manner of the transition can provide evidence as to the topology of the edge.

Early in the decay the test shows the existence of an edge below the decaying trajectory. Using the bisection techniques briefly discussed earlier we can track the dynamics on this edge. Later in the decay of the original trajectory there exists only an edge above the decaying trajectory. Again bisection can be used to track the dynamics of this part of the edge. Figure 3.15 shows the evolution of these two pieces of edge, the edge beneath in green and the edge above in red. The dynamics on these two pieces of edge initially move in different directions, however 200 time units later they become involved in the same dynamics which is maintained for the rest of the time the edge is accurately tracked[2]. This result suggests that the two pieces of edge above and below the trajectory are dynamically connected. Building on the previous result we now have a more complete picture of the route past the edge. The transition from the trajectory lying above the edge to below it, added to the dynamical connection of those two pieces of edge fits with the low dimensional picture built by the 2D model of Lebovitz. The complete geometry of the edge in the full dynamics is much more complicated than a 2D model could hope to model, as shown by the multiple layers of edge observed in figure 3.12. Two further details from this work also suggest agreement with the low dimensional model, that the edge goes up into the turbulent part of phase space. If we examine the location of the transition in relative edge position of a trajectory (from above the edge to below the edge) under the E_{3D} projection of the dynamics we note that this transition occurs at values of E_{3D} associated with turbulent dynamics. This metric is commonly used to evaluation if a flow field is turbulent and therefore suggests the edge also exists near turbulence in phase space. This claim could be proved by developing a method to track the edge into turbulence, however a method to perform this is not clear. The second observation to be made concerns the evolution of the dynamics after the transition in edge location has occurred. As can be seen in figure 3.15, the relaminarizing trajectory tracks the dynamics of the edge for approximately 50 time units before diverging. This picture is consistently observed and helps our understanding of the manner in which trajectories pass by the edge. The trajectories running approximately parallel to the edge in phase space fits the picture produced from the low dimensional model. None of the results found in this work are individually convincing arguments for the

[2]i.e. when the coloured pairs diverge. There is no evidence that if the edge was tracked longer these edge dynamics would separate.

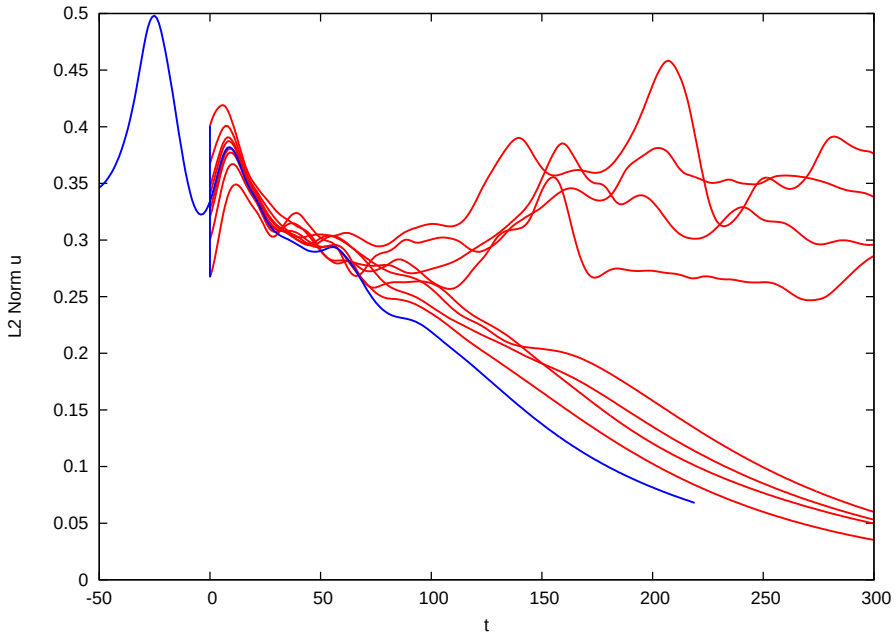

Figure 3.11: L2 norm of **u** against time. Blue curve shows decaying trajectory in full dynamics. Blue straight line shows range of initial condition from λ rescaling. Red curves show selected evolution trajectories from these new initial condition.

spiral topology of the edge. However together they begin to form a body of evidence which supports a more complicated version of this cartoon of the edge geometry. The manner of the transition around the edge appears to agree with the picture constructed. The E_{3D} projection suggests this transition happens near turbulence, and the dynamics of the edge near this transition appear to be connected. The evolution of the trajectory as it leaves turbulence remains close to the edge for a significant amount of time (> 50 time units) both before and after transition, which again is in agreement with the low dimensional model.

3.5 Conclusion

The focus of this work has been understanding the role that the edge plays during decay from turbulence. Beginning from a hypothesis that turbulence decayed through a point in the edge, we examined the statistics and physical processes involved in decay. We finished by comparing the dynamics of the edge in a low dimensional system to the full dynamics of plane Couette flow. There was no evidence to support the hypothesis of a unique decay point, instead what was observed was a wide variety of decay rates and routes back to the laminar state. We statistically confirmed ideas about the physical processes involved during the decay. Statistically all parts of the flow field begin to decay at the same point in time, but the downstream rolls and x-dependent part of the flow field decay at a greater relative rate. The last 200 time units of decay involve only downstream fast and slow streaks. The

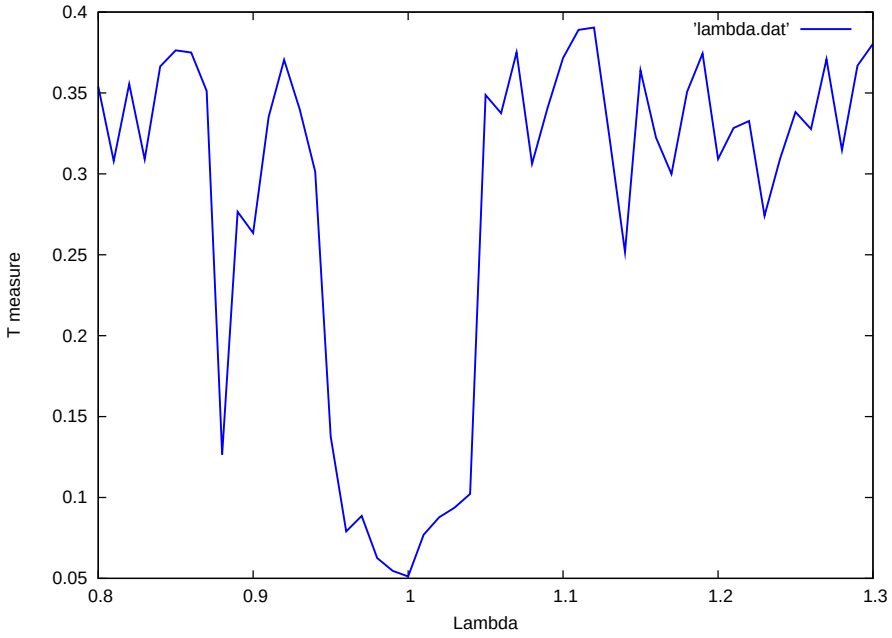

Figure 3.12: T measure against λ for first point in full dynamics. T measure values larger than 0.2 indicate turbulent evolution. Highly complex edge structure evident, with 3 regions of turbulent dynamics and 2 regions of laminar dynamics. Points to 3 individual edge pieces.

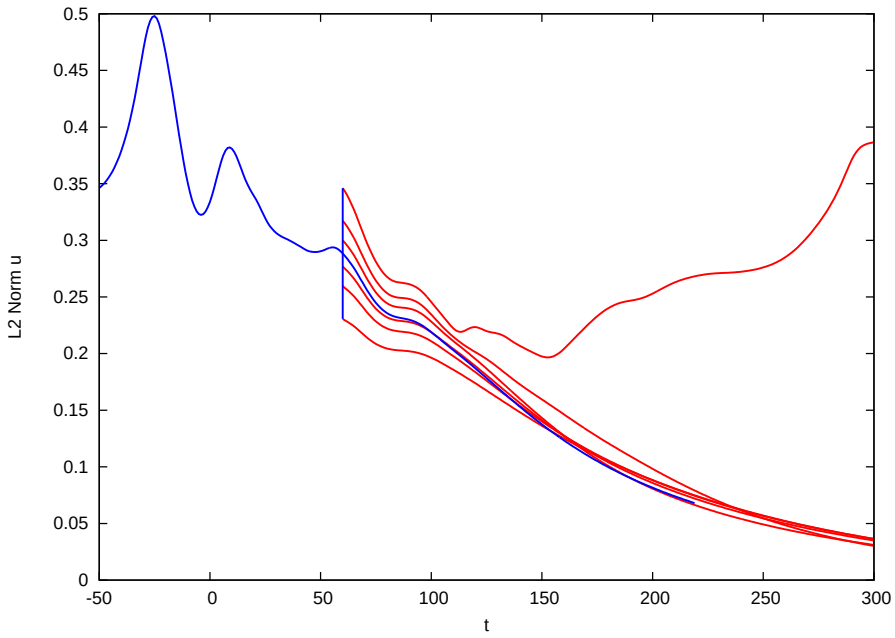

Figure 3.13: L2 norm of **u** against time for second point 60 time units later. Blue curve shows decaying trajectory in full dynamics. Blue straight line shows range of initial condition from λ rescaling. Red curves show selected evolution trajectories from these new initial condition.

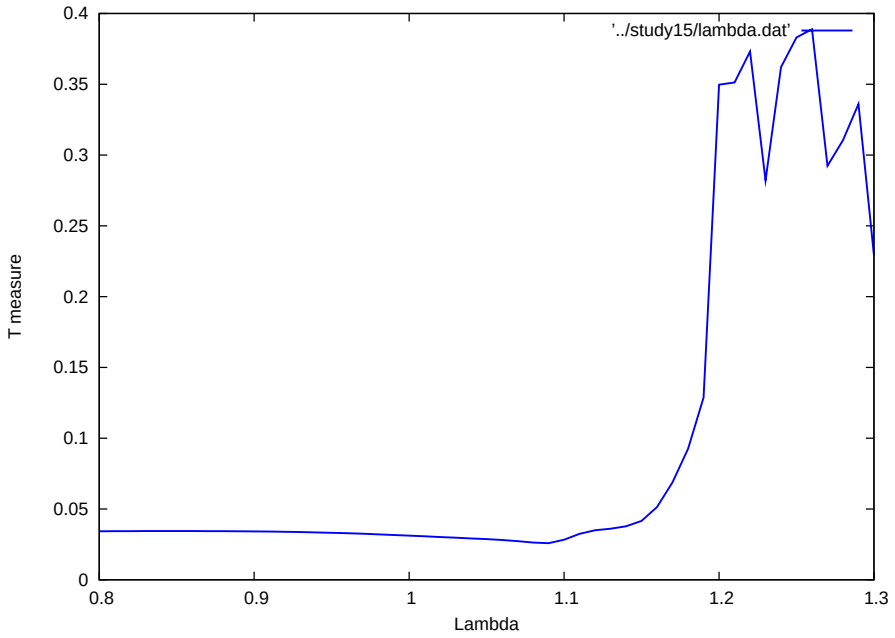

Figure 3.14: T measure against λ for second point. Simpler structure, evidence for single edge piece intersecting the rescaling line. Edge lies above the relaminarizing trajectory.

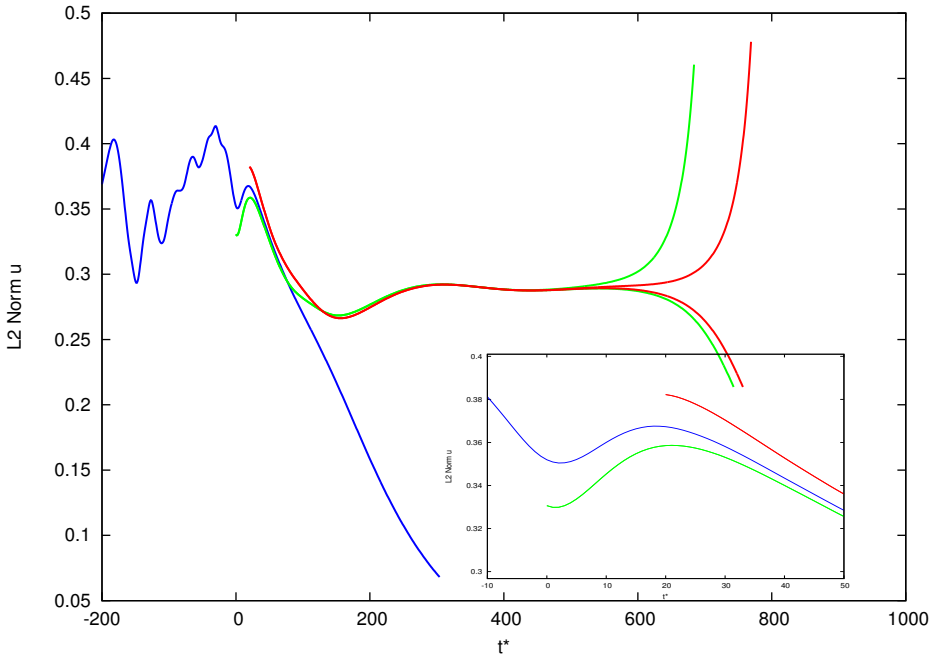

Figure 3.15: L2 norm of **u** against t (relabeled to locate initial edge bisection at zero). Blue curve - relaminarizing trajectory which transitions from having edge below to edge above only. Green curves - bounding curves for edge bisection tracking the dynamics of the edge below the blue curve at $t = 0$. Red curves - bounding curves for edge bisection tracking the dynamics of the edge above the blue curve at $t = 20$. Both pieces of edge become involved in same dynamics, indicating dynamical connection. Inset: close-up around $t = 0$.

rate that these streaks decay is set by the horizontal length-scales involved. The streak structure during decay is simple, involving predominately the first and second horizontal Fourier modes. The relative energy in these two modes sets the decay rate. To understand the geometry of the edge in the full dynamics we ran tests to compare this to a 2D model. This 2D model had been selected as the simplest model containing edge structure seen in several low dimensional models of shear flows. In these models the edge extended to infinity in one direction, but in another wrapped up infinitely many times around a structure (in the case of the 2D model a fixed point). Comparing to this model we saw some evidence in the full dynamics for similar, if more complicated structure. Decaying trajectories passed around the edge, and the parts it passed around were found to be dynamically connected in some cases. The value of E_{3D} at this transition suggests that the edge passes up into phase space. However we do not claim that this evidence proves this model to be accurate. What we have succeeded in doing, is test the validity of this model with a series of tests, and further work is required before stronger conclusions can be made. There are several areas of this work where interesting extensions are clear. Conducting the statistical analysis for a larger domain size would allow study of the conjectures on streak structure. Are six-streak structures observed in larger domains during decay, and at what Reynolds numbers? Another question opened up by this work is into the significance of the location where a decaying trajectory passes around the edge. Does this occur at a specific time before decay, and are there particular characteristics of the flow field as the edge is rounded?

Despite having held attention of great minds since 1883, turbulence in shear flows is an area where real progress is currently being made around the globe. Modern ideas and powerful computers have enabled the discovery of new and complex solutions, which bear resemblance to experimental work. Progress has been made furthering our understanding of the edge, and the role that it plays in the dynamics of turbulent shear flows. The edge itself changes strongly with Reynolds number, with different solutions playing the role as the edge state. The idea that the edge is wrapped and folded around the turbulent dynamics, which a trajectory must negotiate in order to return to the laminar state, is an idea which requires further study before conclusions can be drawn.

3.6 Acknowledgments

This work was carried out thanks to my appointment as a GFD fellow at the Woods Hole Oceanographic Institute. The project was suggested by Tobias Schneider who supervised my work this Summer. Thanks go to John Gibson who offered insight and support with channelflow [24], and to Norm Lebovitz for his advice on low dimensional models. A final thanks to the other GFD fellows and staff who made this Summer very enjoyable.

Bibliography

[1] Hagen, G. H. L. 1839, Über die Bewegung des Wassers in engen zylindrischen Rohren, *Poggendorfs Annal. Physik Chemie*, 16.

[2] Poiseuille, K. L. M., 1840, Recherches experimentales sur le mouvement des liquides dans les tubes de très petits diametres., *CR Acad. Sci.*, 11, 961.

[3] Reynolds, O. 1883, An experimental investigation of the circumstances which determine whether the motion of water shall be direct or sinuous and of the law of resistance in parallel channels., *Phil. Trans. R. Soc.*, 174, 935-982.

[4] Faisst, H. & Eckhardt, B., 2004, Sensitive dependence on initial conditions in transition to turbulence in pipe flow., *J. Fluid Mech.*, 504, 343-352.

[5] Nagata M., 1990, Three-dimensional finite-amplitude solutions in plane Couette flow: bifurcation from infinity. *J. Fluid Mech.*, 217.

[6] Kawahara G. & Kida S., 2001, Periodic motion embedded in Plane Couette turbulence: regeneration cycle and burst. *J. Fluid Mech.*, 449, 291.

[7] Waleffe F., 2003, Homotopy of exact coherent structures in plane shear flows. *Phys. Fluids*, 15.

[8] Faisst, H. & Eckhardt, B., 2003, Travelling waves in pipe flow. *Phys. Rev. Lett.* 91, 224502.

[9] Wedin, H. & Kerswell, R.R., 2004, Exact coherent structures in pipe flow: travelling wave solutions. *J. Fluid Mech.* 508, 333-371.

[10] Pringle, C.C.T. & Kerswell, R.R., 2007, Asymmetric, helical and mirror-symmetric travelling waves in pipe flow. *Phys. Rev. Lett.* 99, 074502.

[11] Viswanath D., 2007, Recurrent motions within plane Couette turbulence. *J. Fluid Mech.*, 580.

[12] Halcrow J., Gibson J.F., Cvitanovi P., & Viswanath D., 2011, Heteroclinic connections in plane Couette flow. *J. Fluid Mech.*

[13] Kerswell, R. R. 2005, Recent progress in understanding the transistion to turbulence in a pipe., *Nonlinearity*, 18, R17-R44.

[14] Itano, T. & Toh, S., 2001, The Dynamics of Bursting Process in Wall Turbulence., *J. Phys. Soc. Japan*, 70, 3, 703-716.

[15] Skufca, J. D., Yorke, J. A. & Eckhardt, B., 2006, Edge of Chaos in Parallel Shear Flow., *Phys. Rev. Let.*, 96, 174101.

[16] Schneider, T. M., Gibson. J. F., Lagha, M., De Lillo, F. & Eckhardt, B., 2008, Laminar-turbulent boundary in plane Couette flow., *Phys. Rev. E*, 78, 037301.

[17] Schneider, T. M., Eckhardt, B. & Yorke, J. A., 2007, Turbulence transition and the edge of chaos in pipe flow., *Phys. Rev. Let.*, 99, 034 502

[18] Waleffe F., 1997, On a self-sustaining process in shear flows. *Phys. Fluids*, Vol. 9, pp. 883-900.

[19] Moehlis, J., Faisst, H. & Eckhardt, B., 2004, A low-dimensional model for turbulent shear flows. *New Journal of Physics*, 6, 54.

[20] Dawes, J.H.P., & Giles, W.J., 2011, Turbulent transition in a truncated 1D model for shear flow. *Proc. Roy. Soc. A.*, To appear.

[21] Lebovitz, N. R., 2009, Shear-flow transition: the basin boundary. *Nonlinearity*, 22, 2645-2655.

[22] Lebovitz, N. R., 2011, Boundary collapse in models of shear-flow transition. *Communications in Nonlinear Science and Numerical Simulations*, accepted.

[23] Gibson J.F., Halcrow J., Cvitanović P., 2008, Visualizing the geometry of state space in plane Couette flow. *J. Fluid Mech.*, 611.

[24] http://www.channelflow.org/

Project 4

A low dimensional model for shear turbulence in Plane Poiseuille Flow: an example to understand the edge

Giulio Mariotti

Boston University

4.1 Introduction

Recent studies of turbulent transition in shear flows [12, 10] have highlighted the presence of a peculiar feature in the phase space: the edge of chaos. The edge of chaos, or simply the edge, is a codimension one invariant set embedded in the basin of attraction of the laminar state, which divides this basin into two subregions: one where orbits decay directly and quite rapidly, and a second where they decay indirectly and more slowly. In terms more familiar to fluid mechanics, the edge divides initial flow conditions that relaminarize rapidly from initial flow conditions that experience transient turbulence and eventually relaminarize.

The edge behavior has been identified both in Direct Numerical Simulations (DNS) [10, 11, 9] and in low dimensional models [12]. In both cases the edge coincides with the stable manifold of an invariant object, the edge state [12], which can be either a simple fixed point [11], a periodic orbit or a higher-dimensional chaotic invariant set [12, 10].

Even though DNS constitutes the ultimate tool to explore turbulence, low dimensional models offer precious insights and analogies on the nature of the edge. A seminal contribution is Waleffe's model for Couette flow [14] (W97), based on a Galerkin truncation of the NS equations. The modes chosen for the truncation stem from a self sustained process between streamwise rolls, streamwise streaks, and streaks instabilities, a triad considered fundamental in turbulent transition [3]. Waleffe proposed an eight modes model and a further reduction to a four modes model, both of which showed a lower branch family of saddle points and an upper branch family of stable or unstable fixed points, analogous to the upper

and lower branches of traveling waves found in DNS [15, 16]. The presence of a dual relaminarization behavior in the W97 model, 'direct' and through 'transient-turbulence', was identified in [1], while the edge structure was studied recently in [4]. A dual relaminarization behavior was also found in a nine modes variation of W97 [6, 7].

A question about the edge remains open: if the edge divides the phase space in two regions, how do trajectories that experience transient turbulence relaminarize? It was initially proposed [12] that initial conditions that experience transient turbulence lie close to the edge, specifically between two symmetric parts of it, but in the laminar basin. The longer relaminarization time was explained by the fractal structure of the edge. It has been suggested [10] that 'the stable manifold of the laminar profile and the stable manifold of the edge state have to intermingle tightly in the region with turbulent dynamics'.

A dynamical description of the edge's 'intermingling' has been drawn by a simple two dimensional model [5], which features only linear and quadratic terms, non-normal matrix for the linear terms and energy conserving nonlinear terms. The idea is that the edge, i.e. the stable manifold of the edge state, does not extend indefinitely over the whole phase space. Indeed, the model shows that part of the stable manifold of a lower branch fixed point, i.e. the edge, coincides with the unstable manifold of an upper branch fixed point. The basic mechanism of the edge is hence the following: trajectories starting below the stable manifold approach the origin directly, while trajectories starting above the stable manifold have to travel around the upper branch fixed point in order to reach the origin. To complicate further the situation, the stable manifold can spiral around the upper branch fixed point. As a result, an orbit starting between the folds of the stable manifold will experience a longer path to the origin, enhancing the edge behavior.

Here we study a sixth-order truncated model of Plane Poiseuille Flow with free-slip boundary conditions. The basic structure is analogous to W97 and indeed the model shows analogous dynamical characteristics. In addition, the model has striking similarities with the two dimensional model in [5]. The main purpose of this work is to identify the edge-like behavior and to explain it in terms of basic dynamical-systems objects. This description will hopefully facilitate the understanding the edge behavior in more complex systems, such as the full NS equations.

4.2 Model description

The coordinate system is chosen such that x is in the streamwise direction, y in the wall-normal direction, and z in the spanwise direction. The domain is $x \in [0, L_x]$, $y \in [-1, 1]$, and $z \in [0, L_z]$, where $L_x = \frac{2\pi}{\alpha}$, $L_z = \frac{2\pi}{\gamma}$. The vertical wave number, β, is chosen equal to $\pi/2$, while the x and z wavenumbers are initially left unconstrained. Periodic boundary conditions are imposed along x and along z. Six solenoidal modes are introduced:

$$\phi_1 = \begin{bmatrix} \sqrt{2}cos(\beta y) \\ 0 \\ 0 \end{bmatrix}, \tag{4.1}$$

$$\phi_2 = \begin{bmatrix} 2\sqrt{2}cos(\gamma z)sin(2\beta y)sin(\beta y) \\ 0 \\ 0 \end{bmatrix}, \tag{4.2}$$

$$\phi_3 = \frac{2}{c_3}\begin{bmatrix} 0 \\ \gamma sin(2\beta y)cos(\gamma z) \\ -2\beta cos(2\beta y)sin(\gamma z) \end{bmatrix}, \tag{4.3}$$

$$\phi_4 = \begin{bmatrix} 0 \\ 0 \\ 2cos(\alpha x)sin(2\beta y) \end{bmatrix}, \tag{4.4}$$

$$\phi_5 = \frac{\sqrt{2}}{c_5}\begin{bmatrix} 2\gamma cos(\alpha x)sin(\gamma z)sin(\beta y) \\ 0 \\ -2\alpha sin(\alpha x)cos(\gamma z)sin(\beta y) \end{bmatrix}, \tag{4.5}$$

$$\phi_6 = \frac{2\sqrt{2}}{c_6}\begin{bmatrix} -\alpha\beta cos(\alpha x)sin(\beta y)sin(2\gamma z) \\ (\alpha^2+\gamma^2)sin(\alpha x)cos(\beta y)sin(2\gamma z) \\ \beta\gamma sin(\alpha x)sin(\beta y)sin(\gamma z)^2 \end{bmatrix}, \tag{4.6}$$

with the following normalization coefficients:

$$c_3^2 = 4\beta^2+\gamma^2, c_5^2 = \gamma^2+\alpha^2, c_6^2 = \alpha^2\beta^2+\gamma^4+2\gamma^2\alpha^2+\alpha^4+3/4\beta^2\gamma^2. \tag{4.7}$$

The first three modes are intended to represent respectively the mean streamwise flow, the streamwise streaks, and the streamwise rolls. The last three modes are intended to represent the 1D, 2D and 3D streak instabilities. The mean flow is approximated by a cosine. The maximum difference in the streamwise velocity is found between the walls, $y = 1$ and the center line, $y = 0$. As a consequence, the roll capable of the most mixing has a wavelength equal to $\beta/2$ (Fig. 4.1). As a comparison, the most mixing efficient roll in Couette Flow has wavelength equal to β. The resulting Galerkin representative of the streaks, ϕ_2, has a maximum at $y = \pm\frac{2}{\pi}\arccos\left(\frac{1}{\sqrt{3}}\right) \sim \pm 0.61$, which is closer to the wall than the centers of the rolls, $y = \pm\frac{1}{2}$ (Fig. 4.1).

The roll mode ϕ_3 has free-slip boundary condition in the z direction, and the 2D and 3D streaks instability modes, ϕ_5 and ϕ_6, have free-slip boundary conditions in both the x and z directions. The six modes are drawn from the 'shift-reflect' class, i.e., equivalent under the transformation:

$$[u(x,y,z);v(x,y,z);w(x,y,z)] \rightarrow [u(x+L_x/2,y,-z);v(x+L_x/2,y,-z);-w(x+L_x/2,y,-z)], \tag{4.8}$$

where u, v, and w are the velocity components along x, y, and z.

Assuming that the modes are fully capturing the dynamics of interest, we truncate the velocity field to the following finite sum:

$$\mathbf{u}(\mathbf{x},t) = \sum_{i=1}^{N} X_i(t)\phi_i(\mathbf{x}), \tag{4.9}$$

where X_i is the amplitude of the mode ϕ_i and N is the number of modes, here equal to 6. The truncated velocity is then substituted in the Navier Stokes equations,

$$\frac{\partial \mathbf{u}}{\partial t} + \mathbf{u}\cdot\nabla\mathbf{u} = -\nabla p + \frac{1}{R}\nabla^2\mathbf{u} \quad + F(y)\hat{\mathbf{X}}, \tag{4.10}$$

and the resulting equation (4.10) is projected into the each mode ϕ_k, by setting the inner product of (4.10) and ϕ_k equal to zero. The spatial integration of the inner product removes the space-dependence and the procedure yields a system of N coupled ODEs for the amplitude X_i. The partial time derivative in (4.10) becomes the total time derivate in the ODEs, the laplacian becomes a linear term, while the advection becomes non-linear terms. Because of the solenoidal condition of the modes and the boundary conditions, the pressure term does not appear in the ODEs, while the body force becomes an inhomogeneous term.

Utilizing the modes 4.1-4.6, we obtain the following system of ODEs for the amplitudes X_i,

$$\dot{\mathbf{X}} = A\mathbf{X} + g(\mathbf{X}) + \frac{k_1}{R}\hat{X}_1. \tag{4.11}$$

The forcing term is present only in the direction of the mean flow mode. The matrix A describes the viscous dissipation,

$$A_{i,j} = -\delta_{i,j}\frac{k_i}{R}, \tag{4.12}$$

where,

$$\boldsymbol{k} = \begin{bmatrix} \beta^2 \\ 5\beta^2 + \gamma^2 \\ c_3^2 \\ \alpha^2 + 4\beta^2 \\ \alpha^2 + \beta^2 + \gamma^2 \\ (\alpha^2 + \beta^2) + (\gamma^2(4c_5^4 + \beta^2(4\alpha^2 + \gamma^2)))/c_6^2 \end{bmatrix}. \tag{4.13}$$

The operator g includes the non-linear terms,

$$g(\mathbf{X}) = \begin{bmatrix} -\sigma_0 X_2 X_3 \\ \sigma_0 X_1 X_3 - \sigma_1 X_4 X_5 \\ -(\sigma_4 + \sigma_5) X_5 X_6 \\ \sigma_2 X_2 X_5 - \sigma_3 X_1 X_6 \\ (\sigma_1 - \sigma_2) X_2 X_4 + (\sigma_4 - \sigma_6) X_3 X_6 \\ (\sigma_5 + \sigma_6) X_3 X_5 + \sigma_3 X_1 X_4 \end{bmatrix}, \tag{4.14}$$

with the following coefficients:

$$\sigma_0 = \frac{\beta\gamma}{c_3}, \sigma_1 = \frac{\gamma^2}{c_5}, \sigma 2 = \frac{\alpha^2}{c_5}, \sigma_3 = \frac{\gamma\alpha\beta}{2c_6}, \sigma_4 = \frac{\beta^2(4\alpha^2 + 5\gamma^2)\alpha}{2c_3c_5c_6}, \sigma_5 = \frac{(\beta^2 - \alpha^2 - \gamma^2)\gamma^2\alpha}{2c_3c_5c_6}, \sigma_6 = \frac{\gamma^2\beta^2\alpha}{4c_3c_5c_6}. \tag{4.15}$$

The non-linear terms are quadratic and conserve energy, i.e. $\langle \mathbf{X} \cdot g(\mathbf{X}) \rangle = 0$. The system of ODEs shows three symmetries: S_1=diag(1,1,1,-1,-1,-1), S_2=diag(1,-1,-1,1,-1,1), and S_3=diag(1,-1,-1,-1,1,-1). The last symmetry comes from the product of the first two. These symmetries are undoubtedly inherited from the shift-reflect symmetry, but the derivation has not been done.

Finally, the transformation $X_1 \rightarrow X_1 + 1$ is introduced, so that the laminar state corresponds to $\mathbf{X} = 0$.

4.3 Analysis of the system

The matrix of the system linearized around the laminar state is non-normal, because of the component $\sigma_0 X_1 X_3$ in the second ODE of (4.11). The laminar state is a fixed point, linearly stable for all R. It is evident that the model is not able to reproduce the linear instability of the laminar state found in Plane Poiseuille Flow for $R > 5772$ [8]. However, it is widely accepted that this instability is not significant for transition to turbulence.

The analytical solution for the steady state of the system (4.11) is found to be a polynomial of 8^{th} order in X_5. Under the explored range of values for the parameter α, γ and R, no real solutions are found, implying that the system (4.11) has no fixed points other than the laminar point. Also an asymptotic analysis shows no presence of fixed points. In order to reduce the number of free parameters, the wavelengths are set constant, $\gamma = 5/3$ and $\alpha = 1.1$, corresponding to the values used for the Couette flow in W97 [14].

The search of other non-trivial solutions is initially performed sampling the direction of the maximum transient linear growth. An approximation of this direction is found to be $\hat{X}_3$, i.e. the rolls component. However, perturbing the laminar state in only one direction is not sufficient to find non-laminar solutions. In fact, the modes $X_{1,2,3}$ constitute a closed set when the initial value of the modes $X_{4,5,6}$ is zero. We therefore introduce a small perturbation, $O(10^{-3})$, on the modes $X_{2,4,5,6}$, and a greater perturbation, $O(10^{-1})$, on the X_3 mode. Fixing $R = 500$, a stable periodic orbit is found.

4.4 Bifurcation analysis

The bifurcations of the stable orbit were followed using the continuation software MatCont [2], using R as control parameter. A saddle node bifurcation appears for $R > R_{sn} \sim 291.7$, giving birth to two branches of periodic orbits (Fig. 4.2A). The lower branch (PO_{lb}), closer to the laminar state, is unstable for all R, with only one real Floquet multiplier greater than one (Fig. 4.2C). The upper branch (PO_{ub}) is initially unstable, with two real multipliers greater than one (Fig. 4.2D). The two multipliers readily become complex conjugate for $R > R_c \sim 292.4$, but they remain greater than one. At $R > R_t \sim 305.5$ the two complex conjugate multipliers become smaller than one, and the periodic orbit becomes stable. Because of the system symmetries, two other couples of upper and lower branches periodic orbits are present.

The bifurcation portrait shows some similarities with the model W97, in which a saddle-node bifurcation gives birth to two branches of fixed points. Also for the W97 model, the lower branch is always unstable, with only one unstable direction, and the upper branch is initially unstable, with two unstable directions. The upper branch is initially an unstable node, and turns readily into an unstable spiral, when the two positive eigenvalues become complex conjugate. For higher value of R the spiral node becomes stable through a Hopf bifurcation. The analogy between the two models is clear when fixed points are replaced with periodic orbits.

4.4.1 Bifurcation at R_t

state ceases to be the only attracting state and PO_{ub} introduces an additional basin $X_1 - R$ plane, with components $X_{2,3,4,5,6}$ kept fixed, is plotted in Figure 4.3. The basin boundary is initial conditions which converge to the laminar state from initial conditions which converge to PO_{ub}. This identification is

When R exceeds R_t, a bifurcation takes place: the laminar state ceases to be the only attracting state and PO_{ub} introduces an additional basin of attraction. A slice of the two basins in the $X_1 - R$ plane, with components $X_{2,3,4,5,6}$ kept fixed, is plotted in Figure 4.3. The boundary is identifiable using the time needed for the orbit to come arbitrarily close to the origin (relaminarization time). Trajectories starting inside the basin of attraction of PO_{ub} have a relaminarization time equal to infinity or to the maximum simulation time. The identification of the basin boundary is complicated, as usual, by the long transient time of trajectories starting close to the basin boundary. As expected the new basin of attraction appears around $R = R_t$, and expands for increasing value of R.

Are there structures embedded in the boundary of the basin of attraction? Since the bifurcation at $R = R_t$ is a subcritical Neimark-Sacker type, we expect the appearance of an invariant two-dimensional torus for $R > R_t$. Indeed we found a periodic orbit lying on a torus embedded in the basin boundary. This orbit was found bisecting initial conditions on different sides of the basin boundary. The orbit on the torus for $R = 307.0$ is shown in Figure 4.4D. The torus orbit has a high-frequency modulation with a period approximately equal to that of PO_{ub}. The total period of the torus orbit is approximately ten times this high-frequency modulation. The multipliers of the orbit are $1.19 \pm 0.45i$; 1; $2\ 10^{-5}$; 1 10^{-10}; $5\ 10^{-8}$. The torus is therefore unstable, with a very attracting stable manifold.

Unfortunately, we were not able to continue the torus orbit for different values of R using Matcont. Computing the torus orbit with the bisection technique for different value of R, we found that the torus shrinks for decreasing values of R and collapses to PO_{ub} at $R = R_t$. We also found that the period of the orbit on the torus can change discontinuously with R. A complete investigation of the torus is left to other studies.

4.4.2 Description of the periodic orbit

For completeness, a brief description of the periodic orbit is presented. The period at the saddle node bifurcation is ∼31.8 time units. The period of PO_{ub}, T, increases monotonically with R, while the period of PO_{lb} decreases monotonically with R (Fig. 4.2B), both approaching an asymptotic value. The structure of PO_{ub} and PO_{lb} is similar for all values of R (Fig. 4.4). The center of both PO_{ub} and PO_{lb} has components $X_{2,3,4,6}$ equal to zero and components $X_{1,5}$ different from zero. In addition, the period of the components X_1 and X_5 is half the period of the other 4 components, i.e. the period of of X_1 and X_5 alone is half the period of the full orbit. The different behavior of the mode X_1 and X_5 compared to the other modes emerges from the symmetry S_3. We have in fact that $S_3(\mathbf{X}(t)) = \mathbf{X}(t + T/2)$, i.e. $S_3(\mathbf{X}(t))$ is not a different periodic solution but just the original solution translated by half period. This implies that the mean of $X_{2,3,4,6}$ over a period must vanish. In general, we don't expect this to be a common feature in other low dimensional models.

A particular behavior of the streaks and rolls mode, ϕ_2 and ϕ_3, was noticed: they seem to have a different relative phase in the stable and unstable periodic orbit. As shown in

Figure 4.4A and B, the streaks precede the rolls in the stable orbit, while the rolls precede the streaks in the unstable orbit. In the $X_2 - X_3$ plane, the former situation corresponds to a counter clockwise rotation of the trajectory and the latter to a clockwise rotation. The phase lag of the streaks relative to the roll is quantified with the maximum of the cross-correlation between X_2 and X_3:

$$\varphi = max(t) \int_T X_3(\tau) X_2(\tau + t) d\tau, \tag{4.16}$$

The lag of the streaks is positive for the whole lower branch and for most of the unstable part of the upper branch. For R just before R_t the lag of the streaks turns negative, and remains negative for the remaining part of the upper branch. The physical interpretation of these behaviors is not clear, and will not be considered further in this work.

4.5 Structure of the edge

The rest of this work is devoted to the search for edge-like structures in the phase space.

4.5.1 $R > R_t$

We first consider the case of $R > R_t$, when both a stable and an unstable periodic orbit are present. The lifetime before relaminarization is used to map the phase space (see [6, 12, 10, 13]). The coordinates X_1 and X_5 seem an intuitive choice, given their different behavior with respect to $X_{2,3,4,6}$. Figure 4.5 shows the relaminarization time for different fixed values of $X_{2,3,4,6}$, keeping R fixed, equal to 307.0. Two regions are distinguished: D, where orbits are attracted to the stable periodic orbit PO_{ub}, and B, where orbits are attracted to the origin in a finite time. In addition, two subregions can be distinguished in B: B_s, where orbits tend to the origin in a relatively short time, and B_l, where orbits tend to the origin in a longer time. In general, while trajectories starting in B_s proceed almost directly to the origin, trajectories starting in B_l take a more convoluted path to the origin, causing the longer relaminarization time.

The different time and pattern of relaminarization in B is now analyzed. Starting with a trajectory in B_s (e.g. trajectory p_1 in Fig. 4.6A), we move the initial condition toward the basin D. We intersect a point after which orbits take a considerably longer path before approaching the laminar state. Using a bisection technique [12], we identify a point in the phase space of initial conditions, say x_0, which determines a sudden change: a trajectory starting just below x_0, x^-, approaches the origin quite directly, while a trajectory starting just above x_0, x^+, takes a longer path to the origin (Fig. 4.6B).

Both trajectory x^- and x^+ approach PO_{lb} arbitrarily closely. Before the two trajectories collapse into PO_{lb}, they separate: x^- goes directly to the origin while x^+ swings up, visits the region near the torus orbit and eventually converges to the origin. The fact that both x^- and x^+ initially converge to PO_{lb} implies that the point x_0 lies on the stable manifold of PO_{lb}, $SM(PO_{lb})$. The different trajectory behavior after PO_{lb} is evidently dictated by the presence of two branches of the unstable manifold of PO_{lb}, $UM(PO_{lb})$.

Because both x^- and x^+ belong to the laminar basin, the point x_0 has the nature of an edge: trajectories starting infinitesimally close but on two opposite sides of x_0 have

different finite-time, but same asymptotic dynamics. This result agrees with the finding that the edge coincides with the stable manifold of an invariant object [10, 9, 6, 12], which in this case corresponds to a lower branch of unstable periodic orbits. In addition, the fact that the trajectory x^+ is approaching the region of PO_{ub} suggests the presence of a connection between the upper and lower periodic orbits.

The way toward multiple edges

In order to navigate the variety of relaminarization patterns in B, we analyze two transects of initial conditions crossing ∂D. For simplicity, the two transects are chosen in the X_1 and X_5 direction, with all the other initial conditions kept fixed (Fig. 4.7). The first point on the transects, p_i, corresponds to a trajectory that relaminarizes 'directly', while the last point on the transects, p_e, corresponds to a trajectory that converges to PO_{ub}. Trajectories are described using two parameters: the time to relaminarization, and the maximum value achieved by the coordinate X_5, a footprint of the trajectory history.

The outcomes for both transects are similar. The relaminarization time is minimum for p_i and maximum, equal to the simulation time, for p_e. The lifetime of the initial conditions between p_i and p_e is characterized by 'steps' and 'spikes'. Starting from p_i and moving toward p_e, the lifetime is approximately constant, it suddenly increases and shortly after decreases. The lifetime then remains steady, higher than before the peak, approximately constant until the next peak. Increasing the number of bisection points, we found that points starting close to each peak come arbitrarily close to PO_{lb}. The interpretation is straightforward: at every peak the vector of initial conditions is intersecting a different fold of $SM(PO_{ub})$. Points lying just below or above $SM(PO_{ub})$ are attracted to PO_{ub} and then are captured by the two opposite arcs $UM(PO_{ub})$. The peak of $max(X_5)$ is evidently a trajectory captured by the arc of $UM(PO_{ub})$ leaving in the direction opposite to the origin.

What happens between the different folds of $SM(PO_{lb})$? We noticed that after every peak in the relaminarization time, the orbit makes an 'extra loop' around the torus orbit. The consequence of these extra loops is manifested as the 'steps' in relaminarization time. Therefore every fold of $SM(PO_{lb})$ determines a band of increasing relaminarization time. This suggests that $SM(PO_{lb})$ is wrapped around ∂D. Different folds of $SM(PO_{lb})$ appear also when other coordinates are chosen to section the phase space (Fig. 4.8). For example, the first 4 folds of $SM(PO_{lb})$ are plotted in Figure 4.8D.

It comes natural to ask what relationship is present between $SM(PO_{lb})$ and the orbits on the basin boundary of PO_{ub}. A simple interpretation would be that $SM(PO_{lb})$ coincides with the unstable manifold of the orbit on the torus, $UM(T)$. The spacing between the folds supports this idea. We found that the distance between the folds is in a geometric succession, approximately equal for both transects studied. Indeed the folds of an unstable manifold spiraling out of a periodic orbit are expected to be in a geometric succession. A cartoon of the various periodic orbits and manifolds is exemplified in Figure 4.7C. This situation is analogous to the 2D model in [5], where the stable manifold of the lower branch fixed point coincides with the unstable manifold of an unstable periodic orbit.

The situation in our case is more complicated than described above. The edge, which coincides with $SM(PO_{lb})$, has codimension one, i.e. dimension 5 in our system. The torus orbit has two complex conjugate unstable multipliers, at least for the value of R

considered. The dimension of $UM(T)$ is 3, considering both the unstable and neutral multipliers. Therefore $UM(T)$ and $SM(PO_{lb})$ cannot coincide. Instead, it is likely that these two objects intersect. A three dimensional cartoon of this intersection is shown in Figure 4.9.

4.5.2 $R < R_t$

When R decreases the basin of attraction of PO_{ub} shrinks and eventually disappears for $R < R_t$ (Fig. 4.3). The origin is a global attractor, except for a measure zero set containing the upper and lower branch unstable periodic orbits. Is the edge structure still present?

$R_c < R < R_t$

First we investigate the case with $R_c < R < R_t$, when the multipliers greater than one are complex conjugate. Again, we use the relaminarization time to map the phase space. All initial conditions relaminarize before the maximum simulation time (Fig. 4.10), in agreement with the absence of no other basins of attraction besides the laminar one. However, both regions with short, B_s, and long, B_l, relaminarization time persist, indicating the presence of the edge.

We study a transect of initial conditions, with the initial point p_i on B_s and the final point p_e on PO_{ub}. The results are analogous to the case with $R > R_t$: the lifetime of p_i is minimum, the lifetime of p_e is equal to the maximum time allowed by the simulation, and the lifetime of the initial conditions between p_i and p_e is characterized by 'peaks 'and 'steps'. Also in this case, trajectories associated with the peaks converge toward PO_{lb}, confirming that the transect of initial conditions is intersecting $SM(PO_{lb})$.

The distance between the peaks continues to be in a geometric succession, which suggests that $SM(PO_{lb})$ is spiraling around PO_{ub}. Is $SM(PO_{lb})$ still related to an unstable manifold? Because the torus orbit disappeared, $UM(PO_{ub})$ is the only candidate to consider. Also in this case the dimension of the unstable manifold is 3, less than the dimension of $SM(PO_{lb})$. Again, $UM(PO_{ub})$ cannot coincide with $SM(PO_{lb})$, but it might intersect it. Interestingly, the dimension of $UM(PO_{ub})$ is one unit smaller than the dimension of $SM(PO_{lb})$, and hence $UM(PO_{ub})$ is a potential candidate for the boundary of $SM(PO_{lb})$.

It is remarkable that, even though the basin boundary of PO_{ub} and the torus orbit are no longer present, the behavior of the edge remains unvaried. Therefore the edge is not related to the presence of a second basin of attraction besides the laminar one.

$R_{sn} < R < R_c$

Finally, we consider the case with $R_{sn} < R < R_c$. The multipliers of PO_{ub} greater than one become real, which forecasts the disappearance of the spiraling behavior of $SM(PO_{lb})$ and $UM(PO_{ub})$. Indeed, a sample of initial conditions from a point in B_s to a point on PO_{ub} shows no 'peaks' and 'steps' in relaminarization time. The lifetime is gradually increasing starting from the point on B_s and moving toward the point on PO_{ub} (Fig. 4.11A,B), where it has a maximum. After PO_{ub} the lifetime decreases and sets to a quite constant value, higher than before the point on PO_{ub}. Only a hint of the edge remained: a single step in lifetime crossing PO_{ub}.

How did $UM(PO_{ub})$ change? Because the multipliers are real, $UM(PO_{ub})$ has two distinct directions: $UM_1(PO_{ub})$, associated with the most unstable eigenvector v_1, and $UM_2(PO_{ub})$, associated with the least unstable eigenvector v_2. $UM1(PO_{ub})$ is easily tracked starting a initial condition along on v_1 and $-v_1$: both arcs of $UM1(PO_{ub})$ are connected directly to the origin. $UM2(PO_{ub})$ is more difficult to follow because initial conditions on v_2 are attracted to $UM1(PO_{ub})$. Using a bisection technique, and exploiting the fact that initial conditions on different sides are attracted to different arcs of $UM1(PO_{ub})$, we find an arc of $UM2(PO_{ub})$ which is connected directly to PO_{lb}, without any spiraling structure (Fig. 4.11C). The bisection technique is not able to find the other arch of $UM2(PO_{ub})$, and we suppose that this arch is connected directly to the origin (Fig. 4.11D).

In this configuration the edge behavior is present but strongly reduced. Trajectories on the upper side of the edge have to circumnavigate PO_{ub} before reaching the origin, but they are not slowed by the complicated path imposed by the spiral.

4.6 Discussion

The following dynamical portrait emerges from the study of a six dimensional model for shear turbulence. For $R > R_t$ there is a stable periodic orbit with a finite basin of attraction D. A periodic orbit on a torus is embedded in ∂D. The unstable manifold of the torus orbit, $UM(T)$, has a convoluted structure, which in a two dimensional projection appears as a spiral. This unstable manifold intersects the stable manifold of an unstable periodic orbit $SM(PO_{lb})$ (Fig. 4.12C).

$SM(PO_{lb})$ is technically part of the boundary of B, because every neighborhood of $SM(PO_{lb})$ contains at least one point of B (e.g., orbits that relaminarize) and at least one point not of B (e.g., orbits that collapse to PO_{lb}). However, the basin boundary nature of $SM(PO_{lb})$ is not intuitive, since orbits on both sides of $SM(PO_{lb})$ relaminarize. $SM(PO_{lb})$ divides orbits with different qualitative behavior belonging to the same basin of attraction, and hence it is an edge. The different qualitative behavior emerges because orbits on the side of the stable manifold opposite to the origin need to circumnavigate this object in order to relaminarize. The path followed by the orbits is complicated by the coiling structure of $SM(PO_{lb})$ around the basin of attraction of PO_{ub}. Orbits starting between the folds of the unstable manifold have to uncoil before reaching the origin. This is apparent in the two dimensional representation in Figure 4.7.

We propose the following analogy: the basin of attraction of PO_{ub} represents persistent turbulence, i.e. flows that never decay to laminar. Trajectories between the folds of $SM(PO_{lb})$ represent instead transient turbulence: complex flows which eventually decay to the laminar state. The edge structure divides orbits that relaminarize in a simple fashion from orbits that experience transient turbulence.

For $R_c < R < R_t$ the upper branch periodic orbit becomes unstable. The basin boundary of this orbit disappears, the torus collapses to PO_{ub}, and $UM(PO_{ub})$ takes the place of $UM(T)$. This unstable manifold continues to be a spiral, and continues to intersect $SM(PO_{lb})$ (Fig. 4.12B). The structure of the edge remains unchanged. To continue the analogy, the case $R_c < R < R_t$ describes a situation in which no sustained turbulence is possible. All the observed turbulence must be transient.

Finally, for $R_{sn} < R < R_c$ the multipliers of PO_{ub} become real, and the spiraling

behavior ceases to exist. One arc of $UM(PO_{ub})$ continues to intersect $SM(PO_{lb})$. Since this stable manifold is no longer a spiral, the edge effect is strongly reduced. The edge is still present as a single fold, which divides trajectories that go straight to the origin from those that have to circumnavigate PO_{ub} (Fig. 4.12A).

These results show many similarities with the two-dimensional model studied by Lebovitz [5]. The model in [5] shows, for a certain range of a Reynolds-like parameter R^*, an upper and lower fixed point and an unstable periodic orbit, which are the analogues of PO_{ub}, PO_{lb} and the torus orbit of our model. For small value of R^* the upper fixed point is stable and the periodic orbit constitutes its basin boundary. The stable manifold of the lower branch point spirals around the periodic orbit and coincides with its unstable manifold. This situation clearly represents a 2D analogue of our model for $R > R_t$. For higher values of R^* the upper fixed point becomes unstable and the periodic orbit disappears. The stable manifold of the lower fixed point is now spiraling around the upper fixed point and coincides with its unstable manifold. This situation is analogous to our model for $R_c < R < R_t$.

Some differences are present between the two models. First, because Lebovitz's model is 2D, the stable and unstable manifolds of the different objects can have the same dimension and hence coincide. Second, the additional basin of attraction is present for small values of R^* and disappears for high R^*, while in our model it appears for high values of R. These differences should warn about the variability of results between simplified models. However, the analogies suggest the presence of common features in shear turbulence models.

The portrait emerging from the model proposed here and the model of Lebovitz give a simple interpretation of the edge. The fact that the edge coincides with a stable manifold of an invariant object was already known [12, 10, 11]. The novelty of our results is that one limb of the edge does not extend to infinity, but connects to another invariant object, which for the case here studied can be a fixed point, a simple periodic orbit or a torus orbit. If this stable manifold is spiraling around the invariant object, then the difference in relaminarization time between trajectories starting on different sides of the edge is enhanced. However, we should stress that the spiral structure is not strictly necessary for the presence of the edge. In higher dimensional models, the full NS as the limit, we expect the invariant objects and the manifolds to be more convoluted than in a two or six dimensional model. As a consequence, we expect a greater difference in trajectories on different side of the edge, with or without the presence of a spiral behavior.

Finally, the edge seems to be related to the unstable manifold of this invariant object, but dimensional considerations imply that these two cannot coincide. We conclude that the stable and unstable manifold intersect, but more investigation is needed to draw more specific conclusions.

4.7 Conclusion

A six-dimensional system of ODEs representing a Galerkin truncated model for Plane Poiseuille Flow was derived and analyzed. In this model the edge behavior is explained by the combination of simple dynamical elements: the stable manifold of an invariant object connected to another invariant object. This configuration is possible with or without the presence of another basin of attraction besides the laminar one, and with or without a spiraling stable manifold.

4.8 Acknowledgment

I would like to thank the directors of the Geophysical Fluid Dynamics Program for the opportunity of this great experience. I would like to thank all the lecturers and speakers for sharing their knowledge. In particular, I'm deeply grateful to Norman Lebovitz for his support on this project. Finally, I would like to thank all the participants and the fellows for the beautiful time spent together.

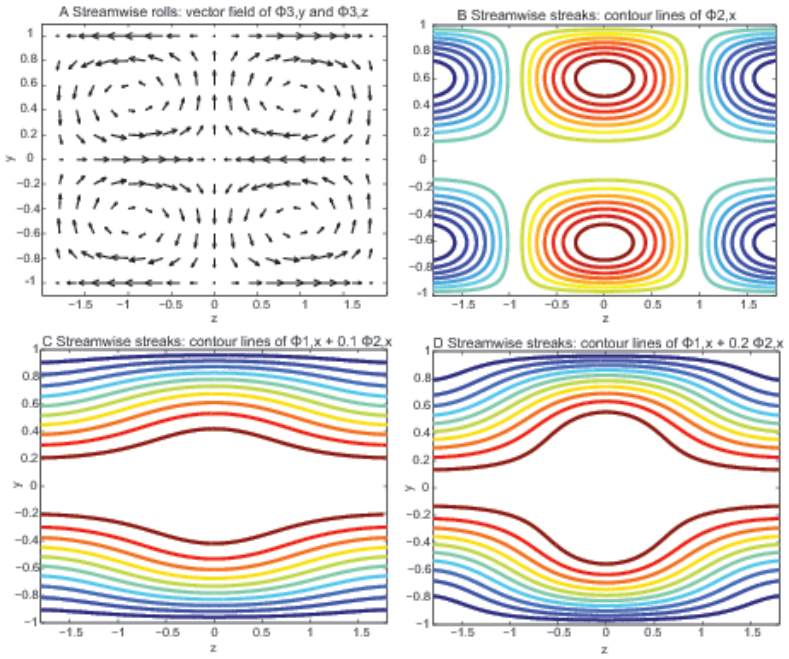

Figure 4.1: A) Vector field of the streamwise rolls (y and z component of ϕ_3). B) Contour lines of the streamwise streaks (x component of ϕ_2). C,D) Redistribution of the streamwise velocity under the combination of the mean flow and the stramwise streaks, for $X_2 = 0.1$ and $X_2 = 0.2$, with $X_1 = 1$. Contour lines every 0.1, from 0 at $y = \pm 1$ to 1 at $y = 0$.

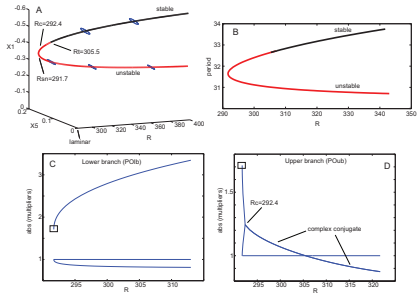

Figure 4.2: A) Coordinate X_1 and X_5 of the center of the upper and lower branches periodic orbits for different value of R. The blue circles represent the periodic orbits at selected value of R. The coordinate $X_{2,3,4,6}$ of the center of both periodic orbits is identically zero for all R. B) Period of the upper and lower branch periodic orbits. C,D) First three greater multipliers of the upper and lower branch periodic orbits. The values in the squares are the same, i.e. the multipliers coincide at the saddle node bifurcation.

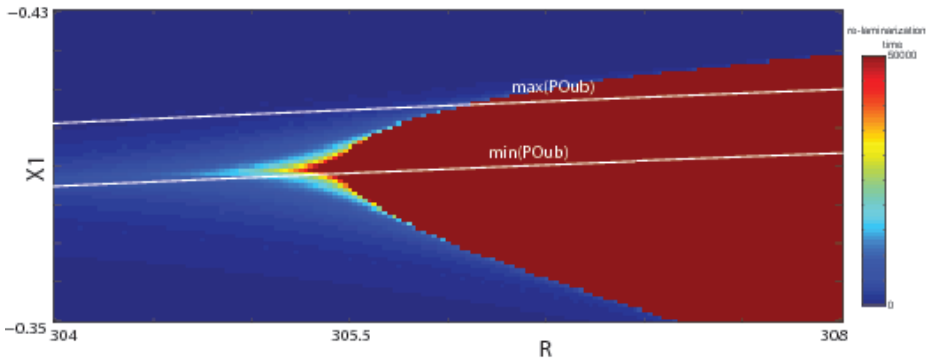

Figure 4.3: Each grid square is colored to show the lifetime before relaminarization for trajectory with initial conditions X_1 and parameter R. The other initial conditions are constant for each cells, $X_2 = -0.0511$, $X_3 = -0.0391$, $X_4 = 0.0016$, $X_5 = 0.1924$, $X_6 = 0.1260$, which correspond to a point on PO_{ub}. The other parameters are $\gamma = 5/3$, and $\alpha = 1.1$. A section of the basin of attraction of PO_{ub} coincides approximately with red region. The lines represent the projection of the minimum and maximum value of PO_{ub}.

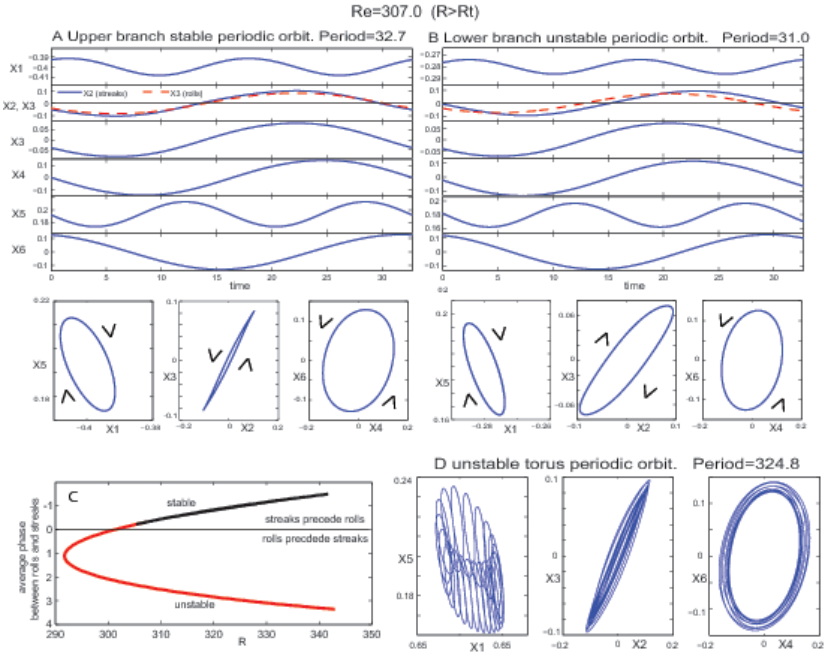

Figure 4.4: A) Upper branch stable periodic orbit, $R = 307.0$ ($R > R_t$). The orbit in the $X_2 - X_3$ plane is counter clockwise. B) Lower branch unstable periodic orbit. The orbit in the $X_2 - X_3$ is clockwise. C) Average phase lag between the mode X_2 (streaks) and mode X_3 (rolls). Positive lag means that the rolls precede the streaks. D) Periodic orbit on the torus, embedded in the basin boundary of PO_{ub}.

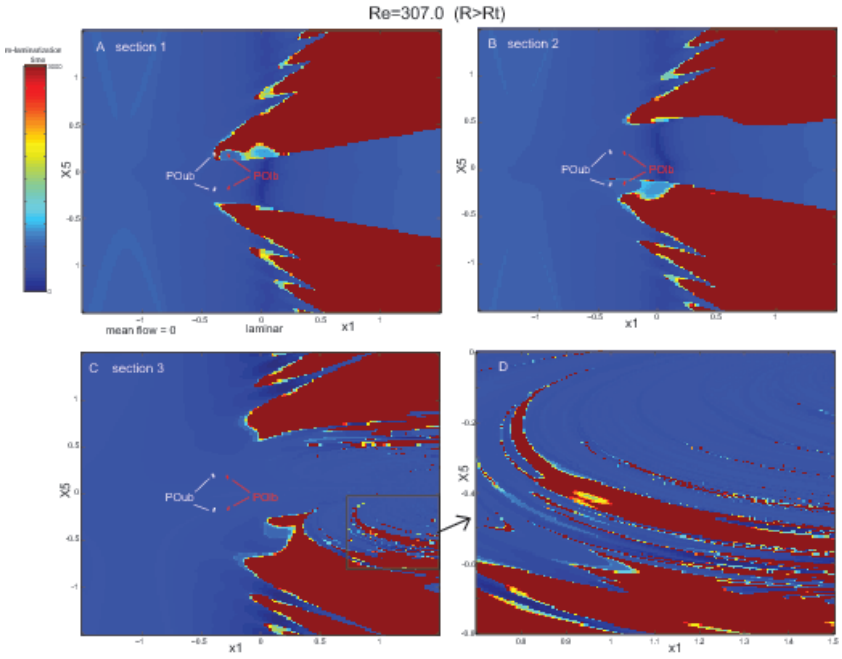

Figure 4.5: A) Two dimensional sample of the phase space, with the laminar state at the origin, for $R = 307.0$ ($R > R_t$). Each grid square is colored to show the lifetime before relaminarization for trajectory with initial conditions X_1 and X_5 and the center of the cell. The other initial conditions are constant for each cells: $X_2 = -0.0511$, $X_3 = -0.0391$, $X_4 = 0.0016$, $X_6 = 0.1260$, which correspond to a point on PO_{ub}. The other parameters are $\gamma = 5/3$, and $\alpha = 1.1$. The upper and lower branch periodic orbits are projected into this plane. B,C) Same as in A, with the coordinate X_3 increased by 0.1 and 0.5 respectively. D) Detail of C.

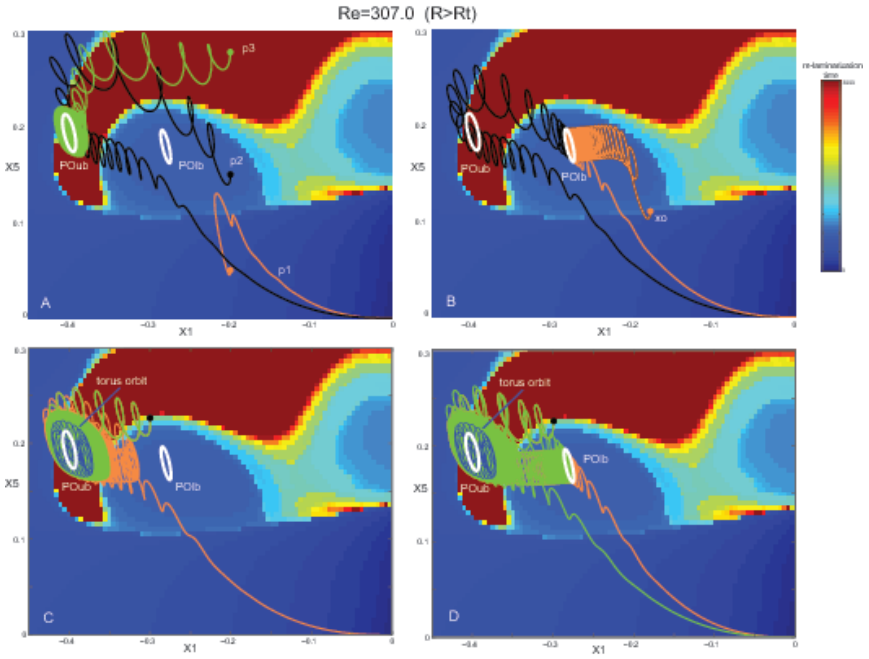

Figure 4.6: On the background, lifetime of trajectories before relaminarization, for $R = 307.0$, as in Figure 4.5. The upper and lower branch periodic orbits, the torus orbit and some significant trajectories are projected into this plane. A) Trajectory p_1 relaminarizes following a short path; trajectory p_2 relaminarizes following a longer path, visiting the region near PO_{ub} and the torus orbit; trajectory p_3 converges to PO_{ub}. B) Trajectories starting infinitesimally close to each other first approach PO_{lb} and then diverge into different path toward the origin. C,D) Trajectories near the basin boundary of PO_{ub} have convoluted paths around PO_{ub} and the torus orbit, and some of them approach PO_{lb} before relaminarization.

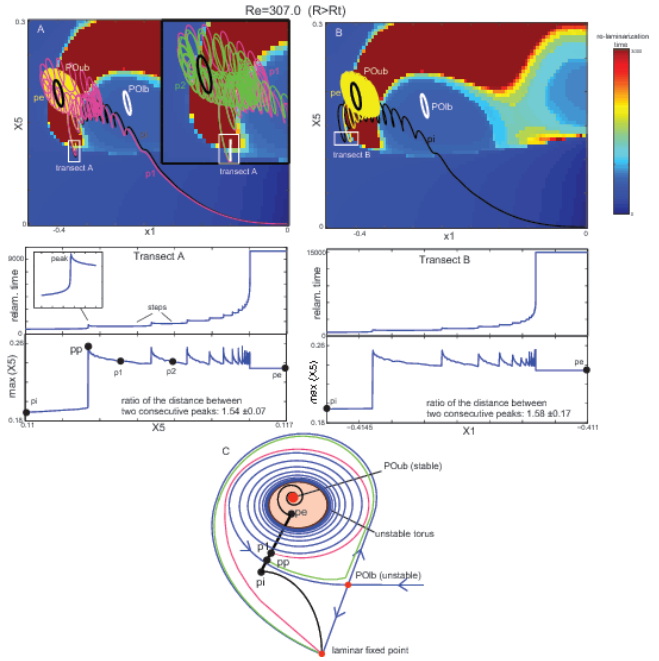

Figure 4.7: A,B) Lifetime of trajectories, as in Figure 4.5. Some trajectories and the periodic orbits are projected into the plane. Two transects of initial conditions crossing ∂D are analyzed. Transect A is aligned along the direction X_5; transect B is aligned along the direction X_1. All the other initial conditions are kept fixed. The first point on both transects, p_i, corresponds to a trajectory that relaminarizes 'directly', while the last point, p_e, corresponds to a trajectory that converges to PO_{ub}. Trajectories corresponding to the initial conditions on the transects are described using two parameters: the time to relaminarization, and the maximum value achieved by the coordinate X_5, a footprint of the trajectory history. C) Cartoon of the phase space, with the laminar fixed point, PO_{ub}, PO_{lb}, the torus orbits and some trajectories as an example.

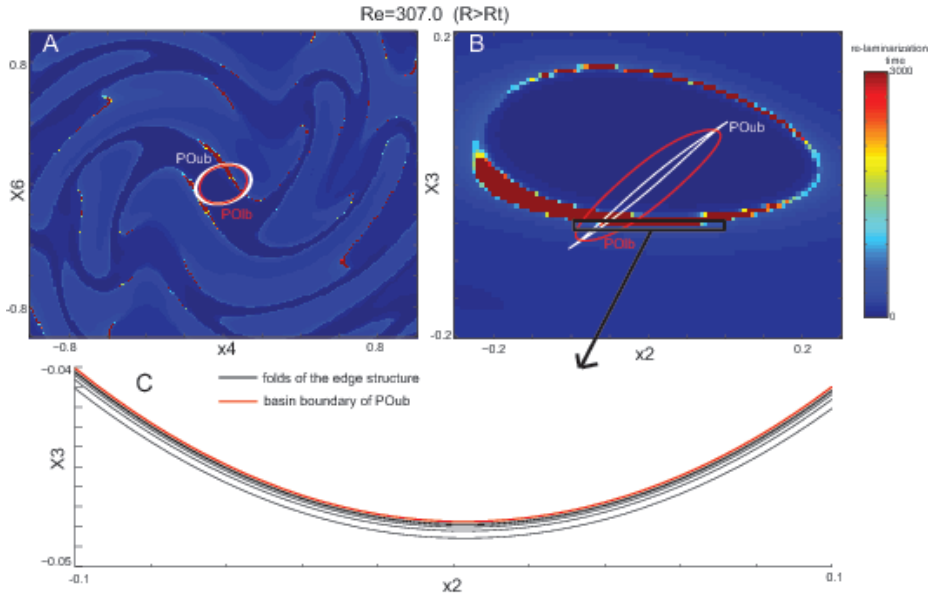

Figure 4.8: A,B) Lifetime of trajectories and projection of PO_{ub} and PO_{lb}, as in Figure 4.5, but utilizing different coordinates: X_4-X_6, and X_2-X_3. C) Representation of the edge's folds, identified using the 'peaks' of relaminarization time as in Figure 4.7.

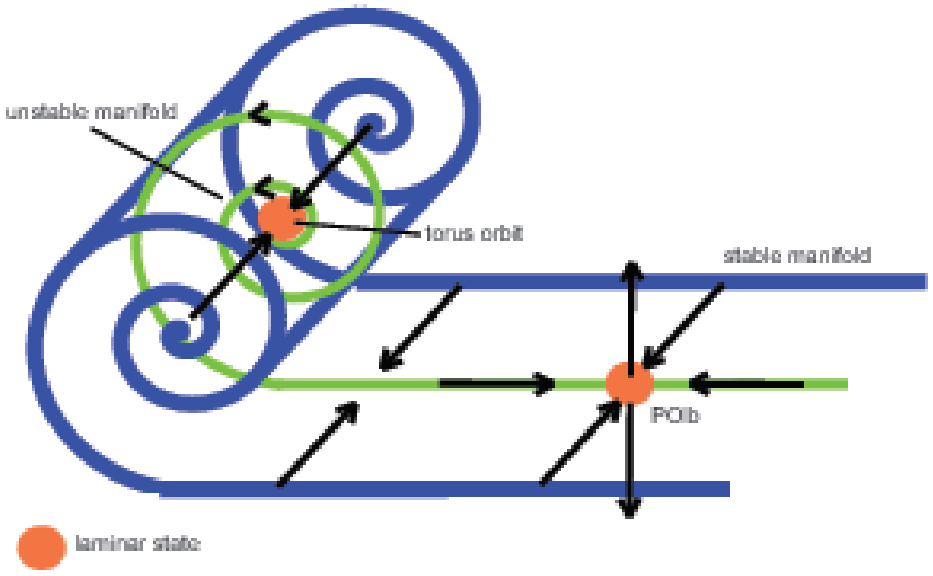

Figure 4.9: Example of how $UM(PO_{ub})$ can intersect $SM(PO_{lb})$, in a three dimensional case. $UM(PO_{ub})$ lies on a vertical plane and the green line is the intersection.

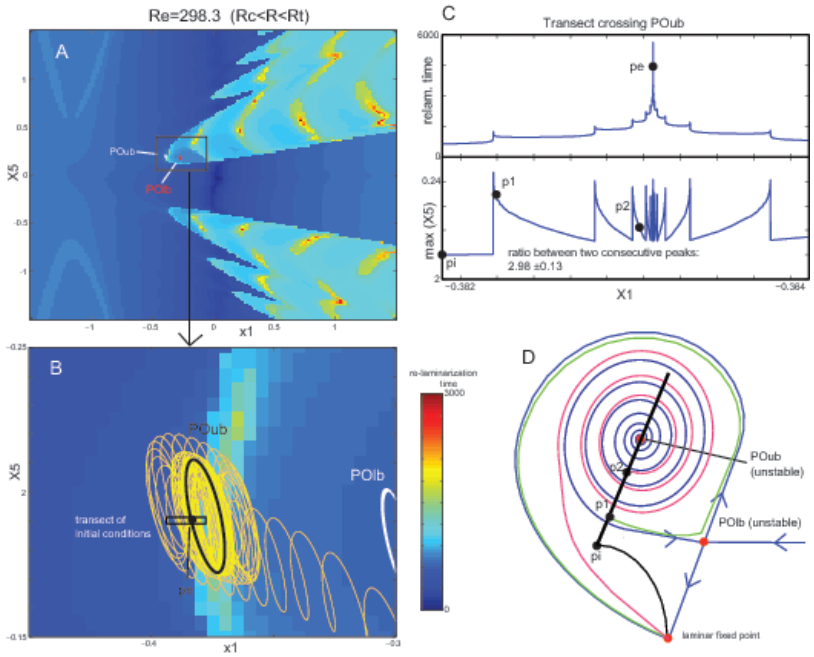

Figure 4.10: A,B) Lifetime of trajectories and projection of PO_{ub} and PO_{lb}, as in Figure 4.5, but with $R = 298.3$ ($R_c < R < R_t$). C) Analysis of a transect of initial conditions crossing PO_{ub}. Trajectories corresponding to the initial conditions on the transect are described using two parameters: the relaminarization time and the maximum value achieved by the coordinate X_5. The point p_i corresponds to an initial condition that relaminarize 'directly', while the point p_e corresponds to an initial condition on PO_{ub}. D) Cartoon of the phase space, with the laminar fixed point, PO_{ub}, PO_{lb}. Trajectory p_1 starts close to $SM(PO_{lb})$, trajectory p_2 starts between two folds of $SM(PO_{lb})$.

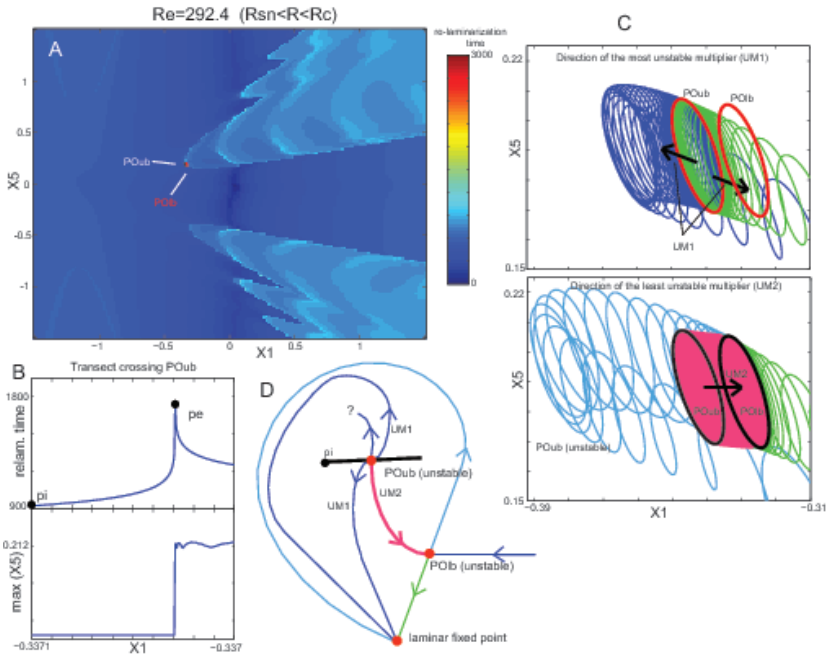

Figure 4.11: A) Lifetime of trajectories and projection of PO_{ub} and PO_{lb}, as in Figure 4.5 and Figure 4.10, but with $R = 292.4$ ($R_{sn} < R < R_c$). B) Analysis of a transect of initial conditions crossing PO_{ub}. The point p_i corresponds to an initial condition that relaminarizes 'directly', while the point p_e corresponds to an initial condition on PO_{ub}. C) Directions of the unstable manifolds of PO_{ub}: UM_1 is associated with the most unstable multiplier, UM_2 is associated with the other unstable multiplier. D) Cartoon of the phase space, with the laminar fixed point, PO_{ub}, PO_{lb}, and unstable manifolds of PO_{ub}.

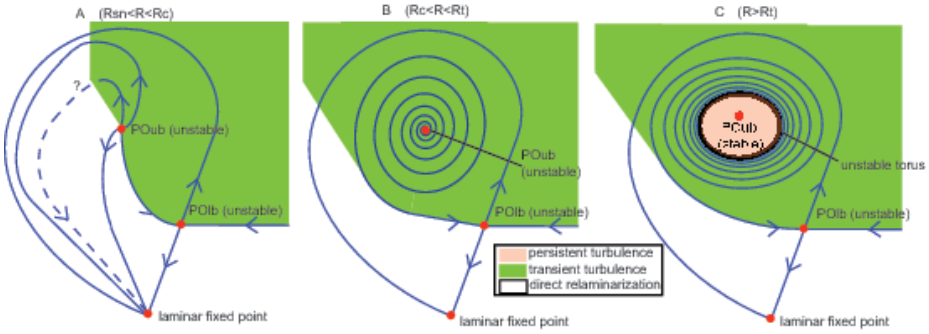

Figure 4.12: Cartoon of the phase space for different values of R. A) $R_{sn} < R < R_c$, two unstable periodic orbits, both with real unstable multipliers. B) $R_c < R < R_t$, two unstable periodic orbits; the upper one with two complex conjugate unstable multipliers, the lower one with a real unstable multiplier. C) $R > R_t$, stable and unstable periodic orbits. The unstable orbit has a real unstable multiplier. The color shading indicates in an approximate way regions with different relaminarization behavior.

Bibliography

[1] O. Dauchot and N. Vioujard, *Phase space analysis of a dynamical model for the subcritical transition to turbulence in plane couette flow*, The European Physical Journal B - Condensed Matter and Complex Systems, 14 (2000), pp. 377–381.

[2] A. Dhooge, W. Govaerts, and Y. A. Kuznetsov, *matcont: A matlab package for numerical bifurcation analysis of odes*, ACM TOMS, 29 (2003), pp. 141–164.

[3] J. M. Hamilton, J. Kim, and F. Waleffe, *Regeneration mechanisms of near-wall turbulence structures*, Journal of Fluid Mechanics, 287 (1995), pp. 317–348.

[4] N. Lebovitz, *Shear-flow transition: the basin boundary*, Nonlinearity, 22 (2009), pp. 2645, 2655.

[5] ——, *Boundary collapse in models of shear-flow turbulence*, Communications in Nonlinear Science and Numerical Simulations, doi:10.1016/j.cnsns.2011.07.023q (2010).

[6] J. Moehlis, H. Faisst, and B. Eckhardt, *A low-dimensional model for turbulent shear flows*, New Journal of Physics, 6 (2004), pp. 1–17.

[7] J. Moehlis, H. Faisst, and B. Eckhardt, *Periodic orbits and chaotic sets in a low-dimensional model for shear flows*, J. Applied Dynamicl Systems, 4 (2005), pp. 352–376.

[8] S. A. Orszag, *Accurate solution of the orr-sommerfeld stability equation*, Journal of Fluid Mechanics, 60 (1971), p. 689703.

[9] T. M. Schneider, F. De Lillo, J. Buehrle, B. Eckhardt, T. Dörnemann, K. Dörnemann, and B. Freisleben, *Transient turbulence in plane couette flow*, Phys. Rev. E, 81 (2010), p. 015301.

[10] T. M. Schneider, B. Eckhardt, and J. A. Yorke, *Turbulence transition and the edge of chaos in pipe flow*, Phys. Rev. Lett., 99 (2007), p. 034502.

[11] T. M. Schneider, J. F. Gibson, M. Lagha, F. De Lillo, and B. Eckhardt, *Laminar-turbulent boundary in plane couette flow*, Phys. Rev. E, 78 (2008), p. 037301.

[12] J. D. Skufca, J. A. Yorke, and B. Eckhardt, *Edge of chaos in a parallel shear flow*, Phys. Rev. Lett., 96 (2006), p. 174101.

[13] J. Vollmer, T. M. Schneider, and B. Eckhardt, *Basin boundary, edge of chaos, and edge state in a two-dimensional model*, New Journal of Physics, 11 (2009), p. 013040.

[14] F. Waleffe, *On a self-sustaining process in shear flows*, Physics of Fluid, 9 (1997), pp. 883–900.

[15] ——, *Homotopy of exact coherent structures in plane shear flows*, Physics of Fluids, 15 (2003), pp. 1517–1534.

[16] J. Wang, J. Gibson, and F. Waleffe, *Lower branch coherent states in shear flows: Transition and control*, Phys. Rev. Lett., 98 (2007), p. 204501.

Project 5

Upstream basin circulation of rotating, hydraulically controlled flows

Adele Morrison

Australian National University

5.1 Introduction

5.1.1 Motivation

The overflows of dense water from the Nordic Seas into the North Atlantic are a key element of the global meridional overturning circulation. The deep southward limb of the overturning is fed primarily by the overflows, and the transport of the deep limb is closely linked to the transport in the warmer northward currents in the upper ocean of the North Atlantic. The threat of potentially significant shifts in climate due to changes in the overturning motivates an improved understanding of the overflows and the associated upstream basin circulation. Despite enhanced recent efforts [1, 2], the source regions and pathways of the deep water masses upstream of the overflows remain uncertain.

Observations of the Denmark Strait and Faroe Bank Channel, the two primary exit points of deep water from the Nordic Seas, indicate that the overflows are hydraulically controlled. Hydraulic control is qualitatively suggested by the characteristic spillage observed in the drawdown of downstream isopycnals (Figure 5.1), the lack of seasonality in overflow transport
and the dependence of the overflow transport on upstream interfacial elevation. The hydraulic control has also been quantitively confirmed by the identification of control sections where the flow undergoes sub-critical to super-critical transitions [4].

A feature of hydraulically controlled flows is that the stratification in the basin upstream of the overflow sill or strait consists of a uniform dense layer overlaid by a dynamically inactive upper layer, as shown in Figure 5.1. It is therefore not unreasonable to model the

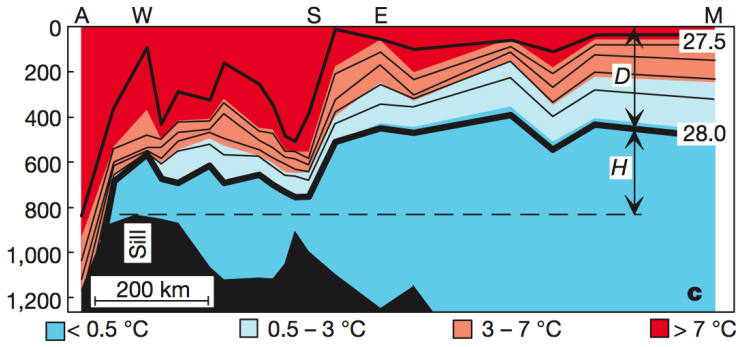

Figure 5.1: An along-stream section of the Faroe Bank Channel indicating the characteristic spillage of hydraulically controlled flows, showing temperature (colour shading) and isopycnals (contours). From Hansen et al. (2001)[3].

upstream basin as a single fluid layer (or $1\frac{1}{2}$ layers with reduced gravity) governed by the shallow water equations.

Here we focus on the nature of the upstream basin circulation in an idealised one layer model with circular basin geometry and varying source location, using a combination of laboratory and numerical experiments.

5.1.2 Overview

Monitoring the transport of the Nordic Sea overflows has long been a goal of the oceanographic community. Direct current measurements are difficult due to the complex structure of the flows. Instead, observational studies have attempted to infer overflow transports from upstream hydrographic measurements [3, 5], as suggested may be reasonable by the rotating hydraulic theory of Gill [6]. Calculation of the overflow transport using Gill's theory, which assumes a uniform potential vorticity flow through a rectangular cross-section channel, requires knowledge of the upstream basin circulation (ie. interfacial height on a boundary), as well as the strait geometry and potential vorticity. On the contrary, Helfrich and Pratt (2003)[7] have shown that the overflow transport in an idealised numerical model depends only on the strait parameters (geometry and potential vorticity) and not the upstream circulation. The simulated basin-strait system selects the Gill solution with maximum potential energy in the basin. This implies that accurate estimates of the transport cannot be gained from upstream information. The original plan for this project was to perform an experimental comparison of the findings of Helfrich and Pratt (2003). However, we were unable to pursue this question very far due to limitations of the experimental parameter range. In particular, the width of the strait in the experiment was small compared with the Rossby radius, placing it in a different regime from the previous numerics.

As an alternative, we have focused on the dependence of the circulation direction in the upstream basin on the potential vorticity flux through the basin, as introduced in Section 5.1.3. We show that, for the parameter regime of the experiments, the relative vorticity component of the potential vorticity flux cannot be ignored and that the commonly

assumed simple dependence of the flow direction on the relative thicknesses of the inflow and outflow does not necessarily hold for hydraulic flows.

5.1.3 Potential vorticity balance of the upstream basin circulation

Previous studies of boundary layer flows in semi-enclosed basins have shown that the direction of circulation (ie. cyclonic or anticyclonic) in the basin is strongly dependent on the potential vorticity (PV) fluxes at the inflow and outflow [7, 8, 9]. Integrating the PV over the entire basin yields a balance between the net PV fluxed in or out of the basin and the dissipation of PV by friction. Here we derive the PV balance, following Yang and Price (2000) [10]. We begin with the shallow water momentum and continuity equations:

$$\frac{Du}{Dt} - fv + g\frac{\partial h}{\partial x} = -\lambda u \tag{5.1}$$

$$\frac{Dv}{Dt} + fu + g\frac{\partial h}{\partial y} = -\lambda v \tag{5.2}$$

$$\frac{Dh}{Dt} + h\left(\frac{\partial u}{\partial x} + \frac{\partial v}{\partial y}\right) = 0, \tag{5.3}$$

where $\frac{D}{Dt}$ is the material derivative, (u, v) are the velocity components, h is the layer depth, f is the Coriolis parameter and λ is the Rayleigh bottom friction coefficient. Given the northerly latitude and small size of the basins under consideration, we take f to be constant. The vorticity equation may be obtained by taking the curl of the momentum equations:

$$\frac{\partial}{\partial t}(\nabla \times \mathbf{u}) + \nabla \times ((f + \nabla \times \mathbf{u}) \times \mathbf{u}) = -\lambda \nabla \times \mathbf{u}. \tag{5.4}$$

Extracting the steady state, vertical component of the vorticity equation (applying incompressibility and noting that the divergence of the vorticity is zero) gives:

$$(\mathbf{u} \cdot \nabla)(f + \zeta) = (f + \zeta)\frac{\partial w}{\partial z} - \lambda\zeta \tag{5.5}$$

where $\zeta = v_x - u_y$ is the vertical component of the relative vorticity and w is the vertical component of the velocity. Rearranging the term on the left (again using incompressibility and separating the divergence into horizontal and vertical parts), we obtain:

$$\nabla \cdot [\mathbf{u_h}(f + \zeta)] + \frac{\partial}{\partial z}[w(f + \zeta)] = (f + \zeta)\frac{\partial w}{\partial z} - \lambda\zeta \tag{5.6}$$

where $\mathbf{u_h} = (u, v)$ is the horizontal vorticity. The second and third terms in this equation are similar in form. The term $\frac{\partial}{\partial z}[w(f + \zeta)]$ represents vorticity transport due to a vertical mass flux into the layer, while $(f + \zeta)\frac{\partial w}{\partial z}$ is the usual vortex stretching term. If adjacent layers have different relative vorticity (ie. $\frac{\partial \zeta}{\partial z} \neq 0$), there is not necessarily a cancellation between the two terms. For downwelling located in the interior of a basin, the upper layer flow will likely be slow and geostrophic, and thus $f \gg \zeta$ is a reasonable assumption. However this is not necessarily the case for downwelling near a basin boundary (within a boundary layer flow). Given this caveat, Yang and Price [10] make the assumption that $f \gg \zeta$, which reduces Equation 5.6 to:

$$\nabla \cdot [\mathbf{u_h}(f+\zeta)] = -\lambda\zeta \tag{5.7}$$

Under the shallow water approximation, all variables are assumed to be depth independent, allowing us to rewrite Equation 5.7 in terms of depth-integrated variables:

$$\nabla \cdot \left[\mathbf{U_h}\left(\frac{f+\zeta}{h}\right)\right] = -\lambda\zeta, \tag{5.8}$$

where $\mathbf{U_h} = \mathbf{u_h}h$ is the depth integrated horizontal velocity and $\frac{\zeta+f}{h}$ is the potential vorticity. Finally, integrating Equation 5.8 over the entire basin and applying the divergence and Stokes theorems, we obtain a balance between the net PV fluxed in or out of the basin and the dissipation of PV by friction:

$$\oint_C (\mathbf{U_h}\cdot\hat{\mathbf{n}})\left(\frac{f+\zeta}{h}\right) ds = -\lambda \oint_C \left(\mathbf{u_h}\cdot\hat{\mathbf{t}}\right) ds \tag{5.9}$$

where C is the boundary of the basin, $\hat{\mathbf{n}}$ is the normal vector across the basin boundary and $\hat{\mathbf{t}}$ is the tangential vector along the boundary. The term on the left of Equation 5.9 is simply the net PV fluxed out of the basin via the open boundaries at the inflow and outflow, ie.

$$Q\left[\left(\frac{f+\zeta_{out}}{h_{out}}\right) - \left(\frac{f+\zeta_{in}}{h_{in}}\right)\right] = -\lambda \oint_C \left(\mathbf{u_h}\cdot\hat{\mathbf{t}}\right) ds. \tag{5.10}$$

Equation 5.10 implies that if the net PV flux through the openings is positive, the average direction of the circulation on the basin boundary must be anticyclonic, so that the dissipation of PV balances the net flux. Similarly, if the net PV flux is negative, the average boundary circulation direction is cyclonic. Yang and Price (2000) [10] simplify this balance even further, by assuming a 'slug' (unidirectional and steady) flow at both the inflow and outflow to argue that the relative vorticity integrated across an opening must be zero. The relative vorticity component will also vanish in a model with no-slip conditions. This assumption leads to:

$$Qf\left[\left(\frac{1}{h_{out}}\right) - \left(\frac{1}{h_{in}}\right)\right] = -\lambda \oint_C \left(\mathbf{u_h}\cdot\hat{\mathbf{t}}\right) ds. \tag{5.11}$$

Numerical simulations of Yang and Price (2000) [10] and Yang (2005) [9], using a free-slip boundary to determine the dissipation given by the circulation integral, and prescribed, uni-directional flows at the openings (so that the simplification of Equation 5.11 holds), show that by changing the relative heights of the inflow and outflow (and therefore the sign of the net PV flux), the circulation can be made to switch direction in the basin, as shown in Figure 5.2. For a net PV flux of zero, the inflow was found to split into two branches, so that the circulation direction differed across the two sides of the basin. This relation between the net PV flux and the direction of basin circulation has been used to explain the puzzling discrepancy of the circulation direction in the models of the Arctic Ocean Model Intercomparison Project [9].

Although the dependence of the circulation direction given by Equation 5.10 relies strongly on the linear friction parameterisation, numerical studies using smaller frictional coefficients, no-slip boundary conditions or lateral friction instead of bottom friction have

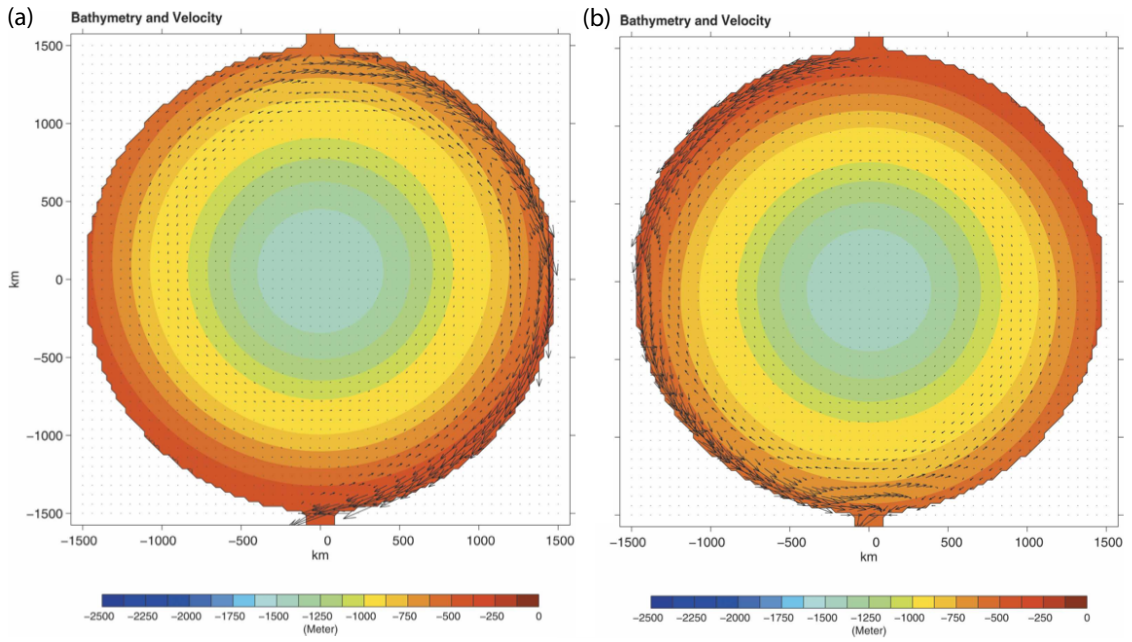

Figure 5.2: Numerical simulations showing the control of the net PV flux through the basin on the circulation direction. The left figure (a) shows the case where the PV flux at the outflow is larger than the inflow, which was achieved by tilting the basin such that $h_{out} < h_{in}$. The right figure (b) shows the effect of tilting the basin in the opposite direction. From Yang (2005) [9].

also found consistency between the sign of the PV flux through the basin and the circulation direction [9, 10].

5.1.4 Review of previous studies of upstream basin flows

In this section, we review past numerical, analytical and experimental studies, which have examined the structure of the flows in basins upstream of a hydraulically controlled sill.

Pratt (1997)[8] derived analytical expressions for the boundary layer currents that link the upstream sources to the overflow strait. The flows are equivalent to the northern or southern boundary layers arising in a homogeneous Stommel circulation in a rectangular basin. Variation in topographic slope near the boundary replaces the latitudinal variation of f. An average estimate of the boundary layer thickness, δ, arises from what is essentially a diffusion equation with angle around the basin replacing the role of time:

$$\delta = \sqrt{R_b}\sqrt{\frac{\lambda}{\beta_T}} \tag{5.12}$$

where R_b is the basin radius, $\beta_T = -f\frac{\partial}{\partial r}\left(\frac{h}{H_o}\right)$ is the topographic beta and H_o is the depth scale. The diffusive nature of the solution gives rise to a spreading of the boundary layer as

the current flows from the inflow source to the exit strait. Pratt matched this solution to various inflow and outflow boundary conditions and found that all of the analysed solutions have the flow entering the strait along the left wall (note we will use 'left' and 'right' as if looking downstream from the basin towards the overflow channel). The left wall may be interpreted as a western boundary with the beta effect arising due to the presence of a topographic slope between the basin and strait. The solution for a source located on the boundary opposite the outflow channel has two opposing boundary layers, as shown in Figure 5.3. The boundary layer along the right wall overshoots the strait to join the left wall boundary layer and enter the strait from the left. Note that the inflow was assumed to split in order to feed the two boundary layers directly.

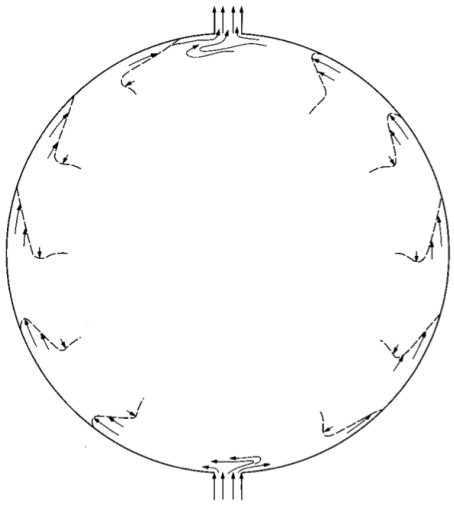

Figure 5.3: Analytical boundary layer solution of Pratt (1997)[8] for basin flow fed by an isolated boundary source and sink.

The primary experimental study that has looked at the nature of the flows upstream of a controlling passage was that of Whitehead and Salzig (2001)[11]. This study observed the qualitative features of the upstream circulation for varying source locations. For all source locations, Whitehead and Salzig observed the current entering the strait from the left, either flowing directly along the left wall or overshooting the strait from the right wall to enter along the left. For a source located on the right hand boundary wall upstream of the strait, the flow formed a boundary layer on the right wall which crossed to the left side of the strait entrance before forming a tightly curving current on the left wall of the exit strait. Fluid entering through a source on the left boundary, just upstream of the channel, was observed to flow directly along the left wall to the overflow channel. A source placed in the centre of the upstream basin formed a clockwise boundary current around the edge of the basin.

Helfrich and Pratt (2003)[7] investigated upstream flows in numerical simulations using two different source locations. A uniform downwelling over the entire basin created a domed interface and an essentially geostrophic, anticyclonic circulation, with fluid approaching the

strait along the left wall. With an inflow on the boundary directly opposite the strait, the flow split into two boundary currents, which rejoined at the strait. An asymmetry was observed between the two currents, with the right wall current stronger and overshooting the strait to enter from the left.

5.2 Laboratory experiments

5.2.1 Apparatus and procedure

The experiments were carried out in a basin on a 1 m diameter rotating table in the geophysical fluid dynamics laboratory at the Woods Hole Oceanographic Institution, as depicted in Figure 5.4. The parabolic basin had a depth of 0.20 m and a radius of 0.46 m. A vertical sidewall of height 0.10 m was attached to the top of the basin edge following the curvature of the basin, except near the side inflow and outflow strait, where the radius of curvature was 0.12 m and 0.20 m respectively, in order to smoothly connect the inflow and outflow channels. For all but one experiment, the overflow sill had a height of 0.025 m and was positioned within the outflow strait, which had a width of 0.13 m, at a distance of 0.20 m from the basin edge.

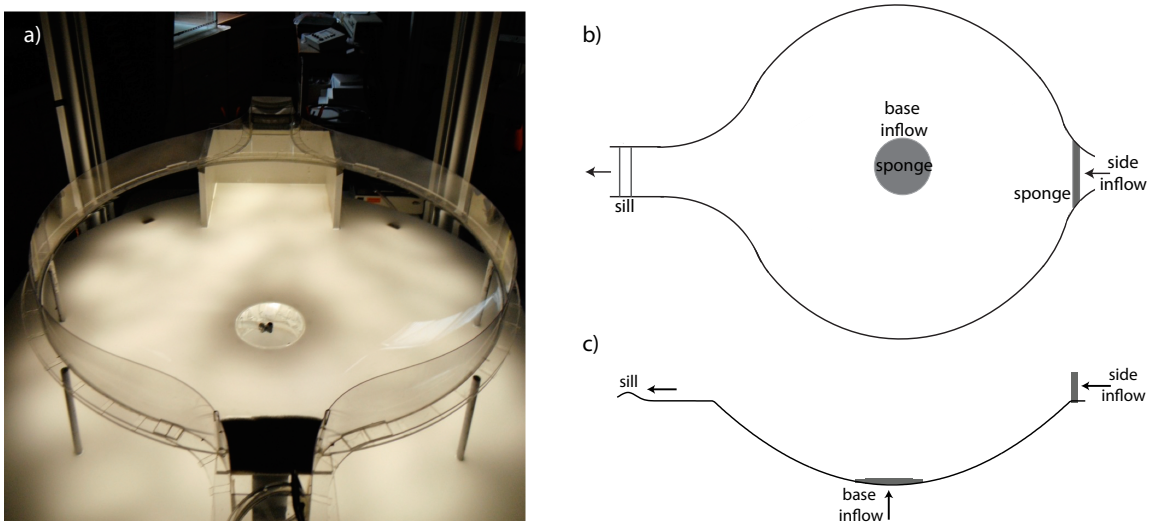

Figure 5.4: The experimental apparatus, shown from a,b) top view and c) side view.

The inflow location was varied between a boundary and centred upwelling region. For the boundary inflow, water entered the basin directly opposite the strait, through a sponge which had a width of 0.12 m and was aligned with the basin edge. For the case of upwelling inflow, water entered through a circular sponge of radius 0.07 m at the bottom of the tank. The overflow water was collected in a basin, before being pumped back to the inflow. Pump rates varied between (10 – 40) mL/s ($(0.77 - 3.08)\times10^{-4}$ m^3/s) and the basin was rotated anti-clockwise with a range of rotation rates corresponding to $f = (1, 1.5, 2)$ s^{-1}.

A lid was fitted on top of the entire basin during all experiments in order to reduce the

effects of surface stress from the overlying air. The basin was lit from below using $\sim$ 300 white LEDs below a diffuser. With the table rotating and the pump switched on, the basin was left to spinup for 30 minutes. Dye was then released into the inflow at a constant rate of $\sim$15 mL/hr. At higher dye release rates, the interface between the central undyed fluid and the dyed right wall current was observed to tilt and become baroclinically unstable. The advection of dye by the flow was imaged from above by a co-rotating black and white camera, with images taken at intervals of 0.5 s.

Using the same scaling for the channel depth h_o as Whitehead and Salzig (2001) [11], gives a Rossby radius ($R_d = \sqrt{gh_o}/f$) in the range of (0.2 – 0.4) m for the range of experimental parameters. The strait width is therefore much less than the Rossby radius and the hydraulic control on the basin will be more similar to the non-rotating case.

Due to the brief nature of the summer project, it was decided not to perform quantitative measures of the circulation, such as particle image velocimetry (PIV), at this time.

5.2.2 Qualitative description of the flows

The flow behaviour observed in the experiments qualitatively agrees with the expected flows from previous numerical simulations [7, 9] and a theoretical boundary layer solution [8], as described in Section 5.1.4, except that the case of boundary inflow is rarely (if ever) observed to split into a left wall and right wall current, as described in these previous studies.

Boundary inflow

Figure 5.5 shows the progress of dye around the basin from the inflow to the strait. The dye was released at a constant rate into the inflow after the circulation had reached steady state. The inflow is entirely deflected to the right, into the cyclonic boundary layer. The cyclonic right wall current overshoots the strait, as also observed in previous numerics and experiments [7, 11]. The overshooting behaviour is a result of the flow looping back to form a nominal 'western' boundary current as it crosses background PV contours on the way out of the basin. Also seen in Figure 5.5c,d is a strip of undyed fluid exiting in the centre of the strait. This undyed fluid is fed from the anticyclonic left wall current, which spirals out of the centre of the basin. Given sufficient time, the overshooting right wall current would spiral inwards to the centre of the basin to eventually feed the outward spiralling left wall current. Similar circulation patterns were observed over a range of inflow fluxes and rotation rates.

Over the range of experimental parameters investigated (perhaps with the exception of the raised sill, discussed below), the inflow was not observed to split into a left wall and a right wall current, as was assumed in the interpretation of both the numerical simulations of Yang (2005) [9] and the analytical solution of Pratt (1997) [8]. In hindsight, reexamining these studies shows that the inflow (except perhaps for the case shown in Figure 5.2a) turns entirely to the right and that the left wall current is fed from the interior of the basin, rather than directly from the inflow.

The separation of the current from the left wall of the exit strait is due to the surface curvature resulting from the centripetal effect of the rotating table. The free surface height increases by an amount $d = \frac{\Omega^2 r^2}{2g}$ where $\Omega = f/2$ and r is the distance from the axis of rotation. For $f = 1$ s^{-1}, the surface is raised by 2.6 mm at the edge of the basin. For

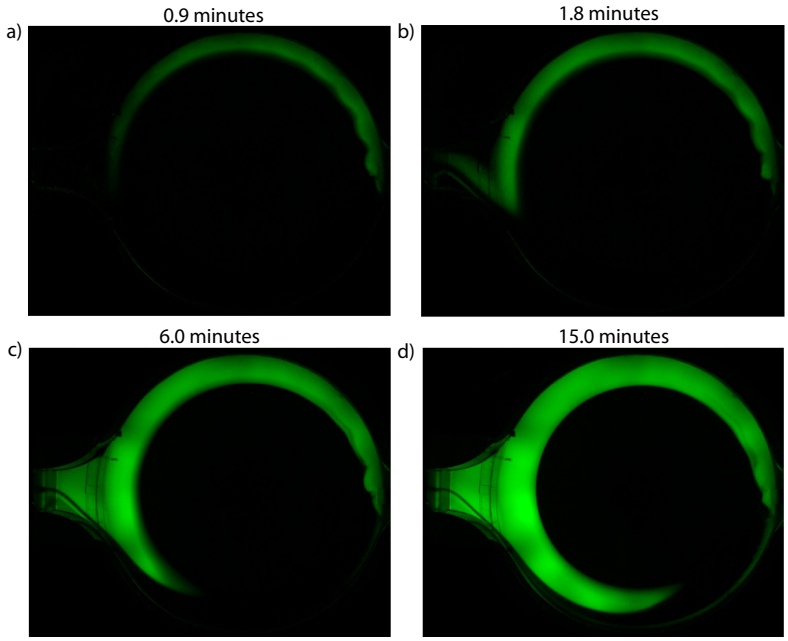

Figure 5.5: A sequence of false-colour photographs from the experiment showing the progression of dye around the basin. The inflow is on the right and strait on the left. The inflow was set to 30 mL/s and the rotation rate was $f = 1.5$ s^{-1}.

$f = 2$ s^{-1}, the effect becomes more significant with the surface raised by 10.6 mm. At higher rotation rates, the gradient of the thickness in the strait increases, resulting in an effective western boundary layer on the right wall of the strait.

Upwelling inflow

The experiments with a central upwelling source behaved much as expected from previous numerical work, with a predominantly anticyclonic geostrophic circulation. Figure 5.6 shows the steady state flow for a typical experiment. Dye enters the basin through the sponge at the center of the tank and gradually spirals outwards in the small ageostrophic component of the flow due to bottom friction. The boundary current around the rim of the basin recirculates as well as feeding the overflow. A persistent feature of the flow is a cyclonic eddy at the entrance to the strait.

Raised sill

To investigate the dependence of the circulation direction on the PV budget, an experiment was carried out with a raised sill, of height 0.045 m. Apart from the location of the sill, the experimental parameters were identical to those of the experiment shown in Figure 5.5. The sill was placed at the edge of the basin to remove the effects of the strait on the circulation. It should be noted that the topographic gradient leading up to the sill was large. With

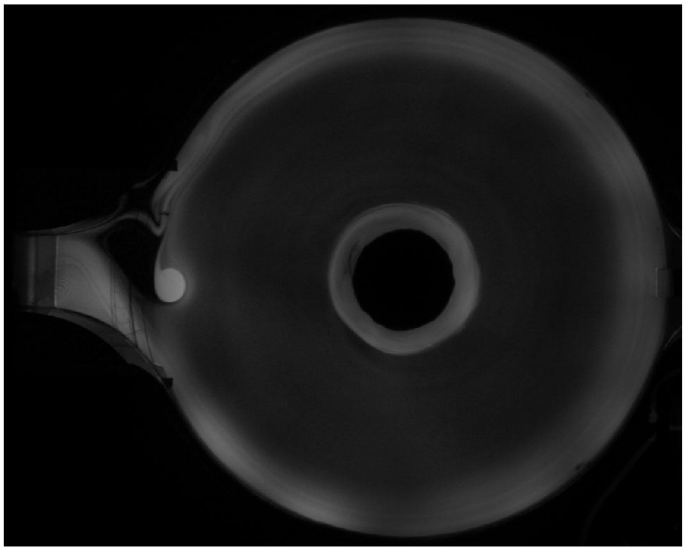

Figure 5.6: False-colour dye image for upwelling inflow through the base of the tank (through the dark patch in the centre). The inflow spirals anticyclonically outwards. Note the concentration of dye in the cyclonic eddy near the entrance to the strait. The inflow was set to 20 mL/s and the rotation rate was $f = 1.5$ s^{-1}.

a raised sill, the net PV flux through the boundary (under Yang's assumption that we can ignore the relative vorticity component) is strongly positive. According to the balance between the net PV flux and PV dissipation (Section 5.1.3) and the numerical simulations of Yang (2005) (Figure 5.2), we would expect the right wall current to be severely diminished (if present at all) and the circulation in the basin to be predominantly anticyclonic.

Figure 5.7 shows a timeseries of dye entering through the inflow. Compared to the experiment with a lower sill, the left wall current is noticeably stronger. It is unclear if the inflow is splitting into two directions, or if the left wall current is entraining dye from the right wall current as it spirals outwards from the centre of the basin. Despite the increased presence of the left wall current, the right wall current remains dominant and the circulation appears predominantly cyclonic. In order for the flow to satisfy the PV balance, either the relative vorticity components of the PV flux through the boundary must be significant, or dissipation along the left wall leading up to the strait dominates, despite the opposing contribution from the dissipation along the right wall.

5.3 Numerical simulations

5.3.1 Methods

Numerical solutions of the shallow water equations were computed in order to gain a more quantitative understanding of the flows seen in the laboratory. The model domain was constructed to closely mimic the experiments. Figure 5.8 shows the bathymetry, using

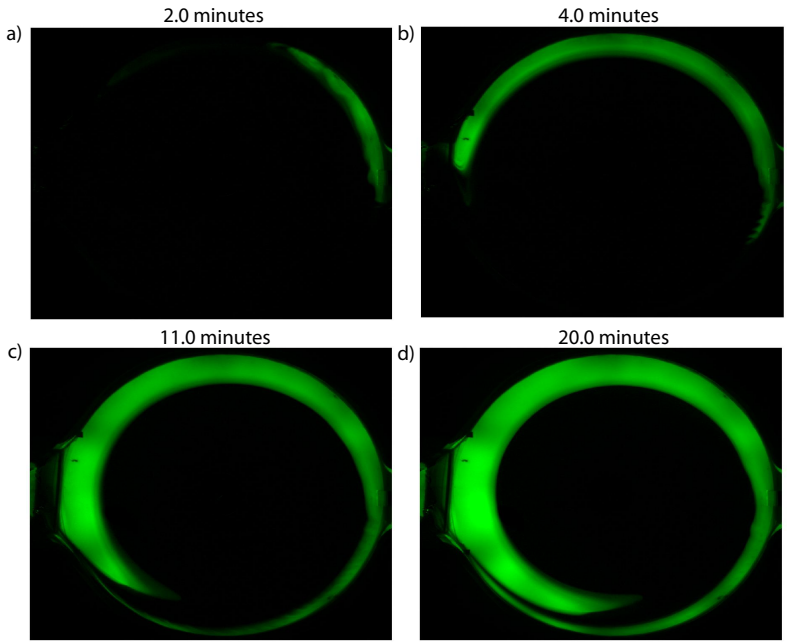

Figure 5.7: A sequence of photographs from the experiment with a raised sill. Apart from the location and height of the sill, the parameters were identical to the experiment shown in Figure 5.5. Note that the view of the strait is obstructed by the placement of the sill at the edge of the basin. The strength of the anticyclonic left wall current noticeably increases when the thickness of the outflow is reduced, though the right wall current remains dominant.

rectangular cells with a resolution of 0.5 cm. The numerical model (described in detail in [12, 7]) solves the shallow water equations in flux form and using a second-order finite-volume method to allow shocks, hydraulic jumps and layer depths approaching zero, as are common in rotating hydraulics. The model was run out to equilibrium and a time mean used for the analysis described in the following sections.

5.3.2 Simulations of the experiments

The simulations described in this section had a no-slip boundary condition, small lateral friction, bottom friction and an added centripetal term to obtain the variation in free surface height seen in the experiments. The numerics reproduced the mean state of the experiments well. Figure 5.9 shows the mean state of the basin circulation with inflow through the side wall and with parameters typical of the experiments. The structure of the circulation is remarkably similar to that observed in the experiments (Figure 5.5) and highlights the spiral structure of the flows, with the left wall boundary current spiralling anticyclonically out from the centre, while the overshooting right wall boundary current spirals cyclonically into the centre of the basin. The simulations show clearly that the left wall current in this case is fed from the interior of the basin, rather than from a direct splitting of the inflow, as was

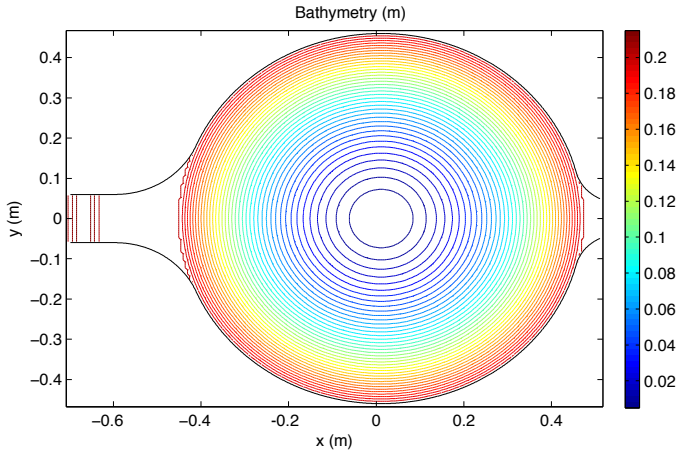

Figure 5.8: Bathymetry used in the numerical simulations.

assumed for the flows in [8, 9].

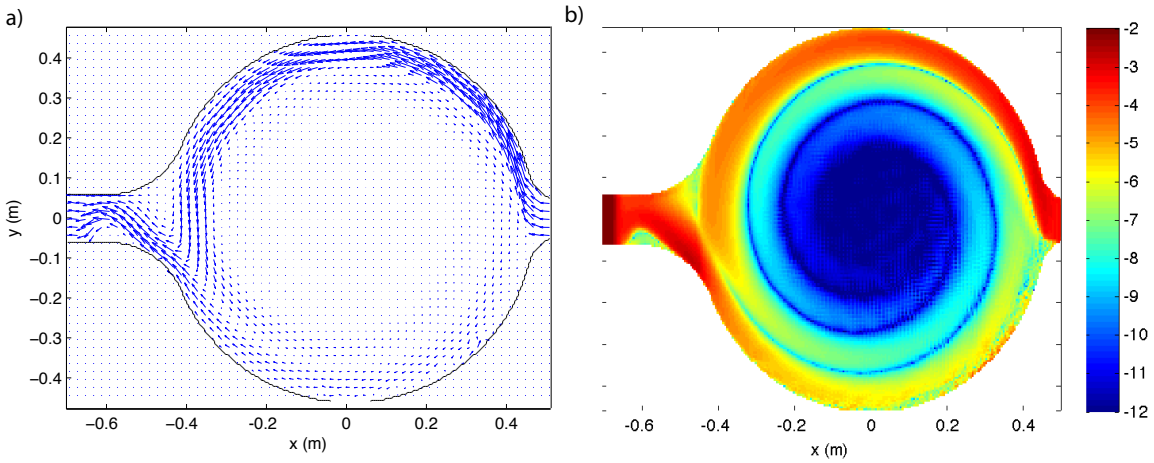

Figure 5.9: Time averaged numerical simulation of an experiment with side inflow = 40 mL/s and $f = 2$ s^{-1}. a) Velocity flow field at equilibrium. b) The log of the velocity magnitude.

The effect of adding the centripetal term ($\Omega^2 r$) to the shallow water momentum equation is shown in Figure 5.10. The simulations demonstrate that the separation of the flow from the left wall of the strait, such as seen in Figure 5.5d, is a result of the enhanced thickness gradient due to the increased surface curvature that is present with the centripetal term.

The numerical simulations with inflow through the bottom of the basin are shown in Figure 5.11. Again, the features seen in the experiment, such as the anticyclonic geostrophic flow and the dominant eddy near the strait are also observed in the numerics.

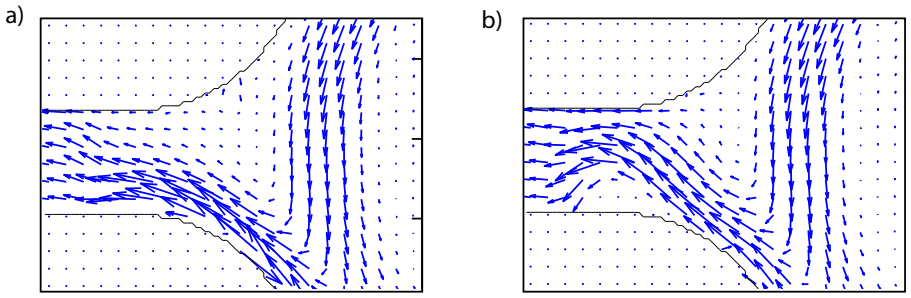

Figure 5.10: The effect of the centripetal term on the strait flow. Centripetal term switched a) off, and b) on.

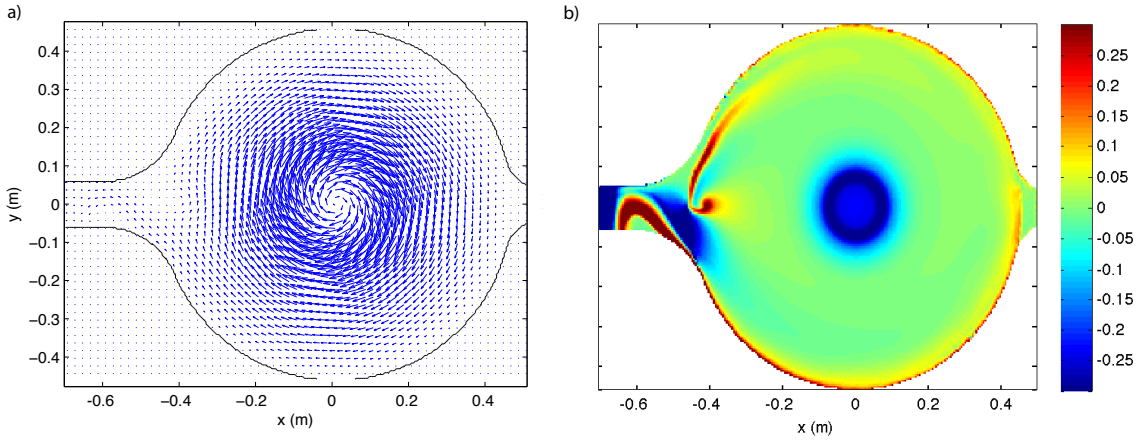

Figure 5.11: Numerical simulation of an experiment with bottom upwelling inflow = 40 mL/s and $f = 2$ s^{-1}. a) Time-averaged flow field at equilibrium. b) Relative vorticity.

5.3.3 Potential vorticity balance

A range of simulations with varying sill height were carried out to investigate the extent of the dependence of the basin circulation direction on the PV flux through the basin. These simulations were performed with free-slip boundary conditions and zero lateral friction, leading to the simple PV balance of Equation 5.10. As outlined in Section 5.1.3, as the height of the sill is raised, we would expect the net PV flux out of the basin to increase and therefore the dissipation should compensate by switching the direction of the flow, so that the inflow feeds the left wall boundary current (ie. the reverse of the flow shown in Figure 5.9).

Figure 5.12 shows the effect of doubling the sill height on the basin circulation. The right wall boundary current weakens as the sill height is increased, but there is no clear switch in direction, as was expected. Alternatives for the flow to satisfy the PV balance without changing the direction of circulation may be either an increase in dissipation on the left wall,

relative to the right wall, as the flow approaches the strait, or compensation by significant relative vorticity fluxes through the openings (previously assumed to be negligible). It seems unlikely that the former is the case, as the left wall boundary current also weakens and breaks up with increasing sill height. It is also apparent here that the jagged boundaries caused by the rectangular grid cells result in anomalies in the weak left wall boundary flows. In order to investigate if the relative vorticity fluxes are significant, the PV flux at the outflow was split into planetary and relative vorticity components, as shown in Figure 5.13 for varying sill height.

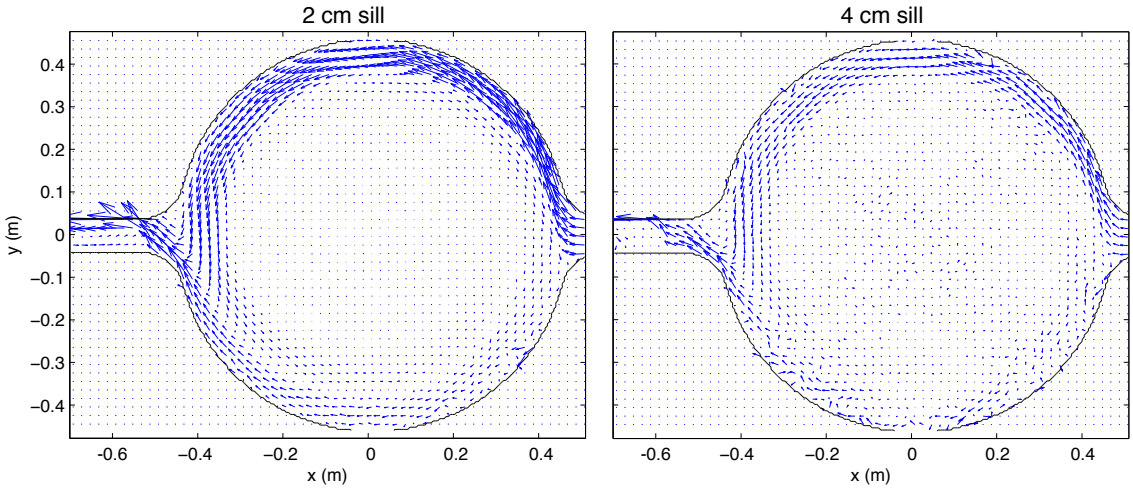

Figure 5.12: Comparison of simulations with varying sill height. The left (right) figure shows the flow for a 2 cm (4 cm) sill.

As the sill height is increased, the outflow layer thins, resulting in an increase in the planetary vorticity. The relative vorticity at the outflow compensates by becoming increasingly negative. Interestingly, the sum of the two vorticity components (ie. the net outflow PV) remains constant as the sill height is varied. Compared with previous work [8, 10, 9], these results show that, at least for the parameter range of the experiments, changes in the outflow planetary vorticity, resulting from changing fluid thickness, may be compensated by changes in relative vorticity at the outflow, rather than changes in basin dissipation (ie. a change in circulation direction). The primary difference between these numerical simulations and those of Yang (2005) is that we have not fixed the direction or transport of the flow at the exit of the basin. The compensation depicted in Figure 5.13 may be due simply to the freedom allowed for the flow to adjust, or perhaps a result of the criticality of the flow at the exit sill. It is possible that the relative vorticity at the North Atlantic overflows is insignificant, as is commonly assumed, and that our experiments and simulations are in a different parameter range. Figure 5.14 shows that we also see significant relative vorticity fluxes over a wider range of parameters (varying rotation rate, f, and transport, Q). However in order to have a closer comparison with the real ocean, rotation rates roughly double these are required. The largest rotation rate ($f = 3$ s^{-1}) of the simulations shown in Figure 5.14 corresponds to a Rossby radius equal to the width of the exit channel.

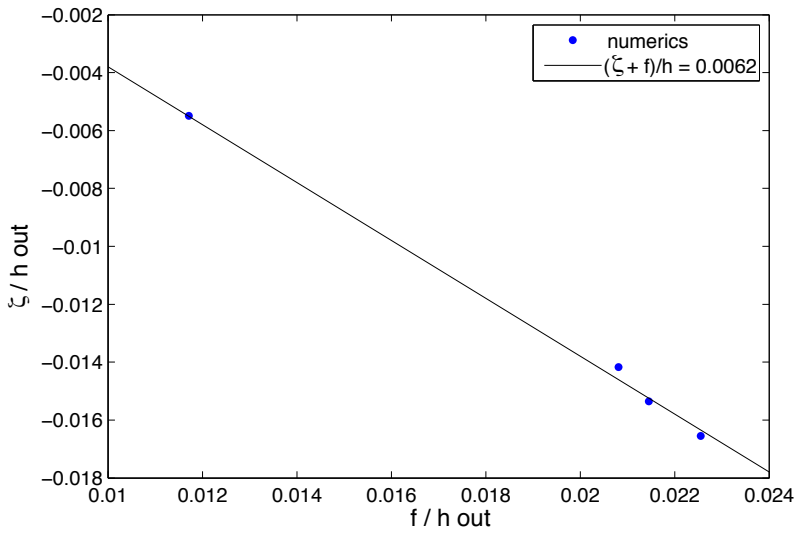

Figure 5.13: Variation of the relative versus planetary components of the potential vorticity flux at the outflow for changing sill height. Sill height increases towards the right of the figure. The line represents constant net potential vorticity at the outflow.

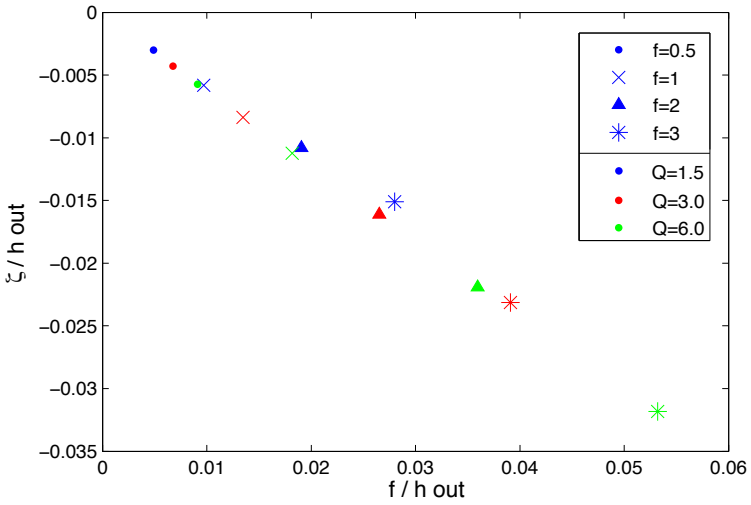

Figure 5.14: Variation of the relative versus planetary components of the potential vorticity flux at the outflow for a range of simulations with varying Coriolis parameter f and outflow transport Q.

The one caveat to these results is that we have had some difficulty in closing the PV budget of the basin. We expect this is due to the noisy boundary dissipation in the regions of low flow, as shown in Figure 5.15. Simulations run at double the resolution have significantly

reduced boundary noise and improved closure of the PV budget, with no noticeable effect on the splitting of the two boundary currents. This suggests that the results of the relative vorticity compensation are generally correct despite the closure problem. Higher resolution or better boundary fitting are needed in order to balance the PV budget.

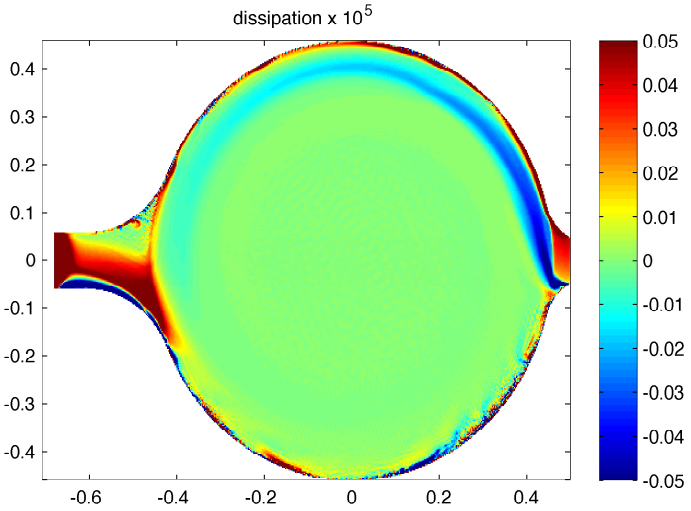

Figure 5.15: Typical spatial dissipation ($-\lambda\nabla\times(u/h)$) for a simulation with side inflow.

5.4 Conclusions and further work

We have performed experiments and numerical simulations to investigate the basin circulation upstream of a hydraulically controlled sill. Previous work by Yang (2005) and Pratt (1997) has shown a simple dependence of the direction of circulation in the basin on the relative thickness of the inflow and outflow. This relationship is based on the assumption of negligible relative vorticity at the basin openings, compared with the component of planetary vorticity in the fluid. Previous numerical studies have enforced this assumption by constraining the direction and transport of the flow through the openings. We have shown in a series of experiments and numerical simulations that, for the parameter range examined here, the relative vorticity may be significant if the flow is given freedom to adjust. Changes in outflow thickness may be compensated by changes in relative vorticity, rather than changes in dissipation brought about by a reversed circulation.

Repeating the analysis of the relative vorticity contribution to the PV budget in additional numerical simulations with an extended parameter range (in particular, increasing f, so that the Rossby radius is a fraction of the strait width) would enable the results to be more readily applied to the ocean. Further work on the PV balance would also require closure of the budget by increasing the resolution of the simulations or using improved boundary fitting.

A further extension of this work would be to compare the response of the PV balance

in flows with subcritical and critical outflows. It is possible that the significant changes in relative vorticity we have observed are a feature of the hydraulic flows and would not be present in the subcritical case.

5.5 Acknowledgements

I would like to thank Karl Helfrich, whose guidance and encouragement throughout the summer made this project possible. I am also grateful to Anders Jensen for devoting so much time on short notice to helping me with the construction of the experiment. Despite a few disgruntlements along the way, George Veronis inspired surprising levels of enthusiasm and success on the softball field. Finally thanks to all the fellows for the cycling and beach adventures, crazy frisbee games, icecreams and beers that made the summer so much fun.

Bibliography

[1] T. Eldevik, J. E. Nilsen, D. Iovino, K. A. Olsson, A. B. Sando, and H. Drange, *Observed sources and variability of Nordic seas overflow*, Nature Geoscience, (2009).

[2] A. Kohl, *Variable source regions of Denmark Strait and Faroe Bank Channel overflow waters*, Tellus Series A-Dynamic Meteorology and Oceanography, (2010).

[3] B. Hansen, W. R. Turrel, and S. Osterhus, *Decreasing overflow from the Nordic seas into the Atlantic Ocean through the Faroe Bank Channel since 1950*, Science, (2001).

[4] J. B. Girton, L. J. Pratt, D. A. Sutherland, and J. F. Price, *Is the Faroe Bank Channel overflow hydraulically controlled?*, Journal of Physical Oceanography, (2006).

[5] A. Nikolopoulos, B. K., H. R., and P. A. Lundberg, *Hydraulic estimates of Denmark Strait overflow*, Journal of Geophysical Research-Oceans, (2003).

[6] A. E. Gill, *The hydraulics of rotating-channel flow*, Journal of Fluid Mechanics, (1977).

[7] K. R. Helfrich and L. J. Pratt, *Rotating hydraulics and upstream basin circulation*, Journal of Physical Oceanography, (2003).

[8] L. Pratt, *Hydraulically drained flows in rotating basins. Part II: Steady flow*, Journal of Physical Oceanography, (1997).

[9] J. Yang, *The Arctic and subarctic ocean flux of potential vorticity and the Arctic ocean circulation*, Journal of Physical Oceanography, (2005).

[10] J. Yang and J. F. Price, *Water-mass formation and potential vorticity balance in an abyssal ocean circulation*, Journal of Marine Research, (2000).

[11] J. A. Whitehead and J. Salzig, *Rotating channel flow: control and upstream currents*, Geophysical and astrophysical fluid dynamics, (2001).

[12] K. Helfrich, A. Kuo, and L. Pratt, *Nonlinear rossby adjustment in a channel*, Journal of Fluid Mechanics, 390 (1999), pp. 187–222.

Project 6

Islands in locally-forced basin circulations

Sam Potter

Princeton University

6.1 Abstract

The circulation response of a square basin with an island and localized surface stress curl is discussed. Attempts in a laboratory were unsuccessful due to unforeseen difficulties in applying a localized surface stress curl to a rotating tank experiment. Numerical simulations show that the effect of an island on the circulation of a square basin with localized forcing can for the most part be characterized by Kelvin's circulation theorem. The circulation response is shown to depend on whether the island has vertical or sloped walls.

6.2 Introduction

6.2.1 Simple gyre circulations

Stommel (1948) and Munk (1950) ([7, 8]) created a simple theory for understanding the gyre circulations of the oceans. Both of these papers solve for the steady state flow field of a homogeneous small Rossby number ocean forced by a wind stress curl. The equation to consider, from [6]

$$\frac{\partial}{\partial t}\nabla^2\psi + \epsilon J(\psi, \nabla^2\psi) + \frac{\partial \psi}{\partial x} = \text{curl}\boldsymbol{\tau} - \mu\nabla^2\psi + E\nabla^4\psi. \tag{6.1}$$

Here ψ is the streamfunction and

$$\epsilon = \frac{U}{\beta L^2} = \left(\frac{\delta_I}{L}\right)^2 \tag{6.2}$$

$$\mu = \frac{r}{\beta L} = \left(\frac{\delta_S}{L}\right) \tag{6.3}$$

$$E = \frac{\nu}{\beta L^3} = \left(\frac{\delta_M}{L}\right)^3. \tag{6.4}$$

U and L are the scaling velocity and length, respectively. r is the bottom friction coefficient, ν is viscosity and $\beta = \frac{df}{dy}$ is the meridional gradient of the Coriolis parameter. The first and second terms on the LHS of (6.1) are the material derivative of the relative vorticity and the third term is the meridional advection of planetary vorticity. The first term on the RHS of (6.1) is the curl of the wind stress and the second and third terms are bottom friction and lateral friction, respectively. δ_I, δ_S, δ_M are the inertial, Stommel and Munk boundary layer widths. Since the nondimensional numbers above are functions of these boundary layer widths, the nonlinearity of the system can be framed in terms of δ_I/δ_S or δ_I/δ_M. A larger δ_I/δ_S means the system is more nonlinear. In this report δ_I is calculated as $\delta_I = \sqrt{U_S/\beta} = \sqrt{\text{curl}\tau/\beta^2}$ where $U_S = \text{curl}\tau/\beta$ is the Sverdrup flow.

Considering a steady state and assuming that ϵ, the Rossby number for this system, is small, the first two terms on the left hand side of (6.1) are dropped. For the Stommel model $\nu := 0$, and vorticity is modified by bottom friction with r^{-1} the frictional timescale. In the Munk model $r := 0$ and lateral viscosity takes the place of bottom friction. The solution streamfunction can be found found by splitting the solution into two parts: a frictionless interior where either viscosity or bottom drag can be ignored and a frictional boundary layer, where length scales are short enough for friction to be important. Following [5] an explicit approximate solution can then be found by asymptotically matching the Sverdrup flow of the geostrophic interior, where $\frac{\partial \psi}{\partial x} = \text{curl}\tau = \mathbf{w_E}$, to the western boundary layer solution where friction is important. For the nondimensional Stommel problem the approximate streamfunction solution with a wind stress of $\boldsymbol{\tau} = (-\cos(\pi y), 0)$ is given by $\psi = \pi(1 - x - e^{x/d})\sin(\pi y)$ (see Figure 6.1). From (6.2), $d = \delta_S/L = \mu$ is the nondimensional width of the frictional western boundary layer and is assumed to be much less than one. The solution of the Munk problem is not shown here but exhibits the same basic characteristics as figure 6.1.

The solution of the Stommel and Munk problems forced with anticyclonic (cyclonic) wind curl exhibit two features: slow anticyclonic (cyclonic) flow in the interior of the ocean and fast northward (southward) flow in the western boundary current. This report will deal with several modifications of this ocean circulation theory. I will be considering how the gyre circulation is changed when (a) the wind forcing is localized, not universal, and (b) there exists an island with or without topography in the basin.

6.2.2 Gyre circulation with islands

Adding an island to the Stommel-Munk setup creates a multiply connected domain. This allows for the existence of an island circulation, defined as the total transport between the island and the outer basin boundary. When the circulation is in steady state and linear and the bulk of the dissipation takes place on the eastern side of the island, which acts as a western boundary for the sub-basin east of the island, the island transport can be solved for using the Island Rule of Godfrey [3, 1].

Following Pedlosky et al. (1997) the Island Rule can be derived starting from the horizontal momentum equations for a single homogeneous layer:

$$\frac{\partial \mathbf{u}}{\partial t} + (\zeta + f)\hat{k} \times \mathbf{u} = -\nabla \left(\frac{p}{\rho} + \frac{|\mathbf{u}^2|}{2} \right) + \text{Diss}(\mathbf{u}) + \mathbf{T} \tag{6.5}$$

where $\mathbf{T}$ is a forcing (e.g. wind stress), Diss($\mathbf{u}$) is dissipation, either bottom friction, lateral friction or both, ζ is relative vorticity, and the first term on the right hand side is the Bernoulli function. The β-plane approximation is made, making $f = f_0 + \beta y$. To determine the island streamfunction it is necessary to integrate around the island, but this creates a problem since the eastern side of the island contains a highly dissipative western boundary. Assuming that the only non-negligible dissipation due to the island occurs on the *eastern* side, the trick of Godfrey is to create a contour that avoids this western boundary (see figure 6.2). Integrating around a circuit that only sees ocean interior and eastern boundaries allows the Diss($\mathbf{u}$) term to be ignored. Assuming that the flow is linear, in a steady state and is non-divergent (so a streamfunction can be defined) integrating (6.5) around the contour C defined in figure 6.2 gives

$$\beta(y_n - y_s)\psi_I = -\oint_C \mathbf{T} \cdot \hat{t} ds, \tag{6.6}$$

where y_s and y_n are the southernmost and northernmost latitudes of the island, respectively, and ψ_I is the island streamfunction, which is assumed to be zero on the eastern basin boundary and a constant on the island. This relation can be further simplified by defining a Sverdrup streamfunction

$$\beta\psi_S = -\int_x^{x_e} \hat{k} \cdot \nabla \times \mathbf{T} dx'$$

where x_e is the x-coordinate of the eastern basin boundary. Using Stokes Theorem the forcing term in (6.6) becomes

$$\oint_C \mathbf{T} \cdot \hat{t} ds = \oint_{C_I} \mathbf{T} \cdot \hat{t} ds + \int\int_R \beta \frac{\partial \psi_S}{\partial x} dx dy \tag{6.7}$$

$$= \oint_{C_I} \mathbf{T} \cdot \hat{t} ds - \beta \int_{y_s}^{y_n} \psi_S(x_+, y) dy, \tag{6.8}$$

Here x_+ is the x-coordinate of the eastern side of the island and C_I is the counter-clockwise circuit around the island. If we assume there is no net tangential force around the island

the first term on the right hand side of (6.8) drops out and (6.6) becomes

$$\psi_I = \frac{1}{y_n - y_s} \int_{y_s}^{y_n} \psi_S(x_+(y), y) dy. \tag{6.9}$$

Therefore the island streamfunction in this idealized setup has a very simple interpretation: it is the average of the Sverdrup streamfunction along the eastern boundary of the island.

The presence of the island circulation changes the standard Stommel-Munk problem. From [1], figure 6.3 shows an anticyclonic gyre circulation in a circular ocean basin with an island in the center of the tank. The flow is forced by a uniform wind stress curl. The circular basin geometry is different than the rectangle of the original Stommel-Munk problem, which changes the form of the Sverdrup flow and western boundary current. The primary change induced by the island is a recirculation region in the eastern sub-basin. The extent of this recirculation is determined by the latitudes where ψ_I is equal to the Sverdrup flow [1, 2]. The existence of the recirculation is demanded by Kelvin's circulation theorem: southerly flow above and below the recirculation is balanced by a patch of northerly flow in the recirculation. If dissipation $\text{Diss}(\mathbf{u})$ is modeled as bottom friction, the contour integral around the island is conserved: $\oint_C \text{Diss}(\mathbf{u}) \cdot \hat{t} = -r \oint_C \mathbf{u} \cdot \hat{t} = 0$ [1]. This relation requires that the contribution by the western side of the island is negligible.

The Godfrey and Pedlosky et al. island studies above assumed that the island had vertical walls – there is no gradual slope leading from ocean bottom to island top. Assuming vertical walls simplifies the analysis considerably since potential vorticity contours simply follow lines of latitude when there is no bottom topography. Pedlosky et al. (2009) studied the gyre circulation with an island of the form in figure 6.4. The resulting circulation is shown in figure 6.5, which can be compared directly to figure 6.3. The recirculation region has for the most part disappeared. A sharp meander has now formed in the western sub-basin, with streamlines sharply breaking from topographic control to rejoin the southward Sverdrup flow.

6.3 This report

I will study the above questions – how basin circulation changes when an island is included – but for localized forcing. The above studies mostly concentrated on the case where the surface forcing was basin-wide, the circulation changes considerably when the wind stress curl is localized in space. The remainder of the paper will be organized as follows. Section 6.4 will describe an unsuccessful attempt to study locally-forced island circulations in a rotating tank experiment and section 6.5 will describe more successful numerical models of the circulations.

Numerical model

For the following numerics the model created by Helfrich et al. (1999) was used [10]. The model solves the single layer rotating shallow water equations with bottom friction and

viscosity:

$$\begin{aligned}
\frac{\partial u}{\partial t} + u\frac{\partial u}{\partial x} + v\frac{\partial u}{\partial y} - fv &= -g\frac{\partial h}{\partial x} - ru + \frac{\nu}{h}\nabla\cdot(h\nabla u) \\
\frac{\partial v}{\partial t} + u\frac{\partial v}{\partial x} + v\frac{\partial v}{\partial y} - fv &= -g\frac{\partial h}{\partial y} - rv + \frac{\nu}{h}\nabla\cdot(h\nabla v) \\
\frac{\partial h}{\partial t} + \frac{\partial (uh)}{\partial x} + \frac{\partial (vh)}{\partial y} &= 0,
\end{aligned}$$

where h is the fluid height, $f = f_0 + \beta y$ and the second and third terms in the horizontal momentum equations are bottom friction and lateral friction, respectively.

The model was made to mimic the laboratory setup (described below). The model is nondimensionalized using the half width of the basin l as a horizontal length scale, the mean depth H as a vertical length scale, the gravity wave speed $\sqrt{gH}$ as the velocity scale, and the advective time $l/\sqrt{gH}$ as the time scale. A 150x150 grid was used and the model was run out to 6.5 Ekman spindown times, though the model only needed 1-2 spindown times to equilibrate. The model's Stommel layer was resolved by 3 grid widths, the Munk layer by 2 grid widths. This western boundary layer resolution is not ideal, however, the results presented below are reasonable.

6.3.1 β-plume circulation

The circulation that results from a localized forcing is called a *β-plume* [4, 5, 9]. Figure 6.6 shows a β-plume circulation in the shallow water model. Unless noted otherwise all wind stress curls are anticyclonic, which induces a southerly Sverdrup flow beneath the forcing. The streamlines roughly follow lines of constant potential vorticity f/H, where H is fluid depth. The edges of the plume expand north and south since the edges of the circulation form small length scales in which friction is important. A zonal boundary layer scaling analysis shows that the plume expands as $\delta_S|x-x_0|)^{1/2}$, where $|x-x_0|$ is the distance from the forcing region located at x_0. Again there is a frictional western boundary current that allows a northward return flow. We will discuss the island results in a later section, but from 6.9 and the arguments made in section 6.2 we can already guess that the β-plume cannot simply use the island to form a western boundary current.

6.4 The laboratory

The tank used for this experiment is shown from above in figure 6.7. The tank is square with sides of 60 cm and an average depth of 25 cm. The bottom of the tank is angled with a slope of 0.15 to create a topographic β effect with the top of the picture the effective north. The topographic β equals $f_0 s/H$ where f_0 is the rotation of the tank, s is the bottom slope, and H is the mean depth. An island of length 30 cm is located 23 centimeters east of the western wall. This island has a sloping topographic 'skirt' going from the island surface to the tank bottom. The flow is driven by a stepper motor attached to a rotating disk of radius 7.5 cm located 45 cm east and 30 cm north of the southwest corner (bottom left). There is a rigid lid above the entire flow, with the disk the only moving piece of the lid.

The water beneath the rotating lid experiences a constant wind stress curl; this curl drives an Ekman pumping that is balanced by a horizontal geostrophic flow. Diluted food dye was used to visualize the flow, with images taken by a videocamera mounted on the rotating table.

For the rotating table experiment the Munk width $\delta_M = 1.33$ cm and the Stommel width $\delta_S = 0.87$ cm for $f_0 = 2$ s^{-1}. The inertial boundary layer width δ_I can be calculated as $\delta_I = \sqrt{U_S/\beta}$ where $U_S = |w_0|/s$ is the Sverdrup flow driven by a surface Ekman pumping under the disk $w_0 = (\frac{\nu}{\Omega})^{1/2}\Delta\Omega$. ν is the viscosity, $\Omega = f_0/2$ is the rotation of the tank and $\Delta\Omega$ is the differential rotation of the forcing disk.

Figure 6.7 shows the steady state flow after ninety minutes of spinup. The dye shows up poorly so the flow is highlighted by black arrows. The table rotation was counterclockwise at $f = 2\Omega = 2$ s^{-1} and the disk rotation was clockwise at $\Delta\Omega = 0.1$ s^{-1}. The nonlinearity measure $\delta_S/\delta_I = 2.78$, so the flow is being forced strongly. This does not change the conclusions of the following paragraphs, however, and the odd behavior found in the lab was also found for weaker forcings. The dye entry point can be seen along the southeastern side of the island. The red dye does not illuminate any dynamics, so it can be ignored here. Following the arrows in the picture, the blue travels north before it heads east towards the disk. The flow wraps under the disk, then heads back west near the location where the dye was entered. The dye then arcs to the northeast where it wraps *behind* the disk. Once the flow has gone behind the disk it heads west to join back up with the flow to create a recirculation.

A northward flow to the *east* of the forcing region is a problem since the tank is a rigid lid system with negligible buoyancy effects. The only method of communicating information in the system is Rossby waves propagating on the topographic β. Since $\beta > 0$ the Rossby waves propagate to the west and consequently a water parcel to the east of the forcing region has no way of knowing that there is any forcing, and thus should not be moving.

The first guess as to what was going wrong was something involving the imperfect laboratory setup: unaccounted for buoyancy effects, incorrect rotation–either from the table itself or from placement on the table, or incorrect forcing. These are issues that do not effect the shallow water model, so we next tried to emulate the laboratory flow in the model.

The result is shown in figure 6.8. A clockwise rotating circulation emanates from the disk and heads towards the island, returning after heading north on a frictional boundary layer. A counter-clockwise rotating circulation can be seen behind the clockwise circulation, very much as in the laboratory experiment. Therefore the problem is not with the laboratory, but with the setup. The laboratory forcing did not turn out as intended.

In the laboratory experiment the azimuthal surface stress is as follows

$$\tau(r) = \begin{cases} \tau_{\max} r/R & : r \le R \\ 0 & : r > R \end{cases}$$

where $\tau_{\max}$ is the maximum stress and r is the radial distance from the disk center. The curl of the stress is

$$\text{curl}\tau(r) = \begin{cases} 2\tau_{\max}/R & : r \leq R \\ -\text{sgn}(\tau_{max})\delta(r-R) & : r = R \\ 0 & : r > R \end{cases}$$

since the there is a discontinuous jump in stress from $r = R$ to $r > R$. This oppositely signed ring of stress curl drives the counter-rotating flow that shows up just to the east of the forcing. Friction causes the circulation to spread in the laboratory; in the model this discontinuity in curl is spread over a grid cell.

This problem was corrected in the model by changing the stress term outside the disk to

$$\tau(r) = \begin{cases} \tau_{\max} r/R & : r \leq R \\ \tau_{\max} R/r & : r > R \end{cases}$$

This gives zero curl outside the disk. The nonzero stress for $r > R$ does generate a small Ekman transport, but this has a negligible effect on the flow for weak forcing. For the remainder of this report I will discuss numerical model runs forced with this corrected stress distribution.

6.5 Numerics

6.5.1 Vertically-walled island

A vertically walled island is now included in the basin. The island is one nondimensional unit long in y centered at $y = 0.7$. The island is two grid cells in width as required by the numerics. The circulation is shown in figure 6.9. The center of the β-plume is interrupted on its way west and a recirculation region the width of the forcing region extends to the island. The outer edges of the plume continue west until intersecting the western side of the domain, forming a boundary layer. The island intersection of these two parts of the β-plume determine stagnation points of the circulation at $y \approx 0.7, 1.3$ along the eastern side of the island.

This flow satisfies the island rule and the structure of the eastern sub-basin circulation is analogous to the circulation on the eastern side of the vertically walled island in figure 6.3 (Pedlosky et al. (1997)). The recirculation region in figure 6.9 is a stretched out form of the recirculation in figure 6.3. Moving south to north along the eastern side of the island in both circulations the velocity changes from southward to northward to southward, again satisfying the circulation constraint $\oint_C \text{Diss}(\mathbf{u}) \cdot \hat{t} = -r \oint_C \mathbf{u} \cdot \hat{t} = 0$, again assuming that the primary dissipative process is bottom friction $\text{Diss}(\mathbf{u}) = -r\mathbf{u}$ acting on the eastern side of the island.

The same considerations apply when the basin geometry is varied. When the island is small relative to the forcing the circulation looks like a β-plume with slightly modified contours where the island lies (figure 6.10). When the island is large relative to the forcing the

western basin response is the scale of the island (figure 6.11). These two figures show that the size western basin response will scale as the larger of the island and forcing meridional lengthscales. This still holds if the forcing region is moved relative to the island. In figure 6.12 the forcing is moved to the south but since a piece of the β-plume hits the island the western sub-basin response is the size of the island.

6.5.2 Island with topography

The topographic island placed in the basin is shown in figure 6.13. The shallow water model used for these numerics becomes unstable when the island reaches to the surface so the island was only made to reach 3/4 of the way to the surface. The dynamics of the 'submerged' island are assumed to be very similar to an island reaching to the fluid top since there are closed f/H contours surrounding the (submerged) island. The submerged island could also be thought of as a seamount.

Adding a topographic island changes the geometry of potential vorticity f/H contours. In the absence of friction a linear flow will follow f/H contours. A topographic island is very different from a vertically-walled island because topography creates closed f/H contours, whereas the vertical island merely disrupts f/H contours, exactly like the eastern and western boundary in the Stommel or Munk problem. We might expect the flow to look like the sketch in figure 6.14, with the flow only leaving an f/H contour when encountering the western boundary. This however, is not what happens, and the the resulting circulation is shown in figure 6.15 for a case with $\delta_I/\delta_S = 0.33$

The circulation has changed drastically compared to the vertically walled island in figure 6.9. There is still a main recirculation region, but it now reaches all the way to the southwestern tip of the island. The topography has a strong control on the flow, with the streamfunction lines for the most part tracking f/H contours, except in small areas where friction is important. The around island flow also differs from the vertically-walled case. As the return flow comes around the northern edge of the island it tracks south on a f/H contour, but then takes a hard left turn and heads *north* towards the forcing region. This sharp meander is reminiscent of the meander in figure 6.5 from Pedlosky et al. (2009). In the Pedlosky et al. paper the meander is in the western sub basin – in the localized forcing case in figure 6.15 the meander is to the east of the island. The meander again allows the circulation to satisfy the circulation constraint, the return flow of the main recirculation cell moves *counterclockwise* (mostly northward) with respect to a closed f/H contour, while the flow returning from the western sub-basin moves *clockwise* (mostly southward). The reason that the flow does not follow the course shown in figure 6.14 is friction: there is enough friction for the flow to 'slide' off of f/h contours and travel all the way around the island. In fact the main recirculation region is simply a truncated version of the sketch in figure 6.14, with the flow only making it to the southern tip of the island before it gets rerouted from its course to the western wall.

With cyclonic forcing the circulation response is the same, but with opposite sign, as expected for the linear regime.

6.5.3 Increasing non-linearity

The numerical model used was designed to study inertial flows and was not ideal for this problem. Thus we were not able to study the entire range of parameter space that we would have liked. For example it was difficult to modify lateral and bottom friction and change the geometry of the sloped island. However we were able to get interesting results for changing δ_I/δ_S, the nonlinearity factor, by increasing the strength of the wind stress curl. Results for both anticyclonic and cyclonic forcing are shown in figures 6.16a-6.16d. Increasing the nonlinearity pushes the center of the western boundary current to the north (south) corner for anticyclonic (cyclonic) forcing. The main recirculation region becomes deformed and stretches to the south. For $\delta_I/\delta_S = 7.37$ with a vertically-walled island the flow is unsteady, with vortices being shed off the southern tip of the island (not shown). This unsteadiness, which was not found in the topographic island circulation, may be a result of flow separation at the sharp corners of the vertically walled island.

6.6 Conclusions

The presence of an island in a basin with localized wind stress curl significantly changes the standard β-plume response. Whether the island has vertical walls or a topographic slope the circulation is split into two components. The bulk of the circulation stays close to the eastern side of the island, forming a small recirculation region that includes most of the forcing area. In the vertically walled case, this recirculation forms a rectangular region with latitudinal scale defined by the size of the forcing region. In the topographic slope case the western side of the main recirculation region is diffused southward, with a small component of the flow reaching the southwestern tip of the island topography. The second component of the flow travels around the island, using the western edge of the basin to form a western boundary current. This flow is for the most part quite similar for both islands – the circulation acts as an interrupted β-plume, extending around the southern and northern edges of the island. This around-island flow does differ significantly on the return by the northern edge of the island. In the topographic case, the return flow tracks almost due south along an f/H contour until sharply jumping north to rejoin the forcing region and forming a meander. All of the around-island dynamics appear for the most part to be governed by Kelvin's circulation theorem about the island: $\oint_C \mathrm{Diss}(\mathbf{u}) \cdot \hat{t} \approx -r \oint_C \mathbf{u} \cdot \hat{t} = 0$. Thus around the island, or in the topographic case around a closed f/H contour about the island, the clockwise flow must balance the counterclockwise flow. In the vertically walled case this requirement creates a recirculation zone analagous to that found in Pedlosky et al. (1997) and in the topographic case it creates a sharp meander in the eastern sub-basin.

An interesting effect of the island is that even when the forcing radius is very small relative to the island length the circulation response *must* be on the scale of the island. This is again due to the circulation constraint on a closed contour of the flow about the island and the act of friction forcing flow off of f/H contours. This dramatic effect of the island on the basin circulation is not seen in the studies with basin-wide forcing.

6.6.1 Future Work

It is easy to change the relative size, shape, and relative position of the forcing region and island within the model. The results found in this study and some results not placed in this report suggest that the bulk of the possible flow types are captured well by the two examples given above. However there are many basin and forcing geometries and some may give fundamentally different circulations. Related to this, it would be nice to replicate the numerical results in this paper with a model more suited to slow, linear ocean circulations. The model used here was created to study inertial flows and worked quite well but was not perfect: it was not amenable to turning off lateral friction or turning down bottom friction, and had issues with some island geometries. Lastly, to study this problem in the lab would require a mass source-sink setup that was either a point source or a source over a general area that induced an Ekman pumping directly. It would be interesting to see if the lab results match up with the numerical results over a wide range of forcings.

Bibliography

[1] Pedlosky, Joseph , Pratt, Lawrence J., Spall, Michael A. & Helfrich,Karl R., 1997 *Circulation around islands and ridges*, Journal of Marine Research, 55 no. 6, 1199-1251.

[2] Pedlosky, Joseph, Iacono, Roberto, Napolitano, Ernesto & Helfrich, Karl, 2009 *The skirted island: The effect of topography on the flow around planetary scale islands* Journal of Marine Research, 67 no. 4, 435-478.

[3] Godfrey, J. S., 1989 *A sverdrup model of the depth-integrated flow for the world ocean allowing for island circulations*, Geophysical and Astrophysical Fluid Dynamics, 45 no.1-2, 89-112.

[4] Stommel, Henry, 1982 Is the South Pacific helium-3 plume dynamically active?, Earth and Planetary Science Letters, 61 no. 1, 63-67.

[5] Vallis, G. K., 2006 *Atmospheric and Oceanic Fluid Dynamics*, Cambridge University Press

[6] Pedlosky, J., 1996 *Ocean circulation theory*, Springer

[7] Stommel, H., 1948 *The westward intensification of wind-driven ocean currents*, Trans. Amer. Geophys. Union, 99, 202-206.

[8] Munk, W. H., 1950 *On the Wind-Driven Ocean Circulation.*, Journal of Atmospheric Sciences, 7, 80-93.

[9] Spall, M.A., 2000 *Buoyancy-forced circulations around islands and ridges* Journal of Marine Research, 58 no. 6, 957-982.

[10] Helfrich,K.R., Kuo, Allen C. and Prattl, L.J., 1999 *Nonlinear Rossby adjustment in a channel* J. Fluid Mech., 390, 187-222.

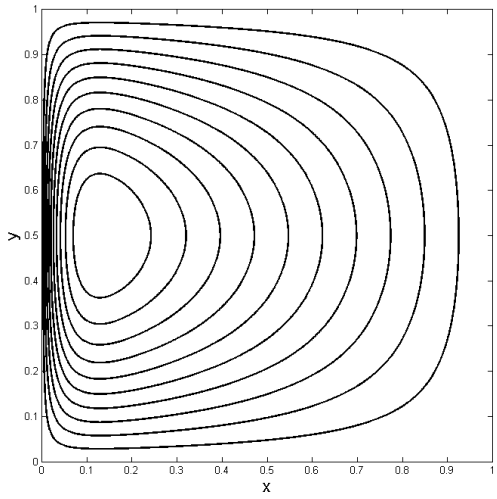

Figure 6.1: Following [5], the solution streamfunction of the Stommel problem with $d = 0.04$.

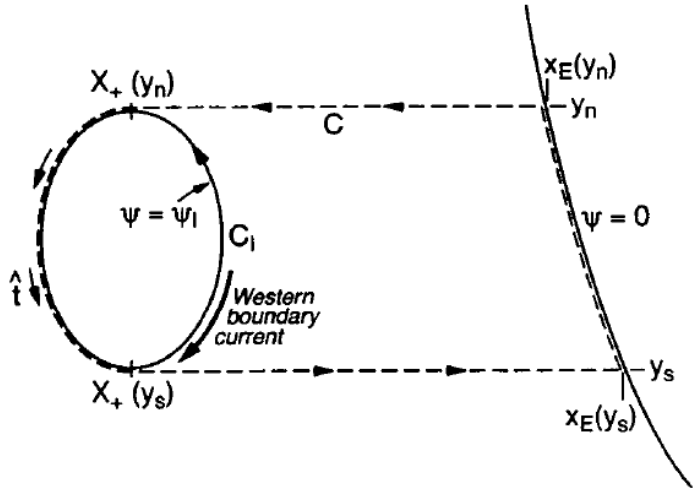

Figure 6.2: The contour integral allowing for the evaluation of the island circulation, from [1].

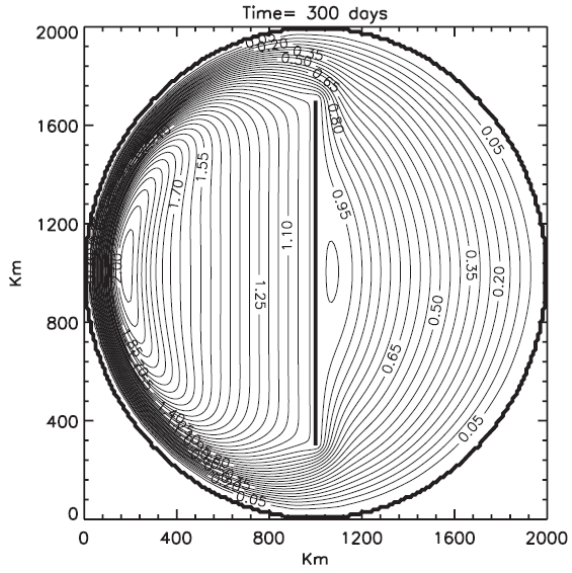

Figure 6.3: Linear gyre circulation in a circular basin with a vertically-walled island [2]. The forcing is anticyclonic. The island is represented by the bar in the center of the basin.

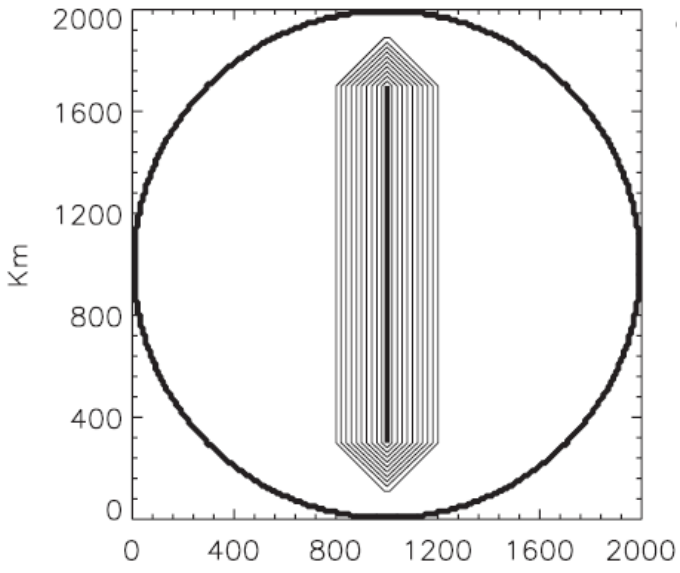

Figure 6.4: The island with topography from [2].

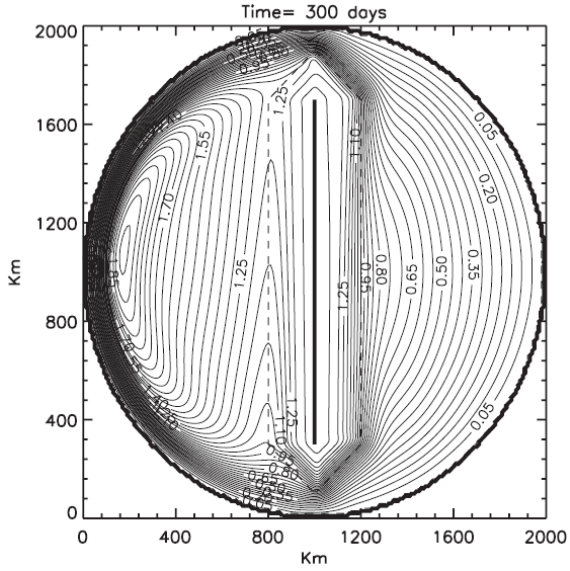

Figure 6.5: The circulation in a gyre with the island from figure 6.4(from [2]). The dashed line marks the outer edge of the island topography.

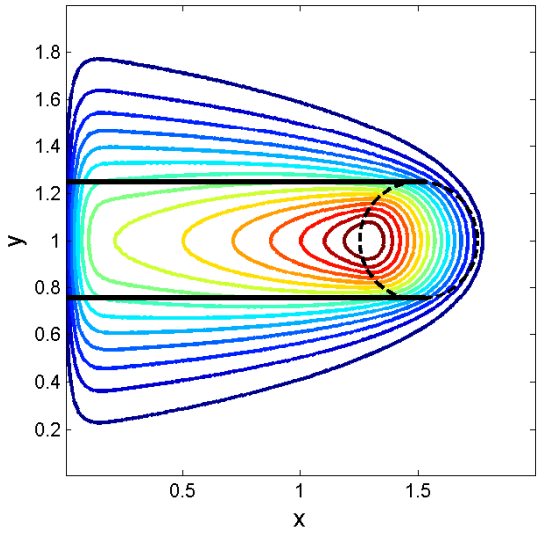

Figure 6.6: A β-plume circulation forced by a disk of constant wind stress curl centered at $(x, y) = (1.5, 1)$ with radius 0.25. The straight black lines indicate the width the beta plume would have if there were no friction. $\delta_I/\delta_S = 0.33$.

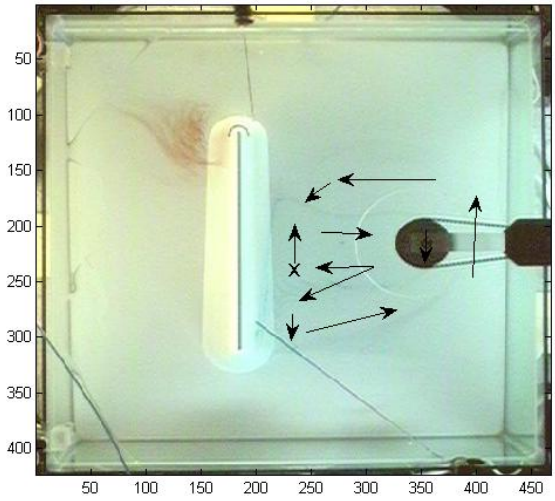

Figure 6.7: A run of the rotating table experiment. Starting at **X** the arrows denote the path of a water parcel through the flow.

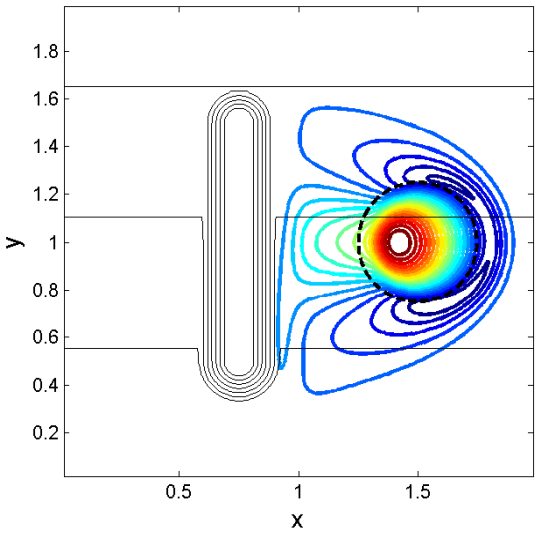

Figure 6.8: Steady state streamfunction from the numerical model in a setup mimicking the laboratory experiment. Black lines denote height contours.

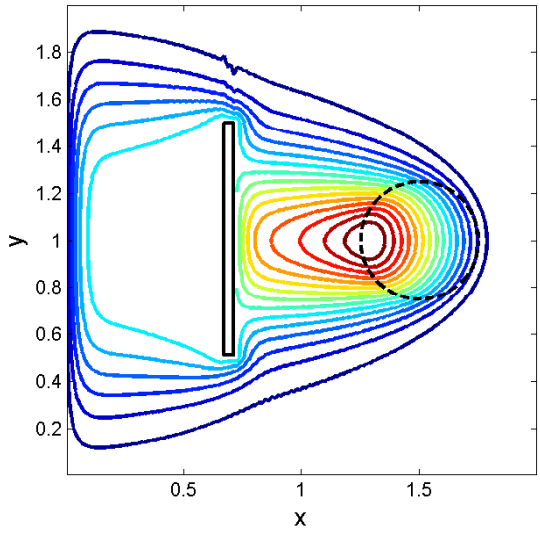

Figure 6.9: Circulation with a vertically walled island. $\delta_I/\delta_S = 0.33$.

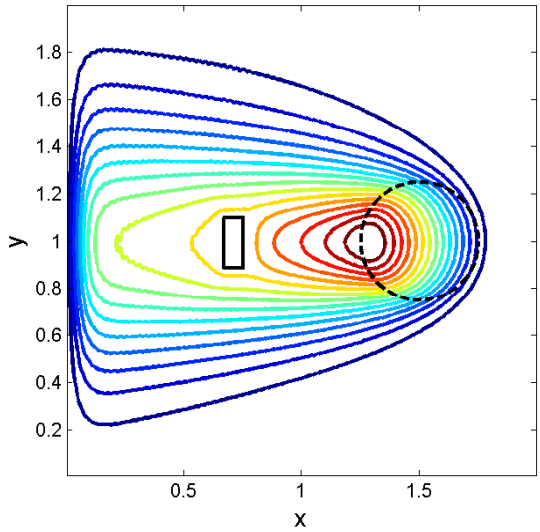

Figure 6.10: Circulation with a vertically walled island with length 0.2. $\delta_I/\delta_S = 0.33$.

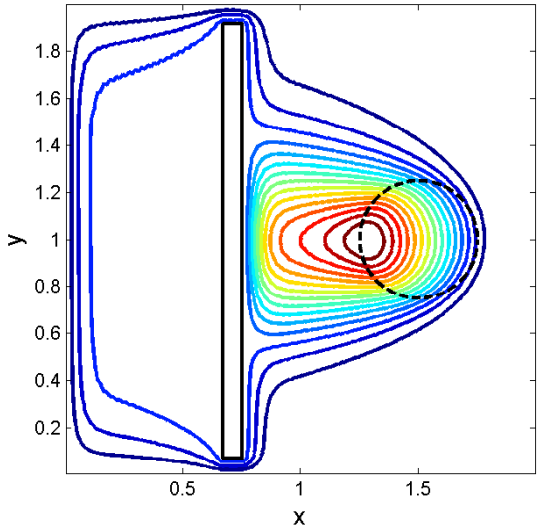

Figure 6.11: Circulation with a vertically walled island with length 1.95. $\delta_I/\delta_S = 0.33$.

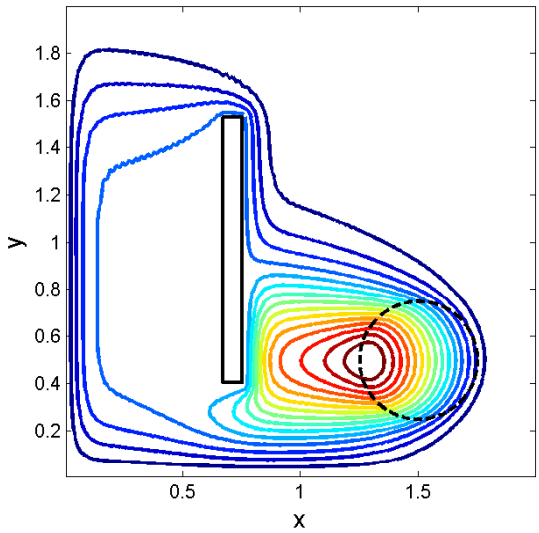

Figure 6.12: Circulation with a vertically walled island and the forcing centered at $(x, y) = (1.5, 0.5)$. $\delta_I/\delta_S = 0.33$.

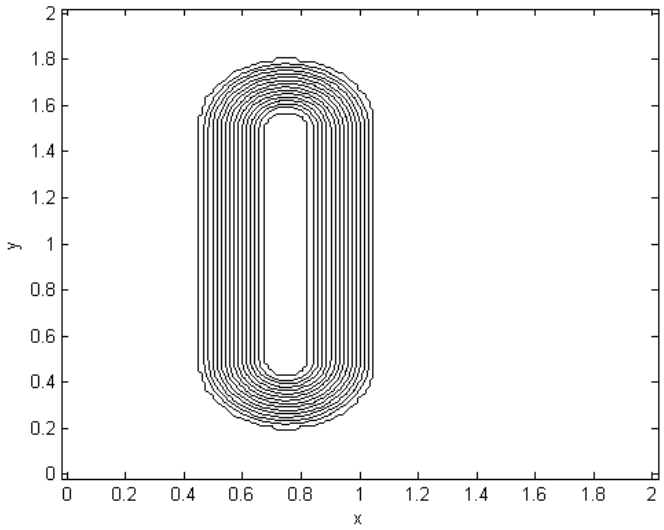

Figure 6.13: Height contours of the topographic island. Contours are spaced 0.05 nondimensional units apart to a maximum of 0.75. The total height of the fluid is 1.

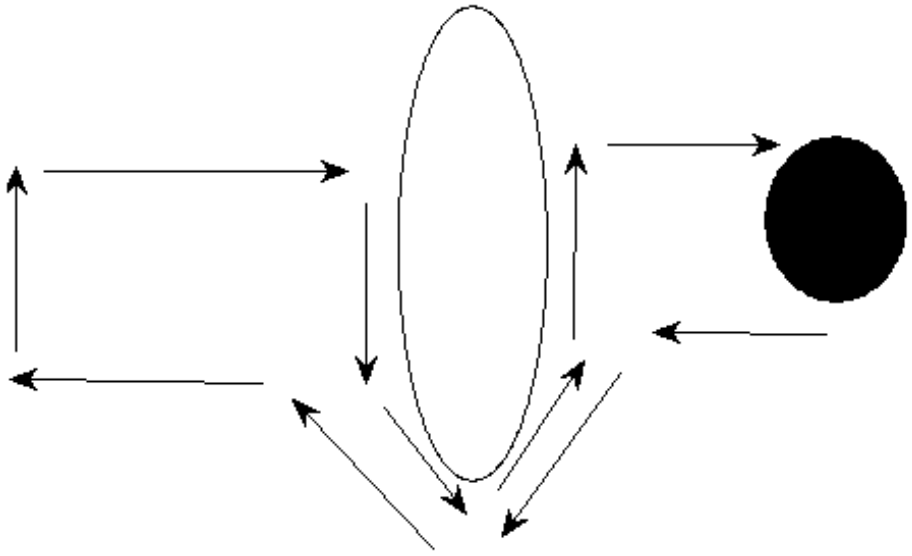

Figure 6.14: A sketch of the expected flow in a basin with a topographic island. The open figure is the outermost closed f/H contour defined by the island, the closed figure is the forcing region.

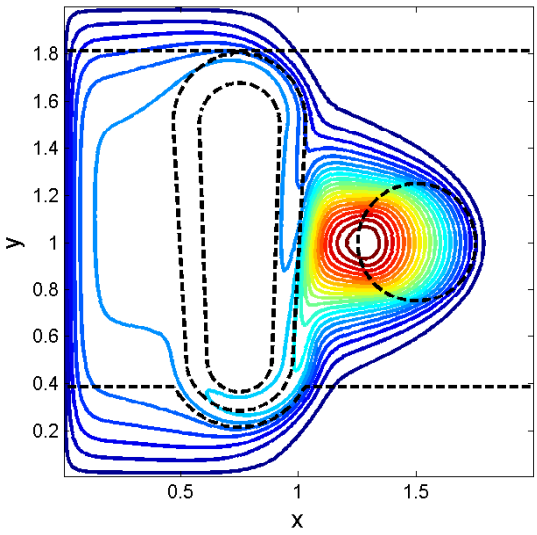

Figure 6.15: Circulation in a basin with the topographic island from figure 6.13. Black contours denote potential vorticity f/H. The largest closed contour is the potential vorticity contour enclosing the island. $\delta_I/\delta_S = 0.33$.

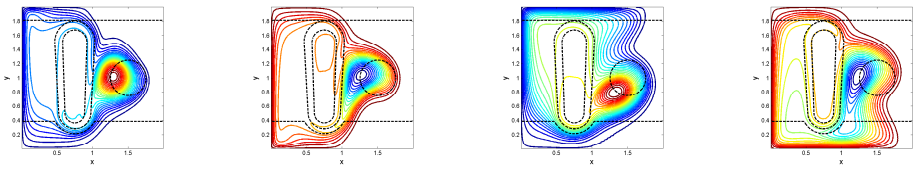

(a) (b) (c) (d)

Figure 6.16: Circulations for increasing non-linearity: (a) Circulation for topographic island with anticyclonic forcing and $\delta_I/\delta_S = 3.30$ (b) Circulation for topographic island with cyclonic forcing and $\delta_I/\delta_S = 3.30$ (c) Circulation for topographic island with anticyclonic forcing and $\delta_I/\delta_S = 7.37$ (d) Circulation for topographic island with cyclonic forcing and $\delta_I/\delta_S = 7.37$.

Project 7

Stability analysis of two-layer immiscible viscous fluids in an inclined closed tube

Zhan Wang

University of Wisconsin

The present investigation is concerned with the role of bottom slope in the stability properties of two-dimensional disturbances in sheared two-layer immiscible fluids with stepwise densities. A linear analysis of normal mode instability of the interface in an inclined closed tube is carried out using full Navier-Stokes equation using Chebyshev-tau method. It has been observed that Reynolds number and the tilt angle both have destabilizing effect on the interface eigenvalue problem of Orr-Sommerfeld equation. As a special example, Stokes flow is proven to be stable for any angles. A weakly nonlinear model equation, which is Kuramoto-Sivashinsky type, for the interface is given using multi-scale method, and the long wave dispersion relation gives a sufficient condition for triggering the instability.

7.1 Introduction

When two fluids of different physical properties are superposed one over the other and are moving with a relative horizontal velocity, the instability occurs at the interface. Two-layer fluids are ubiquitous in both ocean and atmosphere such as the exchange of Atlantic Ocean water with the saltier Mediterranean Sea water through the Strait of Gibralta, light water entering the ocean space from a suddenly broken dam, rapid melting of continental ice, mixing of clouds and etc. The seminal paper on experimental results for two-layer fluid was carried out by Thorpe (1968,1971) for the continuously stratified mixing fluids with acceleration share profile called Kelvin-Helmholtz instability, which revealed the relation-

ship between the lab experiment and the real instability and turbulence in the ocean and atmosphere.

Theoretical approaches for layered viscous channel flow often consider the stability of a basic flow to normal mode type disturbances. The first theoretical study appears to have been a paper by Yih (1967) who discussed the linear stability of two-layer Couette and plane Poiseuille flows using a long-wave approach. He showed that both viscosity and density stratification can generate an interfacial instability, recognized as Kelvin-Helmholtz instability which was also called the interfacial mode, at any Reynolds number. A different, shear type instability mechanism has been found by Hooper & Boyd (1983) occurring primarily for short waves at small Reynolds number. The stability properties at intermediate wavelengths are complicated by mode crossings. Accurate numerical stability studies for the two-layer Orr-Sommerfeld equations (linearized Navier-Stokes) can be implemented recently since the Chebyshev-tau method was developed by Dongarra *et al* (1996) and Boomkamp *et al* (1997). There is a large number of literature in both mixing layers and immiscible fluids for plane channel flows, reader is referred to Hooper & Grimshaw (1985), Yiantsios & Higgins (1988), Pozrikidis (1997), Yecko *et al* (2002), Bague *et al* (2010), Bassom *et al* (2010), Mählmann & Papageorgiou (2010) and the references therein.

Since the instability between two fluids is generated by unbalanced pressure resulting from the perturbation of the velocity shear flow, the combination of external forcing and topographic features, such as sloping bottom, on a two-layer baroclinic flow results in various types of instabilities at the interface. The first paper for viscous fluid moving down an inclined plane was proposed by Yin (1963), which firstly clarified the boundary conditions on the free surface of one layer fluid. Kao (1965) gave the linear analysis for two-layer Poiseuille flow with a sloping bottom in the presence of both interface and free surface using long wave approximation. More recently, Defina *et al* (1999) considered the viscous effect in an inclined tube for the fluid with continuously stratified density, and Negretti (2008) presented more numerical results for an inclined stratified shear flow under Boussinesq assumption. On the experimental side, besides Thorpe's famous work in 70's, Fouli & Zhu (2011) performed a new experiment to understand the generation conditions and development of Kelvin-Helmholtz instabilities in two-layer exchange flows downslope of a bottom sill. The low frequency oscillation were observed to led to the development of large-scale downslope waves that caused significant interfacial entrainment.

Reduced potential models for those fluids which the vorticity is identically zero, and the velocity is thus given by the gradient of a harmonic potential, have also been developed to study the interface stability problem in multi-layer fluids. Purely inviscid potential flow is the simplest nonlinear model, and the vortex sheet method or called boundary integral method is a successful numerical method to simulate the Kelvin-Helmohltz instability (see [14] and the references therein). There are two theories of potential flow of a viscous fluid: viscous potential flow and the dissipation method. In the viscous potential theory, the effects of viscosity on the normal stress are not neglected but the effect of shear stresses are neglected, in other words, the governing equation is Laplace while the viscosity enters through normal stress balance and tangential stresses are not considered on the interface. On the other hand, the dissipative method is a famous theory which was first introduced by Stokes in his study of the decay waves, which based on the basic fact that the viscous stresses of the irrotational flow are self-equilibrated and do not give rise to forces in the

equations but they do work and give rise to energy and dissipation. In a recent paper, Kim *et al* (2011) used the linearized versions of these models to the research of Kelvin-Helmohltz instability.

This work concerns two-layer immiscible fluids in an inclined closed tube and has been extended Thorpe's classic work to the viscous and non-mixing case. The aim of the present linear stability study is to examine the influence of a bottom slope on the stability of the interface under the action of a shear advection. The bottom slope has destabilizing effect of buoyancy at the interface and adds an additional acceleration term which results in a parabola base shear flow. It is much natural than the plane channel flow which needs extra force to maintain the base shear and more realistic in the case of oil & water interface. The primary problem to which we shall address the following analysis is the investigation of the static stability of the interface y=0 in the tilt coordinates between two parallel shear flows $U_{1,2}(y)$ of a light viscous incompressible fluid in y>0 and a heavy one in y<0 when this interface is subjected to the small periodic perturbation.

The rest of the paper is organized as follows. In Sec. II the base shear flow is calculated and the governing equations and the connecting boundary conditions on the interface for the perturbed system are presented. In Sec. III, the Chebyshev-tau method is applied to solve the eigenvalue problem for two-layer Orr-Sommerfeld systems. The results for both Stokes flow and general case are discussed for the additional effect of changing the density ratio, tilt angle, surface tension and Reynolds number. In Sec. IV, a weakly nonlinear PDE model for the long wave perturbation is derived via multi-scale method, and a sufficient condition for generating instability is also obtained automatically. Finally, Sec. V summarizes the results and includes conclusion.

7.2 Formulation

7.2.1 Governing equation

The flow is assumed to be viscous, incompressible fluids at uniform depth inclined tube at an angle θ in a gravitational field with the coordinate axes $x-y$ as shown in Fig.1 with origin at the interface. The upper layer is a fluid of density ρ_1 and the lower layer is of density ρ_2 with $\rho_2 > \rho_1$. The governing Navier-Stokes equations (NSE) in the tilt coordinates read

$$\frac{\partial \widetilde{u}_i}{\partial t} + \widetilde{u}_i \frac{\partial \widetilde{u}_i}{\partial x} + \widetilde{v}_i \frac{\partial \widetilde{u}_i}{\partial y} = -\frac{1}{\rho_i}\frac{\partial \widetilde{P}_i}{\partial x} + g\sin\theta + \frac{\mu_i}{\rho_i}\nabla^2 \widetilde{u}_i \tag{7.1}$$

$$\frac{\partial \widetilde{v}_i}{\partial t} + \widetilde{u}_i \frac{\partial \widetilde{v}_i}{\partial x} + \widetilde{v}_i \frac{\partial \widetilde{v}_i}{\partial y} = -\frac{1}{\rho_i}\frac{\partial \widetilde{P}_i}{\partial y} - g\cos\theta + \frac{\mu_i}{\rho_i}\nabla^2 \widetilde{v}_i \tag{7.2}$$

$$\frac{\partial \widetilde{u}_i}{\partial x} + \frac{\partial \widetilde{v}_i}{\partial y} = 0 \tag{7.3}$$

where $i = 1, 2$ denotes two different fluids. $\widetilde{u}, \widetilde{v}$ are the velocities in x and y directions respectively, $\widetilde{P}$ is the pressure and μ_i represents the dynamic viscosity. For the closed tube,

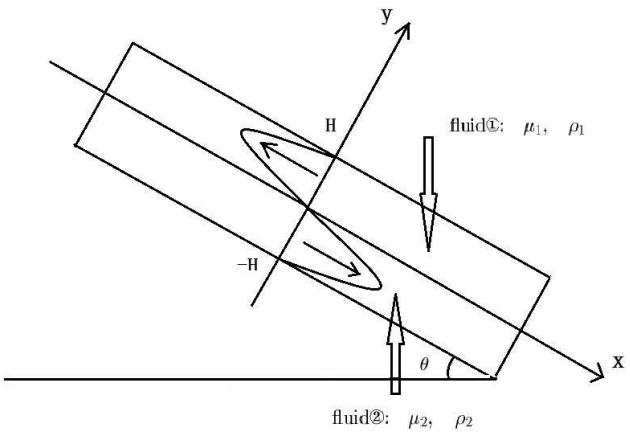

Figure 7.1: Schematic sketch in tilt coordinates of two-layer viscous fluids with parabolic shear flow.

the base shear flow profiles take the form

$$\widetilde{u}_1 = \frac{(1-\gamma)g}{1+m^2+14m}\frac{\rho_2}{\mu_2}\sin\theta\Big[\frac{7+m}{2}y^2 - 4Hy + \frac{1-m}{2}H^2\Big] \tag{7.4}$$

$$\widetilde{u}_2 = \frac{(1-\gamma)g}{1+m^2+14m}\frac{\rho_2}{\mu_2}\sin\theta\Big[-\frac{7m+1}{2}y^2 - 4mHy + \frac{1-m}{2}H^2\Big] \tag{7.5}$$

where $m \triangleq \frac{\mu_1}{\mu_2}$ is the dynamic viscosity ratio, and $\gamma \triangleq \frac{\rho_1}{\rho_2}$ is the density ratio. In the mean time $\widetilde{v}_1 = \widetilde{v}_2 = 0$. Defining $g' \triangleq \frac{\rho_2-\rho_1}{\rho_2}g = (1-\gamma)g$ as the reduced gravity, then we can define the typical velocity scale as

$$U \triangleq \frac{g'}{1+m^2+14m}\frac{\rho_2}{\mu_2}\sin\theta \tag{7.6}$$

Introducing dimensionless variables that are constructed using the velocity scale, U, and the length scale, H, we find that the problem is characterized by the Reynolds number, R_i, the Froude number, F, the surface tension parameter, S. More precisely, rescaling the system by

$$\big(\widetilde{u}_i, \widetilde{v}_i\big) = U\big(u_i', v_i'\big), \quad \big(x, y\big) = H\big(x', y'\big), \quad \widetilde{P}_i = \rho_i U^2 P_i', \quad t = \frac{H}{U}t' \tag{7.7}$$

With a little abuse of notation, we still use (t,x,y) as the time and space coordinates for simplicity, then the governing equations are of the form

$$\frac{\partial u_i'}{\partial t} + u_i'\frac{\partial u_i'}{\partial x} + v_i'\frac{\partial u_i'}{\partial y} = -\frac{\partial P_i'}{\partial x} + \frac{\sin\theta}{F^2} + \frac{1}{R_i}\nabla^2 u_i' \tag{7.8}$$

$$\frac{\partial v_i'}{\partial t} + u_i'\frac{\partial v_i'}{\partial x} + v_i'\frac{\partial v_i'}{\partial y} = -\frac{\partial P_i'}{\partial y} - \frac{\cos\theta}{F^2} + \frac{1}{R_i}\nabla^2 v_i' \tag{7.9}$$

$$\frac{\partial u_i'}{\partial x} + \frac{\partial v_i'}{\partial y} = 0 \tag{7.10}$$

Here $R_i = \frac{\rho_i HU}{\mu_i}$ is Reynolds number, $F = \frac{U}{(gH)^{1/2}}$ is Froude number, and for later use, the dimenionless surface tension is defined as $S = \frac{\sigma}{\rho_2 HU^2}$, where σ is the coefficient of surface tension (assumed constant). Furthermore, we have

$$\frac{R_2}{F^2} = \frac{\rho_2 HU}{\mu_2}\cdot\frac{gH}{U^2} = \frac{1+m^2+14m}{1-\gamma}\frac{1}{\sin\theta} \tag{7.11}$$

$$R_2 S = \frac{\rho_2 HU}{\mu_2}\cdot\frac{\sigma}{\rho_2 HU^2} = \frac{(1+m^2+14m)\sigma}{\rho_2 g' H^2\sin\theta} \tag{7.12}$$

Finally, we can rewrite the base shear flow as

$$U_1 = \frac{\widetilde{u}_1}{U} = \frac{7+m}{2}y^2 - 4y + \frac{1-m}{2} \tag{7.13}$$

$$U_2 = \frac{\widetilde{u}_2}{U} = -\frac{7m+1}{2}y^2 - 4my + \frac{1-m}{2} \tag{7.14}$$

7.2.2 Linearization

Assuming small perturbations from the basic flow in the form,

$$u_i' = U_i(y) + u_i, \quad v_i' = v_i, \quad P_i' = P_i(x,y) + p_i \tag{7.15}$$

neglecting second order terms in the primed quantities, and making use of the fact that U_i and P_i satisfy the basic flow equations, we have, upon substitution of (15) into (8)-(10), the linearized equations governing the disturbance motion,

$$\frac{\partial u_i}{\partial t} + U_i\frac{\partial u_i}{\partial x} + DU_i v_i = -\frac{\partial p_i}{\partial x} + \frac{1}{R_i}\nabla^2 u_i \tag{7.16}$$

$$\frac{\partial v_i}{\partial t} + U_i\frac{\partial v_i}{\partial x} = -\frac{\partial p_i}{\partial y} + \frac{1}{R_i}\nabla^2 v_i \tag{7.17}$$

$$\frac{\partial u_i}{\partial x} + \frac{\partial v_i}{\partial y} = 0 \tag{7.18}$$

where the operator D means the derivative with respect to y. No-slip and no-penetration boundary conditions are posed on the two fixed walls for the perturbation

$$u_1(t,x,1) = Du_1(t,x,1) = u_2(t,x,-1) = Du_2(t,x,-1) = 0 \tag{7.19}$$

Suppose the perturbation of the interface is designated as $y = \eta(t,x)$, then on the interface, the boundary conditions are as follows

- contiunity of velocity: $u_1' = u_2'$, $v_1' = v_2'$
- contiunity of tangential stress: $\mu_1\Big(\frac{\partial v_1'}{\partial x} + \frac{\partial u_1'}{\partial y}\Big) = \mu_2\Big(\frac{\partial v_2'}{\partial x} + \frac{\partial u_2'}{\partial y}\Big)$
- contiunity of normal stress: $\big(-P_2' + \frac{2}{R_2}\frac{\partial v_2'}{\partial y}\big) - \gamma\big(-P_1' + \frac{2}{R_1}\frac{\partial v_1'}{\partial y}\big) - S\frac{\partial^2 \eta}{\partial x^2} = 0$

For two-dimensinal incompressible Navier-Stokes equation, it is convenient to introduce the stream function Ψ_i, such that $u_i = \frac{\partial \Psi_i}{\partial y}$ and $v_i = -\frac{\partial \Psi_i}{\partial x}$. We now assume a sinusoidal disturbance and write

$$\Psi_i = \psi_i(y) e^{ik(x-ct)} + c.c. \tag{7.20}$$

where $c.c.$ denotes complex conjugate. $\psi(y)$ is the complex amplitude, k is the dimensionless real wave number and $c = c_R + ic_I$ is the dimensionless complex wave speed. The real part c_R is the phase velocity of the wave, while kc_I is its growth rate. More precisely, the flow is unstable if $c_I > 0$, stable if $c_I < 0$ and neutrally stable when $c_I = 0$. Substitution of (20) into (16) and (17) yields upon elimination of p_i by taking the curl, the following two Orr-Sommerfeld equations for the two fluids

$$\big(D^2 - k^2\big)^2 \psi_1 = i\frac{k\gamma R_2}{m}\Big[(U_1 - c)(D^2 - k^2) - D^2 U_1\Big]\psi_1 \tag{7.21}$$

for the upper phase $0 < y < 1$, and

$$\big(D^2 - k^2\big)^2 \psi_2 = ikR_2\Big[(U_2 - c)(D^2 - k^2) - D^2 U_2\Big]\psi_2 \tag{7.22}$$

for the lower phase $-1 < y < 0$. The conditions at the interface are the continuity of the velocity components and the balance of the stress components. Formally speaking, these conditions must be evaluated at $y = \eta(x,t)$, the location of the interface in the disturbed situation, and not at the originally interface y = 0. This modification is taken into account by means of a Taylor expansion in η around y = 0. The interface conditions then read $\eta = \frac{\psi_1(0)}{c - U_1(0)} e^{ik(x-ct)}$. Finally we can rewrite the boundary conditions in terms of ψ_i, k, c and R_i correcting to the leading order in η, and the details of the derivation are presented in appendix B.

at $y = 1$: $\psi_1 = D\psi_1 = 0$

at $y = -1$: $\psi_2 = D\psi_2 = 0$

at the interface $y = 0$:

- $\psi_1 = \psi_2$
- $\big(D\psi_1 - D\psi_2\big) + \big(DU_1 - DU_2\big)\frac{\psi_1}{c - U_1} = 0$
- $\big(D^2 + k^2\big)\big(m\psi_1 - \psi_2\big) + \big(mD^2 U_1 - D^2 U_2\big)\frac{\psi_1}{c - U_1} = 0$
- $m\big(D^3 - 3k^2 D\big)\psi_1 - \big(D^3 - 3k^2 D\big)\psi_2 + ik\gamma R_2\big[(c - U_1)D + DU_1\big]\psi_1 - ikR_2\big[(c - U_2)D + DU_2\big]\psi_2 + ikR_2\Big[(1 - \gamma)\frac{\cos\theta}{F^2} + k^2 S\Big]\frac{\psi_1}{c - U_1} = 0$

7.3 Linear stability analysis

Systems (21) and (22) with corresponding boundary conditions have an infinite number of eigenvalues and associated eigenfunctions. Since the real part of the temporal growth rate in (20) is e^{-ikc}; $c = c_R + ic_I$; the eigenvalue which has largest imaginary part is most dangerous in a linear instability analysis. In order to determine the complex eigenvalue c, the eigenfunctions ψ_i are approximated by the Galerkin truncation of the Chebyshev polynomial of first kind. Then the eigenvalue problem is discretized and formed a generalized matrix eigenvalue problem (see details in Appendix C)

$$\mathbf{A}\vec{x} = c\mathbf{B}\vec{x} \tag{7.23}$$

where $\vec{x} = (\psi_1, \psi_2)^\top$. The matrices $\mathbf{A}$ and $\mathbf{B}$ are singular because some of the boundary and interface conditions do not contain the eigenvalue c. This singularity is handled by deflating the infinite eigenvalues using the standard QZ-algorithm. Grid convergence has been checked by varying number of collocation points, and in most calculations 100 collocation points are used. Furthermore, the implemented algorithm has been validated by against the tow-layer plane Poiseuille flow problem in [6] which is also presented in Appendix C. Excellent agreement was found in all cases. The linear stability study will be discussed in the following parts of the section. For simplicity, we assume that two fluid have the same dynamic viscosity from now on.

7.3.1 Stokes flow

For an extreme example, it is interesting to study the inertialess stability and let the Reynolds number be zero. Thus in the absence of the surface tension the linear equations, i.e., the Orr-Sommerfeld equations can be reduced to

$$\begin{cases} \left(D^2 - k^2\right)^2 \psi_1 = 0, & 0 < y < 1 \\ \left(D^2 - k^2\right)^2 \psi_2 = 0, & -1 < y < 0 \\ \psi_1(1) = D\psi_1(1) = 0, & \text{at } y = 1 \\ \psi_2(-1) = D\psi_2(-1) = 0, & \text{at } y = -1 \\ \psi_1 = \psi_2, \quad D\psi_1 = D\psi_2, & \text{at } y = 0 \\ \left(D^2\psi_1 - D^2\psi_2\right)c + 16\psi_1 = 0, & \text{at } y = 0 \\ \left(D^3\psi_1 - D^3\psi_2\right)c + 16ik\cot\theta\psi_1 = 0, & \text{at } y = 0 \end{cases} \tag{7.24}$$

It is easy to find the general solution for Stokes flow

$$\psi_1 = a_1 e^{ky} + b_1 e^{-ky} + c_1 y e^{ky} + d_1 y e^{-ky} \tag{7.25}$$

$$\psi_2 = a_2 e^{ky} + b_2 e^{-ky} + c_2 y e^{ky} + d_2 y e^{-ky} \tag{7.26}$$

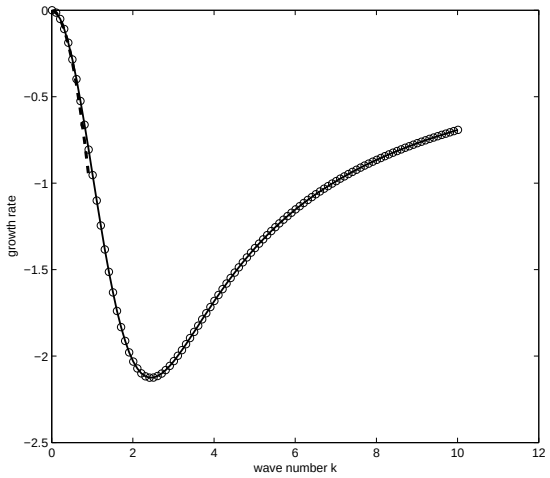

Figure 7.2: Growth rate versus wave number for Stokes wave at $\theta = \frac{\pi}{3}$. Solid line is the theoretical prediction, the circle ones are numerical results, and the dash line is the asymptotic expansion when wave number k is fairly small.

From the boundary conditions, we once more obtain a secular equation by setting the determinant of the coefficients of a_i, b_i, c_i and d_i to zero:

$$\begin{vmatrix} e^k & e^{-k} & e^k & e^{-k} & 0 & 0 & 0 & 0 \\ ke^k & -ke^{-k} & (1+k)e^k & (1-k)e^{-k} & 0 & 0 & 0 & 0 \\ 0 & 0 & 0 & 0 & e^{-k} & e^k & -e^{-k} & -e^k \\ 0 & 0 & 0 & 0 & ke^{-k} & -ke^k & (1-k)e^{-k} & (1+k)e^k \\ 1 & 1 & 0 & 0 & -1 & -1 & 0 & 0 \\ k & -k & 1 & 1 & -k & k & -1 & -1 \\ k^2c+16 & k^2c+16 & 2kc & -2kc & -k^2c & -k^2c & -2kc & 2kc \\ k^3c+iNk & -k^3c+iNk & 3k^2c & 3k^2c & -k^3c & k^3c & -3k^2c & -3k^2c \end{vmatrix} = 0$$

where we define $N \triangleq 16\cot\theta$. Direct computation yields the determinant

$$c = iN\frac{4k^2\sinh(2k) + 4k\cosh(2k) + 2\sinh(2k) - \sinh(4k) - 4k - 8k^3}{4k^2\cosh(4k) - 4k^2 - 32k^4} \tag{7.27}$$

Numerical computation shows that the above expression can not be positive for all wave number k, which implies Stokes flow is always stable for any tilt angle $< \frac{\pi}{2}$. Typical relationship between the wave number k and the growth rate is plotted when the tilt angle is $\frac{\pi}{3}$, together with numerical results using the Chebyshev-tau method and the asymptotic expansion as k is small in Fig.2.

7.3.2 General case

In this part, we consider the effects of density ratio, tilt angle, Reynolds number and surface tension on the linear stability problem for the general Orr-Sommerfeld equation. Fig.3 shows a typical profile of the unstable eigenmode and its velocity field.

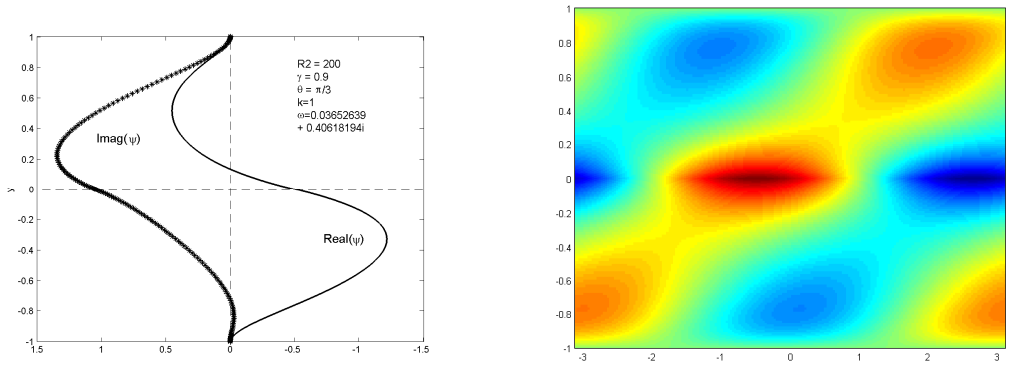

Figure 7.3: Typical steam function of the unstable eigenvalue and its velocity vector field. On the right hand side, the red color means the right direction vector, while the blue color represents the left direction vector.

In Fig.4, the effect density ratio, surface tension, Reynolds number and tilt angle are plotted respectively. The upper left picture shows that the density ratio has little effect on the stability property. We check the density ratio from 0.5 to 0.9, the basic behavior of the growth rate curve does not change much. The upper right picture shows that the surface tension would stabilize the system a little bit but not very significant especially when the wave number k is very small, that is because for long wave approximation, the surface tension is of order k^4 in the Fourier space (See more details in the next section). In the lower-half part of Fig.4, two plots show the Reynolds number and the tilt angle are two main factors in stability analysis. Both of them have destabilizing effect. It is worth mentioning that Reynolds number is not a good parameter in the lab, since

$$R_2 = \frac{\rho_2 HU}{\mu_2} = \frac{\rho_2^2 H g'}{\mu_2^2(1+m^2+14m)} \sin\theta \tag{7.28}$$

It is obvious that $R_2/\sin\theta$ is an appropriate parameter for studying the effect of tilt angle. In the lower right of Fig.4, we fix $R_2/\sin\theta = 10$ instead of fixing the Reynolds number.

Fig.5 plots the relationship between the tilt angle θ and $R_2/\sin\theta$, the parameter used to replace the Reynolds number, for generating the instability. It shows that when $R_2/\sin\theta$ is rather small or big, the curve is quite smooth, but in between the points are a little bit messy due to the modes crossings.

7.4 Weakly nonlinear model for long wave perturbation

In this section, we use multi-scale method to establish a weakly nonlinear model for the interface evolution in long wave perturbation setting. The ansatz for slow-varying small amplitude perturbation is

$$\eta = \epsilon A(X,T) \tag{7.29}$$
$$\Psi_1 = \epsilon\Psi_{10}(X,Y,T) + \epsilon^2\Psi_{11}(X,Y,T) + O(\epsilon^3) \tag{7.30}$$
$$\Psi_2 = \epsilon\Psi_{20}(X,Y,T) + \epsilon^2\Psi_{21}(X,Y,T) + O(\epsilon^3) \tag{7.31}$$

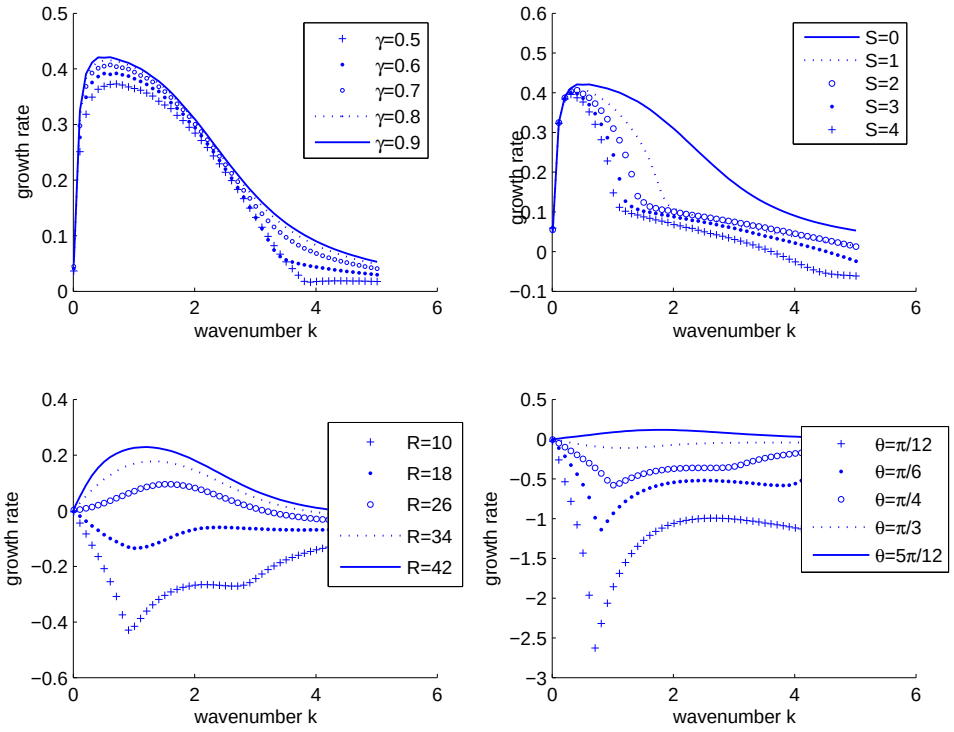

Figure 7.4: Growth rate versus wave number k. Upper left: $R_2 = 200, S = 0, \theta = \pi/3$; Upper right: $R_2 = 200, \gamma = 0.9, \theta = \pi/3$; Lower left: $\gamma = 0.9, \theta = \pi/3, S = 0$; Lower right: $R_2/\sin\theta = 10, \gamma = 0.9, S = 0$.

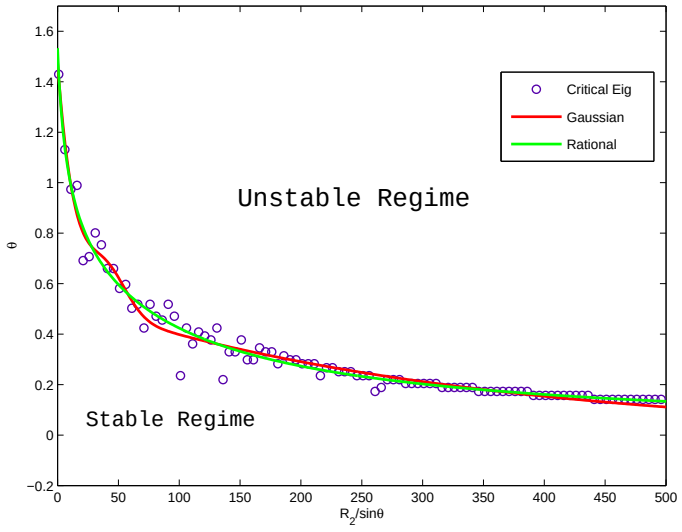

Figure 7.5: Curve for separating stable region and unstable region. The circle ones are the numerical results of Orr-Sommerfeld systems, two solid lines are the fitting curves using different functions: rational function (green) and gaussian function (red).

with $X = \epsilon x$, $Y = \epsilon y$ and $T = \epsilon^2 t$ where ϵ is a small parameter. Due to the expression of η, it is convenient to rewrite Ψ_{10} and Ψ_{20} as

$$\Psi_{10}(X, Y, T) = A(X, T)\phi_0(Y)$$
$$\Psi_{20}(X, Y, T) = A(X, T)\chi_0(Y)$$

Substitution of the above expressions into perturbed full Navier-Stokes equations and corresponding boundary conditions, taking $m = 1$ and collecting terms of first order of ϵ, yield

$$\begin{cases} D^4\phi_0 = D^4\chi_0 = 0, & \text{governing equations} \\ \phi_0(1) = D\phi_0(1) = 0, & \text{no-slip conditions at } y = 1 \\ \chi_0(-1) = D\chi_0(-1) = 0, & \text{no-slip conditions at } y = -1 \\ \phi_0 = \chi_0, \quad D\phi_0 = D\chi_0, & \text{at the interface } y = 0 \\ D^2\phi_0 - D^2\chi_0 + 16 = 0, & \text{tangential stress at } y = 0 \\ D^3\phi_0 = D^3\chi_0, & \text{normal stress at } y = 0 \end{cases} \tag{7.32}$$

After direct calculations, the solutions of this ODE system are

$$\begin{cases} \phi_0 = 2y^3 - 4y^2 + 2y \\ \chi_0 = 2y^3 + 4y^2 + 2y \end{cases} \tag{7.33}$$

Then we turn to the second order of the expansion. The second order approximation is obtained by collecting terms of order ϵ^2, which yields the following inhomogeneous ordinary differential system

$$\begin{cases} D^4\Psi_{11} = R_1 A_X(U_1 D^2 - D^2 U_1)\phi_0, & \text{governing equations} \\ D^4\Psi_{21} = R_2 A_X(U_2 D^2 - D^2 U_2)\chi_0, & \text{governing equations} \\ \Psi_{11}(1) = D\Psi_{11}(1) = 0, & \text{no-slip conditions at } y = 1 \\ \Psi_{21}(-1) = D\Psi_{21}(-1) = 0, & \text{no-slip conditions at } y = -1 \\ \Psi_{11} = \Psi_{21}, & \text{at the interface } y = 0 \\ D\Psi_{11} - D\Psi_{21} = 8A^2, & \text{at the interface } y = 0 \\ D^2\Psi_{11} = D^2\Psi_{21}, & \text{tangential stress at } y = 0 \\ D^3\Psi_{11} - D^3\Psi_{21} + (16A_X \cot\theta - S\epsilon^2 A_{XXX}) = 0, & \text{normal stress at } y = 0 \end{cases} \tag{7.34}$$

Here the surface tension is supposed to be very large between oil and water interface, i.e., $S = O(1/\epsilon^2)$. Observing the governing equations and boundary conditions carefully, we can assume that

$$\Psi_{11} = m_1(Y)A_X + m_2(Y)A^2 + m_3(Y)A_{XXX} \tag{7.35}$$
$$\Psi_{21} = n_1(Y)A_X + n_2(Y)A^2 + n_3(Y)A_{XXX} \tag{7.36}$$

After a tedious computation, we substitute the solution of (34) into the kinematic boundary condition and collect the $O(\epsilon^3)$ terms, then obtain

$$A_T + a_1 A A_X + a_2 A_{XX} + a_3 A_{XXXX} = 0 \tag{7.37}$$

with

$$\begin{aligned} a_1 &= \big(2D^2U_1 + 2D\phi_0 + 2m_2\big)(0) = 8 \\ a_2 &= m_1(0) = \frac{1}{70}(R_1 + R_2) - \frac{2}{3}\cot\theta \\ a_3 &= m_3(0) = \frac{S\epsilon^2}{24} \end{aligned}$$

This is a typical Kuramoto-Sivashinsky equation when a_2 is big than 0, and its steady solution, properties and globally well-posedness have been studied. When $a_2 < 0$, it becomes diffusion equation which is globally well-posed. If neglecting the nonlinear term, using standard Fourier analysis, the dispersion relation reads

$$c = i\big(a_2 k - a_3 k^3\big) \tag{7.38}$$

substitution of the dispersion relation into the Fourier mode $e^{ik(X-cT)}$, one obtains the growth rate equals $e^{(a_2k^2 - a_3k^4)T}$. It shows that the surface tension has stabilizing effect on the system. If neglecting the surface tension term, the sign of a_2 determines the stability property of the system, which gives a sufficient condition between Reynolds number and tilt angle for generating the instability:

$$\cot\theta < \frac{3}{140}\big(R_1 + R_2\big) \tag{7.39}$$

7.5 Conclusion

By the end of the project, I hoped to have an answer, either analytic or numerical, for the stability of the two-layer viscous fluid in an inclined closed tube subject to small perturbations and find the effects of surface tension, tilt angle, Reynolds number, density ratio and wave number in triggering the instability. For the linear stability analysis, Chebyshev-tau method is applied to two-layer Orr-Sommerfeld equations. Tilt angle and Reynolds number both have the effect to destabilize the system, while the surface tension stabilize it. Stokes flow is studied as an extreme example showing that it is stable for any tilt angle. Except this, for any Reynolds number, one can find a tilt angle to generate the instability. Furthermore, a weakly nonlinear model equation for long wave perturbation is derived and found to be Kuramoto-Sivashinsky type. If neglecting the surface tension effects, it offers a sufficient condition on Reynolds number and the tilt angle for generating linear instability, which totally depends on the coefficient of A_{XX} term.

7.6 Acknowledgements

I would like to take the opportunity to thank staff in 2011 GFD summer school, especially the two main lecturers Fabian and Rich and the organizers Norman, Phil and Janet. Also, I'd like to thank Jack, Olivier, Fabian, Leslie, Joe and Phil for their guidance and advice throughout the summer. I would like to thank George for his coaching and enthusiasm through the summer's softball practices and games. Last but not least, I'd like to thank all the fellows for the late nights in Walsh Cottage, fantastic dinners, trips to the beach, and more.

7.7 Appendix A. derivation of base shear flow

In this section the basic unperturbed flow pattern is obtained. The unperturbed flow is parallel to the x-axis and the velocity is a function of y only. Both of the fluids have the same depth H. The Navier-Stokes equations that govern the basic flow are

$$-\frac{1}{\rho_i}\frac{\partial \widetilde{P}_i}{\partial x} + g\sin\theta + \frac{\mu_i}{\rho_i}\frac{\partial^2 \widetilde{u}_i}{\partial y^2} = 0 \tag{7.40}$$

$$-\frac{1}{\rho_i}\frac{\partial \widetilde{P}_i}{\partial y} - g\cos\theta = 0 \tag{7.41}$$

From equation (41), one obtains $\widetilde{P}_i = -\rho_i g\cos\theta y + \big(\text{function of x}\big)$. Since $\frac{\partial^2 \widetilde{u}_i}{\partial y^2}$ is a function of y only, from (40) it is clear that $\frac{\partial \widetilde{P}_1}{\partial x}$ and $\frac{\partial \widetilde{P}_2}{\partial x}$ are both constants. Then the solutions for $\widetilde{u}_i$ take the form

$$\widetilde{u}_1 = (-\frac{\rho_1 g}{\mu_1}\sin\theta + c_1)\frac{y^2}{2} + a_1 y + b_1 \tag{7.42}$$

$$\widetilde{u}_2 = (-\frac{\rho_2 g}{\mu_2}\sin\theta + c_2)\frac{y^2}{2} + a_2 y + b_2 \tag{7.43}$$

where a_i, b_i and c_i are all constants need to be determined by the boundary conditions. Using the boundary conditions at the interface $y = 0$: $\widetilde{u}_1 = \widetilde{u}_2$, $\mu_1\frac{\partial \widetilde{u}_1}{\partial y} = \mu_2\frac{\partial \widetilde{u}_2}{\partial y}$ and $\widetilde{P}_1 = \widetilde{P}_2$, one obtains $a_2 = ma_1$, $b_1 = b_2$ and $c_2 = mc_1$ respectively, where $m = \frac{\mu_1}{\mu_2}$ is the dynamic viscosity ratio. For simplicity, let's denote $c_1 \triangleq c$, $a_1 \triangleq a$ and $b_1 \triangleq b$. On the other hand, because the tube is closed, then there is no flux across any place $x = constant$, which implies

$$\begin{aligned} &\int_{-H}^{0} \widetilde{u}_2 dy + \int_{0}^{H} \widetilde{u}_1 dy = 0 \\ \Longrightarrow\quad & b = \frac{H^2}{12}\Big[\Big(\frac{\gamma}{m}+1\Big)\frac{\rho_2}{\mu_2}g\sin\theta - (1+m)c\Big] - \frac{H}{4}\big(1-m\big)a \end{aligned} \tag{7.44}$$

Finally, applying the no-slip boundary conditions at the fixed walls, one obtains

$$\Big(-\frac{\gamma\rho_2 g\sin\theta}{m\mu_2} + c\Big)\frac{H^2}{2} + aH + \frac{H^2}{12}\Big[\Big(\frac{\gamma}{m}+1\Big)\frac{\rho_2 g\sin\theta}{\mu_2} - (1+m)c\Big] - \frac{H}{4}\big(1-m\big)a = 0$$

$$\Big(-\frac{\rho_2 g\sin\theta}{\mu_2} + mc\Big)\frac{H^2}{2} - amH + \frac{H^2}{12}\Big[\Big(\frac{\gamma}{m}+1\Big)\frac{\rho_2 g\sin\theta}{\mu_2} - (1+m)c\Big] - \frac{H}{4}\big(1-m\big)a = 0$$

Therefore, we solve the linear system for a and c

$$a = \frac{4(\gamma-1)}{1+m^2+14m}\frac{\rho_2}{\mu_2}gH\sin\theta \tag{7.45}$$

$$b = \frac{(1-m)(1-\gamma)}{1+m^2+14m}\frac{\rho_2}{\mu_2}\frac{gH^2\sin\theta}{2} \tag{7.46}$$

$$c = \frac{7m+\gamma+m^2+7m\gamma}{m(1+m^2+14m)}\frac{\rho_2}{\mu_2}g\sin\theta \tag{7.47}$$

Finally, we get the base shear flow

$$\widetilde{u}_1 = \frac{(1-\gamma)g}{1+m^2+14m}\frac{\rho_2}{\mu_2}\sin\theta\Big[\frac{7+m}{2}y^2 - 4Hy + \frac{1-m}{2}H^2\Big] \tag{7.48}$$

$$\widetilde{u}_2 = \frac{(1-\gamma)g}{1+m^2+14m}\frac{\rho_2}{\mu_2}\sin\theta\Big[-\frac{7m+1}{2}y^2 - 4mHy + \frac{1-m}{2}H^2\Big] \tag{7.49}$$

7.8 Appendix B. boundary conditions on the interface

In this part, we give the details of the derivation of the stress continuity on the interface in terms of the stream functions. First of all, we know

$$u_i = \frac{\partial \Psi_i}{\partial y} = D\psi_i e^{ik(x-ct)} \tag{7.50}$$

$$v_i = -\frac{\partial \Psi_i}{\partial x} = -ik\psi_i e^{ik(x-ct)} \tag{7.51}$$

Furthermore, we assume the interface is designated as $\eta(x,t) = \hat{\eta}e^{ik(x-ct)}$. Following the notation in section 2.1, the kinematic boundary condition $\eta_t = v_1' - \eta_x u_1'$ can be linearized as $\eta_t = v_1 - \eta_x U_1$, then one obtains

$$-ikc\hat{\eta} = -ik\psi_1 - ik\hat{\eta}U_1 \Longrightarrow \hat{\eta} = \frac{\psi_1(0)}{c - U_1(0)} \tag{7.52}$$

For the continuity of velocity at the interface, $v_1' = v_2'$ is trivial, while $u_1' = u_2'$ results in

$$\begin{aligned} & U_1 + \eta DU_1 + u_1 + \cdots = U_2 + \eta DU_2 + u_2 + \cdots \\ \Longrightarrow \quad & \big(D\psi_1 - D\psi_2\big) + \big(DU_1 - DU_2\big)\frac{\psi_1(0)}{c - U_1(0)} = 0 \end{aligned} \tag{7.53}$$

Then for the tangential stress, taking expansion about $y = 0$, one obtains

$$\begin{aligned} & m\Big(\frac{\partial v_1'}{\partial x} + \frac{\partial u_1'}{\partial y}\Big) = \frac{\partial v_2'}{\partial x} + \frac{\partial u_2'}{\partial y} \\ \Longrightarrow \quad & m\Big[\frac{\partial v_1}{\partial x} + \frac{\partial(u_1 + U_1 + DU_1\eta + \cdots)}{\partial y}\Big] = \frac{\partial v_2}{\partial x} + \frac{\partial(u_2 + U_2 + DU_2\eta + \cdots)}{\partial y} \\ \Longrightarrow \quad & \big(D^2 + k^2\big)\big(m\psi_1 - \psi_2\big) + \big(mD^2U_1 - D^2U_2\big)\hat{\eta} = 0 \\ \Longrightarrow \quad & \big(D^2 + k^2\big)\big(m\psi_1 - \psi_2\big) + \big(mD^2U_1 - D^2U_2\big)\frac{\psi_1(0)}{\omega - U_1(0)} = 0 \end{aligned} \tag{7.54}$$

For later use, we point out the following formula $\hat{\eta} = \frac{\psi_1(0)}{c-U_1(0)} = -\frac{(D^2+k^2)(m\psi_1-\psi_2)}{mD^2U_1 - D^2U_2}$. In order to obtain the normal stress formula, we need the expression of the presure. Assuming $p_i = \hat{p}_i e^{ik(x-ct)}$, using equation (8), we can get

$$\hat{p}_i = \frac{1}{ikR_i}\big(D^3\psi_i - k^2 D\psi_i\big) + cD\psi_i + DU_i\psi_i - U_i D\psi_i \tag{7.55}$$

Now we can rewrite the normal stress boundary condition in a suitable form,

$$
\begin{aligned}
&\big(-P_2' + \frac{2}{R_2}\frac{\partial v_2'}{\partial y}\big) - \gamma\big(-P_1' + \frac{2}{R_1}\frac{\partial v_1'}{\partial y}\big) - S\frac{\partial^2\eta}{\partial x^2} = 0 \\
\Longrightarrow\quad &\big(-p_2 - DP_2'\eta + \frac{2}{R_2}\frac{\partial v_2}{\partial y} - \cdots\big) - \gamma\big(-p_1 - DP_1'\eta + \frac{2}{R_1}\frac{\partial v_1}{\partial y} - \cdots\big) - S\frac{\partial^2\eta}{\partial x^2} = 0 \\
\Longrightarrow\quad &\big(\gamma\hat{p}_1 - \hat{p}_2\big) + \frac{2ik}{R_2}\big(mD\psi_1 - D\psi_2\big) + \Big[(1-\gamma)\frac{\cos\theta}{F^2} + k^2S\Big]\hat{\eta} = 0 \\
\Longrightarrow\quad &m\big(D^3 - 3k^2D\big)\psi_1 - \big(D^3 - 3k^2D\big)\psi_2 + ik\gamma R_2\big[(c-U_1)D + DU_1\big]\psi_1 \\
&-ikR_2\big[(c-U_2)D + DU_2\big]\psi_2 + ikR_2\Big[(1-\gamma)\frac{\cos\theta}{F^2} + k^2S\Big]\frac{\psi_1}{c-U_1} = 0
\end{aligned}
\tag{7.56}
$$

For numerical purpose, we need rewrite the normal stress in the following way

$$
\begin{aligned}
&m\big(D^3 - 3k^2D\big)\psi_1 - \big(D^3 - 3k^2D\big)\psi_2 + ik\gamma R_2\big[(c-U_1)D + DU_1\big]\psi_1 - ikR_2\big[(c \\
&-U_2)D + DU_2\big]\psi_2 - ikR_2\Big[(1-\gamma)\frac{\cos\theta}{F^2} + k^2S\Big]\frac{(D^2+k^2)(m\psi_1 - \psi_2)}{mD^2U_1 - D^2U_2} = 0
\end{aligned}
\tag{7.57}
$$

7.9 Appendix C. numerical method

Step 1. Coordinate transformation

Chebyshev polynomials are orthogonal on the interval $[-1, 1]$. In order to use the Chebyshev-tau QZ-algorithm to solve the generalized eigenvalue problem, we need transform the Orr-Sommerfeld equations on either of the intervals $[-1, 0]$ and $[0, 1]$ to the interval $[-1, 1]$ by a change of the independent variable y. This is easily achieved by means of the linear transformations

$$
\begin{cases}
z = 2y - 1 & 0 \leqslant y \leqslant 1 \\
z = -2y - 1 & -1 \leqslant y \leqslant 0
\end{cases}
\tag{7.58}
$$

It is noted that $z = -1$ becomes the interface in both cases. Then the Orr-Sommerfeld equations in new coordinates become

$$
\Big(4D^2 - k^2\Big)^2\psi_i - ikR_i\Big[U_i\big(4D^2 - k^2\big) - U_i''\Big]\psi_i = \Big[-ikR_i\big(4D^2 - k^2\big)\psi_i\Big]c \tag{7.59}
$$

Here D presents the derivative with respect to the new variable z and $'$ means the derivative w.r.t the old variable y. Furthermore, the rigid wall boundary condition in the new coordinates become

$$
\psi_1(1) = D\psi_1(1) = \psi_2(1) = D\psi_2(1) = 0 \tag{7.60}
$$

The interface boundary conditions are, on $z=-1$

$$\psi_1-\psi_2=0 \tag{7.61}$$

$$\big(2U_1D-U_1'+U_2'\big)\psi_1+2U_1D\psi_2=\big(2D\psi_1+2D\psi_2\big)c \tag{7.62}$$

$$\big(4mD^2+mk^2-mU_1''+U_2''\big)\psi_1-\big(4D^2+k^2\big)\psi_2=\big(4D^2+k^2\big)\big(m\psi_1-\psi_2\big)c \tag{7.63}$$

$$\begin{aligned}&m\big(8D^3-6k^2D\big)\psi_1+\big(8D^3-6k^2D\big)\psi_2+i\Big[k\gamma R_2\big(U_1'-2U_1D\big)\psi_1\\&-kR_2\big(2U_2D+U_2'\big)\psi_2-k\Big(\cot\theta+\frac{k^2T}{\sin\theta}\Big)\big(4D^2+k^2\big)\big(m\psi_1-\psi_2\big)\Big]\\&=-i\Big(2k\gamma R_2D\psi_1+2kR_2D\psi_2\Big)c\end{aligned} \tag{7.64}$$

where $T\triangleq\frac{\sigma}{\rho_2g'H^2}$ is a new parameter.

Step 2. Galerkin truncation and point collocation

Approximating the eigenfunction ψ_1 and ψ_2 by the truncated Chebyshev expansions

$$\psi_1(z)=\sum_{n=0}^{N}a_nT_n(z),\qquad \psi_2=\sum_{n=0}^{N}b_nT_n(z) \tag{7.65}$$

where $T_n(z)$ is the nth order first-kind Chebyshev polynomial. The high order derivatives of the eigenfunction can be found by differentiating the Chebyshev polynomial. Our goal is to determine the coefficients a_n, b_n and the eigenvalue ω. For this purpose, we need $2(N+1)$ conditions. We collocate the Galerkin truncation at the extrema of the Chebyshev polynomial

$$z=\cos\Big(\frac{j\pi}{M}\Big),\qquad j=1\cdots M-1 \tag{7.66}$$

We pick $M=N-2$, thus if we evluate the Orr-Sommerfeld equation at these extrema points, we obtain $2N-6$ linear algbraic equations. The other eight conditions come from the corresponding boundary conditions mentioned in step 1. Therefore we complete our system.

Step 3. Generalized eigenvalue problem

We denote

$$A_R\triangleq\begin{pmatrix}16D^4-8k^2D^2+k^4 & 0\\ BC1\sim4 & BC1\sim4\\ 0 & 16D^4-8k^2D^2+k^4\\ BC5\sim8 & BC5\sim8\end{pmatrix} \tag{7.67}$$

$$A_I\triangleq\begin{pmatrix}-kR_1\big[U_1(4D^2-k^2)-U_1''\big] & 0\\ BC1\sim4 & BC1\sim4\\ 0 & -kR_2\big[U_2(4D^2-k^2)-U_2''\big]\\ BC5\sim8 & BC5\sim8\end{pmatrix} \tag{7.68}$$

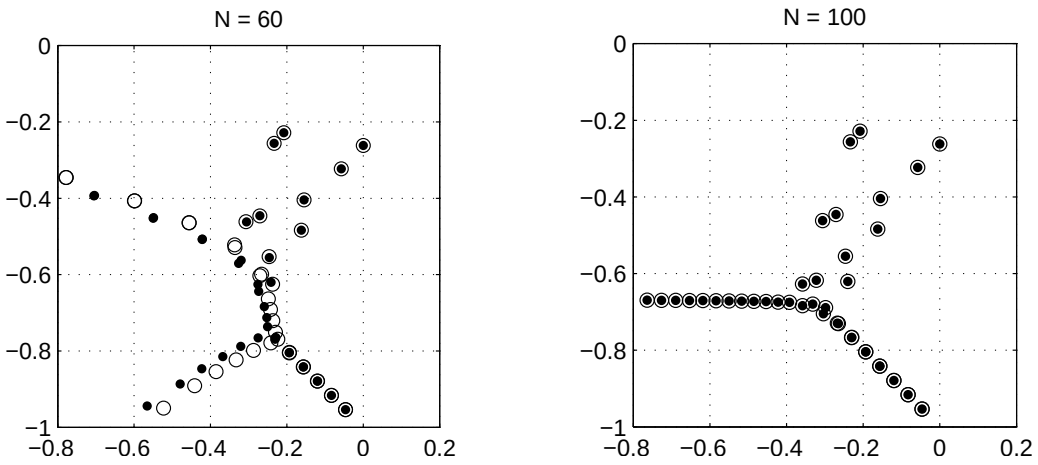

Figure 7.6: Eigenvalues for plane Poiseuille at Raynolds number 5772. The dots are for the general Chebyshev method and the empty circles are for Chebyshev-tau method. Left picture uses 60 collocation points and the right one uses 100 points

$$B_R \triangleq \begin{pmatrix} 0 & 0 \\ BC1 \sim 4 & BC1 \sim 4 \\ 0 & 0 \\ BC5 \sim 8 & BC5 \sim 8 \end{pmatrix} \tag{7.69}$$

and

$$B_R \triangleq \begin{pmatrix} -kR_1(4D^2 - k^2) & 0 \\ BC1 \sim 4 & BC1 \sim 4 \\ 0 & -kR_2(4D^2 - k^2) \\ BC5 \sim 8 & BC5 \sim 8 \end{pmatrix} \tag{7.70}$$

where $BC1 \sim 4$ represents the boundary conditions (60), while $BC5 \sim 8$ the boundary conditions (61)-(64). We therefore can write the system of equations as a generalized eigenvalue problem

$$\Big[A_R + iA_I\Big]\mathbf{x} = c\Big[B_R + iB_I\Big]\mathbf{x} \tag{7.71}$$

where $\mathbf{x} = (a_0, \cdots, a_N, b_0, \cdots, b_N)^\top$. Using QZ-algorithm in MATLAB, it is easy to obtain the eigenvalues and corresponding eigenvectors.

Step 4. Validation

Two examples are presented here for the purpose of validation. The first example is the one-layer plane Poiseuille flow at Reynolds number 5772. The resulting eigenvalues using general Chebyshev method presented in Page 150 of [17] and Chebyshev-tau method are both plotted in Fig.6. It is clear that when collocation points are increased to 100 points, the results for two methods coincide with each other perfectly. For our linear problem in the paper, we use 100 points for all numerical experiments. Another numerical experiment

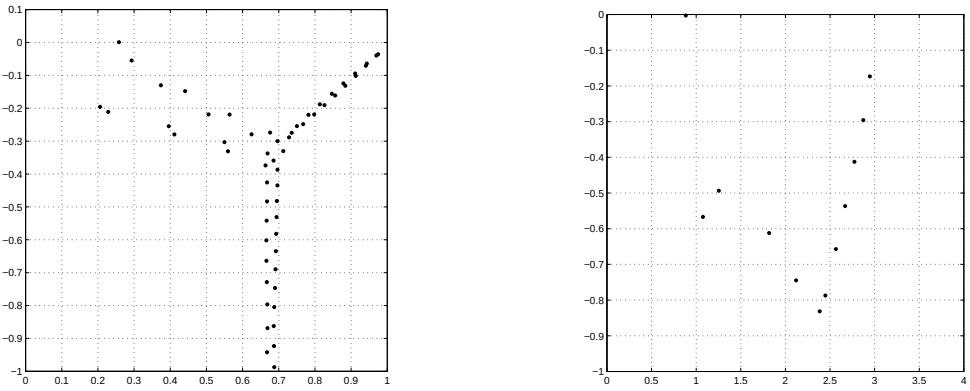

Figure 7.7: Eigenvalues for two-layer plane Poiseuille flow. Left: $Re = 10^4$, $a = 1$, $m = 2$, $n = 1.2$, $u_n = 0$. Right: $Re = 25$, $a = 1$, $m = 2$, $n = 10$, $u_n = 3$

is carried out for the two-layer Poiseuille flow and compared with the results in [6]. In Fig.7 the plots are the eigenvalues for different height ratios and Reynolds numbers. The results agree with the Pic.7 and Pic.9 of paper [6] very well. And numbers in the following table show the comparison of the leading eigenmodes between the left hand-side of Fig.7 and Pic.7 in [6].

Model type	Our codes	Dongarra's results
interface	0.00172758052977	0.00179188368
shear	0.00087962166886	0.0008778915187

Bibliography

[1] A.P. Bassom, M.G. Blyth, D.T. Papageorgiou, Nonlinear development of two-layer Couette-Poiseuille flow in the presence of surfactant, Phys. Fluids, 22(10), 2010.

[2] P.A.M. Boomkamp, B.J. Boersma, R.H.M. Miesen, G.V. Beijnon, A chebyshev collocation method for solving two-phase flow stability problems, J. Comp. Phys., 132, 191-200, 1997.

[3] A. Bague, D. Fuster, S. Popinet, R. Scardovelli, S. Zaleski, Instability growth rate of two-phase mixing layer from a linear eigenvalue problem and an initial-value problem, Phys. Fluids, 22(1), 2010.

[4] C. Cenedese, J.A. Whitehead, T.A. Ascarelli, M. Ohiwa, A dense current flowing down a sloping bottom in a rotating fluid, J. Phys. Oceanogr., 34, 188-203, 2002.

[5] A. Defina, S. Lanzoni, F.M. Susin, Stability of a stratified viscous shear flow in a title tube, Phys. Fluids, 11(2), 1998.

[6] J.J. Dongarra, B. Straughan, D.W. Walker, Chebyshev tau-QZ algorithm methods for calculating spectra of hydrodynamic stability problems, J. Appl. Nume. Math., 22(4), 1996.

[7] H. Fouli, D.Z. Zhu, Interfacial waves in two-layer exchange flows downslope of a bottom sill, J. Fluid Mech., 680, 194-224, 2011.

[8] A.P. Hooper, W.G.C. Boyd, shear-flow instability at the interface between two viscous fluids, J. Fluid Mech., 128, 507-528, 1983.

[9] A.P. Hooper, R. Grimshaw, Nonlinear instability at the interface between two viscous fluids, Phys. Fluids, 28(1), 1985.

[10] T.W. Kao, Stability of two-layer viscous stratified flow down an inclined plane, Phys. Fluids, 8(5), 1965.

[11] H. Kim, J.C. Padrino, D.D. Joseph, Viscous effects on Kelvin-Helmholtz instability in a channel, J. Fluid Mech., 680, 398-416, 2011.

[12] S. Mählmann, D.T. Papageorgiou, Interfacial instability in electrified plane Couette flow, J. Fluid Mech., 666, 155-188, 2011.

[13] O. Marchal, J.A. Whitehead, Penetration of a salinity front into the ocean interior: laboratory experiments and a simple theory, to appear in J. Phys. Oceanogr., 2011.

[14] D.I. Meiron, G.R. Baker, S.A. Orszaga, Analytic structure of vortex sheet dynamics. Part 1. Kelvin-Helmholtz instability, J. Fluid Mech., 114, 283-298, 1982.

[15] M.E. Negretti, S.A. Socolofsky, G.H. Jirka, Linear stability analysis of inclined two-layer stratified flows, Phys. Fluids, 20(9), 2008.

[16] C. Pozrikidis, Instability of two-layer creeping flow in a channel with parallel-sided walls, J. Fluid Mech., 351, 139-165, 1997.

[17] Lloyd N. Trefethen, Spectral Methods in MATLAB, SIAM, Philadelphia, 2000.

[18] S.A. Thorpe, A method of producing a shear flow in a stratified fluid, J. Fluid Mech., 32(4), 693-704, 1968.

[19] S.A. Thorpe, Experiments on the instability of stratified shear flows: miscrible fluids, J. Fluid Mech., 46(2), 299-319, 1971.

[20] C.S. Yin, Stability of liquid flow down an inclined plane, Phys. Fluids, 6(3), 321-334, 1963.

[21] C.S. Yih, Instability due to viscosity stratification. J. Fluid Mech., 27, 337-352, 1967.

[22] S.G. Yiantsios, B.G. Higgins, Linear stability of plane Poiseuille flow of two superpose fluids, Phys. Fluids, 31(11), 1988.

[23] P. Yecko, S. Zaleski, J.-M. Fullana, Viscous modes in two-phase mixing layers, Phys. Fluids, 14(2), 2002.

Project 8

Elliptic vortex patches: coasts and chaos

Andrew Crosby

Cambridge University

We investigate the interaction of ocean vortex patches with boundaries via the elliptic moment model of Melander, Zabusky & Stysek [13], under which vortex patches are approximated as elliptic regions of uniform vorticity. The interaction with a straight boundary is shown to reduce to the problem of an ellipse in constant strain, as previously investigated by Kida [9]. Interactions with more complicated geometries, where we might have expected the motion to be chaotic, are found to be constrained by an adiabatic invariant arising from a separation of time scales between the rotation of the patch and its motion along the coast. A couple of examples where the presence of a background flow does produce clear chaotic motion are also given. Finally a conformal mapping technique is developed to find the motion of vortex patches in geometries where the flow is not so easily calculated.

8.1 Introduction

In many problems in geophysical fluid dynamics the flows of interest are quasi-two dimensional due to the presence of rotation, stratification or shallow water, and a ubiquitous feature of such flows are large-scale vortex structures. Examples include the famous Red Spot of Jupiter's atmosphere, which is thought to be well approximated by the shallow water equations [3]. Closer to home the Atlantic Ocean plays host to Gulf Stream rings, which are rings of hot or cold water formed by an instability of the gulf stream (see Figure 8.1a), and also to Meddies, which are formed by the flow of regions of warm salty water from the Mediterranean into the Atlantic (see Figure 8.1b). Such structures are important for the transport of heat/salt across the Atlantic and, due to their relatively long life-times (O(years) in the case of meddies), will inevitably interact with ocean boundaries; indeed a study by Richardson & Tychensky [15] observed that meddies would interact with sea-mounts and could sometimes be observed to breakup in the process.

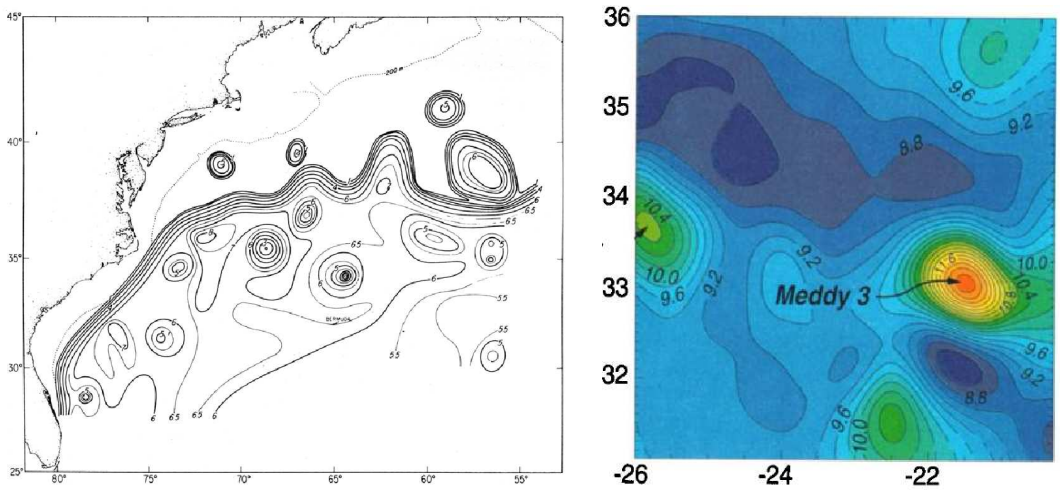

(a) Gulf stream rings visualized by depth in 100m of 15°C isotherm, (Richardson, Cheney & Worthington 1976) [14]

(b) Mediterranean eddies visualized by temperature at 1000m depth, (Richardson & Tychensky 1998) [15]

Figure 8.1: Examples of vortices present in the Earth's oceans

Previous work by Johnson and McDonald [8, 7] had mainly focused on the modelling of such ocean vortices as point vortices and analysing their paths around islands or past coastal gaps. To complement this work they did some contour dynamics calculations to look at the motion of an initially circular patch of vorticity in such situations. The project presented by Ted Johnson at the Woods Hole program was motivated by an observation during this earlier work that, where the point vortex motion had a separatrix, it ought to be possible to find chaotic motion of a patch of vorticity. The two problems presented by Ted were that of motion around a pair of islands (see Figure 8.2a) where the vortex patch might be expected to chaotically switch which island it goes around, and that of motion past a coastal gap where the vortex patch might either go through the gap or continue along the coast in a chaotic scattering problem (see Figure 8.2b).

In the end there was only time to consider the problem of motion around a pair of islands but on route we discovered some interesting phenomena which are presented in the following sections.

8.2 Problem description

We consider the two-dimensional Euler equations, and model regions of vorticity as finite area patches of uniform vorticity. Under certain assumptions the motion of such patches is well approximated by an elliptic moment model developed by Melander, Zabusky & Stysek [13] (MZS from here on in). It is this model that we will utilise here so we begin by briefly describing the important results from its derivation.

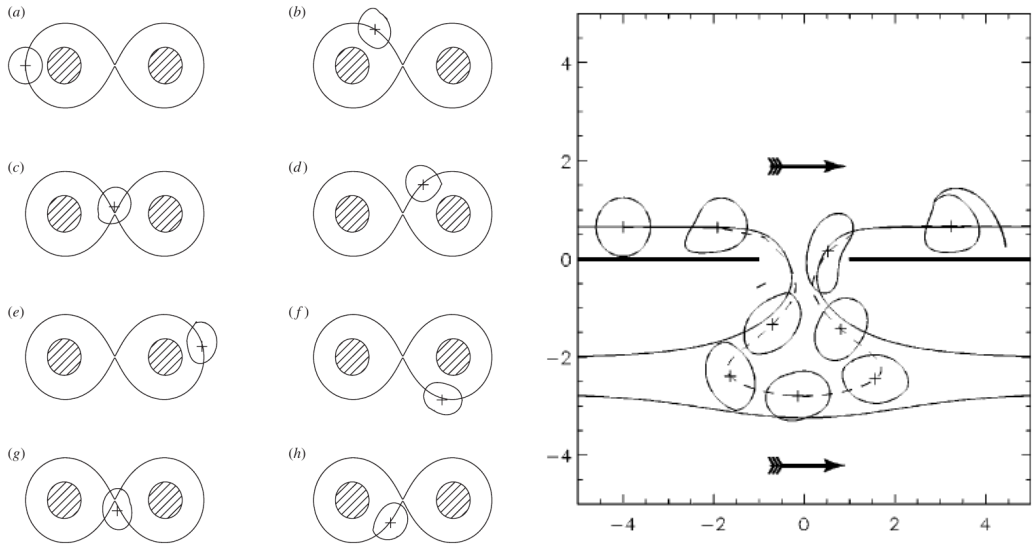

(a) Two islands. (b) Coastal gap with background flow.

Figure 8.2: Contour dynamics simulations results by Johnson and McDonald where vortex patch shape could affect motion near a separatrix.

8.2.1 Elliptic moment model

It is a remarkable result of Kirchoff [10] that an elliptic patch of vorticity in the absence of background flow maintains its elliptical shape and simply rotates about its centre. For a patch of vorticity ω and area A the rotation rate is given by

$$\Omega = \frac{\omega}{2 + r + r^{-1}} \tag{8.1}$$

where $r \geq 1$ is the ratio of the major axis to the minor axis of the ellipse. Furthermore such an elliptic patch remains elliptical under the application of some combination of uniform advection, rotation and strain. It is these results that form the backbone of the model of MZS.

It is worth noting that such elliptic vortex patches are not always stable: it was shown by Love [11] that for $r > 3$ the ellipse becomes unstable in the absence of any background flow, and Dritschel [4] extends this analysis to the case of an ellipse in a straining flow.

MZS considered a collection of uniform vorticity patches whose typical dimension, L, was much less than their typical separation, R. This separation allows the use of a multipole expansion when calculating the interaction between vortex patches. They then represented each vortex patch in terms of its centroid and Fourier modes representing the shape. At second order the model is particularly elegant as, under the extra assumption that the patches are initially approximately elliptical i.e. higher Fourier modes $\ll 1$, the model is closed (requires no knowledge of higher moments). Thus the patches and their motion can be entirely represented in terms of their centroids and their elliptical shape.

Under these approximations patch centroids evolve due to the point vortex and elliptic moments from all the other patches. Meanwhile the elliptic shape of each patch evolves due

Figure 8.3: Approximation of vortex patches as ellipses under the moment model of MZS.

to a self-contribution causing it to rotate (c.f. Kirchoff) and the strain flow generated by the point vortex contributions from the other patches.

8.2.2 Representing an ellipse

It is useful at this stage to consider a couple of methods for representing an elliptical shape, if we assume that the size of the ellipse is fixed then the shape needs two independent quantities to represent it. Perhaps the simplest and most physically intuitive is the following:

$$(r, \theta) \tag{8.2}$$

where $r \geq 1$ is the ratio of the major to minor axis and θ is the angle that the major axis makes to the horizontal. In the following sections it will often be convenient to represent the ellipse in terms of its quadrupole moment

$$\mathbf{q} \equiv \begin{pmatrix} q_{xx} & q_{xy} \\ q_{xy} & q_{yy} \end{pmatrix} \equiv \int (\mathbf{x} - \mathbf{x}_c)(\mathbf{x} - \mathbf{x}_c)\ dS \tag{8.3}$$

where $\mathbf{x}_c$ is the centroid of the ellipse and the integral is over the area of the ellipse. This can be written in terms of (r, θ) as follows:

$$\mathbf{q} = \frac{A^2}{4\pi} \begin{pmatrix} r\cos^2\theta + r^{-1}\sin^2\theta & (r - r^{-1})\sin\theta\cos\theta \\ (r - r^{-1})\sin\theta\cos\theta & r\sin^2\theta + r^{-1}\cos^2\theta \end{pmatrix} \tag{8.4}$$

There are only really two independent quantities here as $\det(\mathbf{q})$ is a function only of the area A and consequently is fixed. Finally we can also represent the ellipse via a complex quadrupole moment

$$q \equiv \int (z - z_c)(z - z_c)\ dS = (q_{xx} - q_{yy}) + 2iq_{xy} \tag{8.5}$$

where $z = x + iy$.

8.2.3 Hamiltonian representation

The underlying two-dimensional Euler equations are Hamiltonian and it was observed by MZS that their elliptic model preserved the Hamiltonian structure. Here we will sketch a

derivation of the Hamiltonian in terms of complex variables, (the use of complex variables allows for a much more compact representation of the quadrupole interactions).

The Hamiltonian for the two-dimensional Euler equations is given by the excess energy [1]

$$H = -\frac{1}{2}\int \omega\psi \; dS - \int \omega\Psi \; dS \tag{8.6}$$

where ψ is the stream function due to the vorticity in the flow and Ψ is the stream function for an externally-imposed irrotational flow. For patches of uniform vorticity, and assuming no background flow for the time being, we can rewrite the above expression as

$$H = -\frac{1}{2}\sum_i \omega_i \int \psi_i \; dS_i - \frac{1}{2}\sum_{i\neq j} \omega_i \int \psi_j \; dS_i \tag{8.7}$$

where $\int \cdot \, dS_i$ is an integral over patch i, ω_i is the vorticity of patch i, and ψ_i is the stream function due to patch i.

The elliptic moment model of MZS is equivalent to integrating over elliptic regions, and expanding ψ_j in the second term as a multipole expansion while keeping terms up to order $(L/R)^2$.

The stream function due to a point vortex of unit strength at $\mathbf{x}_0$ is given by

$$\psi(\mathbf{x}) = -\frac{1}{2\pi}\log\left(|\mathbf{x}-\mathbf{x}_0|\right). \tag{8.8}$$

As the flow due to a point vortex is irrotational this can be written in terms of a complex stream function ϕ which is an analytic function of $z = x + iy$

$$\phi(z) = \frac{1}{2\pi i}\log(z - z_0) \tag{8.9}$$

from which the stream function can be recovered by taking the imaginary part.

The complex stream function due to patch i, ϕ_i can be written as

$$\phi_i(z) = \frac{\omega_i}{2\pi i}\int \log(z-\hat{z}) \; d\hat{S}_i, \tag{8.10}$$

which can then be expanded about the centroid of the patch z_i in a multipole expansion

$$\phi_i(z) \approx \frac{\omega_i}{2\pi i}\int \log(z-z_i) - \frac{\hat{z}-z_i}{z-z_i} - \frac{(\hat{z}-z_i)^2}{2(z-z_i)^2} \; d\hat{S}_i \tag{8.11}$$

the second term disappears as z_i is the centroid of the patch and the third term can be rewritten in terms of the complex quadrupole, q, defined earlier

$$\phi_i(z) \approx \frac{\omega_i}{2\pi i}\left(A_i \log(z-z_i) - \frac{q}{2(z-z_i)^2}\right). \tag{8.12}$$

The contribution to the Hamiltonian from the stream function of patch i evaluated at patch j in Equation (8.7) is calculated by expanding this multipole expansion as a quadratic around z_j

$$\phi_i(z) \approx \frac{\omega_i}{2\pi i}\left(A_i \log(z_j - z_i) - \frac{q_i}{2(z_j-z_i)^2} + \frac{A_i}{z_j - z_i}(z-z_j) - \frac{A_i}{2(z_j-z_i)^2}(z-z_j)^2\right) \tag{8.13}$$

and then integrating over patch j to give

$$\omega_j \int \psi_i \; dS_j = -\frac{\omega_i \omega_j}{2\pi} \mathrm{Re}\left(A_i A_j \log(z_j - z_i) - \frac{A_i q_j + A_j q_i}{2(z_j - z_i)^2} \right). \tag{8.14}$$

Calculation of the self-interaction term is more complicated and here we will just quote the result of MZS rewritten in terms of q:

$$\omega_i \int \psi_i \; dS_i = \frac{(\omega_i A_i)^2}{4\pi} \log\left(\frac{4\pi}{A_i^2} \sqrt{|q_i|^2 + \frac{A_i^4}{4\pi^2}} + 2 \right). \tag{8.15}$$

These results can then be combined to give a full Hamiltonian

$$H = -\sum_i \frac{(\omega_i A_i)^2}{8\pi} \log\left(\frac{4\pi}{A_i^2} \sqrt{|q_i|^2 + \frac{A_i^4}{4\pi^2}} + 2 \right) - \sum_{i \neq j} \frac{\omega_i \omega_j}{4\pi} Re\left(A_i A_j \log(z_j - z_i) - \frac{A_i q_j + A_j q_i}{2(z_j - z_i)^2} \right). \tag{8.16}$$

To complete the model we need to know how to obtain the equations of motion from the Hamiltonian: this can be achieved either by directly deriving the equations of motion and working backwards [13] or directly from the Hamiltonian Euler equations [12]. The resulting equations are as follows:

$$\dot{x}_i = \frac{1}{\omega_i A_i} \frac{\partial H}{\partial y_i} \tag{8.17}$$

$$\dot{y}_i = -\frac{1}{\omega_i A_i} \frac{\partial H}{\partial x_i} \tag{8.18}$$

$$\dot{q}_{xi} = \frac{4\sqrt{|q_i|^2 + \frac{A^4}{4\pi^2}}}{\omega_i} \frac{\partial H}{\partial q_{yi}} \tag{8.19}$$

$$\dot{q}_{yi} = -\frac{4\sqrt{|q_i|^2 + \frac{A^4}{4\pi^2}}}{\omega_i} \frac{\partial H}{\partial q_{xi}} \tag{8.20}$$

Finally we note that (q_x, q_y) do not form a canonical variable pair but MZS observe that the following pair, written here in terms of r and θ do.

$$\left(\frac{\omega_i A_i}{16\pi} \frac{(r_i - 1)^2}{r_i}, 2\theta_i \right) \tag{8.21}$$

8.3 Motion along a coast

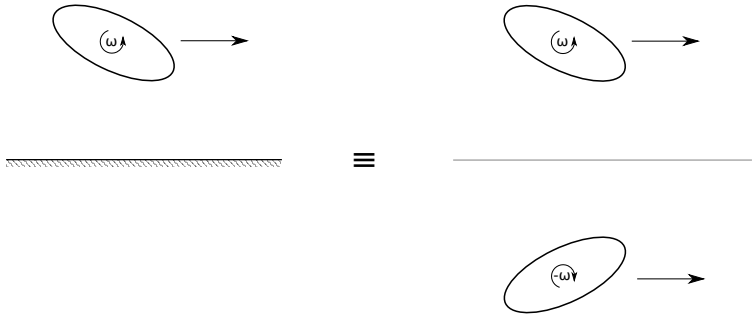

We begin by considering the simple case of a vortex patch moving along a coast or ocean-ridge. Consider the coast to lie along the line $y = 0$. This problem can be solved via a simple image system: the motion is the same as that of two vortex patches where the image vortex is the reflection of the original vortex patch in the line $y = 0$. The image patch will have opposite vorticity and a quadrupole $\bar{q}$. Now from the previous section we can construct the Hamiltonian as follows:

$$H = -\frac{(\omega A)^2}{8\pi}\log\left(\frac{4\pi}{A^2}\sqrt{|q|^2 + \frac{A^4}{4\pi^2}} + 2\right) + \frac{\omega^2}{4\pi}Re\left(A^2\log(z-\bar{z}) - \frac{A(q+\bar{q})}{2(z-\bar{z})^2}\right) \tag{8.22}$$

$$H = -\frac{(\omega A)^2}{8\pi}\log\left(\frac{4\pi}{A^2}\sqrt{(q_x^2+q_y^2) + \frac{A^4}{4\pi^2}} + 2\right) + \frac{\omega^2}{4\pi}\left(A^2\log(2y) + \frac{Aq_x}{4y^2}\right) \tag{8.23}$$

Applying equations (8.17) then gives the following evolution equations:

$$\dot{x} = \frac{\omega A}{4\pi y} - \frac{\omega q_x}{8\pi y^3} \tag{8.24}$$

$$\dot{y} = 0 \tag{8.25}$$

$$\dot{q}_x = -\frac{2\omega q_y}{2 + \frac{4\pi}{A^2}\sqrt{(q_x^2+q_y^2) + \frac{A^4}{4\pi^2}}} \tag{8.26}$$

$$\dot{q}_y = \frac{2\omega q_x}{2 + \frac{4\pi}{A^2}\sqrt{(q_x^2+q_y^2) + \frac{A^4}{4\pi^2}}} - \frac{A\omega}{4\pi y^2}\sqrt{(q_x^2+q_y^2) + \frac{A^4}{4\pi^2}} \tag{8.27}$$

The first thing to notice is that the vortex patch stays at a fixed height above the wall; this is a consequence of the conservation of the y-component of the global centroid. Under the elliptic model the strain experienced by the patch comes only from the point vortex contribution of the image, this is of fixed magnitude and at a fixed distance hence the patch experiences a constant strain rate. This problem of an elliptic patch of vorticity in constant strain has previously been analysed by Kida [9]. By writing q_x and q_y in terms of r and θ we can rewrite the Hamiltonian in a form similar to that given in the paper of Kida

$$H = -\frac{\omega^2 A^2}{8\pi}\log(r + r^{-1} + 2) + \frac{\omega^2 A^2}{4\pi}\log(y) + \frac{\omega^2 A}{16\pi y^2}\frac{A^2}{4\pi}(r - r^{-1})\cos(2\theta) \tag{8.28}$$

and then defining e to be the constant strain rate

$$e \equiv \frac{A\omega}{8\pi y_c^2} \tag{8.29}$$

we have the following for some constant c (dependant on H):

$$\cos(2\theta) = \frac{\omega}{e}\frac{r}{r^2-1}\log\left(\frac{(r+1)^2}{cr}\right). \tag{8.30}$$

Kida showed that there were three types of motion possible: rotation, nutation and extension in which respectively either the major axis of the ellipse oscillates about $\theta = 0$, the

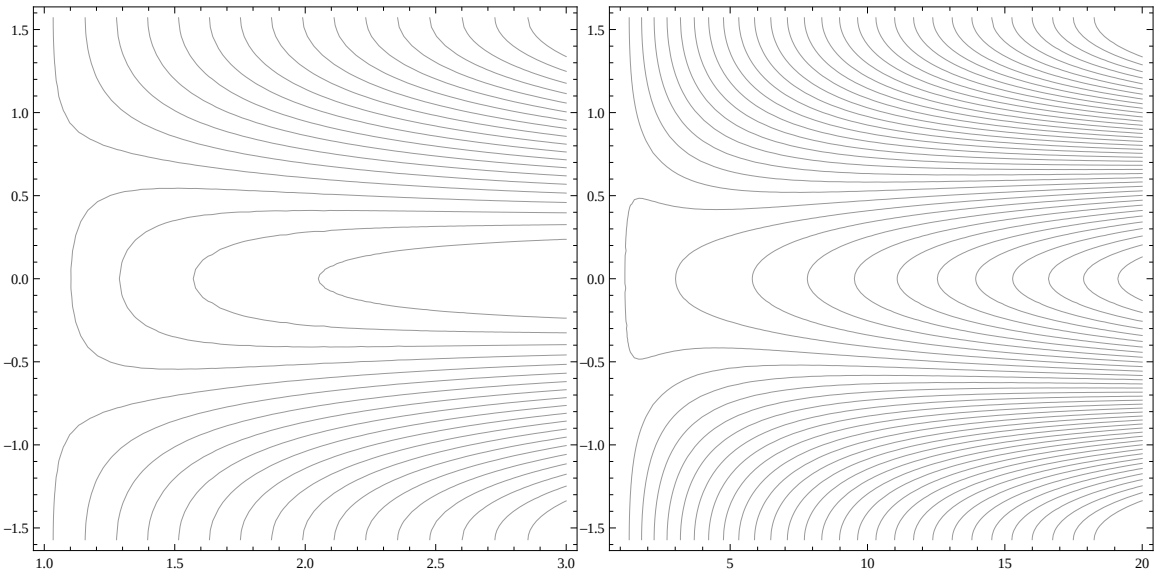

(a) (b)

Figure 8.4: $\frac{e}{\omega} = 0.2$. Contour plots of 2θ vs r.

major axis continually rotates, or the ellipse gets stretched out indefinitely. For $\frac{e}{\omega} > 0.15$ the only possible motion is extension where the ellipse is stretched indefinitely (see Figure 8.4). For our value of e this corresponds to $A > 3.8y^2$ which for a circle would give radius $> 1.2y$. So when vortex patches are sufficiently close to a coast we expect them to break up, although we must be a little careful here because we have assumed that the vortex patch and its image are separated by a large distance in the model derivation so we can not expect this value to be quantitatively correct. There is a small range, $0.15 > \frac{e}{\omega} > 0.13$, where both nutation and extension are possible, and then for $\frac{e}{\omega} < 0.13$ all three types of motion can occur (see Figure 8.5).

8.3.1 Comparison with contour dynamics code

The full solution for the evolution of a patch of uniform vorticity can be calculated numerically using the method of contour dynamics [16]. This method makes use of the fact that the velocity only needs to be known on the boundary in order to evolve the patch position and that the velocity on the boundary can be calculated by an integral round the boundary as follows:

$$\nabla\psi(\mathbf{x}) = -\frac{1}{2\pi}\int \nabla_{\mathbf{x}} \log(|\mathbf{x}-\hat{\mathbf{x}}|)\; d\hat{S} \tag{8.31}$$

$$= \frac{1}{2\pi}\int \nabla_{\hat{\mathbf{x}}} \log(|\mathbf{x}-\hat{\mathbf{x}}|)\; d\hat{S} \tag{8.32}$$

$$= \frac{1}{2\pi}\int \log(|\mathbf{x}-\hat{\mathbf{x}}|)\; d\hat{\mathbf{n}}. \tag{8.33}$$

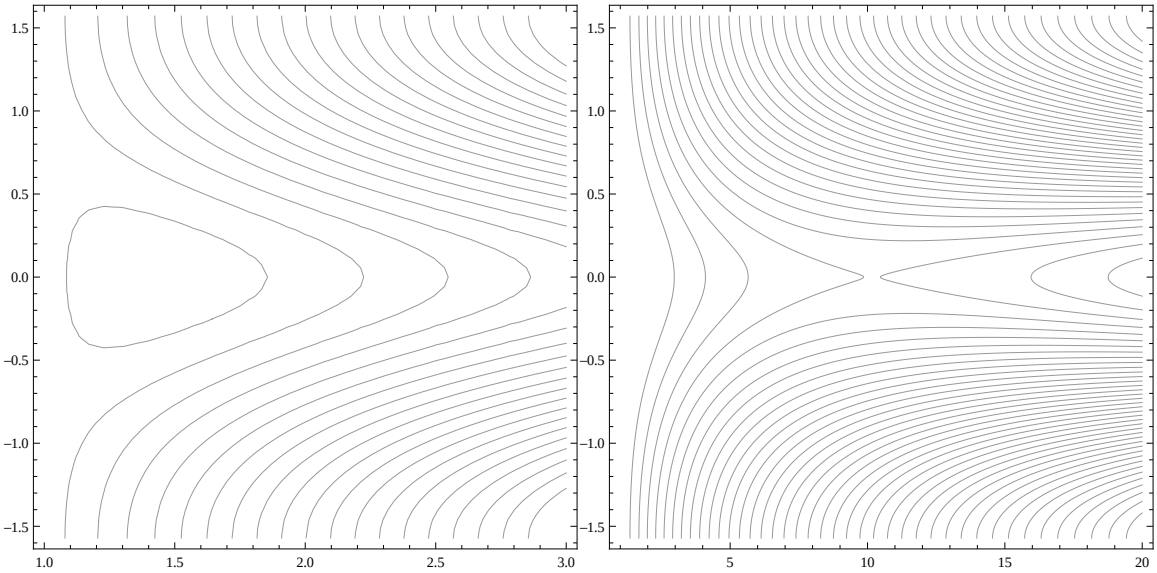

(a) (b)

Figure 8.5: $\frac{e}{\omega} = 0.08$. Contour plots of 2θ vs r.

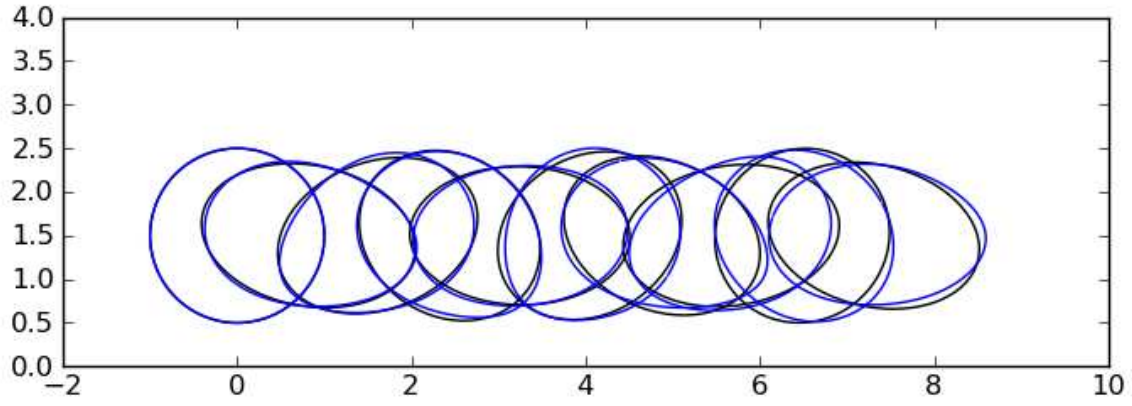

Figure 8.6: Motion of an initially circular patch with centroid at $y = 1.5$. Patch motion is from left to right with time intervals of $5/\omega$. Contour dynamics solution is in blue and the model in black.

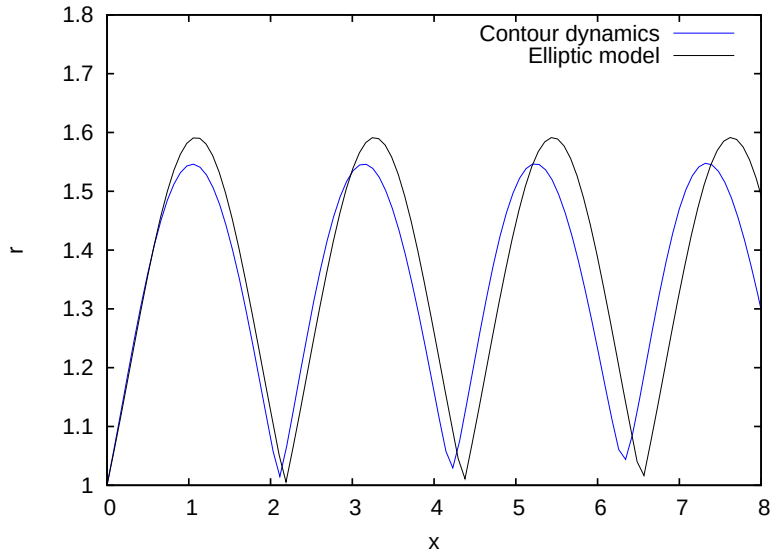

Figure 8.7: r against x for an initially circular patch with centroid at $y = 1.5$. For the contour dynamics solution r is calculated from the quadrupole moment.

A comparison between the model and contour dynamics calculations is shown in Figure 8.6, here the patch has a unit radius and its centroid starts at a distance 1.5 above the coast. The model and full solution agree very well at early times but at later times there is a noticeable phase drift. A more quantitative comparison is made in Figure 8.7, which again clearly shows the phase drift by also shows that the elliptic model overestimates the maximum value of r by $\sim 10\%$.

The good agreement between the model and full solution when $y = 1.5$, despite the technical requirement in the model derivation for the patch and its image to be well separated, raises the question of what happens if we use the model to calculate the motion of a patch of vorticity right next to the wall. The result of such calculations is shown in Figure 8.8. Whilst the elliptic model is clearly unable to capture the formation of a cusp it still does a remarkably good job of predicting the overall shape.

8.3.2 Background tide

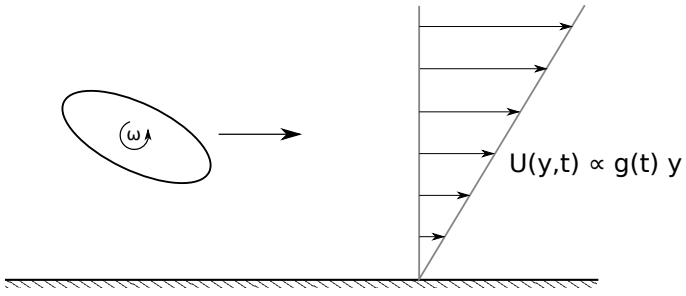

A natural extension to the previous problem is to ask what happens if there is a background flow along the coast. We consider here what happens if a time dependent background

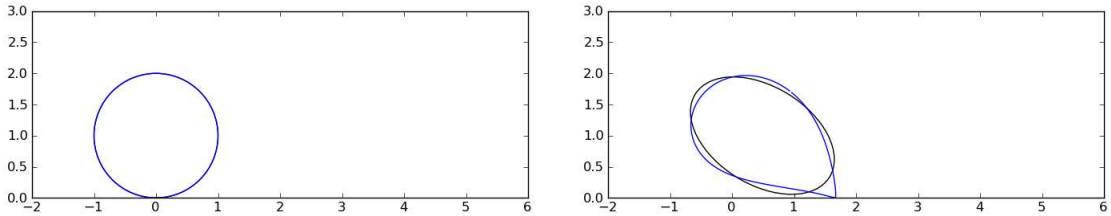

(a) $t = 0$ (b) $t = 2/\omega$

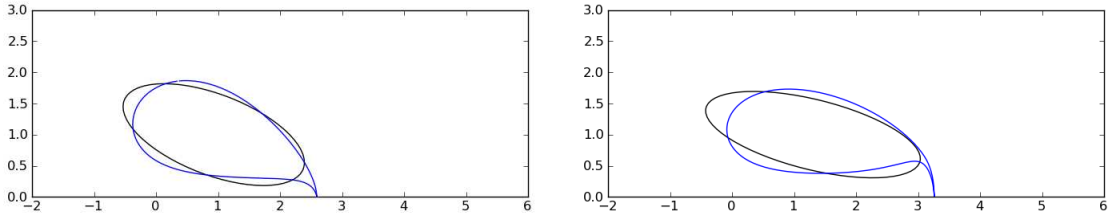

(c) $t = 4/\omega$ (d) $t = 6/\omega$

Figure 8.8: Even when the vortex patch is right next to the wall and consequently the model (black) should be completely invalid it still does a remarkably good job of capturing the overall shape of the region of vorticity (blue).

shear flow is imposed

$$U(y,t) = g(t)y \tag{8.34}$$

where we take the strength of the shear to vary sinusoidally with time

$$g(t) = f \sin\left(\frac{2\pi t}{T}\right). \tag{8.35}$$

Such shear might be caused by the presence of a tidal flow along the coast. It is known that, in the absence of a boundary, such background flows lead to chaotic behaviour [5].

We have to be a little careful when constructing the Hamiltonian for the motion of the elliptic patch in this flow as the background flow has infinite energy and is being driven by some unmodelled mechanism. The extra term that we add is

$$H_{shear} = -\omega \int \Psi_{shear}\, dS \tag{8.36}$$

where Ψ_{shear} is the (non-irrotational) stream function for the background flow

$$\Psi_{shear} = g(t)\frac{y^2}{2} \tag{8.37}$$

consequently we find that

$$H_{shear} = -\frac{\omega g(t)}{2}(Ay^2 + q_{yy}). \tag{8.38}$$

By neglecting any contribution due to the energy in the background flow we are effectively assuming that the background flow is unaffected by the presence of the vortex patch.

As the Hamiltonian is now time dependent we expect to find chaotic behaviour. The patch will still remain at a fixed height above the wall but we find more interesting behaviour if we consider what happens to the shape of the patch; the motion is now determined by three parameters: f, T and the initial distance from the wall y_0 (unless otherwise stated we will take $A = \pi$ and $\omega = 1$).

As an example we focus on the case of $y_0 = 3$. The unforced behaviour ($f = 0$) for this case is shown in Figure 8.9, for this value of y_0 almost all the orbits in the range of interest are rotations. We will consider what happens when we apply forcing with a period $T = 14$, from Figure 8.9b we see that this corresponds to the time period of an orbit with $r \approx 2$ when $\theta = 0$. Figures 8.10a & 8.10b show Poincaré sections of the resulting motion with points plotted every period T (the quantities plotted are actually the earlier canonical variables (Equation (8.21)) relabelled in terms of r and θ).

Initially a weak forcing of $f = 0.001$ is applied and a resonance opens up about the orbit with matching period (Figure 8.10a). In fact a similar resonance opens up about every orbit whose time period is a rational multiple of the forcing [2], but for this weak forcing they are too small to be observable here. An increase in forcing by a factor of 10 to $f = 0.01$ does little to affect the motion apart from increasing the size of the resonance (Figure 8.10b). As the forcing is increased further to $f = 0.05$ many of the higher order resonances become visible (Figure 8.11a). Finally by $f = 0.1$ a 'sea of chaos' has emerged (Figure 8.11b).

The development of resonances could have an impact on whether vortex patches are likely to break up: a sufficiently large resonance can take a vortex patch that is initially near circular and extend it well beyond $r = 3$ where the elliptic patch would become unstable in the absence of background flow. Similarly the emergence of a 'sea of chaos' allows the vortex patch to access all states within a large region of the Poincaré section including some for which the value of r is very large.

We can also consider what happens when the frequency of the forcing is changed: Figure 8.12 shows a Poincaré section when the forcing has a period of $T = 30$. One notable new feature here is that the sea of chaos that exists for most of the region $r \gtrsim 4$ extends out into a region where elliptic patches get extended indefinitely; this is why there aren't many points plotted in it as any solution that started there typically only survived a few periods before being indefinitely extended. This Poincaré section also provides us with an opportunity to observe one of the fundamental building blocks of chaos: the 'heteroclinic tangle' (see Figure 8.12b). When $f = 0$ we have a two-dimensional Hamiltonian system where the only type of fixed points are centres or saddles. A saddle point consists of the intersection of a stable and unstable manifold; in a two dimensional Hamiltonian system these manifolds can only intersect at a fixed point. However this saddle point structure is unstable and once a perturbation is added (here by increasing f away from zero) the two manifolds will typically intersect at a point away from the fixed point. The iterates of such an intersection lead to an infinite number of intersections away from the fixed point. On top of this the area-preserving property of a Poincaré section means that the area of the 'nodes', the regions formed by the two manifolds between intersections, must all be the same. Consequently as the intersections approach the fixed point the nodes get increasingly stretched out until eventually they start to wrap all the way around and overlap the fixed

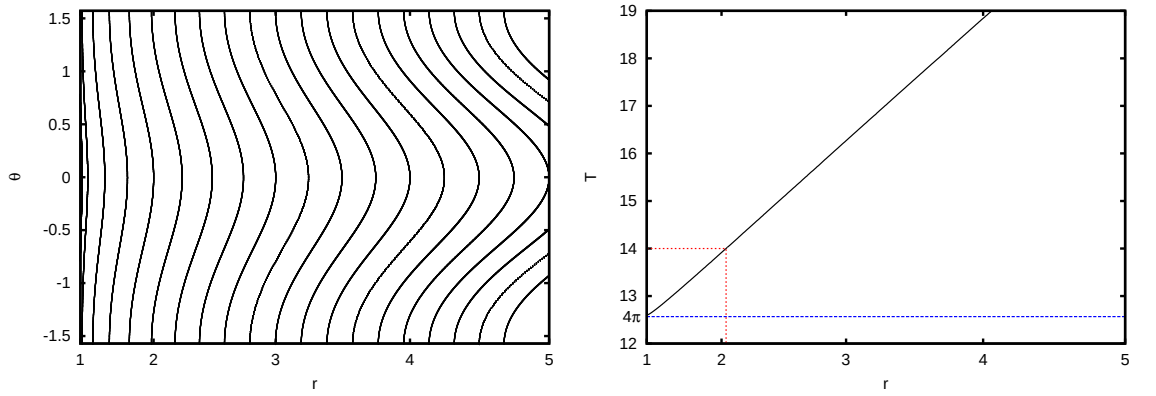

(a) Motion in the (r, θ) plane.

(b) Time period of orbits labelled by value of r at $\theta = 0$. The orbit times are all greater than that of an isolated circular patch for which $T = 4\pi$.

Figure 8.9: Behaviour for $y_0 = 3$ in the unforced case ($f = 0$).

point in the perpendicular direction. It is this 'stretching' and 'folding' that guarantees the presence of a Smale Horseshoe and consequently chaotic behaviour. The presence of such tangles was predicted by Poincaré before we had the ability to calculate such structures numerically!

Finally we note that if the period of the forcing applied is much less or greater than the characteristic period associated with the rotation of the elliptic patch then, unless the forcing is very strong, the motion remains near integrable.

8.4 Motion around a corner

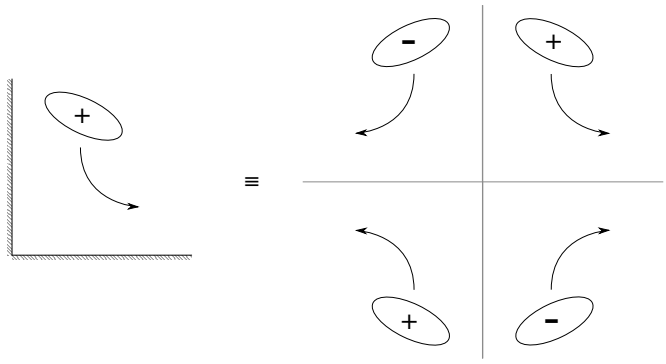

In the case of a patch moving above a straight coast the presence of a second conserved quantity (y component of the global centroid) meant the motion remained integrable. We will now consider what happens when a patch of vorticity moves in a quarter plane for which this extra conserved quantity does not exist. Far away from the corner the patch will remain at a constant distance from the coast but then the interaction with the corner will allow the distance to change. As this is a four-dimensional system we would expect to find

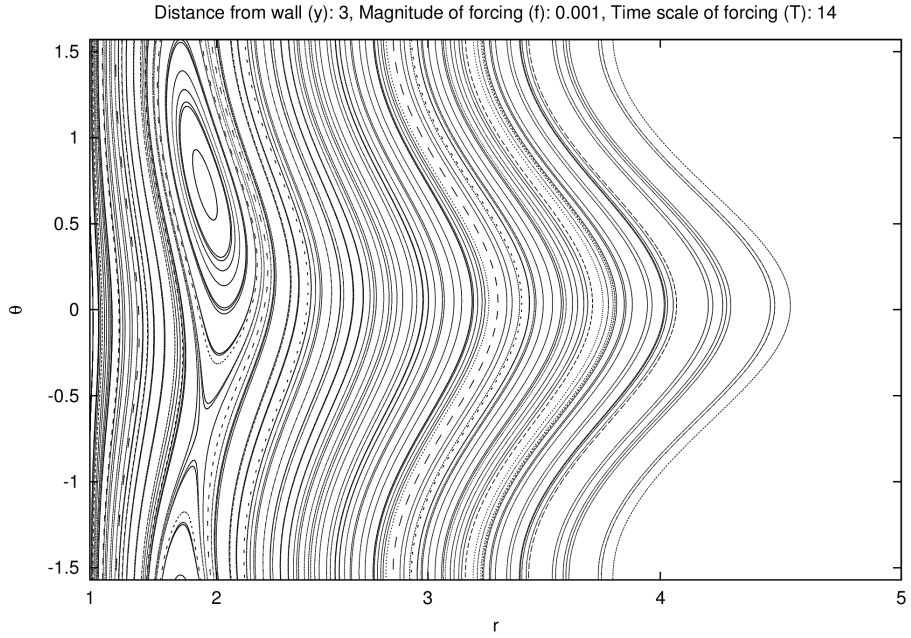

(a) $f = 0.001$

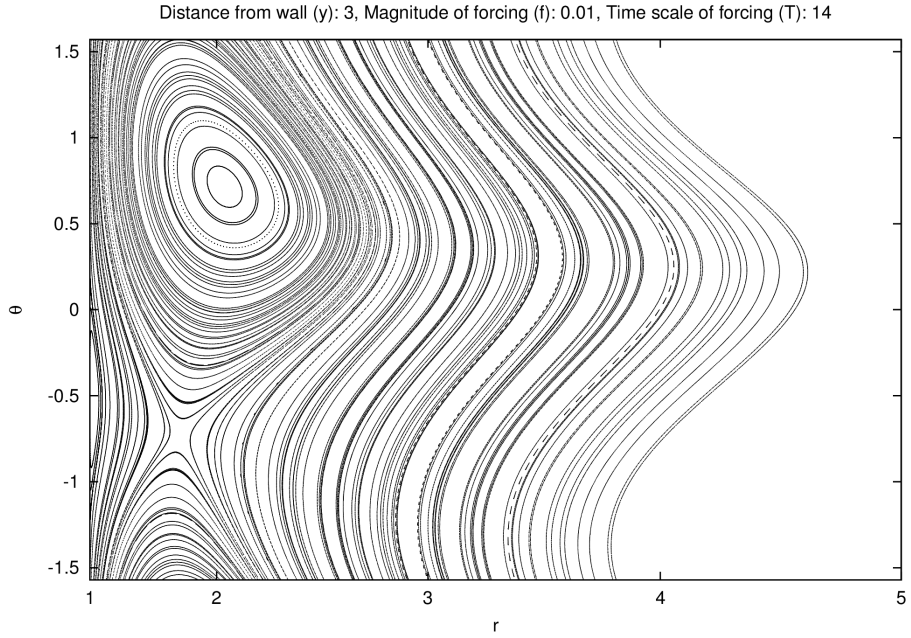

(b) $f = 0.01$

Figure 8.10: Poincaré sections for $y_0 = 3$, $T = 14$.

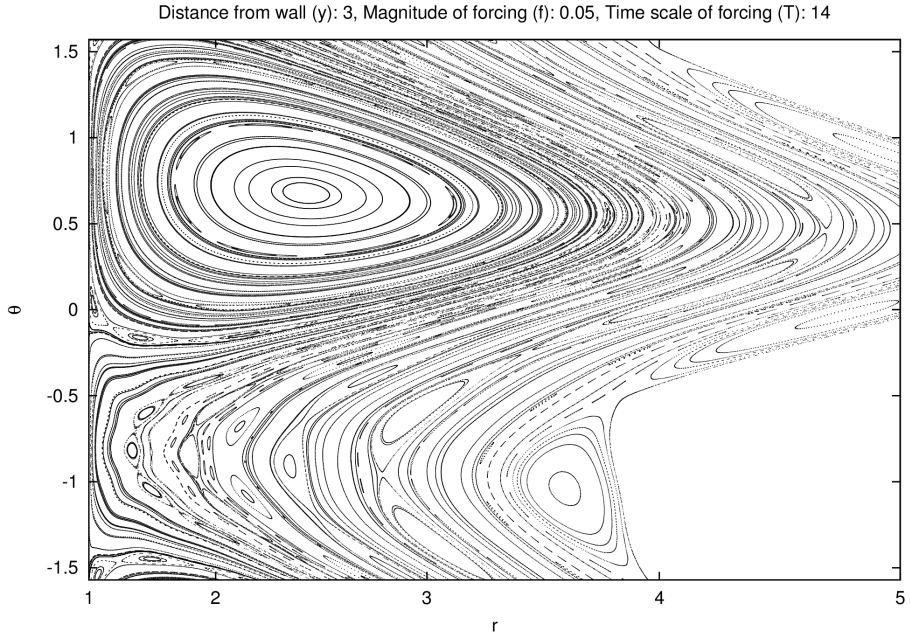

(a) $f = 0.05$

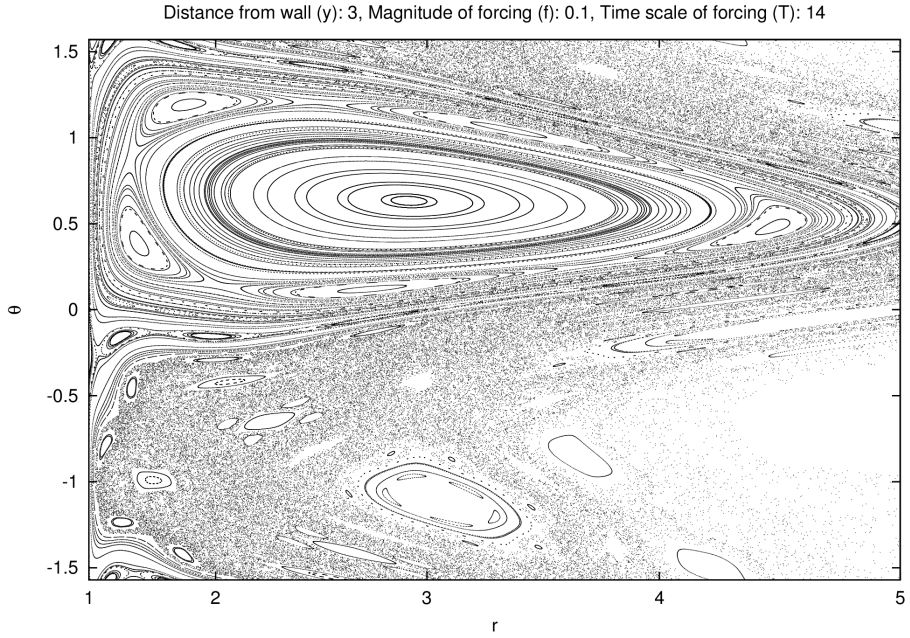

(b) $f = 0.1$

Figure 8.11: Poincaré sections for $y_0 = 3$, $T = 14$.

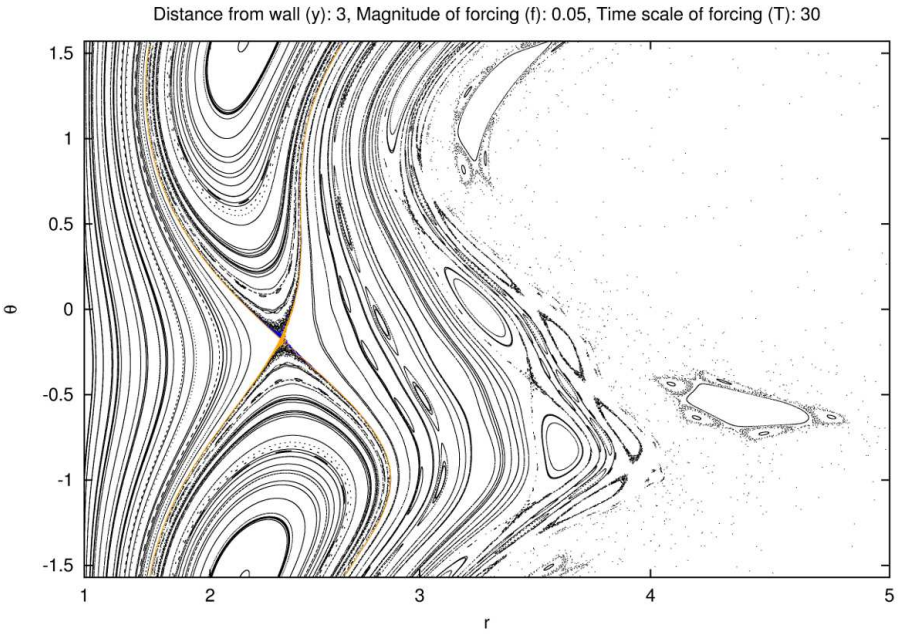

(a)

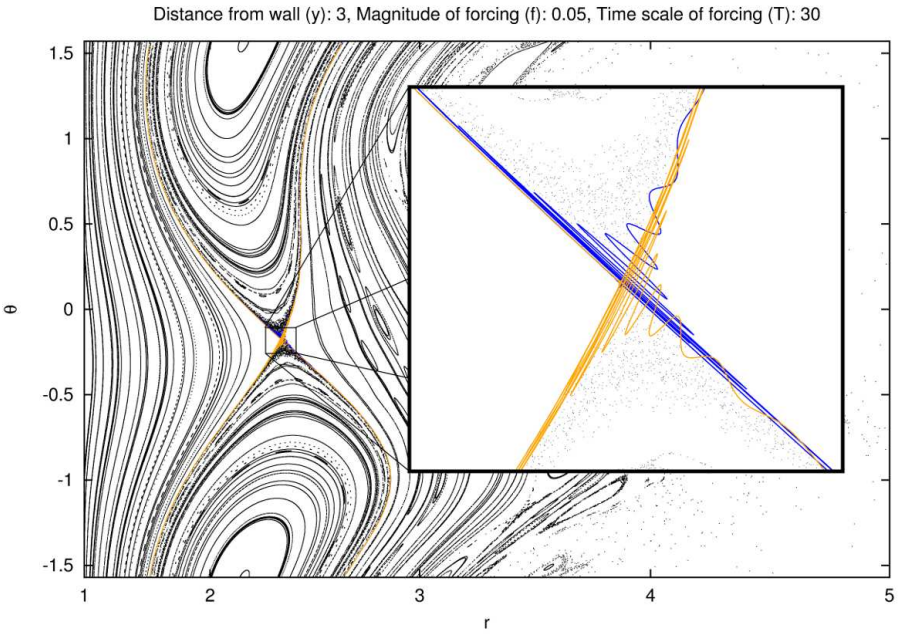

(b) Magnification of heteroclinic tangle.

Figure 8.12: Poincaré sections for $y_0 = 3$, $T = 30$, $f = 0.05$.

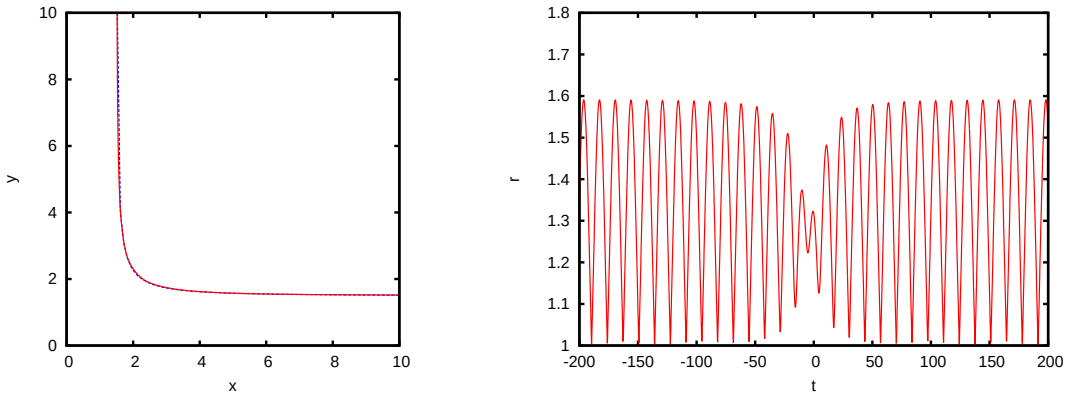

(a) Path of centroid in x-y plane.

(b) Variation of r with t.

Figure 8.13: Typical behaviour of a vortex patch moving round a corner. Initial conditions are $x = 1.5$, $y = 100$, $r = 1$ & $\theta = 0$.

chaotic behaviour.

We can again use the method of images (this time we need three images) to construct the Hamiltonian

$$H = H_{self} + \frac{\omega^2}{4\pi}\left(A^2 \log(\frac{2xy}{\sqrt{x^2+y^2}}) + \frac{Aq_x}{4y^2} - \frac{Aq_x}{4x^2} + \frac{A(q_x(x^2-y^2)+2q_yxy}{4(x^2+y^2)^2}\right) \tag{8.39}$$

from which the motion of patches is easily calculated. Figure 8.13 shows an example of the resulting motion; the distances from the wall before and after the corner are very similar and consequently so is the behaviour of the elliptic shape. This example is typical and, unless patches are started so close to the wall that they extend indefinitely, all patches exit the corner at a similar distance from the wall as they entered, with the maximum deviation being of order 10^{-4}.

The explanation for this surprising behaviour comes from considering the time scales involved in the problem: there is a time scale on which the patch rotates, T_{self}, and a second time scale on which the strain rate experienced by the patch changes as the patch moves through the corner, T_{strain}. T_{strain} is relatively long compared with T_{self}; in Figure 8.13b the ratio of the time scales can be seen to be $T_{strain}/T_{self} \approx 5$. This separation of time scales is sufficient to lead to the phenomenon of adiabatic invariance [6].

If we view this problem as a patch of vorticity in a slowly varying strain field then the theory of adiabatic invariance states that, whilst the Hamiltonian associated with the motion can vary, there exists an adiabatic invariant that is constant to all orders in $\epsilon \equiv T_{self}/T_{strain}$. A first-order approximation to this adiabatic invariant is given by the action

$$J \equiv \oint p\, dq \quad \text{where} \quad p = \frac{\omega A^2}{16\pi}\frac{(r-1)^2}{r}, \quad q = 2\theta \tag{8.40}$$

here p and q are a pair of canonical variables and the integral is over one period of the motion. The variation of this action as the patch passes through the corner for the example

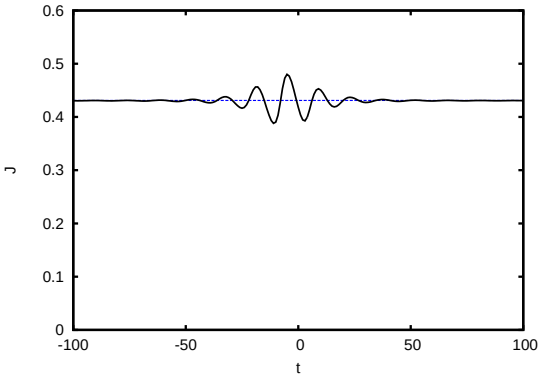

(a) Variation of action as the patch passes through the corner.

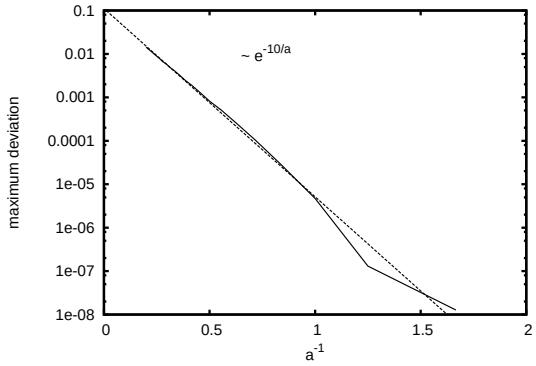

(b) Maximum deviation over all simulations with the same initial energy and action for a range of patch speeds a.

Figure 8.14

given earlier is shown in Figure 8.14a. The presence of the adiabatic invariant means that the action before the interaction with the corner and the action after the interaction, and similarly the distance from the wall, should be the same to all orders. As we have no direct control over the time scales in the problem checking that the distance from the wall is the same to all orders in ϵ is a bit tricky. To get around this we instead consider the related (but unphysical) problem whereby the speed at which the patch centroid moves is changes by a factor a. In this new problem the separation of time scales is $T_{self}/T_{strain} = a\epsilon$; so if the patch centroid moves more quickly, $a > 1$, the strain experienced by the patch varies more quickly and consequently there is less of a separation between the two time scales, conversely if the patch moves more slowly, $a < 1$, there is more of a separation. To see that the distance from the wall is constant at all orders we look at how the change in distance from the wall varies as we vary a, see Figure 8.14b. As a is decreased there is a clear exponential decrease in the deviation corresponding to the adiabatic invariant begin constant at all orders.

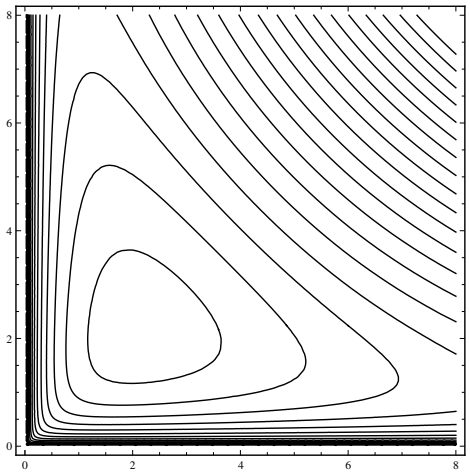

Figure 8.15: Path lines of point vortices in corner with background shear flow.

8.4.1 Corner trapping by an external flow

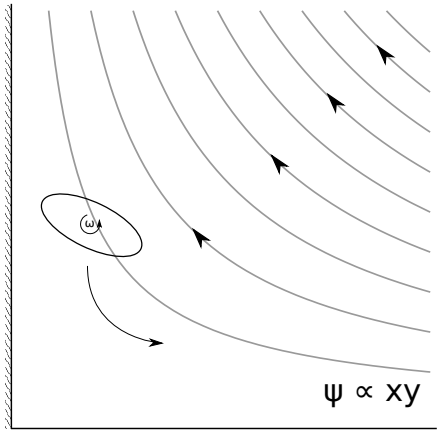

It is possible to add an external straining flow

$$\Psi = \beta xy \tag{8.41}$$

to the quarter-plane motion such that the vortex patch becomes trapped in the corner provided $\beta < 0$; the motion of point vortices in such a flow is shown in Figure 8.15. For elliptic vortex patches this results in the following extra term in the Hamiltonian:

$$H_\Psi = -\omega \left(\frac{\beta q_y}{2} + Axy \right). \tag{8.42}$$

Poincaré sections can be calculated for the resulting motion by plotting all solutions with a fixed value of β and a fixed energy H when they pass forwards through the plane

$\theta = 0$. The resulting Poincaré sections for the x-y plane are shown in Figure 8.16. Also shown by blue lines are the energetically allowable regions of the plane; the asymmetry here is due to the choice of plotting at $\theta = 0$.

For low values of H there is a region of closed streamlines and a second energetically allowable region near $y = 0$ where all patches extend indefinitely. As H is increased the boundaries of these two regions become closer together and at the same time we see the development of resonances in the central region (see $H = 0.25$). By $H = 0.275$ a 'sea of chaos' has emerged around the edge of the central region and at $H = 0.3$, by which time the two regions have merged together, this 'sea of chaos' extends into the region where all patches are indefinitely extended.

The reason that we are able to observe chaotic behaviour here is that the presence of the background straining flow is able to decrease the time scale upon which the vortex patch experiences a change in strain. Unfortunately the emergence of interesting behaviour for $H > 0.25$ also corresponds with the elliptic vortex patches intersecting with the boundaries of the quarter plane, thus the solutions shown become unphysical. So whilst this may still be an interesting mathematical problem we will not spend any more time analysing it here.

8.5 Application to more complicated geometries

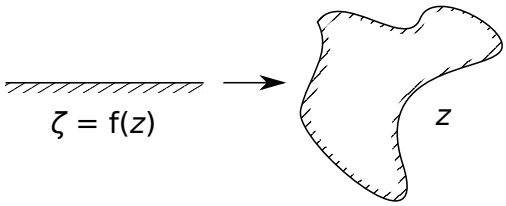

Everything that we've considered so far has been for a 'simple' geometry in which we have been able to construct the solution via the method of images. However the problems that we initially set out to look at featured more complicated geometries in which such methods can not be used. In this section we consider how to make use of conformal transformation techniques to tackle such geometries.

Conformal transformations are a powerful tool for dealing with irrotational flows as for such flows the stream function satisfies Laplace's equation

$$\nabla^2 \psi(z) = 0 \tag{8.43}$$

and under a conformal transformation $\zeta = f(z)$ such functions retain this property

$$\nabla^2 \psi(f^{-1}(\zeta)) = 0. \tag{8.44}$$

Thus we can find the flow in a complicated geometry by finding a map to a simple geometry and solving for the flow in that domain before transforming back. Furthermore such transformations (with a slight caveat) preserve the Hamiltonian; the slight caveat is that, if we have a flow with an infinite energy, such as that for a point vortex, we must take care

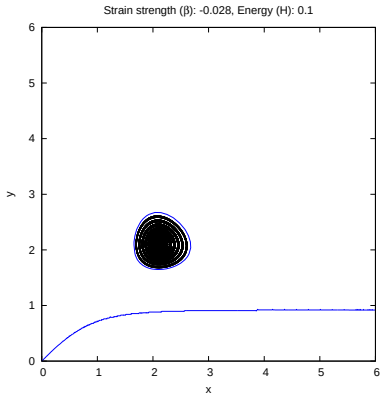

(a) $H = 0.1$

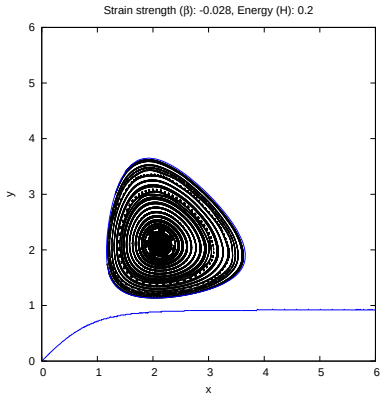

(b) $H = 0.2$

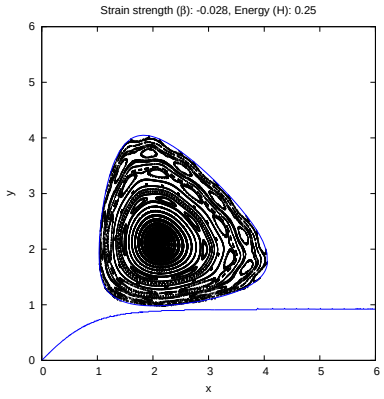

(c) $H = 0.25$

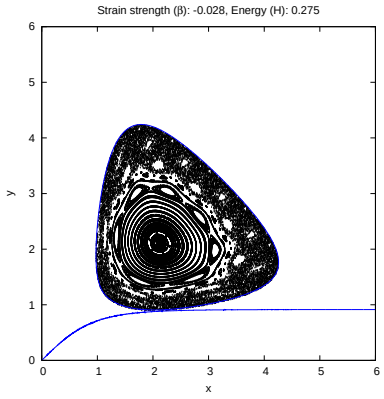

(d) $H = 0.275$

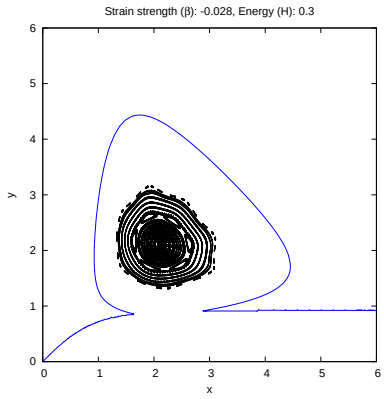

(e) $H = 0.3$

Figure 8.16: Poincaré sections in the x-y plane plotted when $\theta = 0$. The strength of the external strain is fixed at $\beta = -0.028$ and sections are shown for 5 values of the energy H.

over what happens to the 'zero' energy under the transformation. For point vortices Routh showed that the following correction was required

$$H(z) = \hat{H}(\zeta(z)) + \mathrm{Re}\left(\frac{\Gamma^2}{4\pi}\log(f')\right). \tag{8.45}$$

We would like to make use of conformal transformations to calculate the motion of elliptic vortex patches but if we conformally transform such a patch then we will be left with a non-elliptical patch of non-uniform vorticity for which we do not know how to calculate the flow! The solution is to observe that the Hamiltonian can be split into two parts: a self contribution, H_{self}, and an interaction with other vortex patches, H_{int}. The self-contribution does not care about the geometry so is easily calculated in the original geometry. The interaction term represents the energy due to a point vortex and quadrupole, of appropriate strength, located at the centroid of the patch. Such singularities transform nicely under a conformal transformation: a point vortex becomes a point vortex of the same strength and a quadrupole becomes a dipole and a quadrupole of different, but easily calculated, strengths.

Let z be the coordinate of the complicated geometry where the complex stream function is given by $\phi(z)$. Then consider a conformal transformation

$$\zeta = f(z) \qquad z = f^{-1}(\zeta) = F(\zeta) \tag{8.46}$$

which takes this complicated geometry to a simpler one with coordinate ζ and stream function $\Phi(\zeta)$. Now the stream function in the complicated geometry with a point vortex and quadrupole located at z_0 can be written as follows:

$$\phi(z) = \frac{1}{2\pi i}\left(A\log(z-z_0) - \frac{q}{2(z-z_0)^2}\right) + \phi_{z_0}(z). \tag{8.47}$$

In order to calculate H_{int} we need to find $\phi_{z_0}(z)$ and its first two derivatives up to sufficient accuracy for the elliptic model.

A point vortex in the ζ geometry behaves like $\log(\zeta-\zeta_0)$ and to find the corresponding behaviour in the z geometry we expand this in terms of z (all derivatives of f are evaluated at z_0)

$$\log(\zeta-\zeta_0) = \log(z-z_0) + \log f' + \frac{f''}{2f'}(z-z_0) + \frac{4f'''f' - 3f''^2}{24f'^2}(z-z_0)^2 + O((z-z_0)^3) \tag{8.48}$$

from which we see that a point vortex in one geometry corresponds to a point vortex of equal strength in the other geometry. Taking two derivatives with respect to z_0 then gives

$$\frac{f'^2}{(\zeta-\zeta_0)^2} + \frac{f''}{(\zeta-\zeta_0)} = (z-z_0)^{-2} + \frac{4f'''f' - 3f''^2}{12f'^2} + O((z-z_0)) \tag{8.49}$$

which tells us that a quadrupole in the z geometry leads to a both a dipole, $\hat{d}$, and a quadrupole, $\hat{q}$, in the ζ geometry

$$\hat{q} = f'^2 q, \qquad \hat{d} = \frac{f''q}{2}. \tag{8.50}$$

Then the flow in the ζ geometry can be written as

$$\Phi(\zeta) = \frac{1}{2\pi i}\left(A\log(\zeta-\zeta_0) - \frac{qf''}{2(\zeta-\zeta_0)} - \frac{qf'^2}{2(\zeta-\zeta_0)^2}\right) + \Phi_{\zeta_0}(\zeta) \tag{8.51}$$

where we assume that the geometry is sufficiently simple for us to be able to calculate $\Phi_{\zeta_0}(\zeta)$.

By conformal invariance $\phi(z) = \Phi(\zeta)$ and combining this with Equations (8.47) ,(8.48), (8.49) & (8.51) gives the following expression for $\phi_{z_0}(z)$ in which we have neglected terms of too higher order for the elliptic model:

$$\phi_{z_0}(z) = \frac{A}{2\pi i}\left(\log f' + \frac{f''}{2f'}(z-z_0) + \frac{4f'''f' - 3f''^2}{24f'^2}(z-z_0)^2\right) + \frac{q}{2\pi i}\frac{4f'''f'-3f''^2}{24f'^2} \tag{8.52}$$

$$+\Phi_{\zeta_0}(\zeta_0) + \Phi'_{\zeta_0}(\zeta_0)f'(z-z_0) + \frac{\Phi'_{\zeta_0}(\zeta_0)f'' + \Phi''_{\zeta_0}(\zeta_0)f'^2}{2}(z-z_0)^2. \tag{8.53}$$

It follows that

$$\int \phi_{z_0}(z)\,dS = \frac{A^2}{2\pi i}\log f' + \frac{Aq}{2\pi i}\frac{4f'''f'-3f''^2}{12f'^2} + A\Phi_{\zeta_0}(\zeta_0) + \frac{q}{2}(\Phi'_{\zeta_0}(\zeta_0)f'' + \Phi''_{\zeta_0}(\zeta_0)f'^2) \tag{8.54}$$

which upon multiplication by a factor of $-\frac{\omega^2}{2}$ gives us the relation between the interaction Hamiltonians in the two geometries

$$H_{int}(z,q) = \hat{H}_{int}(\zeta(z),\hat{d},\hat{q}) + \mathrm{Re}\left(\frac{(\omega A)^2}{4\pi}\log(f') + \frac{\omega^2 Aq}{4\pi}\frac{4f'''f' - 3(f'')^2}{12(f')^2}\right). \tag{8.55}$$

All that then remains is to add on the self-interaction term to obtain the full Hamiltonian for the motion in the complicated geometry

$$H(z,q) = H_{int}(z,q) + H_{self}(q). \tag{8.56}$$

8.5.1 Flow around an island

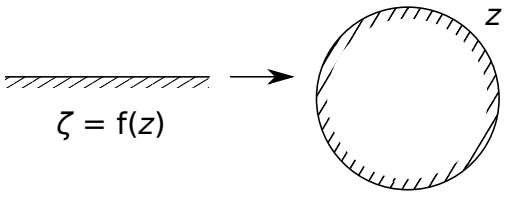

We illustrate this conformal mapping method by considering the evolution of a vortex patch around an island. In this case we can conformally transform back to a half-plane geometry via the following transformation:

$$z = \frac{\zeta + i}{\zeta - i}, \qquad \zeta = f(z) = i\frac{z+1}{z-1}. \tag{8.57}$$

The resulting dipole and quadrupole strengths in the simple geometry are then

$$\hat{d} = \frac{iq}{2}(\zeta - i)^3, \qquad \hat{q} = \frac{-q}{4}(\zeta - i)^4. \tag{8.58}$$

The interaction Hamiltonian in the simple geometry is much the same as that for motion above a coast (Equation (8.22)) but now with an added dipole contribution

$$\hat{H}_{int}(\zeta) = \frac{\omega^2}{4\pi} Re\left(A^2 \log(\zeta - \bar{\zeta}) + \frac{A(\hat{d} - \bar{\hat{d}})}{\zeta - \bar{\zeta}} - \frac{A(\hat{q} + \bar{\hat{q}})}{2(\zeta - \bar{\zeta})^2} \right). \tag{8.59}$$

Then applying the result of the earlier derivation (Equation (8.55)) we can calculate the interaction Hamiltonian in the original island geometry to be

$$H_{int} = \frac{\omega^2 A^2}{4\pi} \log(x^2 + y^2 - 1) - \frac{\omega^2 A}{4\pi} \frac{(x^2 - y^2)q_x + 2xyq_y}{(x^2 + y^2 - 1)^2}. \tag{8.60}$$

This Hamiltonian that we have just found corresponds to the case in which the island has a circulation equal and opposite to that of the vortex patch. This circulation is a constant of the motion (Kelvin's circulation theorem) and if we imagine that our vortex patch has been advected close to the island by some background flow then there is no reason to expect there to be any circulation around the island. The Hamiltonian for this no circulation case is easily found by placing a point vortex of opposite strength to the patch at the point in the ζ plane which is mapped to infinity ($\zeta = i$). The interaction Hamiltonian with this extra point vortex is still easily calculated and the result in the island geometry is

$$H_{int} = \frac{\omega^2 A^2}{4\pi} \log\left(1 - \frac{1}{x^2 + y^2}\right) - \frac{\omega^2 A}{4\pi} \frac{(x^2 - y^2)q_x + 2xyq_y}{(x^2 + y^2 - 1)^2} \frac{2x^2 + 2y^2 - 1}{(x^2 + y^2)^2}. \tag{8.61}$$

This zero-circulation Hamiltonian has a more rapid decay with distance from the island as we would expect.

As a consequence of the rotational symmetry of the island there is another constant of the motion, this is the angular impulse

$$\omega \int \mathbf{x} \cdot \mathbf{x} \, dS = \omega \left(A(x^2 + y^2) + \sqrt{q_x^2 + q_y^2 + \frac{A^4}{4\pi^2}} \right). \tag{8.62}$$

So, whilst the distance of the centroid to the island is able to move, the motion, like the case of a half-plane, is integrable.

An area for further investigation is what happens when we impose a background flow. Such a flow could cause the vortex patch to impact with the island and lead to the break up of the patch as observed in [15].

8.6 Motion around a pair of islands

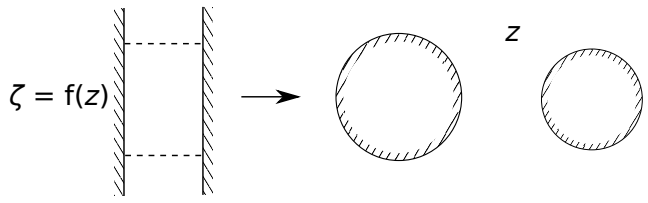

We're now in a position to consider one of the problems that we originally set out to consider: the motion of a vortex patch around a pair of islands. This problem was previously considered by Johnson and McDonald [8] for the case of a point vortex and they showed that the following conformal transformation

$$z = \frac{\sinh((\zeta+\beta)/2)}{\sinh((\zeta-\beta)/2)}, \qquad \zeta = f(z) = \log\left(\frac{\sinh((z+\beta)/2)}{\sinh((z-\beta)/2)}\right) \tag{8.63}$$

maps the $2\pi i$ periodic channel ($0 < \operatorname{Re}\zeta < \gamma$, $-\pi < \operatorname{Im}\zeta < \pi$) onto the exterior of two islands with the values of γ and β setting the relative sizes and separation of the two islands. The flow in this 'simple' geometry can be calculated via the method of images, where the required images are as shown in Figure 8.17. Johnson and McDonald show that for a point vortex in this geometry the resulting stream function is given by

$$\Phi(\zeta) = \frac{\kappa}{2\pi i}\log\left(\frac{\vartheta_1(i/2(\zeta-\zeta_0))}{\vartheta_1(i/2(\zeta+\bar{\zeta}_0))}\right) \tag{8.64}$$

where $\vartheta_1(\zeta)$ is the first Jacobi Theta function with nome $e^{-\gamma}$. Similar stream functions can be calculated for the dipole and quadrupole by taking the appropriate derivatives. For a dipole we get

$$\Phi(z) = \frac{-1}{2\pi i}\left[d\left(\frac{\mathcal{Z}(\pi)}{\pi}(z-z_0) + i\mathcal{Z}(i(z-z_0))\right) + \bar{d}\left(\frac{\mathcal{Z}(\pi)}{\pi}(z+\bar{z_0}) + i\mathcal{Z}(i(z+\bar{z_0}))\right)\right] \tag{8.65}$$

where $\mathcal{Z}(\zeta)$ is the Weierstrass zeta function with half periods π and γi, and for a quadrupole

$$\Phi(z) = \frac{1}{4\pi i}\left[q\left(\frac{\mathcal{Z}(\pi)}{\pi} + \wp(i(z-z_0))\right) - \bar{q}\left(\frac{\mathcal{Z}(\pi)}{\pi} + \wp(i(z+\bar{z_0}))\right)\right] \tag{8.66}$$

where $\wp(\zeta)$ is the Weierstrass elliptic function of the same half periods. From these functions it is relatively easy to construct the function Φ_{z_0} for the stream function due to the appropriate point vortex, dipole and quadrupole combination with the singularities at z_0 subtracted off. Using this we can construct the interaction Hamiltonian

$$\begin{aligned}\hat{H} =& \frac{\omega^2}{4\pi}\operatorname{Re}\left(A^2\log(\vartheta_1(\frac{i}{2}(\zeta+\bar{\zeta})) + A(d+\bar{d})\left(\frac{\mathcal{Z}(\pi)}{\pi}(\zeta+\bar{\zeta}) + i\mathcal{Z}(i(\zeta+\bar{\zeta}))\right)\right.\\ &+ \frac{A(q+\bar{q})}{2}\wp(i(\zeta+\bar{\zeta})) + \frac{A(\bar{q}-q)}{2}\frac{\mathcal{Z}(\pi)}{\pi}\\ &+ 2A^2\log\left(\frac{\vartheta_1(\frac{i}{2}(\zeta-\beta))}{\vartheta_1(\frac{i}{2}(\zeta+\beta))}\right) + 2Ad\left(-2\beta\frac{\mathcal{Z}(\pi)}{\pi} + i\mathcal{Z}(i(\zeta-\beta)) - i\mathcal{Z}(i(\zeta+\beta))\right)\\ &\left.+ Aq\big(\wp(i(\zeta-\beta)) - \wp(i(\zeta+\beta))\big)\right).\end{aligned} \tag{8.67}$$

Here, as with the case of a single island, we have placed a point vortex of opposite strength at the point that gets mapped to infinity ($\zeta = \beta$) to ensure that the circulation around both islands is zero.

Using the above Hamiltonian we were able to calculate some numerical solutions of an elliptic vortex patch travelling around a pair of islands; the path of the centroid in one such

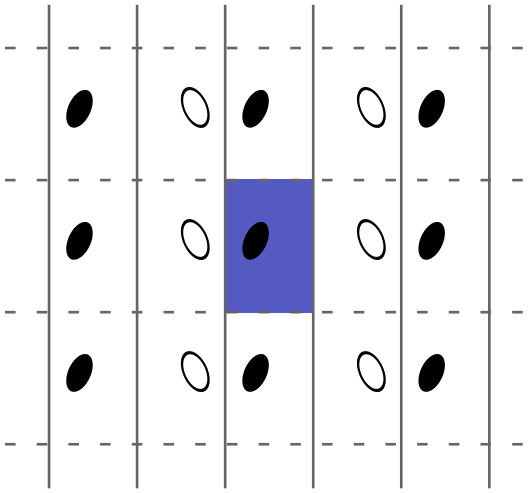

Figure 8.17: Image system for periodic strip. White regions of vorticity have opposite sign to the original patch.

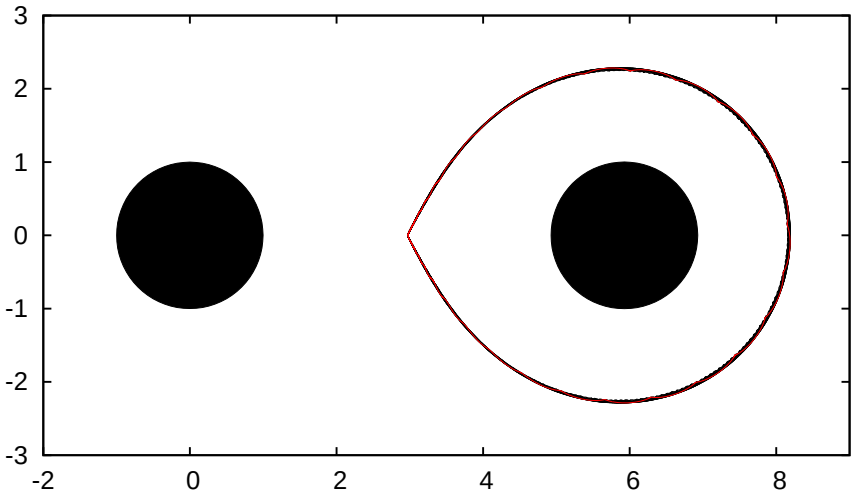

Figure 8.18: Motion of an initially circular patch around a pair of islands as represented by the position of its centroid. $O(10)$ orbits are shown with the first one in red.

simulation is shown in Figure 8.18. We were not able to find any solutions that flipped from going around one island to going around the other, a likely reason for this is that the adiabatic invariance that we found back in the quarter-plane problem is still at work here and consequently the motion is in some sense close to being integrable. We also found that, whilst this elliptic model is much faster than calculating the full solution would be, it is still quite slow to calculate due to the relatively large time taken to calculate the complicated Hamiltonian.

8.7 Conclusion

The elliptic moment model of Melander, Zabusky & Stysek provides a powerful method of analysing the interaction of ocean vortex patches with coastal boundaries, and appears to do a good job of predicting the motion even outside the regime where it is technically applicable. Under this simple model the problem of motion along a coast reduces to that of an elliptic patch in constant strain as analysed by Kida leading to three distinct types of motion depending on the distance of the centroid above the wall and the shape of the patch. The application of a periodic shear flow, as might arise from a background tidal flow, gives rise to chaotic behaviour which could play an important role in causing the break up of vortex patches.

On investigating more complicated geometries where we might expect to find chaotic behaviour we instead find the presence of an adiabatic invariant due to the separation of time scales between the rotation of the patch and the longer time scale on which the strain experience by the patch varies. In the case of motion in a quarter-plane the addition of a background flow was able to reduce this separation and produce chaotic, although unfortunately unphysical, behaviour.

We also demonstrated that, through the use of conformal mapping techniques, it is possible to calculate the motion of an elliptical vortex patch in more complicated geometries. This technique was applied to both the case of motion around a single island and motion around a pair of islands. In the former the motion was found to still be integrable and in the latter the probable presence of the adiabatic invariant meant that the expected chaotic flipping of which island the patch orbited was not observed to occur.

8.8 Future directions

There are a wide range of other problems involving the interaction of elliptic vortex patches with boundaries that we have the machinery to tackle. These include the problem of motion of a vortex patch past a gap in the coast line which was one of the original aims of this project that we ran out of time to investigate. Another possibility is looking at the interaction of a patch with an island in the presence of a background flow, this has been observed to break up actual vortex patches in the ocean. The adiabatic invariance observed could also be investigated further by looking at the motion of a patch above a coastline with more rapidly varying geometry.

8.9 Acknowledgements

I would like to thank Ted Johnson and Phil Morrison for proposing this project and for their continued support throughout the summer. Further thanks go to Fabian Waleffe and Rich Kerswell for two weeks of enlightening lectures, to Norm Lebovitz and Phil Morrison for all their organisational work, and to the other Fellows for making it a thoroughly enjoyable ten weeks.

Bibliography

[1] G. Batchelor, *An introduction to fluid dynamics*, Cambridge mathematical library, Cambridge University Press, 1967.

[2] M. V. Berry, *Regular and Irregular Motion*, in Topics in Nonlinear Mechanics, S. Jorna, ed., 1978, pp. 16–120.

[3] T. E. Dowling and A. P. Ingersoll, *Jupiter's Great Red SPOT as a shallow water system*, J. Atmos. Sci., 46 (1989), pp. 3256–3278.

[4] D. G. Dritschel, *The stability of elliptical vortices in an external straining flow*, J. Fluid Mech., 210 (1990), pp. 223–261.

[5] D. Goldman and R. J. McCann, *Chaotic response of the 2d semi-geostrophic and 3d quasi-geostrophic equations to gentle periodic forcing*, Nonlinearity, 21 (2008), p. 1455.

[6] J. Henrard, *The adiabatic invariant in classical dynamics*, in Dynamics Reported, Springer Verlag, 1993, pp. 117–235.

[7] E. R. Johnson and N. R. McDonald, *The motion of a vortex near a gap in a wall*, Phys. Fluids, 16 (2004), pp. 462–469.

[8] ——, *The motion of a vortex near two circular cylinders*, Proc. Roy. Soc. London, 460 (2004), pp. 939–954.

[9] S. Kida, *Motion of an elliptic vortex in a uniform shear flow*, J. Phys. Soc. Japan, 50 (1981), pp. 3517–3520.

[10] G. Kirchhoff, *Vorlesungen über mathematische Physik.*, Mechanik, Leipzig: Teubner, 1876.

[11] A. E. H. Love, *On the stability of certain vortex motions*, Proc. London Math. Soc., s1-25 (1893), pp. 18–43.

[12] S. P. Meacham, P. J. Morrison, and G. R. Flierl, *Hamiltonian moment reduction for describing vortices in shear*, Phys. Fluids, 9 (1997), pp. 2310–2328.

[13] M. V. Melander, N. J. Zabusky, and A. S. Styczek, *A moment model for vortex interactions of the two-dimensional Euler equations. I - Computational validation of a Hamiltonian elliptical representation*, J. Fluid Mech., 167 (1986), pp. 95–115.

[14] P. L. Richardson, R. E. Cheney, and L. V. Worthington, *A Census of Gulf Stream Rings, Spring 1975*, J. Geophys. Res., 83 (1978), pp. 6136–6144.

[15] P. L. Richardson and A. Tychensky, *Meddy trajectories in the Canary Basin measured during the SEMAPHORE experiment, 1993-1995*, J. Geophys. Res., 1032 (1998), pp. 25029–25046.

[16] N. J. Zabusky, M. H. Hughes, and K. V. Roberts, *Contour dynamics for the euler equations in two dimensions*, J. Comput. Phys., 135 (1997), pp. 220–226.

Project 9

On Brownian Motion in a Fluid with a Plane Boundary

Chao Ma

University of Colorado

9.1 Introduction

Brownian motion was discovered by the botanist Robert Brown in 1827. While studying pollen grains suspended in water under a microscope, Brown observed that particles ejected from the pollen grains executed a jittery motion. After he replaced the pollen grains by inorganic matter, he was able to rule out that the motion was life-related, although its origin was yet to be explained.

In 1905, Einstein[5] explained Brownian motion as the result of bombardment of fluid molecules on the suspended particle. There are two main parts to his paper. First, he finds the following relation of the diffusion coefficient to other physical quantities:

$$D = \frac{k_B T}{6\pi\eta a} = \frac{k_B T}{\zeta},$$

where D is diffusion coefficient, k_B is Boltzmann's constant, a is radius of the particle, η is the dynamic viscosity, and $\zeta = 6\pi\eta a$ is the Stokes drag, which was first calculated by Stokes. Then, Einstein related the diffusion coefficient to the mean square displacement of the particle, $\langle x^2 \rangle = 2Dt$, where D is diffusion coefficient. Specifically, Einstein found that the density of the Brownian particles $f(x,t)$ satisfies the heat equation

$$\frac{\partial f}{\partial t} = D\frac{\partial^2 f}{\partial x^2},$$

and after solving the heat equation, he got that the mean square displacement is proportional to time. However, Einstein also noticed when time is short (in ballistic time regime), the mean square displacement should be different, since during very short times individual particles become significant.

In 1908, Langevin[12] used another point of view, he assumed the particles satisfy the Newtonian equation:

$$m\frac{d\mathbf{v}(t)}{dt} = -\zeta\mathbf{v}(t) + \mathbf{X}\,,$$

where $\zeta = 6\pi\mu a$ is the Stokes drag and $\mathbf{X}$ is a random force describing the bombardment by fluid particles. Using this equation, with the assumption that $\langle\mathbf{X}(t)\mathbf{x}(t)\rangle = 0$, $\mathbf{x}(t)$ being the position of particle, Langevin was able to derive the same relation that Einstein derived, i.e.

$$\langle x^2\rangle = \frac{2k_BT}{\zeta}t\,.$$

This is valid when t is large, but when t is small, a particle's inertia becomes significant. In this inertia dominated regime, termed the ballistic regime, the particle's motion is highly correlated. Langevin's approach also applies to the ballistic regime. In the classical Langevin theory, it is assumed that the autocorrelation function of the random force satisfies

$$\langle X(t_1)X(t_2)\rangle = 2\zeta k_BT\delta(t_1 - t_2)\,.$$

This means that the random force acting on the Brownian particle is memoryless. From the Langevin equation, it can be shown that the velocity autocorrelation function has exponentially decay,

$$\Phi(t) := \langle v(t_0)v(t_0+t)\rangle = \langle v(t_0)^2\rangle e^{-\frac{\zeta t}{m}}\,.$$

However, in the 1960s, the famous "tails" of the velocity autocorrelation function were discovered[14]. It was experimentally obeserved that the velocity autocorrelation does not exponential decay, but rather has an algebraic decay. Then, Langevin's approach was generalized to give a more accurate description. Instead of using the δ correlated random force, it was figured out that one should include the memory effect of the fluid.

The long time behavior of velocity autocorrelation function (VACF) and mean square displacement (MSD) have been observed by both experiment and computer simulation for many years. The ballistic regime (where the inertia of Brownian particle will dominate) is hard to observe in experiments, since it requires the position detector equipment to have extraordinary spatial and temporal resolution. Only very recently has Brownian motion in the ballistic regime been observed[9], and the experiment showed excellent agreement with theoretical predictions[4].

There are two main steps that have been taken to derive the VACF and MSD. A deterministic part where one calculates the response function $\zeta(\omega)$ corresponding to a specific frequency. This step is done by solving the linearized Navier-Stokes equations analytically. The second step is a statistical part, where one uses the fluctuation-dissipation theorem to relate correlation functions to the corresponding response functions. The fluctuation-dissipation theorem is a main tool in statistical mechanics to predict behavior of non-equilibrium thermodynamic systems, as widely observed in nature: for example, the Brownian motion seen in the irregular oscillation of a suspended mirror, the thermal noise in resistor, etc.

An important theorem of Nyquist was the first theorem in this area to be proved (to my knowledge). The idea was discovered by J. Johnson and then proved by H. Nyquist. For any network, the square of the voltage during the frequency range $(\nu, \nu + d\nu)$ is given by:

$$E_\nu^2\, d\nu = 4R_\nu k_BT\, d\nu$$

where E_ν is the electromotive force and R_ν is the real part of the impedance of the network. Using this result, Nyquist proved the following formula that was given in Johnson's paper:

$$I^2 = \frac{2}{\pi} k_B T \int_0^\infty R(\omega)|Y(\omega)|\, d\omega$$

where $Y(\omega)$ is the transfer admittance of any network from the member in which electromotive force in question originates to a member in which the resulting current is measured.

For Brownian motion, the random impact of surrounding molecules has two kinds of effects: first, the molecules act as a random force and second, they give rise to the frictional force. This means the frictional force and random force must be related. This is the essence of the so-called fluctuation-dissipation theorem, which in formulas is given by

$$\zeta(\omega) = \frac{1}{k_B T} \int_0^\infty \langle X(t_0) X(t_0 + t) \rangle e^{i\omega t}\, dt \tag{9.1.1}$$

$$\mu(\omega) = \frac{1}{k_B T} \int_0^\infty \langle v(t_0) v(t_0 + t) \rangle e^{i\omega t}\, dt\,, \tag{9.1.2}$$

where $\zeta(\omega)$ is the response function or friction constant for particular fluid system and $\mu(\omega)$, the admittance, is given by

$$\mu(\omega) = \frac{1}{\zeta(\omega) - im\omega}\,.$$

If we let $s = -i\omega$, then above formulas are just Laplace transformations. Thus, if we want to calculate the autocorrelation function for Brownian particles, we can first calculate the friction constant of the corresponding system, and then use the fluctuation-dissipation theorem to get the final result.

There are several papers[7, 11] that describe the fluctuation-dissipation theorem. Given this theorem, we only need to calculate the response function by solving Navier-Stokes equations. Many people contributed to this area to develop a general theory. The case where Brownian particles are in a viscous, compressible fluid filling the whole of space $\mathbb{R}^3$ has been thoroughly solved[3],[17]. In [4] and [15], the asymptotic behavior of the velocity autocorrelation function(VACF), mean square displacement(MSD), etc. up to higher orders have also been calculated. In this paper, we consider the effect of a plane boundary, i.e., where the fluid occupies only half space, and compute the velocity autocorrelation function for this case.

9.2 Behavior of Brownian particles in different time regimes

The behavior of the VACF and the MSD are different in the different time regimes. On the very short time scale, the inertia of the Brownian particle dominates, while on the longer time scale, the hydrodynamical memory effect plays an important role. There are several characteristic times: $t_p = m/\zeta$, $t_\nu = a^2/\nu$, and $t_c = a/c$, where m is the mass, a is the radius of the Brownian particle, $\zeta = 6\pi\eta a$ is again the Stokes drag, and c is the speed of sound in the fluid. The case $t < t_p$ is the ballistic regime, where as noted above, the inertia of the particle is significant. The case $t \gg t_p$ is the diffusive time regime. When $t \simeq t_\nu$ hydrodynamical effects need to be taken into account, and when $t < t_c$ one must consider

compressibility of the fluid. The two graphs of Figs. 9.1 and 9.2 show experiment data from [9]. The first graph is the MSD vs. time, while the second one is the VACF vs. time. Evidently, the experiment data fits the theory[4] very well. It worth noting that the model of [4] only considers incompressible fluid dynamics. So if we want to test the behavior of Brownian particle into the compressible regime, we need to both enhance the accuracy of the detector into the nanosecond regime but alter the theory as well.

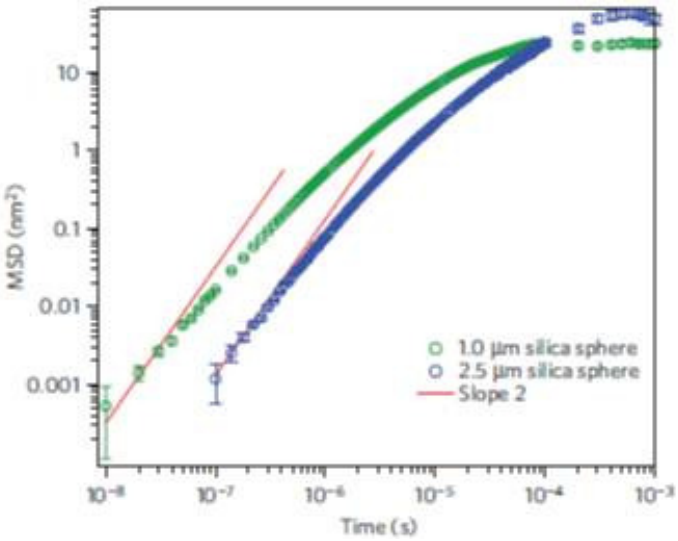

Figure 9.1: The mean square displacement (MSD) vs. time from the experiments of Ref. [9]

The mean square displacement in the ballistic regime is given by $\langle x^2 \rangle = t^2 k_B T/m^*$. Here $m^* = m + \frac{1}{2}M$ is the virtual mass of the body and $M = \rho_f 4\pi a^3/3$ is the mass of the displaced fluid. In ballistic time regime, the velocity autocorrelation function is given by $\langle v^2 \rangle = k_B T/m^*$, a result that seems inconsistent with the equipartition theorem $m\langle v^2 \rangle = k_B T$ when $t \to 0$. This discrepancy is explained as the effect of compressibility. When t is smaller than the characteristic time $t \leq t_c = a/c$, the fluid cannot be regarded as incompressible and, in this case, the particle is decoupled from fluid and the effective mass is m. In Zwanzig and Bixon's paper[18], they describe the decrease from $k_B T/m$ to $k_B T/m^*$.

9.3 Brownian Motion in whole space $\mathbb{R}^3$

We consider a spherical particle oscillating in a fluid with velocity $\mathbf{u}_\omega = \mathbf{u}e^{-i\omega t}$. To find the mean square displacement and autocorrelation function, we first to calculate the force $\mathbf{F}(\omega)$ of the fluid acting on the sphere as $\mathbf{F}(\omega) = -\zeta(\omega)\mathbf{u}_\omega$. This is done by solving the linearized Navier-Stokes equations. After we obtain the solution, we use the fluctuation-dissipation theorem to find the MSD and the VACF of the particle. We first consider the case where the fluid fills all of $\mathbb{R}^3$, and then use the result to find an approximate solution when the fluid is bounded by a plane and occupies half space.

To solve the NS equations in domain $\mathbb{R}^3$, we can fix the sphere to the origin for simplicity.

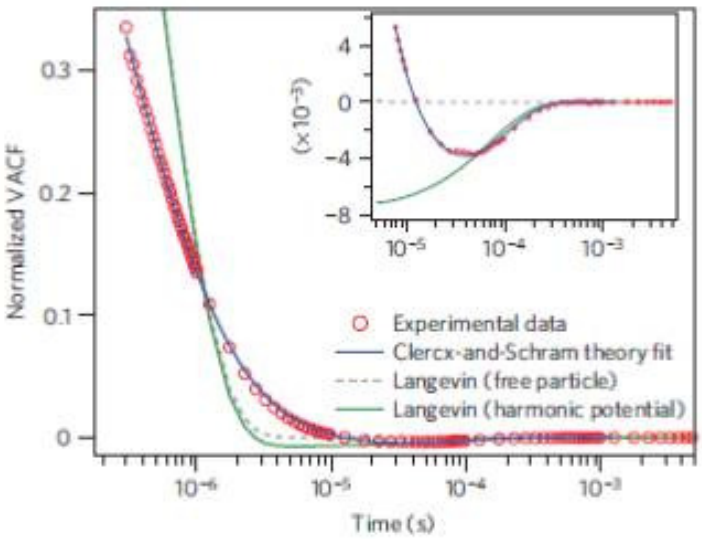

Figure 9.2: The velocity autocorrellation function (VACF) vs. time from the experiments of Ref. [9]

Then, in this frame, the velocity field of the fluid $\tilde{\mathbf{v}}$ changes with time, and satisfies the non-slip boundary condition at the surface of the sphere, i.e., $\tilde{\mathbf{v}} = 0$ on the sphere and $\tilde{\mathbf{v}} = -\mathbf{u}e^{-i\omega t}$ at infinity. Next we decompose the velocity field as $\tilde{\mathbf{v}} = \mathbf{v} - \mathbf{u}e^{-i\omega t}$, where $\mathbf{v}$ does not oscillate with time, and apply the boundary condition $\mathbf{v} = \mathbf{u}e^{-i\omega t}$ at the sphere boundary (non-slip) and $\mathbf{v} = \mathbf{u}e^{-i\omega t}$ at infinity. For fluid motion $\mathbf{v}$ satisfies the following Navier-Stokes (NS) equations:

$$\rho\left(\frac{\partial \mathbf{v}}{\partial t} + (\mathbf{v}\cdot\nabla)\mathbf{v}\right) = -\nabla p + \eta\nabla^2\mathbf{v} + \left(\frac{\eta}{3} + \mu\right)\nabla(\nabla\cdot\mathbf{v}) \tag{9.3.1}$$

$$\frac{\partial \rho}{\partial t} + \nabla\cdot(\rho\mathbf{v}) = 0\,, \tag{9.3.2}$$

with boundary condition $\mathbf{v} = \mathbf{u}e^{-i\omega t}$ at the sphere and $\mathbf{v} = 0$ at infinity. For Brownian motion, the Reynolds is number is very small, so we can consider the linearized NS equations instead

$$\rho_0\frac{\partial \mathbf{v}}{\partial t} = -\nabla p + \eta\nabla^2\mathbf{v} + \left(\frac{\eta}{3} + \mu\right)\nabla(\nabla\cdot\mathbf{v}) \tag{9.3.3}$$

$$\frac{\partial \rho}{\partial t} = -\rho_0\nabla\cdot\mathbf{v}\,, \tag{9.3.4}$$

with the same boundary conditions as above. After solving these equations, we can calculate the drag of the fluid acting on the sphere for arbitrary motion by Fourier decomposing as

$$\mathbf{v}(t) = \int_{-\infty}^{\infty}\mathbf{u}_\omega e^{-i\omega t}\,d\omega \qquad \text{and} \qquad \mathbf{F}(t) = \int_{-\infty}^{\infty}\mathbf{F}_\omega e^{-i\omega t}\,d\omega\,.$$

Because of the linearity assumption, the Fourier component of force is proportional to Fourier component of velocity, $\mathbf{F}_\omega = -\zeta(\omega)\mathbf{u}_\omega$. This means we can find the drag for arbitrary motion if we know each Fourier component.

Now suppose $\mathbf{v}(x,y,z,t) = \mathbf{v}_\omega(x,y,z)e^{-i\omega t}$. To avoid clutter in what follows, we denote $\mathbf{v}_\omega$ by $\mathbf{v}$, and similarly for other quantities. Thus we have

$$\begin{aligned} -i\omega\rho_0\mathbf{v} &= -\nabla p + \eta\nabla^2\mathbf{v} + (\frac{1}{3}\eta + \mu)\nabla(\nabla\cdot\mathbf{v}) && (9.3.5)\\ -i\omega\rho &= -\rho_0\nabla\cdot\mathbf{v}\,, && (9.3.6)\end{aligned}$$

with the pressure and density related by $\nabla P = C^2\nabla\rho$. Combining (9.3.5) and (9.3.6) gives

$$\omega^2\mathbf{v} + C_l^2\nabla\nabla\cdot\mathbf{v} - C_t^2\nabla\times\nabla\times\mathbf{v} = 0\,, \tag{9.3.7}$$

where $C_l^2 = C^2 - i\omega\nu_l$, $C_t^2 = -i\omega\nu_t$, and $\nu_t = \eta/\rho_0$, $\nu_l = (4\eta/3+\mu)/\rho_0$. The boundary conditions are now given by $\mathbf{v} = \mathbf{u}$ at the sphere and $\mathbf{v} = \mathbf{0}$ at infinity, where $\mathbf{u}e^{-i\omega t}$ is the velocity of the sphere in lab frame. Next we decompose as $\mathbf{v} = \nabla\phi + \nabla\times\mathbf{A}$, and obtain the following equations:

$$\nabla^2\phi + \beta^2\phi = 0 \qquad \text{and} \qquad \nabla\times\nabla\times\mathbf{A} - \alpha^2\mathbf{A} = 0\,, \tag{9.3.8}$$

where $\alpha^2 = i\omega\rho_0/\eta$, $\beta^2 = \omega^2/C_l^2$, and boundary condition $\nabla\phi + \nabla\times\mathbf{A} = \mathbf{u}$ on the sphere. The exact solution of this problem is given in [3]:

$$\begin{aligned} v_r &= \left[2A\left(-\frac{1}{r^3} + \frac{i\alpha}{r^2}\right)e^{i\alpha r} + B\left(-\frac{2}{r^3} + \frac{2i\beta}{r^2} + \frac{\beta^2}{r}\right)e^{i\beta r}\right]u\cos\theta && (9.3.9)\\ v_\theta &= \left[A\left(-\frac{1}{r^3} + \frac{i\alpha}{r^2} + \frac{\alpha^2}{r}\right)e^{i\alpha r} + B\left(-\frac{1}{r^3} + \frac{i\beta}{r^2}\right)e^{i\beta r}\right]u\sin\theta && (9.3.10)\end{aligned}$$

where $x = i\alpha a$, $y = i\beta a$, $\Delta = 2x^2(3-3y+y^2) + y^2(3-3x+x^2)$,

$$P = \frac{3}{\Delta}(3-3y+y^2)\,, \qquad Q = -\frac{3}{\Delta}(3-3x+x^2)$$

and

$$A = Pa^3e^{-i\alpha a}\,, \qquad B = Qa^3e^{-i\beta a}\,.$$

The force of fluid acting on the sphere is given by integrating as follows:

$$\begin{aligned} \mathbf{F} &= \oint da\big[-p\cos\theta + 2\eta e_{rr}\cos\theta - 2\eta e_{r\theta}\sin\theta + (\mu - 2\eta/3)(\nabla\cdot\mathbf{v})\cos\theta\big]\\ &= \oint da\big[(\mu - 2\eta/3 + iC^2\rho_0/\omega)(\nabla\cdot\mathbf{v})\cos\theta + 2\eta e_{rr}\cos\theta - 2\eta e_{r\theta}\sin\theta\big]\\ &= 4\pi\eta a x^2\mathbf{u}\big[(1-y)Q + 2(x-1)P\big]/3\,. \end{aligned}$$

9.4 Brownian Motion in the Half Space $\mathbb{R}^+\times\mathbb{R}^2$

Now we suppose the sphere is moving in a fluid that occupies a region bounded by a plane. The perpendicular distance from the center of the sphere to the plane is given by l and the radius of the sphere is given by a. We assume the velocity of sphere is given by $\mathbf{u}e^{-i\omega t}$, as before, and again use the frame of sphere instead of the lab frame, i.e., we let sphere

be fixed and the fluid have velocity $\tilde{\mathbf{v}}$. Then again we decompose as $\tilde{\mathbf{v}} = \mathbf{v} - \mathbf{u}e^{-i\omega t}$. The linearized Navier-Stokes equations are the same as Eqs. (9.3.3) and (9.3.4) that we used for the $\mathbb{R}^3$ case, with boundary condition $\mathbf{v} = \mathbf{u}e^{-i\omega t}$ at the sphere and $\mathbf{v} = 0$ at the plane and at infinity.

If the sphere oscillates in an arbitrary direction, we lose symmetry, and the problem becomes hard to solve. So we first consider the case where sphere oscillates perpendicular to the plane. It seems that the most appropriate coordinate system to use to solve the above equations with the sphere-plane boundary conditions is the bipolar coordinate system. Actually, Brenner and several other authors [10],[2],[8] used bipolar coordinate to solve for the drag force when a sphere is approaching a plane. For their problem this was equivalent to solving a Laplace-type equation in bipolar coordinates. In our case, for simplicity, we consider an incompressible fluid, so we can use a Stokes stream function Ψ. Defining the Laplace-type operator L^2 as

$$L^2 = \frac{\sin^2\theta}{r}\left\{\frac{\partial}{\partial\xi}\left(\frac{1}{r}\frac{\partial}{\partial\xi}\right) + \frac{\partial}{\partial\theta}\left(\frac{1}{r}\frac{\partial}{\partial\theta}\right)\right\},$$

where (ξ, θ) are the bipolar coordinates with

$$r := \frac{c\sin\theta}{\cosh\xi - \cos\theta},$$

and $(0, \pm c)$ being the foci of the bipolar coordinate system. For our problem the stream function satisfies

$$L^4\Psi + \alpha^2 L^2\Psi = 0,$$

where $\alpha^2 = i\omega\rho_0/\eta$. Defining $\Pi = L^2\Psi$, we see Π satisfies a Helmholtz equation of the form

$$L^2\Pi + \alpha^2\Pi = 0.$$

If we let $\Pi = f \cdot \sqrt{r}$, then we can simplify this equation as follows:

$$\frac{\partial^2 f}{\partial\xi^2} + \frac{\partial^2 f}{\partial\theta^2} - \frac{3}{4\sin^2\theta}f + \frac{\alpha^2 r^2}{\sin^2\theta}f = 0.$$

Unfortunately, in bipolar coordinate this kind of Helmholtz equation is not separable[13]. So instead, we resort to approximation.

Our approximation is based on the image method[8]. We first use this method to obtain an approximate solution and then use the fluctuation-dissipation theorem to calculate the VACF for the Brownian particle. As we will see later on, we don't need to restrict to the incompressible case or to perpendicular oscillation. However, the image method of approximation makes the velocity field only satisfy the Neumann boundary condition at the plane. So we have to assume slip boundary condition on the plane instead of the more physical no-slip boundary condition. Using the image method, we can find approximate solution up to some order of $\frac{a}{l}$, which will be a good approximation if the distance of the sphere to the plane l is much larger than radius of the sphere a. Suppose the vector field that satisfies equations (9.3.9) and (9.3.10) is $\mathbf{v}_1$, and $\mathbf{v}_2$ is the image velocity field of $\mathbf{v}_1$ obtained by reflecting through the plane (imagining the plane as a mirror). Then, suppose

$\mathbf{v}_3$ is the velocity field satisfy $\mathbf{v}_3 = -\mathbf{v}_2$ at the sphere and vanishing at infinity, $\mathbf{v}_4$ is image velocity field of $\mathbf{v}_3$, etc. We suppose that $\mathbf{v} = \mathbf{v}_1 + \mathbf{v}_2 + \ldots$ would be the actual solution (with Neumann boundary condition). However, even with this assumption the $\mathbf{v}_i, i = 3, 5, \ldots$ are not easy to obtain. So, instead we seek $\mathbf{v}_3 = -\mathbf{v}_2(2l, \gamma)$ at the sphere, where γ depends on the direction of oscillation of the sphere. Solving for $\mathbf{v}_3$ is the same as solving for $\mathbf{v}_1$, so this simplifies matters. Finally, we suppose that summation of $\mathbf{v}_i$ will converge to actual solution, but this eventually needs to be shown.

In the following, we only consider $\mathbf{v} = \mathbf{v}_1 + \mathbf{v}_2 + \mathbf{v}_3 + \mathbf{v}_4$, which will be a good approximation up to order $O(a/l)$ or $O((a/l)^3)$, depending on whether the frequency is high or low. Let $\mathbf{F}_i$ be the drag force of $\mathbf{v}_i$ acting on sphere, and suppose the angle between the normal component of plane and the velocity of sphere is γ. We calculate the drag force of $\mathbf{v}$ in two cases: first, when the sphere oscillates perpendicular to the plane surface of fluid, i.e., $\gamma = 0$, and then when the sphere oscillates parallel to the plane, when $\gamma = \pi/2$. The general case is a linear combination of the two. Notice that $|\mathbf{F}_2|/|\mathbf{F}_3| = O(a/l)$ and $\mathbf{F}_4$ is even smaller than $\mathbf{F}_2$; therefore, we can just consider the contributions of $\mathbf{F}_1$ and $\mathbf{F}_3$, i.e.,

$$\mathbf{F} \simeq \mathbf{F}_1 + \mathbf{F}_3 \,.$$

The drag force $\mathbf{F}_1$ was given in the previous section as

$$\mathbf{F}_1 = -\zeta(\omega)\mathbf{u}$$

where

$$\zeta(\omega) := -4\pi\eta a x^2 \big[(1-y)Q + 2(x-1)P\big]/3 \,.$$

So, to next order

$$\mathbf{F} \simeq \mathbf{F}_1 + \mathbf{F}_3 = -\zeta(\omega)\mathbf{u} + \zeta(\omega)\mathbf{v}_2(2l, \gamma) \,.$$

When the sphere is moving perpendicular to plane

$$\mathbf{v}_2(2l, 0) = -v_r(2l, 0)\,\frac{\mathbf{u}}{|\mathbf{u}|} \,,$$

while when the sphere is moving parallel to plane

$$\mathbf{v}_2(2l, \pi/2) = v_\theta(2l, \pi/2)\,\frac{\mathbf{u}}{|\mathbf{u}|} \,.$$

For the case of arbitrary motion, supposing the angle between normal component of plane and the velocity of sphere is γ, we obtain

$$\mathbf{v}_2(2l, \gamma) = -\mathbf{n}\, v_r(2l, 0) u \cos\gamma + \mathbf{t}\, v_\theta(2l, \pi/2) u \sin\gamma \,,$$

where $\mathbf{n}$ and $\mathbf{t}$ are unit vectors normal and tangent to the plane, respectively.

Although in principle, we can use the fluctuation-dissipation theorem to find the VACF, the complicated formula of the response function ζ makes it hard to find exact an expression for the VACF. So, we simplify the response function by considering high frequency and low frequency regimes. Let $s = -i\omega$. Define $t_\nu = a^2\rho_0/\eta, t_{\nu'} = a^2\rho_0/(4\eta/3 + \mu), t_c = a/C$ to be three characteristic time scales. In order for $\sqrt{s}$ to make sense, we place a branch

cut along negative real axis, making the square root well defined. Below we make several simplifications, the reasons for which will become clear later.

Low Frequency Case, $s << 1$:

$$\begin{aligned}
x^2 &= -\alpha^2 a^2 = st_\nu\,, \qquad x = -\sqrt{st_\nu} \\
y^2 &= \frac{s^2 t_c^2}{1 + s\left(\frac{t_c}{t_{\nu'}}\right) t_c} \simeq s^2 t_c^2 \left(1 - s\left(t_c/t_{\nu'}\right) t_c\right) \quad \Rightarrow \quad y \simeq -t_c s \\
\triangle &= 2x^2(3 - 3y + y^2) + y^2(3 - 3x + x^2) \simeq 6st_\nu \\
P &\simeq (3 + 3st_c + s^2 t_c^2)/2st_\nu\,, \qquad Q \simeq -(3 + 3\sqrt{st_\nu} + st_\nu)/2st_\nu \\
&\qquad\qquad \zeta(s) \simeq 6\pi\eta a(1 + \sqrt{st_\nu})
\end{aligned}$$

$$\begin{aligned}
v_r(2\theta, 0) &\simeq \left[-\frac{2P}{(2l)^3}\, a^3 e^{i\alpha(2l-a)} - \frac{2Q}{(2l)^3}\, a^3 e^{i\beta(2l-a)}\right] u \\
&\simeq -\frac{2}{8}\left(\frac{a}{l}\right)^3 \left[\left(\frac{3}{2st_\nu} + \frac{3t_c}{2t_\nu}\right) - \left(\frac{3}{2st_\nu} + \frac{3}{2\sqrt{st_\nu}}\right)\right] u \\
&\simeq \frac{3}{8}\left(\frac{a}{l}\right)^3 \frac{u}{\sqrt{st_\nu}} \\
v_\theta(2\theta, \pi/2) &\simeq \left[-\frac{P}{(2l)^3}\, a^3 e^{i\alpha(2l-a)} - \frac{Q}{(2l)^3}\, a^3 e^{i\beta(2l-a)}\right] u \\
&\simeq \frac{3}{16}\left(\frac{a}{l}\right)^3 \frac{u}{\sqrt{st_\nu}}\,.
\end{aligned}$$

High Frequency Case, $s >> 1$:

$$\begin{aligned}
x &= -\sqrt{s\, t_\nu}\,, \qquad y \simeq -\sqrt{st_{\nu'}}\,, \qquad \Delta \simeq 3st_\nu st_{\nu'} \\
P &\simeq \frac{3s^{-3/2}}{t_\nu \sqrt{t_{\nu'}}} + \frac{s^{-1}}{t_\nu}\,, \qquad Q \simeq -\frac{3\, s^{-3/2}}{t_{\nu'}\sqrt{t_\nu}} - \frac{s^{-1}}{t_{\nu'}} \\
&\qquad \zeta(s) \simeq 2\zeta\left[(t_\nu/t_{\nu'} + 2) + (\sqrt{t_\nu/t_{\nu'}} + 2)\sqrt{st_\nu}\right]/9
\end{aligned}$$

$$\begin{aligned}
v_r(2l, 0) &\simeq \left[-\frac{1}{2}\left(\frac{a}{l}\right)^2 e^{-\sqrt{st_\nu}\,2l/a} \frac{1}{\sqrt{st_\nu}} + \frac{a}{2l} e^{-\sqrt{st_{\nu'}}\,2l/a}\right] u \\
v_\theta(2l, \frac{\pi}{2}) &\simeq \left[-\frac{a}{2l} e^{-\sqrt{st_\nu}\,2l/a} + \frac{1}{4}\left(\frac{a}{l}\right)^2 e^{-\sqrt{st_{\nu'}}\,\frac{2l}{a}} \frac{1}{\sqrt{st_{\nu'}}}\right] u\,.
\end{aligned}$$

Now we use the above expressions to calculate the velocity autocorrelation function, which is given by

$$\begin{aligned}
\Phi(t) &= \langle v_i(0) v_i(t)\rangle = \frac{k_B T}{\pi} \int_{-\infty}^{\infty} d\omega e^{-i\omega t} Re \frac{1}{-i\omega m + (1 + c)\zeta(\omega)} \qquad (9.4.1) \\
&= \frac{k_B T}{2\pi i} \int_{\epsilon - i\infty}^{\epsilon + i\infty} ds\, e^{st} \frac{1}{sm + (1 + c)\zeta(s)}\,, \qquad (9.4.2)
\end{aligned}$$

where $s = -i\omega$ and c is a correction term that depends on γ.

Let us first calculate the velocity autocorrelation in the low frequency case, $s << 1$, without the plane ($c = 0$), which will we will use to compare with the plane case. We obtain

$$\frac{\Phi(t)}{k_BT} \simeq \mathcal{L}^{-1}\left(\frac{1}{6\pi\eta a + 6\pi\eta a\sqrt{t_\nu s}}\right) \tag{9.4.3}$$

$$= \frac{1}{6\pi\eta a\sqrt{t_\nu}}\mathcal{L}^{-1}\left(\frac{1}{\sqrt{s} + 1/\sqrt{t_\nu}}\right). \tag{9.4.4}$$

From any table of inverse Laplace transforms, we obtain

$$\mathcal{L}^{-1}\left(\frac{1}{\sqrt{s} + a}\right) = \frac{1}{\sqrt{\pi t}} - ae^{a^2t}\mathrm{erfc}(a\sqrt{t}) \tag{9.4.5}$$

where the erfc function is defined by

$$\mathrm{erfc}(x) = \frac{e^{-x^2}}{x\sqrt{\pi}}\sum_{n=0}^{\infty}(-1)^n\frac{(2n-1)!!}{(2x^2)^n}. \tag{9.4.6}$$

From (9.4.5) we find for the case without the plane, that the asymptotic behavior of velocity autocorrelation as $t \to \infty$ is given by

$$\Phi(t) = \frac{k_BT}{6\pi\eta a\sqrt{t_\nu}}\frac{t_\nu}{2\sqrt{\pi}}t^{-\frac{3}{2}} = \frac{k_BT}{\zeta}\frac{\sqrt{t_\nu}}{2\sqrt{\pi}}\,t^{-\frac{3}{2}}, \tag{9.4.7}$$

where $\zeta := 6\pi\eta a$, for simplicity.

Now, when the fluid is bounded by the plane, I couldn't find a formula in any Laplace inverse transformation table. Thus, we needed to directly calculate it. The following formula will be useful for the case $s << 1$. Suppose $R(\sqrt{s}) = a_0 + a_1\sqrt{s} + a_2s + a_3s^{3/2}$. When t is large, we obtain

$$\Phi(t) = \frac{k_BT}{2\pi i}\int_{\epsilon-i\infty}^{\epsilon+i\infty} ds\, e^{st}\frac{\sqrt{s}}{R(\sqrt{s})} = -\frac{k_BT}{2a_0\sqrt{\pi}}\,t^{-3/2}. \tag{9.4.8}$$

The above follows because

$$\begin{aligned}
\Phi(t) &= \frac{k_BT}{2\pi i}\int_{\epsilon-i\infty}^{\epsilon+i\infty} ds\, e^{st}\frac{\sqrt{s}}{R(\sqrt{s})} \\
&\simeq -\frac{k_BT}{2\pi i}\int_0^\infty dr\,\left[\frac{e^{-tr}\sqrt{r}i}{R(\sqrt{r}i)} + \frac{e^{-tr}\sqrt{r}i}{R(-\sqrt{r}i)}\right] \\
&= -\frac{2k_BT}{\pi}\int_0^\infty d(s/\sqrt{t})\,\frac{e^{-s^2}s^2/t(a_0 - a_2s^2/t)}{(a_0 - a_2s^2/t)^2 + (a_3s^3/t^{3/2} - a_1s/\sqrt{t})^2} \\
&\simeq -\frac{2k_BT}{\pi a_0}t^{-3/2}\int_0^\infty ds\, e^{-s^2}s^2 \\
&= -\frac{k_BT}{2a_0\sqrt{\pi}}\,t^{-3/2}.
\end{aligned}$$

We can switch the order of the limit and the integration in above calculation as long as $a_0 \neq 0$ and $a_0/a_2 \neq a_1/a_3$. The physics of the problem indicates that Φ should approach zero when $t \to \infty$, which means the poles of above integrand are located in the region $Re(s) < 0$. These poles will contribute to exponential decay to $\Phi(t)$, which is much smaller than the contribution from the branch point $s = 0$, which gives algebraic decay. Thus, if we want to know the long time behavior of $\Phi(t)$, we can assume $s << 1$ to simplify our calculation, because the contributions from a_1, a_2, a_3 are much smaller than that from a_0.

When $a_0 = 0$, which corresponds to no plane case ($l = \infty$), we cannot switch the order of limit and integration. We should first set $a_0 = 0$ in the integral, then take limit in t, giving

$$\Phi(t) = \frac{k_B T}{2\sqrt{\pi}} \frac{a_2}{a_1^2} t^{-\frac{3}{2}} . \tag{9.4.9}$$

Notice, by plugging in the a_i, this gives the same formula as we derived above, $\Phi(t) = k_B T \sqrt{t_\nu}\, t^{-3/2}/(2\zeta\sqrt{\pi})$.

Now, consider the long time behavior of $\Phi(t)$ when there is a plane and $\gamma = 0$, i.e., the sphere is moving perpendicular to the plane. Again letting $\zeta = 6\pi\eta a$, we have

$$\begin{aligned} \Phi(t) &= k_B T \mathcal{L}^{-1} \left(\frac{1}{ms + \zeta \left[\sqrt{st_\nu} + (1 - 3(a/l)^3/8) - 3(a/l)^3/(8\sqrt{st_\nu}) \right]} \right) \\ &= \frac{k_B T}{2\pi i} \int_\Gamma ds \, \frac{e^{ts}\sqrt{s}}{ms^{3/2} + \zeta\sqrt{t_\nu} s + \zeta \left[1 - 3(a/l)^3/8\right]\sqrt{s} - 3\zeta(a/l)^3/(8\sqrt{t_\nu})} , \end{aligned}$$

where Γ is a contour from $-\infty$ to 0 and 0 to $-\infty$ and $a_0 = -3\zeta(a/l)^3/(8\sqrt{t_\nu})$. So, when $t \to \infty$ we obtain

$$\Phi(t) = \frac{4k_B T\sqrt{t_\nu}}{3\sqrt{\pi}\zeta} \left(\frac{a}{l}\right)^{-3} t^{-\frac{3}{2}} . \tag{9.4.10}$$

For $\gamma = \frac{\pi}{2}$, i.e., when the sphere is moving parallel to the plane, $a_0 = 3\zeta(a/l)^3/(16\sqrt{t_\nu})$ and

$$\Phi(t) = -\frac{8k_B T\sqrt{t_\nu}}{3\sqrt{\pi}\zeta} \left(\frac{a}{l}\right)^{-3} t^{-\frac{3}{2}} . \tag{9.4.11}$$

For general case, $\mathbf{u} = u[\mathbf{n}\cos\gamma + \mathbf{t}\sin\gamma]$ and

$$\mathbf{F} = -u\,\zeta(\omega)\left[\mathbf{n}\left(1 + v_r(2l, 0)\right)\cos\gamma + \mathbf{t}\left(1 - v_\theta(2l, \pi/2)\right)\sin\gamma\right] .$$

Notice, for general case, the direction of $\mathbf{F}$ is no longer parallel to the direction of $\mathbf{u}$. So must first specify a direction, then calculate correlation function along that direction.

For the short time behavior of $\Phi(t)$, we can perform calculations similar to those above to find the approximate behavior. The branch point $s = 0$ contributes $b_0\sqrt{t}$, while the poles contribute $\sum_i b_i e^{tp_i}$, where p_i denotes the locations of the poles of $R(\sqrt{s})$. So, $\Phi(t) = b_0\sqrt{t} + \sum_i b_i e^{tpi}$. To find exact values of b_i and p_i is very tedious, which we do not do here.

For the future work, the most natural goal would be to find the exact solution for the linearized Navier-Stokes equation, at least for the case $\gamma = 0$. But, this is a difficult problem due to the non-separability of Helmholtz equation in bipolar coordinate. If we try to use another coordinate system, for example spherical coordinates, to find the coefficients of the eigenfunctions that match the boundary condition at the sphere, then matching at the plane will not be likely possible. So, instead of finding an exact solution, it is reasonable to seek a better approximate solution than that provided by the image method.

Acknowledgement

First, I wish to thank Phil Morrison for his guidance and supervision. I also would like to thank Joe Keller for many helpful discussions, as well as Rich Kerswell, Norm Lebovitz, and Steve Childress for helpful suggestions. Many thanks to the GFD faculty and WHOI for giving me the opportunity to join the GFD program this summer. Finally, thanks to all the fellows, whom I hope I will meet again in the future.

Bibliography

[1] G. K. Batchelor, *An Introduction to Fluid Dynamics* (Cambridge University Press, Cambridge, 1967).

[2] H. Brenner, *The slow motion of a sphere through a viscous fluid towards a plane surface*, Chem. Eng. Sci. **16**, 242 (1961).

[3] T. S. Chow and J. J. Hermans, *Brownian motion of a spherical particle in a compressible fluid*, Physica **65**, 156 (1973).

[4] H. J. H. Clercx and P. P. J. M. Schram, *Brownian particles in shear flow and harmonic potentials: A study of long-time tales*, Phys. Rev. A **46**, 1942 (1992).

[5] A. Einstein, *Über die von der molekularkinetischen Theorie der Wärme geforderte Bewegung von in ruhenden Flüssigkeiten suspendierten Teilchen*, Ann. Phys. **322**, 549 (1905).

[6] J. P. Freidberg, *Ideal magnetohydrodynamic theory of magnet fusion systems*, Rev. Mod. Phys. **54**, 801 (1982).

[7] E. J. Hinch, *Application of the Langevin equation to fluid suspensions*, J. Fluid. Mech. **72**, 499 (1975).

[8] J. Happel and H. Brenner, *Low Reynolds Number Hydrodynamics: With Special Applications to Particulate Media* (Kluwer, Dordrecht, The Netherlands, 1983).

[9] R. Huang, I. Chavez, K. M. Taute, B. Lukić, S. Jeney, M. G. Raizen, and E-L. Florin, *Direct observation of the full transition from ballistic to diffusive Brownian motion in a liquid*, Nature Physics **7**, 576 (2011).

[10] G. B. Jeffrey, *On a form of the solution of Laplace's equation suitable for problems relating to two spheres*, Proc. Roy. Soc. Lond. A **87**, 109 (1912).

[11] R. Kubo, *The fluctuation-dissipation theorem*, Repts. Prog. Phys. **29**, 255 (1966).

[12] P. Langevin, *Sur la théorie du mouvement Brownien*, C. R. Acad. Sci. Paris **146**, 530 (1908).

[13] P. Moon and D. E. Spencer, *Seperability in a class of coordinate systems*, J. Franklin Inst. **254**, 585 (1952).

[14] A. Rahman, *Correlations in the motion of atoms in liquid argon*, Phys. Rev. **136**, A404 (1964).

[15] P. P. J. M. Schram and I. P. Yakimenko, *On the theory of Brownian motion in compressible fluids*, Physica A **260**, 73 (1998).

[16] M. S. Tillack and N. B. Morley, *Magnetohydrodynamics*, (McGraw Hill, New York, 1998).

[17] R. Zwanzig and M. Bixon, *Hydrodynamic theory of the velocity correlation function*, Phys. Rev. A **2**, 2005 (1970).

[18] R. Zwanzig and M. Bixon, *Compressibility effects in the hydrodynamic theory of Brownian motion*, J. Fluid Mech. **69**, 21 (1975).

Project 10

Localized solutions for Plane Couette Flow: a continuation study

John Platt

Harvard University

10.1 Introduction

There has been much interest in investigating the transition to turbulence of linearly stable shear flows from a dynamical systems viewpoint [*Lanford*(1982), *Kerswell*(2005), *Eckhardt et al.*(2007)]. Here an instantaneous velocity field is pictured as a point in an infinite-dimensional phase space, with laminar flow being a linearly stable fixed point. Other invariant solutions exist, forming a "scaffold" for turbulent dynamics. Turbulence is imagined as a path in phase space moving between these invariant solutions. In this project we focus on one such invariant solution for plane Couette flow, in which the shear flow is established by moving two parallel plates past each other. A sketch of the geometry of the plane Couette system is shown in Figure 10.1.

The first of these invariant solutions was found by Nagata [*Nagata*(1990)], though many more have been found since [*Gibson et al.*(2009)]. Due to the vast computational expense required to work with these solutions, the majority of these solutions have been found in small domains that are periodic in both span-wise and stream-wise directions. However, observations of turbulent flows show localized turbulent regions coexisting with laminar regions [*Emmons*(1951), *Tillmark*(1992)]. A first invariant solution exhibiting this localized

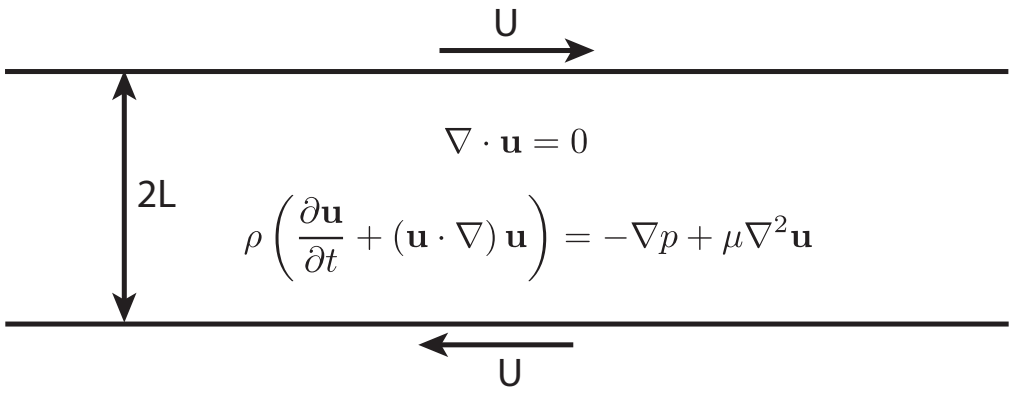

Figure 10.1: A sketch of the plane Couette system. Two plates separated by a distance of $2L$ are moved past each other with a velocity difference of $2U$, establishing a shear flow in the viscous fluid between the plates.

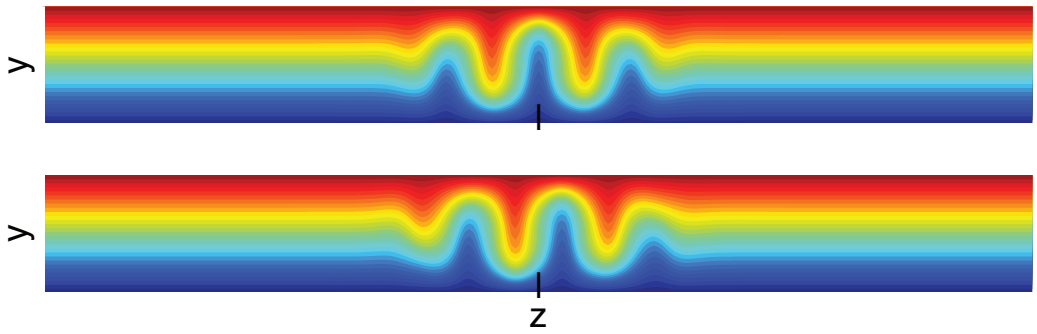

Figure 10.2: Plots of x-averaged streamwise velocity for the two localized solutions presented in [*Schneider et al.*(2010b)].

nature was presented in [*Schneider et al.*(2010a)], with the solution remaining periodic in stream-wise direction, but localized in the span-wise direction. In this project, building on the work outlined above, we try to provide more insight into these localized invariant solutions.

We aim to answer two main questions in this project. Our first goal is to determine what behavior should be expected for localized invariant solutions of plane Couette flow. To investigate this we first review the observations from for the first localized solution [*Schneider et al.*(2010b)], which show a distinctive bifurcation behavior known as homoclinic snaking. We then use continuation methods to investigate the bifurcation structure

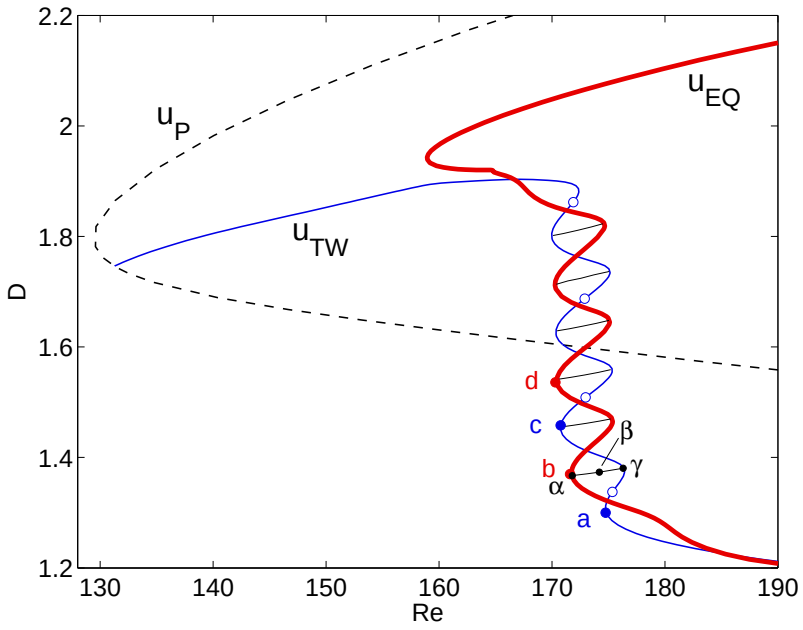

Figure 10.3: A plot of the bifurcation diagram from [*Schneider et al.*(2010b)]. We clearly see the homoclinic snaking structure, and the reattachment to the periodic solution from [*Nagata*(1990)].

of the second solution, and compare the two solutions to see what similarities and differences they share. The second goal is to investigate how more localized solutions could be generated. We analyze the symmetry breaking process during localization, and predict the number of localized "versions" of a periodic solution that may exist. All of the numerical calculations in this project are performed using the Channelflow package developed by John Gibson, and approximately 25,000 hours of CPU time was used to produce the results.

10.2 Review of the first localized solution

[*Schneider et al.*(2010b)] presented a continuation study for the first localized solution ever found for plane Couette flow. The periodic counterpart for this localized solution is the original invariant solution presented in [*Nagata*(1990)], and there exist two distinct versions of the solution, with flowfields shown in Figure 10.2. Continuing the pair of solutions in Re, for a fixed value of the x-dimension of the periodic domain, L_x, produced the bifurcation diagram shown in Figure 10.3. Here D is a volume normalized dissipation rate, and can be

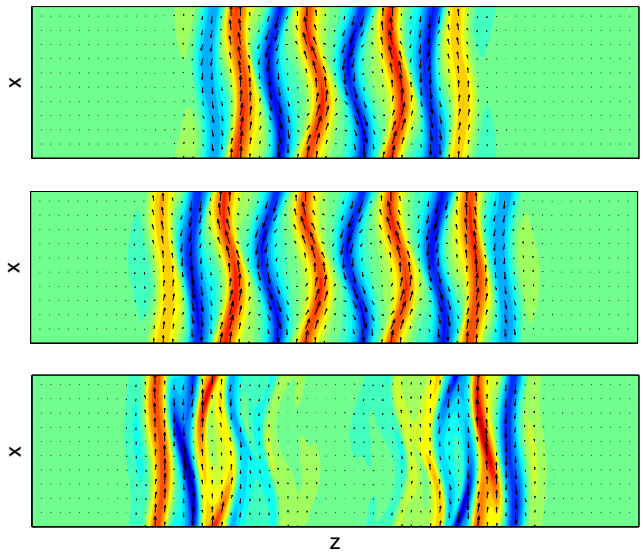

Figure 10.4: Plots showing the velocity field on the midplane. In-plane velocities are indicated with arrows and streamwise velocity is indicated with color. The top pair of plots show the flowfield at two adjacent saddle-node bifurcations on the snake, and the bottom plot show the marginal eigenfunction at the upper bifurcation.

thought of as a measure of how turbulent the solution is. The two solutions intertwine in a sequence of saddle-node bifurcations to form a structure that transitions to higher values of D over a relatively short interval in Re. One of the solutions reattaches to the periodic solution, shown in black, while the other solution follows the upper branch to high Re.

This sort of structure has also been observed in an entirely different system, the Swift-Hohenberg equation,

$$\frac{\partial u}{\partial t} = ru - \left(\frac{\partial^2}{\partial x^2} + q_c^2\right)^2 u + f(u), \tag{10.2.1}$$

where r is the control parameter, q_c is a parameter, and $f(u)$ is a nonlinear function. The phenomena is known as homoclinic snaking [*Burke and Knobloch*(2007)], and describes how a spatially localized solution of the above equation expands to fill the periodic domain it sits in. As the solution grows, structure is added at the edges, while in the internal region the solution does not change. Thus, to further test the similarities between the results in [*Schneider et al.*(2010b)] and homoclinic snaking in the Swift-Hohenberg equation, we can

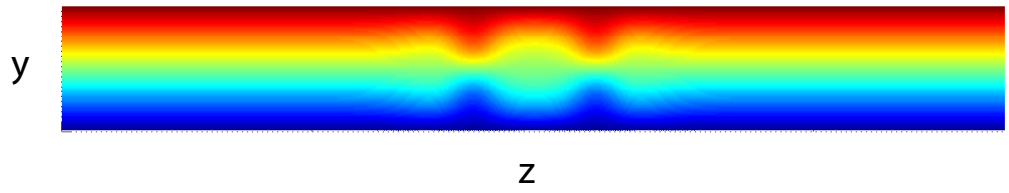

Figure 10.5: A plot of x-averaged streamwise velocity for the new localized solution.

examine the flow fields at different points on the snake. Throughout this project we take $\mathbf{x} = (x, y, z)$ with y being the direction perpendicular to the plates, x parallel to the direction of shear, and z the spanwise coordinate. These coordinate directions are then used to define the velocity vector $\mathbf{u} = (u, v, w)$. Figure 10.4 shows flowfields on the midplane for the first two saddle node bifurcations in Figure 10.3, along with the marginal eigenfunction for the second bifurcation. From the marginal eigenfunction we can clearly see that the solution is adding structure at the edges of the localized solution, while the central part remains relatively unchanged. As we move up the snake the solution achieves higher values of D by expanding the non-laminar region, but keeping the magnitude of the local dissipation rate roughly constant.

In the next section we present the results of a continuation study on a second localized solution. We want to compare the observations of this second solution with the results summarized above, to allow us to see what behavior is generic for localized invariant solutions, and specifically if homoclinic snaking is a feature of all localized solutions of plane Couette flow.

10.3 Continuation of second solution

We now use continuation methods to investigate a second localized solution. This localized solution was found by [*Gibson and Brand*(2011)] based on an understanding of the functional form of the fronts between laminar and turbulent regions. It is a localized version of the periodic solution EQ7 from [*Gibson et al.*(2009)]. Figure 10.5 shows a plot of the x-averaged streamwise velocity, allowing us to directly compare with the previous localized

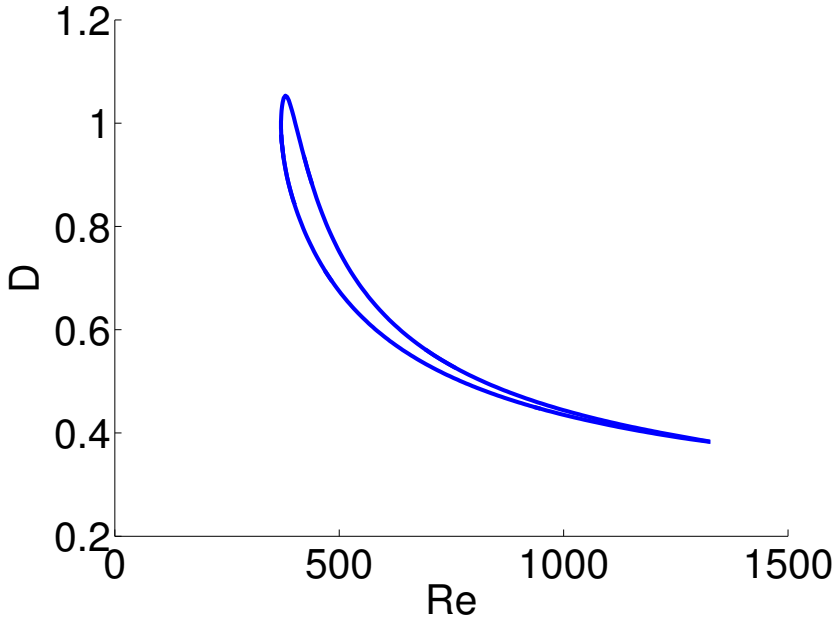

Figure 10.6: A plot of the bifurcation diagram generated by continuing in Re with $L_x = 3\pi$.

solution shown in Figure 10.2. We notice that the variations in velocity for the new localized solution are less pronounced, in agreement with the observation that this new solution exists at a much lower dissipation.

To allow us to plot the bifurcation diagrams, in the following we describe flowfields by the simple measure,

$$D = \frac{1}{2L_x}\int_{-L_z/2}^{L_z/2}\int_{-1}^{1}\int_{-L_x/2}^{L_x/2}\mathbf{v}(\mathbf{x})\mathrm{d}x\mathrm{d}y\mathrm{d}z, \tag{10.3.1}$$

where $\mathbf{v}$ is the velocity perturbation found by subtracting the laminar profile away from the full velocity field, and L_x, L_z are the streamwise and spanwise dimensions of the periodic domain. We do not normalize by L_z since our solutions are localized in L_z, and thus any measure of them should also be independent of L_z. Since the solution is independent of L_z, we have just two controlling parameters Re and L_x to continue in.

10.3.1 Isolas

To begin we continue in Re, fixing $L_x = 3\pi$, producing the results shown in Figure 10.6. We observe a closed isola in the (Re, D) plane, in sharp contrast to the homoclinic snaking

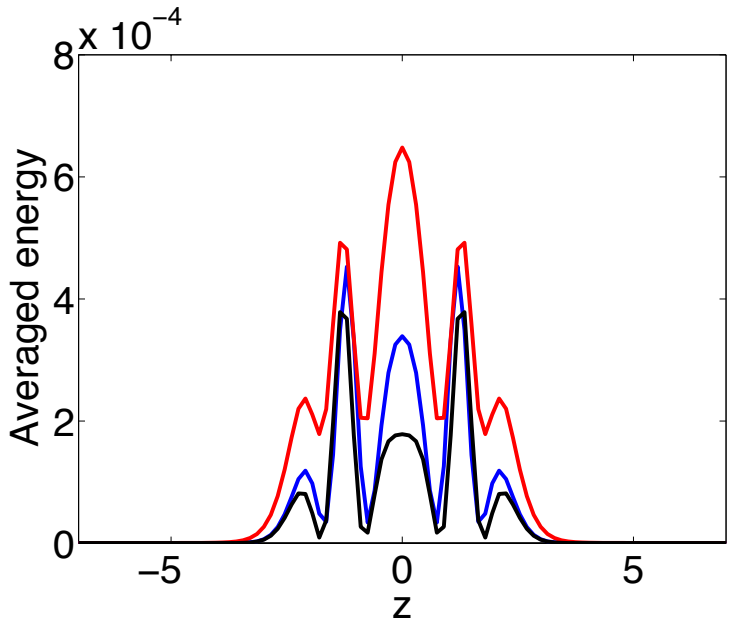

Figure 10.7: A plot of the averaged energy as a function of z for three points on the $L_x = 3\pi$ isola. The solution with the lowest value of Re is plotted in red, the highest value of Re in black, and the intermediate value of Re in blue.

observed with the first localized solution. We also note that the solution is relatively constant over a wide range of Re. Such closed isolas have also been observed in studies of localized solutions in the Swift-Hohenberg equation [*Burke and Knobloch*(2006)]. Recalling that for the previous localized solution higher values of D were attained by approximately fixing the maximum size of the velocity perturbations, but expanding the solution to fill more of the domain, we now plot the energy in the velocity fluctuations, averaged in the x and y-directions, as a function of z at three points on the closed curve; the two extreme values of Re and one intermediate value. This is shown in Figure 10.7. We see that the structure of the solutions remains relatively constant, while changes in D are achieved by varying the amount of energy in each of the oscillations. This is in agreement with the observations of isolas in the Swift-Hohenberg equation in [*Burke and Knobloch*(2006)], which show that around an isola the number of oscillations in the solution is unchanged. We can also compute the spectrum of the solution at a selection of points, finding that at all points the solution has a low number of unstable directions. This is important for

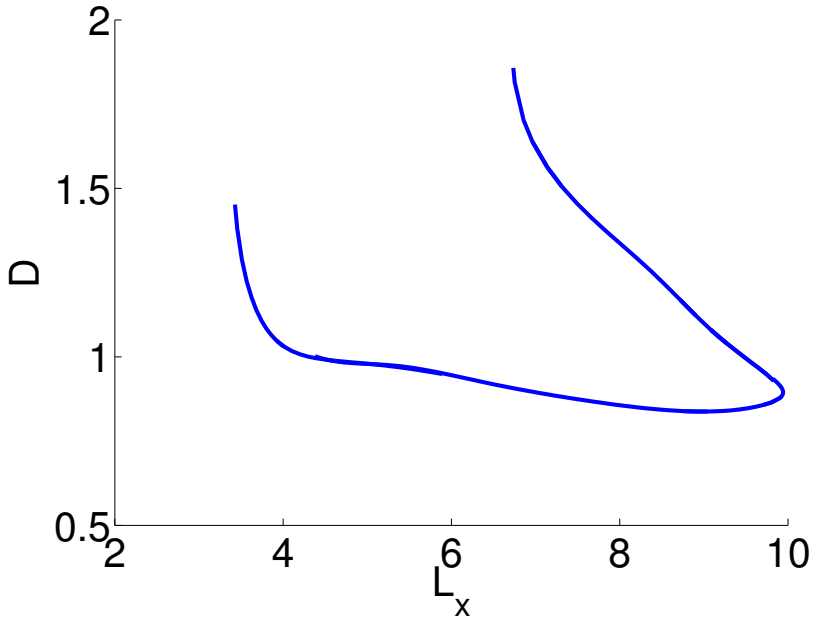

Figure 10.8: A plot of the bifurcation diagram generated by continuing in L_x with $Re = 400$.

the dynamical systems view of turbulence since points in phase space with few unstable directions may be approached more often than ones with many unstable directions.

Next we continue the original localized solution in L_x, producing the results in Figure 10.8. This time we do not observe a closed curve, instead seeing a relatively constant value of D over a range of L_x with the two ends of the curve moving towards higher values of D. Our previous continuation in Re with $L_x = 3\pi$ had two values at $Re = 400$, corresponding to the two points on the curve for $L_x = 3\pi$. As before, when we examine the flowfields along the curve in Figure 10.8 we see relatively little change in the structure, with higher values of D be attained by increasing the magnitude of the velocity fluctuations not increasing the fraction of the domain the localized solution occupies.

Now we use the solutions found at different values of L_x to begin new continuations in Re, shown in Figure 10.9. For $L_x = 2.9\pi, 3\pi, 3.1\pi$ we see very similar behavior to before. However, for $L_x < 2.9\pi$ we see a region of higher curvature developing for low values of Re. For these values of L_x we take the second solution at $Re = 400$, which exists at a higher value of D, and continue in L_x. We discover that the reason for the change in behavior

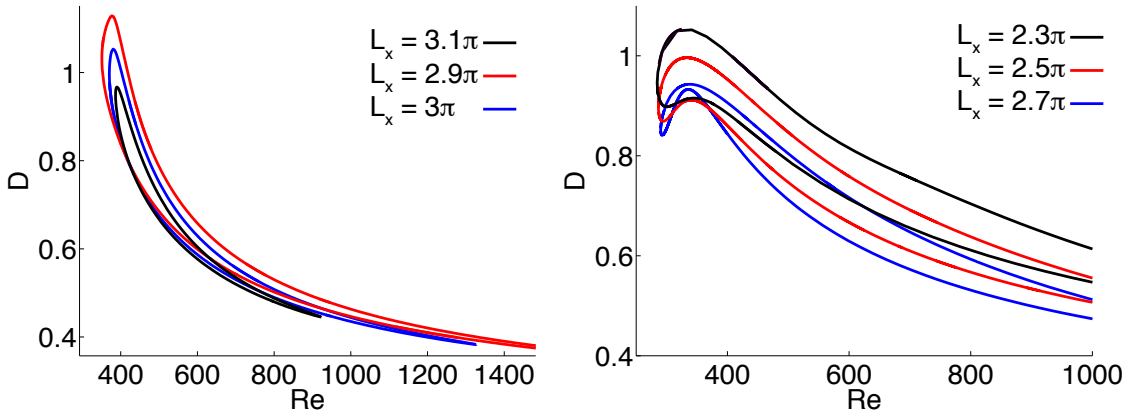

Figure 10.9: A plot of the bifurcation diagrams generated by continuing in Re for a range of L_x values.

around $L_x = 2.9\pi$ is due to the existence of another solution branch, shown in red in Figure 10.10. Continuing the new curve in one direction leads to a roughly constant value of D extending to far higher values of L_x than previously observed. Extending the curve in the other direction we see some curves before the solution branch rapidly moves to higher values of D.

10.3.2 Searching for snaking

So far we have seen no evidence of homoclinic snaking, but the existence of the new curve for $L_x \in [2.9\pi, 3.1\pi]$ demonstrates the existence of further curves in the (Re, D) plane, to go with the isolas already observed. Choosing $L_x = 2.9\pi$ we track this new curve, shown in red in Figure 10.11. We observe dramatically different results, with the new curve showing snaking like behavior and moving to much higher values of D in a relatively narrow range of Re. Similar results are seen when continuing solutions from the new branch in the (L_x, D) plane in Re. Fixing $L_x = 4\pi$ and continuing in Re we produce the results seen in Figure 10.12. As in Figure 10.11 the curve proceeds to high values of D in a narrow range of Re, exhibiting some bends. To test if this could be another instance of homoclinic snaking we examine the flow fields. Figure 10.13 shows the averaged energy as a function of z for three points along the $L_x = 4\pi$ curve. We observe that, while there is some evidence of additional structure being added at the edge of the localized solution, as before the higher

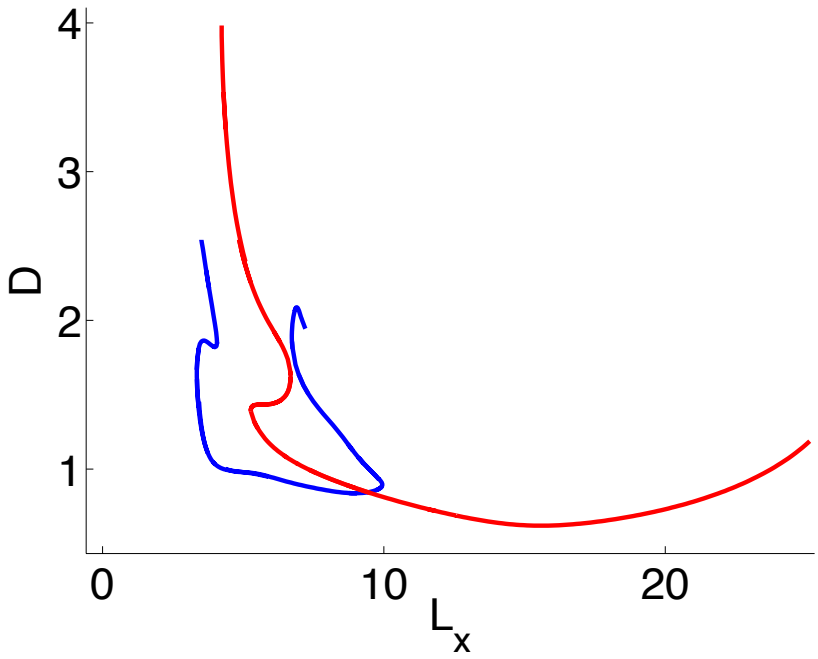

Figure 10.10: A plot of the bifurcation structure in the (L_x, D) plane, for $Re = 400$, with the new branch included.

values of D are achieved by increasing the magnitude of the velocity fluctuations. A similar investigation of the flowfields along the $L_x = 2.9\pi$ curve gives the same result.

10.3.3 Bifurcation behavior summary

To summarize we have found that homoclinic snaking is not a feature of all localized solutions of plane Couette flow. The bifurcation behavior shown by our localized solutions very different to that observed in [*Schneider et al.*(2010b)]. For some continuations in Re we see closed curves, as in some continuation studies of the Swift-Hohenberg equation [*Burke and Knobloch*(2006)]. The physical properties of the solutions also vary considerably. When compared with the first localized solution, our localized solution exists at much lower dissipation values, and remains there for a wide range of Re and L_x. Our solutions also retains the property of having a relatively low number of unstable directions, and important property for the dynamical systems view of turbulence. Several branches at higher

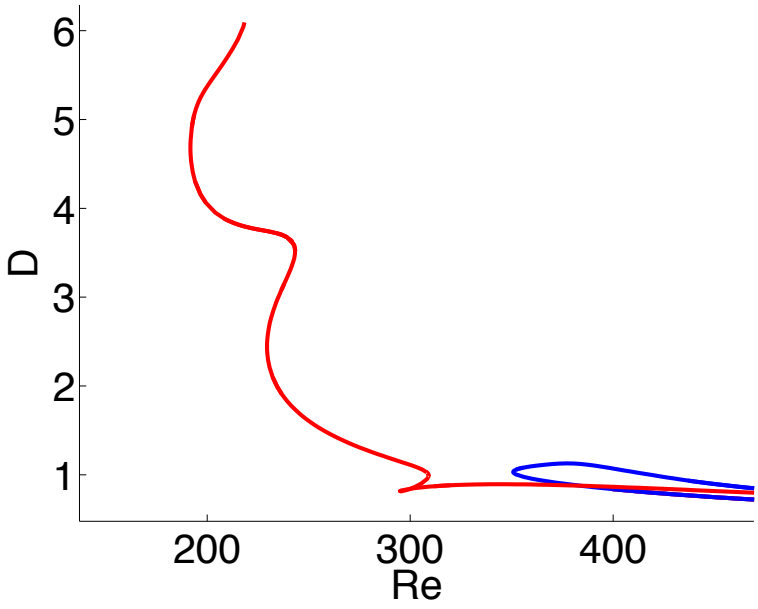

Figure 10.11: A plot of the (Re, D) bifurcation diagram for $L_x = 2.9\pi$, showing the two distinct branches.

values of D are still open for further continuation, and these may provide a route to the values of D seen with the previous solution. Having discussed the bifurcation behavior for localized solutions, we next discuss further work aimed at finding additional localized solutions.

10.4 Symmetry breaking during localization

The localized solution discussed in this project is just the second one discovered, despite the existence of many solutions in spanwise periodic domains. We will now address our second goal of investigating how additional localized solutions could be generated. New work examining the fronts between laminar and turbulent regions has shown how more localized solutions could be constructed using the many periodic solutions currently known [*Gibson and Brand*(2011)]. We now examine the symmetries of both localized solutions, and try to find general relations between these and the symmetry groups of the periodic parent solutions. We hope that this will provide useful guidance when attempting to find

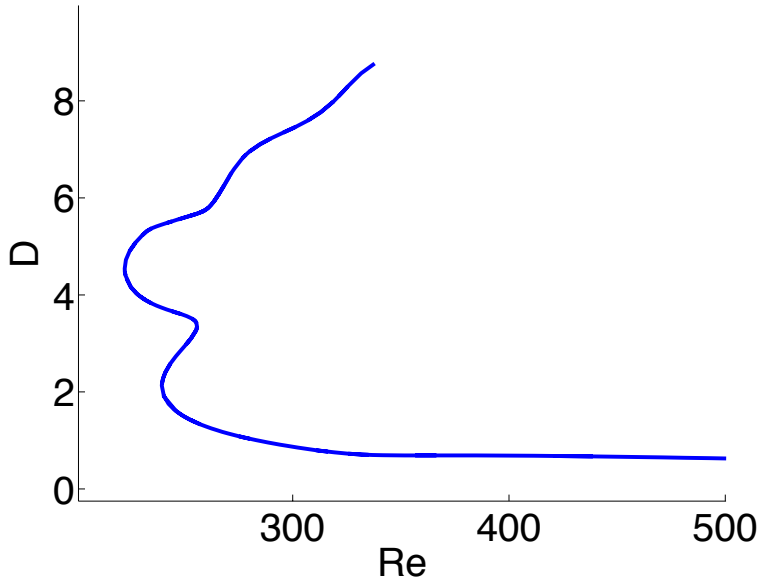

Figure 10.12: Bifurcation diagram generated by continuing in Re with $L_x = 4\pi$.

future localized solutions, and we also make a prediction for the number of localized versions of each periodic solution.

First we define the symmetry groups for the exact solutions using the notation in [*Gibson et al.*(2009)]. Plane Couette flow in a periodic box allows symmetries of the form

$$[u, v, w](x, y, z) = [s_x u, s_y v, s_z w](s_x x + \tau_x L_x, s_y y, s_z z + \tau_z L_z). \tag{10.4.1}$$

Here s_x, s_y and s_z define the reflection symmetries in x, y and z respectively, with τ_x and τ_z setting the shift in the x and z directions. An individual symmetry can then be fully described using the notation

$$(1, s_x, s_y, s_x; \tau_x, \tau_z).$$

Obviously solutions can satisfy multiple symmetries, which themselves can be combined to form a symmetry group for the solution. We can analyze the symmetries of solutions by investigating the generators of the symmetry groups.

First we examine the localized solution presented in [*Schneider et al.*(2010a)], which is a localized version of the first periodic solution found in [*Nagata*(1990)]. The symmetry

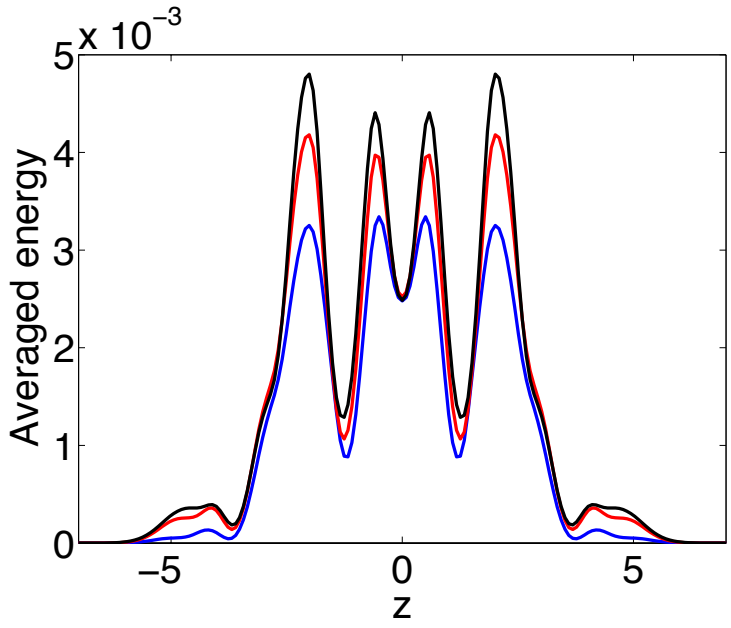

Figure 10.13: A plot of the averaged energy as a function of z for three points on the $L_x = 4\pi$ curve.

group for the periodic solution has two generators,

$$(1, 1, 1, -1; 0.5, 0)$$

$$(1, -1, -1, -1; 0, 0.5)$$

This led to two localized solutions, one a strict equilibrium, the other a travelling wave. Each of these solutions has a symmetry group with a single generator,

$$(1, 1, 1, -1; 0.5, 0)$$

for the travelling wave, and,

$$(1, -1, -1, -1; 0, 0)$$

for the equilibrium.

Next we turn to the localized solution studied in this work. In this case the periodic parent has a symmetry group with three generators,

$$(1, -1, -1, 1; 0, 0)$$

$$(1, 1, 1, -1; 0, 0.5)$$

$$(1, 1, 1, -1; 0.5, 0)$$

This leads to a localized solution that has a symmetry group with just two generators,

$$(1, -1, -1, 1; 0, 0)$$

$$(1, 1, 1, -1; 0, 0)$$

From this limited set of examples we now extrapolate some general rules. The localization process breaks one of the symmetry generators of the periodic parent solution, leading to a symmetry group with one fewer generator. Any shift in the L_z direction is eliminated. In [*Schneider et al.*(2010a)] two solutions were found, corresponding to breaking each of the generators of the Nagata solution in turn. For the new solution discussed here we have broken a single generator, allowing us to tentatively predict the existence of two more localized versions of the periodic solution, corresponding to breaking the other two periodic generators. Even more speculatively we can predict the existence of three more, giving six in total, if localized solutions can be formed from any subgroup of the periodic symmetry group.

10.5 Discussion

In this project we analyzed the physical flowfields and bifurcation structure for a localized exact solution for plane Couette flow. By making comparisons with the first such solution we can begin to determine what behavior is generic for localized solutions of plane Couette flow, and what is specific to individual solutions.

The previous localized solution showed a distinctive bifurcation behavior, identical in form to the homoclinic snaking seen in the Swift-Hohenberg equation. Despite an extensive parameter search we can find no evidence for homoclinic snaking in this solution, suggesting that this bifurcation structure is not an essential feature of all localized solutions. However, we did find closed curves in the bifurcation diagram, similar to the isolas observed in some studies of the Swift-Hohenberg equation. In contrast to the previous study, for which solutions existed in a narrow range of Re, we found relatively unchanged solutions over

a wide range of Re and L_x. The solutions presented in this study also exist at far lower dissipation values than previous observations.

To conclude, localized solutions for plane Couette flow can experience a wider range of behavior than that reported in [*Schneider et al.*(2010b)]. Solutions can exist over a wider range of Re, L_x and D then previously observed, and do not necessarily show the distinctive homoclinic snaking bifurcation behavior. However, there may still be a link to the Swift-Hohenberg equation, as shown by the isolas observed in this study.

Bibliography

[*Kerswell*(2005)] Kerswell, R.R. (2005), Recent progress in understanding the transition to turbulence in a pipe, *Nonlinearity*, 18.

[*Eckhardt et al.*(2007)] Eckhardt, B., T.M. Schneider, B. Hof, and J. Westerweel (2007), Turbulence transition in pipe flow, *Annual Review of Fluid Mechanics*, 39.

[*Lanford*(1982)] Lanford, O.E. (1982), The strange attractor theory of turbulence, *Annual Review of Fluid Mechanics*, 14.

[*Nagata*(1990)] Nagata, M. (1990), Three-dimensional finite-amplitude solutions in plane Couette flow: bifurcation from infinity, *Journal of Fluid Mechanics*, 217.

[*Waleffe*(2003)] Waleffe, F. (2003), Homotopy of exact coherent structures in plance shear flows, *Physics of Fluids*, 15.

[*Gibson et al.*(2009)] Gibson, J.F., J. Halcrow, and P. Cvitanovic (2009), Equilibrium and travelling-wave solutions of plane Couette flow, *Journal of Fluid Mechanics*, 638.

[*Tillmark*(1992)] Tillmark, N., and P.H. Alfredsson (1992), Experiments on transition in plane Couette flow, *Journal of Fluid Mechancis*, 235.

[*Emmons*(1951)] Emmons, H.W. (1951), The laminar-turbulent transition in a bounary layer - Part I, *Journal of the Aeronautical Sciences*, 18.

[*Schneider et al.*(2010a)] Schneider, T.M., D. Marinc, and B. Eckhardt (2010), Localized edge states nucleate turbulence in extended plane Couette cells, *Journal of Fluid Mechanics*, 646.

[*Schneider et al.*(2010b)] Schneider, T.M., J.F. Gibson, and J. Burke (2010), Snakes and ladders: Localized solutions of plane Couette flow, *Physical Review Letters*, 105.

[*Burke and Knobloch*(2007)] Burke, J., and E. Knobloch (2007), Homoclinic snaking: Structure and stability, *Chaos*, 17.

[*Burke and Knobloch*(2006)] Burke, J., and E. Knobloch (2006), Localized states in the generalized Swift-Hohenberg equation, *Physical Review E*, 73.

[*Gibson and Brand*(2011)] Gibson, J., and E. Brand (2011), Spatially localized solutions of plane Couette flow, *64th Annual Meeting of APS Division of Fluid Dynamics*, 56.

Project 11

Maximizing the heat flux in steady unicellular porous media convection

Lindsey T. Corson

St. Andrews University

11.1 Introduction

Convection in a horizontal porous layer heated from below is relevant to a variety of geological and engineering applications (Nield & Bejan [13]; Phillips [16], [17]). Porous media convection has been studied extensively, beginning with the linear stability analyses of Horton and Rogers [9] and Lapwood [11], and the flow dynamics and bifurcation structure for low to intermediate Rayleigh numbers (Ra) have been thoroughly explored both theoretically and numerically (Graham and Steen [7]). Asymptotic descriptions of steady porous media convection have been proposed by Palm *et al.* [15], Robinson & O'Sullivan [18], and Rudraiah & Musuoka [19], although there is a distinct lack of agreement among these and other authors regarding the asymptotic form of the convection.

It has been firmly established that the classical marginally stable boundary layer argument of Howard [10] for Rayleigh-Bénard convection at high Rayleigh number also holds for porous media convection (Horne & O'Sullivan [8]). This argument gives a scaling $Nu \sim Ra$, where the Nusselt number, Nu, represents the heat transport; a result supported by rigorous upper bound theory (Doering & Constantin [5]). However, Graham and Steen [7] note

that this scaling is only valid after the onset of plumes, at approximately $Ra = 700$; for smaller Ra the appropriate scaling is $Nu \sim Ra^{2/3}$ (Cherkaoui & Wilcock [3]).

The high resolution two-dimensional (2D) direct numerical simulations (DNS) of Otero *et al.* [14] in a horizontally periodic layer indicate that as the Rayleigh number is increased, the heat transport shifts from being described by the classical $Nu \sim Ra$ scaling to being better described by $Nu \sim Ra^{0.9}$. Crucially, their simulations show that the spacing between the thermal plumes decreases as Ra is increased. From the data presented, it appears that the inter-plume spacing may scale in direct proportion to the wavelength of the fastest growing linear mode ($\sim Ra^{-1/4}$). The experimental results of Lister [12], by contrast, suggest the inter-plume spacing scales as $(Ra + C)^{-1/2}$, for some constant C.

Motivated in part by these prior investigations, the primary aim of the present study is to determine the maximum heat transport attainable in steady 2D unicellular porous media convection. By focusing on this restricted class of flows we are able to use an efficient iterative numerical scheme to systematically probe the way in which the heat transport depends on the inter-plume spacing. Guided by our numerical results, we also propose a large-Ra asymptotic reduction of the governing equations that yields the asymptotic structure of the solutions giving the maximum heat transport.

The remainder of this report is organised as follows. In §11.2 we formulate the standard mathematical model of porous media convection and recall the key results of linear stability theory for this system. The numerical method used to find (generally unstable) steady-state high-Ra solutions is described in §11.3 along with a synopsis of our numerical results. In §11.4 we propose a multi-region matched asymptotic description of the maximal Nusselt number solutions, motivated by the numerical solutions described in §11.3. In §11.5 we use our steady-state solutions as initial conditions in a time-dependent numerical model and analyse the results. Finally, in §11.6 we summarise our findings and outline avenues for future work.

11.2 Problem formulation

We consider a fluid-saturated porous layer heated from below at $z = 0$ and cooled from above at $z = 1$. The evolution of the 2D velocity $\mathbf{u}(\mathbf{x}, t) = (u, w)$, temperature $T(\mathbf{x}, t)$ and

pressure $p(\mathbf{x}, t)$ fields is governed by the non-dimensional Darcy-Oberbeck-Boussinesq equations (Nield & Bejan [13]) in the infinite Darcy–Prandtl number limit. In streamfunction–vorticity form, these equations can be expressed as

$$\nabla^2 \psi = -Ra \frac{\partial T}{\partial x}, \tag{11.2.1}$$

$$\frac{\partial T}{\partial t} + \frac{\partial \psi}{\partial z}\frac{\partial T}{\partial x} - \frac{\partial \psi}{\partial x}\frac{\partial T}{\partial z} = \nabla^2 T. \tag{11.2.2}$$

Here ψ is the streamfunction describing cellular flow in the (x, z)–plane. The dimensionless parameter $Ra = KHg\beta\Delta T/(\nu\kappa_m)$ is the Rayleigh number, where K is the permeability of the medium, H is the depth of the layer, g is the gravitational acceleration, β is the thermal expansion coefficient, ΔT is the temperature difference across the layer, ν is the kinematic viscosity, and κ_m is the effective diffusivity of heat through the saturated medium.

The non-dimensional temperature at the top and bottom of the layer is held fixed at 0 and 1, respectively, and we seek steady unicellular solutions with discrete translational invariance in the horizontal coordinate x and reflection symmetry about the planes $x = n\pi/k$ for integer n and given cell width $L = \pi/k$, where k is the horizontal wavenumber. Since we are interested in unicellular convection we will take $n = 1$ throughout. Therefore, we impose the following boundary and symmetry conditions:

$$\begin{aligned} &T(x,0,t) = 1, \quad T(x,1,t) = 0, \quad \psi(x,0,t) = 0, \quad \psi(x,1,t) = 0, \\ &\frac{\partial T}{\partial x}(0,z,t) = 0, \quad \frac{\partial T}{\partial x}(L,z,t) = 0, \quad \psi(0,z,t) = 0, \quad \psi(L,z,t) = 0. \end{aligned} \tag{11.2.3}$$

It is useful to recapitulate a few results from linear stability theory (Nield & Bejan [13], Chapter 6). If we define $T = (1-z) + \tilde{\theta}(x, z, t)$, where $1 - z$ is the conduction solution, and search for solutions of the linearised versions of (11.2.1) and (11.2.2) of the form

$$\tilde{\theta}(x, z, t) = \cos(kx)\sin(\pi z)e^{\sigma t}, \quad \psi(x, z, t) = \Psi \sin(kx)\sin(\pi z)e^{\sigma t}, \tag{11.2.4}$$

we find that the (strictly real) growth rate σ is given by

$$\sigma = \frac{Ra}{k^2 + \pi^2} - (k^2 + \pi^2). \tag{11.2.5}$$

From this relationship, it is easily shown that the critical wavenumber $k^{\text{crit}} = \pi$, implying the critical cell width $L^{\text{crit}} = 1$ and that the critical Rayleigh number $Ra^{\text{crit}} = 4\pi^2$. Moreover,

for large Rayleigh number, the wavenumber k_f of the fastest growing linear mode is given by

$$k_f \sim \sqrt{\pi} Ra^{1/4}. \tag{11.2.6}$$

A useful quantity in the study of convection is the normalised volume-averaged vertical heat flux, or Nusselt number,

$$Nu = 1 + \frac{1}{L}\left\langle \int \frac{\partial \psi}{\partial x} T \mathrm{d}x\mathrm{d}z \right\rangle, \tag{11.2.7}$$

where the angle brackets indicate the long-time average

$$\langle f \rangle = \lim_{T\to\infty} \frac{1}{T}\int_0^T f(t)\mathrm{d}t. \tag{11.2.8}$$

From the equations of motion we can derive an equivalent expression for the Nusselt number,

$$Nu = -\frac{1}{L}\left\langle \int_{z=0} \frac{\partial T}{\partial z}\mathrm{d}x \right\rangle. \tag{11.2.9}$$

This expression shows that Nu can also be interpreted as the ratio of the horizontally-integrated, time-averaged vertical heat flux to the corresponding value realized in the absence of convection.

11.3 Numerical simulations

We compute time-independent numerical solutions of (11.2.1)–(11.2.2), subject to the boundary conditions (11.2.3), using a Newton–Kantorovich iteration scheme (Boyd [2], Appendix C). We begin by rewriting the model equations as

$$\nabla^2 \psi = F^{\psi}(T_x), \tag{11.3.1}$$

$$\nabla^2 T = F^{T}(\psi_x, \psi_z, T_x, T_z), \tag{11.3.2}$$

where a subscript denotes a partial derivative with respect to the given variable. Suppose we have iterates $T^{(i)}(x,z)$ and $\psi^{(i)}(x,z)$, which are good approximations to the true solutions $T(x,z)$ and $\psi(x,z)$. Taylor expanding the functions F^{ψ} and F^{T} in (11.3.1) and (11.3.2)

about the ith iterate gives

$$\nabla^2\psi = F^{\psi}(T_x^{(i)}) + F^{\psi}_{T_x}(T_x^{(i)})[T_x - T_x^{(i)}] + \mathcal{O}\left([T_x - T_x^{(i)}]^2\right) \tag{11.3.3}$$

$$\begin{aligned}\nabla^2 T =& F^T(\psi_x^{(i)}, \psi_z^{(i)}, T_x^{(i)}, T_z^{(i)}) + F^T_{\psi_x}(\psi_x^{(i)}, \psi_z^{(i)}, T_x^{(i)}, T_z^{(i)})[\psi_x - \psi_x^{(i)}] \\ &+ F^T_{\psi_z}(\psi_x^{(i)}, \psi_z^{(i)}, T_x^{(i)}, T_z^{(i)})[\psi_z - \psi_z^{(i)}] + F^T_{T_x}(\psi_x^{(i)}, \psi_z^{(i)}, T_x^{(i)}, T_z^{(i)})[T_x - T_x^{(i)}] \\ &+ F^T_{T_z}(\psi_x^{(i)}, \psi_z^{(i)}, T_x^{(i)}, T_z^{(i)})[T_z - T_z^{(i)}] \\ &+ \mathcal{O}\left([\psi_x - \psi_x^{(i)}]^2, [\psi_z - \psi_z^{(i)}]^2, [T_x - T_x^{(i)}]^2, [T_z - T_z^{(i)}]^2\right),\end{aligned} \tag{11.3.4}$$

where, for example, $F^T_{T_x}$ denotes the Frechet derivative of the function $F^T(\psi_x, \psi_z, T_x, T_z)$ with respect to T_x. By defining correction terms

$$\psi^{(i+1)} \equiv \psi^{(i)} + \hat{\phi}, \quad T^{(i+1)} \equiv T^{(i)} + \hat{\theta}, \tag{11.3.5}$$

and computing the Frechet derivatives, the linear differential equations for the corrections are given by

$$\nabla^2\hat{\phi} + Ra\hat{\theta}_x = F^{\psi}(T_x^{(i)}) - \nabla^2\psi^{(i)}, \tag{11.3.6}$$

$$\nabla^2\hat{\theta} + T_z^{(i)}\hat{\phi}_x - T_x^{(i)}\hat{\phi}_z - \psi_z^{(i)}\hat{\theta}_x + \psi_x^{(i)}\hat{\theta}_z = F^T(\psi_x^{(i)}, \psi_z^{(i)}, T_x^{(i)}, T_z^{(i)}) - \nabla^2 T^{(i)}, \tag{11.3.7}$$

subject to the boundary conditions

$$T = 1, \quad \psi = 0, \quad \hat{\theta} = 0, \quad \hat{\phi} = 0 \quad \text{on} \quad z = 0, \tag{11.3.8}$$

$$T = 0, \quad \psi = 0, \quad \hat{\theta} = 0, \quad \hat{\phi} = 0 \quad \text{on} \quad z = 1, \tag{11.3.9}$$

$$T_x = 0, \quad \psi = 0, \quad \hat{\theta}_x = 0, \quad \hat{\phi} = 0 \quad \text{on} \quad x = 0, \tag{11.3.10}$$

$$T_x = 0, \quad \psi = 0, \quad \hat{\theta}_x = 0, \quad \hat{\phi} = 0 \quad \text{on} \quad x = L. \tag{11.3.11}$$

Equations (11.3.6) and (11.3.7) can be rewritten in matrix form

$$\begin{bmatrix} D_{xx} + D_{zz} & RaD_x \\ T_z^{(i)}D_x - T_x^{(i)}D_z & D_{xx} + D_{zz} - \psi_z^{(i)}D_x + \psi_x^{(i)}D_z \end{bmatrix} \begin{bmatrix} \hat{\phi} \\ \hat{\theta} \end{bmatrix} = \begin{bmatrix} -RaT_x^{(i)} - \nabla^2\psi^{(i)} \\ \psi_z^{(i)}T_x^{(i)} - \psi_x^{(i)}T_z^{(i)} - \nabla^2 T^{(i)} \end{bmatrix}, \tag{11.3.12}$$

where, for example, D_x denotes the partial derivative with respect to x.

We iterate the system of equations (11.3.12) for a given Rayleigh number Ra and cell-width – or inter-plume spacing – L, subject to the boundary conditions (11.3.8)–(11.3.11), using a pseudospectral collocation method. A convergence criterion requiring

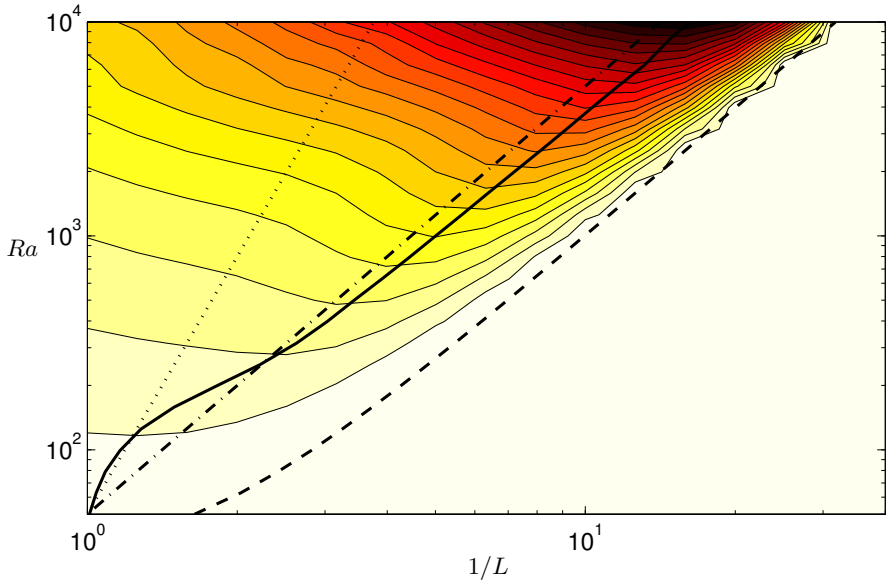

Figure 11.1: Surface plot of Nusselt number in (Ra, L) parameter space. Darker shading represents higher values of Nu. The solid line marks the ridge along which Nu is maximum; the dashed line is the linear stability boundary; the dashed-dotted line is $L = 50^{1/2} Ra^{-1/2}$; and the dotted line is $L = 50^{1/4} Ra^{-1/4}$. The jagged contours at high Ra are resolution artefacts.

$\max(|\hat{\phi}|) < 10^{-10}$ and $\max(|\hat{\theta}|) < 10^{-10}$ was employed. A Chebyshev tensor-product formulation with 60 nodes in both the horizontal and vertical directions was used to provide adequate resolution of the boundary layers.

Simulations were performed starting at $Ra = 50$, just above the critical Rayleigh number $Ra^{\text{crit}} = 4\pi^2 \approx 39.5$, and initial cell width $L = 1$. Once convergence was achieved, Ra was increased by a factor of $10^{1/10}$ with the previous converged state used as the new "initial" condition. This was repeated for cell widths from $L = 1$ to $L = 0.01$, reduced in steps of $10^{1/10}$ in order to thoroughly explore (Ra, L) parameter space. At each point the Nusselt number Nu was recorded.

The results of these simulations are summarized in figures 11.1 and 11.2. In figure 11.1 a surface plot of the Nusselt number in (Ra, L) parameter space is presented. The dashed line indicates the linear stability boundary, $L \sim \pi Ra^{-1/2}$. To the right of this line there is no convection and so $Nu = 1$; the jagged contours at high Ra are resolution artefacts. The solid line denotes the maximum value of Nu, and hence marks a ridge on the surface.

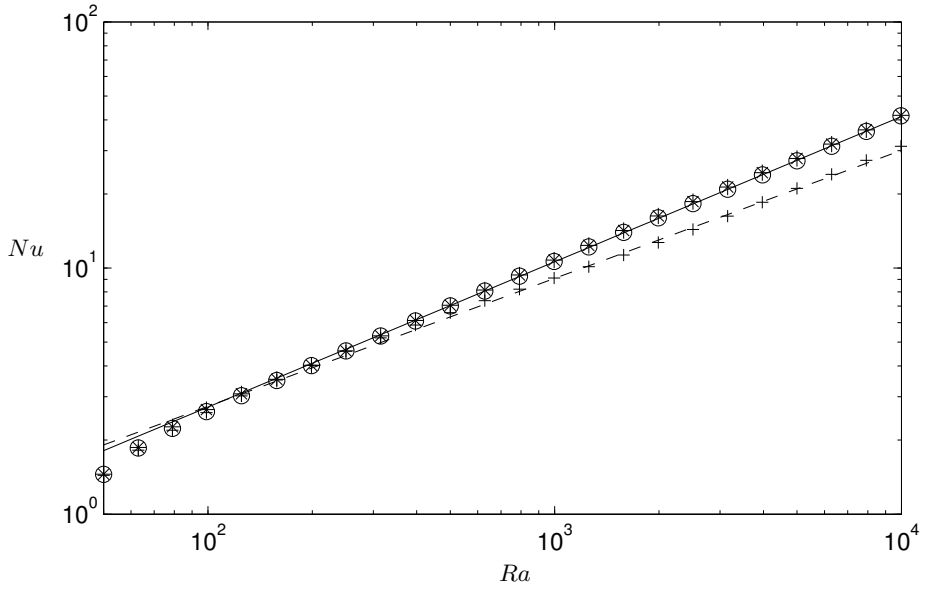

Figure 11.2: Plot of Nu vs. Ra along different paths $L = L(Ra)$. The asterisks are the data along the maximum Nu ridge; the circles are the data along the curve $L = 50^{1/2}Ra^{-1/2}$, and the crosses are the data along the curve $L = 50^{1/4}Ra^{-1/4}$. The solid line is the best fit curve $0.18Ra^{0.59}$, and the dashed line is the best fit curve $0.25Ra^{0.52}$.

To elucidate scalings, the lines $L = 50^{1/2}Ra^{-1/2}$ (dashed–dotted) and $L = 50^{1/4}Ra^{-1/4}$ (dotted) are also plotted. The constants $50^{1/2}$ and $50^{1/4}$ were used so that $L = 1$ when $Ra = 50$ in each case.

As noted in § 11.1, the DNS results presented in Otero *et al.* [14] suggest that the inter-plume spacing scales with the wavelength of the fastest growing linear mode: from (11.2.6), $L \sim \pi/k_f = \sqrt{\pi}Ra^{-1/4}$. However, the experimental results of Lister [12] suggest that the inter-plume spacing scales as $(Ra + C)^{-1/2}$. We can see in figure 11.1 that the maximum Nu ridge satisfies the $L \sim Ra^{-1/4}$ scaling up to $Ra \approx 150$, as it closely follows the dotted line. Above $Ra \approx 150$, the ridge shifts to the right and for $Ra > 500$ it follows the relationship $L \sim 7.02Ra^{-0.52}$. With this scaling, however, the ridge would eventually cross the linear stability boundary into the conduction $Nu = 1$ regime. Therefore, it seems plausible that the maximum Nu ridge (at least for steady 2D unicellular convection) must eventually scale as $L \sim Ra^{-1/2}$, in agreement with Lister's results [12].

Figure 11.2 shows the variation of Nu with Ra along the ridge (asterisks) and along

the curves $L = 50^{1/2}Ra^{-1/2}$ and $L = 50^{1/4}Ra^{-1/4}$ (circles and crosses, respectively). In the range $50 \leq Ra \leq 350$, all three curves lie on top of one another; however, at higher values of Ra the $L = 50^{1/4}Ra^{-1/4}$ curve drops below the other two. Across the range $1000 \lesssim Ra \lesssim 10000$, the data along the curve $L = 50^{1/4}Ra^{-1/4}$ scale as $Nu \sim 0.25Ra^{0.52}$ (dashed line), and the data along the curve $L = 50^{1/2}Ra^{-1/2}$, as well as the ridge, scale as $Nu \sim 0.18Ra^{0.59}$ (solid line). Although none of these steady-state unicellular solutions exhibits the Nu–Ra scaling presented in Otero *et al.* [14], they do reveal a clear and non-trivial dependence of the heat transport on the inter-plume spacing.

11.3.1 Solution structure

In this section, we examine the spatial structure of the numerical solutions across the range $1000 \lesssim Ra \lesssim 10000$, where we obtain the clean $Nu \sim Ra^{0.6}$ relationship with a cell width that scales as $L \sim 50^{1/2}Ra^{-1/2}$, to gain further insight into the steady unicellular flows that maximize the heat transport.

Figure 11.3 shows contour plots of the temperature $T(x, z)$ and streamfunction $\psi(x, z)$ for $Ra = 997$ and $Ra = 9976$. Note the aspect ratio distortion in each set of plots: when $Ra = 997$, $L \approx 0.2239$, and when $Ra = 9976$, $L \approx 0.0708$. Clear evidence of a thermal boundary layer, which thins as Ra is increased, can be seen in figure 11.3(a) and (c). In figure 11.3(b) and (d) there is evidence of a momentum boundary layer that also thins as Ra is increased but remains thicker than the thermal boundary layer. Furthermore, in the centre of the cell, which we will denote the core, the streamlines become vertical as Ra increases, suggesting ψ becomes independent of z there.

To extract scalings from the numerical results, it is convenient to decompose the total temperature into its horizontal mean, denoted with an overbar, and a fluctuation; i.e., $T(x, z) = \overline{T}(z) + \theta(x, z)$, where $\theta(x, z)$ is the fluctuation. We note that with this decomposition, (11.2.1) and (11.2.2) become

$$\nabla^2\psi = -Ra\frac{\partial\theta}{\partial x}, \tag{11.3.13}$$

$$-\frac{\partial}{\partial z}\left(\overline{\frac{\partial\psi}{\partial x}\theta}\right) = \frac{\partial^2\overline{T}}{\partial z^2}, \tag{11.3.14}$$

$$\frac{\partial\psi}{\partial z}\frac{\partial\theta}{\partial x} - \frac{\partial\psi}{\partial x}\frac{\partial\theta}{\partial z} - \frac{\partial\psi}{\partial x}\frac{\partial\overline{T}}{\partial z} + \frac{\partial}{\partial z}\left(\overline{\frac{\partial\psi}{\partial x}\theta}\right) = \nabla^2\theta, \tag{11.3.15}$$

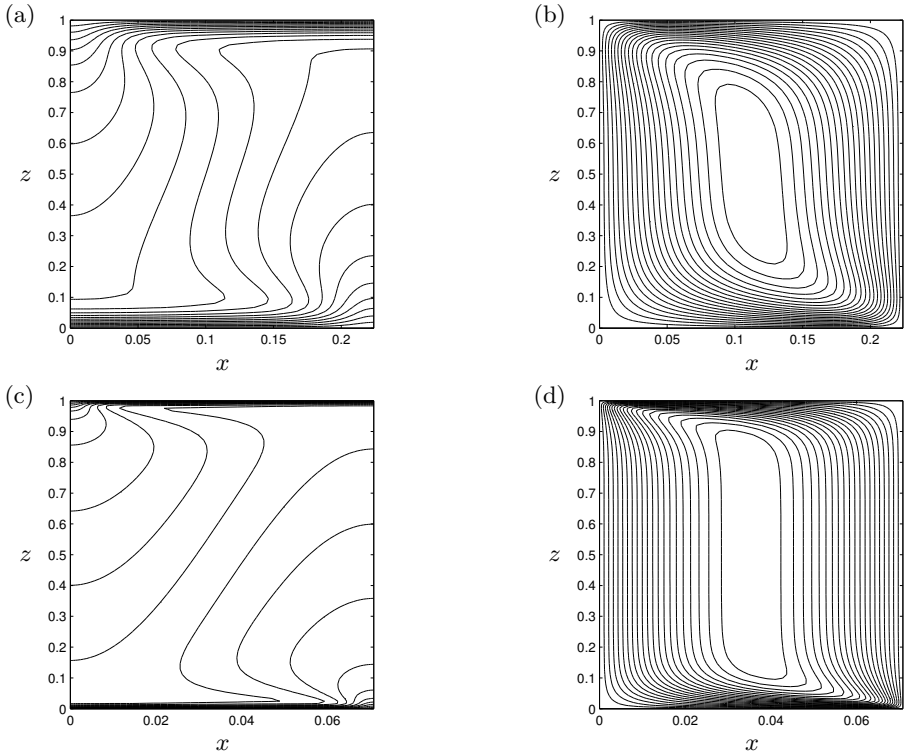

Figure 11.3: Contour plots of (a) temperature $T(x, z)$, (b) streamfunction $\psi(x, z)$ for $Ra = 997$; and (c) temperature $T(x, z)$, (d) streamfunction $\psi(x, z)$ for $Ra = 9976$. In each plot contours are evenly spaced. Note the aspect ratio distortion.

where an overbar again denotes a horizontal average.

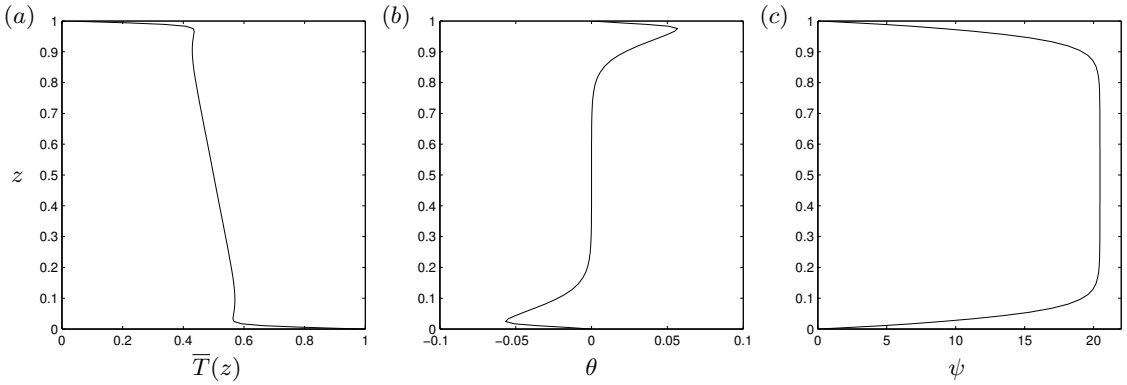

Figure 11.4: Vertical profiles of (a) $\overline{T}(z)$ and (b) θ and (c) ψ at $x = L/2$ for $Ra = 9976$.

Figure 11.4 shows vertical profiles of $\overline{T}$, θ and ψ for $Ra = 9976$. The existence of two distinct boundary layers is now very clear, with the momentum boundary layer being thicker than the thermal boundary layer. In the core, both the temperature fluctuation θ and the streamfunction ψ are independent of z, whereas the average temperature gradient is weakly

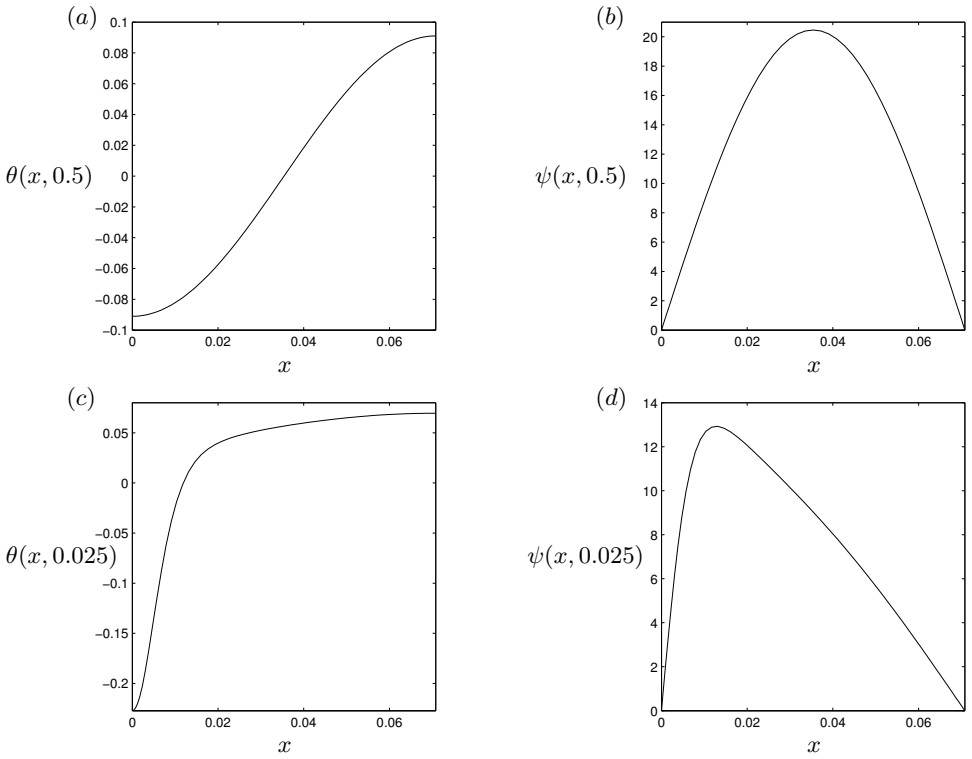

Figure 11.5: Horizontal profiles of the temperature fluctuation θ (left column) and streamfunction ψ (right column) through the centre of the domain (a, b) and near the bottom of the domain, within the thermal boundary layer (c, d), at $Ra = 9976$.

unstable.

Figure 11.5 shows horizontal profiles of θ and ψ in both the core (top row) and the thermal boundary layer (bottom row). In the core, the solution appears to consist of a single Fourier mode, whereas in the boundary layer the solution clearly involves a superposition of many Fourier modes.

Using these numerical results, we can attempt to quantify the dependencies on Ra of the boundary layer thicknesses and the amplitudes of θ and ψ in the core (figure 11.6). Since neither boundary layer is uniformly thick across the domain, we plot both the maximum (crosses) and minimum (asterisks) thicknesses of each layer. Figure 11.6 (a) and (b) shows the results for the thermal and momentum boundary layer, respectively, with the best fit curves for each case shown by the solid and dashed lines. In the thermal boundary layer both the thickest and thinnest parts of the layer scale as $\delta \sim Ra^{-0.6}$. However, in the momentum boundary layer there is quite a difference between the scalings of the thinnest

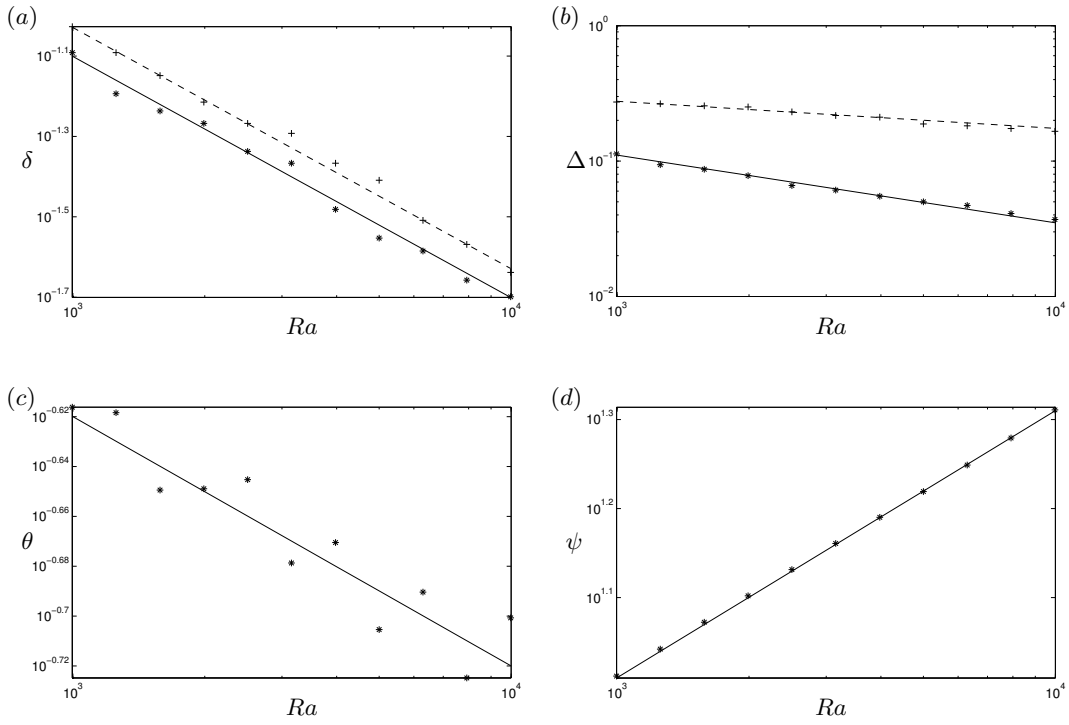

Figure 11.6: (a, b) Approximate location of the minimum (asterisks) and maximum (crosses) thicknesses of the thermal and momentum boundary layers, respectively. The solid lines represent the best fit curve for the minimum thickness: $\delta \sim 5.0Ra^{-0.6}$ for the thermal boundary layer, and $\Delta \sim 3.5Ra^{-0.5}$ for the momentum boundary layer. The dashed lines represent the best fit curve for the maximum thickness: $\delta \sim 5.9Ra^{-0.6}$ for the thermal boundary layer, and $\Delta \sim 1.1Ra^{-0.2}$ for the momentum boundary layer. (c, d) Asterisks represent the approximate maximum values of θ and ψ in the core, respectively. The solid lines in each case indicate the best fit curves $\theta \sim 0.48Ra^{-0.1}$ and $\psi \sim 1.3Ra^{0.3}$.

and thickest parts, with the minimum thickness scaling as $\Delta \sim Ra^{-0.5}$ and the maximum thickness as $\Delta \sim Ra^{-0.2}$.

The amplitude scalings are estimated by plotting the maximum values of θ and ψ in the core region versus Ra, as shown in figure 11.6 (c) and (d), respectively. The solid line in each plot represents the best fit curve. In this way, we find that in the core $\psi \sim Ra^{0.3}$ and $\theta \sim Ra^{-0.1}$.

11.4 Asymptotic reduction

Motivated by the numerical results presented in §11.3, we seek a matched asymptotic description of steady unicellular convection in a cell of varying aspect ratio $L = lRa^{-1/2}$,

with $l = \mathcal{O}(1)$, in the large Rayleigh number limit. The numerics suggest that the flow can be divided into three subdomains as shown in figure 11.7: a core, a momentum boundary layer of thickness Δ, and a thinner thermal boundary layer of thickness δ. This nested boundary layer structure is similar to that presented by Fowler [6] for unicellular porous media convection in a cell of fixed, $\mathcal{O}(1)$ aspect ratio.

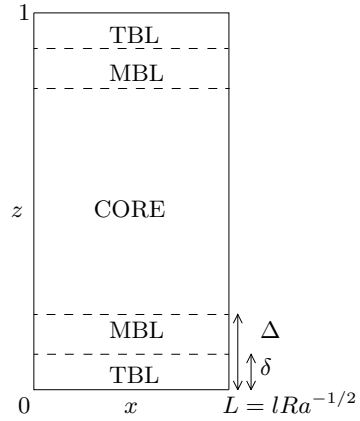

Figure 11.7: Schematic showing hypothesized three-subdomain asymptotic structure for porous media convection at high Rayleigh number.

Each of the subdomains is characterised by a different dominant balance of terms in (11.3.13)–(11.3.15). The various dominant balances are fixed once the Ra dependencies of the dependent and independent variables in the three subdomains is specified. Here, we opt to determine these scalings *a priori* by insisting that four asymptotic constraints are satisfied and subsequently compare our predictions with the scalings extracted from the numerical results in §11.3.

Firstly, in the thermal boundary layer, the mean advective and diffusive heat fluxes are both significant. Hence, (11.3.14) requires

$$\Psi_B \Theta_B = \frac{1}{\delta Ra^{1/2}}, \tag{11.4.1}$$

presuming $\overline{T} = \mathcal{O}(1)$, where Ψ_B and Θ_B are the magnitudes of ψ and θ, at leading order, in the thermal boundary layer. Balancing wall-normal diffusion with advection of the mean temperature in (11.3.15) yields

$$\Psi_B = \frac{1}{\delta} Ra^{-1/2} \Theta_B, \tag{11.4.2}$$

and combining (11.4.1) and (11.4.2) then gives

$$\Theta_B = 1, \quad \Psi_B = \frac{1}{\delta Ra^{1/2}}. \tag{11.4.3}$$

Secondly, given our hypothesized asymptotic structure, we require ψ_z to vary smoothly everywhere *within* the momentum boundary layer. In particular, this implies

$$\frac{\Psi_M}{\Delta} = \frac{\Psi_B}{\delta}. \tag{11.4.4}$$

Thirdly, the existence of the momentum boundary layer requires that z derivatives become comparable to x derivatives in (11.3.13), and hence that $\Delta = Ra^{-1/2}$. Equations (11.4.2) and (11.4.4) then yield

$$\Psi_M = \Psi_B^2 = \frac{1}{\delta^2 Ra}. \tag{11.4.5}$$

The final constraint requires the convective heat flux to dominate the diffusive heat flux in the core,

$$-\overline{\psi_x \theta} \sim Q, \tag{11.4.6}$$

where Q is the constant advective heat flux there. Since integration of (11.3.14) in z gives the exact result

$$-\overline{\psi_x \theta} - \overline{T}_z \equiv Nu, \tag{11.4.7}$$

$Q \sim Nu = \mathcal{O}(1/\delta)$, noting that $1/\delta$ is an estimate of the magnitude of $\overline{T}_z$ near $z = 0$ and $z = -1$. Assuming $\Psi_M = \Psi_C$ (see figure 11.4(c)), then (11.4.6) implies

$$\Theta_C = \delta Ra^{1/2}. \tag{11.4.8}$$

Also, in the core, the leading order balance in (11.3.13) is

$$\psi_{xx} = -Ra\theta_x. \tag{11.4.9}$$

Substituting the scalings for Θ_C and Ψ_C gives $\delta = Ra^{-2/3}$, implying $Nu \sim Ra^{2/3}$.

The complete list of asymptotic scalings is presented in Table 11.1, along with the numerical scalings found in §11.3.1 for finite Ra for comparison. Although they do not match identically, there is general agreement between the numerical and asymptotic scalings. Presumably, the discrepancies are attributable either to finite-Ra effects or to inherent limitations in our method of data processing for the numerics.

	Numerical	Asymptotic
Nu	$Ra^{0.59}$	$Ra^{2/3}$
δ	$Ra^{-0.6}$	$Ra^{-2/3}$
Δ	$Ra^{-0.2}$–$Ra^{-0.5}$	$Ra^{-1/2}$
Θ_C	$Ra^{-0.1}$	$Ra^{-1/6}$
Θ_M	–	$Ra^{-1/6}$
Θ_B	–	1
Ψ_C	$Ra^{0.3}$	$Ra^{1/3}$
Ψ_M	–	$Ra^{1/3}$
Ψ_B	–	$Ra^{1/6}$

Table 11.1: Comparison of numerical and asymptotic scalings.

11.4.1 Core

In the core, the leading order versions of (11.3.13)–(11.3.15) are

$$\psi_{Cxx} = -Ra\theta_{Cx}, \tag{11.4.10}$$

$$-\overline{\psi_{Cx}\theta_C} = Q, \tag{11.4.11}$$

$$-\psi_{Cx}\overline{T}_{Cz} = \theta_{Cxx}, \tag{11.4.12}$$

where a subscript "C" again refers to a core field. Integrating (11.4.10) with respect to x gives

$$\psi_{Cx} = -Ra\theta_C + f(z), \tag{11.4.13}$$

where $f(z) = 0$ from mass conservation, and substituting this expression into (11.4.11) yields

$$Ra\overline{\theta_C^2} = Q. \tag{11.4.14}$$

Thus, we deduce that both θ_C and ψ_C are independent of z, in accord with the results of our numerical calculations. Substituting (11.4.13) into (11.4.12) reveals that the mean temperature gradient within the core must be constant, i.e. $\overline{T}_{Cz} \equiv -g$, say, and that θ_C and hence ψ_C admit single mode solutions:

$$\theta_{Cxx} + Rag\theta_C = 0, \tag{11.4.15}$$

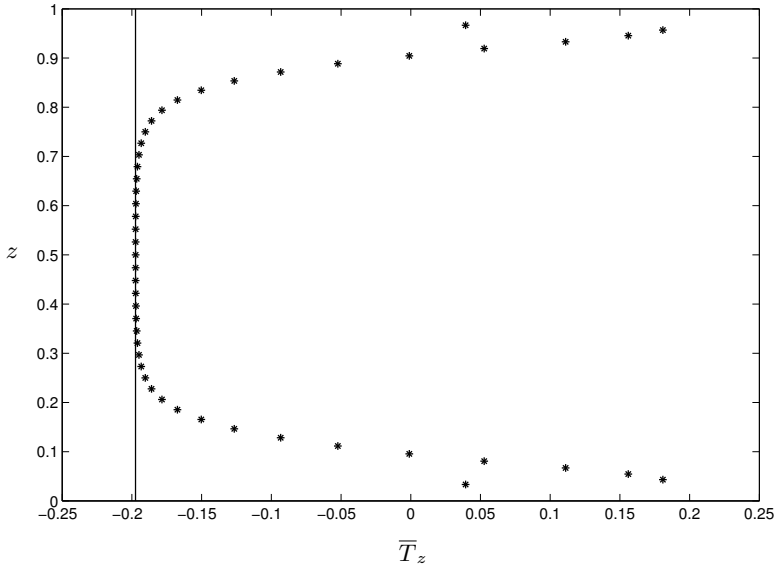

Figure 11.8: Comparison of the numerically computed $\overline{T}_z$ at $Ra = 9976$ and $l = \sqrt{50}$ (asterisks) with the predicted value in the core given by $\overline{T}_{Cz} = (\pi/l)^2$ (solid).

and so

$$\theta_C(x) = -\Theta_C \cos(Ra^{1/2} g^{1/2} x). \tag{11.4.16}$$

A similar asymptotic structure was found by Blennerhassett & Bassom [1] in their study of strongly nonlinear, high wavenumber Rayleigh–Bénard convection. Because the lateral boundary conditions require $\theta_{Cx} = 0$ at $x = 0, L$, $g = (\pi/l)^2$. In figure 11.8, this prediction is compared with the exact (numerically computed) mean temperature gradient at $Ra = 9976$ and $l = \sqrt{50}$; the evident excellent agreement provides strong support for the presumed asymptotic structure of the flow within the core. Specifically,

$$\theta_C(x) = -A\Theta_C \cos(Ra^{1/2} \frac{\pi}{l} x), \tag{11.4.17}$$

$$\psi_C(x) = \frac{l}{\pi} Ra^{1/2} A\Theta_C \sin(Ra^{1/2} \frac{\pi}{l} x), \tag{11.4.18}$$

where $A = \mathcal{O}(1)$ is a constant to be determined, while

$$\overline{T}_C = \frac{1}{2} - \left(\frac{\pi}{l}\right)^2 \left(z - \frac{1}{2}\right). \tag{11.4.19}$$

11.4.2 Momentum boundary layer

In the momentum boundary layer, (11.3.13)–(11.3.15) become, at leading order,

$$\psi_{Mxx} + \psi_{Mzz} = -Ra\theta_{Mx}, \tag{11.4.20}$$

$$-\overline{\psi_{M_x}\theta_{M_z}} = 0, \tag{11.4.21}$$

$$\psi_{Mz}\theta_{Mx} - \psi_{Mx}\theta_{Mz} = \psi_{Mx}\overline{T}_{Mz}, \tag{11.4.22}$$

presuming $\overline{T}_{M_z} = \mathcal{O}(\Theta_M/\Delta)$ – see figure 11.4. From (11.4.22) it follows that

$$\theta_M = F(\psi_M) - \overline{T}_M(z). \tag{11.4.23}$$

Noting that both θ and ψ must smoothly transform from their z-independent profiles in the core to functions of both x and z such that $\theta = F(\psi)$ in the far-field of the momentum boundary layer, we rewrite θ_C as a function of ψ_C:

$$\theta_C(x,z) = F(\psi_C) = \mp A\Theta_C\sqrt{1 - \left(\frac{\pi}{lA\Theta_C}\right)^2 Ra^{-1}\psi_C^2}. \tag{11.4.24}$$

The positive square root applies on the left half of the domain, where $\theta_C < 0$, while the negative square root applies on the right half of the domain, where $\theta_C > 0$. Furthermore, moving from the core to the momentum boundary layer at, say, $z = 0$, $\overline{T}_C \to \overline{T}_M^\infty$, where $\overline{T}_M^\infty$ is the limiting value of $\overline{T}_M(z)$:

$$\overline{T}_M^\infty = \frac{1}{2}\left(1 + \left(\frac{\pi}{l}\right)^2\right). \tag{11.4.25}$$

Hence,

$$F(\psi_M) = \mp A\Theta_C\sqrt{1 - \left(\frac{\pi}{lA\Theta_C}\right)^2 Ra^{-1}\psi_M^2} + \overline{T}_M^\infty. \tag{11.4.26}$$

Equation (11.4.20) becomes a nonlinear Poisson equation for ψ_M:

$$\begin{aligned}\psi_{Mxx} + \psi_{Mzz} &= -RaF'(\psi_M)\psi_{Mx} \\ &= -\psi_{Mx}\frac{\psi_M}{A\Theta_C}\left(\frac{\pi}{l}\right)^2\left(1 - \left(\frac{\pi}{l}\right)^2\frac{\psi_M^2}{RaA^2\Theta_C^2}\right)^{-1/2},\end{aligned} \tag{11.4.27}$$

subject to the boundary conditions

$$\psi_M = 0 \text{ on } x = 0, L \text{ and } z = 0, \text{ and as } Z \equiv \frac{z}{\Delta} \to \infty, \psi_M \to \psi_C. \tag{11.4.28}$$

We can then use (11.4.23) to find $\theta_M(x,z)$ once $\overline{T}_M(z)$ has been determined, presumably by requiring $\overline{\theta}_M = 0$, in which case $\overline{T}_M(z) = \overline{F(\psi_M)}$.

11.4.3 Thermal boundary layer

In the thermal boundary layer, the leading order versions of (11.3.13)–(11.3.15) are

$$\psi_{Bzz} = -Ra\theta_{Bx}, \tag{11.4.29}$$

$$-\overline{\psi_{B_x}\theta_{B_z}} = \overline{T}_{Bzz}, \tag{11.4.30}$$

$$\psi_{Bz}\theta_{Bx} - \psi_{Bx}\theta_{Bz} - \psi_{Bx}\overline{T}_{Bz} + \overline{\psi_{Bx}}\theta_{Bz} = \theta_{Bzz}. \tag{11.4.31}$$

This system is equivalent to

$$\psi_{Bzz} = -RaT_{Bx}, \tag{11.4.32}$$

$$\psi_{Bz}T_{Bx} - \psi_{Bx}T_{Bz} = T_{Bzz}, \tag{11.4.33}$$

which must be solved (e.g., at the bottom of the domain) subject to the boundary conditions

$$\begin{gathered}\psi_B = 0 \text{ on } z = 0, \\ T_{Bx} = 0 \text{ on } x = 0, \quad T_B = 1 \text{ on } z = 0, \\ \text{and, as } \hat{Z} \equiv \frac{z}{\Delta} \to \infty, \psi_B \to \psi_M \text{ and } T_B \to T_M.\end{gathered} \tag{11.4.34}$$

11.5 Time-dependent numerical simulations

Our asymptotic reduction suggests that the heat transport is described by the scaling $Nu \sim Ra^{2/3}$, which differs from the classical scaling $Nu \sim Ra$ of Howard [10] and from that exhibited in the DNS of Otero *et al.* [14]. Therefore, in this section, we employ *time-dependent* simulations to find the heat transport when our steady-state solutions are used as initial conditions.

As before, we consider (11.2.1)–(11.2.2) subject to the boundary conditions given by (11.2.3). Numerical simulations were carried out using a pseudospectral collocation method involving a Chebyshev tensor-product formulation with 70 nodes in both the horizontal and vertical directions to provide adequate resolution of the boundary layers. A semi-implicit time discretization scheme was employed, with the nonlinear and instability terms advanced using a second-order Adams-Bashford method, and the linear diffusive terms advanced using the trapezium rule. The resulting linear algebraic system was solved by direct matrix inversion.

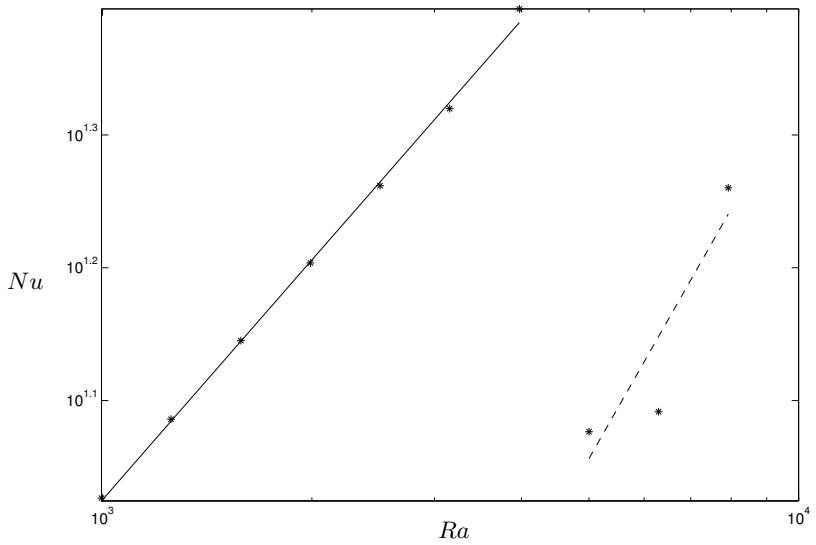

Figure 11.9: Plot of time-averaged Nu against Ra. The solid line is the best fit curve $0.168Ra^{0.6}$, and the dashed line is the best fit curve $0.005Ra^{0.92}$.

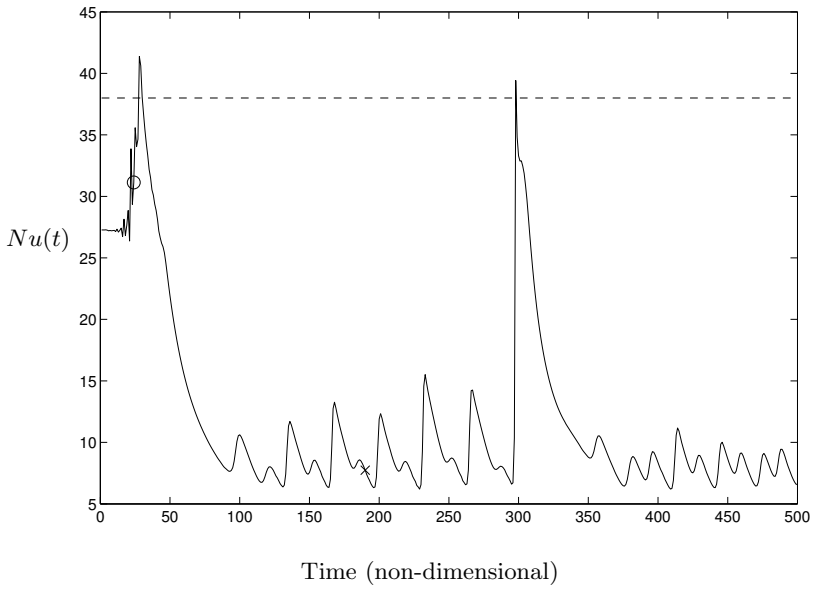

Figure 11.10: Evolution of the Nusselt number for $Ra = 5000$ (solid line). The dashed line represents the approximate value of the long-time average of Nu given by Otero *et al.* [14] at the same Ra in a box of fixed width $L = 1$ (in our notation).

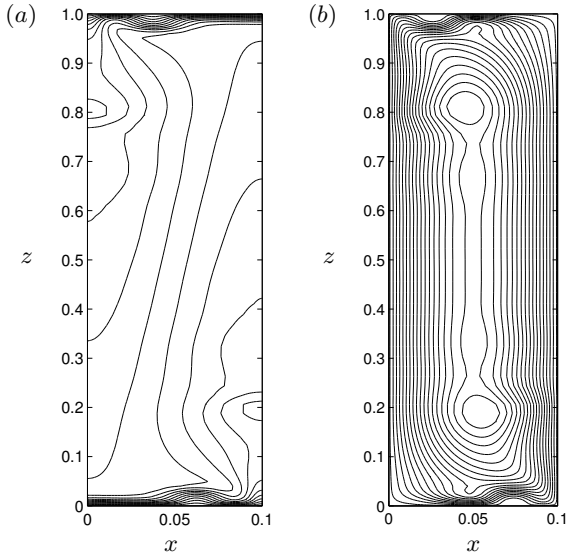

Figure 11.11: Contour plots of (a) $T(x, z)$, (b) $\psi(x, z)$ for $Ra = 5000$ just before the first peak in $Nu(t)$ (denoted by the circle in figure 11.10). In each plot contours are evenly spaced. Note the aspect ratio distortion.

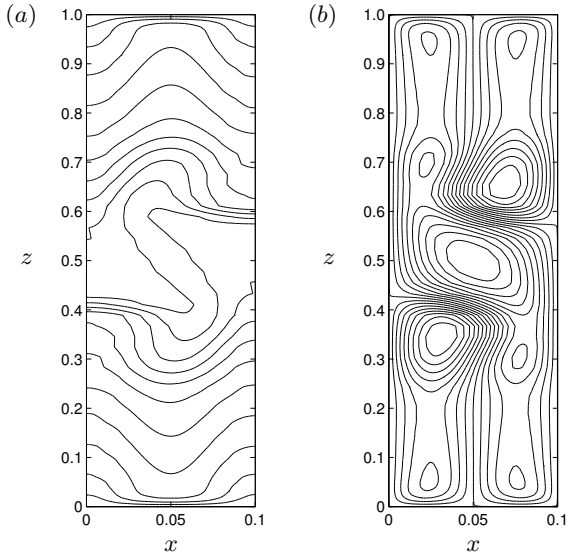

Figure 11.12: Contour plots of (a) $T(x, z)$, (b) $\psi(x, z)$ for $Ra = 5000$ at a later time (denoted by the cross in figure 11.10). In each plot contours are evenly spaced. Note the aspect ratio distortion.

The results of these simulations are summarized in figure 11.9, which shows the variation of the time-averaged Nu with Ra. In the range $1000 \leq Ra \leq 4000$, the data scale as $Nu \sim Ra^{0.6}$, identically to the steady state scaling found in §3. For $Ra > 4000$, however, the data appear to scale as $Nu \sim Ra^{0.92}$, comparable to the $Nu \sim Ra^{0.9}$ scaling found by Otero *et al.* [14] in a domain of *fixed* width $L = 1$. Of course, the accuracy of this scaling may be suspect given the limited data in this region. Nevertheless, these preliminary results are at least suggestive that Nusselt numbers comparable to those achieved in much wider domains might be attained in narrow domains with aspect ratios shrinking according to $L \sim Ra^{-1/2}$.

Figures 11.10–11.12 illustrate the behaviour of the model for $Ra = 5000$, at the start of the $Nu \sim Ra^{0.92}$ regime. Figure 11.10 shows the evolution of the Nusselt number for $Ra = 5000$, with the dashed line denoting the long-time average value of Nu given by Otero *et al.* [14]. The initial steady solution is unstable, and the time-dependent solution quickly deviates away from it, corresponding with the first increase in $Nu(t)$. The Nusselt number then peaks before settling into a roughly periodic dynamic. Eventually, the system is again excited and the Nusselt number peaks a second time before settling back into a time-periodic behavior.

The temperature and streamfunction fields just before the first peak in the Nusselt number (at the time denoted by the circle in figure 11.10) are shown in figure 11.11. In the temperature field (figure 11.11 (a)) there is evidence of a plume (as defined by Graham & Steen [7]) in the lower (upper) thermal boundary layer at $x \approx 0.06$ ($x \approx 0.04$), corresponding with a roll in the streamfunction field (figure 11.11 (b)). As noted in §1, Graham & Steen [7] argue that the classical $Nu \sim Ra$ scaling corresponds to the onset of plume formation, which they define to occur when the isotherms contouring the thermal boundary layer become nearly vertical away from the downstream corner of the cell. Furthermore, both DNS and upper bound theory suggest that convection cells within the thermal boundary layer are required to achieve this scaling (Chini *et al.* [4]).

This simulation does not, however, achieve the same overall long-time average value of Nu as Otero *et al.* [14]. Figure 11.12 illustrates the temperature and streamfunction fields at a later time (denoted by the cross in figure 11.10). The simple unicellular flow has been replaced with an irregular convective pattern. We postulate that this irregular flow pattern

is a result of the way in which our lateral symmetry boundary conditions constrain the system.

11.6 Conclusion

We have presented the results of a set of numerical experiments on a model of steady 2D unicellular convection in a fluid-saturated porous medium and quantified the heat transport over a range of Rayleigh numbers and aspect ratios. We observe that over the decade $Ra = 10^3$–10^4 the maximum value of the Nusselt number occurs in a cell whose aspect ratio scales as $L \sim Ra^{-1/2}$, and not as that of the fastest growing linear mode, i.e. $L \sim Ra^{-1/4}$, which may be postulated from the data presented in Otero *et al.* [14]. Furthermore, in this cell the heat transport is described by the scaling $Nu \sim Ra^{0.6}$.

Guided by our numerical results we have formulated an asymptotic reduction for the structure of the solutions that maximize the Nusselt number. We divide the cell into three subdomains: a central core region, and at both the top and bottom of the layer, a momentum boundary layer with a thinner thermal boundary layer within it. With this reduction the heat transport is described by the scaling $Nu \sim Ra^{2/3}$. To complete the matched asymptotic analysis outlined here, the solutions in the boundary layers must be numerically computed and matched between the layers.

Our heat transport results from both the steady state numerical solutions and the matched asymptotic analysis differ from those given by the DNS of Otero *et al.* [14] and the classical scaling of Howard [10]. Graham & Steen [7] show that this scaling corresponds to the onset of plume formation; until then the appropriate scaling is $Nu \sim Ra^{2/3}$. However, plume formation is a time-dependent process, and therefore is not realisable in our steady model.

Furthermore, both the DNS and upper bound theory suggest that convection cells *within* the thermal boundary layer are required to achieve the $Nu \sim Ra$ scaling (Chini *et al.* [4]). Evidence of this can also be seen when we use our steady solution as the initial condition in a time-dependent model. In this case, at high Ra, Nu periodically approaches values reported by Otero *et al.* [14] and, in fact, appears to achieve the scaling $Nu \sim Ra^{0.92}$. At these times, embryonic rolls in the thermal boundary layer can be seen. However,

the overall behaviour of the temperature and streamfunction fields in this time-dependent model is highly irregular, possibly as a result of the imposed lateral symmetry boundary conditions.

It remains to complete the asymptotic analysis, and to repeat the time-dependent numerical simulations with periodic lateral boundary conditions to see whether Nusselt numbers found by Otero *et al.* [14] are attained more consistently. In addition, it would be interesting to investigate whether a *multicellular* asymptotic structure, supporting convection cells within the thermal boundary layer and achieving the maximal Nu–Ra scaling, can be found.

Acknowledgements

I would like to thank Greg Chini for his supervision over the summer, and for showing me how valuable a tool Skype can be. I would also like to thank Richard Kerswell, Colm Caulfield, and Keith Julien for many useful meetings and discussions throughout the project. Finally, I would like to thank all the participants in the GFD program, both faculty and students, for an inspiring and highly enjoyable summer at Woods Hole.

Bibliography

[1] P. J. Blennerhassett and A. P. Bassom, *Nonlinear high-wavenumber Bénard convection*, IMA J. Appl. Math., 52 (1994), pp. 51–77.

[2] J. P. Boyd, *Chebyshev and Fourier Spectral Methods*, Dover, 2nd ed., 2000.

[3] A. S. M. Cherkaoui and W. S. D. Wilcock, *Characteristics of high Rayleigh number two-dimensional convection in an open-top porous layer heated from below* , J. Fluid Mech., 394 (1999), pp. 241–260.

[4] G. P. Chini, N. Dianati, Z. Zhang, and C. R. Doering, *Low-dimensional models from upper bound theory*, Physica D, 240 (2011), pp. 241–248.

[5] C. R. Doering and P. Constantin, *Bounds for heat transport in a porous layer* , J. Fluid Mech., 376 (1998), pp. 263–296.

[6] A. C. Fowler, *Mathematical models in the applied sciences*, Cambridge University Press, 1997.

[7] M. D. Graham and P. H. Steen, *Plume formation and resonant bifurcations in porous-media convection*, J. Fluid Mech., 272 (1994), pp. 67–89.

[8] R. N. Horne and M. J. O'Sullivan, *Origin of oscillatory convection in a porous medium heated from below*, Phys. Fluids, 21 (1978), pp. 1260–1264.

[9] C. W. Horton and F. T. Rogers, *Convection currents in a porous medium*, J. Appl. Phys., 16 (1945), pp. 367–370.

[10] L. N. Howard, *Convection at high Rayleigh numbers*, in Applied Mechanics, Proc. 11th Congress of Applied Mathematics, H. Gortler, ed., 1964, pp. 1109–1115.

[11] E. R. Lapwood, *Convection of a fluid in a porous medium*, Proc. Camb. Phil. Soc., 44 (1948), pp. 508–521.

[12] C. Lister, *An explanation for the multivalued heat transport found experimentally for convection in a porous medium*, J. Fluid Mech., 214 (1990), pp. 287–320.

[13] D. A. Nield and A. Bejan, *Convection in Porous Media*, Springer, 3rd ed., 2006.

[14] J. Otero, L. A. Dontcheva, H. Johnston, R. A. Worthing, A. Kurganov, G. Petrova, and C. R. Doering, *High-Rayleigh-number convection in a fluid-saturated porous layer*, J. Fluid Mech., 500 (2004), pp. 263–281.

[15] E. Palm, J. E. Weber, and O. Kvernvold, *On steady convection in a porous medium*, J. Fluid Mech., 54 (1972), pp. 153–161.

[16] O. M. Phillips, *Flow and Reactions in Permeable Rocks*, Cambridge University Press, 1991.

[17] ——, *Geological Fluid Dynamics: sub-surface flow and reactions*, Cambridge University Press, 2009.

[18] J. L. Robinson and M. J. O'Sullivan, *A boundary-layer model of flow in a porous medium at high Rayleigh number*, J. Fluid Mech., 75 (1976), pp. 459–467.

[19] N. Rudraiah and T. Musuoka, *Asymptotic analysis of natural convection through horizontal porous layer*, Int. J. Engng. Sci., 20 (1982), pp. 27–39.

Part IV

Lectures and Visitors

Seminars and Visitors 1

Lecture Schedule

GFD Lecture Schedule

Week 1

Introductory lectures will be a total of 2 hours each with a short break.

Monday, June 20 - 9:50 AM

Introduction

Norman Lebovitz and Philip Morrison, GFD Co-Directors

Lecture 1 - 10:00 AM

General Introduction and Overview

Fabian Waleffe, University of Wisconsin

Part 1: 10:00-10:50 AM, Part 2: 10:50-11:50 AM

Tuesday, June 21 - Lecture 2 - 10:00 AM

Viscous derivation of classic inviscid stability results for shear flows. Viscous instability.

Fabian Waleffe, University of Wisconsin

Part 1: 10:00-10:50 AM, Part 2: 10:50-11:50 AM

Wednesday, June 22 - Lecture 3 - 10:00 AM

Diffusion and damping in shear flows: a truly singular limit. Critical layers.

Fabian Waleffe University of Wisconsin

Part 1: 10:00-10:50 AM, Part 2: 11:00-11:50 AM

Thursday, June 23 - Lecture 4 - 10:00 AM

Origin and survival of 3D-ality.

Fabian Waleffe, University of Wisconsin

Part 1: 10:00-10:50 AM, Part 2: 11:00-11:50 AM

Friday, June 24 - Lecture 5 - 10:00 AM

Instability of streaky flows. Asymptotics of self-sustaining process.

Fabian Waleffe, University of Wisconsin

Part 1: 10:00-10:50 AM, Part 2: 11:00-11:50 AM

Week 2

Monday, June 27 - Lecture 6 - 10:00 AM

Spatio-temporal complexity. Spots, puffs and slugs, snakes and spirals.

Fabian Waleffe, University of Wisconsin

Part 1: 10:00-10:50 AM, Part 2: 11:00-11:50 AM

June 27 (continued) - 2:30 PM

Structures of low-Reynolds-number turbulence in a rectangular duct.

Genta Kawahara, Osaka University

Tuesday, June 28 - Lecture 7 - 10:00 AM

Transition scenarios: normality vs non-normality.

Richard Kerswell, Bristol University

Part 1: 10:00-10:50 AM, Part 2: 11:00-11:50 AM

Wednesday, June 29 - Lecture 8 - 10:00 AM

Edge tracking – walking the tightrope.

Richard Kerswell, Bristol University

Part 1: 10:00-10:50 AM, Part 2:11:00- 11:50 AM

Thursday, June 30 - Lecture 9 - 10:00 AM

Triggering transition efficiently.

Richard Kerswell, Bristol University

Part 1: 10:00-10:50 AM, Part 2: 11:00-11:50 AM

June 30 (continued) - 2:30 PM

Vortex-wave interactions/self-sustained processes in shear flows.

Phillip Hall, Imperial College London

Friday, July 1 - Lecture 10 - 10:00 AM

Turbulence: transient or sustained?

Richard Kerswell, Bristol University

Part 1: 10:00:10:50 AM, Part 2:11:00-11:50 AM

Week 3

Monday, July 4

HOLIDAY, INSTITUTION CLOSED

Tuesday, July 5

10:00-10:50 AM

Surface-wave mediated instability of submesoscale ocean fronts.

Greg Chini, University of New Hampshire

— 11:00-11:50 AM

Gravity currents in rotating fluid.

Jack Whitehead, Woods Hole Oceanographic Institution

Wednesday, July 6

10:00-10:50 AM

Ultimate state of two-dimensional Rayleigh-Bénard convection between free-slip fixed-temperature boundaries.

Charles Doering, University of Michigan

— 11:00-11:50 AM

Global stability analysis of fluid flows using Sum-of-Squares of polynominals.

Sergei Chernyshenko, Imperial College, London

Thursday, July 7

10:00-10:50 AM

Generation of magnetic fields by convection in rotating spherical fluid shells.

Friedrich Busse, University of Bayreuth

Friday, July 8

10:00-10:50 AM

Geographically localized coastal trapped waves.

Ted Johnson, University College London

Week 4

Monday, July 11

No lecture scheduled today.

Tuesday, July 12

10:00-10:50 AM

From Swift-Hohenberg to Navier-Stokes: Localization in Plane Couette Flow.

Tobias Schneider, Harvard University

Wednesday, July 13

10:00-10:50 AM

The nonhydrostatic balanced geostrophic equations: the interplay between convective and barotropic dynamics.

Keith Julien, University of Colorado at Boulder

Thursday, July 14

10:00-10:50 AM

Landau damping as a universal description of dissipation.

George Hagstrom, University of Texas at Austin

Friday, July 15

10:00-10:50 AM

New modes of haline convection.

Raymond Schmitt, Woods Hole Oceanographic Institution

Week 5

Monday, July 18

10:00-10:50 AM

Zonostrophic turbulence, zonal jets and the mixing barriers.

Boris Galperin, University of South Florida

Tuesday, July 19

10:00-10:50 AM Anisotropic inverse cascade towards zonal jets in shallow water dynamics.

Alexander Balk, University of Utah

Wednesday, July 20

10:00-10:50 AM

A hierarchy of PDE models for rotating stratified flows.

Leslie Smith, University of Wisconsin, Madison

— 11:00-11:50 AM

Determining macroscopic diffusivity from T, S data: an ongoing study.

George Veronis, Yale University

Thursday, July 21

10:00-10:50 AM

Pseudo spectral reduction of 2D turbulence.

John Bowman, University of Alberta

Friday, July 22

10:00-10:50 AM

Cross-equatorial transport of Antarctic Bottom Water under the complete Coriolis force.

Andrew Stewart, Corpus Christi College

Week 6

Monday, July 25

10:00-10:50 AM

Gyroviscous effects in Braginski magnetohydrodynamic flow between parallel planes.

Paul Dellar, University of Oxford

Tuesday, July 26

10:00-10:50 AM

Self-sinking capsules to investigate Earth's interior and dispose of radioactive waste.

Jesse Ausubel, Rockefeller University

Wednesday, July 27

10:00-10:50 AM

Landau damping as a universal source of dissipation.

George Hagstrom, University of Texas at Austin

Thursday, July 28

10:00-10:50 AM

Stability of vortex and wave flows from bifurcation diagrams exploiting a variational argument.

Paolo Luzzato-Fegiz, Woods Hole Oceanographic Institution

Friday, July 29

10:00-10:50 AM

Coherent vortices in plane Couette flow bifurcation, symmetry and visualization.

Tomoaki Itano, Kansai University

Week 7

Monday, August 1

10:00-10:50 AM

The spring bloom in the oceans.

Amala Mahadevan, Woods Hole Oceanographic Institution

Tuesday, August 2

10:00-10:50 AM

EZ-stability of beta-plane Kolmogorov flow with drag. Yue-Kin Tsang, The Chinese University of Hong Kong

— 11:00-11:50 AM

Stability of swirling flows.

Sherwin Maslowe, McGill University

Wednesday, August 3

10:00-10:50 AM

Questioning the question: The role of nonlinear optimal perturbations in the transition to turbulence of plane Couette flow.

Colm-cille Caulfield, University of Cambridge

— 11:00-11:50 AM

Spatio-temporal chaos in shear flows.

Bruno Eckhardt, Phillips Universitat Marburg

Thursday, August 4

10:00-10:50 AM

Optimal path to turbulence in shear flows.

Dan Henningson, KTH Royal Institute of Technology

— 2:00-5:00 PM: Public Lecture, Redfield Auditorium, reception to follow

On growth and form: geometry, physics and biology.

Lakshiminarayanan Mahadevan, Harvard University

Friday, August 5

10:00:10:50 AM

Simplifying the complexity of turbulent shear flow.

Dwight Barkley, University of Warwick

— 11:00-11:50 AM

On first looking into Chapman and Cowling.

Ed Spiegel, Columbia University

Week 8

Monday, August 8

10:00-10:50 AM

Instabilities and transitions of rotor-stator flows.

Patrice LeGal, IRPHE, France

Tuesday, August 9

10:00-10:50 AM

Topological detection of Lagrangian coherent structures.

Jean-Luc Thiffeault, University of Wisconsin, Madison

Wednesday, August 10

10:00-10:50 AM

Flow through a sudden expansion in a pipe.

Tom Mullin, University of Manchester

— 11:00-11:50 AM

Unbalanced surface dynamics.

Gualtiero Badin, Boston University

Thursday, August 11

10:00-10:50 AM

Laminar-turbulent patterns in plane Couette flow.

Laurette Tuckerman, PMMH-ESPCI, France

Friday, August 12

10:00-10:50 AM

What Phil Morrison wouldn't teach us: how to reduce the symmetry of pipe flows.

Predrag Cvitanovic, Georgia Institute of Technology

Week 9: No lectures scheduled this week

Monday, August 15 – Friday, August 19

Week 10: FELLOWS' PRESENTATIONS

Monday, August 22

2:00 - 3:00 PM

Constraints on low order models: the cost of simplicity.

Martin Hoecker-Martinez, Oregon State University

— 3:00-4:00 PM

A one-fluid MHD model with electron inertia.

Keiji Kimura, Kyoto University

Tuesday, August 23 10:00-11:00 AM

Traversing the edge: how turbulence decays.

Matthew Chantry, University of Bristol

— 11:00- 12:00 PM

A low dimensional model for shear turbulence in Plane Poiseuille flow: an example to understand the edge.

Giulio Mariotti, Boston University

— 2:00-3:00 PM

Upstream basin circulation of rotating, hydraulically controlled flows.

Adele Morrison, Australian National University

Wednesday, August 24

10:00-11:00 AM Islands in locally forced basin circulations.

Samuel Potter, Princeton University

— 11:00 AM-12:00 PM

Two-layer viscus fluid in an inclined closed tube: Kelvin-Helmholtz instability.

Zhan Wang, University of Wisconsin, Madison

— 2:00-3:00 PM

Chaotic interaction of vortex patches with boundaries.

Andrew Crosby, University of Cambridge

— 3:00-4:00 PM

On Brownian motion in a fluid with a plane boundary.

Chao Ma, University of Colorado, Boulder

Thursday, August 25

10:00-11:00 AM

Localized solutions in plane Couette flow: continuation methods.

John Platt, Harvard University

— 11:00 AM-12:00 PM

Ascending the ridge: maximizing the heat flux in steady porous medium convection.

Lindsey Corson, University of Strathclyde

Seminars and Visitors 2

Visitors

2011 GFD Staff and Visitors

Fellows:

Matthew Chantry, University of Bristol

Andrew Crosby, University of Cambridge

Martin Hoecker-Martinez, Oregon State University

Keiji Kimura, Kyoto University

Chao Ma, University of Colorado, Boulder

Guilio Mariotti, Boston University

Adele Morrison, Australian National University

John Platt, Harvard University

Samuel Potter, Princeton University

Lindsey Corson, University of Strathclyde

Zhan Wang, University of Wisconsin, Madison

Staff and Visitors:

Matthew Alford, University of Washington

Michael Allshouse, MIT

James Anderson, Stevens Institute of Technology

Alexander Balk, University of Utah

Dwight Barkley, University of Warwick

John Bowman, University of Alberta

John Burke, Boston University

Joseph Parker, Brasenose College

Tobias Schneider, Harvard University

Leslie Smith, University of Wisconsin, Madison

Edward Spiegel, Columbia University

Andrew Stewart, University of Oxford

Jean-Luc Thiffeault, University of Wisconsin, Madison

Yue-King Tsang, Chinese University of Hong Kong

Laurette Tuckerman, PMMH-ESPCI

Lennaert van Veen, University of Ontario

George Veronis, Yale University

Divakar Viswanath, University of Michigan

Fabian Waleffe, University of Wisconsin, Madison

John Whitehead, Woods Hole Oceanographic Institution